

Highly Loaded Compressors

Anthony Dickens
Corpus Christi College

A dissertation submitted for the degree of
Doctor of Philosophy

May, 2008



Highly Loaded Compressors

Anthony Dickens

Summary

Increasing compressor pressure ratios (thereby gaining a benefit in cycle efficiency), or reducing the number of stages (to reduce weight, cost, etc.), will require an increase in pressure rise per stage. Higher stage pressure rises can be achieved by increasing the stage loading coefficient ($\frac{\Delta h_0}{U^2}$) and it is this topic which forms the focus of this thesis.

Three highly loaded compressor stages were tested in a low speed, single stage, compressor. These three stages had a design stage loading coefficient of 0.65; almost 50% greater than those typically in service today. The highly-loaded Gallimore, Qinetiq and Denton stages achieved peak efficiencies of 83.8%, 85.3% and 85.6% respectively. This compares to a conventionally loaded stage, tested in the same rig, which achieved a peak efficiency of 87.9%. However, contrary to conventional wisdom, the three highly loaded stages did exhibit similar or improved stall margin to the datum stage.

A highly unusual flow breakdown mechanism was observed in one of the highly loaded stages. As the flow coefficient was reduced, large separations formed in the tip region of a few rotor passages. The number of these separations increased on further reductions in flow rate. Unlike conventional rotating stall, each of these separations was fixed to a particular rotor passage and did not propagate. A combination of detailed experiments and CFD was used to develop a model to explain this phenomena.

The experimental results from the four stages tested were also used to successfully calibrate two and three-dimensional CFD programs. Three-dimensional CFD was then used to perform a parametric study into the effects of the choice of design stage inlet angle and stage loading on the performance of several rotor and stator designs. This showed that, as the design stage loading is increased, the locus of peak efficiency moves to lower, even negative, inlet flow angles to control the stator de Haller number and prevent large corner separations.

A theoretical study of the velocities around a generic compressor aerofoil was used to show, for the first time, that profile loss is dependent on both local diffusion factor and on de Haller number (analogous to diffuser area ratio). At a given local diffusion factor the profile loss was shown to be unavoidably greater at low de Haller numbers, typical of those found in highly loaded compressors, than for conventional designs.

Declaration

The research described in this thesis was conducted at the Whittle Laboratory, Cambridge University Engineering department between October 2002 and May 2008. Except where specifically stated to the contrary, this thesis is the work of the author alone and contains nothing which is the result of work done in collaboration. No part of the work contained in this thesis has been submitted to any other University or place of learning. This thesis contains approximately 64,600 words and 189 figures.

Anthony Dickens
April 2008

Acknowledgements

Completing a PhD is as much of a challenge of endurance and mental strength as an academic one. Were it not for the support of several friends, family and colleagues it is unlikely that this thesis would ever have become the finished article you are reading now. I am forever in the debt of those who kept me going in the face of adversity and made this possible.

At the Whittle Laboratory, I am indebted to my supervisor, Ivor Day, for the guidance and all the support he has given me over the past five years. I am also grateful to Chris Freeman for his advice and for sharing a small part of his vast knowledge and experience with me. No experimental program at the Whittle Laboratory would be possible without the support of the workshop staff and technicians. Of these, I would like to thank David Barlow in particular for all his efforts in keeping the experimental program running smoothly, making modifications at short notice and for always impressing me with his skill.

Thinking back over the course of my PhD there are a few encounters that have me helped to focus on the problem(s) at hand and have changed the direction of this work for the better. In particular, the inputs of Simon Gallimore and John Adamczyk are greatly appreciated. Aside from all their other contributions they made the task of finishing a PhD seem achievable.

The work described in this thesis was funded by Rolls-Royce Plc. I am grateful to all those in the Compression Systems department who contributed their thoughts and ideas, especially John Bolger and Mike Howard.

Among my friends I am particularly grateful to Ian Shadforth and Phil Athyade (fellow sufferers of a research life) for their support and understanding. Christian Klostermeier also deserves a mention (despite his misguided support of Michael Schumacher) for the long and enjoyable conversations regarding Formula 1, rowing and life in general (in that order).

Given the (minuscule) likelihood of me winning either a Nobel prize or an Oscar, this is one of the few places I can (publicly at least) say thank-you to my Mum and Dad for their support throughout my education and for the contributions they have made

to my life over the past 29 years. My only regret is that Dad didn't live long enough for me to grow out of the "competitive phase" and I could get round to learning more from him.

Most of all I need to thank my wife, Jenny. For putting up with my lowest moments and helping me out of them. I couldn't have done it without her.

Contents

1	Introduction	1
2	Literature Review	7
3	Experimental Methods	37
4	Three Highly Loaded Stages - Design Attributes	55
5	Measured Performance of Three Highly Loaded Designs	65
6	Investigation into the Unique Stalling Behaviour of the Qinetiq Stage	87
7	Computational Methods and Comparison with Experimental Results	107
8	Design Options for Stages with Increased Loading	123
9	A Simple Model for the Prediction of Profile Losses and the Implications for Highly Loaded Stages	141
10	Conclusions	165

Appendices

A	Experimental Comparison Between the Mini-Deverson Stage and the Original Deverson Build II Stage	173
B	Measured Radial Profiles	177
C	Definition of Non-Dimensional Camber and Thickness Distributions	179
D	Derivation of a Generic Velocity Distribution	181

Nomenclature

Latin Symbols

A	Area & “roof-top” length parameter (Chapter 9)
C_D	Discharge coefficient
C_d	Dissipation coefficient
C_p	Static pressure coefficient
C_{pb}	Base pressure coefficient
c	True chord
c_p	Specific heat
c_x	Axial chord
D_{loc}	Local diffusion factor
DF_{Lieb}	Lieblein diffusion factor
H	Boundary layer shape factor $\left(= \frac{\delta^*}{\theta} \right)$
H_e	Boundary layer energy shape factor $\left(= \frac{\delta_e}{\theta} \right)$
h	Specific enthalpy, stream-tube height & annulus height
hw	Hot-wire
$\frac{\Delta h_0}{U_{mid}^2}$	Stage loading coefficient
i	Incidence
l	Length
M	Mach number
\dot{m}	Mass flow rate
Pr	Prandtl number
p	Pressure
Q	Shaft torque
R	Gas constant
Re	Reynolds number

r	Radius
S	Entropy
\dot{S}_A	Entropy production rate per unit area
s	Pitch & surface distance
T	Temperature
Tu	Turbulence intensity
t	Blade thickness
U	Blade speed
V	Velocity
z	Distance along chord line

Greek Symbols

α	Flow angle
β	Blade metal angle
γ	Ratio of specific heats
$\Delta(\dots)$	Change between stations 1 & 2, i.e. $\Delta x = x_2 - x_1$
δ^*	Boundary layer displacement thickness
δ_e	Boundary layer energy thickness
ϵ	Tip clearance gap height
ζ	Camber angle
η	Efficiency
θ	Boundary layer momentum thickness & circumferential coordinate
Λ	Stage Reaction
λ	Tip flow injection angle or integral length scale
μ	Viscosity
ξ	Stagger angle
ρ	Density
σ	Solidity ($= \frac{c}{s}$)
$\bar{\phi}$	Average inlet flow coefficient $\left(= \frac{\bar{V}_x}{U_{mid}}\right)$
ψ	Non-dimensional pressure rise coefficient $\left(= \frac{\Delta p}{\frac{1}{2}\rho U_{mid}^2}\right)$
Ω	Rotational speed
ω	Stagnation pressure loss coefficient $\left(= \frac{\Delta p_0}{\frac{1}{2}\rho V^2}\right)$

Sub-scripts and Abbreviations

0	Stagnation quantity
1	Inlet
2	Exit
<i>clr</i>	Clearance flow
<i>ex</i>	Exit
<i>fs</i>	Free stream
<i>in</i>	Inlet
<i>LE, le</i>	Leading edge
<i>mid</i>	Mid-span
<i>PS, ps</i>	Pressure surface
<i>r</i>	Radial direction
<i>rx</i>	Rotor exit
<i>SM</i>	Stall margin
<i>SS, ss</i>	Suction surface
<i>s – s</i>	Static to static (e.g. pressure rise)
<i>sx</i>	Stator exit
<i>TE, te</i>	Trailing edge
<i>t – s</i>	Total to static (e.g. pressure rise)
<i>t – t</i>	Total to total (e.g. pressure rise)
<i>x</i>	Axial direction
θ	Circumferential direction

Super-scripts

$\overline{\square}$	Average quantity
$\overline{\square}^M$	Mass average
$\overline{\square}^X$	Mixed out average
$\tilde{\square}$	Magnitude of vector

Chapter 1

Introduction

The increasingly highly competitive airline business and current environmental concerns has led the drive to reduce costs and improve aero-engine efficiency. At cruise, a *Boeing 747* civil airliner consumes approximately 13,000kg of fuel per hour. Flying on average for 4,000 hours per year, this results in an annual fuel bill of £22 million¹. Therefore, even a relatively small fuel consumption improvement (or penalty) can result in significant savings (or costs); a 1% change in fuel consumption results in a £220,000 change in the annual fuel bill.

The key method of increasing the cycle efficiency of a gas turbine is to increase the overall pressure ratio. As new materials have become available² the pressure ratio of aero-engines has increased. Over the past 30 years the pressure ratio across the compression system of a modern civil aero-engine has increased from about 30:1 to almost 50:1. This trend is illustrated in Figure 1.1.

A cut-away view of the compression system found in a modern three-shaft aero-engine is shown Figure 1.2. The pressure rise is achieved over several stages (N.B. one stage consists of one rotor and one stator blade row) each producing an individual pressure ratio of about 1.3 in a current state of the art machine. The number of stages in a compressor is governed by the required overall pressure ratio.

Adding a stage (or stages) increases the manufacturing cost, weight and length. Each

¹At the time of writing the price of aviation fuel was £0.42 per kg.

²The overall pressure ratio is limited by the creep life (i.e. the temperature and material properties) at the rear of the high pressure compressor.

stage costs between £20,000 and £40,000 to manufacture and weighs approximately 75kg (or about 1–2% of the total engine cost/ weight). Increasing the overall length will also increase the size of the ancillary components (e.g. the nacelle) and maintenance requirements. The nacelle is the heaviest and costliest component and therefore the knock-on effect of adding a stage is likely to be significantly greater than the unit cost/ weight penalty alone. Indeed, although the overall pressure ratio has almost doubled in the past 30 years, the total number of compressor stages has only increased from 14 to 15 stages. By the same argument, reducing the number of stages has the potential to yield significant cost and weight benefits.

Increasing the pressure ratio or reducing the number of stages both require a greater pressure rise per stage. This can be achieved by either increasing the blade speed or by increasing the aerodynamic stage loading. The blade speed is limited by mechanical constraints. A modern high-pressure compressor spins at about 10,000rpm, at this speed the centrifugal forces are high enough to induce significant creep reducing the life of the engine. Therefore, higher pressure ratio (or reduced stage count) compressors will require increased aerodynamic loadings and it is this topic which forms the main thrust of this work.

1.1 Loading (and Design Point)

Aerodynamic loading of a stage is often summarised by the so called “stage loading coefficient” defined in Equation 1.1. The stage pressure rise is closely related to the enthalpy rise, Δh_0 , which appears in the numerator of Equation 1.1. This demonstrates the relationship between the pressure rise and the blade speed, U ; pressure rise is approximately proportional to the square of the blade speed.

$$\psi = \frac{\Delta h_0}{U^2} \quad (1.1)$$

The design point of a compressor stage can be displayed on a “Smith Chart”; a plot of stage loading against flow ($\phi = \frac{V_x}{U}$) coefficient. Contours of efficiency (predicted with the one-dimensional correlations of Wright & Miller [99] for a typical modern compressor stage) are shown on a Smith Chart in Figure 1.3. Currently, compressors

are usually designed to operate at points which cover a small area on the Smith Chart where previous designs have been found to be successful. Almost all modern designs lie within the marked ellipse which approximately corresponds to peak efficiency. (The precise location of peak efficiency is dependent on the details of the stage design.) Despite the very significant potential benefits of increasing stage loading, the penalty for producing an inefficient compressor/ engine is so great that adventurous designs, outside this small area, are almost prohibited. The result of this is that there is little experience of highly-loaded designs; a deficiency that this work aims to address.

1.2 Implications of Increasing Stage Loading

Increasing the stage loading will increase the difficulty of the aerodynamic design and therefore the viscous losses. One measure of the difficulty of aerodynamic design is the de Haller number ($\frac{V_2}{V_1}$); the lower the de Haller number, the harder the aerodynamic design becomes. (A commonly accepted rule of thumb suggests that, to achieve a successful compressor design, the de Haller numbers should remain above about 0.7.) The effect of design point on de Haller number³ is illustrated by the blue contours on the Smith Chart of Figure 1.4. As the stage loading is increased (i.e. due North on the Smith Chart) the de Haller number falls, indicating a rapid increase in the difficulty of the aerodynamic design (and therefore viscous losses).

Also shown on Figure 1.4 are lines of constant inlet Mach number (assuming a blade speed of $250ms^{-1}$; typical of that in a modern high-pressure compressor). As the flow and stage-loading coefficients increase (towards the top-right of Figure 1.4) so do the typical Mach numbers and associated losses (e.g. shock losses).

In the worst case, increasing the stage loading too far can lead to surge. This phenomena can have catastrophic consequences and, at the very least, will require a significant engine overhaul.

These potential problems of highly-loaded compressors are starkly illustrated by the experience of *Pratt & Whitney* with their PW6000 civil aero-engine⁴. In its original design, the PW6000 featured a highly-loaded five stage high-pressure compressor. (By

³Calculated for a 50% reaction repeating stage.

⁴Designed for use on the *Airbus A318* aircraft.

way of comparison, the International Aero Engines⁵ V2500 engine featured a 10 stage high-pressure compressor to achieve a similar pressure ratio.) In initial testing, the PW6000 failed to live up to design targets; one report put the specific fuel consumption as 6% above its target due to problems with the high-pressure compressor (Flight International [64]). The net result of this was that the original five stage *Pratt & Whitney* unit had to be replaced by a six stage *MTU* design and a five year delay to its entry into service (Flight International [72]). The difficulty of achieving a successful highly-loaded design clearly cannot be over-stated and provides the motivation for the current work.

1.3 Compressor Design and Correlations

The design of a compressor often starts with mean-line correlations; empirical relationships for loss and surge margin based on one-dimensional (or mean-line) average velocities of the main flow through the compressor. These correlations are empirically derived from previous (successful) designs. This raises a question about the applicability of these correlations to designs well beyond current experience. These correlations predict a drop in efficiency outside the oval zone marked on Figure 1.3.

1.4 Objectives

As previously mentioned, compressors are usually designed at operating points within a small area on the Smith Chart where previous designs have been successful (Figure 1.3). In order to reduce the number of stages in a compressor the design point must move well away from that of existing designs. The inherent risks of increasing stage loading and the very significant (cost and time) penalties for getting a compressor design wrong, mean there is little existing information about adventurous, highly-loaded designs.

This project aims to explore the design space on the Smith Chart at loadings much higher than those currently in use. The knowledge gained by doing so will be used to establish how far blade loadings can be reasonably pushed and how best to imple-

⁵A consortium of aero-engine manufacturers made up of *Pratt & Whitney*, *Rolls-Royce*, *MTU* and the *Japanese Aero Engines Corporation*.

ment highly-loaded stages. Using a combination of low-speed experimental testing and computational fluid dynamics (CFD) allows adventurous designs to be investigated in detail without serious cost implications.

1.5 Structure of Thesis

Chapter 2 contains a review of the literature relevant to highly-loaded blade design. Particular attention is paid to compressor design, current loading limits and basics of the mean-line correlations currently in use. **Chapters 3 and 4** describe the experimental methods/ apparatus used and the design of four stages tested respectively.

As a part of this investigation three highly loaded and one conventionally loaded compressor stages were tested in the Highly Loaded Research Compressor (HLRC) at the Whittle Laboratory, Cambridge. The results from these experiments are presented and discussed in **Chapter 5**.

One of the highly loaded stages tested exhibited a very unusual behaviour as it was throttled towards stall. It is believed that such a flow breakdown mechanism has never been observed before. **Chapter 6** contains the results from an investigation into this phenomena.

Calibration of two and three-dimensional CFD methods (*MISES* and *MULTIP* respectively) against the experimental results is undertaken in **Chapter 7**. The CFD was used to perform a parametric study into the effect of the reaction and stage-loading on rotor and stator aerodynamics. The application of three-dimensional design methods (e.g. sweep and lean) at high loading were also investigated. The results of these studies are presented in **Chapter 8**.

In **Chapter 9**, the one-dimensional correlations for profile and tip clearance loss are investigated. A simple generic velocity distribution based on the physics of the flow is developed and used to estimate profile and tip clearance losses. In particular, the correlation between diffusion factor and profile loss is examined. This differs from conventional wisdom in that it demonstrates that, at high-loading, the profile loss is dependent not only on the diffusion factor but also on the de Haller number.

Finally, the main conclusions from this investigation are summarised in **Chapter 10**.

Chapter 2

Literature Review

2.1 Introduction

This chapter presents a review of the literature relevant to the design of highly loaded axial compressors. This is a wide subject area and includes a review of the few examples of highly loaded compressors reported in the open literature.

Basic descriptions of the flow through a typical compressor blade row and the compressor design process are given. Particular attention is given to the two and three dimensional design methods which have been shown to be able to increase the loading potential of the (blade) boundary layers and the end-wall flows respectively.

The fundamental architecture of a compressor is fixed at the first stage in the design process (e.g. number of stages, rotational speed, etc...); it is very difficult (and expensive) to change the basic layout at a later date. At this stage, simple correlations are used to evaluate the performance of several compressors and eliminate unsuitable designs. Therefore, the ability of these correlations to provide accurate predictions, and the theory behind them, is of considerable interest.

By their very nature, compressor boundary layers are exposed to significant adverse pressure gradients and, therefore, have a tendency to separate. The loading of a compressor stage is restricted by the need to avoid large, lossy, separations. The stage loading coefficient is an imperfect measure of the limiting loading as the detailed design

of the blade row (e.g. solidity, flow angles, etc...) causes considerable scatter. Various loading parameters, intended to give a better idea of the loading capability of a given blade row, are presented and discussed.

Over the years several ingenious attempts have been made to increase the loading capability of axial compressors. These include both passive and active methods. In the former category are slotted/ tandem aerofoils (much like the high-lift devices used on aircraft wings) and attempts to utilize unsteady wake passing effects. Although not within the remit of this thesis, attempts at aspirated blade rows are briefly discussed as they have been shown to increase the loading capability of blade rows beyond current limits.

Stall and surge are one of the most deleterious phenomena to afflict axial compressors. The result of a surge can be catastrophic and therefore compressor designers try to avoid this by allowing sufficient surge margin. Increasing loading is often associated with reduced surge margin. Therefore, it is important to understand some of the basics of stall inception, prediction and prevention.

2.2 Axial Compressor Flows

The details of the flow through axial compressor blade rows have been well documented over the years so only a brief overview will be presented here. Good descriptions of the flow through axial compressors can be found in Cumpsty [12], Hodson [49] and Longley [65].

2.2.1 Boundary Layer Transition

It has been a common assumption that compressor suction surface boundary layers are turbulent over most of the blade surface. Indeed during the design process it is often assumed that the boundary layer is turbulent over the entire blade surface. However, Halstead et al [47] demonstrated that such an approach can lead to an over-prediction of the profile loss by up to 35%.

A comprehensive review of the role of transition in turbo-machines, both steady and

unsteady, is given by Mayle [67]. Mayle categorised the main types of transition found in turbo-machines:

1. **Natural transition:** Once the momentum thickness Reynolds number of a Laminar boundary layer reaches a critical value it becomes unstable and breaks down, via Tollmien-Schlichting waves, into turbulent spots. These turbulence spots propagate downstream and coalesce to form a fully turbulent boundary layer
2. **Bypass transition:** Regions of very high turbulence cause transition directly, i.e. bypassing Tollmien-Schlichting waves. In unsteady bypass transition (e.g. as in wake passing), turbulent spots are followed by a “calmed-region”. This calmed region is laminar in nature (i.e. low loss) but has a full velocity profile (like a turbulent boundary layer). It can therefore briefly tolerate a greater adverse pressure gradient without separating than a normal laminar boundary layer.
3. **Separated flow transition:** A shear layer forms over a laminar separation which breaks down into turbulent flow via a Kelvin-Helmholtz (i.e. shear layer) instability. This turbulent flow can reattach as a turbulent boundary layer.

In multi-stage compressors the adverse pressure gradients, the presence of high ambient turbulence levels and passing wakes means that bypass and separated flow transition tend to dominate. Halstead et al [47] performed a comprehensive set measurements looking at compressor boundary layers. They observed that there were significant regions of laminar and transitional flow on compressor blades. As in similar studies with turbine blades, Halstead et al identified wake induced (i.e. bypass) transition followed by a calmed region.

2.2.2 Secondary Flow

Secondary flows refer to any flows which are not in the primary/ bulk flow direction. The secondary flows present in an axial compressor are illustrated in Figure 2.1. Secondary flows are often vortical in nature and, in compressors, cause losses roughly comparable in magnitude to the blade profile losses. At low aspect ratios secondary flows tend to become more significant.

Cross Passage Flow

The most notorious form of secondary flow is the tangential migration of end-wall boundary layer fluid from the pressure surface, towards the suction surface. It is well established that the end-wall boundary layer is exposed to the pressure field set up by the main passage flow (a common assumption is that the pressure at the hub and casing is equal to that at 10% and 90% of span respectively). The curvature of a streamline exposed to a normal pressure gradient is given by Equation 2.1. The pressure gradient, set-up by the free-stream flow, must induce higher streamline curvature in the slower end-wall boundary layer fluid than in the main-passage flow and is therefore turned beyond the free-stream flow direction. This is illustrated in Diagram 2.1.

$$\kappa = \frac{1}{r} = \frac{1}{\rho V^2} \frac{dP}{dy} \quad (2.1)$$

Where: “ κ ” is the curvature and “ y ” is the direction locally perpendicular to the streamline.

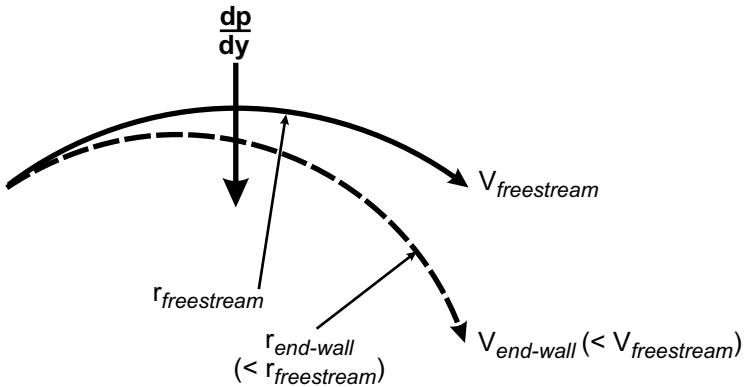


Diagram 2.1: Schematic diagram of end-wall boundary layer overturning.

The overturned end-wall fluid collects in the corner with the suction surface and can migrate, radially, along the suction surface. At the built in ends of blade rows this, almost universally, results in three-dimensional separation (Gbadabo [40]). In their most deleterious form, secondary flows can result in very large, three-dimensional, corner separations despite loading parameters (typically based on two-dimensional, blade to blade flow, e.g. diffusion factor, de Haller number, etc...) being within generally accepted limits. Gbadabo et al [40] demonstrated that the formation and size of three-dimensional

separations are governed by and closely correlated to the number of singularities in the limiting streamlines on the passage surfaces and not by conventional, two-dimensional, boundary layer theory.

Tip Clearance Flows

Tip clearance flows occur at the free end of blades necessary to provide adequate running clearance between the rotating and stationary parts of the compressor, e.g. at the rotor tips. As discussed above, the end-wall fluid is exposed to the pressure field set-up by the main passage flow. This sets up a steep pressure difference across the tip which drives fluid from the pressure side (high pressure), through the clearance gap and ejects it from the suction side (low pressure). The high velocity fluid exiting the tip clearance gap rolls up to form a tip clearance vortex.

Tip clearance flows were studied in detail in a linear cascade by Storer [86]. Storer showed that the flow separates from the pressure side corner of the tip and the resultant shear layer forms a throat, commonly referred to as a “vena-contracta”. In “thick” blades, the shear layer has sufficient time to reattach to the thicker rotor tip before exiting the clearance gap. Storer performed a series of experiments which suggested that the flow would re-attach in cases where the thickness of the blade was greater than approximately 2.5 times the gap height.

Shroud/ Leakage Flow

Shrouded blades (i.e. built in at both ends) often have a leakage path under/ over the shroud. The static pressure rise from inlet to exit of a blade row drives fluid upstream through the shroud, injecting it ahead of the blade row in question. The effect of such leakage flows on an isolated rotor are illustrated by the Shabbir et al [82]; a relatively small leakage flow, 0.25% of the main passage flow, caused a large stagnation pressure deficit near to the hub and reduced the overall pressure rise of the fan.

Demargne & Longley [16] investigated the effects of compressor stator shroud leakage. Demargne & Longley demonstrated that the shroud flow interacts with the cross-passage flow and increases the size of the hub-corner separation. This affected the blockage and turning across the whole span. Demargne & Longley also showed that the

size of this penalty could be reduced or even eliminated, by increasing the tangential velocity of the re-injected shroud flow (i.e. opposing the cross passage flow).

2.3 Axial Compressor Design

Detailed accounts of the design process have been give by various authors, e.g. Gal-limore [36], Brilliant [5] and Cumpsty [12]. Despite the differing provenance of these authors the aerodynamic design of an axial compressor can be split into four, roughly sequential, phases:

1. Initial design
2. Through-flow design
3. Blade-to-blade design
4. Three Dimensional Design/ Modifications

In reality the boundaries between each of these phases is not clear cut and there is always some interaction and iteration between these phases in a successful design process. As the design progresses, so too does the level of detail in the design.

In the design of an aero-engine, typically the required pressure ratio, flow rate and shaft speed will be specified. It is the compressor designer's responsibility to conceive a design to meet these requirements as quickly and cost effectively as possible with best possible efficiency and adequate surge margin.

2.3.1 Initial Design

The fundamental architecture of a new compressor (e.g. number of stages, length, annulus line) is set at the initial design stage. Therefore, the initial design stage is arguably the most important step in the design process. Key design choices must be made which are very difficult (and expensive) to change at a later date; e.g. increasing the number of stages.

Several options are usually evaluated by solving the basic velocity triangles and by using simple, one-dimensional correlations (such as those developed by Koch & Smith [59] and Wright & Miller [99]) to assess the efficiency and surge margin of the compressor. These correlations include empirical relationships for all of the major sources of loss in a compressor blade row (e.g. profile loss, end-wall loss, Mach number loss, etc...). These are discussed further in Section 2.4. This process is repeated/ iterated until one or two suitable configurations are found with sufficient performance to warrant more detailed analysis.

2.3.2 Through-flow Design

It is at the through-flow design stage where the radial dimension is considered. The axisymmetric meridional streamline equations are solved to obtain the radial variation in the flow behind each blade row (i.e. circumferential, blade to blade and three dimensional effects are ignored). The radial variation in axial velocity, pressure and temperature rise is controlled by the span-wise distribution of flow angle. Typically the flow angles at the exit to each blade row are adjusted to achieve the required work input and/ or turning. Regions of excessive loading, or high Mach number, are relieved by adjusting the radial distribution of flow angle; e.g. high hub loading can be reduced by increasing the axial velocity in this region (Gallimore [36]). Once the flow angles are set to give the required pressure rise and acceptable flow across the span, detailed design of blade sections to provide the necessary turning can proceed.

2.3.3 Blade-to-Blade Design

Up until the early 1980s, section design was based on standard families of blades (e.g. double circular arc, NACA-65, Royal Aircraft Establishment C4, etc...). The performance of these sections is well documented; designers looked up appropriate metal angles and loss for the required duty in tables, graphs or correlations produced from detailed cascade testing. The advent of reliable coupled inviscid/ boundary layer prediction programs and increases in computing power led to the development of controlled diffusion aerofoils in the early 1980s.

Hobbs and Weingold [48] describe the development of controlled diffusion blading at

Pratt & Whitney. The strategy they adopted for transonic compressors is summarised in Figure 2.2. Hobbs & Weingold demonstrated an increase in incidence range and diffusion tolerance with controlled diffusion designs. The key feature of controlled diffusion aerofoil design is the smooth, continuously reducing deceleration, chosen to prevent the turbulent boundary layer separating. The strategy behind this “ski-slope” velocity distribution is to have the highest diffusion where the boundary layer is thinnest and most able to tolerate it (i.e. at the start of the blade) and relieve the diffusion as the boundary layer grows towards the trailing edge.

Koller, Kusters et al [60, 61] clearly demonstrated the effect of the transition point on the optimum velocity distribution for compressor aerofoils to be used in an industrial gas-turbine. Koller et al used an automated procedure to arrive at a series of “optimum” velocity distributions (based on a weighted average of design loss and incidence range). These optimum velocity distributions all demonstrated peak suction close to, or shortly downstream of, the transition point.

Industrial gas-turbines are generally larger than their airborne counterparts and operate in the higher density air at ground level. Therefore, they feature higher Reynolds numbers. Typical Reynolds numbers in industrial gas turbines vary between 2×10^6 and 4×10^6 . At these Reynolds numbers the transition point is located near to the leading edge. The optimum velocity distributions developed by Koller, Kusters et al [60, 61] tended to be forward loaded with peak suction, and transition, located at 7-10% of axial chord. The effect of this was to maximise the surface length available for diffusion and therefore reduce the adverse pressure gradient. Original controlled diffusion aerofoils, designed for use in aero-engines (Hobbs & Weingold [48]), have a region of acceleration up to 20-30% of chord, intended to keep the boundary layer laminar for as long as possible. At their higher Reynolds numbers, Koller et al found that this acceleration did not affect the onset of transition (which remained at approximately 10% of axial chord) and therefore there was no benefit in pushing the location of peak suction aft.

The work of Hobbs & Weingold and Koller, Kusters et al highlights that at low Mach numbers (below about 0.8) the key factor determining loss is solidity. The detailed blade shape is most critical at high levels of diffusion and, in particular, affects the maximum tolerable diffusion. This can be exploited for a well designed aerofoil by permitting higher diffusion which allows the solidity, and therefore the loss, to be reduced. The forward loaded aerofoils developed by Koller, Kusters et al [60, 61] had increased

diffusion tolerance which enabled the solidity to be reduced by as much as 29% whilst maintaining (or improving) incidence range. This reduction in solidity resulted in a 20% improvement in loss coefficient.

Koller et al concluded that at Reynolds numbers typically found in aero-engines, with low inlet turbulence ($Tu = 1\%$), a controlled diffusion profile gave better performance. However Camp and Shin [9] report levels of turbulence greater than 4% in three separate multistage compressors. The higher turbulence levels will have a similar effect to increasing Reynolds number (i.e. moving the transition point upstream) and therefore it would not be surprising if the optimum blade shape for aero-engine compressors tended to the forward loaded designs described by Koller et al.

2.3.4 Three Dimensional Design of Axial Compressors

Gallimore et al [37, 38] describe the use of sweep, lean and re-camber in the re-blading of a modern six stage high pressure compressor. The application of three-dimensional techniques to the stators alone allowed a 15% reduction in the number of aerofoils and also gave a 0.7% improvement in peak efficiency. With a three-dimensional rotor an additional 0.2% increase in peak efficiency was realised. In both cases these improvements were achieved without affecting the surge margin. This was based on research carried out by Bolger [4] at the Whittle Laboratory on a low speed, single stage compressor. Unless specified otherwise, lean and sweep will be defined as displacements perpendicular and parallel to the chord line respectively, as used by Gallimore et al [37] and illustrated in Figure 2.3.

Lean/ Dihedral

In calculations and in low speed testing Gallimore et al [37, 38] showed that positive dihedral at the hub and casing reduced the hub corner and tip clearance losses but worsened the performance at mid-span. Negative dihedral had the opposite effect. The “bowed” stators pioneered by *Pratt & Whitney* illustrate a successful application of positive dihedral. Weingold [92] describes an increase of operating line efficiency of 1% with the introduction of bowed stators due to the suppression of corner separations.

Bolger [4] showed that contours of static pressure are not significantly altered by the introduction of lean and remain approximately radial. This is illustrated in Figure 2.4 (reproduced from Bolger [4]). Therefore, the pressure distribution around the blade sections near to the end-walls can be modified by moving them tangentially (i.e. lean) through the approximately stationary contours of static pressure set up by the blade away from the end-walls. To compensate for the reduction in loading at the end-walls (caused by positive lean), the loading (and therefore loss) away from the end-walls increases.

The radial forces applied on the flow by positive lean have two main effects. Firstly, the radial force imposed on the bulk flow tends to drive the main passage flow towards the end-walls, increasing “fullness” of the axial velocity profile at exit to the blade row. And secondly, the reduced suction peak near the end-wall drives suction surface boundary layer fluid towards the blend point(s).

Sweep

Blade sweep originated as a method of controlling the shock losses in transonic compressors. The benefit of positive sweep in transonic machines has been demonstrated by both Wennerstrom [95] and by Wadia et al [91]. In particular, the latter highlighted the benefits that could be obtained from using sweep to control the radial redistribution of flow rather than just as a method of controlling shock losses.

Sweep has since been proved to be beneficial in subsonic designs. This was first shown by Tweedt et al [89] on the stator of a low speed research compressor. Positive sweep at the hub and tip of the stators reduced the losses in the end-wall regions but increased losses and deviation at midspan. Tweedt et al suggested that this had the effect of moving the low momentum fluid near the end-walls inboard, towards midspan. This has since been confirmed by several other researchers, e.g. Inoue et al [54], Bolger [4], Gallimore et al [37, 38] and McNulty et al [68].

Detailed descriptions of the mechanisms behind sweep can be found in Bolger [4] and Denton & Xu [22]. Consider a blade with forward sweep applied to the hub. At the leading edge there is no blade outside of the blade section nearest to the end-wall to support low pressures near to the leading edge. Therefore, the magnitude of peak suction, and the required diffusion along the chord, is reduced near to the end-

wall. Positive sweep also imparts a net radial force on the main passage flow which, particularly in compressors, improves the near wall axial velocity profile (Bolger [4]).

As with lean, the mid-span loading increases to compensate for the reduction in loading caused by sweep at the end-walls and maintain the overall turning. This highlights that three-dimensional design (both sweep and lean) is a trade off. Although benefits are possible from reduced end-wall losses and a more uniform exit flow (i.e. reduced mixing loss) this must be carefully balanced against increased losses at mid-span. Modern three-dimensional CFD programs have allowed compressor designers to realise worthwhile net benefits from such three-dimensional design strategies (e.g. Gallimore et al [37, 38]).

Leading/ Trailing Edge Recamber

Leading edge recamber is perhaps the oldest form of three dimensional modification applied to otherwise two-dimensional blades. The strategy behind leading edge recamber is to align the leading edge with the high incidence flow in the end-wall boundary layer¹.

The strategy behind trailing edge recamber is less clear. It has been implemented by both attempting to counteract the overturning of the end-wall boundary layer by decambering the trailing edge and by increasing the camber to align the overturned flow with the metal. Both these completely opposite approaches have met with some success (Denton et al [21] and Freeman [32] respectively). Cumpsty [12] notes that the latter method is more likely to find success in blades of higher aspect ratios.

2.4 Correlations and the Prediction of Loss

Historically mean-line (or one-dimensional) correlations were used for performance prediction in the absence of other predictive tools. Despite advances in computing power they are still widely used; there is little time available in the modern compressor design cycle to generate specific annulus and blade geometries necessary to use more “up to

¹High incidence flow occurs in the end-wall boundary layers as a result of the change in reference frame. This is illustrated in Figure 2.1.

Name	Definition	Comment
de Haller Number	$\frac{V_2}{V_1}$	Only inlet and exit velocities required
Local Diffusion Factor	$D_{loc} = \frac{V_{ss,max} - V_{te}}{V_{ss,max}}$	Need to know suction surface velocity distribution
Lieblein Diffusion Factor	$DF = \left(1 - \frac{V_2}{V_1}\right) + \frac{\Delta V_\theta}{2\sigma V_1}$	Correlated to D_{loc} , based on velocity triangles and solidity
Diffusion Ratio	$DR = \frac{V_{ss,max}}{V_{te}}$	Rearrangement of D_{loc} : $DR = \frac{1}{1 - D_{loc}}$

Table 2.1: Definition of diffusion parameters.

date” methods (like three-dimensional CFD or through-flow methods). Meanline correlations allow the designer to evaluate different compressor designs quickly and eliminate unsuitable options. It seems appropriate to emphasise the importance of the meanline design here; no amount of profile tweaking or three-dimensional modifications will be able to rectify a poor meanline design (Gallimore [36]).

One of the first correlations for profile loss was that presented by Lieblein [63]. Lieblein showed an almost unique correlation between wake momentum thickness (a measure of loss, see Equation 2.3) and the diffusion factor (either local or his own approximation to it; see Table 2.1) for a series of NACA-65 and C4 type aerofoils of 10% thickness.

Throughout the history of axial compressor design, profile losses (and sometimes also end-wall losses) have been correlated to a series of parameters which give a measure of the adverse pressure gradient (or diffusion) applied to the suction surface. The three most common diffusion parameters (used throughout this thesis) are defined in Table 2.1.

Koch & Smith [59] (of *General Electric*) presented a method for predicting the total loss through a compressor blade row (rather than just the profile loss given by Lieblein’s correlations). The approach used by Koch & Smith was to estimate the total loss as the sum of the individual sources (e.g. profile loss, shock loss, end-wall loss, etc...). At *Rolls-Royce*, Wright & Miller [99] used a similar approach. Although this method

ignores the inherent coupling between these mechanisms it does provide a route to estimating losses of the correct magnitude. Such inaccuracies are glossed over by fitting the empirical correlations to experimental data. However, as a result these correlations are not necessarily reliable for all compressors.

2.4.1 Profile/ Boundary Layer Loss

In an approach similar to Lieblein, Koch & Smith [59] correlated the profile loss to the “diffusion ratio” (DR) presented in Table 2.1. Koch and Smith [59] used an integral boundary layer method to evaluate the total momentum thickness (and therefore the profile loss via Equation 2.3) at the trailing edge of a range of idealised velocity distributions illustrated in Figure 2.5. It is worth noting that these velocity distributions assume that the pressure surface velocity is constant and equal to that at the trailing edge. This method showed good agreement with Lieblein’s experimental data.

To avoid calculating the velocity distribution around each compressor aerofoil, Koch and Smith [59] developed an empirical expression to estimate diffusion ratio. Unlike Lieblein’s diffusion factor, this correlation for diffusion ratio accounted for the effects of blade thickness, Mach number and stream-tube contraction.

Wright & Miller [99] took a similar approach; they correlated a loss parameter (essentially an approximation to the trailing edge momentum thickness) to an empirical diffusion ratio (also including the effects of blade thickness, Mach number, etc...) for a series of double circular arc blade sections.

Denton [18] shows that the rate of entropy production in a boundary layer is given by Equation 2.2 (where C_d is the dissipation coefficient). The variation of the dissipation coefficient with momentum thickness Reynolds number is shown in Figure 2.6 (taken from Denton [18]). Figure 2.6 shows that for turbulent boundary layers C_d is almost constant at a value of approximately 0.002. It can be shown that the entropy production (i.e. loss) per unit surface area in compressor boundary layers is proportional to the *cube* of the edge velocity.

$$\dot{S}_A = C_d \frac{\rho V_{edge}^3}{T} \quad (2.2)$$

Denton [18] used this approach to estimate the loss coefficients of both turbine and compressor blades with generic, rectangular, velocity distributions. Denton found that to predict compressor losses he needed to artificially increase the losses at diffusion factors above 0.55 to model the effects of boundary layer separation (which are not included in Equation 2.2). This had the effect of forcing the choice of solidity to give diffusion factors close to 0.55 for all compressor blade rows.

The approach of Denton [18] only accounts for the losses up to the trailing edge. It does not include losses from the mixing out of the wake. Denton showed that the total entropy loss coefficient is linked to the integral boundary layer parameters by Equation 2.3. For incompressible flow this is equivalent to the stagnation pressure loss coefficient (based on exit velocity). The second term in Equation 2.3 is often neglected (a reasonable assumption for thin, well attached, boundary layers). The final term accounts for the extra loss due to vortex shedding at the trailing edge, commonly termed “base pressure” loss. Typical values of the base pressure coefficient (C_{pb}) are around -0.2 (N.B. C_{pb} is negative).

$$\omega_p = \frac{\Delta P_0}{\frac{1}{2}\rho V_2^2} \approx \frac{T_0 \Delta S}{\frac{1}{2}V_2^2} = \frac{2\theta}{s \cos \alpha_2} + \left[\frac{\delta^* + t_{te}}{s \cos \alpha_2} \right]^2 - \frac{C_{pb} t_{te}}{s \cos \alpha_2} \quad (2.3)$$

2.4.2 Reynolds Number Corrections

The profile loss correlations developed by Koch & Smith [59] and Wright & Miller [99] assume a Reynolds number of 10^6 . The predicted profile loss/ momentum thickness is adjusted to the real Reynolds number via a power law, similar to that derived by Prandtl for a flat plate with a turbulent boundary layer (reproduced in Equation 2.4, Schlichting [79]). In the turbulent regime ($10^5 < Re$) Koch & Smith and Wright & Miller found exponents of -0.17 and -0.19 respectively gave the best fit to their data compared to the value of -0.20 derived analytically by Prandtl.

$$\begin{aligned} Re < 10^5 : \omega_p &\propto Re^{-0.50} \\ 10^5 < Re < Re_{rough} : \omega_p &\propto Re^{-0.20} \\ Re_{rough} < Re : \omega_p &= \omega_{p,Re_{rough}} \end{aligned} \quad (2.4)$$

At Reynolds numbers above which the surface finish can be considered hydraulically rough the loss becomes independent of Reynolds number. Koch & Smith considered blades to be hydraulically rough at “equivalent sand roughness” Reynolds numbers greater than 90. Wright & Miller took a simpler approach and assumed blades to be hydraulically rough at Reynolds numbers above 10^6 . In both correlations this Reynolds number correction is applied to the profile loss *and* end-wall losses², but not to the shock loss.

2.4.3 Shock Loss

Koch & Smith [59] split their shock loss correlation into two parts to account for the shock loss due to blunt leading edges and the passage shock. Koch & Smith arrived at an empirical expression for leading edge bluntness losses which captured the trends seen in a method of characteristics type analysis of the leading edge flow field operating at supersonic relative inlet Mach numbers. The passage shock loss was assumed to be equivalent to that of an oblique shock wave that reduces the representative passage Mach number to the exit Mach number or unity, whichever is greater. Koch & Smith estimated the Mach number of the passage shock with a weighted average of the inlet and peak suction surface Mach numbers (evaluated from their expression for diffusion ratio).

Wright & Miller used an approach similar to Schwenk et al [80]. Schwenk et al suggested that the loss associated with the passage shock could be approximated by that of a normal shock with upstream Mach number equal to the average of inlet and suction surface Mach numbers. Schwenk et al made the following two assumptions to fix the location of the passage shock; (a) that it intersects the leading edge; and (b) it is normal to the camber line at mid-pitch. At the intersection of shock and the suction surface, the Mach number can be evaluated via a Prandtl-Meyer expansion to the local suction surface metal angle (for cases with super-sonic inlet flow). For double circular arc blades the local metal angle can be easily obtained analytically. Wright & Miller found that a value of 65% of that predicted by this method gave a reasonable estimate of the shock loss.

²In the correlation of Koch & Smith, the Reynolds number correction is applied directly to the profile loss and is included in the end-wall loss prediction via the efficiency ratio of Equation 2.5.

For cases with high subsonic inlet flow, Wright & Miller estimated the shock loss via linear interpolation between $M_{crit} < M_{inlet} < 1.0$, where the shock loss at M_{crit} is zero and at sonic inlet flow is estimated via the method described by Schwenk et al [80] (see above). Wright & Miller assumed the shock loss to be zero in cases where the peak suction surface Mach number was below 1.08. Therefore, M_{crit} is the inlet Mach number which gives a peak suction surface Mach number of 1.08 and can be estimated via Wright & Miller's empirical expression for diffusion ratio.

2.4.4 End-wall Loss

Additional losses occur in the end-wall boundary layers. Although sometimes referred to as “secondary losses/ flows”, these end-wall losses are often of a similar magnitude to profile losses. It is therefore imperative that end-wall losses are accounted for when estimating compressor performance.

Equation 2.5, derived by Koch & Smith [59], relates the “free-stream” efficiency (i.e. the efficiency without end-wall effects) to the actual efficiency. Koch & Smith developed correlations for the tangential force deficit thickness (δ_{F_θ}) and the axial velocity (or the mass flow) displacement thickness (δ_x^*)³ against a rotor/ stator averaged static pressure rise coefficient. This latter value is normalised by the maximum static pressure rise coefficient (again averaged across the rotor and stator) and therefore it is not entirely obvious how the latter parameter can be evaluated a priori (without the aid of additional correlations).

$$\frac{\eta}{\eta_{fs}} = \frac{1 - \frac{1}{h} (\delta_{x,hub}^* + \delta_{x,case}^*)}{1 - \frac{1}{h} (\delta_{F_\theta,hub} + \delta_{F_\theta,case})} \quad (2.5)$$

The correlations presented by Koch & Smith showed considerable scatter, especially in the estimate of the tangential force deficit thickness. Nevertheless, they demonstrated that these correlations introduced corrections to the “free-stream” efficiency of approximately the correct magnitude for the range of compressors against which Koch & Smith calibrated their model.

³Physically the tangential force deficit thickness (δ_{F_θ}) and the axial velocity displacement thickness (δ_x^*) represent the reduction in torque (i.e. increase in efficiency) and the increase in loss respectively due to the presence of end-wall boundary layers.

Wright & Miller [99] used the method of Freeman [32] to estimate end-wall loss. Freeman correlated the end-wall axial momentum thickness (normalised on chord) to the diffusion ratio, akin to Lieblein's profile loss correlations. The end-wall momentum thickness is linked to the end-wall loss via Equation 2.6. Equation 2.6 is merely Equation 2.3 applied across the span instead of the pitch; the aspect ratio term appears to relate the wetted area of the end-walls to that of the blade.

$$\omega_{p,ew} = \frac{\Delta P_0}{\frac{1}{2}\rho V_2^2} = \frac{2\frac{\theta_{ex,ew}}{C}}{AR} \quad (2.6)$$

Where: $\theta_{ex,ew}$ is the end-wall boundary layer momentum thickness at blade-row exit.

2.4.5 Tip Clearance Loss

Tip clearance flows occur where fluid is driven through the clearance gap (necessary for mechanical reasons) between the rotor tip and the casing (or the stator and the hub). Tip clearance flows are typically quite strong (where present, they tend to dominate the end-wall flow) and add significant extra loss.

Koch & Smith [59] included the effect of tip clearance in their correlation for end-wall axial velocity displacement thickness. They suggested that the axial velocity displacement thickness was proportional to the ratio of the rotor/ stator averaged tip clearance to the “averaged staggered spacing”⁴. Freeman [32] accounted for tip clearance losses by making his end-wall loss correlation proportional to the tip clearance upon chord.

Storer & Cumpsty [87] developed a method to model tip clearance flow and resulting losses. The tip clearance flow was modelled as a jet driven by the pressure gradient across the blade. The loss of the clearance flow was estimated by a simple control volume calculation of the mixing of a jet into free-stream flow. For the purposes of this mixing calculation the relevant free-stream velocity was that on the suction surface; calculations performance by Storer & Cumpsty showed that the vast majority of the loss was created locally, near to the clearance gap. This approach differed from previous “mixing” models of the tip clearance flow in that it included the effect of the direction of the clearance flow (e.g. Denton & Cumpsty [19], who assumed that the jet was

⁴Staggered spacing, g , is defined as $g = s \cos(\xi)$. In this case “averaged” denotes a rotor/ stator average.

perpendicular to the main flow). Storer & Cumpsty demonstrated very good agreement with the tip clearance losses measured in a cascade.

2.5 Loading Limits for Axial Compressor Blade Rows

De Haller suggested that for satisfactory performance the ratio of exit to inlet velocity across a compressor cascade (now commonly known as the de Haller number) should not drop below about 0.75 (Cumpsty [12]). The obvious simplicity of this method is both an advantage and its greatest disadvantage. Such a simple method does not take into account even the simplest variations between blade rows, most notably solidity (or number of blades).

The most famous and widely used measure of the loading⁵ of compressor blade rows is Lieblein's diffusion factor. Lieblein [63] took data from several cascade tests and showed unique correlation between the local suction surface diffusion factor (defined in Table 2.1) and the wake momentum thickness⁶ (reproduced in Figure 2.7).

Although nowadays it is almost trivial to calculate the velocity distribution around a blade it is still necessary to know the precise geometry. To remove this restriction Lieblein approximated the local diffusion factor around a NACA-65 aerofoil of 10% thickness with the expression presented in Table 2.1; now well known as the Lieblein diffusion factor. The first set of parentheses represents the diffusion due to one-dimensional area change (akin to the De Haller number). A pressure difference between the suction and pressure surfaces is necessary to turn the flow. Therefore the suction surface velocities and diffusion is higher than that suggested by simple one-dimensional area change arguments. The final term accounts for this additional diffusion due to flow turning. The corresponding correlation with exit stagnation pressure loss coefficient is presented in Figure 2.8.

Figure 2.8 shows that the momentum thickness (and therefore profile loss) starts to rise rapidly at Lieblein diffusion factors above about 0.6 (or local diffusion factors

⁵In this case “loading” refers not to stage loading or stage loading coefficient but rather to the level of diffusion (or adverse pressure gradient) along the suction surface.

⁶Momentum thickness is directly related to *exit* loss coefficient via the method of Denton, reproduced in Equation 2.3

above approximately 0.45, see Figure 2.7); denoting the onset and growth of suction surface separations. This has traditionally been taken to be a limit on the acceptable performance of compressor blade rows. In reality the Lieblein diffusion factor rarely goes above 0.5 at the design point of a modern aero-engine compressor (Bolger [3]). It is worth noting here that both Lieblein's, and later Koch & Smith's [59] work concerned only the blade profile losses and does not consider the limits on the stability of the end-wall flow.

More recently Lei et al. [62] developed a criterion for the onset of corner stall. The diffusion parameter that they arrived at is given in Equation 2.7. The precise formulation of this group was arrived at via qualitative arguments, similar to those used in dimensional analysis. Unlike the Lieblein diffusion factor, this new diffusion parameter includes a term to account for inlet boundary layer skew, $\Delta\beta$ (found in the final set of parentheses). This diffusion parameter was shown to be reasonably well correlated with Lieblein's diffusion factor for cases with zero inlet skew.

$$D_{lei} = \frac{1}{\sigma} \left[1 - \left(\frac{\cos\alpha_1}{\cos\alpha_2} \right)^2 \right] (\alpha_2 - \alpha_1 - \Delta\beta) \quad (2.7)$$

Lei et al conducted several numerical simulations of compressor cascades of different geometries and inlet conditions. They showed that hub corner separations (which they defined as flow reversal on the end-wall) occurred when their diffusion parameter was greater than ≈ 0.40 (± 0.05). This was in general agreement with experimental cascade data available in the open literature. Furthermore, Lei et al also demonstrated that the topology of the flow and therefore their criterion, is insensitive to changes in Reynolds number, aspect ratio and inlet boundary layer thickness.

2.6 Novel Concepts for High Loading

2.6.1 Slots and Holes

Most of the early research into highly loaded compressor aerofoils was inspired by successful high lift devices used on isolated aerofoils (i.e. wings), e.g. slots. Slotted aerofoils work by using the pressure difference across the blade to re-energise the suction

surface boundary layer.

Wennerstrom [94] describes experiments carried out in the early 1970s by *NASA* and *Pratt & Whitney*. These showed slots to be less effective in turbo-machines than on isolated wings. This was attributed to their inability to deal with large regions of secondary flow at the end-walls. Slots were shown to be beneficial in some cases and deleterious in others. Griepentrog [46] proposed a set of correlations for slotted aerofoils that suggested slotted aerofoils are more likely to be beneficial at low aspect ratios and Mach numbers. In a later experiment, Wennerstrom [93] eliminated a suction surface separation with the introduction of a slot into a highly loaded, low aspect ratio, stator and realised a 14% reduction in loss.

Dong et al [27] describe the use of a small tip clearance to control hub corner separations. Dong et al yielded a 1.2% efficiency benefit from a clearance gap of 1.7% of chord applied at the stator (stationary) hub of a low-speed, single-stage, research compressor. The clearance gap successfully suppressed the corner separation and prevented radial migration of end-wall fluid on to the suction surface. Perhaps surprisingly, the loss was reduced across most of the blade height from 20% to 80% of span. At the hub the benefit from suppressing the corner separation was almost exactly balanced by the extra loss from the clearance flow.

2.6.2 Wake Passing Effects

Low pressure turbine designers utilize the unsteady effect inherent in turbo-machines for boundary layer control, e.g. Howell [52]. A calmed region forms behind turbulent spots produced by wake induced, or bypass, transition. These calmed regions are laminar in nature and therefore do not produce much loss, however unlike a laminar boundary layer they are more resistant to separation. In low pressure turbines, the resulting time averaged boundary layers are healthier and can tolerate greater levels of diffusion without separation. This enables loss to be reduced by either reducing blade numbers (i.e. reducing the wetted area loss) or by increasing the extent of laminar flow over the front of the suction surface by pushing the peak suction point aft.

Dong & Cumpsty [25, 26] performed a low-speed compressor cascade experiment with moving bars to simulate upstream wakes to investigate unsteady effects in compressors.

The presence of wakes caused premature, bypass, transition close to the leading edge. As in turbines, calmed regions formed behind the turbulent spots caused by the incident wakes. The extra loss associated with premature transition caused by incident wakes was offset by the low-loss calmed region. The net result of this was that the presence of wakes had little effect on the properties of the suction surface boundary layer at the trailing edge.

Ottavy et al [73] performed a detailed study of the effect of incident wakes on a flat plate exposed to a compressor like pressure distribution. At low Reynolds numbers ($Re = 3.5 \times 10^5$), Ottavy et al showed that unsteady effects reduced the loss by as much as 20% from the steady case. As the Reynolds number was increased (to $Re = 5.0 \times 10^5$) the beneficial effects of incident wakes diminished, and even became deleterious. These tests were all performed at a freestream turbulence level of 1.2%; increasing the freestream turbulence to more representative levels is likely to have the same effect as increasing Reynolds number.

Wake passing effects can clearly be beneficial in compressors in certain cases, especially at low Reynolds number and turbulence levels. Whether the effects of wake passing are beneficial or not depends on the details of the flow; in particular, the trade off between reduced losses in the calmed region and the increased losses due to premature, wake induced, transition.

2.6.3 Aspiration

Active boundary layer control has recently received a great deal of attention. Research into aspiration can be split into two, completely opposite, strategies; (a) re-energising the boundary layer by injecting high momentum fluid; and (b) removing the old boundary layer via suction and allowing a new, healthy boundary layer to grow in its place. Aspiration is beyond the scope of this project and so only a brief description follows here.

Kirtley et al [57] performed a CFD analysis which showed that the effectiveness (in terms of preventing separation) of blowing is related to the momentum of the injected flow. They implemented their treatment on a low solidity stator. The number of stators was reduced from the baseline design to increase the design Lieblein diffusion

factor to approximately 0.60. Without blowing, the low solidity stator exhibited a large separation across most of the span. Blowing suppressed the large separation (reducing the stator loss by 54%) and improved the stage efficiency by 0.7%. This was within 0.2% of the datum design with conventional solidity and diffusion factors.

A similar study was conducted by Culley et al [11]. They demonstrated that steady blowing could reduce the stagnation pressure loss on a sector of separated stators by 13%. Culley et al also showed that unsteady injection was more effective than steady blowing for the same, time-averaged, momentum injection coefficient; in the best case, unsteady injection reduced the loss of the same stators by 22%.

Merchant [69] incorporated a suction term in the boundary layer integral momentum equation. He showed that the change in momentum thickness across a slot (closely related to the profile loss) is magnified by an exponential term dependent on the diffusion between the slot and the trailing edge. Merchant therefore argued that to minimise the loss (for the minimum suction), suction should be located immediately upstream of the diffusion region.

Merchant [69] applied this philosophy to CFD designs of a highly loaded ($\frac{\Delta h}{U_{tip}^2} = 0.70$) high-speed fan and a highly loaded stator (similar in duty to the non-aspirated highly loaded stators described later in this thesis). In both cases the Lieblein diffusion factors were above 0.60 (the nominal limit for attached flow). Despite the extreme diffusion, a relatively small amount of suction (1.5-2.0% and 0.5% of bulk flow respectively) prevented boundary layer separation over most of the span (although not at the non-aspirated end-walls) and enabled predicted stage efficiencies of 86% and 91% respectively.

Although aspiration can be used to improve the state of the boundary layers on a blade row in isolation and enable greater diffusion to be tolerated, its impact on the whole engine cycle must be considered. Aspiration requires energy to be expended on compressing air which does no useful work, i.e. is either recycled (e.g. blowing) or thrown overboard (e.g. suction). This reduces the overall efficiency. The question arises: do the benefits in performance outweigh this cost? Kirtley et al [57] attempted to address this issue for their flow controlled stator. Figure 2.9 (reproduced from Kirtley et al [57]) shows the trade off between the change in stage efficiency with potential stator loss reduction accounting for the penalty for implementing active flow control.

For the case tested (with 1% blowing), a 54% drop in stator total pressure loss resulted in a 2.1% drop in overall stage efficiency, i.e. the cost of implementing the flow control out weighed the reduction in stator loss. At high speed blowing is less deleterious due to the greater pressure ratios; in similar analysis for a high-speed stage, Kirtley et al estimated a 0.5% drop in overall stage efficiency for a flow controlled stator.

2.7 Rotating Stall in Axial Compressors

Rotating stall is one of the most deleterious phenomena that an axial compressor can undergo. In high speed machines it often results in significant damage. It is also one of the least well understood phenomena to afflict axial compressors.

2.7.1 Stall Inception

Rotating stall occurs when the low flow/ high pressure rise stability limit is exceeded. It actually manifests itself as a sector of disturbed flow (i.e. a stall cell) which rotates around the annulus in the same direction as the rotor. Stall inception is the process by which a stall cell comes into being. Two separate stall inception mechanisms have been documented in axial compressors; short length scale “spike” type and long length scale “modal” inception (Camp and Day [8]).

Spike type stall is a short length scale phenomena associated with the break down of the flow in the tip region of a single blade passage. This disturbance develops into a stall cell over the time taken for a few rotor revolutions. As the stall cell grows it slows down; it is well known that the larger the stall cell, the slower it rotates (e.g. Day [14]). Camp & Day [8] also showed that spike type stall inception occurs at a certain critical incidence.

Modal type stall inception is characterised by wave like circumferential variations in velocity around the annulus. Modal disturbances appear as a result of a system instability which occurs when the slope of the total-to-static pressure rise characteristic becomes zero or positive (first predicted by Moore [70]). Infinitesimal disturbances gradually grow in amplitude into a stall cell. Unlike spike type stall there is little change in rotation speed from the initial disturbance to the fully developed stall cell.

The type of inception process which occurs is dependent not only on the compressor design but also on the stage matching in multi-stage machines. Modal stall typically occurs when the compressor is well matched (i.e. at design speed) and spike types stall occurs off design at part speed (Day et al [15]).

2.7.2 Stall Prediction

The tools for stall prediction are little changed from those developed almost 30 years ago by Koch [58]. Koch developed a parameter akin to the length-to-width ratio of a diffuser and came up with a similar correlation to that of Slovran and Klomp for two dimensional diffusers. Koch's parameter is averaged over both the rotor and stator passages and includes corrections for various geometric variables (e.g. stagger, tip clearance, Reynolds number, etc...). Despite the simplicity of this model it gives remarkably accurate predictions of the stalling point of several different compressor stages.

Moore & Greitzer [71] also produced an analytical study of stall inception based on the axisymmetric (i.e. averaged around the circumference) pressure rise characteristic and momentum of the air in the blade passages. This analysis predicted that a compressor becomes unstable at the peak of its steady-state, axisymmetric, pressure rise characteristic.

The proliferation of three-dimensional CFD has led to detailed investigations into the flow over the rotor tips in an attempt to understand the mechanisms behind spike type stall inception. Vo et al [90] proposed a criteria for spike inception of rotating stall based on steady and unsteady calculations of the low Mach number E^3 compressor. Vo et al proposed two key criteria which must be met for spike stall inception to occur:

1. The alignment of the interface between the oncoming and tip clearance flows with the leading edge plane⁷.
2. Net reversed flow across the trailing edge plane at the casing.

These conclusions were in general agreement with those of other authors, e.g. Deppe et al [24]. Vo et al demonstrated that single passage, unsteady (i.e. time accurate)

⁷N.B. as the flow rate is reduced the trajectory of the tip leakage flow swings upstream.

calculations are sufficient to evaluate these criteria. Even given today's computing power, unsteady predictions of a multi-stage compressors are prohibitive in the time scales of a typical design exercise.

It seems appropriate to add a note of warning here. Unpublished data taken on low speed research compressors at the Whittle Laboratory has identified spike type inception in compressors where the interface between the main passage and clearance flow still lies well aft of the leading edge plane at the stall point. It seems more likely that spike stall occurs as a result of a fundamental unsteadiness in the tip clearance flow which is tripped by some external disturbance.

2.7.3 Casing Treatment

One of the approaches used to extend the stall margin of a compressor is casing treatment. In axial compressors it is usually installed in the casing over the rotor tips; casing treatment has been shown to only be effective at increasing the surge margin of tip stalling (i.e. spike-type) compressors (Greitzer [44]). Currently casing treatment is only used to correct surge margin *problems*; i.e. the stage is designed for a smooth wall and when a lack of surge margin becomes apparent casing treatment is added in an effort to correct this. In most cases this stall margin gain is achieved at the expense of efficiency.

2.8 Previous Attempts at High Loading

Various accounts of "highly-loaded" compressors designs and their performance are available in the open literature. In general these papers are specific design/ test reports of individual designs rather than investigations into the limits and effects of high loading. The latter is the principal focus of the current work.

Wennerstrom [94] presented a review of the attempts to achieve high loadings in axial compressor up to the 1970s. As elsewhere in the open literature, the definition of "high-loading" used by Wennerstrom refers to the overall enthalpy change and not solely to high stage-loading coefficient⁸. These were all supersonic designs which attempted very

⁸The stage loading coefficient is defined as the overall enthalpy rise, Δh_0 , normalised by the square

high pressure ratios via a combination of high stage loading and high wheel speed. Many early attempts at highly loaded designs failed because generally accepted loading limits (e.g. diffusion factor) were ignored, e.g. the Curtis-Wright counter rotating compressor which had diffusion factors above 1.0 and an overall efficiency barely above 73%. One conclusion Wennerstrom [94] reached was that “it is often easier and more successful to design for increased Mach number than to achieve the same objective with exceptionally high diffusion levels”.

Lyes and Ginder [66] tested a highly loaded stage in a low-speed, four stage research compressor. The design of this stage was a scaled version of stage four of the *Qinetiq* (formerly the *Defence Evaluation and Research Agency*) C147 highly loaded compressor. The low-speed stage had the same design flow and stage loading coefficients, 0.60 and 0.50 respectively, as the high speed compressor. This compressor achieved a efficiency of 88.5% and a stage loading coefficient of 0.54 at the design flow rate. At the design flow rate the measured rotor and stator de Haller numbers (at mid-height) were 0.663 and 0.656 respectively (de Haller suggested a minimum limit of 0.75). Design diffusion factors for the rotor and stator were fairly conventional at 0.48 and 0.44 respectively (in modern aero-engines typical values are generally below 0.5, Bolger [3]).

McNulty et al [68] performed one of the few direct comparisons between a highly loaded and lightly loaded stage available in the open literature. The highly loaded stage had a typical diffusion factor of 0.47. Although not explicitly reported, the mid-span stage loading coefficient can be estimated from other information presented in the paper (e.g. radial profiles, pressure rise characteristics). The estimated stage loading coefficient is approximately 0.54 (assuming repeating stage conditions) and the efficiency is approximately 89%; approximately 2% lower than the efficiency of the conventionally loaded stage. The highly loaded stage also had considerably less stall margin (defined in Equation 2.8) than the conventionally loaded stage, 15% and 45% respectively. The conventionally loaded stage had typical rotor diffusion factor 0.41 and was estimated to have a stage loading coefficient of approximately 0.39.

$$SM = \frac{\overline{\phi_{\eta_{max}}} - \overline{\phi_{stall}}}{\overline{\phi_{\eta_{max}}}} \quad (2.8)$$

of the blade speed, i.e. $\frac{\Delta h_0}{U_{mid}^2}$. The stage loading coefficient is independent of blade speed and shows that enthalpy rise (closely related to pressure rise) can be increased by either increasing the blade speed or the stage loading coefficient.

McNulty et al [68] focused on the effect of forward sweep on tip clearance flows. Figure 2.10 is reproduced from McNulty et al [68] and shows that the highly loaded “Configuration 1” is more sensitive to changes in tip clearance than the conventionally loaded “Configuration 2”; in terms of efficiency, a 1% of chord change in clearance gap leads to an efficiency drop of almost four times that for the lightly loaded stage. The rate of reduction in surge margin also increased with loading. This was mitigated somewhat by forward sweep which halved this penalty. McNulty et al attributed this to double leakage⁹ which was reduced by forward sweep. The more lightly loaded stage was almost insensitive to forward sweep.

Kirtley et al [57] designed an aspirated stator for the high-reaction stage described by McNulty et al. The solidity was reduced to increase the diffusion and encourage separation; the Lieblein diffusion factor increased from approximately 0.50 to 0.60 (the generally accepted limit for attached flow). This stator was tested both with and without blowing. The effects of aspiration are discussed elsewhere (Section 2.6.3) and so only the case without aspiration shall be covered here. Although absolute levels of efficiency were not reported, the high diffusion stator reduced the stage efficiency by 0.9% (without aspiration). Traverse measurements made behind the stator showed a very thick (approximately 20% of pitch), separated, wake over most of the span and a large hub loss core at 15% of span. High blockage was present over most of the pitch at the casing as a result of the high end-wall loading. In general, it can be concluded that attempts at high-diffusion factor stages have not been successful, typically suffering from large separations and corresponding efficiency penalties.

2.8.1 Highly Loaded Fans

Very high loadings do regularly occur at the fan hub in a high-bypass ratio engine; the low hub to tip ratio causes a large variation in stage loading from hub to tip in order to maintain constant work input across the span.

Bryce et al [7] describe the testing of a highly loaded single stage transonic fan. The

⁹Double leakage (discussed by Khalid et al [56]) is where the low total pressure/ high loss tip clearance flow is ingested by the adjacent tip gap, i.e. the clearance flow passes over *two* rotor tips (hence the name “double-leakage”) before exiting the rotor row. This leads to increased mixing losses because of the larger velocity difference between the clearance flow (slower due to reduced total pressure) and the free stream flow.

stage loading coefficient at hub, mid-span and tip were approximately 1.22, 0.54 and 0.34 respectively. At the hub the stator diffusion factor was 0.56, dropping to an approximately constant 0.43 from mid-span to the casing. Unsurprisingly, given the high loading, a large separation is present at the stator hub. Contour plots of stator exit Mach number presented by Bryce et al. show a large loss core/ three-dimensional separation at 11% of span on the stator suction surface which reduces in extent towards the hub. The result was that, despite the reasonable loadings elsewhere, this fan only achieved a peak efficiency of 84% at design speed (although some allowance must be made for Mach number effects).

Friedrics et al [35] had a similar experience with a low speed, low hub to tip ratio compressor. The stage in question had an average stage loading coefficient of 0.56 (based on mid span blade speed) and achieved an efficiency of approximately 88%. Despite the high loading, diffusion factors were well within accepted limits (0.45-0.50 at mid-span), however, the low hub-tip ratio results in an extremely highly loaded hub; the stator hub de Haller number and diffusion factors were 0.56 and 0.62 respectively. As above, a large separation was present in the stator hub.

2.9 Summary

Compressor design typically starts with one-dimensional, mean-line, correlations. However, these generally rely on empirical data from previous conventionally loaded designs. Any errors in the design at this stage are invariably very difficult and expensive to address. The accuracy of these mean-line correlations is therefore of paramount importance. The basis for some of the most widely used loss correlations has been discussed.

Two and three dimensional design has progressed significantly with the development of two and three-dimensional CFD. Controlled diffusion blades and later three-dimensional modifications (e.g. sweep and lean) have increased operating range, tolerable diffusion and efficiency.

In general the highly loaded and high diffusion designs have suffered from poor efficiency and restricted stall margin. Many of the early attempts exceeded now commonly accepted loading limits, such as de Haller number and diffusion factor. Most of the highly-loaded designs discussed above concerns attempts to design and test a specific

fan or compressor. The purpose of the current work is to provide a more general study of the problems associated with the design of compressors which operate well beyond conventional loading levels.

Chapter 3

Experimental Methods

3.1 Introduction

There is currently very little practical experience with stages of very high loading. A detailed experimental investigation was carried out on three highly loaded stages (and one conventionally loaded datum stage) to address this deficiency. The purpose of this experimental program was to generate a body of data which could be used to identify key flow features at high stage loadings and ultimately establish a limit, below which compressor designs of satisfactory performance can be achieved. In addition, this data can be used to calibrate the accuracy of computational fluid dynamics (CFD) programs. Key measurements taken as a part of this program included:

- Area traverses, carried out with pneumatic and hot-wire probes, to investigate the rotor and stator flow.
- Unsteady casing static pressure measurements to study the rotor tip leakage flow.
- Pressure rise, torque and efficiency characteristics to record the overall stage performance.

Experimental analysis is still the only method of generating reliable data on stall-inception and stall margin. Stall can have catastrophic consequences in a real aero-engine and therefore stall margin is one of the most important parameters that must be considered during compressor design. Information on stall, and how it is affected by increasing stage loading, is therefore also of great interest to the compressor designer.

This chapter documents the procedures and techniques used to achieve a high degree of confidence in this experimental investigation, in particular the consistency of the measurements between each of the four stages tested. To this end, the uncertainty in each measurement has been estimated and is shown to be well within tolerable limits.

3.2 Highly Loaded Research Compressor

The Highly Loaded Research Compressor (HLRC) is a single stage, low-speed test facility at the Whittle Laboratory, Cambridge. It rotates at 3000rpm giving a mid-span blade speed of $63.62ms^{-1}$ and average rotor and stator Reynolds numbers of 2.6×10^5 and 2.0×10^5 respectively (see Table 4.1). It is a low speed version of a typical stage in a high pressure compressor of a modern aero-engine. All the stages described in this thesis were tested in this rig under the same conditions and with the same techniques. The arrangement of the HLRC is illustrated in Figure 3.1.

The HLRC is a vertical axis machine with air flowing from top to bottom. Air enters the rig through a honeycomb screen and into a large plenum in order to remove any long length scale disturbances. It then passes through an inlet contraction before entering the working section. The mass flow rate through the machine is controlled by a variable throttle downstream of the working section. The exit flow is ducted away from the HLRC. This is intended to minimise the re-ingestion of highly turbulent exit flow. A schematic of the parallel working section is shown in Figure 3.2. The working section has a hub-to-tip ratio of 0.8.

A turbulence grid and boundary layer spoilers are present up-stream of the research stage to attempt to mimic the turbulence levels and end-wall boundary layers observed in multistage machines. A similar approach was adopted by Place et al [75] on the Deverson rig (another single stage, low-speed, research compressor at the Whittle Laboratory). For the datum and Denton builds a row of inlet guide vanes (IGVs) was present upstream to provide the required swirl into each stage.

Place et al [75] also included a pressure loss screen down-stream of the research stage to mimic the axisymmetric potential effects of a down-stream stage. The additional pressure loss that this method incurs significantly reduces the operating range of the compressor. Place et al were able to maintain operating range by using an auxiliary

fan downstream of the research stage to overcome the additional pressure loss. As no auxiliary fan is present on the HLRC it was not possible to use such a down-stream pressure loss screen and maintain adequate operating range.

The design of each of the four stages tested is described in detail in Chapter 4 and so only the stage installation will be discussed here. The roots of the rotor and the stator blades (at the hub and casing respectively) were sealed with a small silicone fillet to prevent leakage. Two of the stages tested (the datum and Gallimore stators, see Chapter 4) were designed to be “built in” at the stator hub. Physical constraints precluded the use of a similar silicone fillet to seal the stator hub. In these cases, care was taken to ensure a very tight fit.

The rotating hub extends approximately 0.64 axial chord lengths upstream of the leading edge and ends approximately 0.09 axial chord lengths downstream of the rotor trailing edge. In all cases the stator hub was stationary. In cases with clearance at the stator hub the rotation of the end-wall, found in cantilevered engine geometries, cannot be modelled in the HLRC. Similarly, in cases with built in stators, no attempt was made to model or include the effects of the shroud flow; effectively the built in stators were cantilevered with zero clearance.

The Gallimore, Qinetiq and Mini-Deverson stages were all run with a stationary tip clearance of 1.1% of span (an average of 1.0% of true chord). The Denton stage was run with an increased stationary clearance as the lean at the rotor tip was observed to straighten out under centripetal acceleration. It was therefore decided to increase the stationary clearance of this stage to 1.4% of span (1.0% of chord). The magnitude of this effect is unclear and therefore so is the running tip clearance.

3.3 Data Acquisition

Signals from the various transducers used in this work were recorded by a personal computer fitted with data acquisition hardware. The data acquisition hardware used was a *National Instruments* PCI-MIO-16E-1. This consisted of a 12 bit analogue to digital converter and a (up to) 16 channel multiplexer. The resolution of the analogue to digital converter is given in Table 3.1 for each of the different types of transducer used.

Transducer	Voltage Resolution	Real Units Resolution
Steady Pressure	$\pm 0.6mV$	$\pm 0.6Pa$
Unsteady Pressure	$\pm 1.2mV$	$\pm 0.6Pa$
Hot-wire “DC” signal	$\pm 0.6mV$	$\pm 0.010ms^{-1\dagger}$
Hot-wire “AC” signal	$\pm 0.24mV$	$\pm 0.003ms^{-1\dagger}$
Torque	$\pm 0.6mV$	$\pm 0.005Nm$

Table 3.1: Transducer resolution. ([†]At typical velocities.)

In theory this hardware allowed a minimum inter-channel delay of $1\mu s$, i.e. the maximum sampling rate for 1 channel was 1Mhz, for 10 channels it was 100kHz and so on. In practice the maximum sampling rates achievable were below these figures to ensure adequate settling time between adjacent channels. The magnitude of the required settling time and the cross talk between adjacent channels was dependent on the nature of the signals being recorded. Care was taken to ensure this effect was insignificant even at the highest sampling rates used.

The data acquisition and control of the traverse gear (described in Section 3.8) was controlled by a series of bespoke programs written in the *LabVIEW* programming language.

3.4 Pressure Measurements

Steady state pressure measurements (such as those taken during pneumatic probe area traverses and to record pressure rise characteristics) were obtained with *SensorTechnix* +1psi pressure transducers. These were calibrated against an inclined silicone manometer. The calibration coefficients did not change over the period of 18 months during which all the experiments described were carried out.

These pressure transducers have a zero pressure offset. These were fairly constant over time but to eliminate this potential source of error the zero offset was recorded before every experiment and accounted for in the data logging software. The offset was also recorded after each experiment as a check. The maximum offset drift observed was

$\pm 2.4mV$ or $\pm 2.2Pa$ over the course of a stator exit area traverse; the longest experiment performed, taking about 100 minutes. Along with the discretization error this a total accuracy of $\pm 2.8Pa$ or 0.1% of expected total pressure rise.

All pressure rise and flow rate measurements were referenced to the stagnation pressure upstream of the inlet contraction measured by three pitot probes at this location (see Figure 3.1). The upstream pitots and the casing static pressure tappings at each axial location were connected to a single manifold whose common pressure was recorded. This pneumatically averaged pressure was shown to be within 0.05% of the true arithmetic value.

3.5 Torque Measurements

It is vital to measure the work input into the compressor to accurately establish the stage efficiency. The work input to each compressor stage was found from the product of the rotational speed and the measured shaft torque.

The motor driving the HLRC is mounted on low friction gimbals. The rotational movement of the motor is resisted by an arm resting on a load cell. The output from this strain gauge can be used to measure the torque applied by the motor to the research rotor.

Before and after each set of measurements the load cell was calibrated. A series of known loads was applied to the torque arm at a known radius via a mass and pulley system. The observed maximum drift in the calibration coefficient over a series of experiments was within $\pm 0.5\%$. Before and after each measurement, the torque meter zero offset was recorded and accounted for in the data logging program. The maximum drift in this offset was observed to be $\pm 1.2mV$ or $\pm 0.01Nm$.

Assuming a stage loading coefficient of 0.65 at a flow coefficient of 0.50 (typical of the three highly loaded stages), the accuracy of the torque measurement was assessed as $\pm 0.06Nm$ or $\pm 0.3\%$ of a typically expected value.

3.6 Mass Flow Rate

The mass flow rate through the HLRC was determined from the inlet total pressure and the casing static pressure measured immediately downstream of the inlet contraction (Figure 3.2, Plane “a”). The mass flow rate (or average axial velocity) is given by Equation 3.1. The calibration coefficient, K , was obtained from a series of pneumatic probe traverses at the inlet to the working section; a value of 0.981 was found to be appropriate.

$$\dot{m} = \rho A \bar{V}_x = \rho A \times K \sqrt{\frac{2(P_{0,in} - P_{in})}{\rho}} \quad (3.1)$$

The aforementioned error in steady pressure measurement translates to a possible error of $\pm 0.2\%$ in measured mass flow rate between builds. Allowing for errors during the calibration traverse this rises to an absolute uncertainty in mass flow rate of approximately $\pm 1\%$.

3.7 Pressure Rise and Efficiency Characteristics

The pressure rise and efficiency characteristics are one of the most important methods of assessing the performance of a compressor. For this reason their measurement and derivation needs to be well defined.

3.7.1 Pressure Rise and Torque Characteristics

The casing static pressures and torque were measured continuously as the mass flow rate was reduced until the stage dropped into rotating stall, at which point data acquisition was stopped. Throughout this work characteristic measurements are presented in the non-dimensional forms given in Table 3.2.

By continuously reducing the mass flow rate slowly it is reasonable to assume that the compressor is operating in a quasi-equilibrium state during the time taken to record

Variable	Nomenclature	Non-dimensional Group
Flow coefficient	$\bar{\phi}$ or $\frac{V_x}{U_{mid}}$	$\frac{\dot{m}}{\rho A U_{mid}}$
Total-to-total pressure rise	ψ_{t-t}	$\frac{P_{0,ex} - P_{0,in}}{\frac{1}{2}\rho U_{mid}^2}$
Total-to-static pressure rise	ψ_{t-s}	$\frac{P_{ex} - P_{0,in}}{\frac{1}{2}\rho U_{mid}^2}$
Static-to-static pressure rise	ψ_{s-s}	$\frac{P_{ex} - P_{in}}{\frac{1}{2}\rho U_{mid}^2}$
Stage loading coefficient	$\frac{\Delta h_0}{U^2}$	$\frac{Q}{\dot{m} r_{mid}^2 \omega}$

Table 3.2: Characteristic non-dimensional groups.

a single characteristic point. Each characteristic point is derived from the mean of 2000 pressure or torque measurements over a period of 0.2s. To ensure consistency the characteristic was typically repeated several times for each configuration tested.

This method has two key advantages over a discreet point method (as is usually performed); (1) it allows characteristic to be obtained quickly, typically in under 2-3 minutes; and (2) it allows the stall point, and the shape of the characteristic near to stall, to be accurately determined.

The inlet total pressure pitot probes are situated upstream of the inlet bell-mouth, turbulence grid, end-wall boundary layer spoilers and IGVs (Figure 3.1). Therefore, they do not account for the total pressure drop across these obstacles. The total pressure drop between the inlet pitot probes and the inlet to the working section (downstream of the IGVs if present) was recorded by pneumatic probe area traverses at a range of different flow coefficients. These were reduced to a single loss coefficient (averaged across all flow rates) for each stage which was used to derive the inlet total pressure.

3.7.2 Efficiency Characteristics

Discrete efficiency characteristics were derived from three-hole pneumatic probe area traverses and the continuously measured torque characteristic described in Section 3.7.1. The area traverse data was averaged to obtain the total-to-total pressure rise across each stage at typically five to six of flow coefficients. The torque at each of these flow coefficients was obtained by evaluating a polynomial fitted to the continuous torque characteristic. The efficiency can then be evaluated by Equation 3.2.

$$\eta = \frac{\psi_{t-t}}{2\frac{\Delta h}{U^2}} = \frac{\dot{m}\Delta P_0}{\rho Q\Omega} \quad \text{where: } Q = \text{total shaft torque} \quad (3.2)$$

Equation 3.2 assumes that the flow is incompressible. This is a reasonable assumption as the density rise across the HLRC is only about 1.8% of the inlet value.

The uncertainty in the absolute efficiency measurements is $\pm 1.5\%$ or $\pm 0.6\%$ between builds. The higher error in the measurement of the absolute efficiency is due to the uncertainty in the measurement of the absolute mass flow rate.

For a repeating stage, a good estimate of the total-to-total pressure rise is given by the static-to-static pressure rise across the stage. The static-to-static pressure rise was also used in Equation 3.2 to estimate the continuous efficiency characteristic of each stage.

3.8 Traverse Procedure

The flow at inlet to each stage and immediately down-stream of the rotor and stator were investigated with area traverses performed with hot-wire and three-hole pneumatic probes.

Probe access to the working section is effected via a series of slots. The location of these slots is shown in Figure 3.2 (labelled “T”). These slots cover a circumferential distance of approximately 27.5° . This is roughly equivalent to 2 to 3 stator pitches depending on the stage in question.

A tight fitting foam seal is used to minimise leakage flow through the slot (Figure 3.3).

This foam is laced with graphite powder to reduce the drag on the probe when it is in motion. The face of this foam seal lies flush with the casing of the compressor when in place. One end of the foam seal is open ended so that a fragile hot-wire probe could be mounted without damage. The probe would be positioned in the working section before slipping the foam seal over the probe stem and locating it in the slot. Once in place the open end of the foam seal is blocked up with plasticine (Figure 3.3B). When not in use this foam seal was replaced with a solid aluminium blank.

Both the pneumatic three-hole and the hot-wire probes were carefully aligned with the flow direction at the inlet traverse plane (Figure 3.2). No IGVs or turbulence grids were present during this process and therefore the flow was assumed to be aligned with the rig axis. This null position was accurate to within $\pm 0.05^\circ$ and $\pm 0.4^\circ$ for the three-hole and hot wire probes respectively. All the probes used were fitted with an offset dowel (Figure 3.4). This mated with the probe-rotation traverse to locate the probe angle accurately. This allowed the probe to be removed and replaced at the same angular position to within $\pm 0.02^\circ$.

The probes were positioned radially in the compressor by gently touching them on the hub. In the case of the hot-wire probe a dummy probe was used to prevent damage to the hot-wire. The hot-wire was then mounted and the probe offset radially by the difference in length between the dummy and real probes.

3.8.1 Traverse Gear

Circumferential and spanwise traversing is provided by a commercially available X-Y traverse mounted in the $R - \theta$ plane. A bespoke yaw traverse was also fitted to rotate the probe along its own axis. All three axes were driven with stepper motors with micro-stepping enabled. On the Cartesian traverse this gave a step size of 0.0025mm and on the yaw axis this gave a step size of 0.09° . Both the X and Y axes were fitted with home switches. This allowed the traverse gear to be positioned accurately to within one step or $\pm 0.0025\text{mm}$ before the start of each traverse.

No home switch was fitted to the probe rotation axis. Instead a dowel pin was used to ensure the yaw traverse was aligned with a fixed datum before the start of each traverse. This method was accurate to within one step of the yaw traverse or $\pm 0.09^\circ$ of probe

yaw. The fit of the dowel pin was checked at the end of each traverse. At no point was any slip or change in the fit of the dowel pin observed.

The probe head followed the same route for all traverse experiments, moving from hub to casing during radial traverses and as illustrated in Figure 3.5 for a typical area traverse. When determining the probe position, the traverse control program accounted for the probe yaw angle and the perpendicular offset between the measurement point and the probe stem. The available traverse gear did not allow similar correction for the corresponding change in the axial position of the measurement point with yaw angle.

The traverse gear could be moved to different axial locations in the compressor by a series of spacer blocks placed between the Cartesian traverse gear and the yaw traverse gear.

3.8.2 Pneumatic Probe Traverse

A three-hole pneumatic probe was used to measure total pressure, swirl angle and dynamic head. In particular, it is necessary to measure the total pressure to determine the useful work done on the flow, i.e. the total pressure rise, and therefore efficiency of the stage. Total pressure measurements can also be used to give a good estimate of loss generation through a blade row. A photograph of the probe used is shown in Figure 3.4.

The pressures at each traverse point were measured over a period of 2s at 1000Hz and the mean taken. The probe was then moved to the next traverse point and then allowed to settle for 2s before logging the next point. Pressures were recorded with the transducers described in Section 3.4.

Typically three-hole probe traverses were performed over two stator pitches (or two IGV pitches) and consisted of 25 radial points and 41 circumferential points. The radial points were clustered towards the hub and the casing to better resolve the boundary layer and three dimensional flow in these regions. An example of a typical traverse grid is given in Figure 3.5. The radial grid extended to within 2.5% span of the endwalls. This was felt to be a sensible limit given the size of the probe head and the range of yaw angles at which it was required to be used at.

This probe was calibrated in a (steady flow) calibration wind tunnel for total pressure, dynamic head and yaw coefficients (as described by Place [74]) over a wide range of yaw angles. Calibration was performed at two Reynolds numbers. The calibrations for yaw and total pressure coefficient were observed to be Reynolds number independent at all but the most severe yaw angles. The calibration for dynamic head coefficient did have a slight Reynolds number variation; in the range $\pm 15^\circ$ from the nulled position the difference between the high and low Reynolds number calibrations was 1.5%. This corresponds to a 0.75% error in measured velocity. This was deemed to be acceptable. In practice the higher Reynolds number calibration was used as this was typical of the Reynolds numbers expected in the HLRC.

In traverses behind the rotor, an automated probe nulling routine was employed to align the probe approximately to the oncoming flow before a measurement was taken. At each point the probe was aligned to within $\pm 5^\circ$ and then calibration curve was used to obtain a more precise value. This procedure of “near-nulling” the probe ensured that the flow was well within the range at which the calibration was most reliable and was wide enough such that the time penalty was small.

The “near-nulling” routine was not used at stator exit or behind the IGVs at inlet. It was found that in the stator wakes the dynamic head was so low that the flow angle was effectively indeterminate. The probe nulling algorithm had difficulty dealing with this and the time penalty became impracticable. Therefore the probe nulling algorithm was disabled behind stationary blade rows and the probe yaw angle was fixed to approximately the design intent. This did not significantly affect the quality of the results as behind a stationary blade row the flow angle does not vary significantly across the span or with flow coefficient.

The uncertainty in yaw coefficient was assessed to be within ± 0.03 of the true value at typical conditions in the HLRC. This is equivalent to an error of $\pm 0.3^\circ$. When combined with the set-up and calibration errors described above this gives the total accuracy of the flow angle measurement as $\pm 0.5^\circ$. The uncertainty in the measurement of stagnation pressure is within $\pm 0.5\%$ of the expected dynamic head.

The calculated uncertainty in the dynamic head measurement was $\pm 3\%$ or $\pm 1.5\%$ of velocity. Three-hole probes are known to be deficient in the measurement of velocity. Increasing the distance between the pressure tappings and the probe stem has been

shown to reduce the errors in velocity measurement, especially when close to the end-walls (Smout & Ivey [83]). Care was taken to select a pneumatic probe with pressure tappings protruding well forward of the probe stem (by approximately 2.5 stem diameters) but allowing sufficient clearance between the trailing edge and the measurement point. Rotor exit radial velocity profiles measured by a three-hole probe were compared to the velocity profiles derived from a phase locked hot-wire traverse. The difference between these two was less than $\pm 1.5\%$ across the whole span. This gives confidence in both methods of velocity measurement.

Due to the small-scale of the HLRC the probe head occupies a significant fraction of pitch; approximately 7% of stator pitch. Early on in the project traverse data was compared with and without a spatial correction routine. This did not significantly change the results and therefore the subsequent data was analysed without the spatial correction routine for the sake of simplicity.

Another possible source of error is the use of a probe calibrated in a steady flow in a highly unsteady environment and the natural averaging that occurs in the probe and pressure measurement system. The precise nature of this error is dependent on the specifics of the probe geometry and plenum volume (Samoilovich & Yablokov [78] and Grant [42]). These errors are small and usually within tolerable limits.

3.8.3 Hot-wire Traverse

A single element hot-wire was used to measure the turbulence intensity at rotor inlet and phase locked velocities and flow angles at rotor exit. These measurements are not possible with a steady-state probe such as the three-hole probe described above and give some additional insight into the rotor flow. Directly before and after each series of experiments the hot-wire was calibrated in a steady flow calibration wind tunnel. A King's law calibration for velocity measurement was used. Over the course of a day or a series of experiments (whichever was shorter) the uncertainty due to calibration drift was observed to be within 2.5% of the typical velocities observed in the HLRC.

The temperature at the start and end of each hot-wire traverse was recorded and the mean of these two values used to apply a temperature correction (of the form presented by Bearman [2]) to the hot-wire measurements.

Build	Turbulence Intensity [%]	Integral Length Scale [mm]	Integral Length Scale ($\frac{\lambda}{C}$) [%]
Mini-Deverson	5.9	2.4	6.7
Gallimore	5.5	2.7	4.7
Qinetiq	5.5	2.9	5.4
Denton	5.1	2.5	4.0

Table 3.3: Area averaged inlet turbulence characteristics at stage inlet.

At each traverse point unsteady hot-wire data was recorded at 100kHz typically over a period of 2s (100 rotor revolutions). This gives a minimum of 40 points per blade passage in the datum case and more in the cases of the three highly loaded designs. To prevent aliasing the unsteady signal was low-pass filtered at 30kHz.

Inlet Hot-Wire Traverses

Hot-wire traverses were performed at stage inlet (behind the turbulence grid and IGVs, if present) primarily to measure the turbulence properties entering each stage. These traverses covered one IGV or stator pitch and extended to within 2.5% span of the endwalls. The hot-wire probe angle at each point was set to the flow angle measured during the three-hole pneumatic probe traverse described above.

Turbulence intensity and length scale were derived using the method described by Camp and Shin [9]. Fluctuations due to blade passing (e.g. the wake at rotor exit) and to a lesser extent once per revolution variations, can unrealistically inflate turbulence measurements. In the method of Camp and Shin, these deterministic periodic fluctuations and their harmonics are filtered out of the hot-wire signal before calculating the turbulence properties. The averaged turbulence intensity and integral length scales of the flow for all four stages tested are given in Table 3.3.

Rotor Exit Hot-Wire Traverses

Radial traverses with a hot-wire probe were performed to resolve circumferential variations in the flow field downstream of the rotor (e.g. the rotor wakes). A once per revolution signal also recorded from an optical sensor switch which detected the position of a reflective indicator mounted on the rotor disc. During post processing, the once per revolution signal was used to phase-lock and ensemble average the hot-wire data over approximately 100 rotor revolutions. This allowed blade to blade variations in velocity and flow angle to be resolved with a stationary probe. Unlike previous phase-locked and ensemble averaged measurements (which only typically measured over a few rotor pitches), the data logging equipment and custom software allowed the flow downstream of *every* rotor blade to be recorded. Due to the time and data storage requirements these traverses typically consisted of measurements along a single radial line.

A method similar to that described by Dambach & Hodson [13] was used to measure the ensemble average flow direction and velocity with a single element hot-wire. At each traverse point the velocity field was sampled at 19 angular positions over a range of $\pm 45^\circ$ about the flow angle measured by the three-hole probe described above.

The velocity measured by a hot-wire is approximately a linear function of $\tan(\alpha)$ and the magnitude of the velocity vector (in the range $-90^\circ < \alpha < +90^\circ$). This is a simple rearrangement of the result presented by Bruun [6]; that the velocity measured by a hot-wire is approximately equal to the component of the velocity vector normal to the sensing element (Equation 3.3) and is illustrated in Figure 3.6A. Equation 3.3 can be rearranged to form Equation 3.4. Definitions of the angles used are illustrated in Figure 3.6 (inset).

$$V_m = \tilde{V} \cos(\alpha - \alpha_{hw}) \quad (3.3)$$

$$\frac{V_m}{\cos \alpha_{hw}} = \tilde{V} \sin \alpha \tan \alpha_{hw} + \tilde{V} \cos \alpha \quad (3.4)$$

Where:

\tilde{V} = magnitude of the velocity vector

V_m = velocity derived from the hot-wire probe

α = flow angle

α_{hw} = hot-wire probe yaw angle

Equation 3.4 is in the form of a straight line:

$$Y = mX + c \quad (3.5)$$

Where:

$$\begin{aligned} X &= \tan \alpha_{hw} \\ Y &= \frac{V_m}{\cos \alpha_{hw}} \\ m &= \tilde{V} \sin \alpha \\ c &= \tilde{V} \cos \alpha \end{aligned}$$

The flow angle can be determined from the coefficients of Equation 3.4 (i.e. “m” and “c”) which are found by fitting a straight line to the ensemble averaged measurements using a least squares method. At probe angles greater than about $\pm 30^\circ$ from the flow direction the deviation from the cosine approximation of Equation 3.3 becomes significant. Therefore points greater than $\pm 30^\circ$ from the maximum measured velocity are excluded from the line fit. The line fitting process is illustrated in Figure 3.6B. Evaluating the flow angle in this manner gave good results even in cases where the straight line fit was poor. However, in the few cases where the straight line fit was poor (usually in slow, highly turbulent flow, e.g. near to the end-walls), evaluating the flow velocity from the coefficients of the best fit line gave significant errors. In order to make the algorithm robust and reliable for all cases the flow velocity was obtained by interpolation rather than from the best fit coefficients.

The mass averaged flow angle derived via this method was within $\pm 0.5^\circ$ of that measured with the three hole probe. Furthermore the accuracy of this method was established to be $\pm 0.1^\circ$. When setup uncertainties are included, this value rises to $\pm 0.5^\circ$.

3.8.4 Derivation of Averaged Quantities

Area traverse data was reduced to radial profiles by performing a mixed out average in the pitch-wise direction. A detailed description of the method used is given in Bolger [4]. A mass averaging procedure was then used to reduce the radial profile to a 1D value. Again this is similar to the method used by Bolger. The argument behind

Traverse Location	Variable	
	Total Pressure	Velocities
Inlet	$\frac{P_0 - P_{upstream}}{1/2\rho V_x^2}$	$\frac{V}{\overline{V}_x}$
Rotor Exit	$\frac{P_0 - \overline{P}_{0,inlet}}{1/2\rho U_{mid}^2}$	$\frac{V}{U_{mid}}$
Stator exit	$\frac{P_0 - \overline{P}_{0,inlet}}{1/2\rho U_{mid}^2}$	$\frac{V}{U_{mid}}$

Table 3.4: Non-dimensional groups used to present traverse data. *N.B.* the overbar represents pitch and span-wise averaged quantities.

this averaging strategy is that pitch-wise variations, i.e. wakes, mix out quickly whereas span-wise variations persist much further downstream.

3.8.5 Presentation of Traverse Data

Throughout this work, traverse results are presented in terms of the non-dimensional forms given in Table 3.4.

3.9 Unsteady Pressure Measurement

Unsteady casing static pressures were used to resolve the blade to blade pressure field over the rotor tip and also to record stall-inception. Figures 3.2 and 3.7 show the locations of the pressure transducers for each of these types of measurement. In both cases the transducers were mounted flush to the casing.

The fast response pressure transducers chosen for this application were of the type manufactured by *Kulite Semiconductor*. These were statically calibrated before use. Before and after each series of experiments the zero pressure voltages were recorded and used to account for the offset in the recorded pressure signal. These measurements were assessed to be accurate to within $\pm 2Pa$ or $\pm 0.3\%$ of the expected dynamic head at inlet.

3.9.1 Rotor Tip Static Pressure Measurements

The effect of stage loading on the rotor tip clearance flow was studied by recording the casing static pressure over the rotor tip. Thirteen fast response pressure probes were mounted as illustrated in Figure 3.7. The signals from these were logged at 71.4kHz (as high as was possible to allow adequate settling time between adjacent channels). This is equivalent to more than 33 points per blade passage in cases of the three highly loaded designs and 28 points per blade passage in the case of the datum stage. A selection of the fast response pressure probes were logged at a higher frequency to check for aliasing. The spectra were identical indicating that aliasing was not a problem.

Similar data reduction techniques to those employed in the analysis of the hot-wire data were used to resolve the blade to blade pressure field at the rotor tip. The once per revolution signal was used to phase lock the pressure signals to the rotor position which were then ensemble averaged over approximately 250 rotor revolutions.

3.9.2 Stall Inception

Stall is one of the most catastrophic phenomena to afflict axial compressors. The stall inception mechanism of the three highly loaded stages tested is therefore of interest. Stall inception was recorded with six kulites equispaced around the circumference, mounted between 10% and 20% of rotor chord upstream of the rotor leading edge (Figure 3.2). The signal from these probes was logged at 5000Hz and filtered at 1000Hz to prevent aliasing. This also removed the deterministic fluctuations from the blade passing (occurring between 1800Hz and 2550Hz) which can mask small scale rotating disturbances, e.g. nascent modal disturbances. The inlet static pressure signal was also recorded and used to stop data acquisition once the inlet mass flow dropped below the stalling value. This ensured the stall point was always included in the range of data capture. Data from approximately 200 rotor revolutions before stall to approximately 50 rotor revolutions after stall were saved.

Stall inception data is presented in the form of Figure 5.33. The data from each kulite is offset along the ordinate by an amount proportional to its position. In this way, rotating disturbances (e.g. stall cells) can be tracked from one kulite to the next and their speed easily determined by the gradient of the line passing through a given disturbance.

3.10 Flow Visualisation

Boundary layer separation and transition are likely to become more significant at increased loading. Oil and dye flow visualisation has been previously used to diagnose separations and boundary layer transition. This approach is also widely used to obtain skin friction patterns on blade surfaces and end-walls (e.g. Deppe et al [23, 24] and Gbadebo [39]) and is described by Hodson [50]. Oil and dye flow visualisation was used on the stator blades, stator end-walls, rotor casing and on the rotor hub.

Fluorescent paint pigment was mixed with a silicone oil. This was applied to the relevant surfaces. Typically, red paint was used on blade surfaces and green paint on the end-walls to allow easy identification of the source. The compressor was then run at the appropriate operating point until this mixture had dried. This typically took about one hour. The results were then photographed under ultra-violet light for maximum contrast.

Some success was had with this technique in diagnosing a separation bubble on the rotor suction surface of the Qinetiq stage. The edges of the separation bubble showed up clearly as two dark lines (Figure 6.3). This is discussed in more depth in Chapter 6.

3.11 Summary

The experimental methods and apparatus used to measure the performance of a single stage have been described. Estimates of the experimental errors associated with the techniques and data reduction methods described have been made and are well within tolerable limits. Where appropriate presentation techniques have been explained and discussed. The methods described have been used to obtain a comprehensive and consistent set of data which can be used to compare stage designs with a high degree of confidence.

Chapter 4

Three Highly Loaded Stages - Design Attributes

4.1 Introduction

Three highly-loaded stages were designed and tested in the Highly Loaded Research Compressor (HLRC) at the Whittle Laboratory. These stages were designed by Gal-limore¹, a team at Qinetiq² and by Denton³. Additional design details of the former two stages are given by Hughes [53] and Horton [51] respectively.

A conventionally loaded stage was also manufactured for testing in the HLRC as a datum stage against which the three highly loaded stages could be compared. This was a scaled version of the Deverson Build II stage; another well studied low-speed research compressor at the Whittle Laboratory.

The design points of these four stages are illustrated on the Smith Chart ($\frac{\Delta h}{U^2}$ vs. $\frac{V_x}{U}$) presented in Figure 4.1. The range of design points typical of modern civil aero-engines is also marked. All three highly loaded stages were designed to give a stage loading coefficient of 0.65 at flow coefficients of 0.50, 0.60 and 0.65 respectively. It should be noted that these stage loadings are almost 50% higher than currently in mainstream

¹Rolls-Royce plc.

²G.C. Horton et al

³Whittle Laboratory, Cambridge University Engineering Department

use. Such highly-loaded stages offer the potential to reduce the number of compressor stages in a civil core by one third, however, these stages feature de Haller numbers and (Lieblein) diffusion factors well beyond commonly accepted limits. Thus, understanding their aerodynamic performance should be of considerable interest.

This chapter presents key aspects of all four stages and discusses their design.

4.2 Mini-Deverson (Datum)

A conventionally loaded stage was manufactured as a datum to which the three highly loaded designs could be compared. A scaled version of the Deverson Build II stage was chosen for this role. The design and measured performance of this stage is comprehensively documented by Place [74] and Bolger [4]. This is a low speed model of a stage typical of a middle stage in the high-pressure compressor of a 1990s civil aero-engine.

As both the Deverson Rig and the HLRC have a hub to tip ratio of 0.8 the scaling process is straightforward; there was no need to compromise the design by adjusting blade numbers or aspect ratio. However, it was necessary to increase the spacing between rotor and stator in order to leave enough space to fit the necessary probes. To maintain the overall length of the HLRC hub the length of the rotating hub was unchanged from the three highly-loaded stages. This had the effect of increasing the extent of the rotating hub upstream of the rotor leading edge from 51% to 136% of rotor mid-span axial chord. In order to maintain consistency with the other stages tested the tip clearance was increased from 0.96% to 1.11% of span (or 1.4% of chord).

The reduction in compressor size (from a casing diameter of 1.524m to 0.450m) results in a lower Reynolds number. This is partially compensated for by the increased rotational speed of the HLRC. The Reynolds number of the scaled stage is 54% of the larger machine; 1.4×10^5 for the miniature versions of both the rotor and stator.

Despite the geometric differences the performance and behaviour of the scaled stage was very similar to that measured by Bolger [4]. The reduced Reynolds number led to slightly lower turning and higher losses. The measured efficiency of the Mini-Deverson stage was 87.9% compared with 88.7% for the larger machine. Similarly the reduced rotor turning led to a 4.3% reduction in stage loading and pressure rise. As stall is ap-

proached, the flow at the stator hub collapses in both stages and the stall points (and the stall inception mechanisms) were almost indistinguishable between the two machines. A more detailed comparison between the two machines is given in Appendix A.

4.3 One-Dimensional Design

Key one-dimensional, or mean-line, design parameters for all four stages are presented in Table 4.1. All three of the highly loaded stages are designed to be repeating, i.e. the inlet flow angle is equal to that at exit.

The Gallimore stage is the most extreme in terms of design de Haller number and diffusion factor. Common rules of thumb suggest that to achieve a successful compressor design the de Haller number should be kept above 0.7 and the Lieblein diffusion factor below 0.5. The Gallimore stage is well beyond these limits.

The Qinetiq and Denton stages are to the right of the Gallimore stage on the Smith Chart. It can be seen from Table 4.1 (and from Figure 1.4) that the aerodynamic demands on these stages are reduced by the increase in design flow coefficient.

The solidity of all three highly loaded stages is significantly higher than the datum design; typically between 20% and 30% greater, depending on the stage. It is necessary to increase the solidity to limit the suction surface diffusion (a measure of which is given by the diffusion factor) to reasonable levels. The relatively modest diffusion factor of the Denton stator might suggest that it is somewhat over-bladed compared to the other blade rows documented here.

Both the Mini-Deverson and Denton stages were fitted with inlet guide vanes (IGVs) to introduce swirl at inlet to the stage. The IGVs upstream of these two stages turned the flow in opposite directions; in the same sense as the rotor (i.e. co-swirl) upstream of the Mini-Deverson stage and against the rotor direction (i.e. counter-swirl) ahead of the Denton stage.

The effect of counter swirl in the Denton stage is to increase the stage reaction and offload the stator. In a counter-swirl design the average flow through the stator re-accelerates as it turns past the axial direction. This results in a more benign stator de Haller number and diffusion factor than the datum (Mini-Deverson) stage. The use

	Mini- Deverson	Gallimore	Qinetiq	Denton
Stage				
$\frac{V_x}{U}$	0.51	0.50	0.60	0.65
$\frac{\Delta h}{U^2}$	0.46	0.65	0.65	0.65
α_{in} [°]	25.2	0.0	0.0	-15.0
Reaction (Λ)[%]	54.5	67.5	67.5	84.9
Rotor				
Number of blades	51	43	43	35
Pitch (s)[mm]	24.9	28.3	28.3	36.4
Chord (c)[mm]	35.7	57.7	53.7	63.1
σ (c/s)	1.43	1.95	1.81	1.73
Aspect Ratio ($\frac{h}{C}$)	1.26	0.78	0.84	0.71
Reynolds no.	1.4×10^5	2.8×10^5	2.7×10^5	3.6×10^5
de Haller no. ($\frac{V_{2,rel}}{V_{1,rel}}$)	0.65	0.55	0.60	0.62
Diffusion Factor	0.53	0.60	0.55	0.51
Stator				
Number of blades	49	35	35	42
Pitch (s)[mm]	26.0	36.4	36.4	30.3
Chord (c)[mm]	37.2	61.9	64.1	48.1
σ (c/s)	1.43	1.70	1.76	1.58
Aspect Ratio ($\frac{h}{C}$)	1.21	0.73	0.70	0.94
Reynolds no.	1.4×10^5	2.2×10^5	2.5×10^5	1.7×10^5
de Haller no. ($\frac{V_2}{V_1}$)	0.68	0.61	0.68	0.84
Diffusion Factor	0.49	0.62	0.59	0.42

Table 4.1: Key 1D design parameters of the four stages tested in the HLRC.

of counter-swirl was made in response to initial measurements and calculations which indicated problems in both the Gallimore and Qinetiq stators.

4.4 Two-Dimensional Design

All three highly loaded stages were designed to give uniform work addition across the span. The design inlet flow conditions (i.e. flow angle, velocity, stagnation pressure and temperature) were also assumed to be uniform across the span in all but the end-wall boundary layers. All three highly-loaded stages were designed to be repeating stages, i.e. the stator exit flow angle was designed to be uniform across the span and equal to that at inlet.

The design methodology for both the Gallimore and Qinetiq stages was very similar. Once the throughflow design was fixed, a two-dimensional coupled Euler/ integral boundary layer code was used to design constant diffusion aerofoils to give the necessary turning. The leading edge geometry used in both stages was circular. The resulting blades were then checked with a three-dimensional CFD code (*MULTIP71*⁴ and *TRANSCODE* respectively) and minor adjustments made accordingly. Key section design parameters of all four stages are given in Table 4.2.

The Qinetiq stage was scaled from a high speed design of similar duty. This involved adjusting the low-speed blade shapes to match the non-dimensionalised velocity distribution to that of a high speed blade. This technique has been previously described by Wisler [98]. Although the Gallimore stage has not been scaled from a high-speed design, the blade thickness, the leading edge and trailing edge radii have been taken from another scaled blade, albeit at lighter loading, to get appropriate dimensions.

Denton took a fully three-dimensional approach and used the three-dimensional CFD code *MULTIP99* to develop the stage. The Denton stage used an approximately elliptical leading edge geometry. Elliptical leading edges have been shown to reduce the size of the leading edge over-speeds, prolong the extent of low-loss laminar flow and reduce the overall profile loss (e.g. Tain [88]).

The original Deverson stage (Build I) was designed by Place [74] to be a low-speed model

⁴A Rolls-Royce development of the code first described by Denton [17]

	Mini-Deverson	Gallimore	Qinetiq	Denton
Rotor				
t_{max}/C [%]	10.0	10.0	10.0	8.9
Wedge angle [°]	37	20	35	n/a
r_{le}/C [%]	0.9	0.9	1.8	0.5 [†]
r_{te}/C [%]	1.3	1.3	0.9	0.5 [†]
β_1 [°]	-55.6	-64.9	-59.6	-56.0
β_2 [°]	-24.3	-27.8	-24.5	-32.1
Stator				
t_{max}/C [%]	10.0	10.0	10.0	10.0
Wedge angle [°]	36	15	21	n/a
r_{le}/C [%]	0.8	0.9	1.0	0.5 [†]
r_{te}/C [%]	1.2	1.2	0.8	0.5 [†]
β_1 [°]	54.7	59.7	54.2	39.8
β_2 [°]	23.5	-5.1	-5.9	-23.1

Table 4.2: Key section design parameters of the four stages tested in the HLRC at mid-span. ([†]Non-circular leading and trailing edge geometry. Specified leading/ trailing edge half-thickness given, i.e. $\frac{t_{le}}{2C}$ or $\frac{t_{te}}{2C}$.)

of stage eight of the International Aero Engines (IAE) V2500 high-pressure compressor. This is a controlled diffusion aerofoil representative of design practice at the time. A two-dimensional coupled potential flow/ boundary layer solver (*FINSUP*) was used to design a low-speed blade with the same non-dimensional velocity distribution as in the engine; a technique originally described by Wisler [98].

The Deverson Build II stage (on which the Mini-Deverson stage described here is based) is a re-staggered version of the Build I stage. (One of the requirements of the original Deverson design was to allow sufficient incidence range to allow changes to the stage loading to be achieved by re-staggering alone.) Bolger [4] re-staggered the Deverson stage in order to increase the design stage loading from 0.42 to 0.45. The inlet flow angle was left unchanged from the original (Build I) design. Therefore, to maintain the design point incidence onto the rotor and stator at mid-span, the nominal design flow coefficient was reduced from 0.59 to 0.51.

The rotor and stator mid-span sections of the three highly loaded stages and the Mini-Deverson stage are presented in Figures 4.2 and 4.3.

Differences are apparent in the section design of all three stages. The camber distributions given in Figure 4.4 shows that Gallimore, Qinetiq and, to a lesser extent, the datum rotor have high curvature at the leading edge. This is typical of modern controlled diffusion aerofoils. In contrast the curvature of the Denton stage is more constant along its length and closer to a circular arc camber line.

The corresponding thickness distributions, presented in Figure 4.5, show that the location of maximum thickness occurs further aft (at approximately 45% of chord) on both the Gallimore rotor and stator than on the other blades. Conversely, the peak thickness of the Qinetiq rotor is well forward (at approximately 22% of chord) of that on other rotors. Aside from the changes to the aerofoil shape (i.e. velocity distribution) the increased thickness at the leading edge increases the wedge angle⁵ (Table 4.2). Similar to elliptical leading edges, high wedge angle aerofoils have been shown to reduce the leading edge over-speed and delay transition leading to improved loss and incidence tolerance (e.g. Sofia [84]).

⁵N.B. The Qinetiq rotor wedge angle is not as high as might be expected from the thickness distributions due to its larger leading edge circle.

4.5 Three-Dimensional Design

Separate design investigations into three-dimensional modifications (e.g. sweep and lean) to the Gallimore and Qinetiq stages both concluded that there was little or no performance benefit to be gained from such an approach. The Gallimore stage (i.e. rotor and stator) was therefore left as a two-dimensional design. The Qinetiq study did however predict a clear benefit in applying 6° of leading edge re-camber to the rotor hub and this was included in the final design of the Qinetiq rotor. No similar benefit was predicted for the Qinetiq stator which was left as a two-dimensional design. In contrast, the Denton stage was a fully 3D design; sweep and lean were employed in both the rotor and stator geometries.

The final rotor and stator blades for all four stages can be seen in Figures 4.6 and 4.7 respectively.

4.6 Effect of Compressibility

The air density rises by 1.2-1.5% across each of the highly loaded rotors and by 1.8% across the stages. During design, Denton ran calculations at almost double speed (5880rpm) to aid convergence. The higher design speed increased the density rise to 6.6% across the rotor and 7.5% across the stage. Compressibility across the rotor increases the work input and hence the design calculations over-predicted the stage loading. The stage loading coefficient expected experimentally from this stage (i.e. at 3000rpm) is therefore reduced from 0.65 to 0.62.

4.7 Blade Manufacture

All four sets of blades were manufactured in plastic with a glass reinforced core. Stereolithography was used to generate a master blade from which silicone-rubber moulds were made ready for vacuum casting.

4.7.1 Qinetiq Stage Manufacture

Small differences were discovered between the Qinetiq rotor as designed and that tested. These were attributed to errors in the manufacturing process, in particular the clamping of the moulds. The tested blades were physically measured to obtain the correct geometry. The resolution of these measurements was, however, insufficient to adequately resolve the leading and trailing edge geometry and therefore these were assumed to be as designed (i.e. circular). The circular leading and trailing edge geometries were joined to the measured surfaces such that there were no discontinuities in the slope of the blade at the blend points.

The measured geometry was used in all subsequent CFD calculations. A comparison between the design and measured sections at mid-span is shown in Figure 4.8. The manufacturing error had the effect of increasing the turning through the rotor row and consequently increasing the stage loading.

No similar problems were detected with the Qinetiq stators or with any of the other blades tested.

4.8 Summary

The design of three highly loaded stages has been discussed. These all had design stage loading coefficients ($\frac{\Delta h_0}{U^2}$) of 0.65 (almost 50% higher than those currently in use) and featured de Haller numbers and (Lieblein) diffusion factors well beyond commonly accepted limits. A conventionally loaded stage ($\frac{\Delta h_0}{U^2} \approx 0.46$) was also manufactured to be used as a datum stage for measurement and calculation purposes. The design points of all four stages are summarised in Figure 4.1 and key features of each design include:

1. The **Gallimore** stage is a two-dimensional (i.e. does not feature any sweep or lean), axial inflow design. The Gallimore stage is the most extreme in terms of de Haller number and (Lieblein) diffusion factor.
2. Like the Gallimore stage, the **Qinetiq** stage is an axial inflow design and is predominantly two dimensional, however, leading edge re-camber has been applied to the rotor hub. Errors in the manufacturing process increased the rotor camber

and therefore the expected stage loading.

3. The **Denton** stage used counter-swirl at rotor inlet to reduce the aerodynamic demands on the stator (identified as a problem in initial testing of the Gallimore and Qinetiq stages). This was a fully three-dimensional design featuring sweep and lean on both the rotor and the stator. Artificially increased rotational speed in the design calculations caused the stage loading coefficient to be over-predicted. As a result the stage loading expected experimentally from the Denton stage is reduced from 0.65 to 0.62.
4. The conventionally loaded, **Mini-Deverson**, stage is a scaled model of another low-speed research compressor at the Whittle Laboratory (the “Deverson” Build II stage), itself a model of a typical mid-stage of the high-pressure compressor of a 1990s civil aero-engine. A row of IGVs provides the required co-swirl into the approximately 50% reaction stage (i.e. similar rotor and stator velocity triangles).

Chapter 5

Measured Performance of Three Highly Loaded Designs

5.1 Introduction

There is currently little practical experience with stages of very high loading. This chapter describes the results of a detailed experimental investigation carried out on three highly loaded stages (and one conventionally loaded stage). The purpose of this experimental program was to generate a body of data which could be used to identify key flow features at high stage loadings and ultimately go some way towards establishing a limit, below which compressor designs of satisfactory performance can be achieved. In addition, this data can be used to calibrate the accuracy of computational fluid dynamics (CFD) programs.

For the sake of brevity, only the key features of the flow through each of the four stages tested are discussed here. A comprehensive set of radial profiles (including axial velocity, stagnation pressure rise, flow angles, diffusion factors and loss coefficients) can be found in Appendix B. Where relevant to the discussion these plots have been reproduced along with the main text.

Finally, this chapter reports the stalling behaviour of all four stages tested. Experimental analysis is still the only method of generating reliable data on stall; potentially one of the most catastrophic phenomena to affect axial compressors. Knowledge of

the effect(s) of increasing stage loading on stall inception and stall margin is therefore critical for the successful implementation of future highly loaded designs.

All three highly loaded stages exhibited disappointing efficiency when compared with the datum stage. Despite the extreme stage loading and poor efficiency of these designs, all three stages did demonstrate good stall margin.

5.2 Inlet Conditions

The inlet conditions to the HLRC are illustrated by the radial profiles of axial velocity, stagnation pressure loss and swirl angle measured upstream of the Gallimore stage and shown in Figure 5.2. This data was derived from pitch-wise averaging area traverse measurements made with a pneumatic probe. Regions of high stagnation pressure loss at 17%, 50% and 83% span correspond to the circumferential bars of the turbulence grid positioned 91 bar widths (or 2.5 annulus heights) upstream of the Gallimore rotor leading edge (Figure 3.2). It is apparent that the wakes from the turbulence grid have not fully mixed out by rotor inlet.

The interaction between the wakes from the turbulence grid and the Mini-Deversen IGVs led to a slight error in the measurement of the stagnation pressure at the inlet plane. Ninety radial bars and 49 IGVs are present in this build. As these two numbers are not perfectly divisible, nor have any common factors, the relative position of the turbulence grid to the IGVs varies around the circumference. This leads to a circumferential variation in the loss across the combined turbulence grid and IGVs. The inlet stagnation pressure derived from an area traverse carried out over two stator pitches is thought to be lower than the true average over the whole circumference. For this reason the values of efficiency quoted for the Mini-Deversen stage have been taken from the continuous static to static characteristic. This is justified by the excellent agreement between this characteristic and the traverse data shown in the other three stages tested.

No similar error affected the Denton stage. In this case 30 IGVs are used with the same turbulence grid. As there are exactly three turbulence grid pitches per IGV passage the relative position of the turbulence grid to the IGVs does not vary circumferentially.

Stage	$\bar{\phi}$	Design	Measured	$\eta [\%]$
		$\frac{\Delta h_0}{U_{mid}^2}$	$\frac{\Delta h_0}{U_{mid}^2}$	
Mini-Deverson	0.510	0.463	0.445	87.9
Gallimore	0.500	0.650	0.659	83.8
Qinetiq (design)	0.600	0.650	0.700	85.3
Qinetiq (peak-efficiency)	0.682	n/a	0.666	86.4
Denton	0.650	0.650	0.596	85.6

Table 5.1: Peak efficiency/ design point performance of the Mini-Deverson, Gallimore, Qinetiq and Denton stages.

5.3 Overall Performance

Performance characteristics for each of the four stages tested are given in Figures 5.3 to 5.6. The three highly loaded stages achieved peak efficiencies of 83.8%, 86.4% and 85.6% (Gallimore, Qinetiq and Denton stages respectively). In the case of the Gallimore and Denton stages these occurred approximately at the design flow coefficient (0.50 and 0.65 respectively). The Qinetiq stage achieved peak efficiency at a flow coefficient of 0.69, 15% above the design value. These values of efficiency are disappointing when compared to the peak efficiency measured in the conventionally loaded Mini-Deverson stage of 87.9% at a flow coefficient of 0.536 (slightly above the design flow coefficient of 0.510).

The performance of each of the four stages tested is summarised and compared to their respective design intents in Table 5.1. At their design flow coefficients the highly loaded Gallimore, Qinetiq and Denton stages achieved stage loading coefficients of 0.659, 0.700 and 0.596 respectively. The conventionally loaded Mini-Deverson stage achieved a stage loading coefficient of 0.445 at a flow coefficient of 0.510 (the nominal design value). As expected the Denton stage did not achieve the target stage loading coefficient of 0.65, partly due to the effects of compressibility present in the design CFD but not in the real machine (Section 4.6).

The measured stage loading coefficient of the Qinetiq stage at the design flow rate ($\bar{\phi} = 0.600$, $\frac{\Delta h_0}{U^2} = 0.700$) is well above the design value of 0.650. This was expected from the nature of the errors in the manufacture of this stage, in particular the increased

camber at the trailing edge (described in Section 4.7.1). Therefore, it is hardly surprising that the peak efficiency does not lie at the design flow coefficient and occurs where both the rotor and stator are less highly loaded.

Increases in stage loading are commonly associated with a reduction in stall margin. The definition of stall margin used here is that given in Equation 5.1 and the measured stall margins of all four stages tested are listed in Table 5.2. Contrary to this expectation, all three highly loaded stages demonstrated stall margin similar to, or greater than, that observed in the Mini-Deverson stage.

$$SM = \frac{\overline{\phi_{\eta_{max}}} - \overline{\phi_{stall}}}{\overline{\phi_{\eta_{max}}}} \quad (5.1)$$

Stage	Stall-Margin [%]
Mini-Deverson	22
Gallimore	22
Qinetiq	31
Denton	34

Table 5.2: Measured stall margin of the four stage designs tested in the HLRC.

5.4 Mini-Deverson

The Mini-Deverson stage is a conventionally loaded stage representative of a mid-stage found in the high-pressure compressor of a 1990s civil aero-engine. It is a reduced size version of the Deverson Build II stage comprehensively documented by Bolger [4] (details of the scaling process and original design are given in Chapter 4).

The contours of stator exit stagnation pressure in Figure 5.7 (presented as psuedo-pressure loss, see Section 3.8.5) show the dominant feature of the Mini-Deverson flow is the collapse of the flow at the stator hub near to stall. This corner separation forms at the stator hub at the design flow rate ($\bar{\phi} = 0.51$) and grows significantly as the stage is throttled. The appearance of this corner separation corresponds to the sharp change in gradient observed in the pressure rise characteristics at a flow coefficient of 0.51 and is accompanied by a steep drop in efficiency (Figure 5.3).

The collapse of the flow at the stator hub is starkly illustrated by the flow-visualisation photographs in Figure 5.8. Red paint was initially applied to the stator suction surface and green paint to the end-walls. At the design flow coefficient ($\bar{\phi} = 0.511$) fluid from the hub reaches 38% of span. The change in the flow visualisation pattern is dramatic near to stall ($\bar{\phi} = 0.435$); reverse flow exists from the hub to approximately 30% of span and over 60% of the suction surface span is affected by the corner separation.

The “dark” line marked in Figure 5.8A is thought to be caused by boundary layer transition. Bolger [4] correlated similar feature with a perturbation in the static pressure distribution typical of a time averaged transition region.

Contours of relative velocity measured downstream of the rotor are shown in Figure 5.9. As the flow coefficient is reduced the rotor wakes get progressively thicker and deeper, especially from the hub to mid-span. The preferential degradation of the flow at the rotor hub is associated with the formation of the large hub corner separation in the stator (as described above) and its upstream potential effect.

The tip clearance flow, highlighted in Figure 5.9 at the design flow rate ($\bar{\phi} = 0.509$), collects at approximately 80% of pitch from the suction surface¹. As the flow rate is reduced the structure of the tip clearance flow changes; near to stall ($\bar{\phi} = 0.436$) low momentum fluid covers the whole pitch at the casing and the clearance loss core appears much closer to the suction surface. Similar behaviour was observed in all four rotors tested and will be discussed further in Section 5.10.

Despite the differences between the Mini-Deverson and its larger counterpart (most notably Reynolds number), the Mini-Deverson produced very similar results to those obtained earlier by Bolger [4]. A more detailed comparison between the Mini-Deverson stage and its larger counterpart is given in Appendix A. As expected from a well designed, conventionally loaded stage, the Mini-Deverson demonstrated good efficiency, pressure rise and stall margin.

¹N.B. For the remainder of this chapter, fraction of pitch is defined to increase from the suction surface towards the pressure surface.

5.5 Gallimore Stage

The Gallimore stage was designed to achieve a stage loading coefficient of 0.65 (almost 50% greater than those typically in service today) at a flow coefficient of 0.50. In terms of de Haller number and (Lieblein) diffusion factor the Gallimore stage is the most extreme design tested and it exceeds the commonly accepted limits of both of these parameters. More details of the Gallimore design can be found in Chapter 4.

5.5.1 High Flow Performance

One of the most noticeable features of the Gallimore characteristics (Figure 5.4) is the steep drop in efficiency with increasing the flow rate above design (i.e. $\bar{\phi} > 0.50$). This occurs as a result of negative incidence separations on both the rotor and stator at high flow rates.

The stator pressure surface loss is more severe than in the rotor and therefore the high-flow behaviour of the stator is discussed here first. At the highest flow coefficient measured (Figure 5.10A) a region of high loss extends across the whole height of the stator pressure surface. In particular, there is a collection of high loss fluid in the corner between the hub and the pressure surface. The severity of this feature reduces with flow rate (i.e. increasing incidence) and moves towards mid-span. However it is still evident even at the design flow coefficient (highlighted in Figure 5.10D).

Similarly, a collection of low momentum fluid (highlighted in Figures 5.11B) can be seen on the rotor pressure surface at high flow rates (i.e. low incidence) greater than or equal to 0.598. This behaviour is consistent with that expected from a negative incidence separation from the leading edge of the pressure surface.

Negative incidence separations particularly affect the Gallimore stage for two reasons. Firstly, the Gallimore rotor and stator are likely to have lower tolerance to extreme incidence as a result of their lower leading edge wedge angles (see Table 4.2). Secondly, both the rotor and stator have been designed with high camber at the leading edge so that the blade is aligned with the oncoming flow at a flow rate below the design value (Hughes [53]). This is especially true in the case of the stator which exhibits the more severe pressure surface separation.

5.5.2 Stator Flow

The result of the extreme stator de Haller number and diffusion factor can be seen in the contours of stagnation pressure presented in Figure 5.10. By the design flow rate ($\bar{\phi} = 0.50$) a large separation has formed on the suction surface, located at approximately 30% of span. This separation spreads across the whole suction surface as the stage is throttled further; near to stall (Figure 5.10F) it almost appears two-dimensional in nature.

Above the design flow rate (i.e. $\bar{\phi} \geq 0.549$) the stator wakes are relatively thin and the suction surface flow is well behaved. Two loss cores sit on the stator suction surface at approximately 16% and 80% of span, the innermost of which develops into the large suction surface separation described above as the flow rate is reduced.

5.5.3 Rotor Flow

The behaviour of the Gallimore rotor is illustrated in Figure 5.11 by contours of relative velocity. As the stage is throttled the rotor wakes get progressively thicker and deeper, particularly between 4% and 67% of span. Like the stator, the Gallimore rotor appears to suffer from a suction surface separation at low flow rates, possibly even at design ($\bar{\phi}_{design} = 0.500$); near to stall the rotor wakes occupy almost 50% of the rotor pitch (Figure 5.11F).

At high flow rates, low momentum fluid from the tip clearance flow collects in the pressure surface/ casing corner. Between flow coefficients of 0.598 and 0.549 the structure of the clearance flow changes (Figure 5.11B & C). Although this behaviour is similar to that seen in the Mini-Deverson stage this occurs further away from stall, above the design flow rate ($\bar{\phi}_{design} = 0.500$). As the stage is throttled past this point, low momentum fluid begins to collect preferentially near to the suction surface (instead of the pressure surface) and the velocity deficit at the casing increases. Near to stall high loss fluid extends across the whole pitch and the casing flow appears to have completely collapsed (Figure 5.11F).

5.6 Qineticq

Like the Gallimore stage the Qineticq stage was designed to achieve a stage loading coefficient of 0.65 with axial inlet flow (i.e. without upstream IGVs). The Qineticq stage was also predominately two-dimensional design; the only three dimensional modification incorporated was 6° of leading edge recamber applied to the rotor hub. Errors in the blade manufacturing process increased the rotor camber towards the trailing edge and therefore the expected stage loading. Details of the Qineticq design and manufacture process can be found in Chapter 4.

Figure 5.12 shows contours of relative velocity measured downstream of the Qineticq rotor. At high flow coefficients a loss core can be seen in the rotor wake at 22% of span as a result of the hub secondary flow. At the casing, the tip clearance flow collects at approximately 75% of pitch from the suction surface. As the stage is throttled below $\bar{\phi} = 0.682$ the rotor wake thickens drastically on separation of the suction surface between the hub and approximately 70% of span. Near to stall the rotor exit flow is dominated by this suction surface separation. Despite the extreme loading, the blockage at the casing does not approach that seen at the Gallimore or Denton rotor tips near to stall; possibly due to the high blockage at the hub diverting flow towards the tip.

The Qineticq stator flow is illustrated by the contours of stagnation pressure presented in Figure 5.13. In contrast to the previous two stages described this stator was run with a 1.1% clearance gap at the hub. Fluid originating from the tip clearance gap collects at approximately 25% of pitch from the suction surface. The size, position and structure of the tip clearance flow remains similar with reducing flow coefficient.

At the highest flow coefficient tested a loss core is visible on the suction surface at approximately 79% of span. No loss core is visible near the hub as the clearance gap prevents the migration of the hub boundary layer onto the suction surface. The loss core and stator wake gradually gets thicker and deeper as the stage is throttled down to a flow coefficient of 0.541. Any further reduction in the flow rate leads a catastrophic stator suction surface separation from approximately 30% of span to the casing. This collapse of the stator suction surface flow causes a kink in the pressure rise characteristics at a flow rate of about 0.52 (Figure 5.5) and the corresponding sharp drop in efficiency.

5.7 Denton

Unlike the other two highly-loaded stages tested, the Denton stage featured 15° of counter-swirl at rotor inlet in order to reduce the aerodynamic demands placed on the stator (identified as a problem in initial testing of the Gallimore and Qinetiq stages). It was designed to achieve the same stage loading as the other highly loaded designs (i.e. $\frac{\Delta h_0}{U_{mid}^2} = 0.65$) at flow coefficient of 0.65. The Denton stage was also the only fully three-dimensional design tested and featured both sweep and lean on both the rotor and stator. More details of the Denton stage design can be found in Chapter 4.

Contours of relative velocity measured at rotor exit are shown in Figure 5.14. At the design flow rate ($\bar{\phi} = 0.650$), a region of increased velocity deficit is visible in the wake at approximately 85% of span. No such feature is apparent in the other stages tested and is possibly caused by sweep and lean at the rotor tip driving boundary layer fluid towards mid-span. Although the loss cores at approximately 12% and 85% of span get more severe with reducing the flow coefficient this is accompanied by a general, progressive, increase in the depth and width of the rotor wake across the whole span; in other stages the rotor hub loss core has grown preferentially on throttling.

At high flow rates ($\bar{\phi} \geq 0.551$) the structure of the tip clearance flow (highlighted in Figure 5.14B) remains similar. Low momentum fluid, originating from the tip clearance, collects in the corner between the pressure surface and the casing. The extent and depth of this low momentum fluid appears to be less than that seen in the other three stages tested. The loss near to the casing is also unusually low at high flow rates (shown in Figure 5.15). Sweep and lean at the tip have been shown to reduce the strength of clearance flows. Another possible explanation is the closing of the tip gap as a result of the “straightening” of the lean under centripetal acceleration. As the flow coefficient is reduced to 0.498 the tip clearance flow is no longer restricted to the pressure surface/casing corner and begins affect the whole pitch.

Contours of stator exit stagnation pressure are presented in Figure 5.16. The Denton stator was designed to be run with a clearance gap of 1.1% span at the hub. At every flow rate tested, the hub clearance flow can be seen to roll up and collect on the hub at approximately 45% of pitch away from the suction surface. As the stage is throttled the Denton stator wakes remain similar until all but the lowest two flow coefficients tested.

At flow rates below 0.503 the rotor tip flow collapses and low momentum fluid dominates the entire casing pitch (Figure 5.14F). The effect of this on the downstream stator can be seen in the stator casing flow visualisation shown in Figure 5.17C; the flow at stator inlet is almost tangential and therefore the stator separates from the leading edge due to excessive incidence at the casing.

The suction surface flow visualisation in Figure 5.18C shows that the separated casing flow offers little resistance to radial migration and traverses across the blade, almost reaching the hub by the trailing edge. At mid-span it causes a catastrophic suction surface separation (Figure 5.16F). At the casing, this fluid is replaced with attached boundary layer fluid driven from the casing onto the suction surface by the secondary flow and by the three-dimensional design.

In terms of diffusion factor and de Haller numbers the Denton stage is less ambitious than the other two highly loaded stages tested. Whereas the other two highly loaded stages suffer from large separations due to very high levels of diffusion, the lower levels of diffusion mean that the Denton stage fails suddenly, via excessive incidence at the stator casing.

The Denton pressure rise characteristics (Figure 5.6) rise strongly until a flow coefficient of about 0.48. At this flow rate the breakdown of the rotor tip clearance flow and the resultant collapse of the stator suction surface causes the characteristic to flatten off. The efficiency characteristic also shows a sudden drop in efficiency. Although the root cause is breakdown of flow at the rotor tip it is the increased stator loss which has the biggest effect on the stage efficiency; the rotor efficiency only drops by about 3% between the near stall and design flow rates whereas the corresponding value for the stage is approximately 10%.

5.8 Profile/ Mid-Span Loss

As might be expected from the efficiency measurements, the loss across each blade row increases with design stage loading. One of the key analyses on the effect of loading on loss was performed by Lieblein [63] in the 1950s. In this work Lieblein correlated the wake momentum thickness to his so called diffusion factor for several aerofoils operating at their minimum loss incidence. The corresponding peak efficiency

values, mass averaged from the radial profiles between 30% and 70% of span (assuming constant stream-surface radii across each blade row), for the four stages described herein are presented in Figure 5.19. The ordinate shows a generalised loss parameter originally suggested by Lieblein as an approximation to the total wake momentum thickness.

In Figure 5.19 a correction has been applied to the present data for the base pressure loss attributable to thicker trailing edges². For the same reason, Lieblein's data has also been adjusted to a mixed out value; the values he presented were mass averaged values measured between 0.5 and 1.5 chord lengths downstream of the trailing edge³. No similar correction for Reynolds number effects was necessary as both the current data and that presented by Lieblein were recorded at similar Reynolds numbers of about 2×10^5 .

Figure 5.19 shows that at diffusion factors below about 0.5 the loss parameters measured as a part of the present work are roughly comparable to those reported by Lieblein. Lieblein's data increases steadily with diffusion factor up to a diffusion factor of about 0.6. Above this value the loss parameter increases rapidly, which Lieblein took to indicate the onset of separation. The current data for highly loaded stages indicates that this sudden increase in loss occurs at lower diffusion factors (between 0.50-0.55) and is more severe.

The key difference between Lieblein's experiments and the current data is that the present values were recorded in a rotating rig. In contrast, Lieblein's experiments were

²The correction for trailing edge thickness takes the form presented by Denton [18] and reproduced in Equation 5.2. A base pressure coefficient of -0.2 has been assumed. Trailing edge thickness in the present work ranged from 1.7% to 2.5% of chord (Chapter 4). This correction has not been applied to Lieblein's data as this term is not significant (Liblein used much thinner trailing edges, $\frac{t}{c} = 0.3\%$) nor was solidity data readily available.

$$\Delta\omega_{p,x} = -\frac{C_{pb} \left(\frac{t}{c}\right) \sigma}{\cos \alpha_2} \quad (5.2)$$

³Lieblein's loss parameter has been corrected to a mixed out value via Equation 5.3. At the measurement plane a shape factor ($H = \frac{\delta^*}{\theta}$) of 1.1 was representative (Koch [59]). The energy shape factor ($H_e = \frac{\delta_e}{\theta}$) was estimated from this value via the method presented by Stewart [85].

$$\frac{\overline{\omega_{p,x}}^M}{\overline{\omega_{p,x}}^X} = \frac{H_e}{2H} \quad (5.3)$$

carried out in a carefully controlled cascade with end-wall suction to ensure constant axial velocity. The three-dimensional nature of the flow through compressor blade rows, in particular the secondary flows migrating onto the suction surface, are thought to contribute to the premature increase in loss observed in the current data. This is illustrated by flow visualisation experiments performed on the Mini-Deverson stator and shown in Figure 5.8. The end-wall fluid (i.e. green paint) migrates a significant distance (greater than 30% of span) radially onto the suction surface despite predominantly attached flow at the design flow rate.

This has implications for the choice of the limiting (Lieblein) diffusion factor in highly loaded stages, if not for rotating rigs in general.

5.9 Secondary Flows

Secondary flows are expected to be more significant in highly loaded stages than in conventional designs. This stems from the higher tangential pressure gradients across each passage which drive these flows. The increase in tangential pressure gradient is unavoidable; it is required to provide the extra turning necessary to achieve increased loading. Although the increased solidity⁴ of highly loaded blades reduces the pressure difference across the passage it also reduces the tangential distance over which this pressure difference is applied. The distance the flow must travel before it impinges on the suction surface thus also reduces.

The results presented here show that this is indeed the case. One of the most obvious examples of the increase in the strength of the secondary flow can be seen by comparing the component of the flow perpendicular to the chord line in rotor hub flow visualisation results from the Mini-Deverson and Gallimore stages shown in Figure 5.20.

5.9.1 End-Wall Overturning

One measure of the strength of secondary flows is the over-turning of the end-wall flow. Figure 5.21A shows the variation in the radial extent of the overturning adjacent to the

⁴Solidity generally increases with stage loading in order to maintain acceptable levels of diffusion along the suction surface.

rotor hub and stator casing with the flow turning at mid span for all four stages tested. The flow turning at mid-span ($\frac{\Delta V_\theta}{U}$) is roughly equivalent to stage loading coefficient. The values at the rotor casing and stator hub have not been included in this graph so as to prevent any possible confusion caused by the presence of clearance flows. This plot shows a clear trend; as stage loading increases so does the radial penetration of the overturning due to the secondary flow.

A similar trend can be seen in the magnitude of the overturning; shown in Figure 5.21B. The magnitude of the over-turning was defined as the difference between the maximum turning adjacent to the end-wall (i.e. the rotor hub or stator case) and the turning at the edge of the end-wall boundary layer. This was estimated from radial profiles of tangential velocity change (i.e. $\Delta V_\theta = V_{\theta,2} - V_{\theta,1}$) across each blade row tested. The Denton rotor is the most significant outlier in Figures 5.21B. This is perhaps due to the higher axial velocity and/ or reduced blade count leading to a greater tangential blade force driving the secondary flow. Another possible contributing factor is the reduced aspect ratio of this rotor.

The precise nature of the secondary flows is dependent on the specific blade design and not just on the very general stage loading coefficient. Despite the differences in the four designs tested and their inlet conditions, Figure 5.21 clearly demonstrates that as the stage loading coefficient increases so does the radial extent and magnitude of the over-turning due to secondary flows.

5.9.2 End-Wall Losses

In certain cases the secondary flows are beneficial in terms of end-wall loss, especially at the rotor hub. A good illustration of this is at the Gallimore rotor hub. The cross passage pressure gradient drives the low momentum hub boundary layer fluid (marked in Figure 5.11B) towards and onto the suction surface leaving behind a new, thinner, boundary layer. As the flow rate is reduced this scrubbing effect strengthens with the secondary flow and therefore the loss at the rotor hub falls (Figure 5.22). By the design flow rate ($\bar{\phi} = 0.500$, Figure 5.11D) there is almost no evidence of the hub boundary layer at rotor exit.

The reduction in the pitch-wise extent of the hub boundary layer can be seen in the

contours of relative velocity measured downstream of the Qinetiq and Denton rotors (Figures 5.12 and 5.14). As expected, this effect is less obvious in the more lightly loaded (i.e. weaker secondary flows) Mini-Deverson stage; at the near stall operating point ($\bar{\phi} = 0.432$, Figure 5.9D) the hub boundary layer is still evident over more than 50% of pitch whereas there it is all but absent in the case of the Gallimore rotor.

The reduction in loss at the end-walls due to secondary flows is not genuine but rather a redistribution of high entropy fluid. However, we shall see that this scrubbing effect does help the end-wall flow to withstand greater adverse pressure gradients without separating.

5.9.3 Stator Flow Separation

The Mini-Deverson stator behaves in a fairly conventional way; a corner separation develops at approximately the design flow rate and grows as the stage is throttled until it dominates the stator flow near to stall. Figure 5.23 shows the results of flow visualisation performed on the stator (recall that red and green paint was initially applied to the suction surface and end-walls respectively); near to stall this corner separation clearly affects a large region of both the suction surface and the hub.

The breakdown of the flow in the three highly loaded stators as the flow rate is reduced is different. The end-wall flow visualisation in 5.25 and 5.24 shows that despite the extreme de Haller numbers and large suction surface separation there is no evidence of the Gallimore end-wall boundary layers separating. The present data suggests that as the stage loading increases, so will the tendency of a blade to separate from the suction surface, away from the end-walls.

The loss cores, formed by the secondary flows, are highlighted for each of the stators tested in the contours of stator stagnation pressure loss (measured at the peak efficiency flow rate) shown in Figure 5.26. As the design stage loading is increased these loss cores move towards mid-span as a result of the stronger secondary flows. (The reduced aspect ratio of the highly-loaded stators is possibly also a compounding factor.) In the conventionally loaded Mini-Deverson stage the critical loss core sits less than 3% of span away from the hub, whereas in the highly loaded Gallimore and Qinetiq stators the corresponding loss cores lie at 16% and 21% of span respectively from the relevant

end-wall. A similar trend can be seen in the position of the loss core at the rotor hub.

As the flow coefficient is reduced in the Mini-Deverson, Gallimore and Qinetiq stages, large separations grow out of these loss cores. Due to the differences in the position of these loss cores, large separations form at (or close to) the hub/ suction-surface corner in conventionally loaded stators (e.g. the Mini-Deverson stator) whereas at high-loading (e.g. the Gallimore and Qinetiq stators) they form on the suction surface. (The exception to this is the Denton stator which separates due to excessive incidence at the casing; see Section 5.7.) Additionally, the increased strength of the secondary flows at high-loading restricts the pitch-wise extent of any separation near to the end-walls and therefore precludes the formation of traditional corner separations (e.g. the Mini-Deverson stator).

5.10 Rotor Tip Clearance Flows

Although increased loss as a result of double-leakage is well known and has been reported by various authors (e.g. Khalid et al [56] and McNulty et al [68]), details of the structure of the clearance flow as a result of “double-leakage” have not been previously readily available. By combining casing static pressure with rotor exit hot-wire measurements it has been possible to experimentally correlate the structure (and loss) of the clearance flow to the position of the tip vortex, in particular the presence of “double-leakage”, for (what is believed to be) the first time.

The behaviour of the Mini-Deverson tip clearance flow is summarised in Figure 5.27. Contours of rotor exit relative velocity are shown on the left and contours of casing static pressure are shown on the right. At the design flow coefficient ($\bar{\phi} = 0.510$, Figure 5.27A) the tip clearance flow collects at approximately 80% of pitch from the suction surface. An additional region on high loss fluid is also visible directly above the rotor tip. The contours of static pressure indicates that the trajectory of the low pressure core of the tip clearance vortex passes through the passage without impinging on the pressure surface of the adjacent blade.

As the flow rate is reduced the structure of the tip clearance flow changes. This is most clear near to stall ($\bar{\phi} = 0.436$, Figure 5.27C); low momentum fluid covers the whole pitch at the casing and only one (severe) loss core is visible located close to the suction

surface. This is accompanied by a marked increase in loss at the casing (Figure 5.28). The contours of static pressure indicate that this coincides with the trajectory of the tip clearance vortex intersecting the pressure surface of the adjacent blade. At $\bar{\phi} = 0.471$ it hits the adjacent blade at approximately 90% of axial chord and moves upstream with reducing flow rate; by $\bar{\phi} = 0.436$ the intersection point has advanced to approximately 70% of axial chord.

The behaviour of the Qinetiq and Gallimore tip clearance flow is summarised in Figures 5.30 and 5.29 respectively. Although only one loss core (located between 75% and 100% of pitch from the suction surface) is resolved at the high flow rates by measurements taken behind the Gallimore rotor (Figure 5.29A), its location and magnitude lead us to believe that it is in fact a composite of the two loss cores seen at high flow rates in the Mini-Deverson and Qinetiq stages. Broadly speaking the Mini-Deverson, Gallimore and Qinetiq tip clearance flows all behave in the same manner; once the clearance vortex first intersects the adjacent blade (at $\bar{\phi} \approx 0.548$ in the Gallimore stage and at $\bar{\phi} \approx 0.540$ in the Qinetiq stage) the structure of the tip clearance flow changes. In the Qinetiq stage this is accompanied by marked increase loss near to the casing (shown in Figure 5.32).

Unlike the Mini-Deverson and Qinetiq stages, the Gallimore tip clearance flow breaks down much further away from stall, in fact above its design flow rate ($\bar{\phi} = 0.500$). Throttling the Gallimore stage past this point leads to further degradation of the flow over the entire pitch and a progressive increase in casing loss (Figure 5.22). Despite the breakdown of the casing flow it remains stable as the stage is throttled further.

The impact of the tip clearance vortex onto the adjacent blade at the same flow coefficient as the change in the behaviour of the clearance flow implies convincingly that so called “double-leakage” is the cause. Double leakage (discussed by Khalid et al [56]) is where the low total pressure/ high loss tip clearance flow is ingested by the adjacent tip gap, i.e. the clearance flow passes over *two* rotor tips (hence the name “double-leakage”) before exiting the rotor row. This leads to increased mixing losses because of the larger velocity difference between the clearance flow (slower due to reduced total pressure) and the free stream flow. The reduced momentum of the double leakage flow means that it struggles to make it across the pitch and instead collects on the casing near to the suction surface as highlighted in Figures 5.27C, 5.29C and 5.30C.

The trajectory of the Denton clearance flow, shown in Figure 5.31, is more tangential than in the other three stages tested and appears to intersect the adjacent pressure surface at even the highest flow rate tested. However, it is difficult to draw any conclusions similar to those discussed above (or otherwise) from these results as the tip clearance flow is considerably weaker in the Denton stage than in the other three stages tested; possibly as a result of the sweep and lean applied to the rotor tip or because of the suspected reduced clearance gap (due to mechanical effects; see Section 5.7).

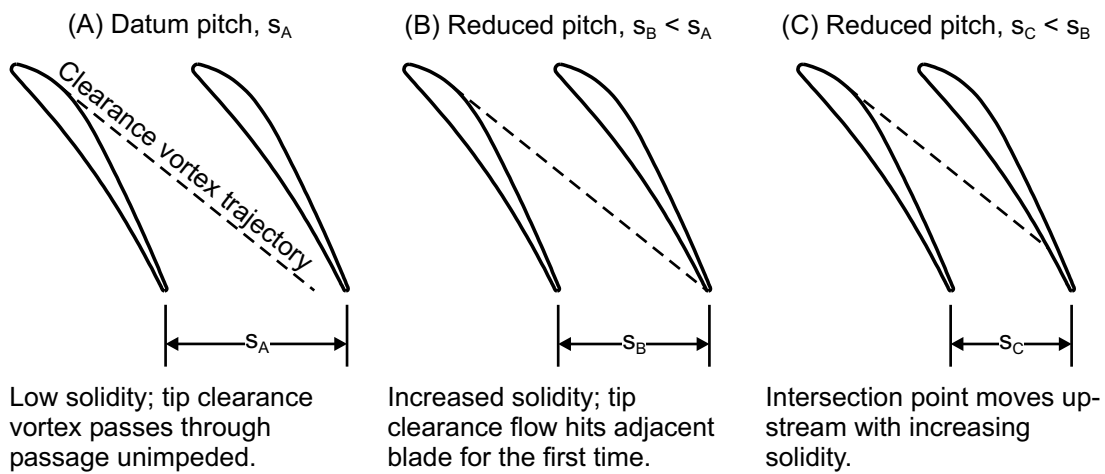


Diagram 5.1: Schematic diagram illustrating the effect of increasing rotor solidity (or loading) on “double-leakage”. (N.B. Dashed line denotes clearance vortex trajectory.)

To determine the effect of stage loading on “double-leakage” let us first consider a hypothetical blade with a vortex core of constant trajectory (as illustrated in Diagram 5.1); as the solidity increases the clearance vortex core intersects the adjacent blade and moves forward into the passage. Solidity tends to increase with design stage loading in order to maintain acceptable diffusion levels. This is obviously an over simplification; increasing the solidity alone will tend to move the clearance vortex downstream, however this is opposed by the increased pressure difference across the blade required to raise the loading. Therefore, increasing the design stage loading will tend increase the probability of double-leakage at flow rates further away from stall and possibly even above design; indeed this is the case with the Gallimore rotor.

Stage	Inception	Spikes	Modes
	Mechanism	Present?	Present?
Mini-Deverson	spike	✓	✗
Gallimore	spike	✓	✓
Qinetiq	mode	✓	✓
Denton	mode	✗	✓

Table 5.3: Stall inception mechanisms observed in the conventional and three highly loaded stages tested in the HLRC.

5.11 Stall Inception

Two distinct mechanisms of stall inception have been identified in axial compressors; long length scale “modal” inception and short length scale “spike” type inception. A more detailed description of each mechanism and its characteristics is given in Chapter 2. Stall inception events in each of the four stages tested were recorded with fast response casing static pressure transducers (Section 3.9). Typical examples of the results from these tests for each of the four stages are shown in Figures 5.33 to 5.35. The dominant stall inception mechanism of each stage is summarised in Table 5.3.

Spikes and modes are physically two completely separate phenomena and therefore not mutually exclusive; both spikes and modes can exist in a compressor simultaneously. Indeed a spike can be triggered by a modal disturbance. For this reason, the presence of spikes and modes has also been recorded in Table 5.3 even if they do not directly lead to rotating stall.

The Mini-Deverson stage stalls via spike type inception. The inception pattern is shown in Figure 5.33. A disturbance occurs in one or two blade passages which propagates around the annulus at high speed; in this case approximately 68% of rotor speed. The Mini-Deverson is atypical in that up to four additional spikes occur approximately one rotor revolution behind the appearance of the original spike. As these short length scale disturbances propagate they grow and eventually fuse to form a fully developed stall cell. The fusing of adjacent short length scale disturbances is accompanied by a sudden reduction in the propagation speed.

The Gallimore stage also stalls via spike type inception. Here, however, a mode propa-

gating at approximately 30% of rotor speed can also be detected in Figure 5.34 immediately prior to stall. A spike forms at the peak of this mode in an area of high static pressure (hence low velocity and high incidence), propagates at approximately 70% of rotor speed and develops into a slower moving rotating stall cell.

The Qinetiq and Denton stages both stall modally. Figure 5.35 shows a classic example of modal inception in the Denton stage. A long length scale disturbance propagating at approximately 35% of rotor speed grows in amplitude as the stall point is approached. A large, well developed, stall cell grows out of this mode.

In the case of the Qinetiq stage mode and spike type disturbances are present together (Figure 5.36). The spikes form, propagate at high speed (approximately 85% of rotor speed) and die out within the time taken for the disturbance to complete one revolution. Despite the presence of these seemingly random spikes the stall cell can be seen to grow smoothly from a modal disturbance. It appears as if the spikes form in a region of high static pressure (and therefore low velocity/ high incidence) near to the peak of the modal disturbance and then die away as the spike and modal disturbance move out of phase. Due to the large difference in propagation speeds there is insufficient time for the spike to develop beyond a point at which it can survive the suppression provided by the trough of the modal disturbance (i.e. high velocity/ low incidence).

5.11.1 Effect of Loading and Rotor Flow on Stall Inception

Both modal and spike type disturbances have been detected in the highly loaded stages tested here. The increased likelihood of serious flow separation and loss at high loading means “turned-over” characteristics (and therefore modal stall inception) are likely to become more prevalent as the stage loading is increased. Although this is supported by the presence of modal disturbances in all three of the highly loaded compressors tested here, this hypothesis would benefit from further supporting evidence.

The pattern of near stall rotor loss is compared in Figure 5.37 and, qualitatively in Table 5.4. The pattern of rotor loss is also compared to the stall inception mechanism in Table 5.4. Although it is not possible to make a definitive conclusion, Table 5.4 indicates that high loss at the rotor hub (e.g. due to a corner separation) is associated with the presence of spikes. Conversely, high tip clearance losses (at the rotor case) seem

Stage	Spikes?	Modes?	Hub Loss	Casing Loss
Mini-Deverson	✓	✗	high	low
Gallimore	✓	✓	high	high
Qinetiq	✓	✓	high	low
Denton	✗	✓	low	high

Table 5.4: Correlation between the rotor loss distribution and the stall inception mechanism.

to be linked to modal inception. This seems to be counter-intuitive when considering the results of Camp & Day [8] and Seitz [81]. They established that spike type stall inception occurred as a result of a local flow breakdown in the rotor tip clearance flow and modal inception was attributed to flow separation near to the hub.

The results in Table 5.4 demonstrate that spike type stall inception is more subtle than a general breakdown of the flow at the rotor tip. The change to the tip pressure distribution, which occurs as the result of flow redistribution around a large hub blockage, seems to promote the specific instability leading to spike type disturbances. In the Mini-Deverson and Gallimore stages these spikes grow into a fully fledged stall cell whereas in the Qinetiq stage they die out before they can cause rotating stall.

The apparent link between high rotor casing loss and modal inception is less clear than for spikes and is probably a little misleading. Modal stall occurs as a result of a system instability when the total to static pressure rise characteristic becomes sufficiently positive (i.e. “turned over”) as a result of high loss. Therefore the high loss at the casing contributes to that necessary⁵ to “turn over” the characteristic but its location is less likely to be significant.

5.12 Summary and Conclusions

The performance and behaviour of three highly loaded stages has been measured in detail. A conventionally loaded datum stage was also tested in the same facility, under

⁵N.B. Near to stall the Gallimore, Qinetiq and Denton stages also exhibit large separations in the stator.

similar conditions. The results of these tests have been discussed in detail above.

It is inherently difficult to draw comparisons between four completely different stage designs and isolate the effect of a single design variable, in this case stage loading coefficient. Nevertheless some general trends attributed to increased stage loading have been identified and discussed. Some of the key aspects regarding the performance of highly loaded stages are summarised below.

1. All three highly loaded stages demonstrated disappointing efficiency when compared to that of the datum stage. The Gallimore, Qinetiq and Denton stages achieved peak efficiencies of 83.8%, 86.4% and 85.6% respectively. The conventionally loaded Mini-Deversen stage achieved a peak efficiency of 87.9%.
2. Below diffusion factors of about 0.50 the values of mid-span loss parameter measured in the HLRC are roughly comparable to those originally presented by Lieblein [63]. Increasing the diffusion factor beyond 0.50-0.55 leads to a rapid increase in mid-span loss. This occurs at a lower diffusion factor and is more severe in a highly-loaded, single-stage compressor than suggested by Lieblein's cascade data.
3. The three highly loaded stages demonstrated reasonable operating range. The measured stall margin of the three highly loaded stages was greater than or equal to that of the datum stage. This is contrary to conventional wisdom which suggests a reduction in stall margin with increased loading.
4. All three highly loaded stages exhibited modal disturbances prior to stall whereas the conventionally loaded Mini-Deversen stage stalled via spike type inception only. This led to the tentative conclusion that the probability of modal stall inception increases with stage loading. Two of the highly loaded stages also exhibited spike type disturbances. Perhaps counter-intuitively, the appearance of spikes was well correlated with the presence of high loss at the rotor hub (e.g. from a corner separation).
5. The impact of secondary flows, in terms of both magnitude (overturning) and radial penetration, increases with stage loading. This occurs due to the increase in tangential pressure gradient and increased solidity inherent in stages of increased turning.

At increased loading, separations tend to form on the suction surface rather than in the corner between the endwall and the suction surface. Separations grow out of loss cores which move towards midspan with increasing design loading. The increased strength of secondary flows at high loading restrict, or eliminate, the pitchwise extent of separations at the endwall.

6. Two loss cores, present in the rotor tip clearance flow, merge into a single loss core as the stage is throttled. This is associated with a significant increase in loss at the casing and coincided with intersection of the trajectory of the centre of the clearance vortex with the adjacent blade. It is believed that this is the first time that the structure of the clearance flow has been correlated experimentally with the position of the tip vortex, or more specifically, the phenomena of “double-leakage”. It was also argued that this is likely to be more significant at high design stage loadings than in conventional stages.

Chapter 6

Investigation into the Unique Stalling Behaviour of the Qinetiq Stage

6.1 Introduction

A highly unusual flow breakdown mechanism was observed in the Qinetiq rotor at low flow coefficients. As the mass flow rate was reduced below $\bar{\phi} \approx 0.65$ large separations appeared in the tip region of a few rotor passages. As the mass flow rate was reduced further the number of these large separations increased until almost every second blade passage was separated. Further reduction in the flow rate led to conventional rotating stall.

Unusually these separations were fixed to individual rotor passages and did not propagate as would be expected from Emmons' model of stall cell propagation. It is believed that this is the first time such a flow breakdown mechanism has been recorded.

Such a flow breakdown mechanism is highly deleterious to performance and, in a high-speed compressor, such a phenomena would induce large, periodic, stresses and is potentially a cause of mechanical failure. It is therefore important to understand the causes behind this and whether or not it is likely to occur in high-speed, highly-loaded, compressors. Detailed measurements and numerical simulations of the Qinetiq stage

have both been used to develop a model which may explain this phenomena.

This flow breakdown mechanism was only observed in the low inlet turbulence configurations of the Qinetiq stage. Details of the three levels of inlet turbulence at which the Qinetiq stage was tested are given in Table 6.1. Except where stated otherwise the remainder of this chapter discusses the performance of the Qinetiq stage in the low turbulence configuration.

	Turbulence Intensity [%]	Integral Length Scale ($\frac{\lambda}{C}$)[%]
Low	2.5	6.6
Medium	5.5	5.4
High	6.4	4.6

Table 6.1: Mid-span turbulence properties at inlet to the Qinetiq stage.

6.2 Macroscopic Effects of Inlet Turbulence Intensity

6.2.1 Performance

The effect of inlet turbulence on the pressure rise and efficiency characteristics is shown in Figure 6.1. At high flow rates the characteristics of all three cases are similar. As the flow coefficient is reduced below a critical value, about 0.65, the difference between the low and high inlet turbulence cases becomes significant. The reduction in inlet turbulence level causes a 12% drop in peak pressure rise and a 38% reduction in stall margin. The efficiency also drops off prematurely as the flow rate is reduced. The characteristics of rotor and stator pressure loss coefficient given in Figure 6.2 indicate that this additional loss occurs in the rotor.

6.2.2 Flow Visualisation

Such a sensitivity to inlet turbulence suggests that boundary layer transition has a significant effect on the performance of the Qinetiq rotor. There is some evidence to support the presence of a separation bubble in oil-dye flow visualisation performed on the rotor suction surface (Figure 6.3A). Oil-dye flow visualisation is usually only considered to be useful on surfaces being subjected to either negligible acceleration or acceleration normal to the surface of interest. In this case however, the two dark lines at 17% and 26% of chord identify the up and downstream extents of a separation bubble. Between these lines the streaks are almost entirely radial (more so than elsewhere), indicating low shear stress in the streamwise direction.

To confirm this interpretation boundary layer trips were placed upstream of the foremost line. By prematurely forcing laminar to turbulent transition (hence suppressing the hypothesised separation bubble) the dark lines were eliminated (Figure 6.3B).

The response of the separation bubble to changes in flow coefficient (i.e. incidence) and inlet turbulence is summarised in Table 6.2. Increasing the inlet turbulence level reduced the length of the separation bubble (but did not eliminate it) and reducing the flow coefficient moved the laminar separation point (i.e. the start of the bubble) towards the leading edge.

Inlet Turbulence [%]	$\bar{\phi} = 0.736$		$\bar{\phi} = 0.638$		$\bar{\phi} = 0.540$	
	$\frac{s_{start}}{C}$	$\frac{l_{bubble}}{C}$	$\frac{s_{start}}{C}$	$\frac{l_{bubble}}{C}$	$\frac{s_{start}}{C}$	$\frac{l_{bubble}}{C}$
2.5	0.18	0.083	0.17	0.093	n/a [†]	
5.6	0.18	0.065	0.17	0.074	0.15	0.074
6.4	n/a		0.17	0.055	0.15	0.074

Table 6.2: Details of the rotor suction surface separation bubble. ([†]Due to the flow breakdown in the rotor at these inlet conditions, the start and length of the rotor suction surface separation bubble cannot be reduced to a single value.)

6.3 Rotor Exit Flow

The source of this additional loss was investigated further with phase locked hot-wire measurements taken at rotor exit. Using the method described in Chapter 3 it was possible to resolve the (ensemble averaged) flow angle and velocity in both the circumferential and radial directions. Figure 6.4 shows contours of ensemble averaged relative velocity behind all 43 rotor blades at a range of flow coefficients approaching stall.

Figure 6.4A was taken at the highest flow rate presented here. The wakes, the tip clearance flow and the hub corner separation have all been successfully resolved behind each rotor passage. As expected the flow is approximately periodic.

As the flow rate is reduced the rotor exit flow becomes more unusual (Figure 6.4B). Large separations appear over the outboard 50% span of four rotor passages. The flow through those passages not immediately adjacent does not seem to be significantly altered.

As the flow rate is reduced further the number of these separations increase until almost every second blade passage is separated (Figures 6.4C to E). Once the rotor has reached this “saturated” condition a small number of these separations seem to jump between adjacent passages as the flow redistributes itself to achieve a separation in every other blade passage. This cannot be achieved in the Qinetiq stage as the rotor has an odd number of blades. Any further reduction in the flow rate from this point leads to conventional rotating stall.

The flow coefficient at which a particular passage stalls is repeatable across several different experiments. It therefore seems likely that the stalling flow coefficient of a given blade passage is inherent in the build of the compressor (i.e. small variations in stagger angle or other manufacturing/ set-up errors) rather than due to random fluctuations in the flow. Examination of the rotor exit flow field shows no obvious correlation between the wake thickness and its separating flow coefficient.

At the stalling flow rate of a given passage a separation will first appear intermittently. As the flow rate is reduced the frequency of this separation will increase until it is present permanently. This process is completed over a narrow band of flow coefficients. On opening the throttle, this process is reversed; no hysteresis was observed between the stalling and unstalling flow rates.

The effect of increasing the inlet turbulence to this stage is shown in Figure 6.5. This was taken at the same flow coefficient as the data presented in Figure 6.4E for the low inlet turbulence case. The large separations have been suppressed and the flow-field is approximately periodic. The hub corner separation is larger with the higher inlet turbulence as the flow is no longer being diverted towards the hub by the flow breakdown at the rotor case described above.

6.4 Propagation

These separations do not appear to be stall cells in the conventional sense; they appear to be fixed in the rotor frame of reference. The contour plots presented in Figure 6.4 are produced from ensemble averaged data. Were these separations propagating the ensemble average picture would be “smeared” over the whole annulus. To confirm this, the propagation of each large separation was tracked with six fast response static pressure probes, located 20% of axial chord upstream of the leading edge (Figure 3.2, plane “d”) and equispaced around the circumference.

Figure 6.7 shows a typical set of unsteady casing static pressure traces. The particular results presented here were taken at a flow coefficient of 0.589. The bold line is drawn with a slope equivalent to the rotational speed of the rig and highlights the same separation over three rotor revolutions. Figure 6.7 shows clearly that each separation precesses with the rotor and is fixed to a single rotor passage over the course of several revolutions¹.

6.5 Notation

To aid the discussion of this flow breakdown phenomena it is useful to define a set of consistent notation. The nomenclature scheme illustrated in Diagram 6.1 has been adopted for this purpose. The separated blade will be referred to as blade “S”. With the rotor moving from right to left, the blades to the left and right of S will be labelled “L” and “T” respectively. A stationary observer will encounter blade L before blade S

¹N.B. The “background” amplitude of the rotor passing changes as a result of the variation in the relative positions of the pressure transducers to the downstream stator blades.

and therefore it is said to *lead* blade S. Conversely, the same observer will see blade T after blade S and therefore it is said to *trail* blade S.

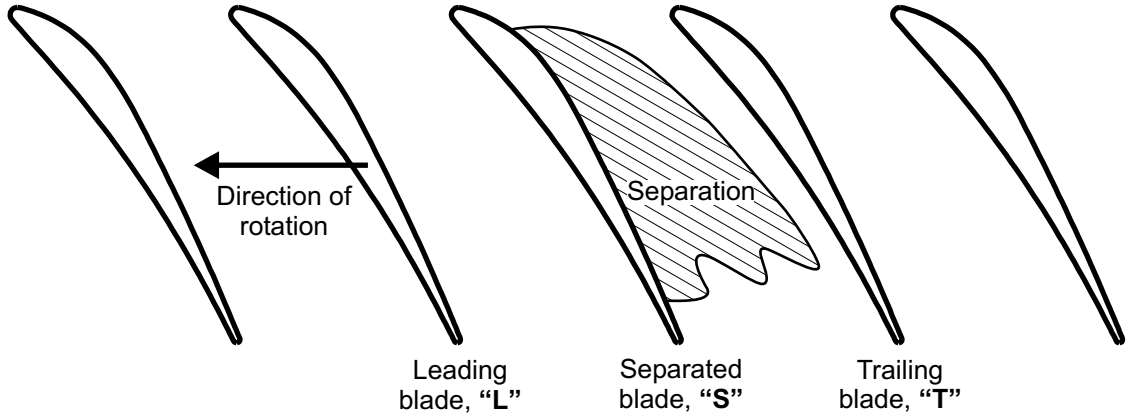


Diagram 6.1: Summary of notation.

6.6 Flow Visualisation

Flow visualisation on the rotor suction surface (as described in Section 6.2.2) was carried out in an attempt to gain some insight into this flow breakdown phenomena. Figure 6.6 shows a photograph of the results taken at a flow coefficient of 0.540.

Analysis of rotor exit hot-wire data showed blades 2, 4 and 43 (immediately ahead of the visible sector) to exhibit large scale separations. Blade 2 shows a dark separation line at approximately 12% of chord similar to that seen at higher flow rates (e.g. Figure 6.3A). The stream-wise extent of the (almost) purely radial streak-lines immediately downstream of this separation line has increased to approximately 16% of chord (from 9.3% at $\bar{\phi} = 0.638$). At the downstream edge of this region a dark re-attachment line is no longer obvious. Although not shown in Figure 6.6, similar changes occur to the patterns formed on blade 4.

Both blades 1 and 3 trail a large separation. The length of the separation bubble on blade 1 has been shortened to approximately 7% of chord (from 9.3% of chord at $\bar{\phi} = 0.638$). However, the patterns produced on blade 3 are less conclusive.

6.7 Emmons' Model of Stall Cell Propagation

Emmons [30] first proposed a simple model explaining the propagation of stall cells in axial compressors (illustrated in Diagram 6.2). The blockage presented by a separation in one passage (like the one illustrated on blade S), or by a larger stall cell, diverts the oncoming flow such that the incidence onto the leading blade (i.e. blade L) is reduced and the incidence onto the trailing blade (i.e. blade T) is increased. The blade exposed to increased incidence (blade T) will separate, whereas the blade with reduced incidence (blade L) is unloaded, mitigating any separations on this blade. Hence, in the rotating frame of reference, the stall cell propagates against the direction of rotation.

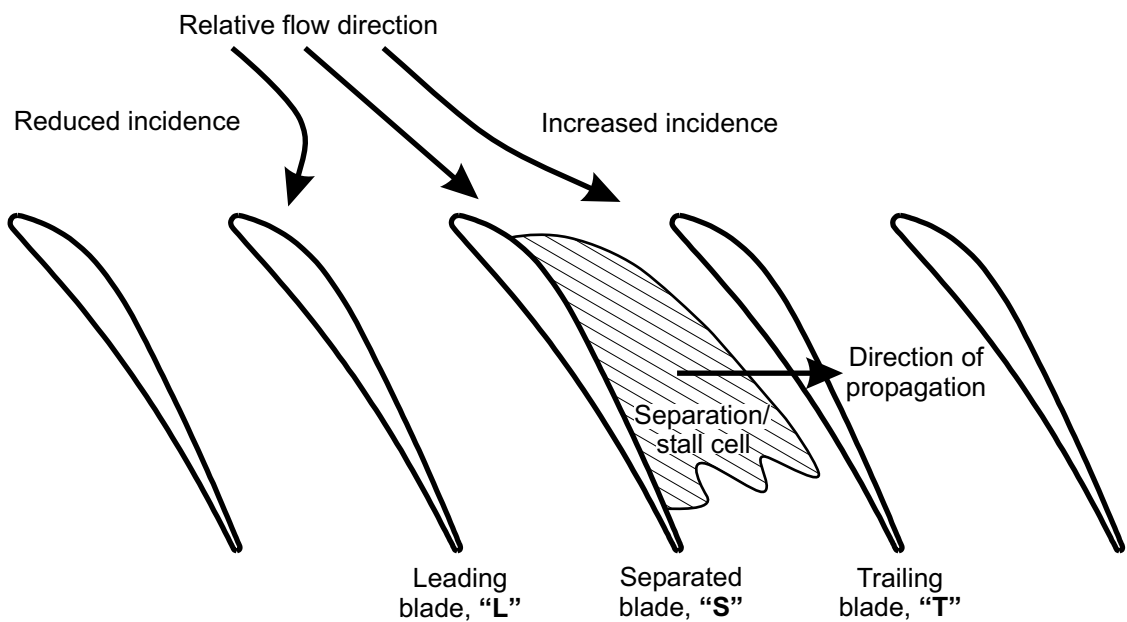


Diagram 6.2: Schematic diagram illustrating Emmons' model of stall cell propagation.

As the propagation speed of a stall cell is less than the blade speed, in the stationary frame of reference the stall cell appears to rotate in the same direction as the rotor. It can be shown that as the number of stages are increased the propagation speed tends to approximately 50% of rotor speed (Greitzer [45]). In fact this is a reasonable approximation for most single stage machines.

6.7.1 Leading Edge Relative Flow Angle

Given their size, it is surprising that the separations observed in the Qinetiq rotor do not propagate in the manner suggested by Emmons' model. The flow immediately (20% of tip axial chord) upstream of the rotor leading edge was investigated further to see if it agreed with Emmons' model. The method described in Chapter 3 was used to resolve the phase-locked velocity and flow angle with a sub-miniature hot-wire probe.

The circumferential variation in axial velocity and incidence (presented as the variation in inlet relative flow angle about the pitch-wise average value) at 75% of span is shown in Figure 6.8. At high flow rates ($\bar{\phi} \geq 0.638$) the traces of axial velocity and incidence variation are approximately sinusoidal with the passing of each blade.

As the overall flow rate through the stage is reduced, the axial velocity in the passage highlighted by the grey band drops (i.e. blade S) disproportionately on the formation of a large scale separation. Both axial velocity and incidence traces become aperiodic. Figure 6.8B shows that once a separation forms on blade S, the incidence onto the trailing blade, T, increases by approximately 3° . Conversely, the incidence onto the leading blade, L, decreases by about 2° . As the stage is throttled further, the blockage in passage S and the corresponding incidence changes onto blades L and T become more severe. These measurements support the flow re-distribution model proposed by Emmons' (Diagram 6.2).

6.7.2 Casing Static Pressure Distributions

Fast response static pressure probes were used in the arrangement shown in Figure 3.7 to resolve blade-to-blade static pressure fields at the casing. This data was ensemble averaged over approximately 250 rotor revolutions. In order to extract the static pressure distribution around each blade from this data it is necessary to fix the precise location of the blade relative to the measured static pressure field. This was done by assuming that the peak pressure recorded by the probe located at the leading edge corresponded to the stagnation point and lay on the blade surface. Examination of CFD solutions indicated that this was a good assumption. The static pressure distribution around each blade at the casing was then extracted by interpolating the static pressure field at the coordinates of the tip section. The surface static pressure distributions were

normalised by the circumferentially averaged relative inlet dynamic head at 90% span; just outside the casing boundary layer.

The effect of the measured incidence change on the static pressure distributions around three blades is shown in Figure 6.9. At high flow rates (e.g. $\bar{\phi} = 0.613$) the static pressure distributions around all three blades are very similar (Figure 6.9A). The key difference between the three pressure distributions at this flow rate (i.e. $\bar{\phi} = 0.613$) is the slightly increased diffusion over the suction surface of blade S.

As the flow rate is reduced (e.g. $\bar{\phi} = 0.589$, Figure 6.9B) the peak suction on blade S collapses on the formation of a large separation. Also shown in Figure 6.9B (in black) is the average (across blades L, S & T) pressure distribution measured with high inlet turbulence ($Tu_{in} = 6.4\%$). This allows the pressure distributions around blades L and T to be compared to the “clean flow” pressure distribution at the same flow rate. (Recall from Section 6.3 that high inlet turbulence suppresses the large aperiodic separations described above.) The increased incidence onto blade T (see Figure 6.8 & Diagram 6.2) reduces the suction surface pressure and increases the diffusion over the foremost 28% of axial chord. The reduced incidence onto blade L has the opposite (albeit smaller) effect.

Once a large separation forms, the increased incidence onto the trailing blade raises the diffusion to beyond the level at which the separation initially occurred. In the case of the three blades examined above, the local diffusion factor² on the trailing blade, T, rises from 0.37 at $\bar{\phi} = 0.613$ to 0.44 at $\bar{\phi} = 0.564$; this compares to a local diffusion factor of 0.38 experienced by Blade S immediately prior to the onset of separation (i.e. at $\bar{\phi} = 0.613$). Despite the increased diffusion, the flow in the trailing passage is stable and any separations in this passage remain small. The suction surface boundary layer on blade T must therefore be more resistant to separation than its neighbour (blade S). Furthermore, as two separations *never* occur in adjacent passages, it is probable that it is the large separation on blade S which causes the stabilisation of the boundary layer on the trailing blade, T; it is highly unlikely that manufacturing, set-up or other random errors are distributed in such a way as to prevent *any* adjacent passages stalling.

The flow breakdown phenomena measured in the Qinetiq rotor differs from Emmons’

²The local diffusion factor (D_{loc}), developed by Lieblein [63], gives a measure of the deceleration applied to the suction surface boundary layer and its tendency to separate. It is defined as $D_{loc} = \frac{V_{max} - V_2}{V_{max}}$, where V_{max} is the peak suction surface velocity and V_2 is the velocity at the trailing edge.

model in that the large separations do not propagate. The boundary layer on Blade T is somehow stabilised by the presence of a separation on Blade S. This outweighs the destabilising effect of the increase in incidence onto Blade T and prevents the separation propagating and growing into a fully fledged rotating stall cell. A model has been proposed to explain this stabilisation effect and its development is described below.

6.8 Proposed Model

The data presented above has been used to propose a simple model to explain the flow breakdown phenomena observed in the Qinetiq stage. In particular, the stabilisation of the flow on the blade trailing a large separation (i.e. blade T) is addressed. This model is illustrated in Diagram 6.3 and summarised below.

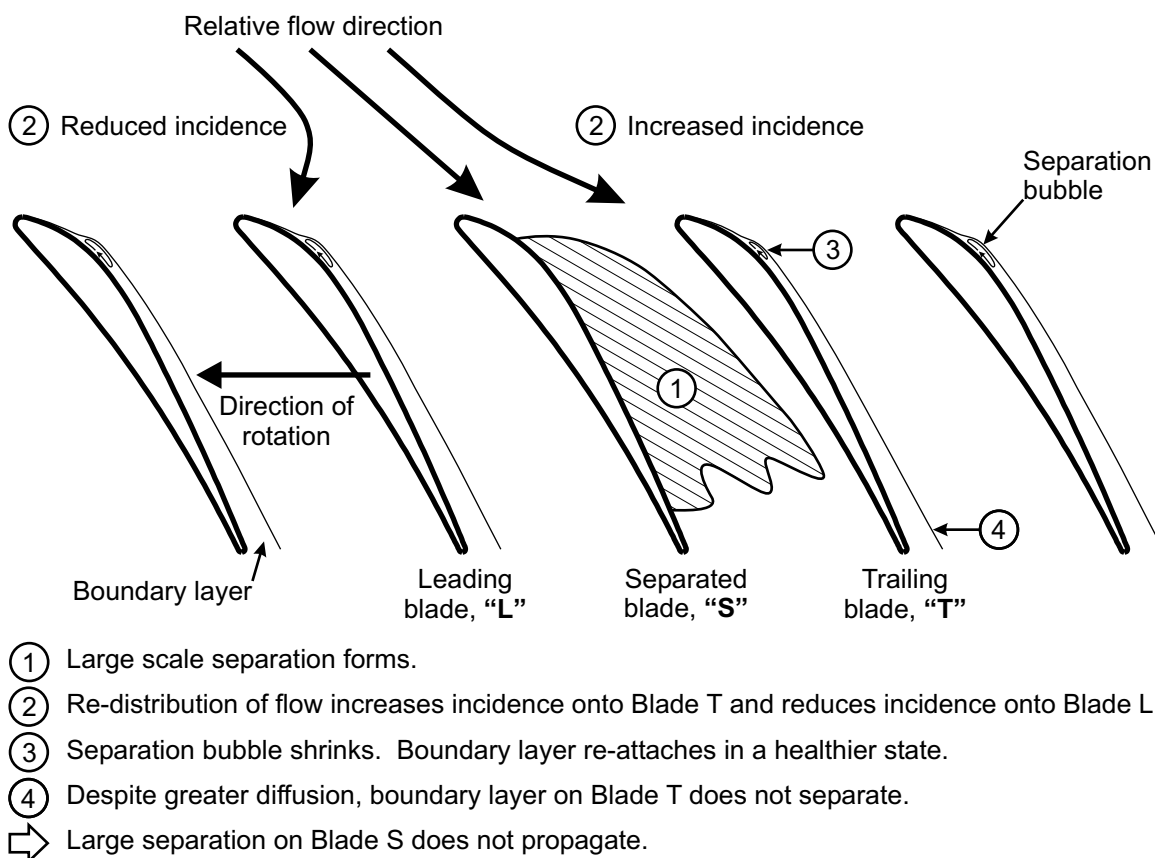


Diagram 6.3: Schematic diagram illustrating proposed model.

1. Due to small geometric differences (e.g. manufacturing or set-up errors) the diffusion on a particular blade (i.e. blade S) is slightly higher than experienced by other blades. As the flow rate is reduced, a point is reached where the suction surface boundary layer on this blade separates first.
2. The resulting large scale separation on blade S diverts the flow into the adjacent passages reducing the incidence onto blade L and increasing it onto blade T. The diffusion across the suction surface of blade T is correspondingly increased.
3. The sensitivity of this phenomena to inlet turbulence and evidence from rotor suction surface flow visualisation suggests that the suction surface separation bubble, plays a significant role. The presence of the separation on blade S reduces the size of the separation bubble on blade T and allows the boundary layer to re-attach in a healthier state (much like the effect of an increase in free-stream turbulence).
4. The healthier boundary layer downstream of the separation bubble on the suction surface of blade T can withstand greater diffusion (i.e. greater than blade S immediately prior to the separation) and does not separate. Therefore, the large scale separation on blade S does not propagate.

As the flow rate is reduced further this process is repeated; the flow over the blade exposed to the next highest diffusion (and not already stabilised) will be the next to collapse and so on. This process continues until eventually (almost) every second blade passage exhibits a large separation. In this condition, (almost) every unseparated blade is stabilised and therefore any further reduction in flow rate will lead to conventional rotating stall.

6.9 Prediction of the Flow Around Two Adjacent Blades with a Two-Dimensional Coupled Inviscid/ Boundary Layer Solver

The coupling between the boundary layers on two adjacent blades investigated further with the *MISES* two-dimensional Euler/ integral boundary layer solver (discussed fur-

ther in Chapter 7). The modelling of this phenomena in two-dimensions is clearly a gross simplification of the three-dimensional nature of the flow around such a large separation. However the aim of this exercise is not to replicate the specifics of this phenomena but to gain some insight into the coupling effects between adjacent blades whilst exhibiting separations.

The expected role of the suction surface separation bubble meant it was important to select a CFD tool that adequately models boundary layer transition. This precluded the use of the three-dimensional CFD codes available as they all assumed fully turbulent boundary layers. *MISES* models boundary layer transition via a modified version of the Abu-Ghannam and Shaw [1] transition criterion (its implementation in *MISES* is described by Drela [29]).

6.9.1 Method

A schematic diagram of the calculation domain is given in Figure 6.10. Blade B has been re-staggered “open” by 0.2° to provide a site for non-periodic flow to nucleate. This re-stagger is within the variation of the measured experimental stagger angles ($\pm 0.7^\circ$ for this build). Figure 6.11 shows the performance of these two blades when simulated individually. Not surprisingly, the plots for the re-staggered blade (i.e. blade B) appear shifted to the left by a similar magnitude as the imposed change in stagger angle. Nevertheless, the difference in performance between the datum and re-staggered blades is insignificant for the current purpose.

Calculations with more than two blades were attempted, however it was not possible to generate a mesh which gave satisfactory convergence for higher numbers of blades.

The results presented and discussed in the remainder of this section are taken for a blade section at 70% span. The stream-tube height was assumed to be constant throughout the computational domain.

It is known from flow visualisation experiments (Section 6.2.2), that the suction surface boundary layer remains laminar over the foremost 15% chord where a separation bubble begins. The behaviour of this separation bubble was thought to play an important role in the flow breakdown mechanism described above. In order to capture the observed separation bubble at all inlet flow angles it was necessary to reduce the computational

Reynolds number from 2.7×10^5 to 1.0×10^5 .

6.9.2 Results

Figure 6.12 shows the calculated displacement and momentum thickness at the trailing edge over a range of inlet flow angles. The re-staggered blade (blade B) separates at about 4° of incidence; prematurely when compared to the single blade calculation. Despite the increase in incidence and loading that this separation causes, the rapid increase in the thickness of the wake downstream of blade A is delayed by almost 2° ; approximately 1° beyond the limit suggested by the single blade calculations.

The predicted static pressure distributions over both blades are shown at three inlet flow angles in Figure 6.13; respectively corresponding to before, during and after the occurrence of this non-periodic separation. The change in the position and extent of separation and reattachment lines with inlet flow angle on both blades is shown by the contours of zero skin friction in Figure 6.14. The variation in transition point with inlet flow angle is also marked (dashed line) on both Figures.

Before the non-periodic separation forms (on blade B) the static pressure distribution over both blades is similar (Figure 6.13A). Furthermore the separation bubbles start at the same point and have similar extents (Figure 6.14). Transition is predicted to occur at approximately the same location. As observed experimentally, the diffusion over blade B is slightly greater than that across blade A.

Once the re-staggered blade (B) separates, the incidence and loading on blade A increases (Figure 6.13B). The increase in incidence causes a separation bubble to form at the leading edge (Figure 6.14). This flow reattaches as a laminar boundary layer due to the favourable pressure gradient. It can be seen in Figure 6.15 that the Reynolds stress coefficient³, akin to intermittency, increases rapidly over this separation bubble. The result of this is to promote the reattachment of the “main” separation bubble, therefore allowing greater diffusion to be tolerated.

Coupled with the increase in incidence is the diversion of extra flow into passage A. This raises the trailing edge velocity on blade A and partially mitigates the increase

³The Reynolds stress coefficient presented here is that embedded in the *MISES* transition model and a modification of the one described by Green et al [43].

in diffusion factor. Therefore the diffusion across blade A increases more slowly with incidence than would be expected from a single blade (or blades operating periodically).

As the inlet flow angle is increased further the stabilised boundary layer on blade A also separates. Once this condition is surpassed, flow around both blades once again becomes similar in terms of static pressure distribution (Figure 6.13C), separation point and the onset of transition.

The predicted behaviour of the boundary layers (described above) is illustrated schematically in Diagram 6.4.

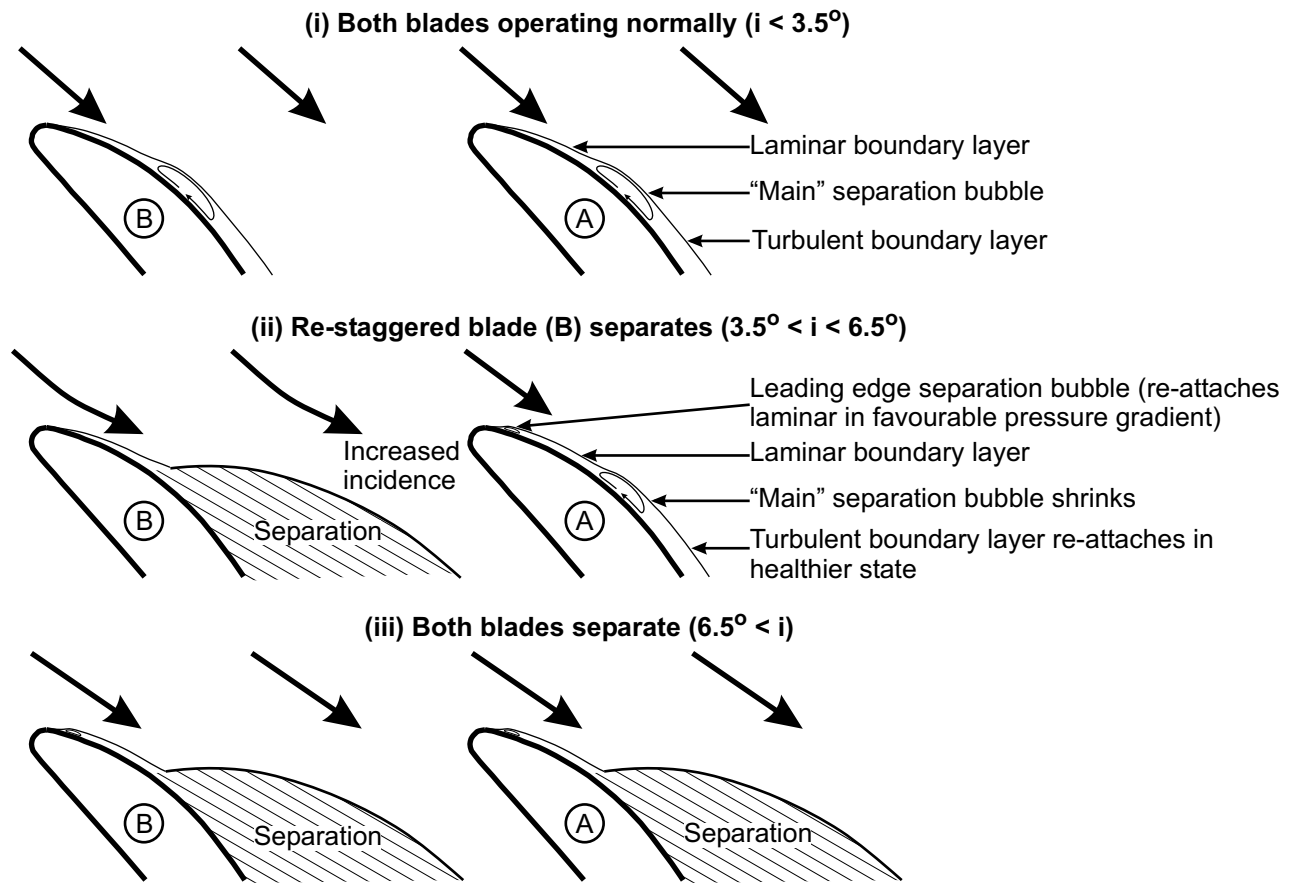


Diagram 6.4: Schematic diagram of MISES “double-blade” results.

6.9.3 Notes on Predictions

The calculations described above exhibit the same, qualitative, symptoms as those observed experimentally. Although this mechanism may not be correct in all its details,

the calculations have clearly demonstrated strong coupling between the boundary layers in adjacent passages.

The measured size of these separations is such that it is not possible to accurately describe the flow in two-dimensions. Calculations along an axisymmetric stream-surface cannot resolve the radial flow re-distribution around large scale separations. Nor can a two-dimensional code model the interaction between the tip clearance flow and the suction surface boundary layer. As such, predictions of this flow breakdown mechanism made with the *MISES* code can only be considered to be qualitative.

Although it was not possible to see the effects of the leading edge separation bubble in the rotor suction surface flow visualisation the presence of such bubbles has been documented by other authors, e.g. Tain [88] and Wheeler [96]. In detailed experimental measurements made on a low speed research compressor, the latter reports the laminar reattachment of this bubble in the favourable pressure gradient immediately downstream of the leading edge. Furthermore, Wheeler [96] also noted that *MISES* prematurely predicted boundary layer transition at the leading edge hence (incorrectly) eliminating the “main” separation bubble.

The *MISES* predictions are also dependent on the accuracy of its transition model. Weaknesses in this are apparent; most notably in the failure to capture the suction surface separation bubble at the test Reynolds number in this case (and in that of Wheeler [96]). In broad terms however, the calculations are realistic enough to provide a plausible explanation of the stalling behaviour of the Qineticq compressor.

In order to confirm the mechanism predicted above detailed measurements of the suction surface shear stress on several adjacent blades are required, e.g. hot-film data. This was not possible within the time available and remains as “work still to be done”.

6.10 Discussion

6.10.1 Why Does the Qinetiq Stage Exhibit Such Unusual Stalling Behaviour?

No similar flow breakdown mechanism has been observed in other compressors. The obvious question arises; why does this phenomena only appear in the Qinetiq stage? Without further (very detailed) work it is not possible to identify with any certainty the answer to this question. However, the differences between the Qinetiq rotor and other compressors, most likely to be significant in the formation of large non-propagating separations, are its leading edge geometry, extreme level of loading and the test Reynolds number.

The Qinetiq rotor features a high wedge angle of approximately 43° . (This compares to between 20° and 37° measured on the other rotor blades tested.) High wedge angles reduce the size of the leading edge over-speeds (or “spikes”) and delay the formation of leading edge separation bubbles until much higher incidence. *MISES* predictions indicate that the formation of a leading edge separation bubble at high incidence is a key factor in the coupling of the boundary layers on adjacent blades. Moreover, the trailing blade (i.e. blade T or A) *cannot* be effectively stabilised if a leading edge separation bubble is present at incidences below that at which the separation first occurs (i.e. on blade S or B). The Qinetiq rotor also features a leading edge circle of double the radius of the other blades tested which is likely to have a similar effect as increasing the wedge angle.

One might reasonably expect flow breakdown to be prevalent in highly loaded designs where boundary layers are operating close to their separation limit. This is especially true of the Qinetiq rotor which is even more highly loaded than the design intent and therefore subject to more severe adverse pressure gradients. Furthermore, the Qinetiq rotor is a “forward-loaded” design (more so than other designs tested), i.e. the peak suction point has been deliberately pushed forward to maximise the surface length available for diffusion. The result of this is a severe adverse pressure gradient over the separation bubble which cannot re-attach and therefore “bursts” at high incidence. It is the stabilisation of this failure mode which prevents the large separation propagating (as described by Emmons) and developing into a fully fledged stall cell.

Also relevant to the stability of the “main” suction surface separation bubble is the free-stream turbulence and Reynolds number. It was shown in Section 6.2.2 that an increase in the inlet turbulence reduced the size of the suction surface separation bubble and stabilised it sufficiently that the non-periodic flow breakdown mechanism was suppressed (Section 6.3 and Figure 6.5). It is likely that an increase in Reynolds number will have a similar effect on the “main” separation bubble and will prevent it bursting.

6.10.2 Implications for Real Aero-Engines

Given the sensitivity to inlet turbulence levels (and Reynolds number) the phenomena observed and described above is most likely to be a problem for the front stages (i.e. low inlet turbulence) of smaller (i.e. low Reynolds number) engines, such as those used on cruise missiles and unmanned aerial vehicles (UAVs). In the case of the latter the high altitude at which they operate reduces the Reynolds number further.

Calculations were performed on the same blade(s) at a Reynolds number of 1.0×10^6 ; representative of the values expected in large aero-engines. These predictions also showed strong coupling between the boundary layers, although in these cases the mechanism is slightly different. Such coupling may enable circumferentially non-periodic flow breakdown, similar to that observed in the Qinetiq stage, to occur in full size compressors or fans. This is a topic requiring more detailed investigation.

There is a current trend in the aero-engine industry to reduce the magnitude of leading edge spikes via high-wedge angles or elliptical leading edge geometry. This promotes the extent of laminar flow and therefore reduces the profile loss. It is therefore expected that such leading edge geometries will strengthen the coupling between the boundary layers on adjacent blades and will increase the probability of similar non-periodic flow breakdown. The experiments presented above have demonstrated that particular care must be taken when modelling such designs at low Reynolds number.

The physical variation in rotor blades and their set-up has been shown to be significant in causing non-periodic flow breakdown. The current work demonstrates how a small stagger variation can result in flow breakdown occurring at significantly lower incidences than that predicted by considering a single blade. The imposed stagger change applied in these predictions is below the variation expected in a real compressor; a variation

of $\pm 0.5^\circ$ is typical (Freeman [33]). The effect of larger stagger angle (or other set-up) variations is not clear and needs more attention.

6.11 Conclusions

Detailed measurements have been made on a, previously unreported, flow breakdown mechanism in the Qinetiq rotor. Calculations have been used to demonstrate coupling between boundary layer transition on adjacent blades and to develop a possible explanation for this phenomena. The major conclusions from this chapter, and recommendations for further work, are summarised below.

1. Due to small geometric differences (e.g. manufacturing or set-up errors) the diffusion on a particular blade is slightly higher than experienced by other blades. As the flow rate is reduced, the suction surface boundary layer on this blade separates first. Unlike a rotating stall cell these separations remain fixed to a particular rotor passage. As the flow rate is reduced further the next highest loaded blade separates and so on until (almost) every second passage exhibits a large separation. Further reduction in the flow rate from this saturated condition leads to conventional rotating stall.
2. It has been shown that the presence of such a separation has a stabilising effect on the flow in the trailing blade passage. In particular, the “bursting” of the suction surface separation bubble is prevented. This effect overcomes the destabilising effect of the increase in incidence (and the corresponding increase in diffusion) predicted by Emmons’ model of rotating stall. Hence these large scale separations do not propagate.
3. A two-dimensional coupled Euler/ integral boundary layer CFD code has been used to demonstrate significant coupling between a large separation and the boundary layer on the adjacent blade. The results from these calculations demonstrated the same qualitative symptoms as measured experimentally. In particular, they predicted the formation of a leading edge separation bubble on the blade adjacent to a large separation (i.e. Blade A or T). This bubble reattaches as a laminar boundary layer in the favourable pressure gradient. The intermittency produced in the shear layer over the leading edge separation bubble shortens

the “main” suction surface separation bubble (over which transition occurs) and prevents it bursting under the same (or greater) diffusion.

4. It has been shown that this flow breakdown mechanism is related to the “bursting” of a large suction surface separation bubble. Increasing the free-stream turbulence allowed the suction surface separation bubble to survive without bursting to lower flow rates and suppressed the large non-periodic separations. It is expected that increasing Reynolds number will have a similar effect. These results highlight a limitation in low speed, low Reynolds number testing of compressor stages and demonstrates the need for care in the design of such experiments.

The turbulence (and Reynolds number) dependency of this phenomena suggest that it is not likely to afflict embedded stages or large compressors. It may be significant for the front stages of smaller engines or those operating at very high altitude such as those used for cruise missiles and UAVs.

Recommendations for future work include:

1. In order to confirm the proposed model and the *MISES* predictions it is necessary to directly measure the suction surface shear stress (e.g. with hot-films) on several adjacent rotor blades. Particular attention must be paid to the resolution of such measurements at the leading edge.
2. It is not clear why this flow breakdown mechanism affects only the Qinetiq stage. Differences between the Qinetiq stage and other compressors likely to affect the formation of such flow breakdown mechanisms were identified; including its extreme loading and leading edge geometry (in particular the high wedge angle). However, this remains a question yet to be definitively answered. It would be instructive to extend an investigation into this question to include other design parameters; e.g. loading, leading edge geometry and manufacturing/ set-up errors.

Chapter 7

Computational Methods and Comparison with Experimental Results

7.1 Introduction

Computational fluid dynamics (CFD) allows the flow to be predicted through an axial compressor, or any other arbitrary geometry. The recent increase in computing power allows steady, multi blade-row, predictions to be made within the time scales necessary for compressor design. Several designs can be evaluated with CFD in the time required to test a single design experimentally and at a fraction of the cost. Nevertheless approximations exist in such methods, e.g. turbulence modelling and the assumption of steady flow¹. To understand the effect and limitations that these approximations and assumptions impose on the solution(s) it is necessary to calibrate the computer codes against known experimental measurements.

The bulk of the three-dimensional calculations presented in this thesis were carried out with the steady flow *MULTIP03* viscous CFD computer code. The two-dimensional coupled Euler/ boundary layer code *MISES* was also used to tailor blade sections, set

¹Higher fidelity methods do exist which address some, or all, of these approximations (e.g. multi-row unsteady, higher order schemes, large eddy simulation, direct numerical simulation). From a design point of view, the increased time and computational cost of such methods is currently prohibitive.

metal angles and set blade numbers.

The objective of using CFD in the present work is to investigate the effect of the choice of velocity triangles and stage loading. In particular CFD will be used to design and assess the performance of several rotor and stator designs of widely different duties in Chapter 8. The current chapter aims to calibrate the *MULTIP03* and *MISES* CFD programs so that the results of this study can be used with confidence. With this in mind, CFD predictions are compared to experimental measurements of the four very different (one conventionally loaded and three highly loaded) stages presented in Chapter 5.

7.2 MULTIP03

The bulk of the three dimensional calculations presented in this thesis were carried out with the *MULTIP03* code, developed by John Denton at the Whittle Laboratory. *MULTIP03* will be shown to give good predictions of the four stages tested as a part of the present work (see Chapter 5) and was much faster than other three-dimensional Navier-Stokes solvers.

7.2.1 Description

MULTIP03 is a development of the code originally described by Denton [17]. It solves the steady, three-dimensional, Navier-Stokes equations through a single blade passage via a time marching (explicit), finite volume method. The flow is calculated over three levels of multi-grid to speed up convergence. Multiple blade rows are calculated via a mixing plane approach. *MULTIP* is a well developed code and is widely used throughout the turbo-machinery industry.

Satisfactory convergence was typically obtained in 20,000 time steps. With a standard grid run on a single processor desktop PC, this took under three hours for a single blade row and under six hours for a stage. In the context of design, this gave *MULTIP* a significant advantage over “higher fidelity” codes which, in initial testing, took almost an order of magnitude longer to converge for little benefit in accuracy.

MULTIP uses a simple mixing length turbulence model to estimate the magnitude of the Reynolds stresses. The maximum mixing length adjacent to each wall is specified as a fraction of pitch in the input file. At solid boundaries the flow is modelled via a slip condition and wall functions (used to obtain the correct shear stress). Throughout the present work all boundary layers were assumed to be fully turbulent.

Procedure

The flow at the inlet to the computational domain was set to be equal to that measured experimentally at rotor inlet (i.e. downstream of the IGVs if present). Specifically, the pitch-wise averaged stagnation pressure and absolute swirl angle profiles were input to the code. The radial flow angle was not measured experimentally and was assumed to be aligned with the annulus and equal to zero (the annulus remains parallel approximately four annulus heights upstream of the rotor inlet traverse plane).

The mass flow through the calculated compressor is controlled by specifying the exit static pressure. At the exit to the computational domain the casing static pressure was specified and simple radial equilibrium used to obtain the variation in static pressure from hub to tip.

Grid

The mesh generator, embedded in *MULTIP03*, produces a single block, sheared “H” type mesh. The single passage grids used in the present calculations typically consisted of 55 pitch-wise, 58 span-wise and 80 stream-wise points on each blade surface. The number of upstream and downstream stream-wise points were chosen to control and/or match cell sizes at the edges of these regions. A typical grid is shown for the Gallimore stage in Figure 7.1.

The clearance gaps between the tip of the rotor and the casing are modelled by tapering the blade thickness to zero over a few cells. This treatment is commonly referred to as a “pinched tip” and is illustrated in Figure 7.1. It was found to be necessary to artificially reduce the size of the clearance gap to 75% of the physical clearance to achieve the correct radial penetration of the rotor clearance flow.

It was not possible to obtain a converged solution for the Qinetiq stage with the pinched tip model of the stator clearance gap. The resulting clearance jets typically had unrealistically low tangential momentum as a result of high loss in the tip gap. In the case of the Qinetiq stator the clearance fluid collected close to the suction surface causing it to catastrophically separate at all operating points.

Instead, a periodic tip treatment was employed to model the stator clearance flows in both the Qinetiq and Denton stators. In this method the blade thickness is maintained all the way to the end-wall (in this case the hub) and a periodic boundary condition applied tangentially across (non-continuous) points on the edges of the clearance gap. Although a periodic treatment does not model the physics of the flow in the clearance gap it does give more realistic predictions of the clearance flow in both the Qinetiq and Denton stators.

MULTIP uses a “cusp” model at the trailing edge. This uses a non load bearing extension to the trailing edge of the blade to prevent fishtailing². Although non-physical, this approach has been shown to be superior to modelling the trailing edge explicitly, especially in terms of the accuracy of the exit flow angle (Denton & Dawes [20]).

A preliminary grid dependency study was carried out by simulating the Gallimore stage with both 55 and 73 radial grid points. Although small differences were apparent in the prediction of the rotor tip clearance flow and the stator suction surface separation, the increase in grid resolution made very little difference to the predicted radial profiles over the majority of the span. The purpose of the current work is to investigate the effects of several design decisions and therefore, in this case, run-time has a greater significance than when using CFD in an pure analysis role. The grid selected gave a good compromise between reasonable accuracy and run time.

²“Fishtailing” refers to the unrealistic negative blade loading at the trailing edge. This occurs as a result of trying to model fundamentally unsteady flow (i.e. vortex shedding) with a steady method. The pressure surface remains attached beyond the true time-averaged separation point and accelerates around the high curvature at the trailing edge, hence creating a region of unrealistically low static pressure.

Post-processing

Analysis of the CFD solutions was performed at axial cut planes, chosen to coincide, as closely as possible, with the experimental traverse locations. This had to be compromised at rotor exit due to the proximity of the mixing plane. Custom programs were used to pitch and span-wise average each *MULTIP* solution at the analysis planes. These used the same method(s) to average the CFD data as were used experimentally (described in Section 3.8.4 and by Bolger [4]).

7.2.2 Comparison with Experimental Results

The calibration exercise was carried out by comparing *MULTIP* predictions to the detailed experimental measurements made of the four stages tested (described in Chapter 5). This allows the strengths and weaknesses of the *MULTIP* code to be assessed and, most importantly, it gives confidence in its use for the design study presented in Chapter 8.

7.2.3 Rotor Exit Flow

Contours of measured and predicted relative velocity at rotor exit are shown for the nominal design and near stall operating points in Figures 7.2, 7.3, 7.4 & 7.5 for the Mini-Deversen, Gallimore, Qinetiq and Denton stages respectively.

Design Flow

At the design flow rate *MULTIP* predicts the structure of the rotor wakes quite well. In general the predicted rotor wakes are deeper (i.e. increased velocity deficit) and thinner than those measured. In the experiments this could be a consequence of natural averaging along the length of the hot-wire element (aligned with the circumferential direction); the wire length was between 3.4% and 5.0% of the mid-span pitch (depending on the number of rotor blades). In spite of this, the overall level of pitchwise averaged loss at the design point is in reasonable agreement.

The measured rotor wakes, shown in Figure 7.5A, indicate that high loss at the Denton rotor hub comes from two sources; a collection of low momentum fluid in the suction surface/ hub corner and a three-dimensional separation visible at about 16% of span. Of these two, it is the corner loss which is more severe. Although the *MULTIP* predictions of the Denton rotor show both sources of loss the relative magnitude of the three-dimensional separation is over-predicted (when compared to the corner loss). The high corner loss also appears closer to the hub and smaller than measured. This is partly due to *MULTIP*'s tendency to under-predict the radial penetration of secondary flows onto the suction surface. In the predictions of the Qinetiq rotor the hub corner separation lies too close to the hub at 15% of span when compared to the measured corner separation at 21% of span (Figure 7.4).

It is apparent that the biggest weakness in *MULTIP* is in its prediction of the tip clearance flow. *MULTIP* struggles to resolve the roll up and collection of the clearance flow in the casing/ pressure surface corner. *MULTIP* under-predicts the pitch-wise penetration of the clearance flow. In all four cases these features are unrealistically smeared across the pitch and the predicted velocity deficits are deeper than measured. This is thought to be due to the simple mixing length model employed by *MULTIP*. In particular the assumption of a constant mixing length across the whole pitch which causes the clearance jet to mix out prematurely. At the Denton rotor casing (Figure 7.5A) *MULTIP* also fails to predict the loss core seen at 85% of span in the experimental measurements.

The prediction of the Mini-Deversen and Denton rotor clearance flows can be slightly improved by reducing the mixing length at the casing, however high mixing lengths are required to keep the Gallimore and Qinetiq calculations stable. The purpose of the current chapter is to calibrate the *MULTIP* CFD code for use with a wide range of stage designs. It is impossible to know appropriate mixing length modifications *a priori* and therefore mixing lengths were kept constant throughout all the simulations presented here.

Near Stall

MULTIP correctly predicts the observed trends between the design and near stall operating points for each stage, i.e. the growth of the hub corner loss cores and thickening

of the wakes. Despite the obvious weakness in the predictions of tip clearance flows, the collapse of the Gallimore and Denton clearance flows is predicted well enough (Figures 7.3B & 7.5B) for this problem to be identified and addressed during the design process.

Radial Profiles

Comparisons of the pitch-wise averaged radial profiles measured and calculated at rotor exit are presented in Figures 7.6, 7.7, 7.8 and 7.9 for the Mini-Deverson, Gallimore, Qinetiq and Denton rotors respectively. *MULTIP* correctly resolves the radial profiles of axial velocity at the design flow rate. Near to stall discrepancies in the predicted blockage of the outer 25% of span cause “see-saw” errors over the remainder of the annulus in order to maintain the required mass flow rate, chosen to match the experimental values. Nevertheless the radial *variations* in axial velocity from hub to about 75% of span are reasonably well predicted.

The shape of the total pressure rise profiles at design are reasonably well predicted. Offsets between measured and predicted pressure rise through the Gallimore and Denton rotors are mostly due to over-prediction of the mid-span axial velocity (as a result of unrealistically high tip clearance blockage) and turning respectively (Figures 7.7 and Figures 7.9). Downstream of the Qinetiq rotor, the predicted defect in total pressure rise (Figure 7.8B), at approximately 10% of span, is smaller and closer to the hub than measured. A similar defect exists in the measurements at approximately 20% span and affects the blade from the hub to almost mid-span. As a result the agreement is compromised in this region, especially near to stall.

At the design flow rate (red symbols) *MULTIP* provides good predictions of the relative flow angle at rotor exit; the maximum difference between the predicted and measured mid-span relative flow angle is $\pm 0.6^\circ$. In general, the agreement near to stall (blue symbols) at mid-span is not much worse. The exception to this is the Denton rotor which under predicts the mid-span turning by 3.8° near to stall (Figure 7.9C), possibly as a result of the high blockage at the casing (recall that the Denton tip clearance flow collapses near to stall; see Figure 7.5) off loading the rotor between the hub and approximately 70% of span.

7.2.4 Stator Exit Flow

Contours of measured and predicted stagnation pressure (presented in terms of a pseudo-loss coefficient; see Section 3.8.5) at stator exit are shown for the nominal design and near stall operating points in Figures 7.10, 7.11, 7.12 & 7.13 for the Mini-Deverson, Gallimore, Qinetiq and Denton stages respectively.

Design

The contours of stagnation pressure shown in Figures 7.10 to 7.13 show good agreement between the measured and predicted stator exit flow. The key flow features of each stator are generally well captured. The agreement between the measured and predicted wake depths is much closer than in the case of the rotors, although they are still over-predicted. The clearance flows at the hub in the Qinetiq and Denton stators (Figures 7.12A & 7.13A) are well captured in terms of both size and position.

In general the radial penetration of the loss cores at the casing is under-predicted (as seen at the rotor hub); this is particularly noticeable in the Mini-Deverson and Qinetiq predictions (Figures 7.10A & 7.12A) where the predicted loss cores do not make it onto the suction surface as observed experimentally. At the Mini-Deverson stator hub (Figure 7.10A) the prediction shows the corner separation is further developed than measured at the nominal design point.

Although *MULTIP* does predict a negative incidence separation in the Gallimore stator (Figure 7.11), it struggles to capture the details of the measured flow. This is possibly due to poor grid resolution at the leading edge inherent with a sheared “H” type mesh.

Near Stall

Near to stall, *MULTIP* qualitatively captures the key features of the measured stator exit flow (Figures 7.10B to 7.13B). In all four cases the correct flow breakdown mechanisms have been predicted, although the details of the large separations are not always captured. In the Mini-Deverson, Gallimore and Qinetiq cases the size of the predicted separations are larger than measured. This is unsurprising given the limitations of the simple mixing length turbulence model. By its very nature the assumption of a constant

mixing length cannot model the dramatically increased mixing inherent in separated flows. The size of predicted separations could be restricted by globally increasing the mixing length limit through the stator row, however the datum mixing lengths were maintained for the sake of simplicity.

Although the size and overall loss of the predicted clearance flow at the Denton stator hub is captured, the predicted structure and pitch-wise location differs from that measured. This occurs as a result of additional loss at the hub. As in the rotor (Section 7.2.3), the assumption of constant mixing length in tip clearance flows is overly deleterious.

Radial Profiles

Comparisons of the pitchwise averaged radial profiles measured and calculated at stator exit are presented in Figures 7.14, 7.15, 7.16 and 7.17 for each of the four stages tested. In general the agreement between the measured and predicted radial profiles at stator exit is less good than downstream of the rotor.

At the design flow rate (shown in red) the axial velocity profiles are well predicted. The size and extent of deficits associated with three-dimensional separations are moderately well captured. Near to stall (shown in blue), the over-predicted separations in the Mini-Deverson, Gallimore and the Qinetiq stators lead to greater velocity deficits than measured. This also results in unrealistically high predictions of flow angle. As in the rotor, discrepancies in the predicted blockage lead to “see-saw” errors over the remainder of the annulus in order to maintain continuity. The accuracy of the near stall prediction of the Gallimore stator profiles (Figure 7.15) suffers across the whole span as a result of the large separation that dominates the stator passage and the significant flow re-distribution towards the casing.

The agreement between the measured and predicted stagnation pressure rise profiles is reasonably good, in particular the span-wise variations are well resolved. The deficit in predicted stagnation pressure in Figure 7.14B indicates that the loss is over-predicted through the Mini-Deverson stator. The opposite is true in Denton stator near to stall (Figure 7.17B).

At the design point the predicted mid-span flow angle downstream of the Mini-Deverson

Stage	$\bar{\phi}$	$\eta_{measured}$ [%]	$\eta_{predicted}$ [%]
Mini-Deverson	0.528 [†]	87.3	86.7
Gallimore	0.499	83.8	83.9
Qinetiq	0.688	86.4	85.6
Denton	0.652	85.6	85.5

Table 7.1: Comparison between measured and *MULTIP* predictions of stage efficiency at the traverse point nearest to peak efficiency. ([†]Nearest CFD point to measured peak efficiency.)

stator lies within 0.5° of the measured value. Near to stall *MULTIP* under-predicts the turning by approximately 1.0° . The predictions of the flow angle at the exit of the three highly loaded stators is less good. Neglecting regions affected by large separations (e.g. the Gallimore stator from 0% to 50% of span), *MULTIP* over-predicts the mid-span stator turning by 1.0° , 2.5° and 3.2° for the Gallimore, Qinetiq and Denton stages respectively at the design flow rate. Nevertheless, at the design point, *MULTIP* resolves the spanwise trends in stator exit flow angle and differences between each of the blades tested. Somewhat perversely, the agreement in flow angle at exit to the Qinetiq stator (Figure 7.16C) is better when operating near to stall than at design. The over-predicted separation leads to the spurious prediction of the correct flow angle.

7.2.5 Characteristic Performance

A comparison between the predicted and measured characteristics (pressure rise, torque and efficiency) are presented in Figures 7.18, 7.19, 7.20 and 7.21 for the Mini-Deverson, Gallimore, Qinetiq and Denton stages respectively. Given the agreement between the velocities, pressures and flow angles at stator exit it is perhaps unsurprising that that *MULTIP* resolves the shape of the pressure rise characteristics reasonably well. The measured and predicted nominal design point efficiencies of all four stages are shown in Table 7.1. *MULTIP* predicts the nominal design point efficiency of all four stages to within 0.8%. The agreement is worst in the Qinetiq stage (the efficiency was under predicted by 0.8%), perhaps because of the unrealistically high loss in the rotor tip clearance flow (Figure 7.4A).

Towards stall the agreement is less good as regions of separated flow grow and become significant; it has been shown above that *MULTIP* struggles to accurately predict large separations. As the flow rate through the Mini-Deverson and Denton stages is reduced below the design value, the predicted drop off in efficiency is more benign than measured (Figures 7.18 & 7.21). This is partly due to the under-prediction of separations at the Mini-Deverson rotor hub and on the Denton stator suction surface (Figures 7.2 & 7.13 respectively).

At high flow rates (i.e. above design), the predicted performance of the Gallimore stage is well above that measured (Figure 7.19). Although *MULTIP* does predict the presence of negative incidence separations on both the rotor and stator, the magnitudes of these are below that observed experimentally.

7.2.6 Summary: *MULTIP*

MULTIP has been shown to provide reasonable predictions of four completely different stages. Key features of the flow in both the rotor and stator are captured, however, quantitatively, the predictions of the stator exit flow are less good than for the rotor. In both the rotor and the stator, *MULTIP* under-predicts the radial penetration of the secondary flows.

MULTIP resolves the changes in efficiency between stages to within 0.8%. In cases which do not suffer from large separations (e.g. a well designed stage operating at its design point), this allows a high degree of confidence in the efficiency predictions of very different loadings, design points and methodologies.

Near to stall, *MULTIP* correctly predicts the failure mechanism in the rotor and stator of each of the four stages tested. However, large separations tend to be over-predicted and their precise nature (e.g. span-wise extent, blockage, flow angle, etc...) is not well captured. This is almost certainly as a result of the crude mixing length turbulence model which does not model the increased mixing in separated flow.

The key weakness of *MULTIP* is in predicting tip clearance flows with a pinched tip model. This is thought to be due to a combination of the crude turbulence model (which assumes a constant mixing length over the whole pitch) and the approximations inherent in tapering the blade thickness over a few grid points to model a square tip.

Despite not modelling the physics of the clearance flow, a “periodic” tip treatment gave good results for cantilevered stators.

The quality of the *MULTIP* predictions over the majority of the flow coupled with its fast turn around time makes *MULTIP* particularly attractive for use in design and, in particular, for assessing several different design options such as the design study presented in Chapter 8.

7.3 MISES

MISES consists of coupled two-dimensional Euler (i.e. inviscid) and boundary layer solvers. It was developed by Drela [28] at Massachusetts Institute of Technology. By only modelling the flow in two dimensions and by capturing boundary layer effects via an integral method only small grids are required. Run times are therefore very quick; typically a converged solution can be obtained in under 30s for a single blade section. However this rapid turn around is achieved at the expense of modelling the true three-dimensional nature of the flow through a turbomachinery blade row.

The *MISES* code was used during the course of this work for two-dimensional blade design, i.e. setting blade numbers, metal angles and tailoring of blade profiles to achieve optimum velocity distributions. *MISES* is widely used in this role throughout the turbomachinery industry.

7.3.1 Description

An example of a typical *MISES* grid is shown in Figure 7.22 for the Qinetiq stator. A typical grid consisted of 20 points across the pitch and approximately 100 stream-wise points on each blade surface. *MISES* grids are displaced from the blade surface to account for the blockage (often referred to as displacement thickness) presented by the boundary layers. This displacement is calculated by solving the integral boundary layer equation along each surface with the velocities calculated at the adjacent edge of the grid (i.e. calculated by the Euler solver).

The boundary layer solver in *MISES* incorporates a hybrid Abu-Ghannan and Shaw [1]

and “ e^n ” laminar to turbulent transition model; full details are given in Drela [29].

The three-dimensional flows through a real compressor blade row clearly cannot be captured by a two-dimensional solver. However, the effect of stream-tube contraction and radius change, so called quasi three-dimensional effects, are included by specifying the stream-tube coordinates (i.e. radius and thickness) in an additional input file.

The mixed out average of the inlet and exit flow properties are assessed at the lines of constant meridional coordinate indicated in Figure 7.22. Profile and any shock losses are also assessed at the latter location.

7.3.2 Calibration

For the purposes of calibration the measured performance of the mid-height sections of all four stators tested was compared to that predicted by *MISES*. The stream-tube radius and height was assumed to be constant throughout the blade row. Conditions were set to be those measured at the nominal design point of each stator. Off-design performance was estimated by varying only the inlet flow angle.

Deviation

A comparison between the measured exit deviation and that predicted by *MISES* is shown in Figure 7.23. At the design point (the solid symbols) *MISES* gives a good estimate of the Mini-Deverson stator exit flow angle to within 0.3° . Towards stall the agreement is less good, no doubt because of the large three-dimensional hub corner separation present at low flow rates which cannot be accounted for by a two-dimensional code such as *MISES*.

The agreement between the measured and predicted exit flow angles is less good for the three highly loaded stages (within $\pm 3.0^\circ$). This suggests that three-dimensional effects become more significant with highly loaded designs. Gbadebo [39] demonstrated a mechanism whereby three-dimensional cross passage flow adds to the mid-span deviation. Another possible cause is the reduced aspect ratio of the three highly loaded stators which increases the three-dimensional effects. Despite this, *MISES* correctly resolves the trends with varying inlet flow angle across the four stators tested.

Boundary Layer Parameters

Figure 7.24 shows the corresponding comparison between predicted and measured³ integral boundary layer/ wake parameters (i.e. displacement and momentum thickness). For each stator the predicted and measured boundary layer parameters were evaluated at the same axial location.

Near to the design point (solid symbols) *MISES* gives a reasonable prediction of the measured displacement and momentum thicknesses. In general, the design point predictions are most accurate for the conventionally loaded Mini-Deverson stator and the agreement is worst for the Gallimore stator. Nevertheless, *MISES* does capture the trends exhibited by the Gallimore and Qinetiq stators, in particular the rapid increase in displacement thickness and shape factor at high incidence. In the case of the Gallimore stator the thickening of the wake at negative incidence due to a separation from the leading edge of the pressure surface is also resolved, as can be seen by the “bucket shape” of the results.

At high incidence, *MISES* does not capture the increase in displacement and momentum thicknesses seen experimentally downstream of the Mini-Deverson and Denton stators. This is perhaps unsurprising from a two-dimensional calculation; near to stall the flow through both of these stators is highly three-dimensional. In the former case this is due to the formation of a large three-dimensional separation at the hub corner (Section 5.4) affecting the flow through the whole passage. In the latter case the flow separates from the leading edge at the casing due to excessive incidence and convects to mid-span (see Section 5.7).

Transition

Without detailed suction surface measurements (e.g. hot-film or boundary layer traverses) it is impossible to assess the accuracy of the transition model in *MISES* with any certainty. However, flow visualisation can be used to give an indication of the location

³Experimental values of boundary layer/ wake integral parameters were estimated from area traverse data by evaluating the appropriate integral from the centre to each edge of the wake and summing the two components. The edge of the wake, and appropriate edge velocity, was identified with a method similar to that employed by Khalid et al [56] as the point where the magnitude of the normal velocity gradient ($\frac{dU}{dy}$) drops below a threshold value.

Stage	<i>MISES</i> Prediction $(\frac{L_{trans}}{C})$	Flow-vis “dark-band” $(\frac{L}{C})$
Mini-Deverson	33%	22-36%
Gallimore	27%	17-28%
Qinetiq	25%	n/a
Denton	37%	27-38%

Table 7.2: *MISES* predictions of suction surface transition point at design as a fraction of true chord.

of transition; Bolger [4] correlated the “dark bands” observed in the flow-visualisation exercise (Chapter 5) with a time averaged transition region. The transition locations predicted by *MISES* are presented in Table 7.2. It can be seen that the predicted transition points agrees well with the downstream limit of these “dark bands”.

7.3.3 Summary: *MISES*

MISES has been shown to give an acceptable estimate of the stator exit flow angle. The conventionally loaded Mini-Deverson stage showed good agreement. The predictions were less good for the three highly loaded designs as a result of increased three dimensional flow and therefore care must be taken when setting the blade exit angle of highly loaded blade rows with *MISES*. Predictions of boundary layer parameters and loss coefficients were also shown to be reasonable at, or near to, the design incidence of each stator.

Most importantly *MISES* correctly predicts the onset/ growth of suction surface separations and the corresponding rapid increase in loss when the flow is not dominated by three-dimensional separations. This justifies its use as a design tool to set acceptable levels of diffusion (i.e. number of blades).

7.4 Summary

The objective of using CFD in the present work is to investigate the effect of the choice of velocity triangles and stage loading. In particular three-dimensional CFD will be

used to design and assess the performance of several rotor and stator designs of widely different duties in Chapter 8.

The *MISES* code was used during the course of this design study for two-dimensional blade design, i.e. setting blade numbers, metal angles and tailoring of blade profiles to achieve optimum velocity distributions. The very fast run times typical of a two-dimensional coupled Euler/ integral boundary layer solver such as *MISES* allows suitable two-dimensional blade designs to be arrived at quickly, ready for assessment in a three-dimensional program like *MULTIP*.

The *MULTIP* three-dimensional CFD code has been shown to provide reasonable predictions of four completely different stages. Key features of the flow in both the rotor and stator are captured (both at the design point and near to stall) and the correct flow breakdown mechanisms are predicted near to stall. *MULTIP* resolved the changes in design point efficiency between stages to within 0.8%. The quality of the *MULTIP* predictions over the majority of the flow coupled with its fast turn around time makes *MULTIP* particularly attractive for use in design and, in particular, for assessing several different design options.

Chapter 8

Design Options for Stages with Increased Loading

8.1 Introduction

Although various highly loaded stages have been attempted over the years (with varying degrees of success), a systematic investigation into the effects of increasing loading and the choice of design velocity triangles has not been previously reported in the open literature. This chapter strives to address this deficiency; a parametric study (conducted with three-dimensional CFD) into the effects of varying loading and stage inlet flow angle on the individual performance of the rotor and stator is presented.

Using three dimensional design techniques, it is possible to exert some control on secondary flows (e.g. Bolger [4]) and increase permissible diffusion (e.g. Gallimore et al [37, 38]). The exploitation of sweep and lean as a potential means of achieving acceptable efficiency at higher loadings seems obvious and therefore warrants investigation; the results from such a study are presented in this chapter.

This study shows that employing high-reaction, counter-swirl, designs is the best strategy for minimising the efficiency penalty at high stage loading. Finally, the implementation of such stages designs in a high-speed, multi-stage compressor is briefly discussed.

	<i>min</i>	Δ	<i>max</i>
$\frac{\Delta h_0}{U_{mid}^2}$	0.35	0.10	0.75
α_{in} ($= \alpha_x$) [$^\circ$]	-20	10	30

Table 8.1: Range and increment (Δ) of nominal stage loading coefficient ($\frac{\Delta h_0}{U^2}$) and inlet/ exit flow angle ($\alpha_{in} = \alpha_x$) tested.

8.2 Method

To assess the impact of stage loading ($\frac{\Delta h_0}{U_2}$) and inlet flow angle (α_{in}) on rotor and stator loss (and therefore overall efficiency), the rotor and stator were considered separately. Several rotor and stator designs were generated and their performance assessed using the three-dimensional CFD code *MULTIP03*. In comparison with measured results, *MUTLIP* gave reasonable predictions of each of the four stages tested (despite their very different designs), especially in cases which did not suffer from large separations (e.g. at design). A detailed description of this CFD program and its use can be found in Chapter 7.

Each blade row was designed as if it were part of a “repeating stage” (i.e. $\alpha_{in} = \alpha_{exit}$). The design flow coefficient was fixed at 0.50 (as for the Gallimore stage) for all designs while the stage inlet angle (or, in other words reaction) and nominal stage loading coefficient were varied. This study is illustrated schematically by the velocity triangles shown in Diagram 8.1. The range and increment of the stage inlet/ exit angles and nominal stage loading coefficients are given in Table 8.1. In all calculations, the rotor blade speed was set to be equal to that in the Highly Loaded Research Compressor (i.e. $U_{mid} = 63.6ms^{-1}$).

The most obvious problem with the Gallimore stage observed during testing was the catastrophic stator separation at the design flow rate. Diagram 8.1B illustrates the increased diffusion and turning required from the stator as a result of higher stage loading. (The rotor also sees increased turning and diffusion, however, as shall be demonstrated later, this is less deleterious in the rotor than the stator.) The effects of stage loading and inlet flow angle on the stator flow were therefore investigated before a similar study was performed on the rotor.

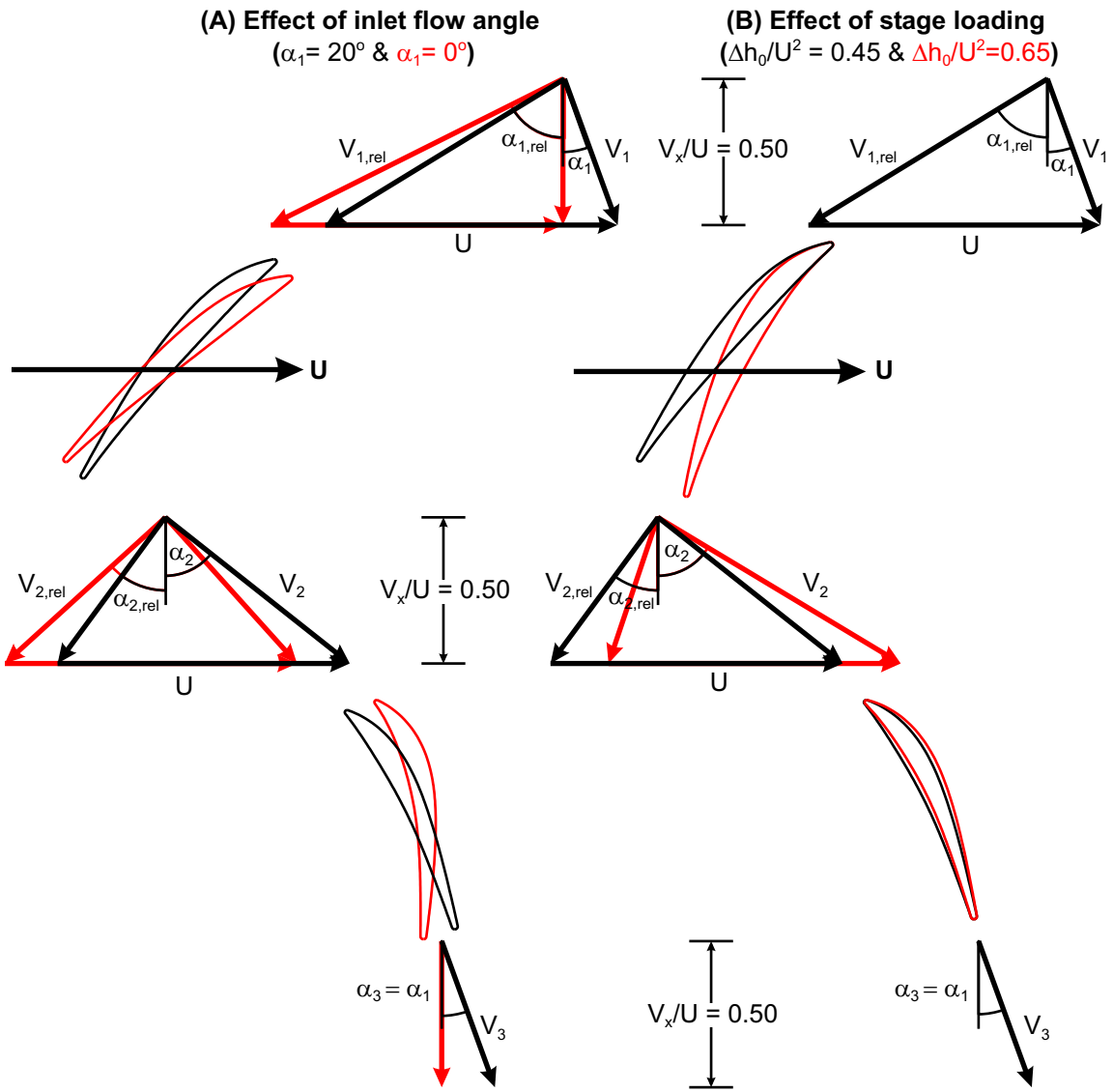


Diagram 8.1: Schematic diagram showing the effects of varying design inlet angle and stage loading on the velocity triangles of a repeating stage. ($\bar{\phi} = 0.50$.)

8.2.1 Blade Definition and Generation

General Configuration

The blades generated for the loading/ inlet flow angle study are loosely based on the existing Gallimore stage; the most extreme design tested so far in terms of rotor/ stator de Haller numbers. The general configuration of this stage and the HLRC has been maintained for the loading and reaction parametric study, including chord length, leading/ trailing edge radii and annulus geometry.

	Rotor	Stator
c [mm]	57.5	61.2
h [mm]	45.0	45.0
r_{hub}/r_{case}	0.80	0.80
$AR (= h/c)$	0.78	0.74
t_{max}/c	0.10	0.10
r_{le}/c	0.009	0.009
r_{te}/c	0.009	0.012
ϵ/c	0.010	0.000

Table 8.2: Summary of rotor and stator geometry (held constant across all designs).

To account for the effects of compressibility, the artificially increased thickness used in the Gallimore stage was maintained for this study. These geometric parameters are summarised in Table 8.2 and apply to all blades produced for the loading/ reaction study described herein.

Blade Design

Each blade was split into seven span-wise sections, each lying on an axi-symmetric stream-surface. The Euler/ integral boundary layer code *MISES* was run for each section and the results used to guide the choice of inlet & exit metal angles and solidity (i.e. number of blades). For the purposes of the *MISES* calculations, turbulence levels were set to those measured in the Gallimore stage (i.e. 2.5% and 4.0% at rotor and stator inlet respectively). (More details on *MISES* can be found in Chapter 7.) The inlet metal angle was chosen to align the leading edge with the oncoming flow and the trailing edge metal angle was adjusted to provide the required turning. The trailing edge metal angles were chosen to give uniform work input (Δh_0) across the span at rotor exit and uniform flow angle at stator exit.

The leading edge angle differs from the oncoming flow angle due to the local effects of the blade circulation. The leading edge metal angle was iteratively adjusted to give equal magnitude over-speeds at the leading edge; a good first approximation to zero incidence. These over-speeds, or “spikes”, are highlighted in the example velocity distribution shown in Diagram 8.2. They occur as a result of the flow accelerating

around the high-curvature leading edge and decelerating as it blends into the (lower curvature) main blade surface.

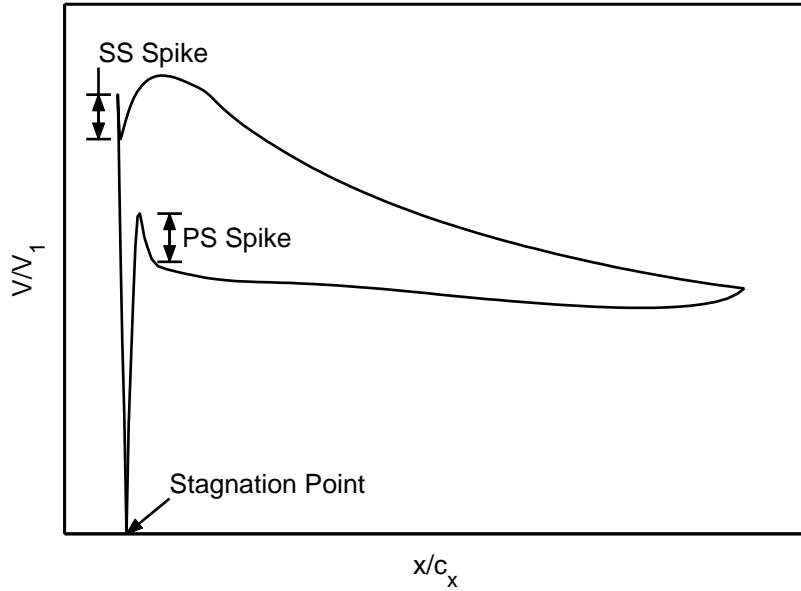


Diagram 8.2: Schematic velocity distribution showing leading edge “spikes”.

This process was repeated for all sections in the span-wise direction apart from the two end-wall sections. The increased incidence at the end-walls meant that these sections could not be calculated with a two-dimensional method. Instead, the inlet and exit metal angles were smoothly extrapolated radially to the end-wall sections. The two dimensional sections produced in this manner were conventionally stacked along a radial line passing through the centroid of each section (i.e. sweep and/ or lean was not deliberately introduced) to produce the final blade.

The number of blades (i.e. solidity) was primarily chosen by considering the mid-span section and was chosen to give a predicted (with *MISES*) suction surface boundary layer with a shape factor of between 2.3 and 2.4 at the trailing edge; i.e. just prior to the onset of separation (separated shape factors for a turbulent boundary layers are usually greater than 2.5).

The shape of each section was controlled primarily by a user specified non-dimensional camber and thickness distribution. (Definitions of the non-dimensional camber and thickness distributions can be found in Appendix C.) For the current study, the same non-dimensional camber line and thickness distribution was used for all sections. These were defined as functions of distance along the chord line by cubic spline curves with

up to six control points. By specifying the camber line angle non-dimensionally, the inlet and exit metal angles can be adjusted to give the necessary incidence and turning independently of the camber distribution.

At a given chord-wise position, the blade thickness was applied perpendicularly to the camber line. An iterative procedure was used to adjust the leading and trailing edge thickness and smoothly blend circular geometries (of specified radius) into the main section profile.

A datum set of rotor and stator blades were designed to give a stage loading coefficient ($\frac{\Delta h_0}{U^2}$) of 0.65 with axial inlet flow (i.e. the Gallimore design point). The result was controlled diffusion rotor and stator designs with improved (two-dimensional) performance over the Gallimore stage. The non-dimensional camber and thickness distribution from these datum blades were maintained for all other blades used in this study. The non-dimensional camber lines and thickness distributions developed for the rotor and stator loading/ inlet flow angle studies (described in this chapter) are shown in Figure 8.1.

8.2.2 Assumed Flow Conditions

Rotor Inlet

For the purposes of the current study, the conditions specified at inlet to the rotor were the radial profiles (i.e. pitch-wise averaged) measured experimentally upstream of the Gallimore stage. At the inlet to the Gallimore stage the flow is axial and uniform across the span. To vary the inlet flow angle, the measured flow angle across the span was incremented by a uniform amount to achieve the desired mass-averaged value. The total pressure, total temperature and axial velocity profiles were left unchanged. The radial flow angle was not measured and assumed to be zero (a reasonable assumption for a parallel annulus machine).

Stator Inlet

The inlet conditions to the stator are not as trivial. Diagram 8.1 shows how the stator inlet flow angle varies with stage inlet flow angle (α_1) and stage loading coefficient

$(\frac{\Delta h_0}{U^2})$. Furthermore, it is important to model the end-wall boundary layers to accurately capture the stator secondary flows. At stator inlet (i.e. rotor exit) the direction of the flow in the end-wall boundary layers varies across their height. It is therefore preferable, in the first instance, to use the measured conditions (or, in the second instance, the profile calculated by a three-dimensional CFD computer program).

In the absence of calculated profiles (the stator design was investigated prior to the rotor), the stator inlet profile adopted was based on that measured in the Gallimore stage. The variation in stator inlet flow angle was captured by bulk shifting the radial profile of flow angle to give a profile with the correct average swirl. Within the chosen range of loadings and stage inlet angle tested this approach gave a maximum error of less than 2° from that given by simple radial equilibrium across the entire span. As at rotor inlet, the radial flow angle was not measured and assumed to be zero.

Although the overall magnitude of the stagnation pressure at rotor exit/ stator inlet will vary with loading, it is the radial variation which is most significant for the stator performance; the magnitude of the stator inlet total pressure drops out of the stator performance analysis when using appropriate non-dimensionalisation. As almost all compressors are designed to give a uniform stagnation pressure rise across the span, the underlying shape of total pressure profile is unlikely to change significantly with design point. Assuming that the upstream rotor is well designed (i.e. no large corner separations), it is therefore reasonable to use the total pressure profile measured behind the Gallimore rotor unchanged as this captures typical span-wise variations found downstream of a rotor.

8.3 Effect of Stage Inlet Angle and Loading on Stator Performance

8.3.1 Performance

The effect of the choice of design point on stator performance is summarised in terms of loss coefficient in Figure 8.3. At low stage loading coefficients (e.g. $\frac{\Delta h_0}{U^2} \approx 0.45$) there is little variation in stator loss with inlet flow angle, α_{in} ($= \alpha_x$, recall repeating stage assumptions). As the stage loading is increased beyond conventional levels (i.e.

$\frac{\Delta h_0}{U^2} \geq 0.55$) this variation becomes more pronounced; as the inlet flow angle is increased (i.e. moving towards 50% reaction) the stator losses rise dramatically. The rate of this increase gets steeper with increasing loading.

The steep rise in loss with increasing inlet flow angle at high loadings is caused by the formation of large corner separations at/ near to the hub. The onset of these separations is marked on Figure 8.3 (by the filled symbols) and illustrated in contours of stagnation pressure loss parameter shown in Figure 8.4 for a stator of nominal loading equal to 0.65. Despite being well designed (i.e. attached) in the two dimensional design, the three dimensional flow is unacceptable. This demonstrates clearly that loading limits based on two dimensional theory, e.g. diffusion factor or two-dimensional boundary layer calculations, are not necessarily suitable for highly loaded designs.

In Chapter 9 it is argued that the velocity distribution around a compressor aerofoil is primarily dependent on the required loading (i.e. turning) and the de Haller number; in fact the velocity distribution is only weakly dependent on the inlet and exit flow angles. The effect of the loading and de Haller number on the calculated stator loss coefficient is shown in Figure 8.5; at each design point the predicted stator loss is labelled and the solid lines show approximate contours of loss coefficient.

At high de Haller numbers, above about 0.65, the stator losses are almost flat and there is mainly a dependency on loading. Highly loaded blades must produce a greater (total) tangential force to provide the necessary turning. This is achieved in two ways; (1) by increasing the pressure difference across each blade; and/ or (2) by increasing the number of blades. The former leads to higher velocities and therefore loss (recall that the entropy production in a turbulent boundary layer is approximately proportional to V_{edge}^3) and the latter increases the wetted area loss. In fact, increasing the suction surface velocities generally requires the addition of more blades to prevent boundary layer separation.

The stator losses increase rapidly as the de Haller number is reduced below about 0.64. At such low de Haller numbers, the contours of stator loss in Figure 8.5 tend towards the vertical, indicating that this rapid increase in loss is only weakly dependent on nominal stage loading. Further reduction in the de Haller below about 0.6 leads to the formation of large corner separations (indicated by the shaded symbols).

8.3.2 Recommendations for Stator Design

In term of compressor design, it is more instructive to consider the stator performance in terms of its impact on stage efficiency rather than the stagnation pressure loss coefficient. The drop in stage efficiency associated with each of the stator designs¹ is shown in Figure 8.6.

Figure 8.6 shows similar trends to the plot of loss coefficient (Figure 8.3). Although the penalty for reducing the stage reaction (i.e. increasing α_{in}) is modest at conventional stage loadings (making 50% reaction machines feasible), the increased variation in loss with α_{in} as the loading increases makes this approach prohibitive at high stage loadings. As the nominal stage loading (i.e. the required stator turning, ΔV_θ) increases, it is necessary to reduce the stage inlet angle to achieve acceptable stator performance. Such high reaction designs off-load the stator by turning the flow past the axial (sometimes referred to as “counter-swirl”). The flow re-accelerates as it is turned past the axial (recall from continuity that $V = \frac{V_x}{\cos \alpha}$) reducing the overall de Haller number hence making the stator design (aerodynamically) easier. In this sense such a blade behaves partially like a turbine blade which acts to accelerate the flow.

The stator de Haller number can also be increased by *increasing* the stage inlet angle (i.e. reducing the reaction), however, at high-loading, this requires very high inlet flow angles which are impractical in a real machine. Simple, repeating stage, velocity triangle calculations can be used to show that to keep the stator de Haller number above 0.65 (the approximate limit suggested by Figure 8.5) the inlet flow angle (α_{in}) must be either less than 4° or greater than 57° at a stage loading coefficient of 0.55. As the loading increases, the gap between these two values increases further and the locus of minimum de Haller number (i.e. the point of hardest aerodynamic design) moves towards lower inlet angles. This trend further encourages high-reaction, counter-swirl stator designs at high loading.

At low stage inlet flow angles (at or below approximately 0°) the penalty for a modest increase in stage loading (i.e. to $\frac{\Delta h_0}{U^2} \approx 0.55$) is relatively small; 0.6% and 0.2% (stage efficiency) for α_{in} equal to 0° and -10° respectively. As the stage loading is increased, it is necessary to reduce the stage inlet angle further to guard against higher efficiency

¹For the purposes of calculating the stator lost efficiency a stage enthalpy rise equivalent to the nominal stage-loading coefficient was assumed.

penalties. However, it is not sufficient to consider the stator lost-efficiency alone; it is also imperative to consider the effect of loading and inlet flow angle on the rotor efficiency.

8.4 Effect of Stage Inlet Angle and Loading on Rotor Performance

8.4.1 Performance

The effect of inlet flow angle and stage loading coefficient on the rotor stagnation pressure loss coefficient is shown in Figure 8.8. The rotor losses show a slight increase with inlet flow angle, especially at higher loadings (i.e. $\frac{\Delta h_0}{U^2} = 0.55 \text{ \& } 0.65$), however, compared to the corresponding curves for the stator (Figure 8.3), the rotor loss coefficients are much flatter at all stage loadings. This can be understood by considering the rotor and stator de Haller numbers, shown in Figure 8.9. Unlike, in the stator (red lines), the rotor de Haller numbers (black lines) are primarily dependent only on the stage loading and is relatively independent of inlet flow angle (for the current range of inlet flow angles).

The effect of inlet angle on the flow thorough a rotor passage is illustrated in Figure 8.10 for a highly loaded design. The contours of axial velocity (shown on the left) show that as the inlet flow angle is reduced a separation forms and grows in the hub/ suction surface corner. This trend is also repeated at lower stage loadings. Low inlet flow angle rotors are particularly susceptible to hub corner separations due to the increased spanwise variation in de Haller number, in particular, their lower hub de Haller numbers (i.e. increase aerodynamic difficulty). However, unlike in the stator the contours of relative velocity (shown in Figure 8.10 on the right) show that the pitch-wise extent of this corner separation is limited and therefore it is much less deleterious than the corner separations observed in the stator. Detailed CFD indicates that similar separations are present on all four of the rotors tested at their respective design points (and over almost all of the characteristic) and do not overly compromise stall margin.

Figure 8.11 shows that although the predicted rotor loss does increase steadily as the de Haller number is reduced, there is no rapid increase in loss below a critical de Haller

number (as caused in the stator by the growth of large corner separations), even at de Haller numbers as low as 0.53. One possible explanation for the differences between the rotor and stator corner separations is the centrifuging of the suction surface boundary layer outboard (therefore thinning any separated regions) to a location where suction surface boundary layers are healthier².

8.4.2 Recommendations for Rotor Design

The rotor performance is presented in terms of lost efficiency in Figure 8.12. Despite reducing the rotor loss coefficient (albeit slightly), the rotor efficiency penalty increases as the inlet flow angle is reduced (i.e. opposite to the trend seen in the stator, see Figure 8.6).

The lost efficiency can be found from Equation 8.1 (assuming that the pressure loss coefficient is approximately equal to the entropy rise coefficient; reasonable for an incompressible flow). As the inlet flow angle is reduced, the benefit in terms of loss coefficient as a result of the higher de Haller numbers (Term A in Equation 8.1), is outweighed by the increase in the normalised inlet relative velocity (Term B in Equation 8.1). In a stage with loading coefficient equal to 0.65, reducing the inlet flow angle from 0° to -20° increases the inlet velocity term in Equation 8.1 by almost one third, far greater than the predicted improvement in loss coefficient.

$$1 - \eta = \frac{T_{0,x}\Delta S}{\Delta h_0} = \underbrace{\frac{\rho}{2 \frac{\Delta h_0}{U^2}}}_{\text{(A) Loss coefficient}} \times \underbrace{\omega_p}_{\text{(B) Relative inlet velocity}} \times \underbrace{\left(\frac{V_{1,rel}}{U} \right)^2}_{\text{(B) Relative inlet velocity}} \quad (8.1)$$

At stage loading coefficients at or below 0.55 (i.e. conventional to moderately high loading) the predicted rotor efficiencies are similar at a given flow angle. As the stage loading coefficient is increased to 0.65, the rotor efficiency penalty increases by approximately 1.2% over the entire range of flow angles tested, i.e. the rotor efficiency begins

²To achieve constant work addition across the span the loading at the hub (i.e. $\frac{\Delta h_0}{U_{local}^2}$) must be greater than at the tip. This results in higher de Haller numbers and reduced diffusion towards the casing.

to drop sharply at a stage loading somewhere between 0.55 and 0.65 irrespective of inlet flow angle.

8.5 Three Dimensional Design

It is possible to exert some control on secondary flows (e.g. Bolger [4]) and increase permissible diffusion (e.g. Gallimore et al [37, 38]) with three-dimensional design (i.e. sweep and lean). The large loss cores and corner separations present in some of the stators assessed in Section 8.3 present an obvious target for such methods. A design study into the exploitation of sweep and lean as a potential means to allow higher loadings was therefore carried out on a highly loaded stator.

8.5.1 Method

For the current study, sweep and lean are defined parallel and perpendicular to the chord line respectively (the same definition as used by Gallimore et al. [37] and illustrated in Figure 2.3). The three-dimensional stacking line(s) used are illustrated in Figure 8.13. Sweep and lean were blended into a radial staking line by 33% of span away from each end-wall. These resulted in a lean/ sweep angle³ of 9.5° and 18.4° for the datum and “double” three-dimensional staking lines respectively. These three dimensional stacking lines were initially applied to a version of the Gallimore stator (nominal stage loading and inlet flow angle of 0.65 and 0°).

8.5.2 Gallimore Stator; $\frac{\Delta h_0}{U^2} = 0.65, \alpha_{in} = 0^\circ$

The main trends and conclusions of this work are unaffected by the various combinations of pure sweep, pure lean and combinations of the two (i.e. sweep and lean have similar effects when applied alone). Therefore, except where explicitly relevant, only the application of a combination of sweep and lean together (as shown in Figure 8.13)

³The definition of the sweep or lean angle used here is that adopted by Bolger [4]; i.e. the angle subtended by the end-wall normal direction and a straight line connecting the end-wall section to the blend point.

	ω_p
2D	0.130
Sweep & lean	0.117
$2 \times$ sweep & lean	0.122

Table 8.3: The effect of sweep and lean on the average stagnation pressure loss coefficient.

is described here.

The effect of adding varying degrees of positive sweep and lean on the contours of stator exit stagnation pressure loss parameter is shown on the left in Figure 8.14. The application of sweep and lean causes a modest reduction in the pitch-wise extent of the hub loss core (Figure 8.14B). This is accompanied by a modest reduction in the passage averaged stagnation pressure loss (Table 8.3). As the degree of sweep and lean is increased further (Figure 8.14C) the loss cores moves towards midspan and the loss begins to increase. The loss cores are moved towards mid-span by the increased radial migration of boundary layer fluid promoted by positive sweep and lean.

The high loss feature located near to the pressure surface at approximately 30% of span (Figure 8.14C) is primarily a result of the sweep (although, lean does augment this effect). This blade suffers from a negative incidence separation from the leading edge of the pressure surface (see Chapter 7). In the two-dimensional blade this fluid collects on the hub and moves across the passage (with the over-turned end-wall flow) into the hub/ suction surface corner. Sweep (and to a lesser extent lean) inhibits the radial migration of this low-momentum separated fluid towards the hub and therefore it remains near to the pressure surface. It is difficult to quantify this effect as, in the case of the two-dimensional blade (i.e. the datum blade), the fluid from the negative incidence separation is indistinguishable from the end-wall flow.

Figure 8.14 (right) shows the effect of sweep and lean on the extent of the separated flow on the suction surface (N.B. regions of negative axial velocity are coloured red). Sweep and lean prolong the attached region until further aft, however, the extent of the suction surface separation is not significantly affected (indeed the casing separation grows). The motion of the separations away from the end-walls corresponds to the movement of the loss cores observed in contours of stagnation pressure.

Sweep and lean reduce the diffusion applied to the hub and casing sections. This prevents the hub/ suction surface corner separation forming (at approximately 35% of axial chord) and reduces the loss at the end walls (note the thinner end-wall boundary layers in Figure 8.14). Sweep and lean increase the adverse pressure gradient to which the end-wall sections are subjected in order to compensate for the decrease in loading at the end-walls and maintain the same turning (Bolger [4]). From approximately 14% of span outwards the required diffusion is increased. The hub loss core lies at approximately 21% of span and is also subjected to this increased diffusion; the local diffusion factor (at a constant radius of 21% of span) is increased from 0.49 to 0.51 (at mid-span the local diffusion factor rises from 0.48 to 0.50).

The benefits of three-dimensional design techniques seem to be relatively modest at high stage loadings. The effect of increased diffusion away from the end-walls on an already highly diffusing blade and the additional radial migration of boundary layer fluid (induced by positive sweep and lean) seem to work against any benefit in terms of end-wall losses.

8.6 Recommendations for the Design of a Highly Loaded Stage

Having demonstrated the effects of stage loading and inlet flow angle on the rotor and stator individually, the results can now be combined to give some idea of the overall penalty for increasing the stage loading and the optimum choice of inlet flow angle. The effect of stage loading and inlet flow angle on the total stage lost efficiency (i.e. $1 - \eta_{rotor} - \eta_{stator}$) is shown in Figure 8.15.

At high inlet flow angles, the effect of the large corner separations in the highly loaded stators dominates the efficiency curves in Figure 8.15. Low stator de Haller numbers and the resulting corner separations preclude successful highly loaded stages with positive/ high inlet flow angles (i.e. co-swirl). Therefore, as the design stage loading is increased, the locus peak efficiency (show in black) moves to lower, even negative, inlet flow angles to control the stator de Haller number. To the left of this line, the total efficiency begins to fall as a result of the efficiency lost in the rotor at low inlet flow angles.

This suggests that a suitable strategy for designing a highly loaded stage would be to choose the maximum inlet flow angle possible which ensures the stator does not suffer from a corner separation. Figure 8.5 suggests that (for stators similar to those analysed here) a stator de Haller number of approximately 0.64 would be an appropriate minimum limit for this purpose. At conventional stage loadings, the higher de Haller numbers and absence of large corner separations mean that the choice of inlet flow angle is less restricted.

The predicted peak efficiency drops by 0.9% as the stage loading is increased from 0.45 to 0.55 and by a further 2.5% between stage loadings of 0.55 and 0.65 (i.e. a total efficiency penalty of 3.4% when compared to conventional loadings, i.e. $\frac{\Delta h_0}{U^2} = 0.45$). Although an efficiency penalty of 0.9% may be tolerable, the rapid drop in efficiency above stage loadings of approximately 0.55 is likely to make such highly loaded stages impracticable for efficiency critical applications (i.e. civil aero-engines).

8.7 Implementation of a High Reaction Stage(s) in a Multi-Stage Compressor

It has been demonstrated above that high-reaction stages are necessary to avoid large stator separations and to achieve good overall efficiency at high loadings. However, at high rotational speeds, such an approach introduces a trade off with higher shock losses on account of the increased relative Mach number into the rotor blade rows. At very high speeds counter-swirl designs are unlikely to be tenable.

In modern high-pressure compressors the Mach numbers drop towards the rear of the machine to provide low Mach number flow, $M_{exit} \approx 0.3$, into the combustor (necessary to achieve adequate combustion). This gives some scope to introduce very highly loaded, high-reaction, stages into the rear stages of the high-pressure compressor.

The transition into the high reaction, high-loaded stages should be possible across a single stator. Behind the second rotor of a high-pressure compressor the flow angle is typically between 35° and 45° . To introduce high-reaction, highly-loaded stages at this location, the second stator is required to introduce $10 - 20^\circ$ of counter-swirl at inlet to the next stage. This stator is roughly comparable to a repeating stage stator of nominal

loading $\frac{\Delta h_0}{U^2} = 0.55 - 0.65$, much like those demonstrated in Section 8.3.

An approach of this type should also yield benefits for the stator row immediately prior to the combustion chamber (i.e. the outlet guide vane or OGV). Normally, the OGV must remove all the, typically positive, swirl that exists between adjacent stages and therefore does more turning (i.e. is more highly loaded) than any other stator. A high-reaction, counter-swirl, design has the opposite effect and alleviates the required OGV turning.

In theory, highly-loaded counter-swirl designs, like those discussed above, could be incorporated into the rear of a modern high pressure compressor. However, they are unlikely to be suitable for the front one or two stages due to the higher Mach numbers and corresponding additional losses.

8.8 Conclusions

A parametric study into the effect of design stage loading and inlet flow angle (i.e. reaction) on the rotor and stator flow fields and performance has been conducted with three-dimensional CFD. The application of three-dimensional design methods to a highly-loaded stator has also been investigated. The main conclusions from this work are:

1. At conventional loading levels ($\frac{\Delta h_0}{U^2} \leq 0.45$) the stator loss is roughly constant with inlet flow angle. As the stage loading increases the variation in stator loss with inlet flow angle becomes more pronounced and the stator losses rise dramatically with increasing inlet flow angle (i.e. reducing reaction).
2. Despite being well attached in the two-dimensional design stage (i.e. in two-dimensional CFD), three-dimensional corner separations form and grow at the stator hub at de Haller numbers below approximately 0.62. This limit is only weakly dependent on stage loading. (Although beyond the scope of the current work, it would be a useful future exercise to investigate if/ how this limit varies with other variables, e.g. aspect ratio.) Increasing the inlet flow angle reduces the stator de Haller number and therefore highly loaded stages (which tend to

have low de Haller numbers anyway) are particularly susceptible to such corner separations.

3. The rotor loss coefficient is primarily dependent on the stage loading. This effect dominates the slight increase seen in rotor loss at high inlet flow angles. At stage loadings up to and including 0.55 the rotor efficiencies are similar, however further increases (i.e. to $\frac{\Delta h_0}{U^2} = 0.65$) in loading lead to a sharp drop in rotor efficiency of approximately 1.2%.
4. As the inlet flow angle is reduced, separations form and grow at the rotor hub/suction surface corner. However, the pitch-wise extent of this corner separation is limited and it is much less deleterious than corner separations observed in the stator. Although the predicted rotor loss increases steadily as the de Haller number is reduced, there is no rapid increase in rotor loss below a critical de Haller number (as caused in the stator by the formation/growth of corner separations), even at de Haller numbers as low as 0.53.
5. At high inlet flow angles, the effect of the large corner separations in the (highly-loaded) stators dominates the predicted stage efficiency. Therefore, as the design stage loading is increased, the locus of peak efficiency (shown in black on Figure 8.15) moves to lower, even negative, inlet flow angles to control the stator de Haller number. However, the gains in stator efficiency with reducing inlet flow angle are tempered with efficiency losses in the rotor. This suggests a suitable strategy for designing a highly loaded stage would be to choose the maximum inlet flow angle possible which ensures the stator does not suffer from a corner separation.

The predictions presented in this chapter suggest that the efficiency penalty for increasing the stage loading from 0.45 (fairly typical of a modern aero-engine stage) to 0.55 results in a modest efficiency penalty 0.9%. However, as the stage loading is increased further the efficiency penalty becomes more severe; between $\frac{\Delta h_0}{U^2} = 0.55$ and 0.65 the efficiency drops by an additional 2.4%.

6. Three-dimensional design methods (e.g. sweep and lean) only offers modest benefits at high loading. Sweep and lean increase the diffusion away from the end-walls and induce radial migration of boundary layer fluid. In an already highly loaded blade row this tends to overload the boundary layers away from the end-walls and makes corner separations difficult to control with three-dimensional design

methods. Therefore, the increased losses at mid-span mitigate any gains in terms of end wall loss.

7. The rear of a high-pressure compressor has been identified as the most suitable location for the introduction of high-reaction, highly-loaded stages. Very high-reaction, counter-swirl, stages are unlikely to be tenable in the front stages of a high-speed compressor due to the higher relative rotor inlet Mach numbers and the corresponding increase in shock losses. The trade off between shock and viscous losses was identified as a critical area for the practical implementation of highly loaded, high-reaction (i.e. counter-swirl), stages and warrants further research.

Chapter 9

A Simple Model for the Prediction of Profile Losses and the Implications for Highly Loaded Stages

9.1 Introduction

The fundamental architecture of a new compressor (e.g. number of stages, length, annulus line, etc...) is set early on in the design process (sometimes referred to as “mean-line” design). Typically, several different compressor configurations are evaluated by working out the basic velocity triangles and by using simple empirical correlations to estimate the major sources of loss (e.g. profile, Mach number, end-wall and tip clearance losses) and surge margin. Despite advances in computing power these correlations are still widely used; there is little time in the design process to use higher-fidelity methods (e.g. three dimensional CFD and streamline curvature calculations) until several initial designs have been refined to one or two “best” options.

The success (or failure) of a compressor design is dependent on the quality of the mean-line design. No amount of profile tweaking or three-dimensional modifications will be able to rectify a poor mean-line design, and changes to the basic configuration (e.g. adding a stage) late in the design process is likely to be very difficult and expensive.

The accuracy of the empirical correlations is therefore of paramount importance.

In the 1950s, Lieblein used the results from a carefully controlled set of cascade tests to demonstrate an almost unique correlation between profile loss and local diffusion factor (a measure of the adverse pressure gradient applied to the suction surface boundary layer). The difficulty in using the local diffusion factor is that it requires knowledge of the velocity distribution around the blade and therefore the precise geometry. To circumvent this Lieblein developed his diffusion factor; a parameter well correlated to the local diffusion factor and only based on velocity triangles and solidity ($\sigma = \frac{c}{s}$). Although over the past 50 years several correlations have been developed and improved, they are still based on the same principle established by Lieblein; that profile losses (and even end-wall losses, e.g. Wright [99]) are uniquely correlated to local diffusion factor.

Correlations, by their very nature, are empirically derived from previous (successful) designs. In light of the current work this raises the question; are these correlations still valid when applied to very highly loaded compressors lying far outside the current design envelope? To illustrate this point, the calculated performance of the series of stators described in Chapter 8¹ is compared with output from a set of one-dimensional correlations currently in use in industry in Figure 9.1. The one-dimensional correlations do not adequately pick up the variation in loss coefficient with increasing exit flow angle demonstrated by CFD, especially at high stage loadings.

The consequences of this could be disastrous; on the basis of these one dimensional correlations a designer could be misled into reducing the stage reaction of a highly loaded design (possibly to reduce the rotor inlet Mach number and corresponding loss) incorrectly believing the penalty in boundary layer loss to be small. It is clear that these one dimensional correlations do not appear sufficient to determine the “best” velocity triangles at high loading and it is therefore important to understand why.

This chapter introduces a simple, generic, approximation to the velocity distribution around a compressor aerofoil which can be shown to accurately mimic the observed changes with increasing loading and varying solidity. The boundary layer and tip clearance losses of this generic velocity distribution can then be estimated. Reducing the problem to such simple, physical, terms allows two of the key components of mean-line

¹These stators are based on a repeating stage design of constant flow coefficient ($\frac{V_{x,avg}}{U_{mid}}$) equal to 0.50. The nominal stage loading coefficient and exit flow angle (α_2) were varied between approximately 0.35 to 0.75 and -20° to 30° respectively.

prediction programs, namely the profile and tip clearance loss correlations, to be evaluated easily without any limitations at high stage loading. In particular, this approach shows that a Lieblein style correlation between local diffusion factor and profile loss has a loading dependency at low de Haller numbers. Furthermore, by combining the generic velocity distribution with a simple boundary layer method and tip clearance loss model, this work establishes the basis of a useful mean-line correlation (or design tool) which includes these effects and is not restricted to designs close to current loading levels.

9.2 Assumed Velocity Distribution

A generic model of the velocity distributions around a compressor (rotor or stator) blade must satisfy two key criteria; (a) it must be consistent with the inlet and exit velocities; and (b) it must provide the correct turning, i.e. the pressure difference from pressure to suction surface must agree with the required change in tangential momentum.

Koch & Smith [59] used an integral boundary layer method to estimate the profile loss of a series of idealised velocity distributions (shown in Figure 2.5). These velocity distributions assumed that the pressure surface velocity is constant and equal to that at the trailing edge. The peak suction surface velocity was set from a correlation which took into account the velocity triangles, solidity, Mach number and thickness. Although this generic velocity distribution was adequate for their purposes it is not truly physical. By choosing the peak suction surface velocity in this manner the tangential (pressure) force on the flow due to the assumed velocity distribution does not necessarily match the required tangential momentum change. To ensure maximum generality it is this deficiency that the present work seeks to address.

The objective of the current work is to develop a simple method for predicting blade profile loss which can be used for both conventional and advanced blade loadings. To develop such a model we begin with the simplified, “straight-line”, approximation to the velocity distribution around a blade as shown in Diagram 9.1. It consists of a rectangular “roof-top” at the leading edge followed by a triangular diffusion to the velocity at the trailing edge. The length of the “roof-top” is controlled by the user defined non-dimensional parameter “ A ”, which defines the roof-top length as a fraction of axial chord. The suction and pressure surface velocities at the leading edge are set

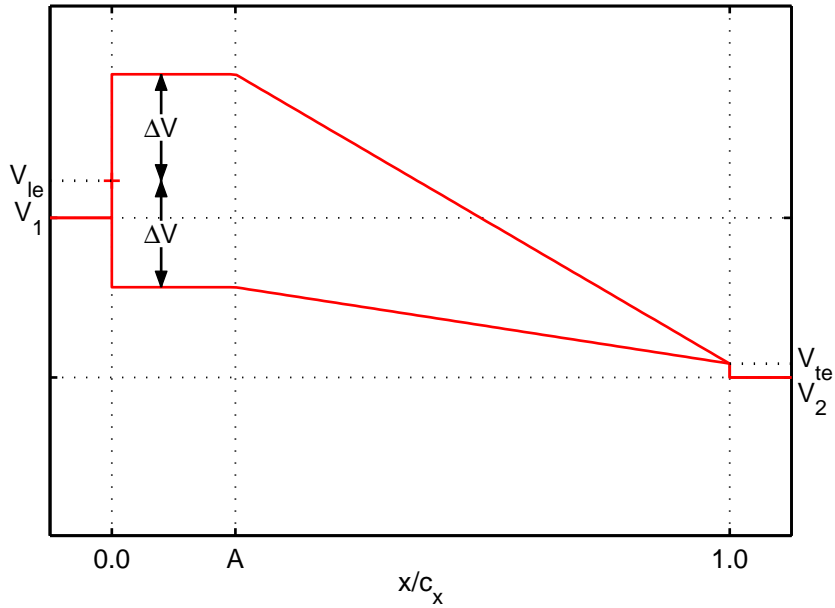


Diagram 9.1: Schematic diagram of the assumed generic velocity distribution around a compressor aerofoil.

such that they lie ΔV (i.e. equidistant) from the average velocity at the leading edge, V_{le} . Similarly, the velocity at the trailing edge (on both surfaces) is set to the average value, V_{te} . As we shall see later, although V_{le} and V_{te} are closely related to V_1 and V_2 respectively they are not necessarily equivalent (hence the step at the trailing edge), for example, due to blockage effects.

In the present approach the suction surface *and the pressure surface* velocities are chosen to provide the pressure difference necessary to achieve the required turning. It can be shown that for incompressible flow through a control volume of constant height (i.e. no stream-tube contraction) the velocity difference at the leading edge, $2\Delta V$, is given by Equation 9.1. A full derivation of Equation 9.1 can be found in Appendix D.

$$\Delta V = \frac{3V_1 \cos \alpha_1 \Delta V_\theta}{\sigma \cos \xi \left(2(1 + 2A) V_{le} + (1 - A) V_{te} \right)} \quad (9.1)$$

Both the representative average velocities at the leading and trailing edges (V_{le} and V_{te} respectively) in Equation 9.1 need to be defined empirically. The physics of the problem suggest that the average leading and trailing edge velocities should be closely related to

the inlet and exit velocities respectively. Figure 9.2 shows that a good approximation to the trailing edge velocity (for a series of low-speed aerofoils²) can be obtained from a correlation based on continuity arguments, of the form presented in Equation 9.2³.

$$\frac{V_{te}}{V_2} = \left[1 - \sigma \left(\frac{\frac{t_{te}}{c} + \frac{\delta_{ss}^* + \delta_{ps}^*}{c}}{\cos \alpha_2} \right) \right]^{-1} \quad (9.2)$$

Where: “ t_{te} ” is the thickness of the blade at the trailing edge and “ δ_{ss}^* ” & “ δ_{ps}^* ” are the displacement thickness of the suction and pressure surface boundary layers respectively.

Estimating the leading edge velocity is not as straightforward. Figure 9.3 shows the results of *MISES* predictions of several low speed blade designs (of varying solidity, turning and inlet flow angle). The leading edge velocity in Figure 9.3 has been plotted against a blockage parameter, σ_c^t . Although it is obvious from Figure 9.3 that the leading edge velocity is proportional to blockage, there is significant variation in the results with turning and inlet flow angle.

Inspection of Figure 9.3 indicates that the leading edge velocity is proportional to axial velocity ($\frac{V_x}{U}$) and inversely proportional to turning ($\frac{\Delta V_\theta}{U}$). A correlation of the form presented in Equation 9.3 may therefore be appropriate. This is confirmed by Figure 9.4, which demonstrates that the leading edge velocity is well correlated to Equation 9.3, with arbitrary constants “ k_1 ” & “ k_2 ” approximately equal to 0.98 and 0.50 respectively.

$$\frac{V_{le}}{V_1} = k_1 + k_2 \frac{\sigma_c^t V_{x,1}}{\Delta V_\theta} \quad (9.3)$$

The non-dimensional group $\frac{\sigma_c^t \max V_x}{\Delta V_\theta}$ has been derived empirically rather than from physical arguments and therefore it is difficult to make an assessment of its generality beyond

²*MISES* was used to predict the velocity distribution around a series of low-speed aerofoils ($M_{in} = 0.21$). Sections were designed to give three levels of turning (equivalent to $\frac{\Delta V_\theta}{U} = 0.40, 0.50 \& 0.60$ assuming a flow coefficient of 0.50) at a uniform inlet flow angle. Solidity ($1.2 \leq \sigma \leq 2.4$), maximum thickness ($0.04 \leq \frac{t_{max}}{c} \leq 0.10$), leading edge radius ($0.005 \leq \frac{r_{le}}{c} \leq 0.010$) and trailing edge radius ($0.010 \leq \frac{r_{te}}{c} \leq 0.080$) were varied systematically.

³The cosine of the flow angle at the trailing edge has been assumed to be equal to that at the exit plane.

the data presented here. Although Equation 9.3 has been shown to be also applicable to a series of high speed designs, at high inlet Mach numbers ($M_1 = 0.75$) appropriate values of the constants “ k_1 ” & “ k_2 ” become approximately 0.9 and 1.0 (rather than 0.98 and 0.50 as reported above). The precise values of the arbitrary constants should therefore be chosen with care, based on previous experience of similar designs. Having established correlations for the leading and trailing edge velocities, the simplified generic velocity distribution can now be fully defined for a compressor blade of any given duty.

A comparison between the generic velocity distributions based on Equations 9.1, 9.2 & 9.3 and those predicted by *MISES* for a range of low-speed aerofoils of different duty is presented in Figure 9.5. For the sake of simplicity the roof-top length parameter, “ A ”, has been assumed to be equal to zero (i.e. a simple triangular velocity distribution). The blockage presented by the boundary layers at the trailing edge has also been ignored. The error introduced by the latter assumption only becomes significant in the most highly loaded cases (Figures 9.5E & F) where the diffusion factor and boundary layer thickness are greatest. Despite its obvious simplicity, the generic velocity distribution gives a reasonable approximation to the velocity distribution around a wide range of compressor blades and, importantly, it correctly models the trends with varying turning, solidity and de Haller number.

It is instructive to return briefly to Equation 9.1. Although Equation 9.1 clearly depends upon required turning (ΔV_θ) and solidity ($\sigma = \frac{c}{s}$), it is not immediately obvious how the velocity and angle terms relate to parameters more familiar to compressor designers (e.g. de Haller number, $\frac{V_2}{V_1}$). By making some sensible approximations and observing that $\frac{\cos \alpha_1}{\cos \xi}$ is almost a linear function of de Haller number, Equation 9.1 can be rearranged into Equation 9.4 (see Appendix D).

$$\Delta V \approx \frac{3 \left(a \frac{V_2}{V_1} + b \right) \Delta V_\theta}{\sigma \left(2(1+2A) + (1-A) \frac{V_2}{V_1} \right)} \quad (9.4)$$

Where: a and b are arbitrary constants (approximately equal to one and zero respectively).

Equation 9.4 shows that that ΔV (and therefore the whole pressure distribution) is

primarily dependent on three variables; the required turning, the specified solidity and the de Haller number. When presented in this form, it can be seen that the effect of de Haller number on ΔV is perhaps counter-intuitive; reducing the de Haller number (i.e. increasing the one dimensional diffusion) *reduces* the required pressure difference between the suction and pressure surfaces for a given amount of turning. This occurs as a result of the effect of de Haller number on the ratio of cosine terms in Equation 9.1 and, as shall be shown in Section 9.3.3, plays a role in the effect of low de Haller numbers (typical of high stage loadings) on profile and tip clearance losses.

9.3 Profile Loss

Almost all profile loss correlations in use today are based on the work of Lieblein [63]. Lieblein took the results from a series of carefully controlled cascade experiments (conducted at *NACA*) and demonstrated that the wake momentum thickness (a measure of profile loss) was well correlated with the local diffusion factor.

Having established that the generic velocity distribution described in Section 9.2 gives realistic predictions, the simple velocity distribution can be input into an integral boundary layer solver and the predicted boundary layer parameters used to estimate profile loss. First, the results from such a coupled boundary layer/ generic velocity distribution method are compared to Lieblein's data for a blade with a moderate stage loading. Having demonstrated the accuracy of the method, the effect of increasing stage loading on profile loss is then discussed.

9.3.1 Approach

The profile loss of any given velocity distribution can be calculated from the boundary layer properties at the trailing edge. At each design point, the boundary layers on both surfaces of the generic velocity distributions (described in Section 9.2) were calculated by the integral method embedded in *MISES*⁴. For added simplicity, the velocity distri-

⁴The *MISES* boundary layer sub-routine was called independently (from a custom *FORTRAN* program) to evaluate the state of boundary layers exposed to a user specified edge velocity distribution (in this case from the generic velocity distributions described above). Further details of the coupled Euler/ integral boundary layer solver *MISES* can be found in Chapter 7.

bution roof-top length parameter, “A”, was set equal to zero. In all the calculations, transition was forced at 2% of chord, effectively rendering the boundary layers fully turbulent.

9.3.2 Comparison with Lieblein’s Data

The predicted wake momentum thickness for a conventionally loaded blade row ($\frac{\Delta h_0}{U^2} = 0.35$, $\alpha_1 = 63.4^\circ$) is compared to Lieblein’s [63] measurements in Figure 9.6. As in Lieblein’s cascade tests, the flow was effectively incompressible (inlet Mach number was set to 0.2) and the Reynolds number was set to 2.5×10^5 . Base pressure loss has not been included in the current analysis; the cascades tested by Lieblein had a thin trailing edge (with thickness of 0.3% of chord) and therefore the corresponding base pressure losses are negligible. The data presented by Lieblein was measured between 0.5 and 1.5 chord lengths downstream of the cascade and the boundary layers had therefore partially mixed out. Therefore, to allow comparison with Lieblein’s data, it was necessary to calculate the momentum thickness of a wake with shape factor equal to 1.1 (typical of that measured by Lieblein) which gives the same profile loss as the calculated integral boundary layer parameters at the trailing edge. It is this, adjusted, momentum thickness which is plotted in Figure 9.6.

The predicted wake momentum thickness lies well within the scatter of Lieblein’s data and captures the trend with increasing local diffusion factor. At high local diffusion factors, above about 0.43, the curve suddenly flattens off. This corresponds to a predicted suction surface boundary shape factor above 3.0, this being indicative of a large separation. In its stand alone form, the *MISES* boundary layer calculation struggles to predict large separations and therefore the predicted results above this value are nonsensical. Koch & Smith [59] circumvented a similar problem by simply extrapolating their boundary layer predictions to high diffusion factors. Overall, for local diffusion factors below 0.43, the predictions from the coupled generic velocity distribution/ boundary layer calculation method, described above, agree remarkably well with Lieblein’s data.

9.3.3 Effect of Increasing Loading

Having demonstrated the validity of this coupled generic velocity distribution/ boundary layer calculation method for a conventional aerofoil, the methods can now be used to investigate the effects of increasing stage loading. Figure 9.7 shows the predicted trailing edge momentum thickness⁵ for a series of aerofoils of different loadings between $\frac{\Delta h_0}{U^2} = 0.25$ (lightly loaded) and $\frac{\Delta h_0}{U^2} = 0.75$ (very highly loaded). The inlet flow angle was held constant at 63.4° and the Reynolds number was set to 1.0×10^6 (representative of engine Reynolds numbers).

The vast majority of profile loss correlations, based on conventional aerofoils (e.g. Koch & Smith [59] and Wright & Miller [99]), assume that the trailing edge momentum thickness (closely related to the mixed out loss via Equation 2.3) is a unique function of only local diffusion factor. It is clear from Figure 9.7 that the correlation between trailing edge momentum thickness and local diffusion factor is not a unique curve and exhibits a loading dependency. This dependency works against the designer trying to increase stage loading; as the loading increases, so does the profile loss at a given local diffusion factor.

Based on the current generic velocity distribution model, the contribution to the total momentum thickness from the suction and pressure surfaces individually is shown in Figure 9.8. When plotted individually, the suction surface momentum thickness collapses onto an almost unique curve (Figure 9.8A). However, Figure 9.8B shows that the dependency of the total loss on loading comes from an increase in pressure surface momentum thickness with loading.

The source of the change in pressure surface loss with blade loading can be explained using the generic velocity distributions shown in Figure 9.9 for a series of blades with local diffusion factor equal to 0.45. The suction surface velocity is fixed by the local diffusion factor (and therefore the upper lines of the velocity distributions in Figure 9.9 are all almost parallel). As the loading increases (blue to red to green) so does the solidity required to maintain acceptable levels of suction surface diffusion. Increasing the solidity also reduces the net tangential force (i.e. the area within the velocity

⁵N.B. The trailing edge momentum thickness plotted in Figure 9.7 (i.e. $\theta_{tot} = \theta_{ss} + \theta_{ps}$) differs from the wake momentum thickness plotted previously in Figure 9.6 which was adjusted to allow comparison with Lieblein's data (see Section 9.3.2).

distribution) which each blade is required to exert on the flow. Therefore, the pressure surface velocities increase in line with the reduction in tangential force. (In the limit, as the number of blades tends to infinity, the pressure surface velocities must tend to that of the suction surface.) The increase in pressure surface loss comes from this increase in pressure surface velocity (recall that the entropy rise in a turbulent boundary layer is approximately proportional to the *cube* of the free-stream velocity; see Equation 2.2).

It has been observed that large extents of laminar flow may exist on the pressure surface of compressor blades (e.g. Halstead et al [47]). This will in part reduce the pressure surface loss and hence the aforementioned loading dependency. However, the pressure surface boundary layer is unlikely to remain laminar when exposed to adverse pressure gradients as demonstrated above for high loading/ high solidity cases.

Let us introduce the concept of individual suction and pressure surface local diffusion factors. Defining the suction and pressure surface diffusion factors separately gives a measure of the adverse pressure gradient applied to *both* the suction surface and to the pressure surface. These are defined in Equation 9.5. The suction surface diffusion factor is equivalent to the more usual local diffusion factor. By plotting the individual suction and pressure surface diffusion factors on the abscissa in Figure 9.10, the suction and pressure surface momentum thicknesses collapse onto a single curve irrespective of loading.

$$D_{loc,ss} = \frac{V_{ss,max} - V_{te}}{V_{ss,max}} \quad , \quad D_{loc,ps} = \frac{V_{ps,max} - V_{te}}{V_{ps,max}} \quad (9.5)$$

So far, we have demonstrated that profile loss is dependent on local diffusion factor and on stage loading for a series of compressor aerofoils with a fixed inlet flow angle ($\alpha_1 = 63.4^\circ$), but how does this change if the inlet flow angle is varied?

The generic velocity distribution is (almost) completely defined by the specified local (suction surface) diffusion factor and de Haller number irrespective of inlet flow angle. The suction surface velocity is fixed by the local diffusion factor. Assuming that the leading and trailing edge velocities are closely linked to those at inlet and exit (as shown in Section 9.2), the de Haller number ($\frac{V_2}{V_1}$) then sets the velocity difference (ΔV) between the suction surface and average velocity at the leading edge (\bar{V}_{le}) and thus also fixes the pressure surface velocity (recall that $V_{max,ss} = V_{le} + \Delta V$ and $V_{max,ps} = V_{le} - \Delta V$,

see Diagram 9.1). In other words, the loading dependency discussed above is, more accurately, a dependency on de Haller number.

As expected, Figure 9.11 shows that for a fixed (suction surface) diffusion factor ($D_{loc} = 0.45$), the pressure surface momentum thickness, as a fraction of the total, is a function of only the de Haller number for all inlet flow angles. At a de Haller number of 0.75 (the limit suggested by de Haller) the pressure surface accounts for only about 20% of the profile loss. As the de Haller number drops the proportion of loss from the pressure surface asymptotes towards 50%. At a de Haller number of 0.55 the pressure surface loss accounts for more than 35% of the total loss. Reducing the specified local (suction surface) diffusion factor will increase the solidity and therefore pressure surface loss, i.e. the proportion of loss due to pressure surface plotted in Figure 9.11 will move upwards.

The dashed line in Figure 9.7 denotes the onset of large suction surface separations (i.e. $H_{ss} > 3.0$). This line also has a slight loading dependency (i.e. negative slope) which punishes higher loadings. The variation in separation limit with loading is caused by a Reynolds number effect; the average suction surface velocity, and therefore the mean suction surface Reynolds number, decreases with de Haller number (e.g. Figure 9.9). Nevertheless, the gradient of the dashed line plotted in Figure 9.7 is steep enough that, for most purposes, it is probably reasonable to assume that the suction surface boundary layer starts to separate at a constant value of local (suction surface) diffusion factor of about 0.47 (at a Reynolds number of 1.0×10^6 ; see Figure 9.7).

9.3.4 High Speed

So far, a coupled generic velocity distribution/ integral boundary layer method has been used to demonstrate that trailing edge momentum thickness (closely related to profile loss) is dependent on local diffusion factor and on loading. In traditional correlations, such as those of Lieblein [63], Koch & Smith [59] or Wright & Miller [99], this loading dependency has not been previously acknowledged. The conclusions reached with the generic velocity distribution model will now be tested against two-dimensional CFD predictions of a series high-speed blade designs.

To simplify blade generation, a high Mach number controlled diffusion aerofoil ($\frac{V_x}{U} & \frac{\Delta h_0}{U^2} = 0.50$) was designed and the resulting non-dimensional camber and thickness

distributions used for all other designs. The inlet Mach number and flow angle were held constant at 0.74 and 63.4° respectively. The maximum blade thickness was set to 5% of chord and the leading & trailing edge radii were both set to 0.8% of chord (or 16% of max thickness); chosen to be representative of a mid-stage in a state of the art high-pressure compressor.

The local diffusion factor was controlled by adjusting the solidity. At each solidity *MISES* was used to tweak the inlet and exit blade metal angles to set the incidence (to give equal magnitude over-speeds) and to give the required turning. At each loading, the stream-tube contraction was set to give constant axial velocity at one value of solidity (chosen to ensure an attached suction surface boundary layer). This ratio was left unchanged for all blades of the same duty; the maximum observed deviation from constant axial velocity was within $\pm 1\%$ of inlet velocity.

Figure 9.12 shows the *MISES* predictions of the total momentum thickness at the trailing edge for a series of blades with increasing stage loading. Reducing the de Haller number from 0.70 to 0.57 (i.e. increasing the loading) leads to approximately a 60% increase in the trailing edge momentum thickness (i.e. profile loss) at the same local diffusion factor. The trailing edge momentum thickness is clearly not a unique function of local diffusion factor but is also dependent on the de Haller number for these engine representative aerofoils.

The increase in profile loss with reducing de Haller number comes from the pressure surface. Figure 9.13 shows that if the de Haller number is reduced from 0.70 to 0.57 (i.e. increasing loading) whilst maintaining a constant local (suction surface) diffusion factor of 0.40, the pressure surface momentum thickness increases from 19% to 36% of the total value at the trailing edge. By plotting the suction and pressure surface momentum thicknesses individually against their respective local diffusion factors (see Equation 9.5) the de Haller number dependency is almost entirely removed and the data for both surfaces is reduced to an almost unique curve⁶. The source of the increased pressure surface loss must therefore come from greater pressure surface diffusion.

The conclusion that the trailing edge momentum thickness (at a given local diffusion factor) is dependent on de Haller number found by the generic velocity distribution

⁶Figure 9.14 does show some loading dependency at high diffusion factors. This is caused by increased suction surface velocities (recall that boundary layer loss is proportional to the velocity cubed at high solidity) due to slight differences in the velocity distributions.

approach at low speed (Section 9.3.3 & Figure 9.7) clearly is also valid for high-speed compressor aerofoils.

Inevitably there is some variation between in the velocity distributions around the high-speed compressor blades. Increasing the camber (i.e. the loading) tends to move the position of peak suction forward and increases the available surface length available for diffusion. This allows greater diffusion to be achieved without suction surface separation. However this does not significantly affect the pressure surface and therefore the main conclusion of the above work; namely that at low de Haller numbers (i.e. high loading), Lieblein style correlations for trailing edge momentum thickness should be dependent on both local diffusion factor *and* on de Haller number.

9.4 Simple Analytical Methods for Estimating Profile Loss

The coupled generic velocity distribution/ boundary layer method, discussed above, can be developed into a useful profile loss prediction tool. Although the numerical boundary layer method used above can be used to obtain profile losses, it becomes cumbersome when evaluating several blade rows and/ or exploring the design space. Instead a simple analytical method of estimating boundary layer losses is developed.

Unlike in existing correlations/ predictive methods, by coupling such a simple method with the generic velocity distribution of Section 9.2, the effect of de Haller number on pressure surface loss (which has been shown to be significant at high loadings) is included in a mean-line predictive tool for the first time. It should be noted that the method presented here does not represent a definitive method of predicting profile losses but rather a reasonable approximation which, it is believed, captures the physical effects relevant to profile loss. Finally, the improvement that such a method gives over existing correlations (especially at high loading) is demonstrated.

An alternative method would be to evaluate a set of separate correlation curves for the suction and pressure surface losses, such as those shown in Figure 9.10. However, the disadvantage of a correlation based method is that every time the velocity distribution is modified or adjusted a new set of correlations must be generated.

9.4.1 Boundary Layer Loss

A control volume calculation (performed between the trailing edge and a location far downstream) can be used to show that the entropy rise coefficient (related to the pressure loss coefficient by the velocity ratio at low Mach numbers) can be found from Equation 9.6 (Denton [18]). Equation 9.6 links the integral boundary layer properties at the trailing edge to the profile loss coefficient.

$$\frac{T_0 \Delta S}{\frac{1}{2} V_2^2} = \frac{2\sigma \left(\frac{\theta}{c} \right)}{\cos \alpha_2} + \left[\frac{\sigma \left(\frac{\delta^*}{c} + \frac{t_{te}}{c} \right)}{\cos \alpha_2} \right]^2 \approx \frac{\Delta P_0}{\frac{1}{2} \rho V_2^2} = \omega_p \times \left(\frac{V_1}{V_2} \right)^2 \quad (9.6)$$

The momentum thickness is related to the displacement (δ^*) and energy thicknesses (δ_e) by the shape factors H and H_e respectively (Equation 9.7). Weighart (see Schlichting [79]) showed that the shape factors are uniquely linked via the relationship reproduced in Equation 9.8, which Weighart derived for a series of power law boundary layer profiles. Therefore, if a shape factor (H or H_e) is known (or assumed) only one of the integral boundary layer parameters δ^* , θ or δ_e is needed to find the profile loss coefficient (via Equation 9.6).

$$H = \frac{\delta^*}{\theta} \quad , \quad H_e = \frac{\delta_e}{\theta} \quad (9.7)$$

$$H = \frac{H_e}{(3H_e - 4)} \quad (9.8)$$

It can be shown that the rate of entropy production in a boundary layer is given by Equation 9.9 (e.g. Denton [18]). Cumpsty [12] and Denton argued that, for a turbulent boundary layer, it is reasonable to assume a constant value of the dissipation coefficient (C_d) approximately equal to 0.002 (see Section 2.4.1) for a high Reynolds number boundary layer⁷. The total entropy production in the boundary layer and therefore the energy thickness at the trailing edge can be evaluated by integrating Equation 9.9 along the surface length, i.e. Equation 9.10.

⁷N.B. It is necessary to increase the value of the dissipation coefficient, C_d , to account for lower Reynolds numbers.

$$T\dot{S}_A = C_d \rho V^3 \quad (9.9)$$

$$\delta_e = \frac{2}{V_{te}^3} \int_0^c C_d V^3 dz \quad (9.10)$$

Where: “z” is the distance along the chord line

The profile loss of any specified velocity distribution can therefore be estimated by assuming a sensible trailing edge shape factor and solving Equations 9.6, 9.7, 9.8 and 9.10. The benefit of assuming the trailing edge shape factor is that even relatively large errors in the assumed value do not significantly affect the estimated momentum thickness and therefore the loss coefficient (for attached flow, the momentum thickness term in Equation 9.6 is dominant). For example, increasing the assumed shape factor from 2.0 to 2.4 only causes a 3% variation in the momentum thickness estimated from Equations 9.7 & 9.10.

Figure 9.15 shows another advantage of using the trailing edge shape factor (for the coupled generic velocity distribution/ integral boundary layer data used in Section 9.3.3); unlike momentum thickness for example, the trailing edge shape factor is almost independent of de Haller number.

It is also necessary to specify a local diffusion factor to fully define the generic velocity distribution currently in question (i.e. to set the solidity). For maximum efficiency the suction surface boundary layer should be close to separation at the trailing edge; more blades (i.e. reduced diffusion) increases the loss (N.B. Equation 9.6 is proportional to solidity, σ), whereas fewer blades (i.e. increased diffusion) introduces high loss from large separations. For well designed blades on the point of separation this corresponds to a local (suction surface) diffusion factor of about 0.45. At this local diffusion factor, Figure 9.15 suggests that a suitable value of the trailing edge shape factor would be approximately 2.1.

A simple analytical method of estimating the profile loss of the generic velocity distribution of Section 9.2 has been described. This method only depends on two empirical variables which must be set by the user based on their experience; the local diffusion factor and the corresponding trailing edge shape factor. Furthermore, this method can easily be extended to modified/ other velocity distributions by simply changing one or

both of these parameters. The profile loss model is completed by the inclusion of so called “base pressure losses” below.

9.4.2 Base Pressure Loss

The total profile loss is made up of the boundary layer losses (described above) and the so called “base pressure loss”. The control volume calculation used to derive Equation 9.6 assumes that the static pressure applied to the upstream boundary (i.e. at the trailing edge) is uniform across the pitch. In reality this is not the case; a region of lower static pressure exists behind blades with thick trailing edges as a result of unsteady effects, e.g. vortex shedding. Including this in the control volume mixing calculation yields an additional loss term in Equation 9.6, (highlighted in Equation 9.11). Roberts & Denton [77] studied base pressure losses in turbines and suggested a suitable approximate value of the base pressure coefficient (C_{pb}) would be -0.20 (N.B. the base pressure coefficient is a negative value).

$$\frac{T_0 \Delta S}{\frac{1}{2} V_2^2} = \underbrace{\frac{2\sigma(\frac{\theta}{c})}{\cos \alpha_2} + \left[\frac{\sigma(\frac{\delta^*}{c} + \frac{t_{te}}{c})}{\cos \alpha_2} \right]^2}_{\text{Equation 9.6}} + \underbrace{\frac{-C_{pb}\sigma(\frac{t_{te}}{c})}{\cos \alpha_2}}_{\text{base pressure loss}} \quad (9.11)$$

9.4.3 Effect of Mach Number on Profile Loss

The aforementioned method of predicting profile loss can also be used to give reasonable estimates at the sort of Mach numbers representative of those found in aero-engine compressors. However, at higher Mach numbers it is necessary to use the compressible version of Equation 9.10, shown below in Equation 9.12. The density ratio term in the integral of Equation 9.12 is related to the velocity distribution via the Mach number in Equation 9.13. In the rear stages of a high pressure compressor Mach numbers are typically subsonic. Shock losses are therefore unlikely to be relevant and have not been considered in the current analysis.

$$\delta_e = \frac{2}{V_{te}^3} \int_0^c C_d \left(\frac{\rho}{\rho_{te}} \right) V^3 dz \quad (9.12)$$

$$\frac{\rho}{\rho_{te}} = \left[\frac{1 + \frac{1}{2}(\gamma - 1) M_{te}^2}{1 + \frac{1}{2}(\gamma - 1) M^2} \right]^{\frac{1}{\gamma-1}} \quad (9.13)$$

There is little data available on the effect of Mach number on the dissipation coefficient (C_d , which appears in Equation 9.10). For the subsonic Mach numbers in question here, the variation of skin friction with Mach number is usually considered to be small; the skin friction coefficient varies by approximately 8% in this range (Schlichting [79]) and the effects of Mach number on dissipation are often assumed to be similar (Denton [18]).

The variation in the average dissipation coefficient⁸ with Mach number has been calculated for various diffusing velocity gradients with the *MISES* integral boundary layer method. The result of this analysis are shown in Figure 9.16. For turbulent boundary layers, *MISES* uses the empirical correlation for skin friction coefficient proposed by Swafford (see Drela [28]) to solve the integral boundary layer equations. For a local diffusion factor of 0.45 (typical of those found on compressor blades) the variation in the dissipation coefficient is less than 3% for peak Mach numbers below one. Even for more modest diffusion factors, the variation does not exceed 13% of the incompressible value.

For the current, approximate, purpose it is therefore reasonable to assume that the dissipation coefficient, C_d , is constant. This demonstrates that the analytical method of Section 9.4.1 for estimating profile loss is sufficiently robust to be used for all compressors operating at Mach numbers up to and including those typically found in aero-engine compressors.

9.4.4 Results

An example of the results from this profile loss model (i.e. boundary layer and base pressure losses) are shown in Figure 9.17 for a series of stators of varying duty. The generic velocity distribution used is that described above with a roof-top length parameter (A) set to zero and the leading edge velocity determined empirically from Equation 9.3 (with constants k_1 and k_2 equal to 0.98 and 0.50 respectively).

⁸The average dissipation coefficient presented in Figure 9.16 is the dissipation coefficient which, when used in Equation 9.12, gives the same energy thickness at the trailing edge as the integral boundary layer calculation.

This figure compares the output from the profile loss model to three-dimensional CFD calculations of comparable stator designs; the same data was compared with an existing profile loss model at the start of this chapter in Figure 9.1.

The profile loss model developed here captures the relative differences in loss with increasing stage loading. Three dimensional separations are not taken account of in this model (or the model of Wright & Miller [99]) and therefore the sudden increase in loss, caused by large corner separations (denoted by the filled symbols), at high exit flow angles cannot be captured. At high stage loadings, the previous Wright & Miller model (demonstrated in Figure 9.1) gave much flatter curves of loss coefficient than predicted by three-dimensional CFD. The profile loss model developed above addresses this deficiency and correctly predicts the slope of the curves, even at high stage loadings.

9.5 Tip Clearance Flows

Another major source of loss in axial compressors are tip clearance flows. These occur as a result of flow escaping through the running clearance (necessary for mechanical reasons) between the rotor blades and the casing (or, in the case of cantilevered stators, between the stators and the hub). Like existing correlations for profile loss, tip clearance losses are included in current mean-line prediction methods without consideration of the effects of loading.

The generic velocity distribution, developed in Section 9.2, can be used to estimate the driving pressure difference behind the tip clearance flow and therefore its resulting loss. This results in a loss model based on the physics of tip clearance flows (rather than on purely empirical arguments) which can be used to say something about the likely effects of loading on tip clearance losses. This tip clearance loss model can be combined with the profile loss model of Section 9.4 to account for tip clearance losses in a mean-line prediction tool.

Storer & Cumpsty [87] developed a method of estimating tip clearance loss based on a control volume analysis of a jet mixing into a main-stream flow. Assuming the jet speed is equal to the suction surface velocity flow (a reasonable assumption for a clearance flow⁹) the mixing loss coefficient can be obtained from Equations 9.14 and 9.15. Phys-

⁹Storer & Cumpsty [87] showed that the clearance jet loses little stagnation pressure through the

ically, the parameter “ χ ” is the ratio of the jet area to main stream passage area and the physical tip gap area is scaled by an empirical discharge coefficient, $C_{D,clr}$. Storer & Cumpsty suggested an appropriate value for $C_{D,clr}$ of 0.80.

$$\omega_{clr} = \frac{\Delta P_0}{\frac{1}{2}\rho V_1^2} = \chi \sin \bar{\lambda} \left[\frac{2 + \chi \sin \bar{\lambda} - 2 \cos \bar{\lambda}}{(1 + \chi \sin \bar{\lambda})^2} \right] \times \left(\frac{V_2}{V_1} \right)^2 \quad (9.14)$$

$$\chi = \frac{A_{jet}}{A_{main}} = C_{D,clr} \frac{\sigma(\frac{\epsilon}{c})}{\left(\frac{h}{c}\right) \cos \xi} \quad (9.15)$$

Where: “ ϵ ” is the height of the tip clearance gap and “ $\bar{\lambda}$ ” is the average jet injection angle (see Diagram 9.2).

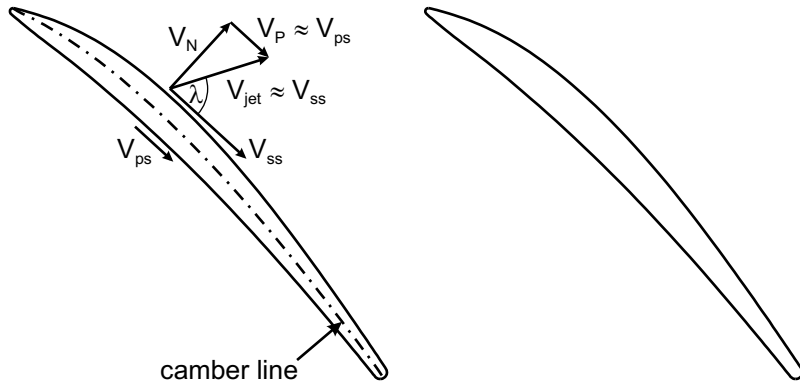


Diagram 9.2: Schematic illustration of local jet injection angle (λ) and relevant velocities.

Although the magnitude of the jet velocity is similar to the suction surface velocity⁹, it is necessary to know its direction, $\bar{\lambda}$, to use Equation 9.14. This can be estimated via the method of Storer & Cumpsty [87]. Storer & Cumpsty made two key assumptions; that the suction and pressure surface velocities are parallel to the camber line (i.e. thin blades) and that the pressure gradient along the camber line is much less than that perpendicular to the blade (valid for most compressors). If the pressure gradient along the camber line is neglected, the component of velocity parallel to the camber line (V_P) will be unchanged as it passes through the clearance gap. The net assumption from this is that the component of jet velocity parallel to the blade is equal to that

clearance gap. Therefore, the jet stagnation pressure is similar to that in the main passage flow. At the exit of the tip gap, the clearance flow is exposed to the suction surface static pressure and therefore, by Bernoulli's equation, the jet velocity must have the same magnitude (but not direction) as the suction surface velocity.

on the pressure surface. The local injection angle (λ) can therefore be estimated by Equation 9.16 at a particular chord-wise location. This is illustrated schematically in Diagram 9.2. Finally, the local injection angle (λ) is mass averaged along the chord to give the average injection angle ($\bar{\lambda}$) used in Equation 9.14.

$$\cos \lambda = \frac{V_P}{V_{jet}} = \frac{V_{ps}}{V_{ss}} \quad (9.16)$$

The limitation of this method is that it is necessary to know the suction and pressure surface velocities a priori. This would usually mean that the precise blade geometry is required. The generic velocity distribution model developed in Section 9.2 has been shown to give a good approximation to the velocity distributions around a wide range of compressor blades. Furthermore, the model is based only on a few simple mean-line parameters. To turn the tip clearance loss model of Storer & Cumpsty [87] into a useful mean-line prediction tool, the suction and pressure surface velocities of the generic velocity distribution shown in Diagram 9.1 are substituted into Equation 9.16 and mass averaged. The associated tip clearance loss can then be estimated via Equation 9.14.

The results from the coupled generic velocity distribution/ clearance loss model are compared to the experimental results of Storer & Cumpsty [87] in Figure 9.18. For reference, the results of the clearance loss model calculated by Storer & Cumpsty and based on the measured injection angle is also shown (black). The coupled generic velocity distribution/ clearance loss model successfully models the overall tip clearance loss and the trends with increasing clearance gap. The injection angle was estimated as 49.3° ; close to the measured values of between 49.4° and 51.6° .

Thus, a mean-line tip clearance loss model has been developed by coupling the generic velocity distribution of Section 9.2 to the clearance loss model of Storer & Cumpsty [87]. Unlike existing, empirical, clearance loss correlations (based on previous, conventionally loaded, designs) this model is based purely on physical arguments. It can now be added to the profile loss model of Section 9.4 to form the back-bone of a useful mean-line performance prediction tool. In the next section, this model is used to investigate the effects of stage loading on clearance loss.

9.5.1 The Effect of Loading on Tip Clearance Loss

The tip clearance loss model, developed above, is based on physical arguments and no assumptions about loading were made in its derivation. This model can therefore be used to investigate the likely effects of increasing stage loading on tip clearance loss. First, a case with fixed inlet flow angle ($\alpha_1 = 63.4^\circ$) is considered while the loading ($\frac{\Delta V_\theta}{U} \approx \frac{\Delta h_0}{U^2}$) is varied. At each loading the solidity was set to maintain a specified local diffusion factor of 0.45. A tip clearance of 1% of chord and an aspect ratio of 1.0 were assumed (N.B. these assumptions only affect the magnitude of the clearance loss and not the trends).

Somewhat counter-intuitively, Figure 9.19A shows the tip clearance loss *decreasing* as loading rises. Similarly, the average injection angle drops (Figure 9.19B), i.e. the clearance flow swings aft. As the design loading increases (i.e. dropping the de Haller number) so too does the number of blades required to maintain acceptable suction surface diffusion. The effect of this is to reduce the pressure difference between the suction and pressure surfaces (directly related to ΔV in Equation 9.1) which drives the tip clearance flow. In Section 9.3 it was shown how the same effect increased the pressure surface boundary layer loss.

The effect of increasing the tip clearance gap on efficiency (presented in terms of the “lost efficiency”) is shown in Figure 9.20 for three rotors of increasing loading (as above; $\alpha_1 = 63.4^\circ$ & $D_{loc} = 0.45$). The efficiency penalty for increasing the tip clearance at the highest loading shown ($\frac{V_\theta}{U} = 0.60$) is less than half that at the lowest ($\frac{V_\theta}{U} = 0.40$).

It is necessary to sound a note of caution here. The simple clearance loss model developed by Storer & Cumpsty [87] takes no account of the phenomena of “double-leakage”. This is where the clearance flow is ingested through the tip gap of the adjacent blade and has been shown to dramatically increase clearance loss (see Chapter 5 and McNulty [68]). As the solidity increases double-leakage becomes more likely. Thus, the benefit of increasing loading on tip clearance loss will not continue indefinitely but will start to decrease once the solidity gets high enough for double-leakage to become significant.

To separate the effects of de Haller number and loading on tip clearance loss, the parameter space is now extended to include inlet angle . The tip clearance loss is governed

by two, opposing, effects. Figure 9.21 shows that at constant stage loading, reducing the de Haller number reduces the tip clearance loss; the greater solidity necessary at low de Haller numbers reduces the pressure gradient driving the clearance flow (as discussed above). Conversely, for a fixed de Haller number, a greater number of blades are required to provide the higher tangential force necessary to increase the turning¹⁰, thus increasing the area ratio parameter, χ (Equation 9.15), and therefore the clearance loss (Equation 9.14). The gradient of the contours in Figure 9.21 (i.e. tending towards vertical) indicate that, at higher loadings, the tip clearance loss is primarily dependent on de Haller number and is less sensitive to changes in loading.

The coupled generic velocity distribution/ tip clearance loss model of Storer & Cumpsty [87] indicates that increasing stage loading does not necessarily punish tip clearance losses. At high loading, the effect of the typically lower de Haller numbers (i.e. higher solidities) generally outweigh any increase in clearance losses due to greater turning.

9.6 Summary and Conclusions

A generic velocity distribution representing the pressure and suction surface velocities of a typical compressor blade has been developed. This generic velocity distribution has been shown to accurately mimic observed velocity distributions over a wide range of design points and loadings. The level of empiricism used in the definition of this velocity distribution has been kept to a minimum to ensure its generality for a wide range of design points not necessarily restricted to those close to previous experience, e.g. at very high stage loading.

This generic velocity distribution has been used to investigate the effect of high stage loadings on both profile and tip clearance losses. This shows, for the first time, that momentum thickness at the trailing edge (closely related to profile loss) is dependent on both local diffusion factor *and* on stage loading, or more specifically on de Haller number. At a given local diffusion factor the profile loss is greater at low de Haller numbers, typical of highly loaded compressors, than for conventional designs. In traditional profile loss correlations (e.g. Lieblein [63], Koch & Smith [59] and Wright &

¹⁰Recall from Section 9.3.3 that for a specified local diffusion factor, fixing the de Haller number effectively fixes the velocity distribution.

Miller [99]) this de Haller number dependency has not been acknowledged.

The concept of a generic velocity distribution has been included in a framework for estimating the profile and tip clearance losses suitable for incorporation into a mean-line design tool. At high stage loadings previous mean-line correlations under-predicted the variation in loss coefficient with stage exit flow angle (i.e. reaction). The model developed in this chapter addresses this deficiency and correctly captures the relative differences in loss with stage loading and exit flow angle, even at elevated stage loadings. The inclusion of an end-wall loss model would be a useful addition, however this remains as “work to be done”.

The main implications of this work are as follows:

1. The generic velocity distribution model shows that as the de Haller number is reduced (typical of increasing stage loading) the solidity required to maintain acceptable diffusion must increase. Increasing the number of blades reduces the tangential force on each blade necessary to give the required turning, and therefore the pressure difference between the suction and pressure surfaces reduces. This results in higher pressure surface velocities and therefore increased profile loss.

This conclusion was confirmed by two-dimensional CFD of a series of compressor blades, typical of those found in modern aero-engines.

2. The tip clearance loss model indicates that the tip clearance loss decreases with de Haller number (for a fixed local diffusion factor) as a result of the reduced pressure gradient across the blade (which drives the clearance flow). On increasing stage loading (typically associated with a reduction in de Haller number) this effect generally outweighs the increase in tip clearance loss due to the greater turning required.
3. The profile and tip clearance loss models demonstrate, for the first time, the importance of considering both the suction *and* the pressure surface velocities when estimating compressor losses. It has been shown that, at high stage loading it is not sufficient to assume that the pressure surface velocity is constant and equal to that at the trailing edge.

Chapter 10

Conclusions

10.1 Introduction and Summary

Over the past 30 years aero-engine pressure ratios have increased from approximately 30:1 to 50:1 in a quest for improved (cycle) efficiency. Despite the increase in pressure ratio, the total number of compressor stages has only increased by one. Further increases in pressure ratio, or a reduction in the number of stages for mechanical reasons (e.g. weight, cost, etc...), will require even greater pressure rise per stage.

One method of achieving higher stage pressure rise is by increasing the stage loading coefficient ($\frac{\Delta h_0}{U^2}$) and it is this topic which forms the focus of the present work. To this end, three highly loaded compressor stages were tested in a low speed, single stage, research compressor. These three stages had a design stage loading coefficient of 0.65; almost 50% greater than those typically in service today. A conventionally loaded stage was also tested in the same rig as a datum.

Compared to the datum stage, the three highly loaded stages showed disappointing efficiency. The highly-loaded Gallimore, Qinetiq and Denton stages achieved peak efficiencies of 83.8%, 85.3% and 85.6% respectively whereas the conventionally loaded Mini-Deversen stage achieved a peak efficiency of 87.9%. However, contrary to conventional wisdom, the three highly loaded stages did exhibit similar or improved stall margin to the datum stage.

Previous investigations into highly loaded stages have tended to be design/ build/ test studies of a specific stage design and have not considered the more global question of how best to design a highly loaded stage. This has been addressed in the current work by a CFD study into the effects of inlet flow angle and stage loading on the flows through, and the performance of, several different rotor and stator designs. This study identified stator de Haller number as a critical parameter; below de Haller numbers of approximately 0.62 three-dimensional corner separations form and grow in the stator hub/ suction surface corner. This limit was insensitive to stage loading for the stators simulated as a part of this study.

In highly loaded stages (which tend to have low de Haller numbers), the effect of stator corner separations dominates the predicted stage efficiency at high inlet flow angles (N.B. the stator de Haller number decreases with increasing stage inlet flow angle). Therefore, to achieve peak efficiency as the stage loading is increased, it necessary to move the stage inlet flow angle to lower, even negative, values to control the stator de Haller number and prevent large corner separations.

The effects of increasing the stage loading on the velocity distribution around a compressor aerofoil have been modelled with a simple generic velocity distribution (based on physical arguments). This generic velocity distribution was used to show, for the first time, that momentum thickness at the trailing edge (closely related to profile loss) is dependent on both local diffusion factor and on de Haller number. At a given local diffusion factor the profile loss was shown to be greater at low de Haller numbers, typical of highly loaded compressors, than for conventional designs. In traditional profile loss correlations (e.g. Lieblein [63], Koch & Smith [59] and Wright & Miller [99]) this de Haller number dependency has not been previously acknowledged.

The rotor and stator CFD studies suggest that the efficiency penalty for increasing the stage loading from 0.45 (fairly typical of a modern aero-engine stage) to 0.55 results in a modest efficiency penalty of 0.9%. However, as the stage loading is increased further the efficiency penalty becomes more severe; between $\frac{\Delta h_0}{U^2} = 0.55$ and 0.65 the efficiency drops by an additional 2.4%.

Throughout the remainder of this chapter more specific conclusions are given along with proposals for future research.

10.2 Measured Flow Through Highly Loaded Stages

The impact of the cross passage end-wall flows increases with stage loading as a result of higher tangential pressure gradients. As the stage loading is increased, loss cores formed by these secondary flows move towards midspan, along the suction surface. Separations grow out of these loss cores and therefore separations on highly loaded blades tend to occur on the suction surface rather than in the end-wall/ suction surface corner(s) at low flow rates .

As the flow rate through a compressor stage is reduced there comes a distinct point where the structure of the rotor tip clearance flow changes. This is associated with a significant increase in loss at the casing and coincides with intersection of the trajectory of the clearance vortex with the trailing edge of the adjacent blade. It is believed that this is the first time that the structure of the clearance flow has been correlated experimentally with the position of the tip vortex, or more specifically, the phenomena of “double-leakage”. So called “double-leakage” becomes more significant as the stage loading is increased as a result of the higher solidities generally required for highly loaded blade rows.

All three highly loaded stages exhibited modal disturbances prior to stall whereas the conventionally loaded Mini-Deverson stage stalled via spike type inception only. This led to the tentative conclusion that the probability of modal stall inception increases with stage loading. Perhaps counter-intuitively, the appearance of spikes (two of the highly loaded stages also exhibited spike type disturbances) was correlated with the presence of high loss at the rotor hub (e.g. from a corner separation). It would be an interesting extension to study the effect of the change in tip pressure distribution (which occurs as the result of flow redistribution around a large hub blockage) on stall inception. By doing so, it would be hoped to gain an insight on how to tailor the tip pressure distribution to obtain maximum stall margin.

10.3 Modelling Losses in Highly Loaded Stages

A generic velocity distribution for the flow around a compressor aerofoil has been developed which has been shown to accurately mimic observed velocity distributions. The level of empiricism used in the definition of this velocity distribution has been kept to a minimum to ensure its generality for a wide range of design points not necessarily restricted to those close to previous experience, e.g. at very high stage loading.

As the de Haller number is reduced (typical of increasing stage loading) the solidity required to maintain acceptable diffusion must increase. The generic velocity distribution model shows that increasing the solidity reduces tangential force on each blade and therefore the pressure difference between the suction and pressure surfaces reduces. This results in higher pressure surface velocities and increased profile loss from the pressure surface. At high stage loading it is not sufficient to neglect the pressure surface loss. The model shows, for the first time, that the momentum thickness at the trailing edge (closely related to profile loss) is dependent on both local diffusion factor *and* on de Haller number; a result which has been confirmed (with two-dimensional CFD) for a series of high Mach number blades representative of those found in typical aero-engine compressors.

The concept of a generic velocity distribution has been included in a framework for estimating the profile and tip clearance losses suitable for incorporation into a mean-line design tool. At high stage loadings previous mean-line correlations under-predicted the variation in loss coefficient with stage exit flow angle (i.e. reaction). The model developed in Chapter 9 addresses this deficiency and correctly captures the relative differences in loss with stage loading and exit flow angle, even at high stage loadings.

10.4 Recommendations for the Design of Highly Loaded Stages

A parametric study into the effect of design stage loading and inlet flow angle (i.e. reaction) on the rotor and stator flow fields and their respective performance has been conducted with three-dimensional CFD.

As the inlet flow angle is increased, the stator de Haller number falls. In highly loaded stages (which tend to have low de Haller numbers) three-dimensional separations form and grow at de Haller numbers below approximately 0.62. This limit is only weakly dependent on stage loading. (Although beyond the scope of the current work, it would be a useful future exercise to investigate if/ how this limit varies with other variables, e.g. aspect ratio.) The opposite trend is seen in the rotor; as the stage inlet angle is reduced three-dimensional separations form at the rotor hub. However, the rotor separations are much less deleterious than corner separations observed in the stator. Therefore, as the design stage loading is increased, the locus of peak efficiency moves to lower, even negative, inlet flow angles to control the stator de Haller number. This suggests a suitable strategy for designing a highly loaded stage would be to choose the maximum inlet flow angle possible which ensures the stator does not suffer from a corner separation.

A study into the effects of three dimensional design techniques showed that sweep and lean only offered modest benefits when applied to a highly loaded blade. Sweep and lean increase the diffusion away from the end-walls and induce radial migration of boundary layer fluid. In an already highly loaded blade row this tends to overload the boundary layers away from the end-walls. Therefore, the increased losses/ separations at mid-span mitigate any gains in terms of end wall loss.

The conclusions from the CFD design study presented above are based on individual blade row (i.e. rotor or stator) calculations operating at their design points. This study would benefit from being extended to cover full stage (i.e. rotor and stator) calculations over the whole characteristic range. Finally, it is recommended that the most promising of these designs are tested in the Highly Loaded Research Compressor.

10.5 The Unique Stalling Behaviour of the Qinetiq Stage

A highly unusual flow breakdown mechanism was observed during testing of the Qinetiq rotor for (what is believed to be) the first time. As the flow coefficient was reduced below about 0.65 large separations formed in the tip region of a few rotor passages. Unlike conventional rotating stall, each of these separations was fixed to a particular

rotor passage and did not propagate. As the flow rate was reduced further the number of these separations increased until (almost) every second passage was stalled. Unlike in Emmons' model of stall cell propagation, the presence of these large separations stabilised the flow in the rotor passages on both sides of the stalled passage. Further reduction in the flow rate from this saturated condition lead to conventional rotating stall.

It has been shown via a combination of experiment and two-dimensional CFD (i.e. a coupled Euler/ integral boundary layer method with transition model) that this phenomena appears to be related to boundary layer transition. In particular, the "bursting" of the suction surface separation bubble is prevented by the presence of a large separation in an adjacent rotor passage. This effect overcomes the destabilising effect of the increase in incidence (and the corresponding increase in diffusion) predicted by Emmons' model of rotating stall and therefore these large scale separations do not propagate.

Increasing the free-stream turbulence allowed the suction surface separation bubble to reach lower flow rates without bursting and suppressed this phenomena. It is expected that increasing Reynolds number will have a similar effect. These results highlight a limitation in low speed, low Reynolds number testing of compressor stages and demonstrates the need for care in the design of such experiments.

It is not clear why this flow breakdown mechanism affects only the Qinetiq stage. The differences between the Qinetiq stage and other compressors likely to affect the formation of such flow breakdown mechanisms were identified; including its extreme loading and leading edge geometry (in particular its high wedge angle). However, this remains a question yet to be definitively answered.

10.6 Closure

In the light of the experimental and numerical results presented in the current work, modest increases in stage loading appear to be feasible. However, the rapidly increasing efficiency penalty for increasing the stage loading further precludes very highly loaded designs for efficiency critical applications (e.g. civil aero-engines). Nevertheless, the present work has demonstrated that very highly loaded stages may be suitable for

applications where efficiency is secondary to other considerations (e.g. cost, weight, etc...), for example in military aero-engines. Furthermore, limitations in existing loss correlations at high loading have been identified, an improved loss model demonstrated and a strategy for the design of highly loaded stages proposed.

Appendix A

Experimental Comparison Between the Mini-Deverson Stage and the Original Deverson Build II Stage

A.1 Introduction

The Mini-Deverson stage is a conventionally loaded stage representative of a mid-stage found in the high-pressure compressor of a 1990s civil aero-engine. It is a reduced size version of the Deverson Build II stage comprehensively documented by Bolger [4] (details of the scaling process are given in Chapter 4). This appendix compares the measured performance of the Mini-Deverson stage to the original Deverson Build II stage measured by Bolger [4].

A.2 Overall Performance

The pressure rise and efficiency characteristics of the Mini-Deverson stage and its larger counterpart are shown in Figure A.1. The Mini-Deverson stage is down on stage loading and hence pressure rise when compared to the original build. At the nominal design flow rate ($\bar{\phi} = 0.51$) this amounts to 4.3% of design stage loading coefficient.

The measured peak efficiency of the Mini-Deverson stage was 87.9% at a flow coefficient of 0.54. This compares to the value reported by Bolger [4] of 88.7%, at a flow coefficient of 0.51. The difference in the flow coefficient at which peak efficiency occurs is consistent with the higher axial velocity over the mid-span region due to the thicker end-wall boundary layers in the original Deverson rig.

A.3 Radial Profiles

The radial profiles of axial velocity, stagnation pressure rise and flow angle measured in the Mini-Deverson stage are compared to those measured by Bolger [4] in the section below. Similar measuring and data reduction techniques were used to record the behaviour of both stages. The following discussion is split into three sections, each corresponding to an area traverse location (i.e. inlet, rotor exit and stator exit).

A.3.1 Inlet Conditions

Despite the presence of upstream boundary layer trips, Figure A.2 shows that the end-wall boundary layers are thinner in the Mini-Deverson stage. At the same mid-span axial velocity (which sets the velocity triangles for the bulk of the flow), the Mini-Deverson will have a greater average flow rate and therefore its characteristics will tend to be shifted to the right. The thicker end-wall boundary layers in the original Deverson stage also cause greater over-turning of the end-wall flow through the IGV passage (this shows up in Figure A.2C as a higher inlet flow angle between 0-10% and 90-100% of span). However, over most of the span the radial profiles of inlet flow angle are very similar.

A.3.2 Rotor Flow

Downstream of the rotor the radial profiles measured behind both rotors (shown in Figure A.3) are very similar. At the nominal design point the plot of relative flow angle shows slightly more turning from the original rotor; as would be expected from the higher Reynolds number. The higher turning provides some explanation for the greater

work input (i.e. Δh_0) and pressure rise measured across the Deverson stage.

Near to stall the profiles measured downstream of the rotor and presented in Figure A.3 indicate a healthier clearance flow at the casing behind the original Deverson rotor. This is probably due to the higher tip clearance of the Mini-Deverson stage; the Mini-Deverson was run at a clearance of 1.40% of chord (increased from 1.24% of chord in the original build) for mechanical reasons (see Chapter 4). At the near stall operating point the plot of relative flow angle in Figure A.3 shows that Mini-Deverson rotor exhibits much higher deviation than the Deverson. One possible cause of this could be premature separation across the suction surface as a result of reduced Reynolds number.

A.3.3 Stator Flow

At the nominal design point the measured profiles at stator exit in Figure A.4) indicate that there is very little difference between the behaviour of Mini-Deverson and Deverson stators.

Near to stall, the increase in deviation and axial velocity deficit indicate that the hub-corner separation is more severe in the Mini-Deverson stage. To mimic the potential effect of a down-stream stage a pressure loss screen was fitted behind the Deverson stator. This smooths out any non-uniformities and tends to reduce the size of any stator separations. A similar screen was omitted from the HLRC to maintain adequate flow range (see Section 3.2); this goes some way to explaining the greater severity of the flow collapse at the Mini-Deverson stator hub.

A.4 Summary

Despite the differences between the Mini-Deverson and its larger counterpart (most notably Reynolds number), the Mini-Deverson produced very similar results to those obtained earlier by Bolger [4]. As expected from a well designed, conventionally loaded stage, the Mini-Deverson demonstrated good efficiency, pressure rise and stall margin.

Appendix B

Measured Radial Profiles

For the interested reader, the radial profiles measured in each of the four stages tested are presented in this appendix. A look-up table of the measured variables and corresponding figure numbers are given below.

	Mini- Deverson	Gallimore	Qinetiq	Denton
Inlet				
Axial velocity (V_x)				
Stagnation pressure (p_0)		B.1	B.9	B.17
Flow angle (α)				B.25
Rotor				
Relative inlet flow angle (α_{rel})	B.2	B.10	B.18	B.26
Axial velocity (V_x)				
Stagnation pressure (p_0)		B.3	B.11	B.19
Flow angle (α_{rel})				B.27
de Haller number ($\frac{V_2}{V_1}$)				
Lieblein Diffusion Factor (DF)	B.4	B.12	B.20	B.28
Loss coefficient (ω_p)				
Stage loading coefficient ($\frac{\Delta h_0}{U^2}$)	B.5	B.13	B.21	B.29

Stator

Inlet flow angle (α)	B.6	B.14	B.22	B.30
Axial velocity (V_x)				
Stagnation pressure (p_0)	B.7	B.15	B.23	B.31
Flow angle (α)				
de Haller number ($\frac{V_2}{V_1}$)				
Lieblein Diffusion Factor (DF)	B.8	B.16	B.24	B.32
Loss coefficient (ω_p)				

Appendix C

Definition of Non-Dimensional Camber and Thickness Distributions

The angle subtended by the camber line and the axial direction was specified along the chord non-dimensionally as a fraction of total camber (i.e. $\beta_2 - \beta_1$). The definition of non-dimensional camber angle used is given in Equation C.1. The coordinates of the camber line (relative to the chord line) were then found by evaluating the integral in Equation C.2.

$$f(z)_{cmbr} = \frac{\beta(z) - \beta_{le}}{\beta_{te} - \beta_{le}} \quad (\text{C.1})$$

$$y = \int_0^z \tan(\beta(z) - \xi) dz \quad (\text{C.2})$$

Where: “ z ” & “ y ” are the distances parallel and perpendicular to the chord line respectively and “ β ” is the local camber line angle.

At a given chord-wise position, the blade thickness was applied perpendicularly to the camber line. As with the camber line, the thickness distribution was specified non-dimensionally (defined in Equation C.3). The inclusion of the leading and trailing edge thickness term (t_{le} & t_{te} respectively) allow a finite thickness to be specified at the two ends of the section without introducing discontinuities into the first derivative of

the thickness distribution. An iterative procedure was used to adjust the leading and trailing edge thickness and smoothly blend circular geometries (of specified radius) into the main section profile. The blade thickness was scaled by a constant (10% for all the blades discussed here) prior to adding it to the camber line to achieve an aerofoil of the specified thickness.

$$f(z)_{thk} = \begin{cases} \frac{t - t_{le}}{t_{max} - t_{le}} & \text{for } 0 \leq \frac{z}{c} \leq z_{t_{max}} \\ \frac{t - t_{te}}{t_{max} - t_{te}} & \text{for } z_{t_{max}} \leq \frac{z}{c} \leq 1.0 \end{cases} \quad (\text{C.3})$$

Appendix D

Derivation of a Generic Velocity Distribution

D.1 Introduction

A generic velocity profile must satisfy two key criteria; a) it must be consistent with the inlet and exit velocities; and b) it must provide the correct turning, i.e. the pressure difference from pressure to suction surface must match the required change in tangential momentum. In the current approach the suction surface *and* the pressure surface velocities are chosen to provide pressure difference necessary to achieve the required turning.

The development of the generic velocity distribution is described in Chapter 9. For convenience a schematic of the velocity distribution is reproduced here in Diagram D.1. The idealised velocity distribution is completely defined by the velocity difference at the leading edge ($2\Delta V$), the representative velocities at the leading and trailing edges (V_{le} and V_{te} respectively) and the length of the “roof-top” (A). It is worth noting that velocity distribution is defined against axial position (rather than against surface distance or distance along the chord line). The advantage of this approach will be seen later (Section D.2.3).

This Appendix presents a derivation for the velocity difference at the leading edge, necessary to define a generic velocity distribution to give the specified turning (ΔV_θ).

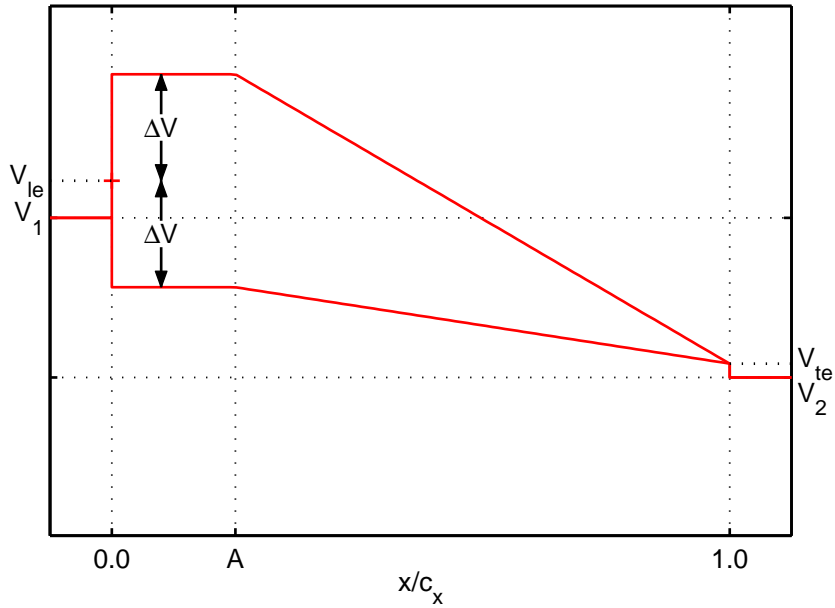


Diagram D.1: Schematic diagram of the assumed generic velocity distribution around a compressor aerofoil.

D.2 Calculation of ΔV

D.2.1 Tangential Momentum

Consider the conservation of tangential momentum across the control volume illustrated in Diagram D.2. The stream-wise boundaries (labelled I_1 & I_2) are chosen such that they are periodic, i.e. there is no net tangential momentum flux nor a net pressure force. The tangential force imposed on the flow by the blade must therefore be given by Equation D.2

$$F_\theta = \dot{m} \times [V_{\theta,2} - V_{\theta,1}] \quad (\text{D.1})$$

$$F_\theta = \rho s V_1 \cos \alpha_1 \Delta V_\theta \quad (\text{D.2})$$

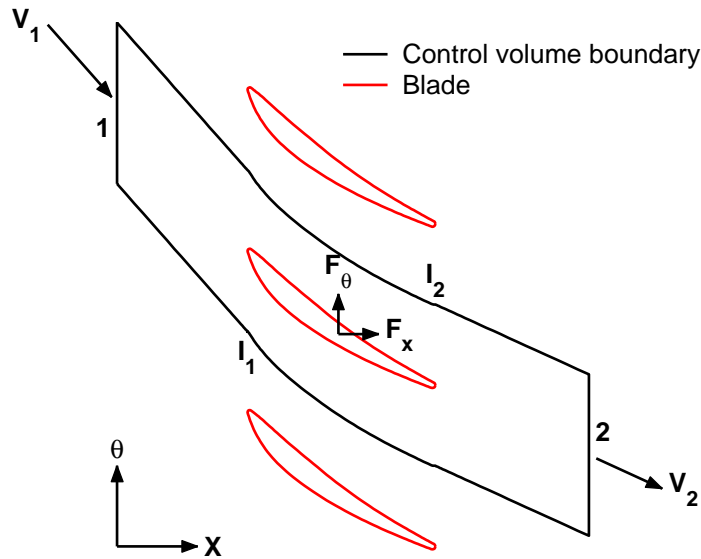


Diagram D.2: Schematic diagram of control volume.

D.2.2 Static Pressure Distribution

The static pressure distribution over the blade surface is uniquely linked to the velocity distribution. Let the velocity at the leading edge of the suction and pressure surfaces be denoted by $V_{0,ss}$ and $V_{0,ps}$ respectively, i.e.:

$$V_{0,ss} = V_{le} + \Delta V \quad (D.3)$$

$$V_{0,ps} = V_{le} - \Delta V \quad (D.4)$$

The velocity on the suction and pressure surfaces of the assumed generic velocity distribution of Diagram D.1 is therefore given by Equations D.5 and D.6.

$$V_{ss}(x) = \begin{cases} V_{0,ss} & \text{for } 0 \leq \frac{x}{c_x} \leq A \\ \left(\frac{V_{0,ss} - AV_{te}}{1-A} \right) - \left(\frac{V_{0,ss} - V_{te}}{1-A} \right) \frac{x}{c_x} & \text{for } A < \frac{x}{c_x} \leq 1.0 \end{cases} \quad (D.5)$$

$$V_{ps}(x) = \begin{cases} V_{0,ps} & \text{for } 0 \leq \frac{x}{c_x} \leq A \\ \left(\frac{V_{0,ps} - AV_{te}}{1-A} \right) - \left(\frac{V_{0,ps} - V_{te}}{1-A} \right) \frac{x}{c_x} & \text{for } A < \frac{x}{c_x} \leq 1.0 \end{cases} \quad (D.6)$$

Assuming that the flow is incompressible and that the static pressure is uniform throughout the boundary layer, the surface static pressure can be linked to the velocity distribution (Equations D.5 and D.6) via Bernoulli's equation. Evaluating Bernoulli's equation along the suction surface yields:

$$p_{ss}(x) = p_0 - \frac{1}{2}\rho V_{ss}^2(x)^2 \Rightarrow$$

$$p_{ss}(x) = \begin{cases} p_0 - \frac{1}{2}\rho V_{0,ss}^2 & \text{for } 0 \leq \frac{x}{c_x} \leq A \\ p_0 - \frac{1}{2}\rho \left[\left(\frac{V_{0,ss} - AV_{te}}{1-A} \right) - \left(\frac{V_{0,ss} - V_{te}}{1-A} \right) \frac{x}{c_x} \right]^2 & \text{for } A < \frac{x}{c_x} \leq 1.0 \end{cases} \quad (\text{D.7})$$

And similarly along the pressure surface:

$$p_{ps}(x) = p_0 - \frac{1}{2}\rho V_{ps}^2(x)^2 \Rightarrow$$

$$p_{ps}(x) = \begin{cases} p_0 - \frac{1}{2}\rho V_{0,ps}^2 & \text{for } 0 \leq \frac{x}{c_x} \leq A \\ p_0 - \frac{1}{2}\rho \left[\left(\frac{V_{0,ps} - AV_{te}}{1-A} \right) - \left(\frac{V_{0,ps} - V_{te}}{1-A} \right) \frac{x}{c_x} \right]^2 & \text{for } A < \frac{x}{c_x} \leq 1.0 \end{cases} \quad (\text{D.8})$$

Only the pressure difference between the suction and pressure surfaces is relevant for the current purpose, therefore p_0 can be eliminated by subtracting Equation D.8 from Equation D.7. Expanding and collecting similar terms yields:

$$\Delta p(x) = \begin{cases} \frac{1}{2}\rho (V_{0,ss}^2 - V_{0,ps}^2) & \text{for } 0 \leq \frac{x}{c_x} \leq A \\ \frac{1}{2}\rho \frac{V_{0,ss} - V_{0,ps}}{(1-A)^2} \left[(V_{0,ss} + V_{0,ps} - 2AV_{te}) - \dots \right. \\ \left. 2(V_{0,ss} + V_{0,ps} - (1+A)V_{te}) \frac{x}{c_x} + \dots \right] \\ (V_{0,ss} + V_{0,ps} - 2V_{te}) \left(\frac{x}{c_x} \right)^2 & \text{for } A < \frac{x}{c_x} \leq 1.0 \end{cases} \quad (\text{D.9})$$

Substituting expressions D.3 and D.3 for $V_{0,ss}$ and $V_{0,ps}$ respectively gives Equation D.10.

$$\Delta p(x) = \begin{cases} 2\rho\Delta VV_{le} & \text{for } 0 \leq \frac{x}{c_x} \leq A \\ \frac{2\rho\Delta V}{(1-A)^2} \left[(V_{le} - AV_{te}) - \dots \right. \\ \left. (2V_{le} - (1+A)V_{te}) \frac{x}{c_x} + \dots \right] \\ (V_{le} - V_{te}) \left(\frac{x}{c_x} \right)^2 & \text{for } A < \frac{x}{c_x} \leq 1.0 \end{cases} \quad (\text{D.10})$$

D.2.3 Tangential Blade Force

The tangential force exerted on the blade (by the flow) can be obtained by integrating the static pressure difference (between suction and pressure surfaces) along the axial projection of the blade and is given by Equation D.11. It is here where the advantage of defining the generic velocity distribution against axial distance becomes apparent. For a pressure (neé velocity) distribution defined against true chord (or surface length) it is necessary to know (or assume) the surface angle or coordinates to calculate the tangential component of the pressure force. By defining the velocity distribution against axial coordinate this restriction is removed and it becomes trivial to find the net pressure acting on the axial projection of the blade.

$$F_\theta = \int_0^{c_x} \Delta P(x) dx \quad (\text{D.11})$$

For the current velocity distribution, the integral of Equation D.11 is equivalent to that of Equation D.12 for a blade section of constant height (here assumed to be unity).

$$F_\theta = c_x \int_0^A \Delta P \left(\frac{x}{c_x} \right) d \left(\frac{x}{c_x} \right) + c_x \int_A^1 \Delta P \left(\frac{x}{c_x} \right) d \left(\frac{x}{c_x} \right) \quad (\text{D.12})$$

Substituting the expression for pressure difference derived in Section D.2.2 (Equation D.10) into Equation D.12 and evaluating gives:

$$F_\theta = 2c_x \rho \Delta V \left[V_{le} \frac{x}{c_x} \right]_0^A + \frac{2\rho c_x \Delta V}{(1-A)^2} \left[(V_{le} - AV_{te}) \frac{x}{c_x} - \dots \right. \\ \left. \frac{1}{2} (2V_{le} - (1+A)V_{te}) \left(\frac{x}{c_x} \right)^2 + \frac{1}{3} (V_{le} - V_{te}) \left(\frac{x}{c_x} \right)^3 \right]_A^1 \quad (\text{D.13})$$

$$F_\theta = \frac{1}{3} \rho c_x \Delta V \left(2(1+2A)V_{le} + (1-A)V_{te} \right) \quad (\text{D.14})$$

D.2.4 Solving for ΔV

The axial chord is linked to the true chord by the stagger angle ($c = c_x \cos \xi$). Equating D.2 to D.14 and rearranging gives an expression for ΔV (Equation D.15).

$$\Delta V = \frac{3V_1 \cos \alpha_1 \Delta V_\theta}{\sigma \cos \xi \left(2(1+2A)V_{le} + (1-A)V_{te} \right)} \quad (\text{D.15})$$

D.3 Discussion

Although Equation D.15 clearly depends upon required turning (ΔV_θ) and solidity, it is not immediately obvious how the velocity and angle terms relate to parameters more familiar to compressor designers (e.g. de Haller number). A reasonable first guess is to assume that the velocities at the leading edge and trailing edge are close to the inlet and exit values (i.e. $V_{le} \approx V_1$ and $V_{te} \approx V_2$ respectively). This allows Equation D.15 to be rearranged into Equation D.16.

$$\Delta V \approx \frac{3 \left(\frac{\cos \alpha_1}{\cos \xi} \right) \Delta V_\theta}{\sigma \left(2(1+2A) + (1-A) \frac{V_2}{V_1} \right)} \quad (\text{D.16})$$

The physical meaning of $\frac{\cos \alpha_1}{\cos \xi}$ is not obvious. Inlet flow angle, α_1 and stagger angle, ξ , are not independent variables; the stagger angle can be approximated by a weighted average of the design inlet and exit flow angles (see Equation D.17). Diagram D.3 shows

that $\frac{\cos \alpha_1}{\cos \xi}$ is an almost linear function of de Haller number for a wide range of velocity triangles¹.

$$\xi = k\alpha_1 + (1 - k)\alpha_2 \quad (\text{D.17})$$

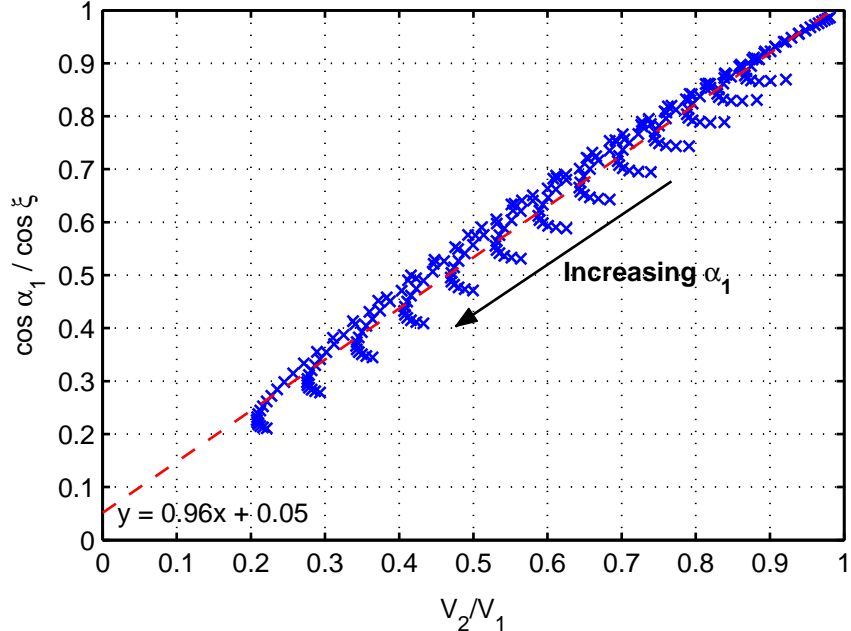


Diagram D.3: Variation of $\frac{\cos \alpha_1}{\cos \xi}$ with de Haller number ($\frac{V_2}{V_1}$) for compressor blade rows ($30^\circ \leq \alpha_1 \leq 80^\circ$, $-20^\circ \leq \alpha_2 \leq 60^\circ$ and $k = 0.3$).

Substituting a best fit straight line into Equation D.16 for $\frac{\cos \alpha_1}{\cos \xi}$ (with arbitrary constants a and b) gives Equation D.18. Equation D.18 shows that ΔV is primarily dependent only on the required turning (ΔV_θ), solidity (σ) and de Haller number ($\frac{V_2}{V_1}$).

$$\Delta V \approx \frac{3 \left(a \frac{V_2}{V_1} + b \right) \Delta V_\theta}{\sigma \left(2(1 + 2A) + (1 - A) \frac{V_2}{V_1} \right)} \quad (\text{D.18})$$

¹Figure D.3 shows the value of $\frac{\cos \alpha_1}{\cos \xi}$ evaluated for inlet flow angles (α_1) between 30° & 80° (increment 4°) and exit flow angles (α_2) between -20° & 60° (increment 4°), assuming constant axial velocity. This range covers almost all practical compressor stages. The stagger angle (ξ) has been estimated from the inlet and exit flow angles via Equation D.17 with $k = 0.3$ (a reasonable estimate for controlled diffusion aerofoils).

Where: a and b are arbitrary constants approximately equal to unity and zero respectively.

D.4 Restrictions and Extensions

The two main restrictions on the analysis above are the assumptions of incompressibility and the assumption of uniform stream-tube height. Extending this method to account for compressibility requires substituting the compressible gas relation of Equation D.19 for Bernoulli's equation in Equations D.7 and D.8 (Section D.2.2). At transonic and supersonic Mach numbers the presence of shocks will cause large changes to the surface pressures and is likely to compromise the generality of an assumed velocity distribution.

$$\frac{p}{p_0} = \left(1 - \frac{\gamma - 1}{2} M^2\right)^{-\frac{\gamma}{\gamma-1}} \quad (\text{D.19})$$

Similarly, changes to stream-tube height must be accounted for *inside* the integral of Equation D.11 as a function of axial coordinate, $h(x)$, as illustrated in Equation D.20.

$$F_\theta = \int_0^{c_x} h(x) \Delta P(x) dx \quad (\text{D.20})$$

The assumed velocity distribution was chosen to give reasonable agreement to that of real compressor blades and for its simplicity; it does not necessarily represent the best fit to real compressor velocity distributions. There is no reason why a more sophisticated parameterisation (e.g. a quadratic or spline fit) of the surface velocities cannot be substituted for Equations D.5 and D.6 to give an improved approximation of real velocity distributions.

The corrections described above are necessary to use this method on typical aero-engine compressors, however absolute applicability is not necessary for the current work, which is concerned with identifying trends with increasing stage loading. Although these extensions are relatively trivial to implement (as long as the assumed velocity distribution remains realistic) the additional mathematical complexity detracts from its

clarity for little benefit in terms of physical understanding of the effects of increasing stage loading.

Bibliography

- [1] B.J. Abu-Ghannam and R. Shaw. Natural Transition of Boundary Layers - The Effects of Turbulence, Pressure Gradient and Flow History. *Journal of Mechanical engineering Science*, 22(5), 1980.
- [2] P.W. Bearman. Corrections for the Effect of Ambient Temperature Drift on Hot-Wire Measurement in Incompressible Flow. *DISA Information*, pages 25–30, 1971.
- [3] J. J. Bolger. Private communication.
- [4] J.J. Bolger. *Three Dimensional Design of Compressor Blades*. PhD thesis, University of Cambridge, 1999.
- [5] L. Brilliant, S. Balamucki, G. Burger, Y. Dong, and C. Lejambre. Application of Multistage CFD Analysis to Low Pressure Compressor Design. In *A.S.M.E. Turbo Expo 2004*, number GT2004-54363. A.S.M.E, 2004.
- [6] H.H. Bruun. *Hot-Wire Anemometry*. Oxford University Press, 1995.
- [7] J.D. Bryce, M.A. Cherret, and P.A. Lyes. Three-Dimensional Flow in a Highly Loaded Single Stage Transonic Fan. *A.S.M.E. Journal of Turbomachinery*, 117:22–28, 1995.
- [8] T.R. Camp and I.J. Day. A Study of Spike and Modal Stall Phenomena in a Low-Speed Axial Compressor. *A.S.M.E. Journal of Turbomachinery*, 120:393–401, 1998.
- [9] T.R Camp and H.W. Shin. Turbulence Intensity and Length Scale Measurements in Multistage Compressors. *A.S.M.E. Journal of Turbomachinery*, 117:38–46, 1995.
- [10] CFM International. CFM56 Engine Family. <http://www.cfm56.com/index.php?level2=engines>, January 2008.

- [11] D.E. Culley, M.M. Bright, P.S. Prahst, and A.J. Strazisar. Active flow separation control of a stator vane using surface injection in a multistage compressor experiment. In *A.S.M.E. Turbo Expo*, number GT2003-38863. A.S.M.E, 2003.
- [12] N.A. Cumpsty. *Compressor Aerodynamics*. Longman Scientific and Technical, 1989.
- [13] R. Dambach and H.P. Hodson. A New Method of Data Reduction for Single-Sensor Pressure Probes. In *A.S.M.E. Turbo Expo 1999*, number 99-GT-304. A.S.M.E, 1999.
- [14] I.J. Day. Stall and Surge. In *Cambridge Turbomachinery Course Notes*. Whittle Laboratory, Cambridge University Engineering Department, 2004.
- [15] I.J. Day, T. Breuer, J. Escuret, M Cherret, and A. Wilson. Stall Inception and the Prospects for Active Control in Four High-Speed Compressors. *ASME Journal of Turbomachinery*, 121:18–27, 1999.
- [16] A.A.J. Demargne and J.P. Longley. The Aerodynamic Interaction of Stator Shroud Leakage and Mainstream Flows in Compressors. In *A.S.M.E. Turbo Expo 2000*, number 2000-GT-570. A.S.M.E, 2000.
- [17] J.D. Denton. The Calculation of Three-Dimensional Viscous Flow Through Multistage Turbomachines. *A.S.M.E. Journal of Turbomachinery*, 114:18–26, 1992.
- [18] J.D. Denton. Loss Mechanisms in Turbomachines. *A.S.M.E. Journal of Turbomachinery*, 115:621–656, 1993.
- [19] J.D. Denton and N.A. Cumpsty. IMechE International Conference Turbomachinery - Efficiency Prediction and Improvement. In *I.G.T.I Gas Turbine Congress*, number C260/87, 1987.
- [20] J.D. Denton and W.N. Dawes. Computational Fluid Dynamics for Turbomachinery Design. *Proceedings of the IMechE (Part C)*, 213:107–124, 1999.
- [21] J.D. Denton, A.M. Wallis, D. Borthwick, J. Grant, and I. Ritchley. The three-dimensional design of low aspect ratio 50% reaction turbines. Number S461/008/96 in Latest Advances in the Aerodynamics of Turbomachinery with Special Emphasis Upon Secondary Flows. IMechE, 1996.

- [22] J.D. Denton and L. Xu. The Exploitation of Three-Dimensional Flow in Turbomachinery Design. *Proceedings of the IMechE, Part C: Journal of Mechanical Engineering Science*, 213(2), 1999.
- [23] A. Deppe, H. Saathoff, and U. Stark. Stall Inception Phenomena in Three Single-Stage Low-Speed Axial Compressors. In *The 10th International Symposium on Transport Phenomena and Dynamics of Rotating Machinery*, number FD048, 2004.
- [24] A. Deppe, H. Saathoff, and U. Stark. Spike-Type Stall Inception in Axial-Flow Compressors. In *Proceedings of the 6th European Conference on Turbomachinery - Fluid Mechanics and Thermodynamics*, 2005.
- [25] Y. Dong and N.A. Cumpsty. Compressor Blade Boundary Layers: Part 1 – Test Facility and Measurements with No Incident Wakes. *A.S.M.E. Journal of Turbomachinery*, 112:222–230, 1990.
- [26] Y. Dong and N.A. Cumpsty. Compressor Blade Boundary Layers: Part 2 – Measurements with Incident Wakes. *A.S.M.E. Journal of Turbomachinery*, 112:231–240, 1990.
- [27] Y. Dong, S.J. Gallimore, and H.P. Hodson. Three-Dimensional Flows and Loss Reduction in Axial Compressors. *A.S.M.E. Journal of Turbomachinery*, 109:354–361, 1987.
- [28] M. Drela. Two-Dimensional Transonic Aerodynamic Design and Analysis Using the Euler Equations. Technical Report GTL Report No. 187, Massachusetts Institute of Technology, 1986.
- [29] M. Drela. MISES Implementation of Modified Abu-Ghannam/ Shaw Transition Criterion. Technical report, M.I.T. Aero/ Astro, 1998.
- [30] H.W. Emmons. A Survey of Stall Propagation - Experiment and Theory. *Trans. A.S.M.E.*, (409-416):183–226, 1956.
- [31] Engine Alliance LLC. Engine Specifications. <http://www.enginealliance.com/gpspec.html>, January 2008.
- [32] C. Freeman. Effects of Tip Clearance Flow on Compressor Stability and Engine Performance. Number LS-1985-05. VKI Lecture Series, 1985.
- [33] C. Freeman. Private communication. 2007.

- [34] C. Freeman and R.E. Dawson. Core Compressor Developments for Large Civil Jet Engines. In *International Gas Turbine Congress, Tokyo*, number 83-Tokyo-IGTC-46, October 1983.
- [35] J. Friedrichs, S. Baumgarten, G. Kosyna, and U. Stark. Effect of Stator Design on Stator Boundary Layer Flow in a Highly-Loaded Single Stage Axial Flow Compressor. *A.S.M.E. Journal of Turbomachinery*, 123:483–489, 2001.
- [36] S.J. Gallimore. Axial Compressor Design. In *Cambridge Turbomachinery Course*, 2004.
- [37] S.J. Gallimore, J.J. Bolger, N.A. Cumpsty, M.J. Taylor, P.I. Wright, and J.M.M Place. The Use of Sweep and Dihedral in Multistage Axial Flow Compressor Blading – Part I: University Research and Methods Development. *ASME Journal of Turbomachinery*, 124:521–532, 2002.
- [38] S.J. Gallimore, J.J. Bolger, N.A. Cumpsty, M.J. Taylor, P.I. Wright, and J.M.M Place. The Use of Sweep and Dihedral in Multistage Axial Flow Compressor Blading – Part II: Low and High-Speed Designs and Test Verification. *ASME Journal of Turbomachinery*, 124:533–541, 2002.
- [39] S.A. Gbadebo. *Three Dimensional Separations in Compressors*. PhD thesis, University of Cambridge, 2003.
- [40] S.A. Gbadebo. Three Dimensional Separations in Axial Compressors. *ASME Journal of Turbomachinery*, 127:331–339, 2005.
- [41] General Electric Aircraft Engines. GE - Aviation: Commercial. <http://www.geaviation.com/engines/comercial/index.html>, January 2008.
- [42] H.P. Grant. Measuring Time-Averaged Stagnation Pressure in Pusatile Airflow. In *23rd International Instrumentation Symposium*. Instrument Society of America, Las Vegas, Nevada, 1977.
- [43] J.E. Green, D.J. Weeks, and J.W.F. Brooman. Prediction of Turbulent Boundary Layers and Wakes in Compressible Flow by a Lag-Entrainment Method. Technical Report R & M Report 3791, Aeronautical Research Council, HMSO London, 1977.
- [44] E.M. Greitzer, J.P. Nikkanen, D.E. Haddad, R.S. Mazzawy, and H.D. Joslyn. A Fundamental Criterion for the Application of Rotor Casing Treatment. *A.S.M.E. Journal of Fluids Engineering*, 101:237–243, 1979.

- [45] E.M. Greitzer, C.S. Tan, and M.B. Graf. *Internal Flow: Concepts and Applications*. Cambridge University Press, 2004.
- [46] H.F.L. Griepentrog. Performance Prediction of High Turning Low Aspect Ratio Stator Cascades in the Transonic Regime. *A.S.M.E. Journal of Engineering for Power*, 92:390–398, 1970.
- [47] D. E. Halstead, D. C. Wisler, T. H. Okiishi, G. J. Walker, H. P. Hodson, and H.-W. Shin. Boundary Layer Development in Axial Compressors and Turbines: Parts 1 to 4. *ASME Journal of Turbomachinery*, 119:114–127, 1997.
- [48] D.E. Hobbs and H.D. Weingold. Development of Controlled Diffusion Airfoils for Multistage Compressor Application. *ASME Journal of Engineering for Gas Turbines and Power*, 108:274–278, 1984.
- [49] H.P. Hodson. Blade to Blade Flowfields and Blade Surface Boundary Layers in Axial Flow Turbo-Machines. In *Cambridge Turbomachinery Course Notes*. Whittle Laboratory, Cambridge University Engineering Department, 2004.
- [50] H.P. Hodson. Experimental Methods for Turbomachinery Aerothermal Research. In *Cambridge Turbomachinery Course Notes*. Whittle Laboratory, Cambridge University Engineering Department, 2004.
- [51] G.C. Horton. The Aerodynamic Design of a Highly-Loaded Low-Speed Compressor Stage. Technical Report Qinetiq/FST/CAT/TR020761, Qinetiq, 2002.
- [52] R.J. Howell, O.N. Ramesh, H.P. Hodson, N.W. Harvey, and V. Schulte. High Lift and Aft-Loaded Profiles for Low-Pressure Turbines. *A.S.M.E. Journal of Turbomachinery*, 123:181–188, 2001.
- [53] J.D. Hughes. Design of a Highly-Loaded Low-Speed Compressor Stage. Technical Report RCR 91343, Rolls-Royce plc., 2000.
- [54] M. Inoue, M. Kuroumaru, M. Furukawa, Y. Kinoue, T. Tanino, S. Maeda, and K. Okuno. Controlled Endwall-Flow Blading for Multistage Axial Compressor Rotor. Number 97-GT-248. ASME, 1997.
- [55] International Aero Engines. V2500 Applications. <http://www.i-a-e.com/engine/applications.shtml>, January 2008.

- [56] S.A. Khalid, A.S. Khalsa, I.A. Waitz, C.S. Tan, E.M. Greitzer, Cumpsty N.A., J.J. Adamczyk, and F.E. Marble. Endwall Blockage in Axial Compressors. *A.S.M.E. Journal of Turbomachinery*, 121:499–509, 1999.
- [57] K.R. Kirtley, P. Grazosi, P. Wood, B. Beacher, and H.W. Shin. Design and Test of an Ultra-Low Solidity Flow Controlled Compressor Stator. In *A.S.M.E. Turbo Expo 2004*, number GT2004-53012. A.S.M.E, 2004.
- [58] C.C. Koch. Stalling Pressure Rise Capability of Axial Flow Compressor Stages. *A.S.M.E. Journal of Engineering for Power*, 103:645–656, 1979.
- [59] C.C. Koch and L.H. Smith. Loss Sources and Magnitudes in Axial Flow Compressors. *A.S.M.E. Journal of Engineering for Power*, pages 411–424, 1976.
- [60] U. Koller, R. Monig, B. Kusters, and H.A. Schreiber. Development of Advanced Airfoils for Heavy-Duty Gas Turbines – Part I: Design and Optimization. *ASME Journal of Turbomachinery*, 122:397–405, 2000.
- [61] B. Kusters, H.A. Schreiber, U. Koller, and R. Monig. Development of Advanced Airfoils for Heavy-Duty Gas Turbines – Part II: Experimental and Theoretical Analysis. *ASME Journal of Turbomachinery*, 122:406–415, 2000.
- [62] V.M. Lei, E.M. Spakovszky, and E.M. Greitzer. A Criterion for Axial Compressor Hub-Corner Stall. In *A.S.M.E. Turbo Expo 2006*, number GT2006-91332. A.S.M.E, 2006.
- [63] S. Leiblein. Experimental Flow in Two-Dimensional Cascades. *Reprinted NASA SP-36: Aerodynamic Design of Axial Compressors*, pages 183–226, 1965 (originally 1956).
- [64] P. Lewis and A. Doyle. MTU Set to Solve PW6000 Problem. *Flight International*, 28th May 2002.
- [65] J.P. Longley. Introduction to 3D Flows. In *Cambridge Turbomachinery Course Notes*. Whittle Laboratory, Cambridge University Engineering Department, 2004.
- [66] P.A. Lyes and R.B. Ginder. Experimental Evaluation of the High-to-Low Speed Transformation Process for a Highly Loaded Core Compressor Stage. In *International Gas Turbine & Aeroengine Congress and Exhibition*, number 98-GT-334. A.S.M.E, 1998.

- [67] R.E. Mayle. The Role of Laminar-Turbulent Transition in Gas Turbine Engines. *ASME Journal of Turbomachinery*, 113:509–537, 1991.
- [68] G.S. McNulty, J.J. Deckers, B.F. Beacher, and S.A. Khalid. The Impact of Forward Swept Rotors on Tip-Limited Low-Speed Axial Compressors. 126:445–454, 2004.
- [69] A. Merchant. Aerodynamic Design and Performance of Aspirated Airfoils. In *A.S.M.E. Turbo Expo*, number GT2002-30369. A.S.M.E, 2002.
- [70] F.K. Moore. A Theory of Rotating Stall of Multistage Axial Compressors: Part I - Small Disturbances. *A.S.M.E. Journal of Engineering for Gas Turbines and Power*, 106:313–326, 1984.
- [71] F.K. Moore and E.M. Greitzer. A theory of post-stall transients in axial compression systems: Part i - development of equations. *A.S.M.E. Journal of Engineering for Gas Turbines and Power*, 108(1):68–76, 1986.
- [72] G. Norris and J. Moxon. PW6000 Lands Long-Awaited Launch Deal as LAN Signs Up. *Flight International*, 23rd August 2005.
- [73] X. Ottavy, S. Vilmin, H.P. Hodson, and S. Gallimore. The Effects of Wake-Passing Unsteadiness Over a Highly-Loaded Compressor-Like Flat plate. *A.S.M.E. Journal of Turbomachinery*, 126:13–23, 2004.
- [74] J.M.M Place. *Three Dimensional Flow in Core Compressors*. PhD thesis, University of Cambridge, 1997.
- [75] J.M.M. Place, M.A. Howard, and Cumpsty N.A. Simulating the Multi-Stage Environment for Single Stage Compressor Experiments. *A.S.M.E. Journal of Turbomachinery*, 118:706–716, 1996.
- [76] Rolls-Royce Plc. *The Jet Engine*. Rolls-Royce Technical Publications, 6th edition, 2005.
- [77] Q.D. Roberts and J.D. Denton. Loss Production in the Wake of a Simulated Subsonic Turbine Blade. In *I.G.T.I Gas Turbine Congress*, number 96-GT-421, 1996.
- [78] G.S. Samoilovich and L.D. Yablokov. Measurement of Periodically Fluctuating Flows in Turbo-machines by Ordinary Pitot Tubes. *Journal of Thermal Engineering*, 17(9):105–110, 1970.

- [79] H. Schlichting. *Boundary-Layer Theory*. McGraw Hill, 7th edition, 1979.
- [80] F.C. Schwenk, G.W. Lewis, and M.J. Hartman. A Preliminary Analysis of the Magnitude of Shock Losses in Transonic Compressors. Technical Report RN E57A30, NACA, 1957.
- [81] P.A. Seitz. *Casing Treatment for Axial Flow Compressors*. PhD thesis, University of Cambridge, 1999.
- [82] A. Shabbir, Celestina, Adamczyk J.J. M.L., and A.J. Strazisar. The Effect of Hub Leakage Flow on Two High-Speed Axial Flow Compressor Rotors. In *International Gas Turbine & Aeroengine Congress and Exhibition*, number 97-GT-346. A.S.M.E, 1997.
- [83] P.D. Smout and P.C. Ivey. Investigation of Wedge Probe Wall Proximity Effects: Parts 1 & 2. *A.S.M.E Journal of Engineering for Gas Turbines and Power*, 119(3):598–611, 1997.
- [84] A. Sofia. The Effect of Wakes on Leading Edge Loss. Master's thesis, ETH Zrich, 2006.
- [85] W.L. Stewart. Analysis of Two-Dimensional Compressible-Flow Loss Characteristics Downstream of Turbomachine Blade Rows in Terms of Basic Boundary Layer Characteristics. Technical Report TN 3515, NACA, 1955.
- [86] J.A. Storer. *Tip Clearance Flow in Axial Compressors*. PhD thesis, University of Cambridge, 1991.
- [87] J.A. Storer and N.A. Cumpsty. An Approximate Analysis and Prediction Method for Tip Clearance Loss in Axial Compressors. In *International Gas Turbine & Aeroengine Congress and Exhibition*, number 93-GT-140. A.S.M.E, 1993.
- [88] L. Tain. *Compressor Leading Edges in Incompressible and Compressible Flows*. PhD thesis, University of Cambridge, 1998.
- [89] D.L. Tweedt, T.H. Okisshi, and M.D. Hathaway. Stator Endwall Leading-Edge Sweep and Hub Shroud Influence on Compressor Performance. *ASME Journal of Turbomachinery*, 108:224–232, 1985.
- [90] H.D. Vo, C.S. Tan, and E.M. Greitzer. Criteria for Spike Initiated Rotating Stall. In *A.S.M.E. Turbo Expo 2005*, number GT2005-68374. A.S.M.E, 2005.

- [91] A.R. Wadia, P.N. Szucs, and P.W. Crall. Inner Workings of Aerodynamic Sweep. *ASME Journal of Turbomachinery*, 120:671–682, 1998.
- [92] H.D. Weingold, R.J. Neubert, R.F. Behlke, and G.E. Potter. Reduction of Compressor Stator Endwall Losses Through the Use of Bowed Stators. Number 95-GT-380. ASME, 1995.
- [93] A.J. Wennerstrom. Some Experiments with a Supersonic Axial Compressor Stage. *A.S.M.E. Journal of Turbomachinery*, 109:388–397, 1987.
- [94] A.J. Wennerstrom. Highly Loaded Axial Flow Compressors: History and Current Developments. *A.S.M.E. Journal of Turbomachinery*, 112:567–577, 1990.
- [95] A.J. Wennestrom. Experimental Study of a High Throughflow Transonic Axial Compressor Stage. *ASME Journal of Turbomachinery*, 106:552–560, 1984.
- [96] A. Wheeler. *The Effect of Unsteady Flows on Compressor Performance*. PhD thesis, University of Cambridge, 2007.
- [97] Pratt & Whitney. Products: Commercial. <http://www.pratt-whitney.com>, January 2008.
- [98] D.C. Wisler. Loss Reduction in Axial-Flow Compressors Through Low-Speed Model Testing. *A.S.M.E. Journal of Turbomachinery*, 107:354–363, 1985.
- [99] P.I. Wright and D.C. Miller. An Improved Compressor Performance Prediction Model. In *European Conference on Turbomachinery: Latest Developments in a Changing Scene*, number C423/028. IMechE, 1991.

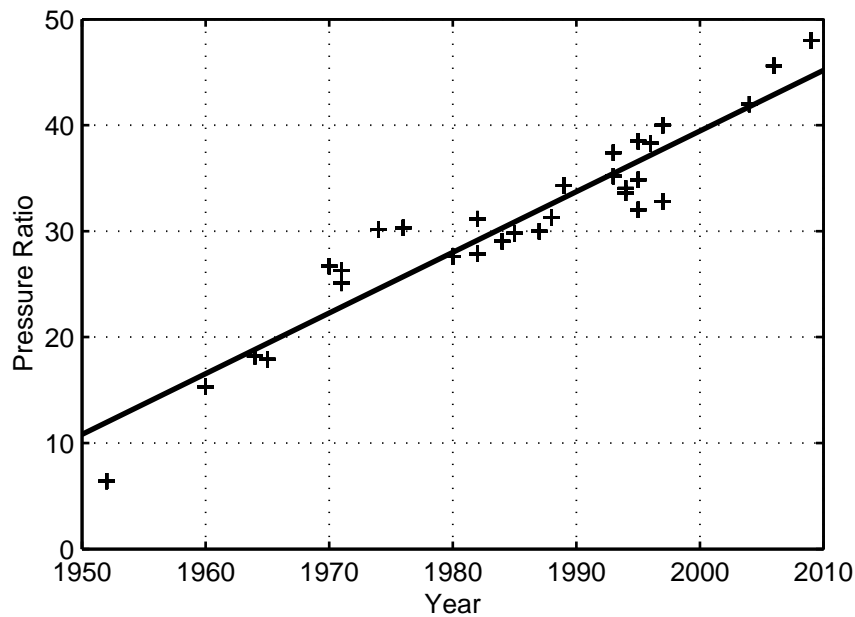


Figure 1.1: Large civil aero-engine pressure ratios from 1950 to 2007. Trend indicated by solid black line. (Sources: Pratt & Whitney [97], General Electric [41], CFM56 [10], International Aero Engines [55], Engine Alliance [31] and Freeman & Dawson [34].)

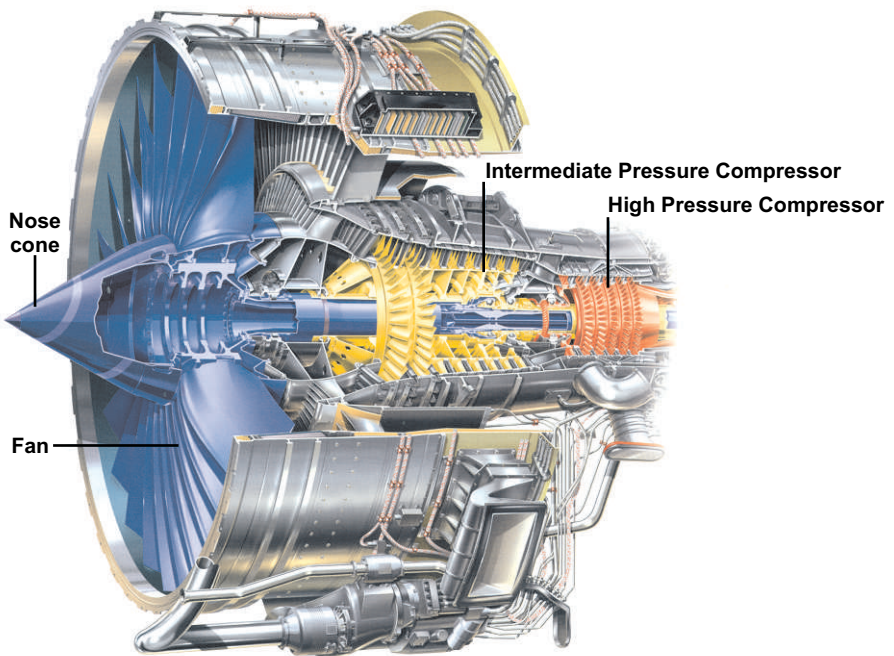


Figure 1.2: Cut-away view of a large civil three-shaft engine. Taken from Rolls-Royce [76]

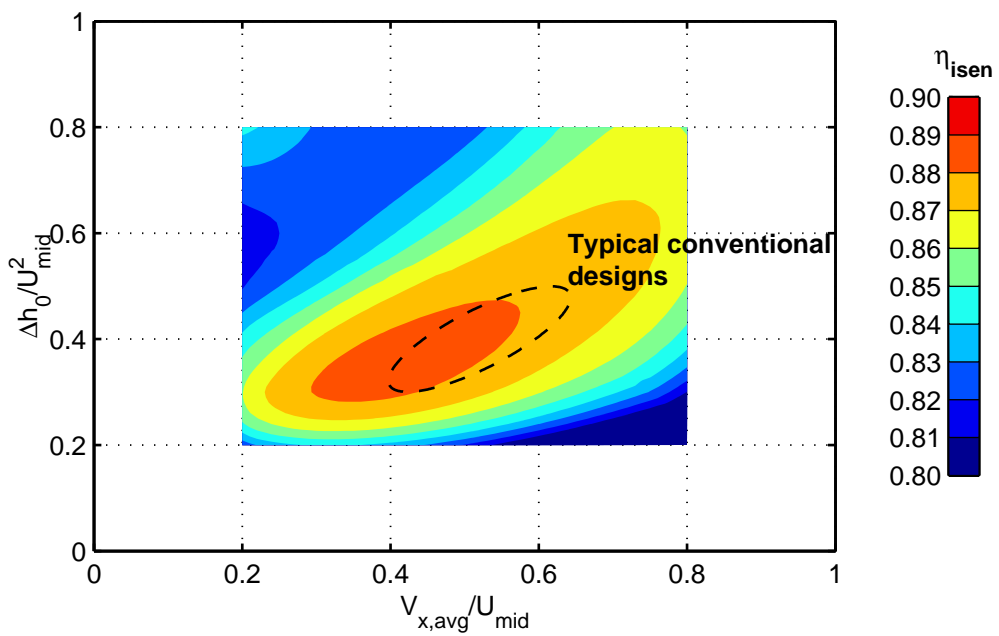


Figure 1.3: Compressor Smith Chart showing contours of efficiency. Efficiency calculated from the one-dimensional correlations of Wright & Miller [99] for a typical high-pressure compressor stage.

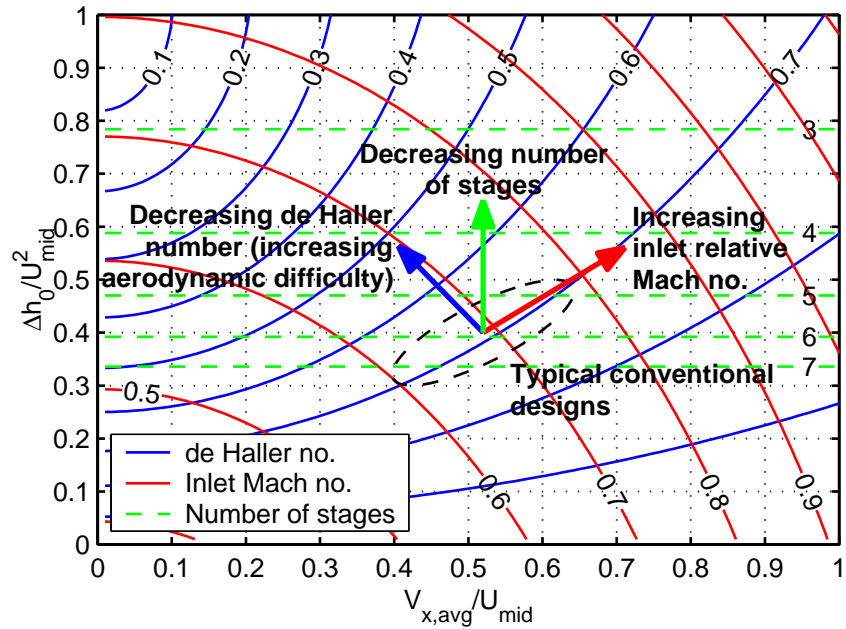


Figure 1.4: Smith Chart showing contours of de Haller number (blue) and inlet relative Mach number (red) for a 50% reaction stage. Number of stages (green) calculated to achieve a overall pressure ratio of 5.0 at engine representative conditions.

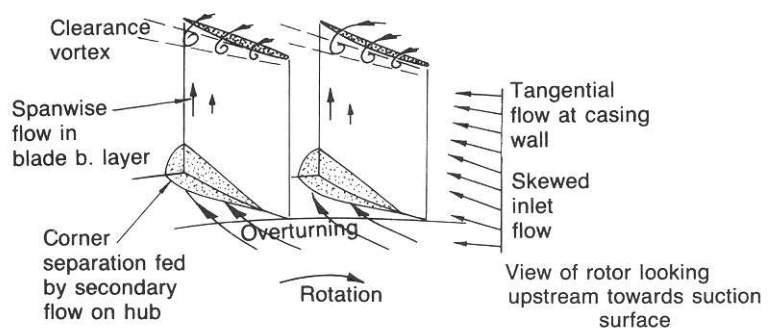


Figure 2.1: Diagram of the secondary flows in a typical compressor blade row. Taken from Cumpsty [12].

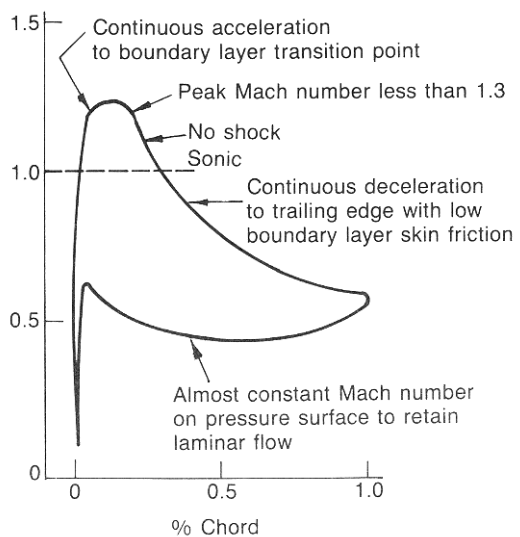


Figure 2.2: Diagram showing the features of super-critical (controlled diffusion) Mach number distribution. Taken from Hobbs & Weingold [48].

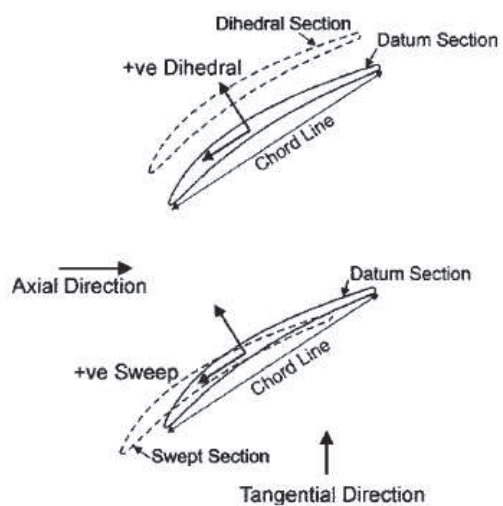


Figure 2.3: Definition of sweep and lean (dihedral). Taken from Gallimore et al [37].

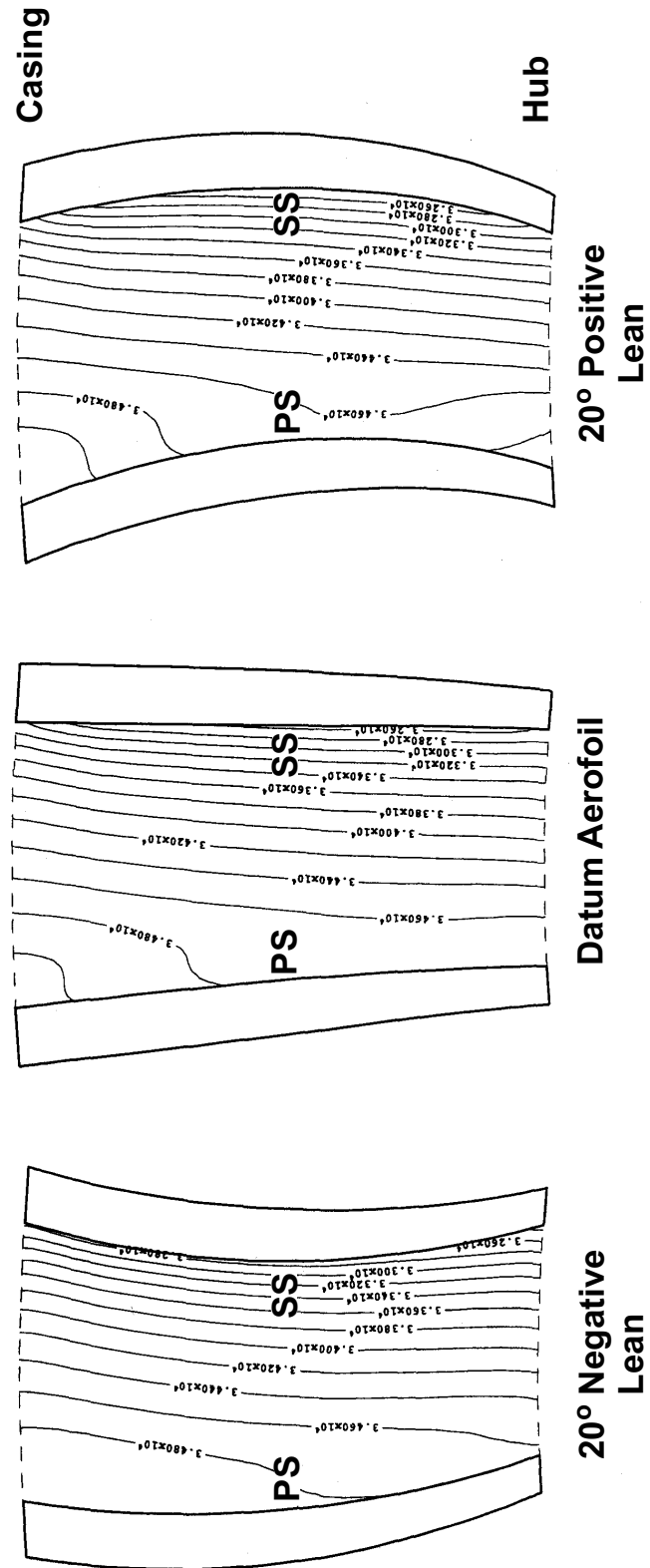


Figure 2.4: Effect of lean on contours of (calculated) static pressure at 14% axial chord.
Reproduced from Bolger [4].

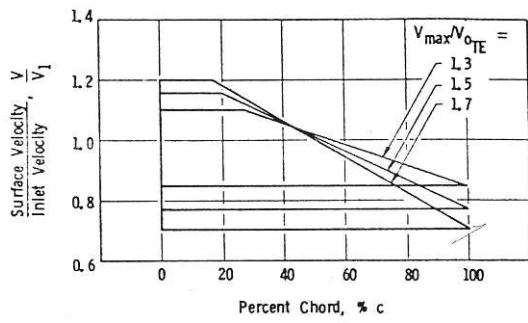


Figure 2.5: Generic velocity distributions used by Koch & Smith [59] to estimate profile losses.

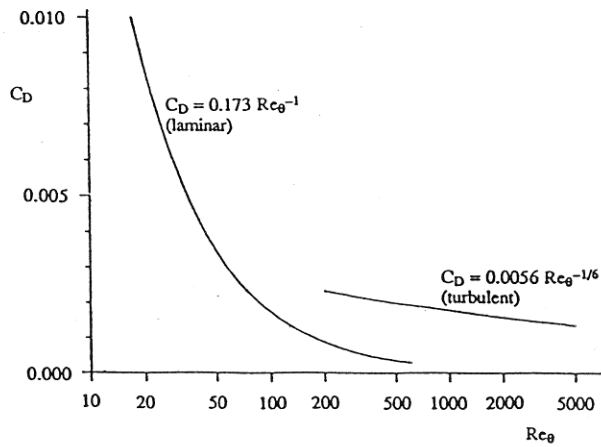


Figure 2.6: Variation of dissipation coefficient (C_D) with momentum thickness Reynolds number (Re_θ). Taken from Denton [18].

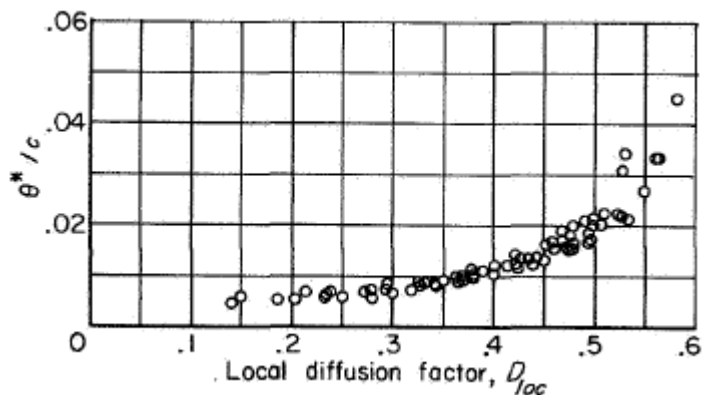


Figure 2.7: Trailing edge momentum thickness ($\frac{\theta}{c}$) against local diffusion factor (D_{loc}). Taken from Lieblein [63].

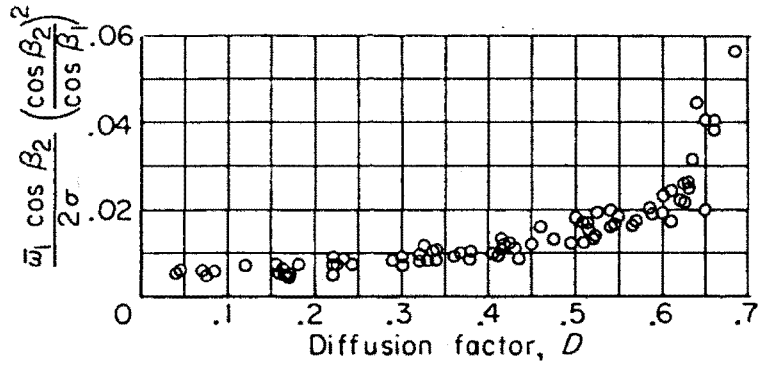


Figure 2.8: Lieblein loss parameter ($\omega_p \frac{\cos \alpha_2}{2\sigma} \left[\frac{\cos \alpha_2}{\cos \alpha_1} \right]^2 \approx \frac{\theta}{c}$) against Leiblein diffusion factor (D). Taken from Lieblein [63].

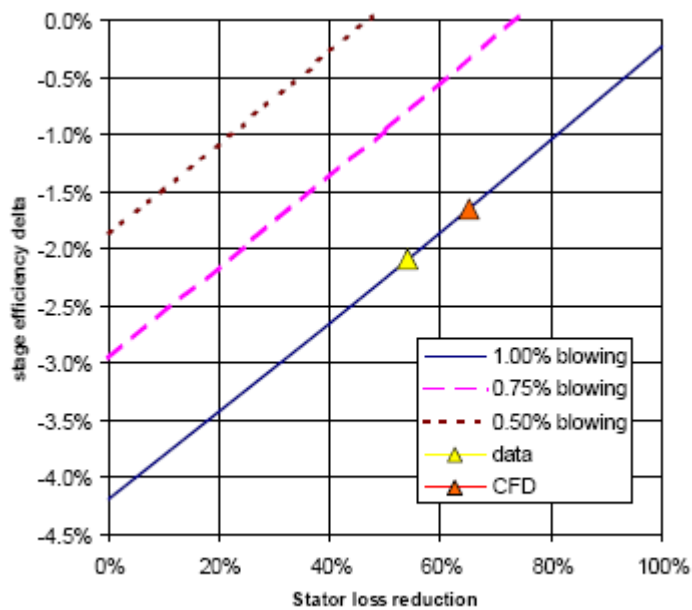


Figure 2.9: Impact of aspiration on compressor cycle performance. Taken from Kirtley et al [57].

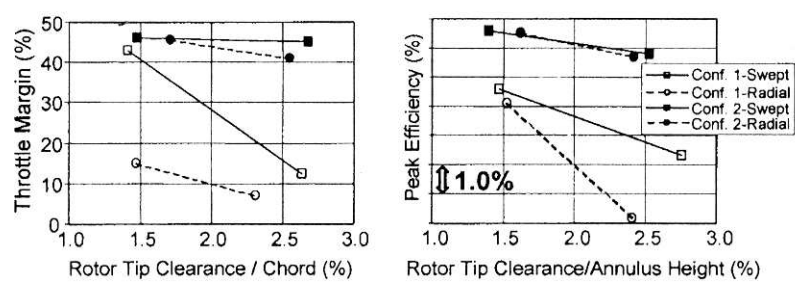


Figure 2.10: Effect of loading on clearance gap sensitivity. (Configuration 1 is highly loaded and Configuration 2 is conventionally loaded.) Taken from McNulty [68].

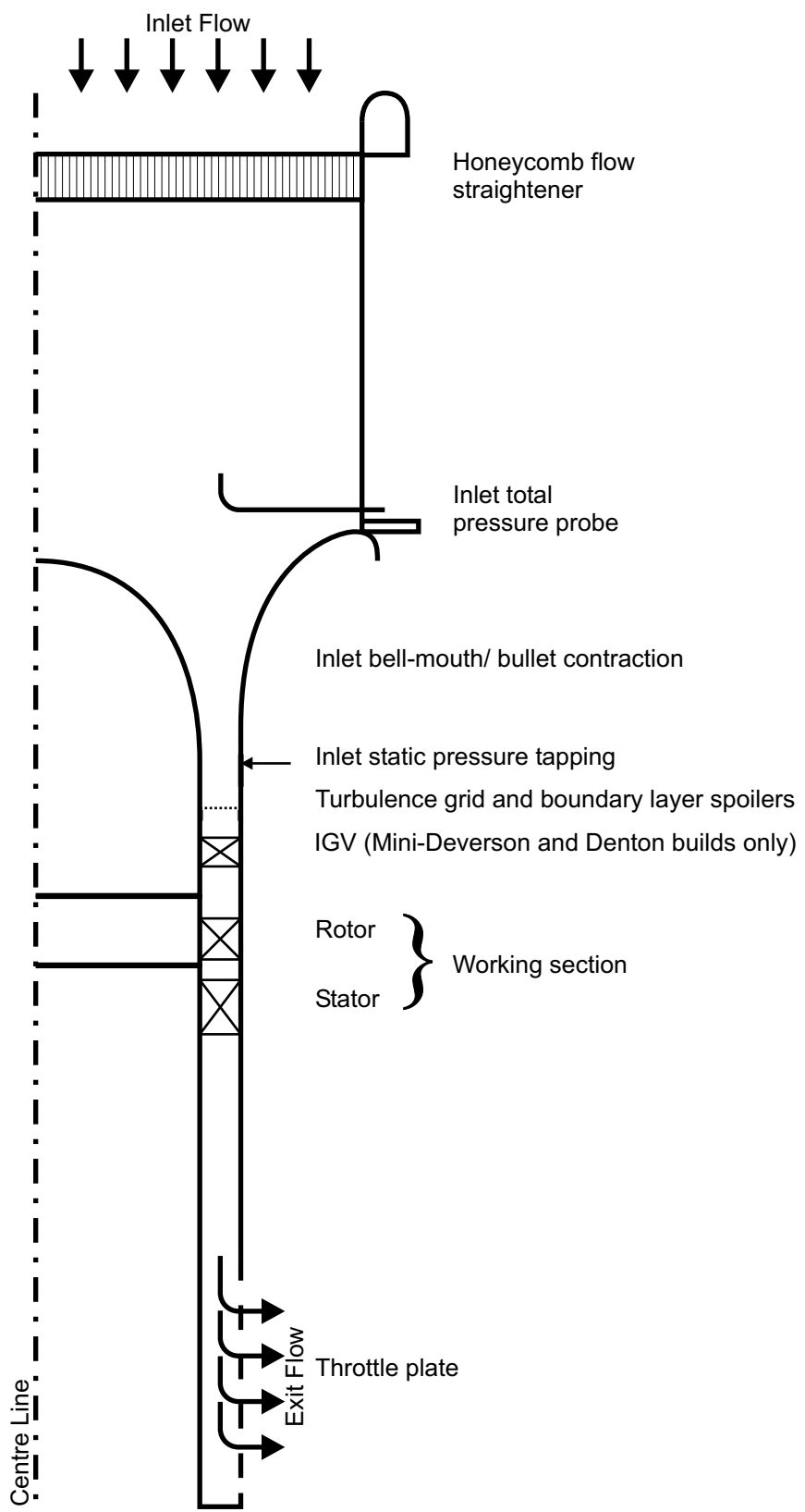


Figure 3.1: Schematic diagram of the Highly Loaded Research Compressor.

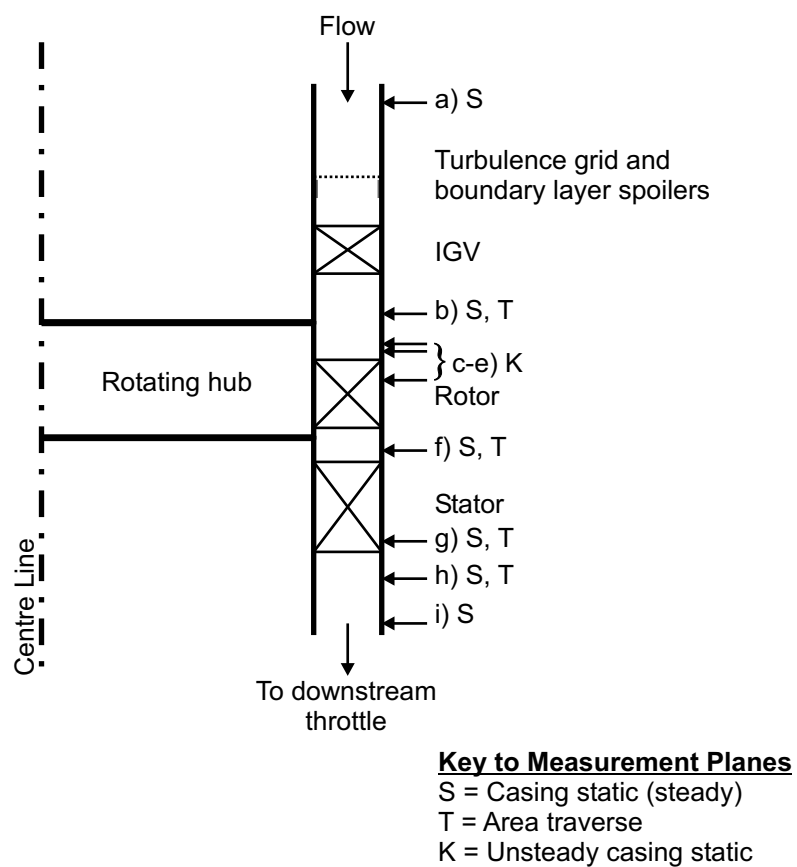
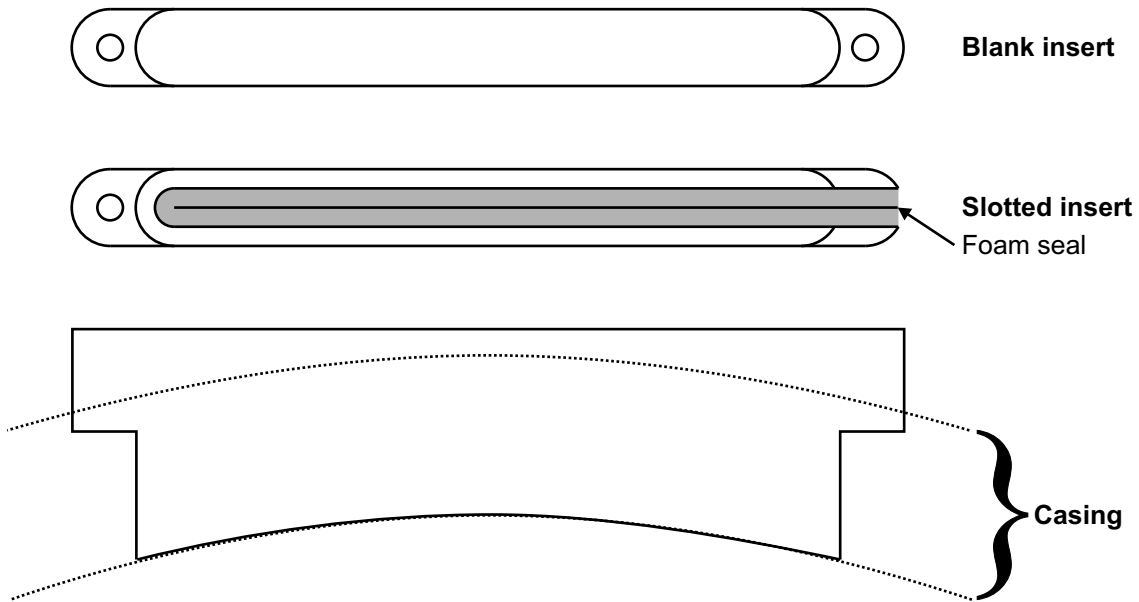


Figure 3.2: Working section detail. Key measurement planes indicated with “ \leftarrow ”. *N.B.* IGVS only present for Mini-Deverson and Denton builds.

(A) Traverse slot detail



(B) Traverse slot in situ

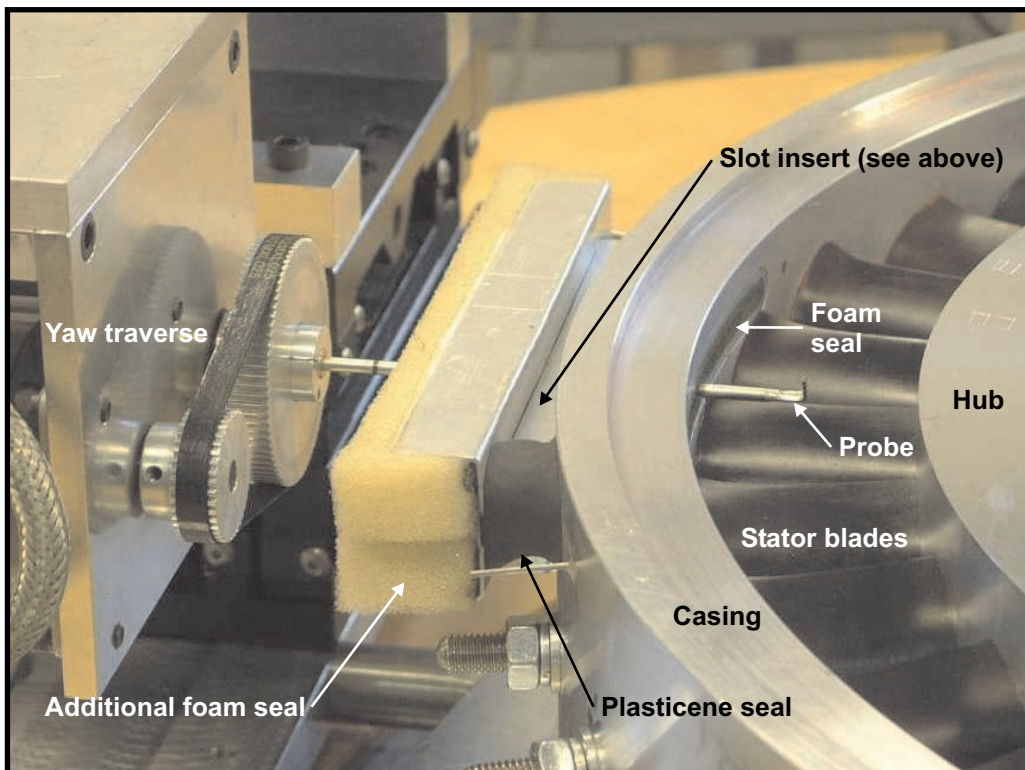


Figure 3.3: Traverse slot detail.

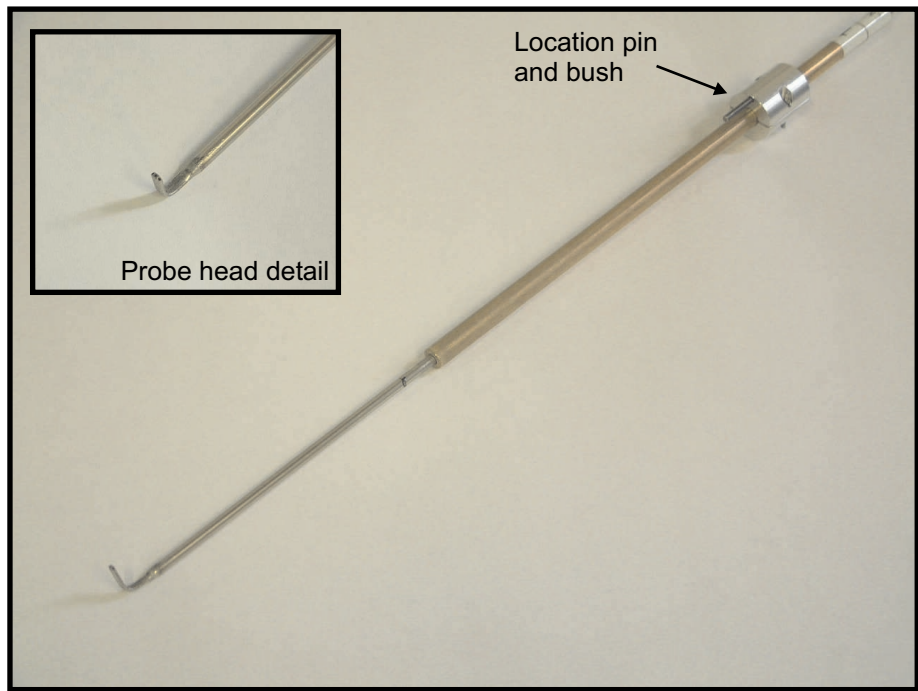


Figure 3.4: Photograph of the three-hole probe used.

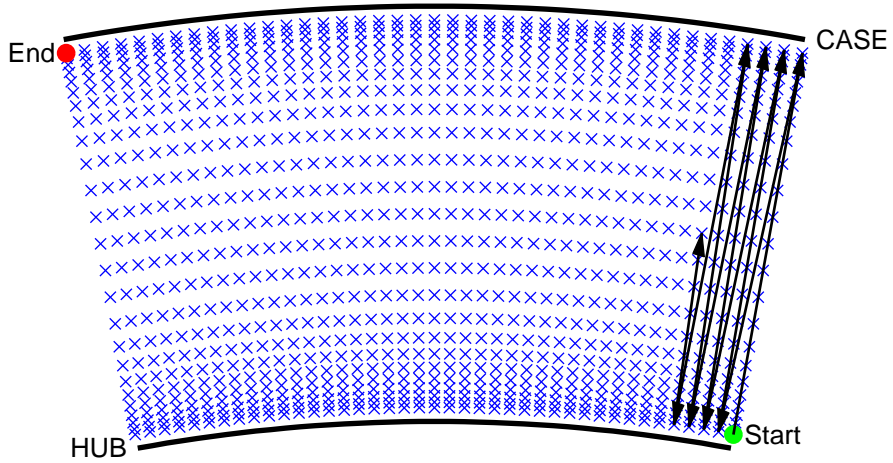
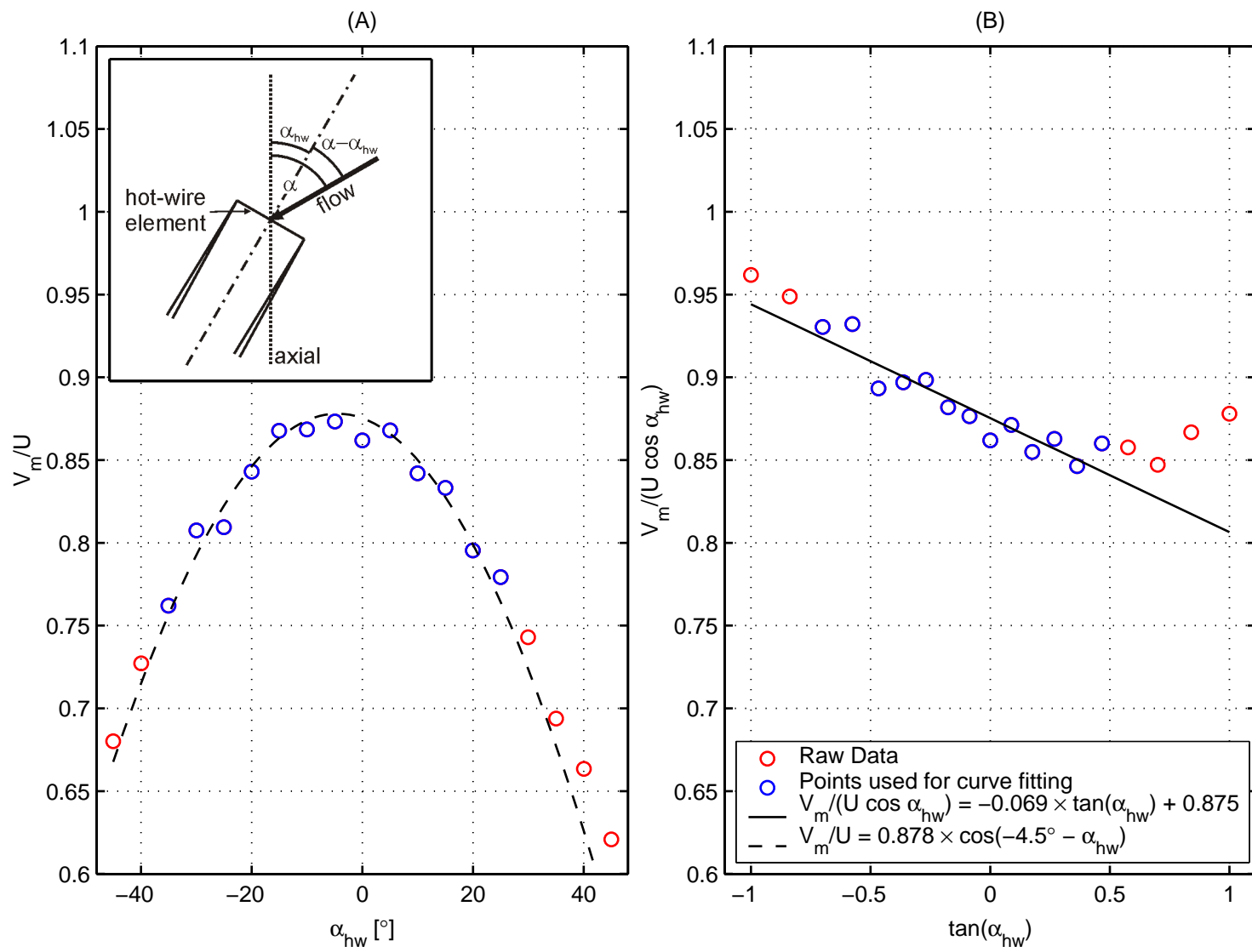


Figure 3.5: Stator exit traverse grid (25×41 points). Probe route illustrated by black arrows.

Figure 3.6: Illustrated example of the determination of flow angle with a single element hot-wire.



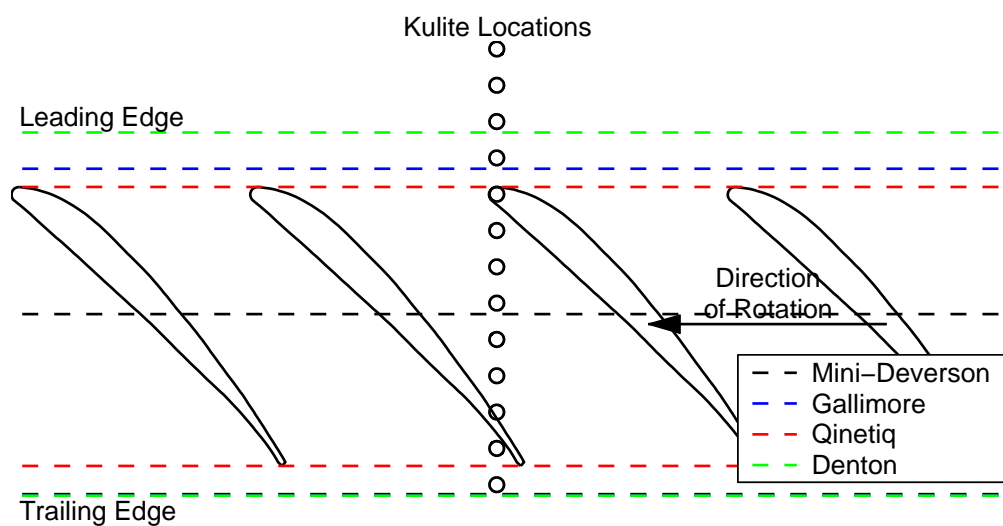


Figure 3.7: Overtip Kulite locations.

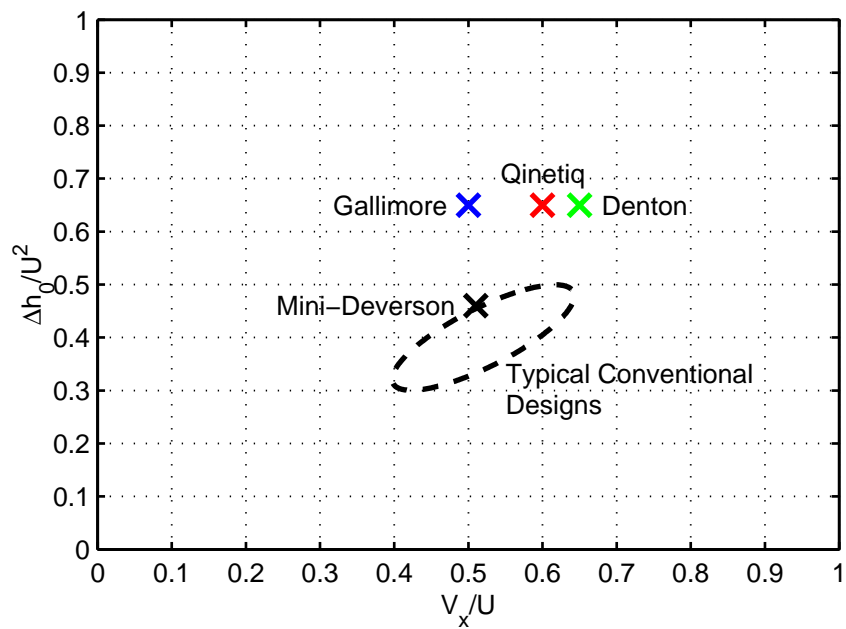


Figure 4.1: Smith Chart illustrating the design points of the four designs tested.

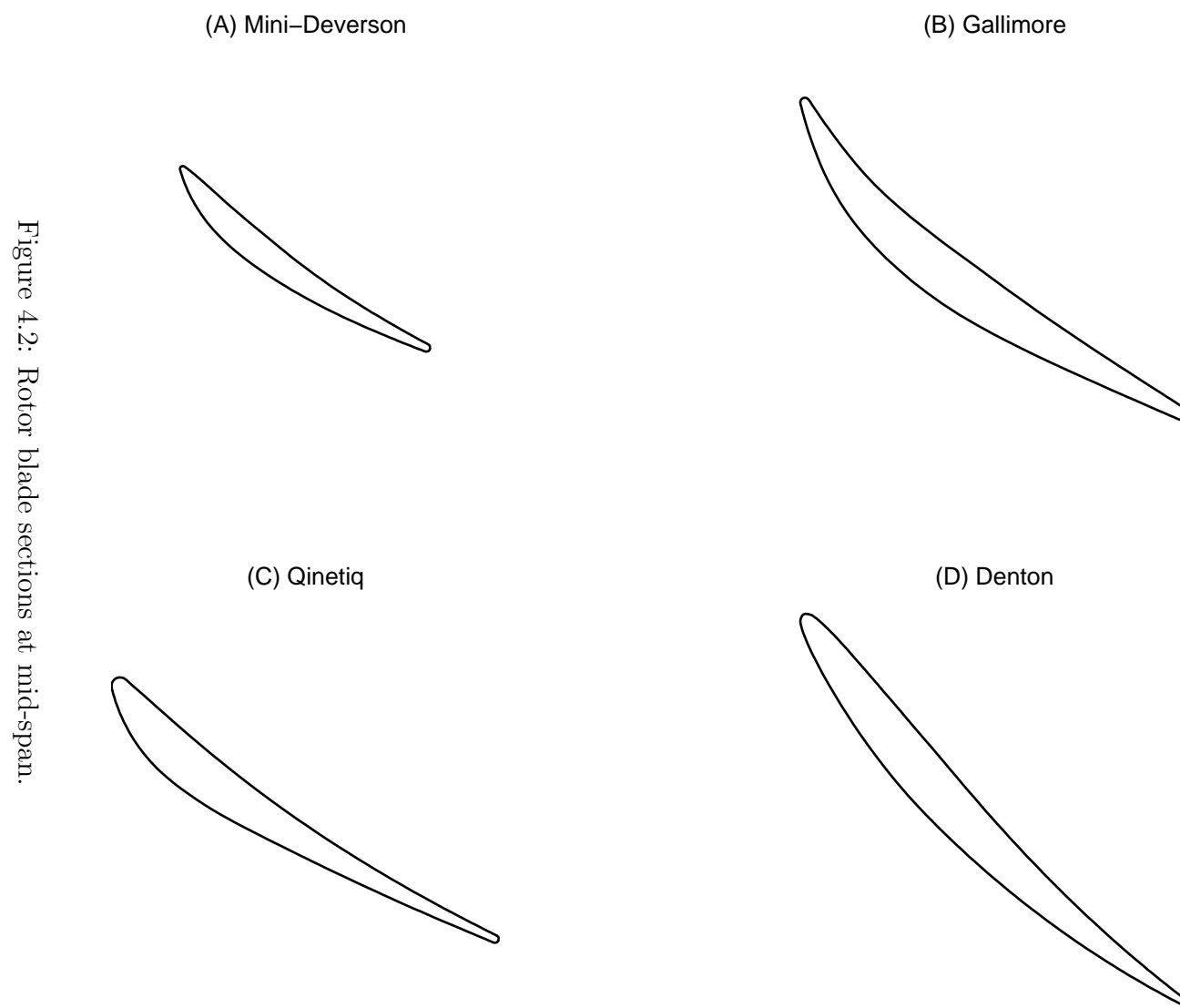
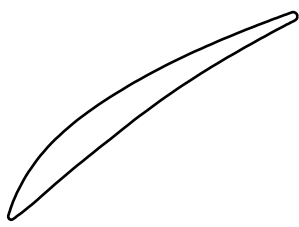
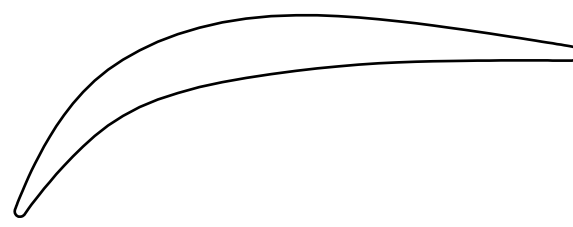


Figure 4.3: Stator blade sections at mid-span.

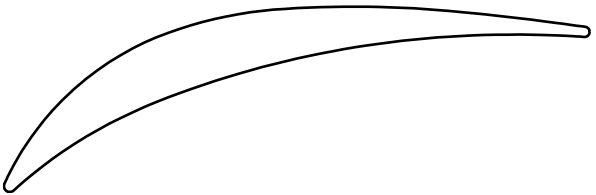
(A) Mini-Deverson



(B) Gallimore



(C) Qinetiq



(D) Denton



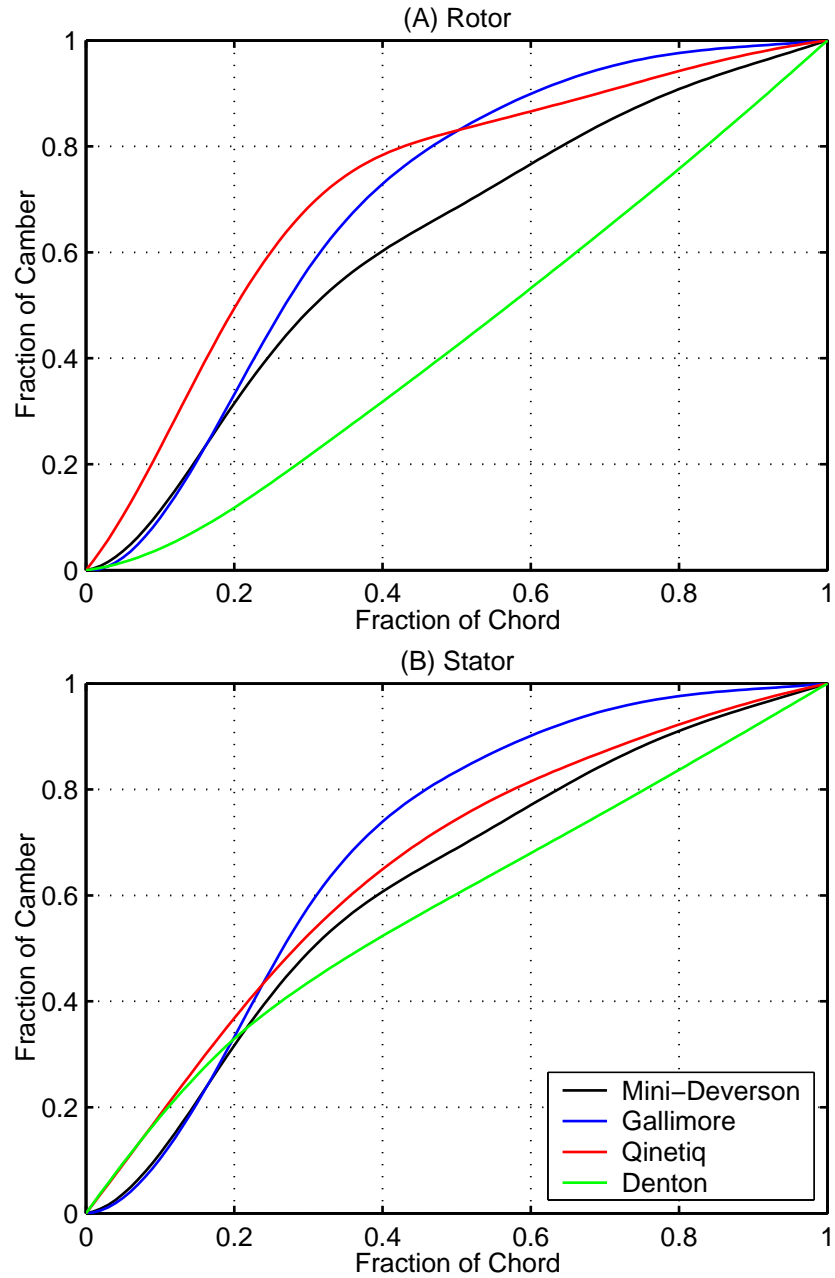


Figure 4.4: (A) Rotor and (B) stator mid-span camber distributions. (N.B. Qinetiq design intent shown.)

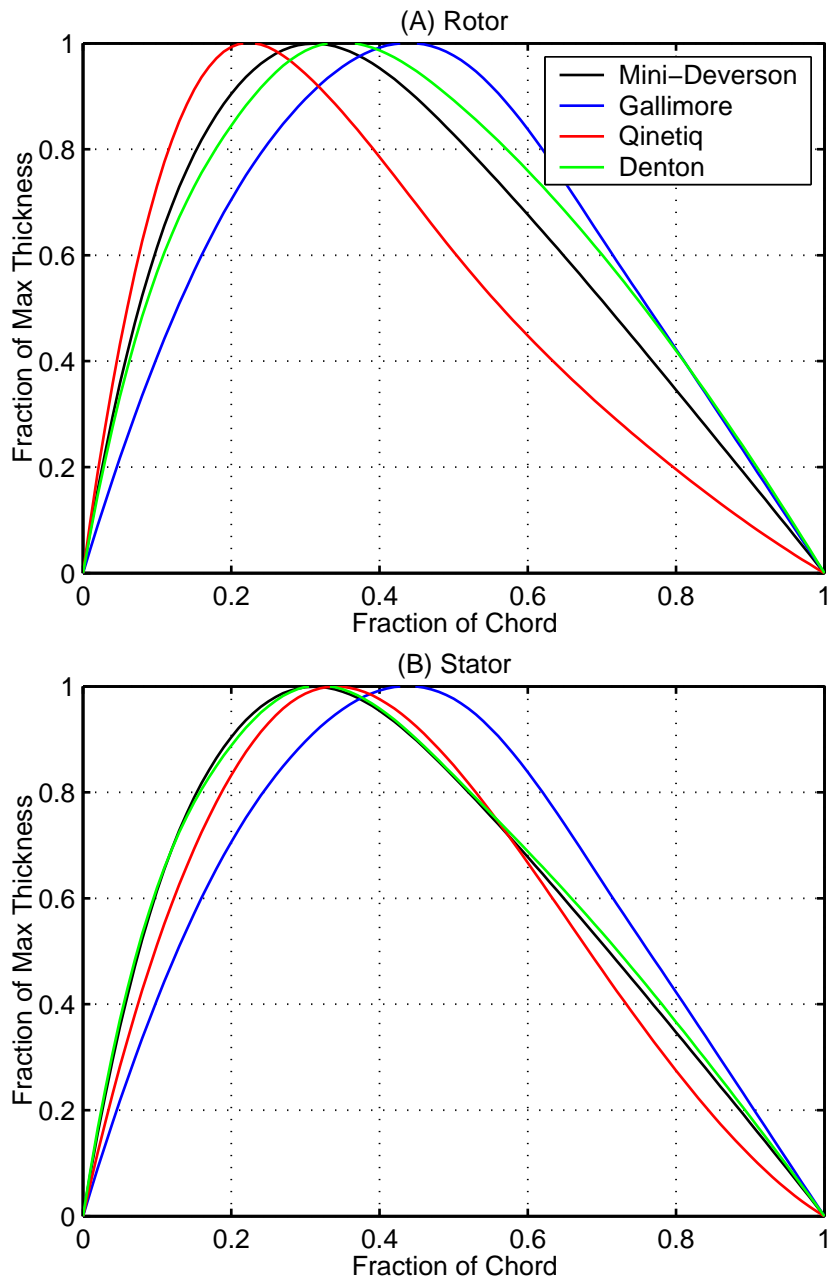


Figure 4.5: (A) Rotor and (B) stator mid-span thickness distributions. (N.B. Qinetiq design intent shown.)

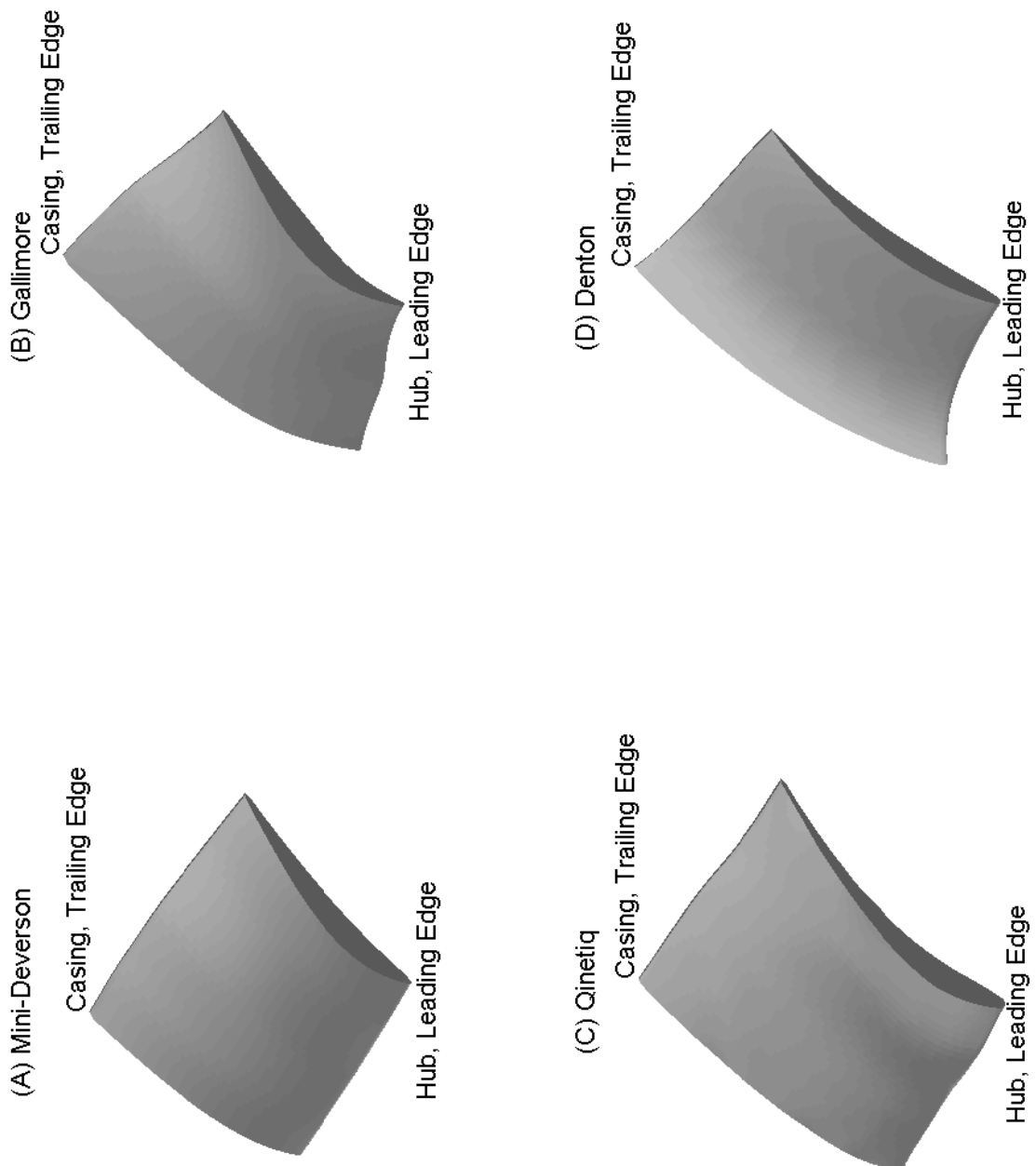


Figure 4.6: Visualisation of the four rotors tested.

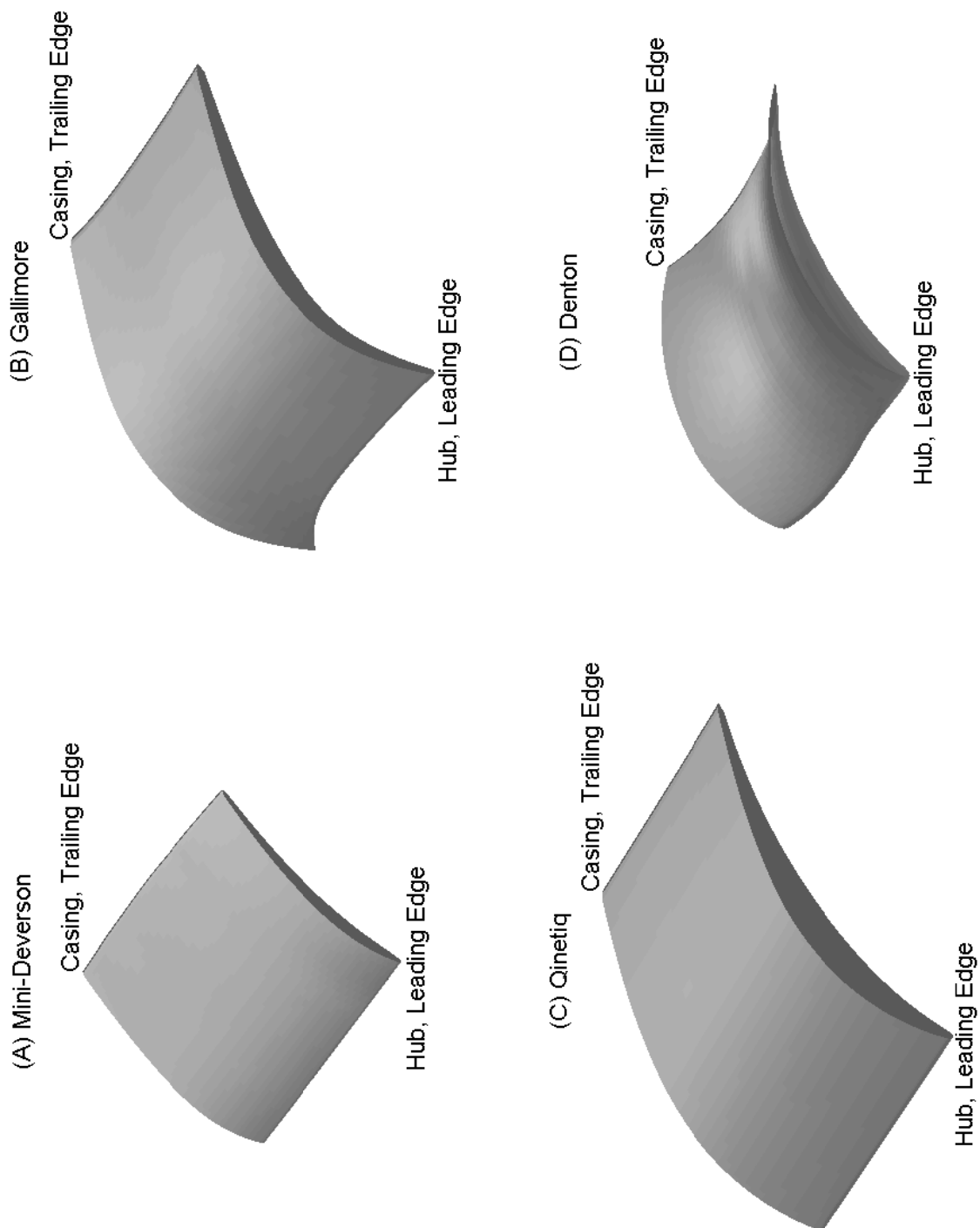


Figure 4.7: Visualisation of the four stators tested.

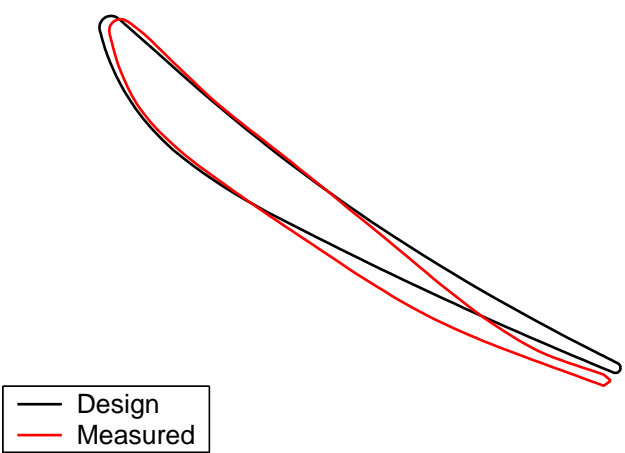
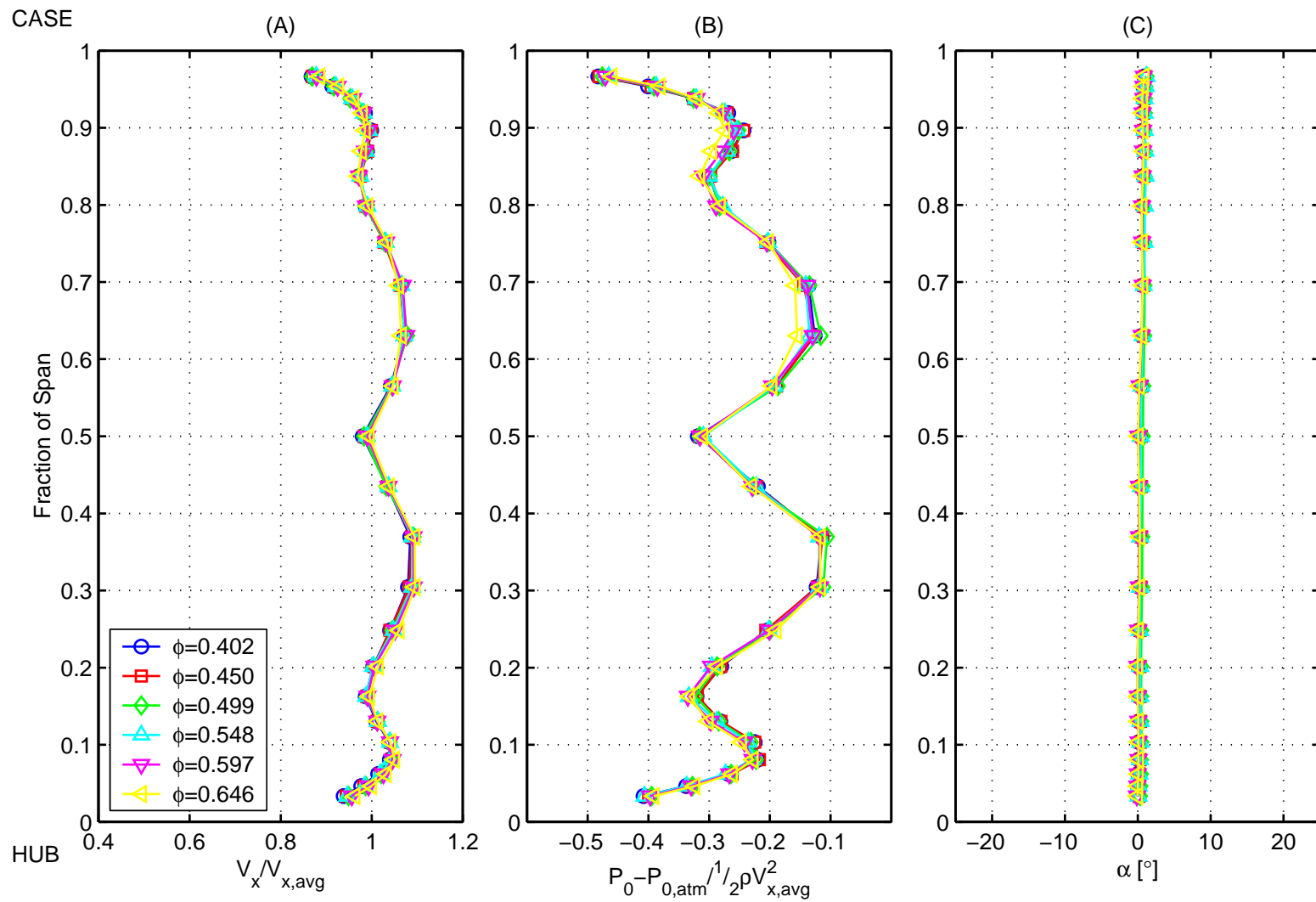


Figure 4.8: Comparison of the design and measured mid-span section of the Qinetiq rotor.

Figure 5.2: Inlet conditions to the Gallimore stage.



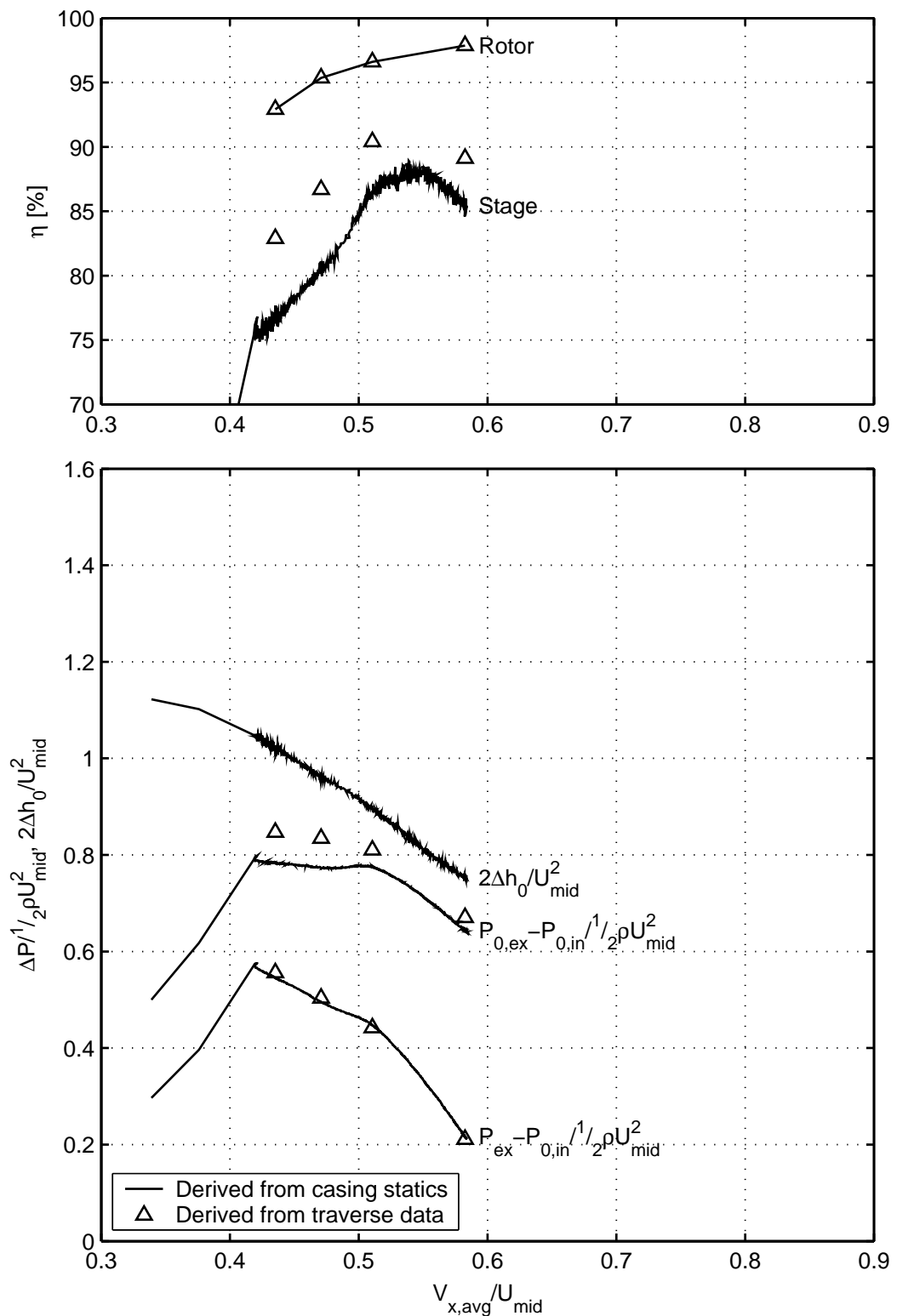


Figure 5.3: Pressure rise, torque and efficiency characteristics of the **Mini-Deverson** stage.

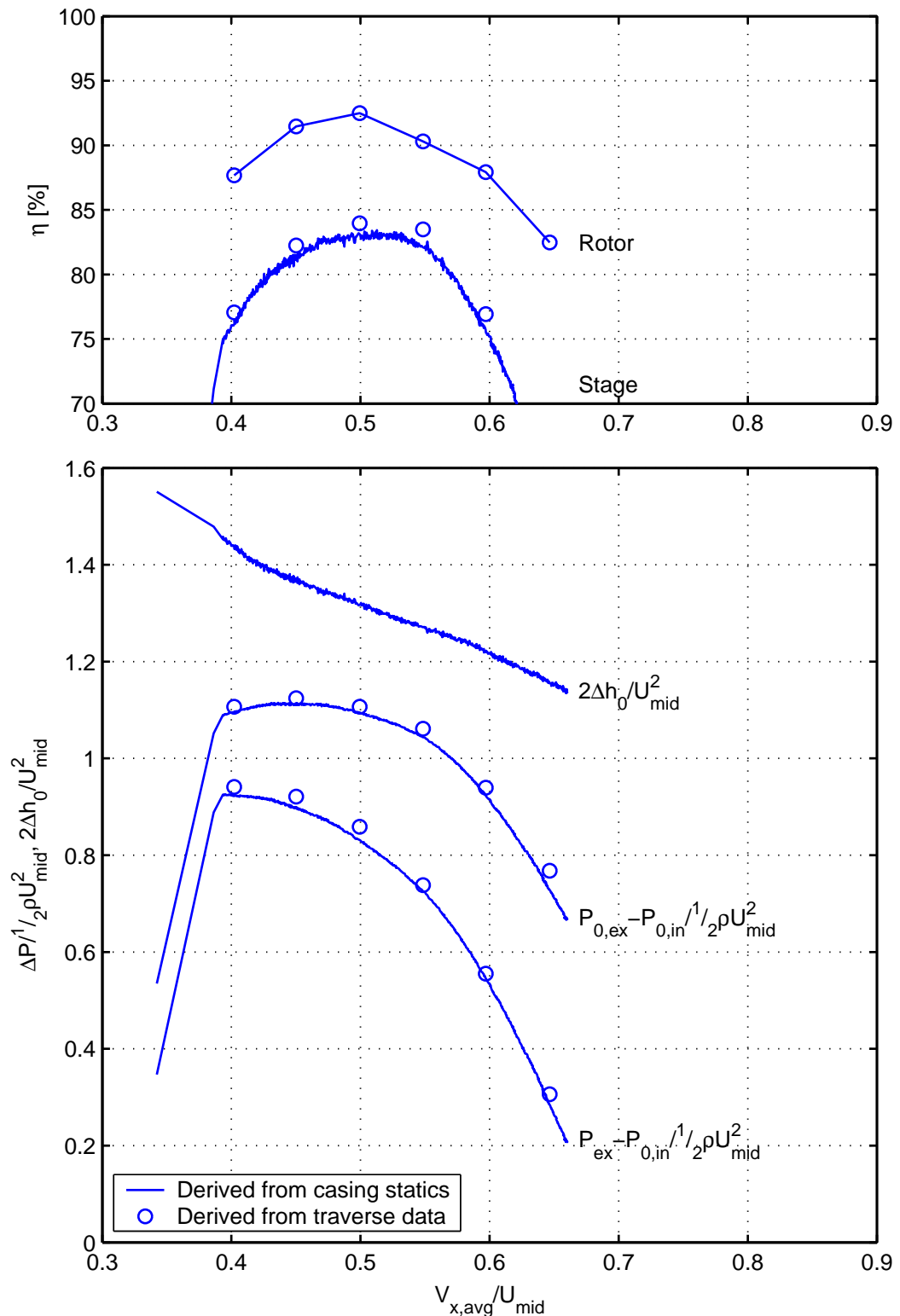


Figure 5.4: Pressure rise, torque and efficiency characteristics of the **Gallimore** stage.

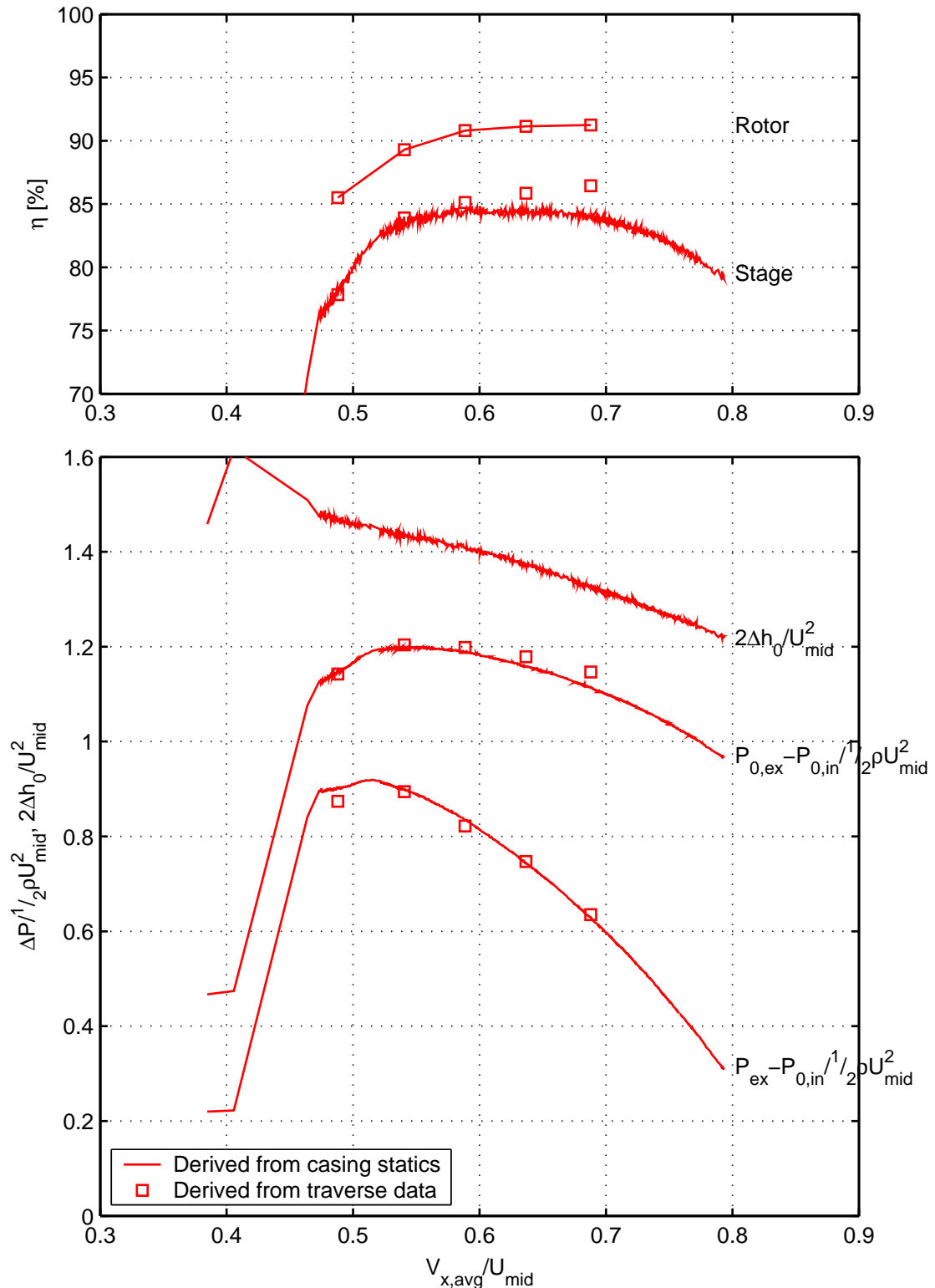


Figure 5.5: Pressure rise, torque and efficiency characteristics of the **Qinetiq** stage.

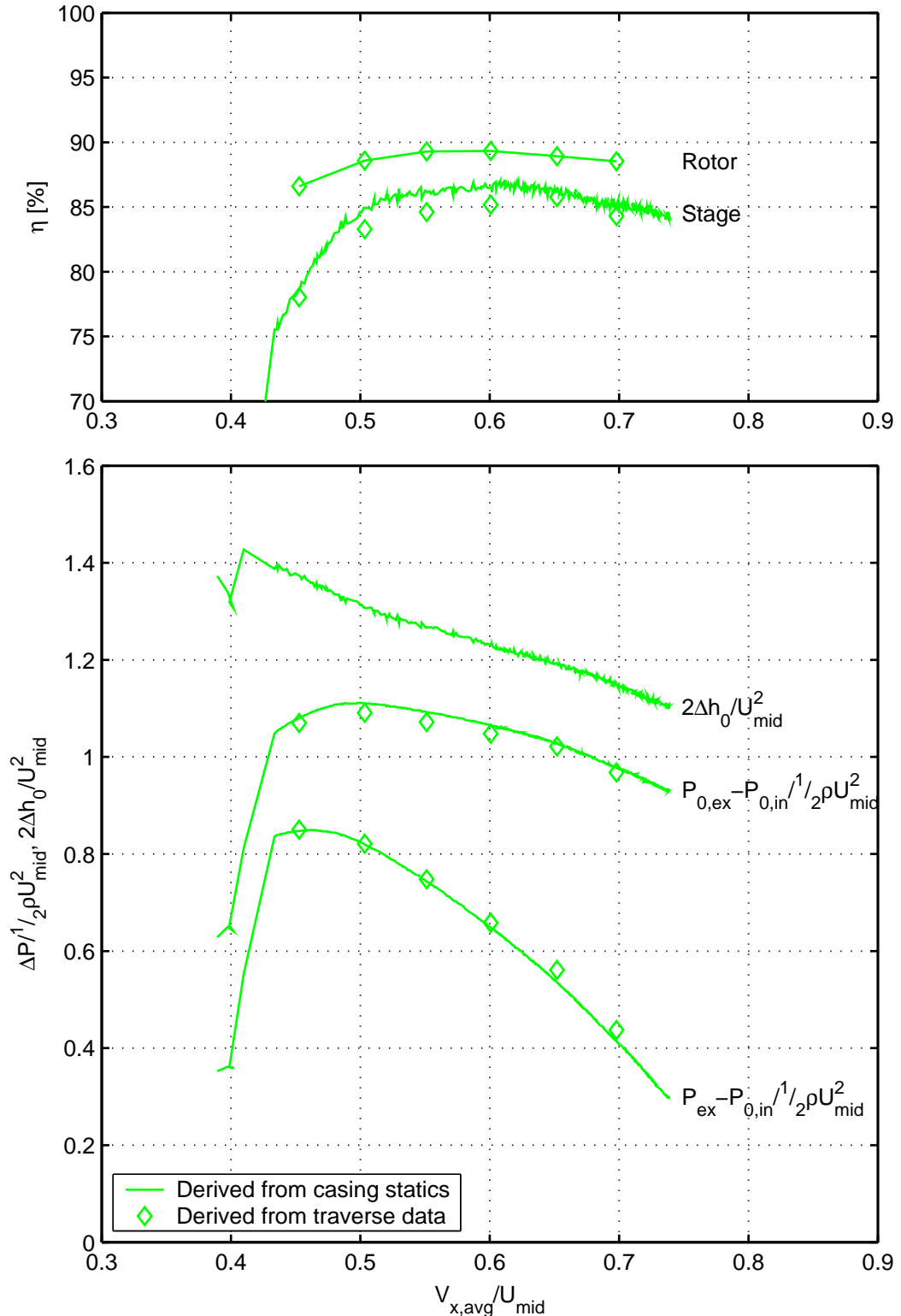


Figure 5.6: Pressure rise, torque and efficiency characteristics of the **Denton** stage.

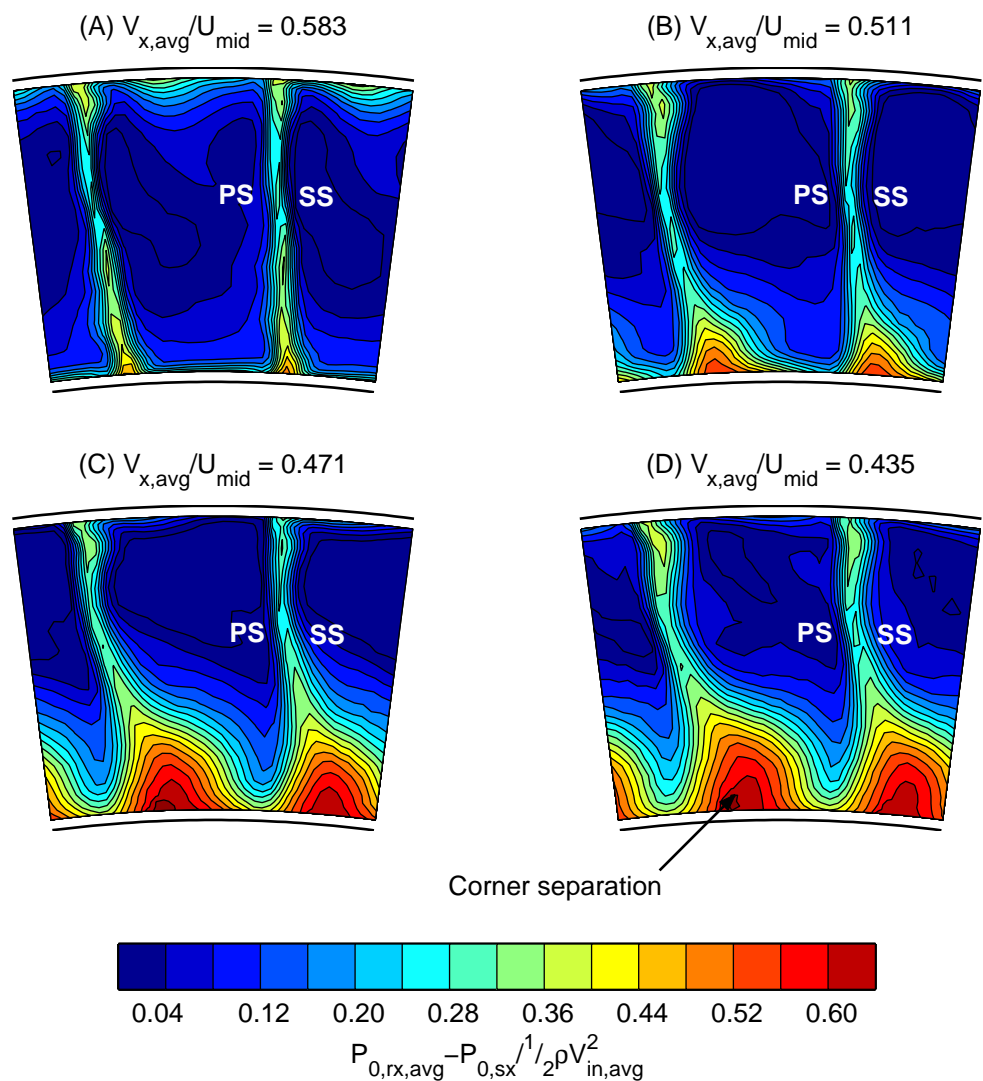


Figure 5.7: Stagnation pressure measured downstream of the **Mini-Deverson** stator.

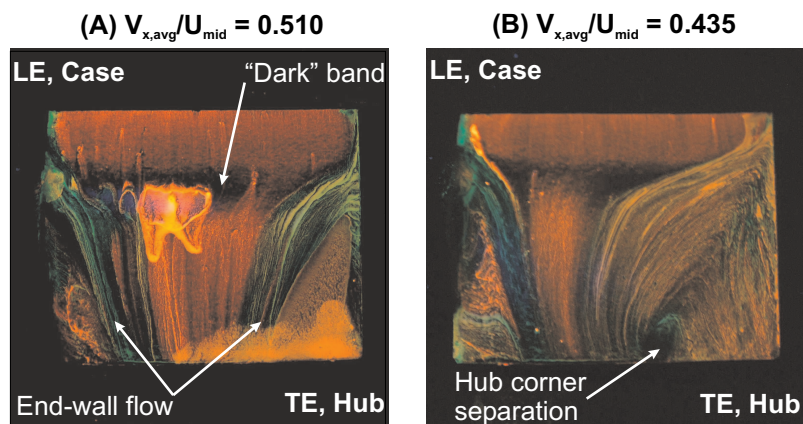


Figure 5.8: Oil and dye flow visualisation on the **Mini-Deverson** stator suction surface. Red and green paint initially applied to suction surface and end-walls respectively.

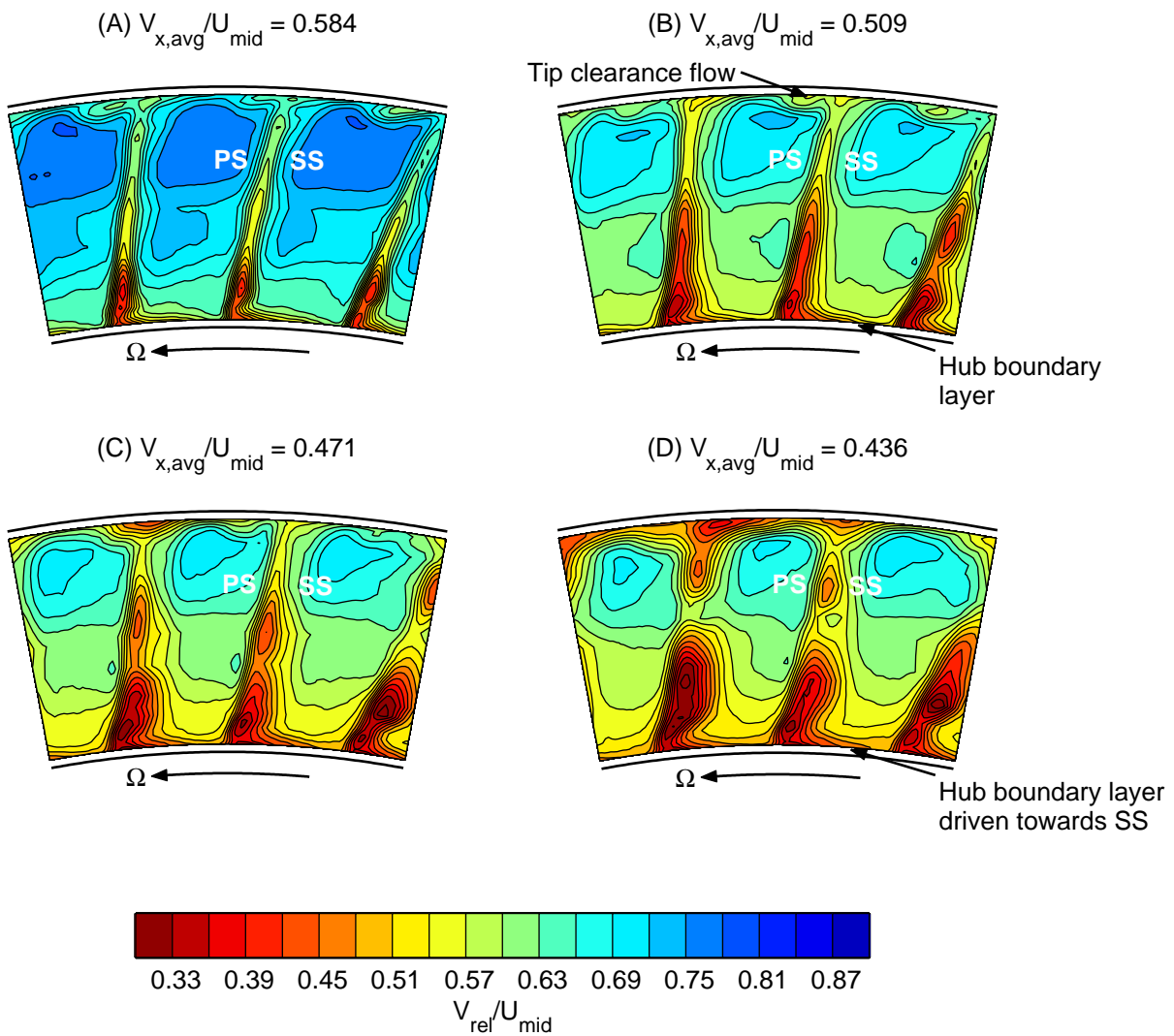


Figure 5.9: Relative velocity downstream of the **Mini-Deverson** rotor.

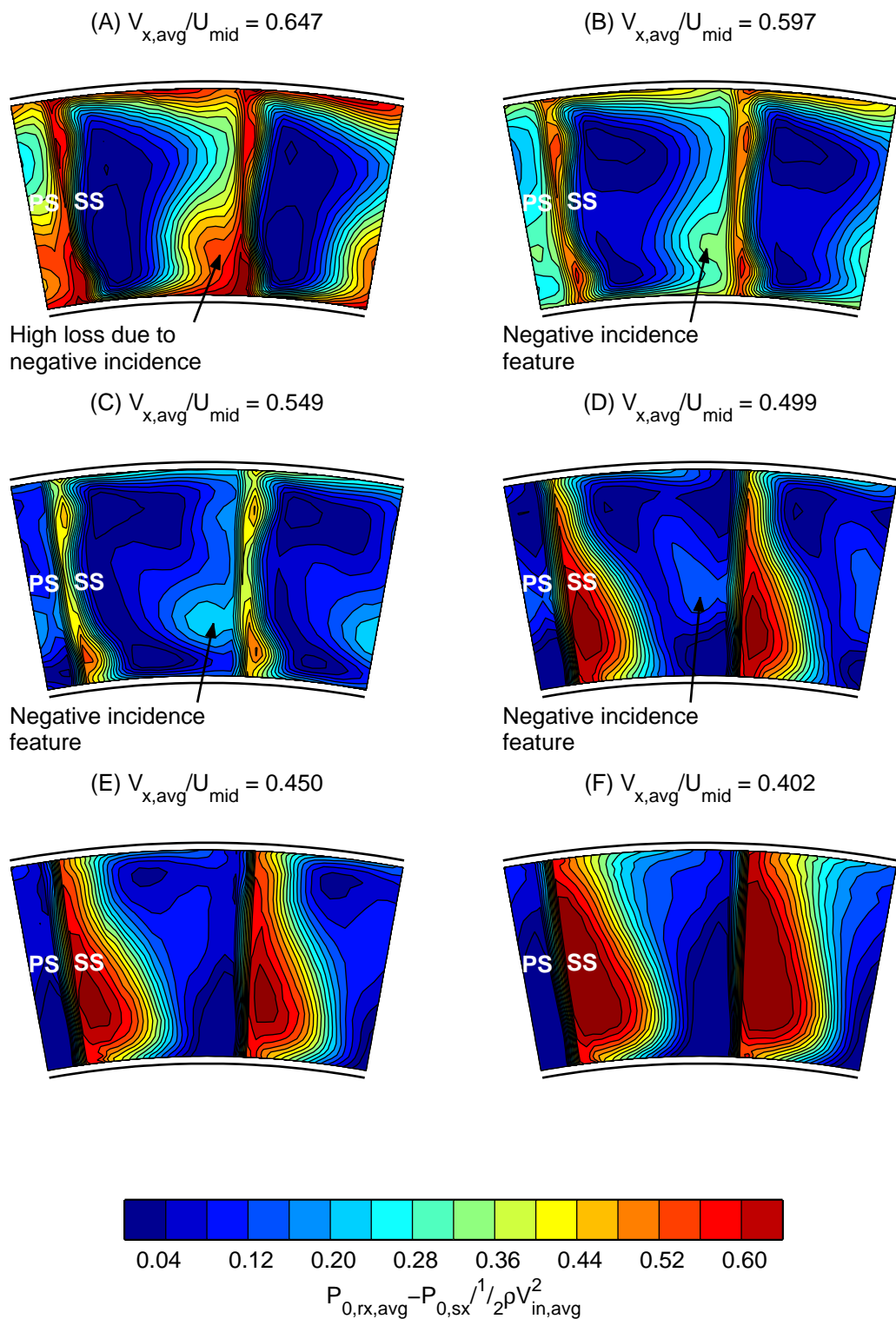


Figure 5.10: Stagnation pressure measured downstream of the **Gallimore** stator.

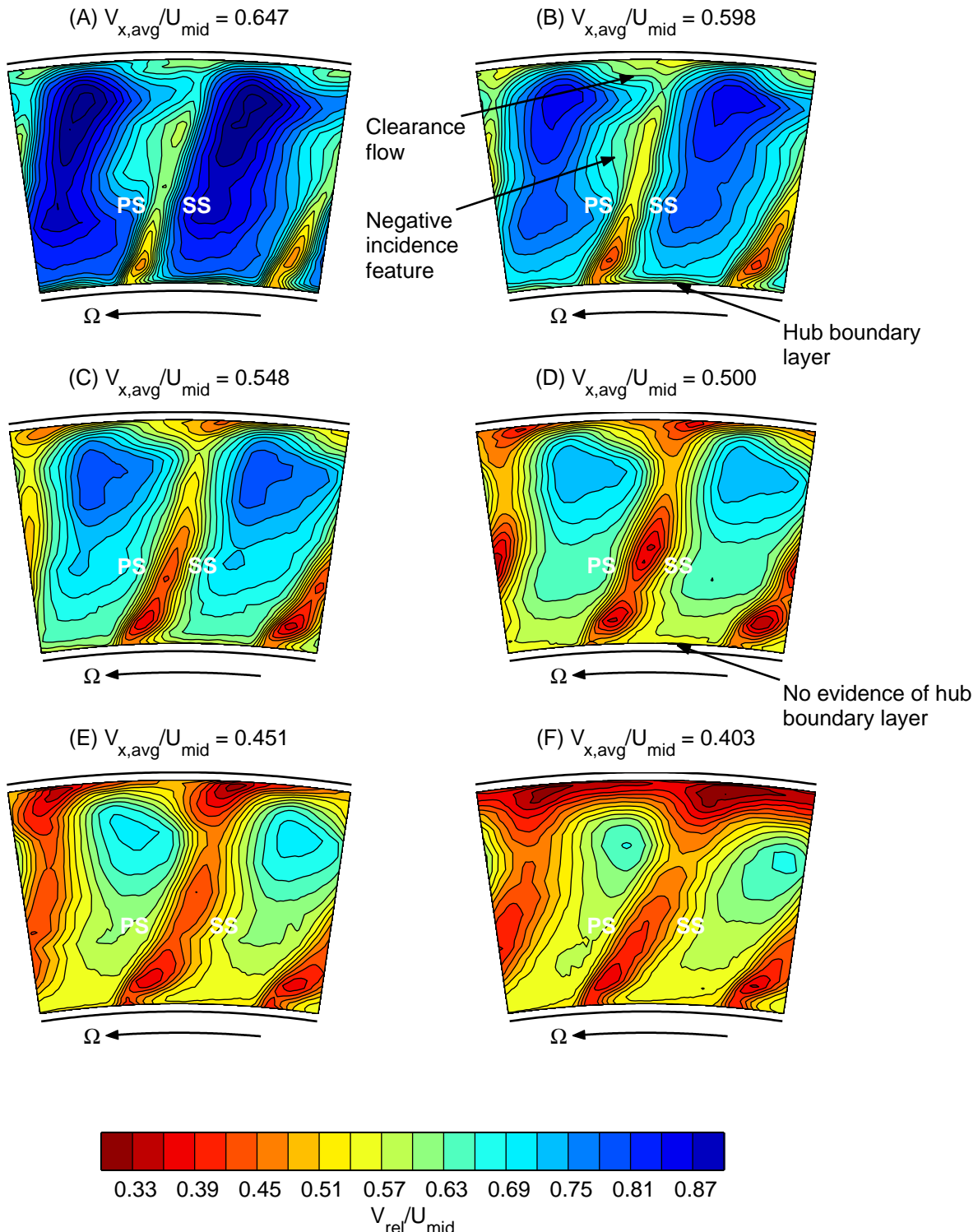


Figure 5.11: Relative velocity downstream of the **Gallimore** rotor.

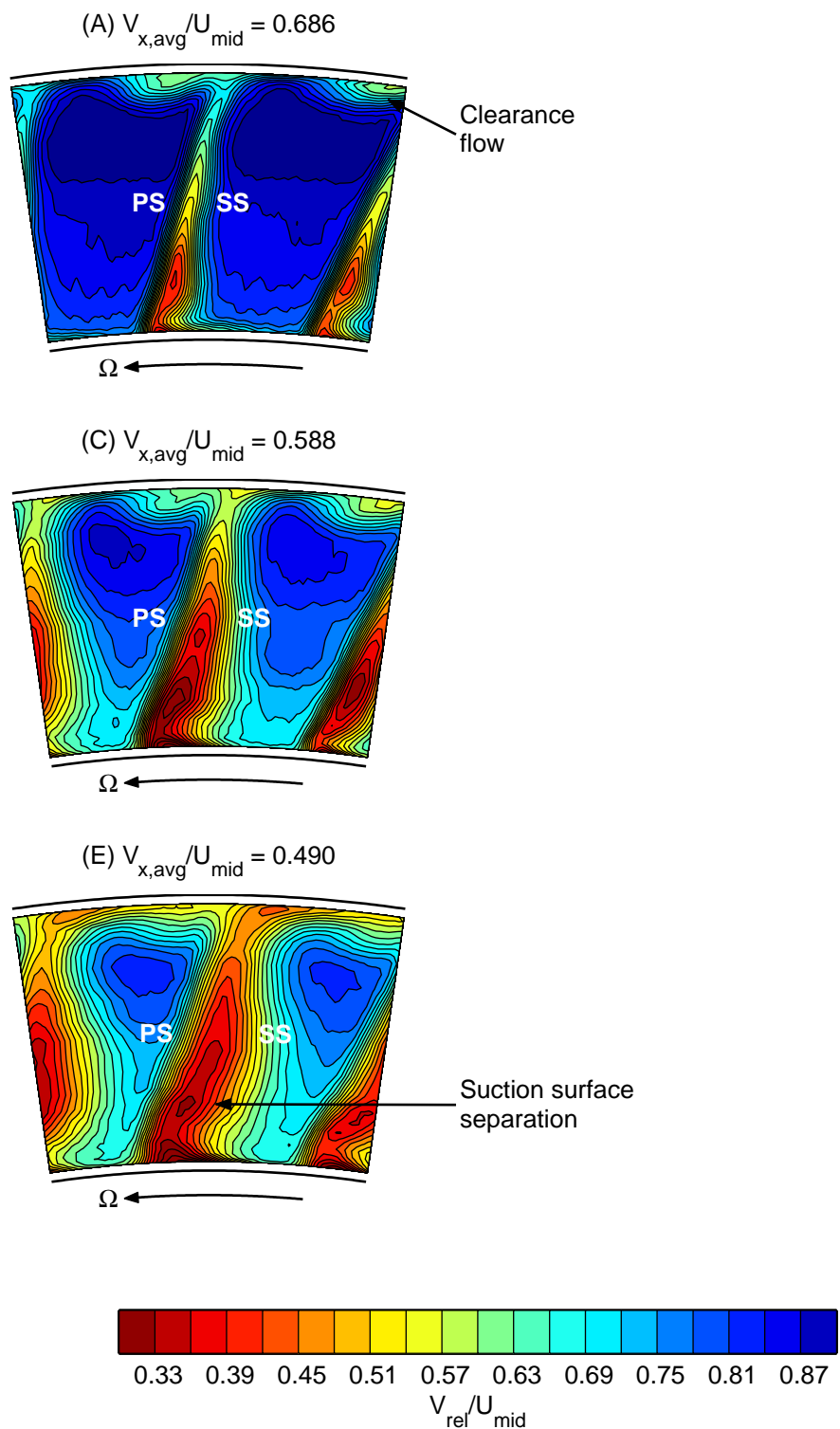


Figure 5.12: Relative velocity downstream of the **Qinetiq** rotor.

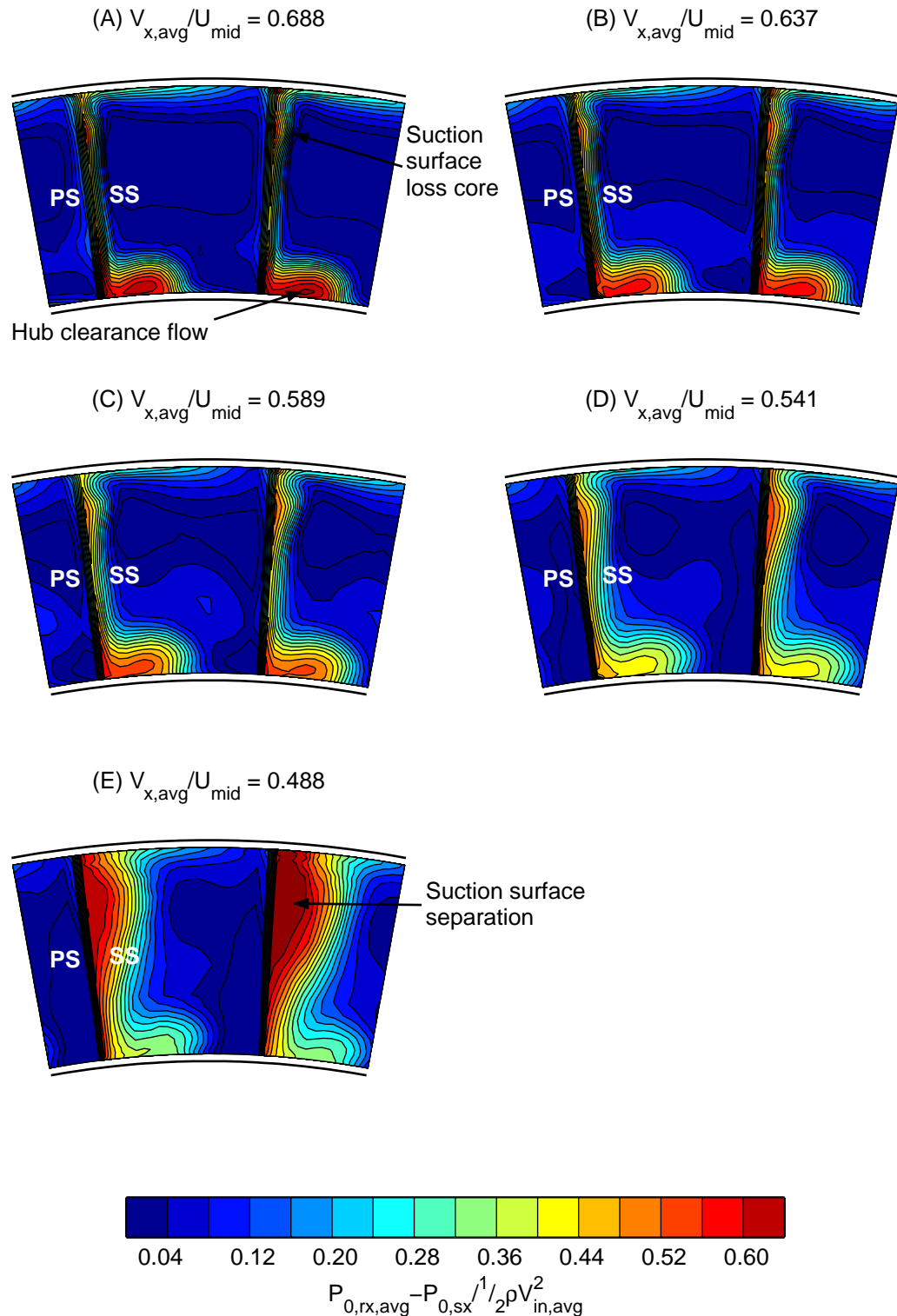


Figure 5.13: Stagnation pressure measured downstream of the **Qinetiq** stator.

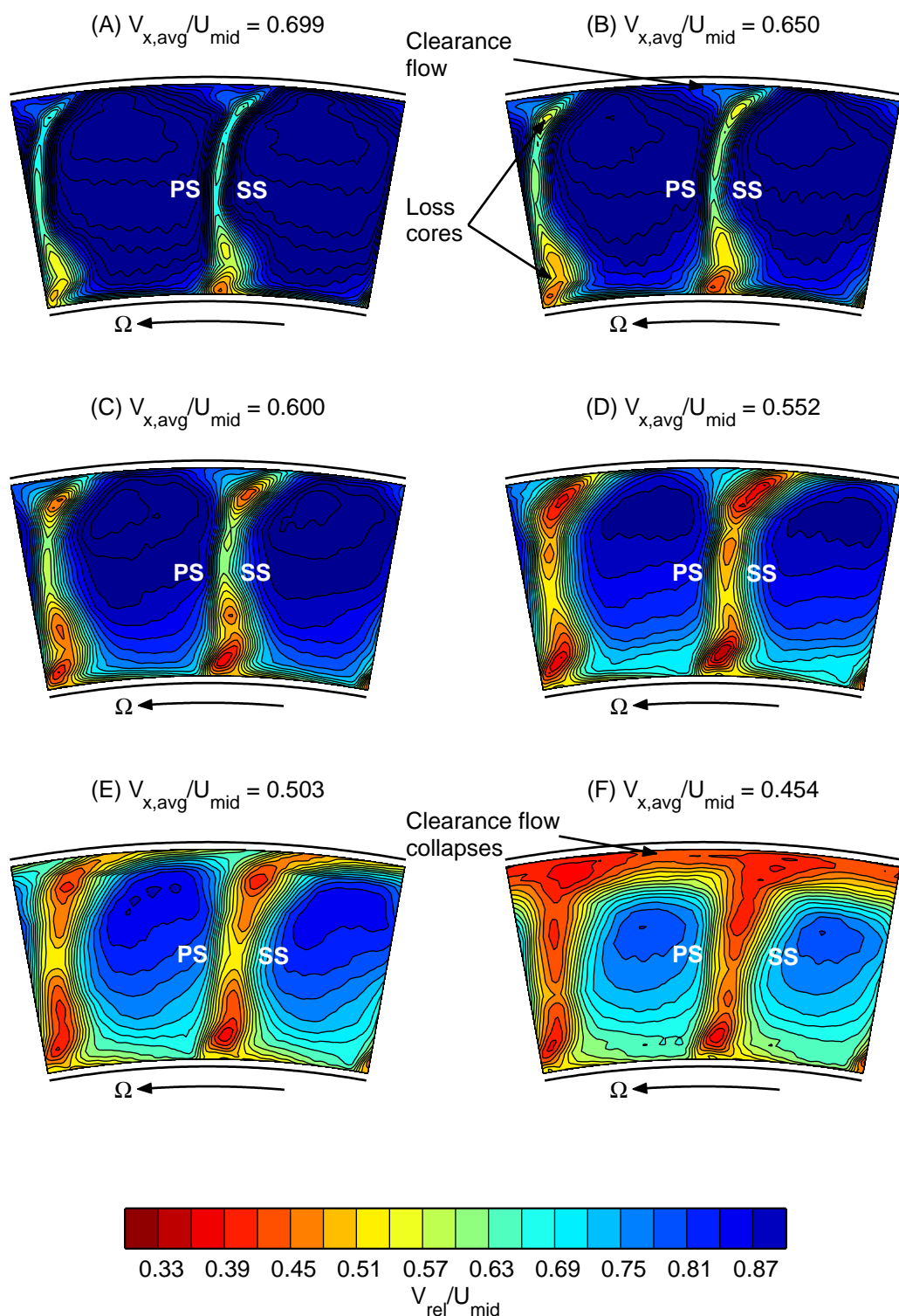


Figure 5.14: Relative velocity downstream of the **Denton** rotor.

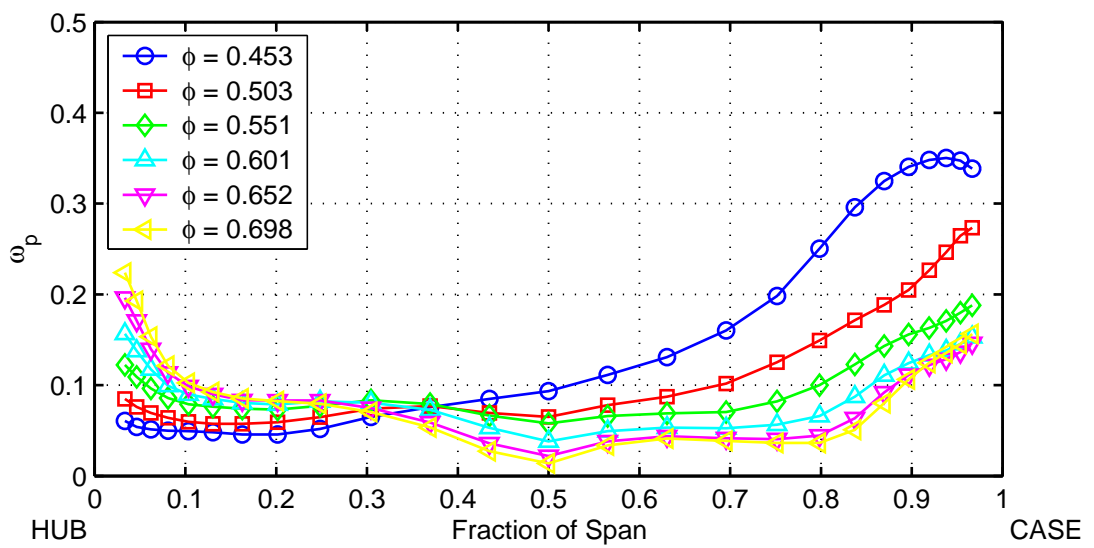


Figure 5.15: **Denton** rotor loss coefficient.

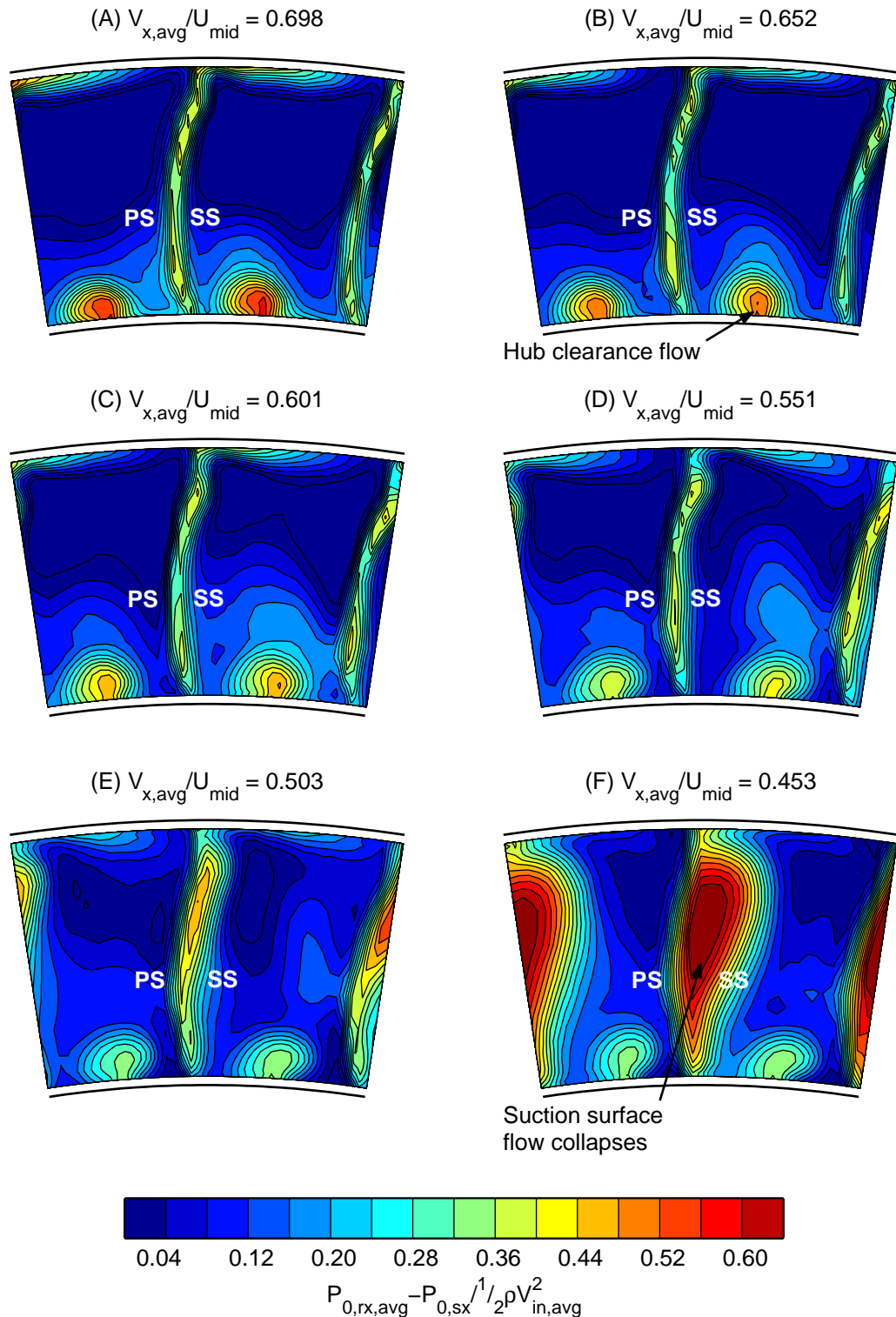


Figure 5.16: Stagnation pressure measured downstream of the **Denton** stator.

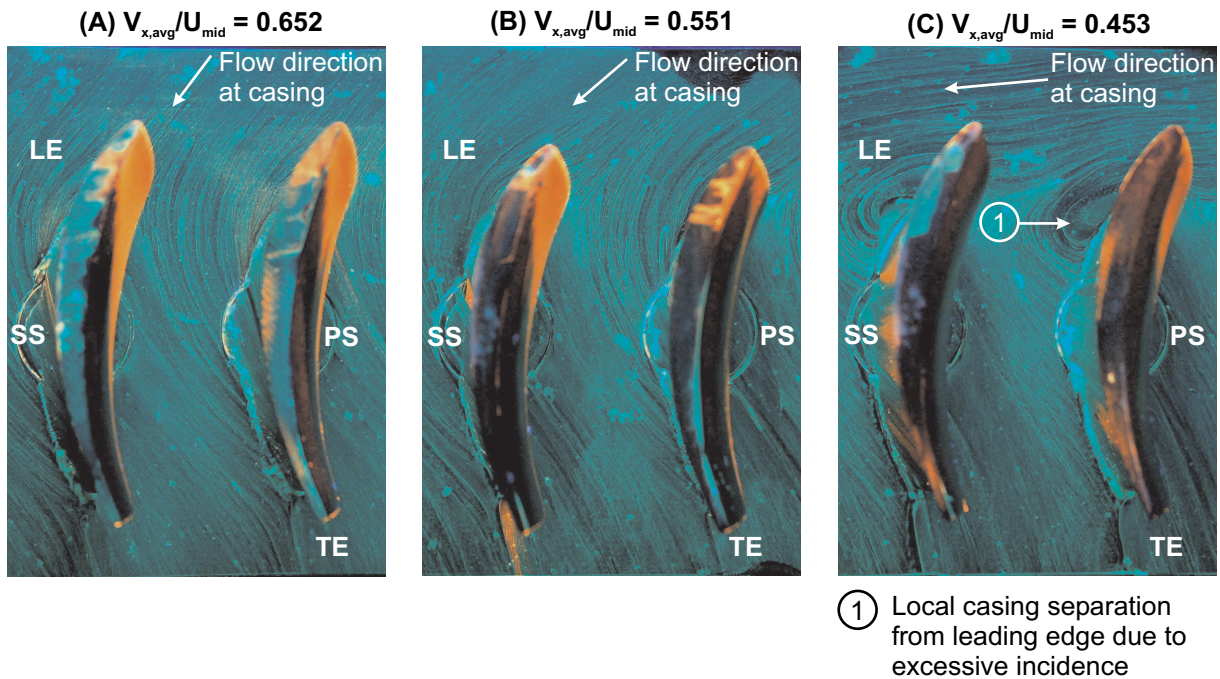


Figure 5.17: Oil and dye flow visualisation on the **Denton** stator; casing view.

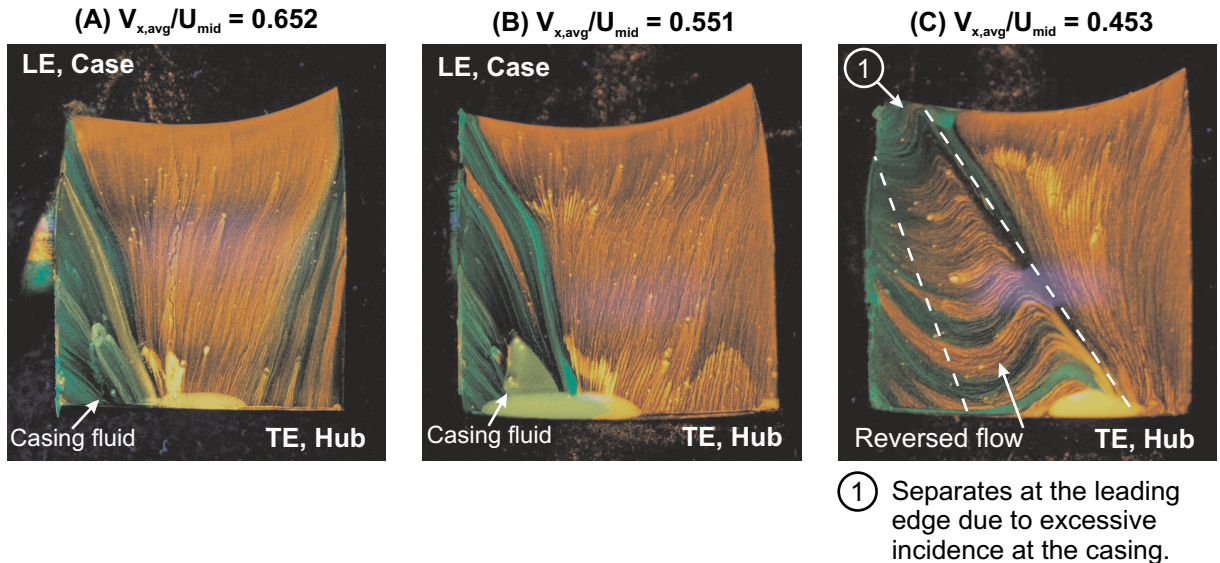


Figure 5.18: Oil and dye flow visualisation on the **Denton** stator suction surface. Red and green paint initially applied to suction surface and end-walls respectively.

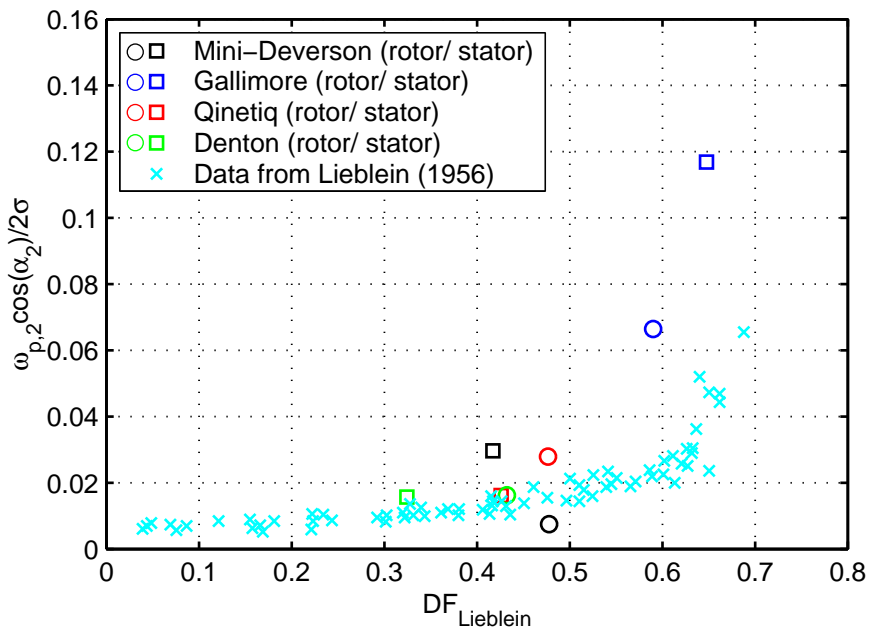


Figure 5.19: Lieblein loss parameter versus diffusion factor. Open circles and squares denote rotor and stator values respectively. “ \times ” symbols indicate data taken from Lieblein [63].

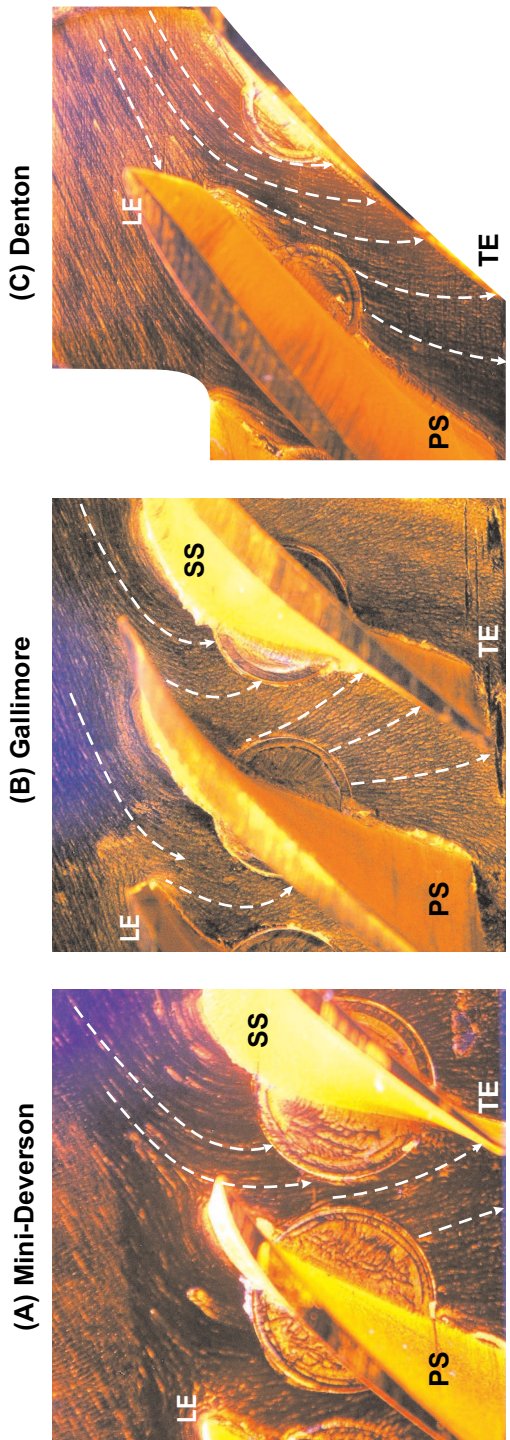


Figure 5.20: Oil and dye flow visualisation performed on the (A) **Mini-Deverson**, (B) **Gallimore** and (C) **Denton** rotor hubs. Dotted lines denote approximate streak lines.

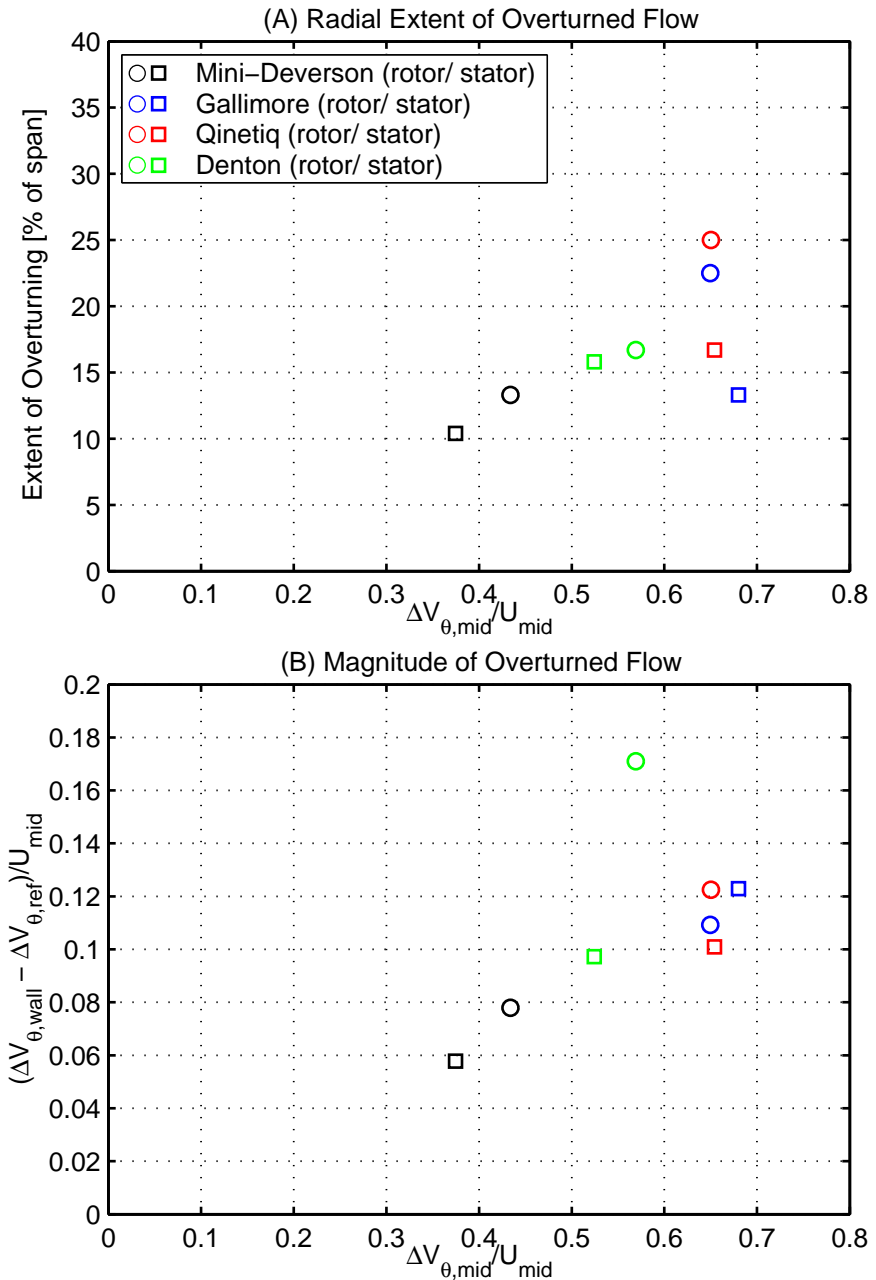


Figure 5.21: Effect of increasing design turning ($\frac{\Delta V_\theta}{U} \approx \frac{\Delta h_0}{U^2}$) on the (A) radial extent and (B) magnitude of the overturned regions at the rotor hub (circles) and stator case (squares).

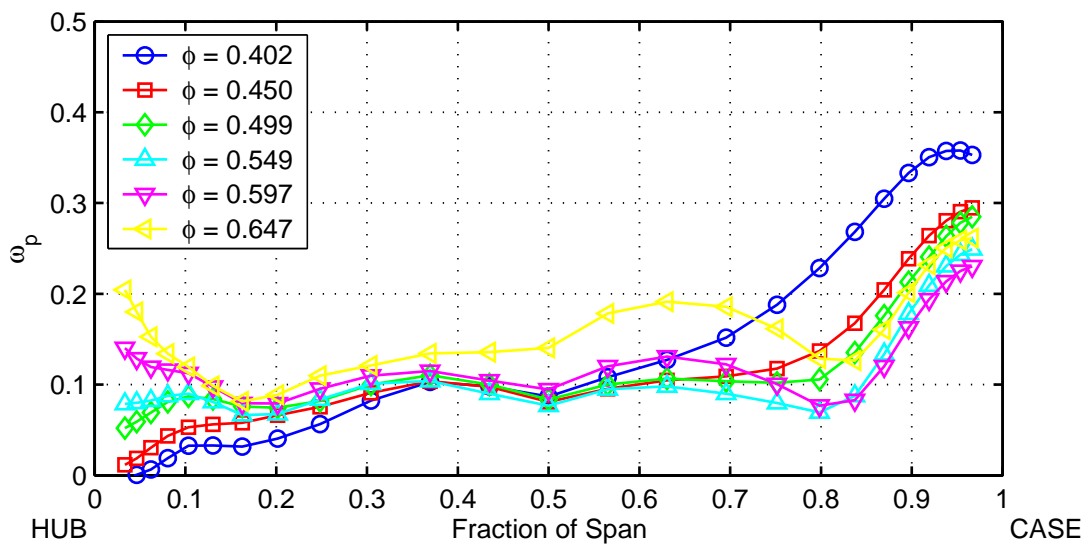


Figure 5.22: **Gallimore** rotor loss coefficient.

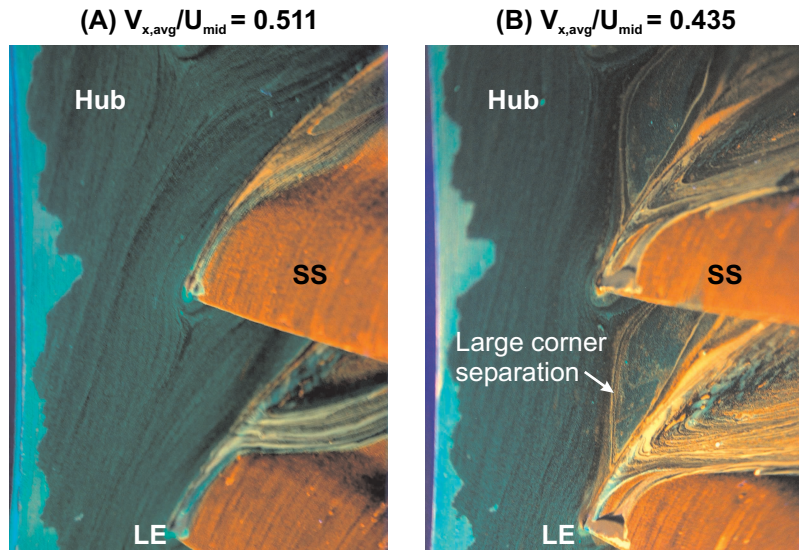


Figure 5.23: Oil and dye flow visualisation on the **Mini-Deverson** the stator; hub and leading edge shown.

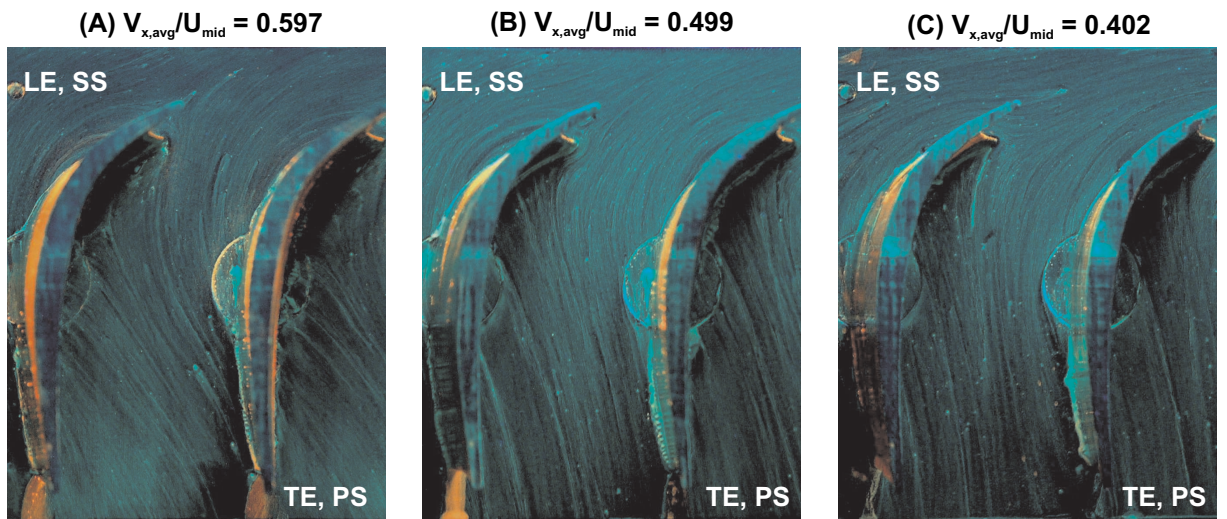


Figure 5.24: Oil and dye flow visualisation on the **Gallimore** stator; casing view. (N.B. Red and green paint initially applied to suction surface and end-walls respectively.)

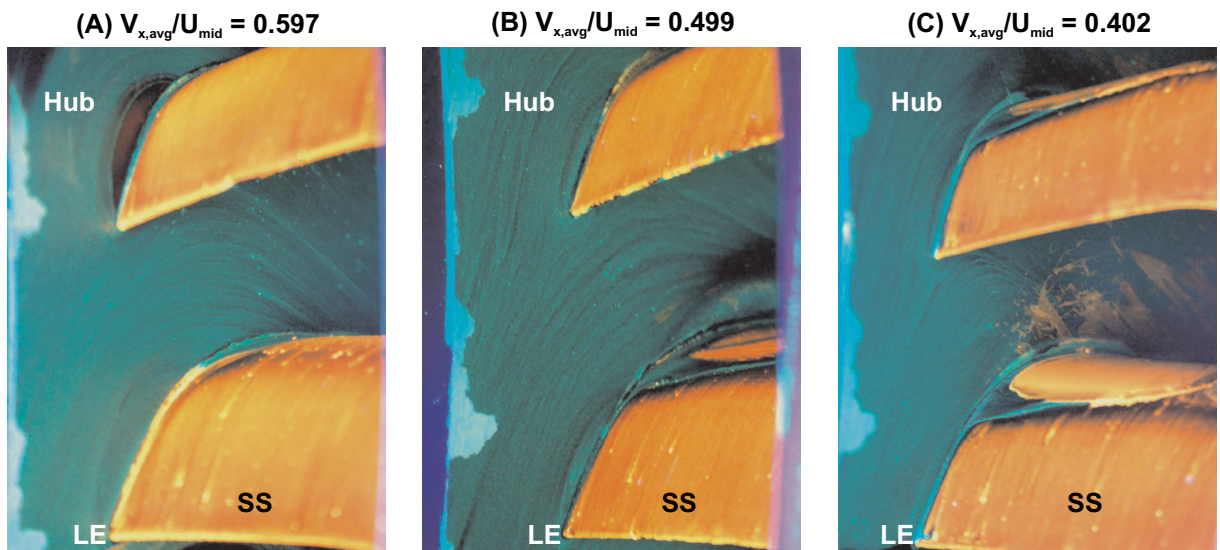


Figure 5.25: Oil and dye flow visualisation on the **Gallimore** the stator; hub and leading edge shown. (N.B. Red and green paint initially applied to suction surface and end-walls respectively.)

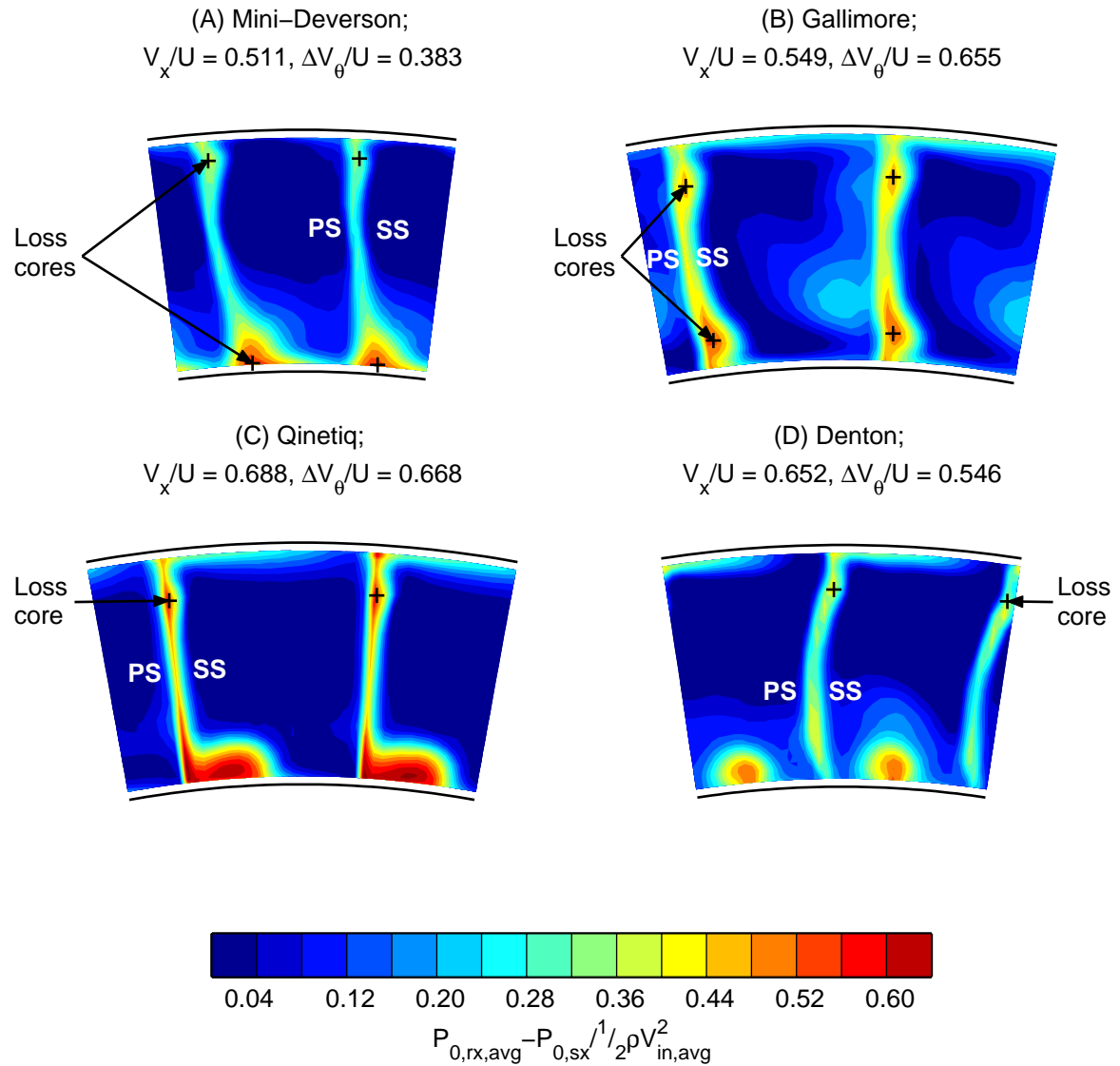


Figure 5.26: Variation in the position of stator loss cores with turning ($\frac{\Delta V_\theta}{U}$). Approximate centre of loss cores marked with “+” symbol.

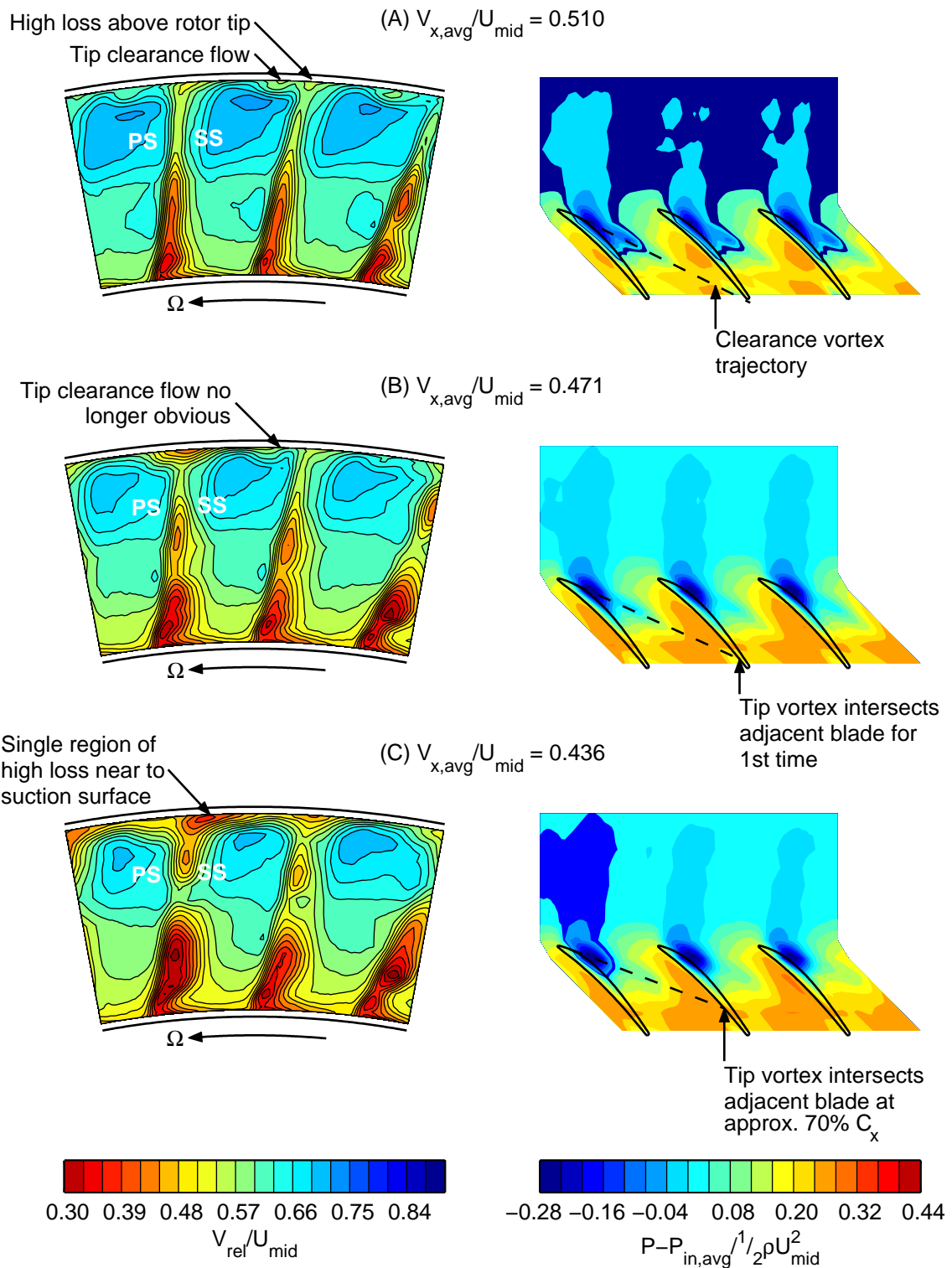


Figure 5.27: Comparison between the structure of the **Mini-Deverson** rotor clearance flow (left) and casing static pressure field (right). Dashed line indicates approximate trajectory of the tip clearance vortex.

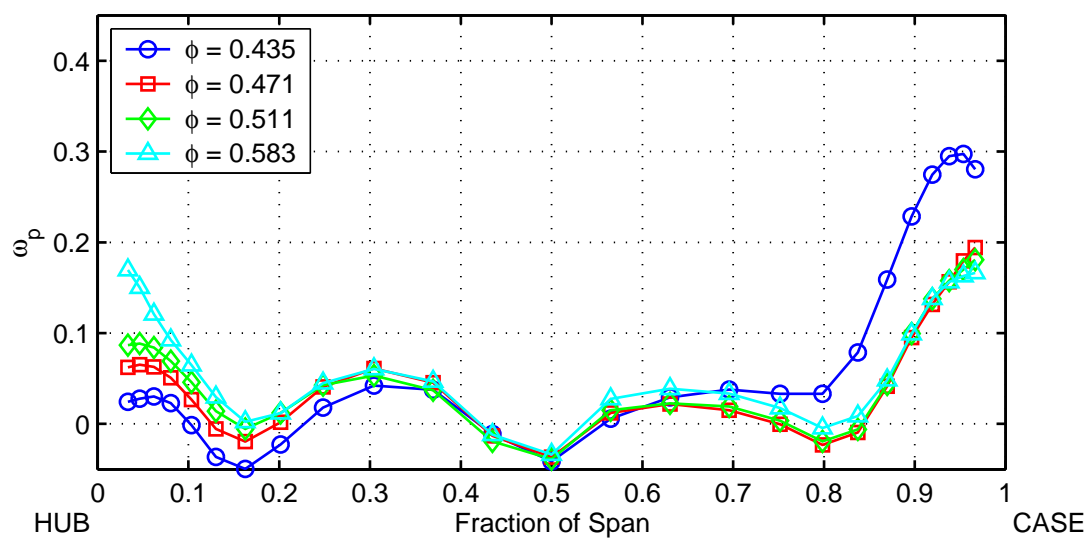


Figure 5.28: **Mini-Deverson** rotor loss coefficient.

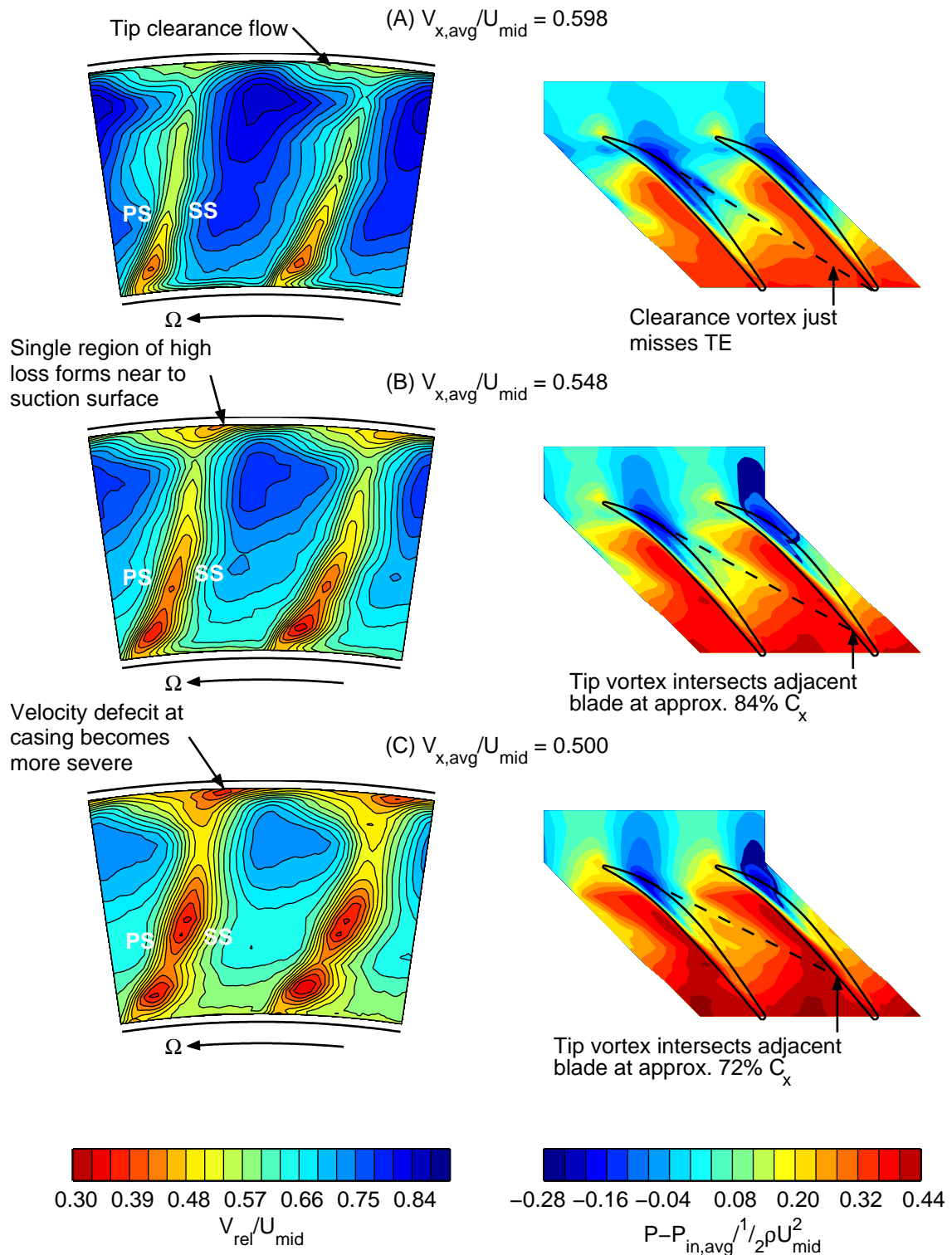


Figure 5.29: Comparison between the structure of the **Gallimore** rotor clearance flow (left) and casing static pressure field (right). Dashed line indicates approximate trajectory of the tip clearance vortex.

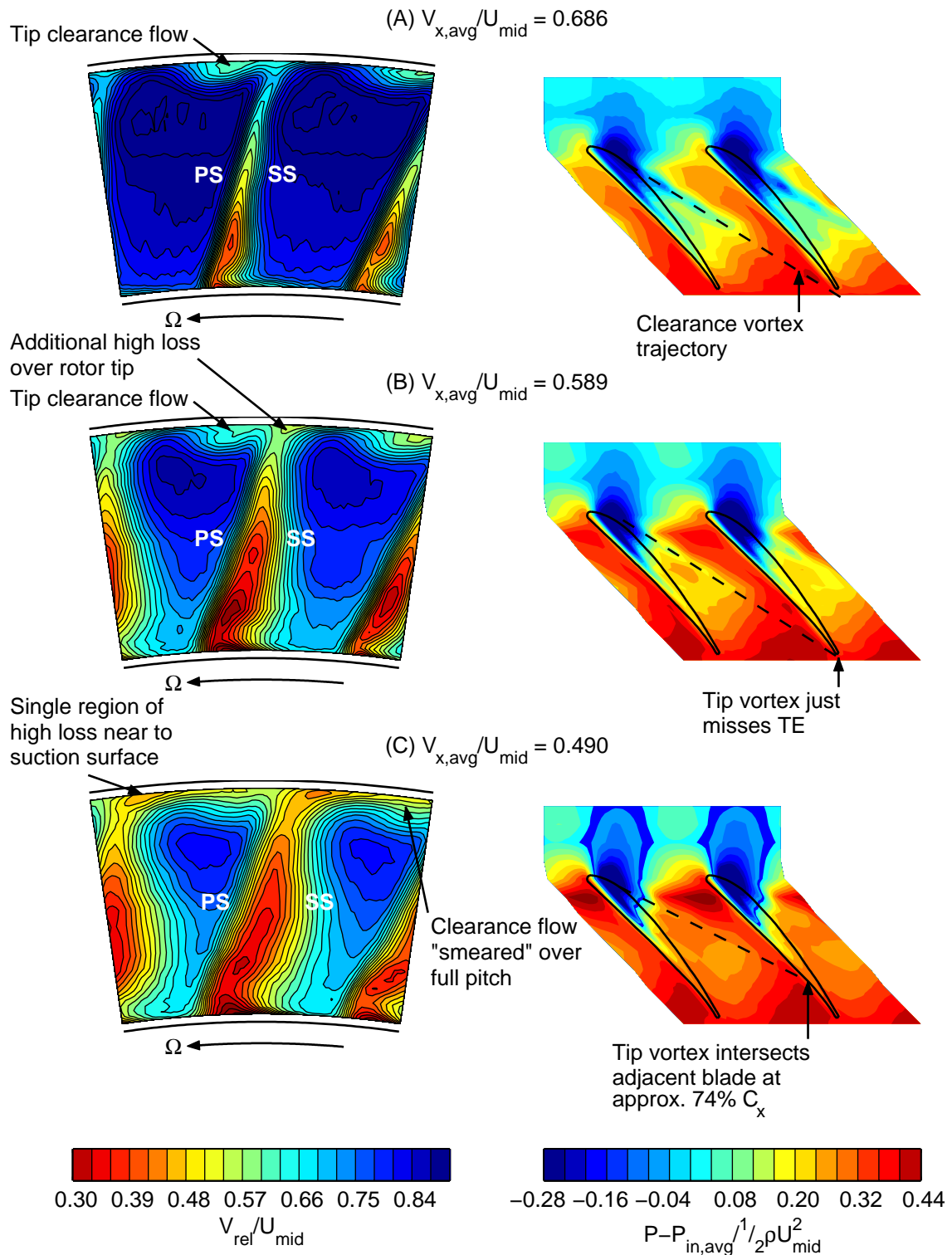


Figure 5.30: Comparison between the structure of the Qineticq rotor clearance flow (left) and casing static pressure field (right). Dashed line indicates approximate trajectory of the tip clearance vortex.

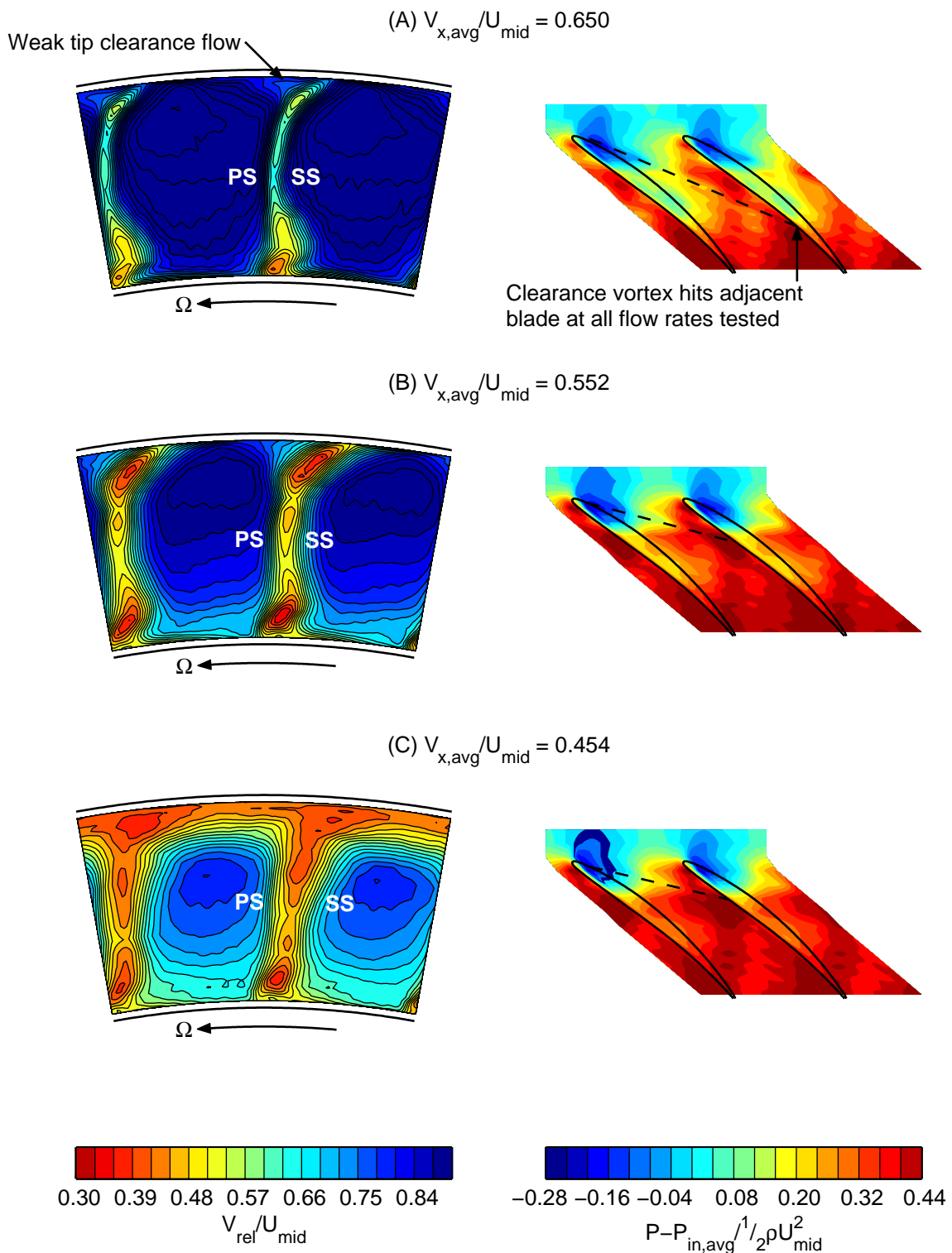


Figure 5.31: Comparison between the structure of the **Denton** rotor clearance flow (left) and casing static pressure field (right). Dashed line indicates approximate trajectory of the tip clearance vortex.

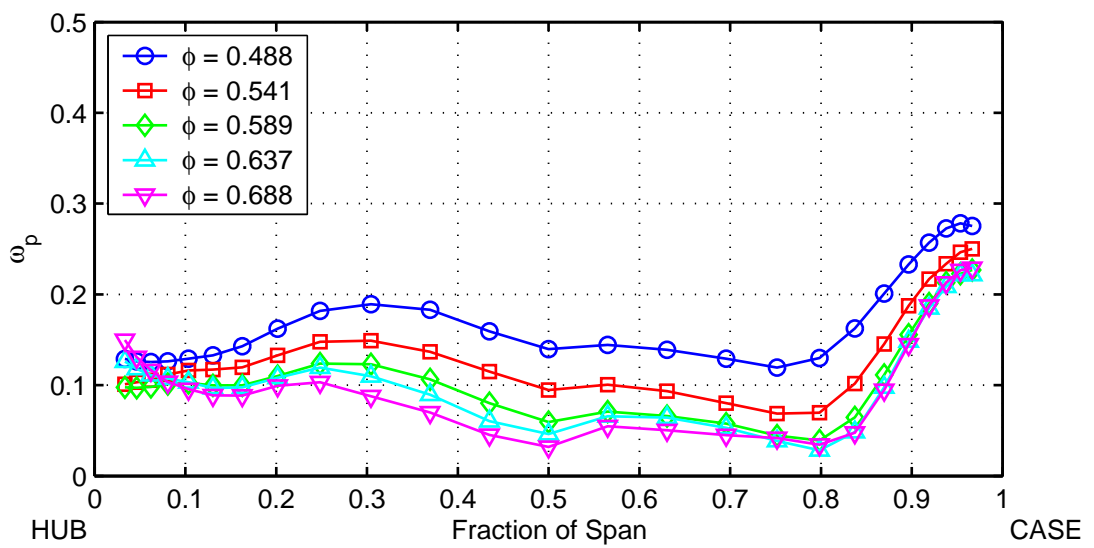


Figure 5.32: Qinetiq rotor loss coefficient.

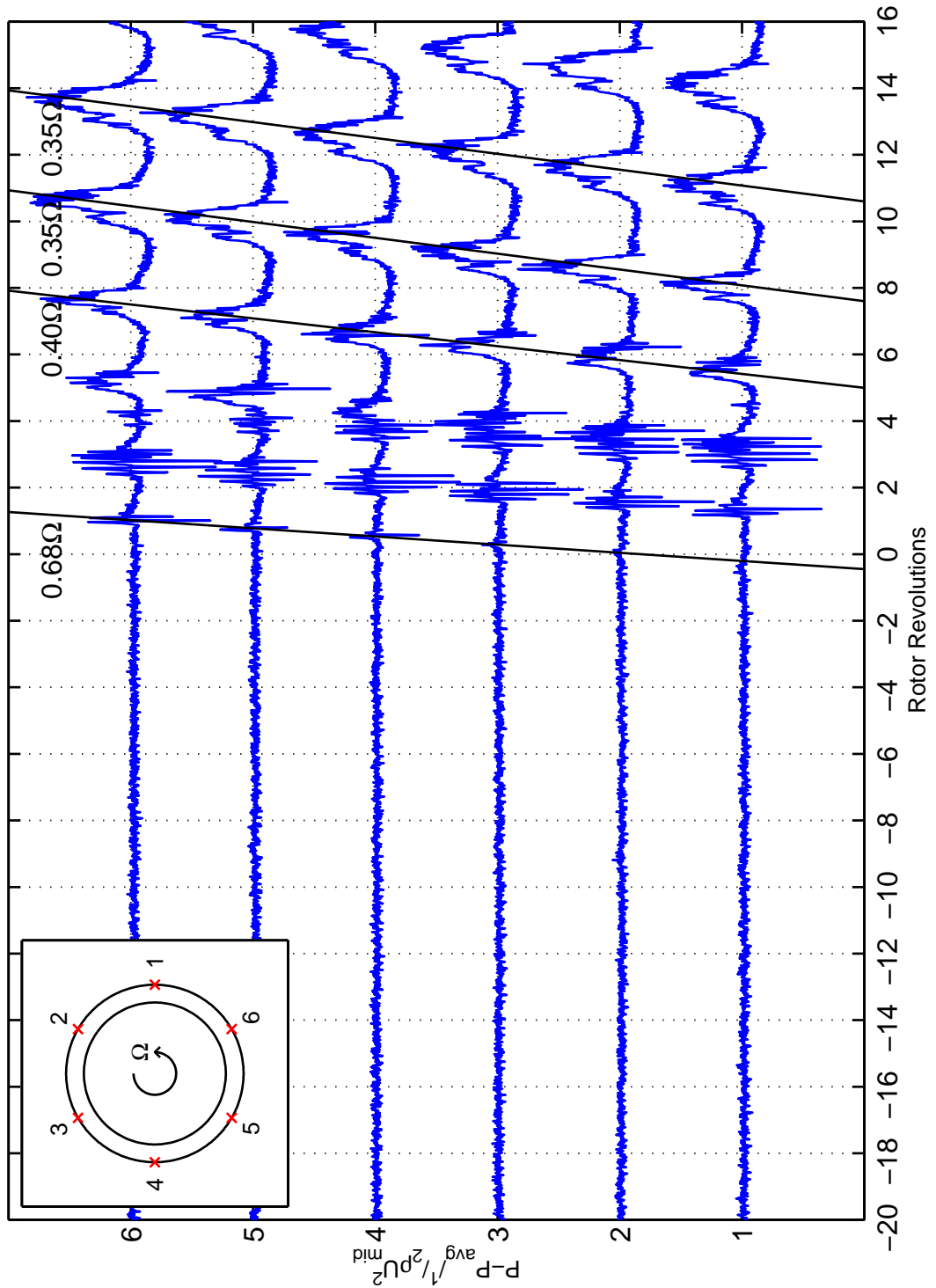


Figure 5.33: Stall inception event in the **Mini-Deverson** stage. Unsteady casing static pressures measured 26% of C_x upstream of the rotor shown. Black lines track stall cell propagation.

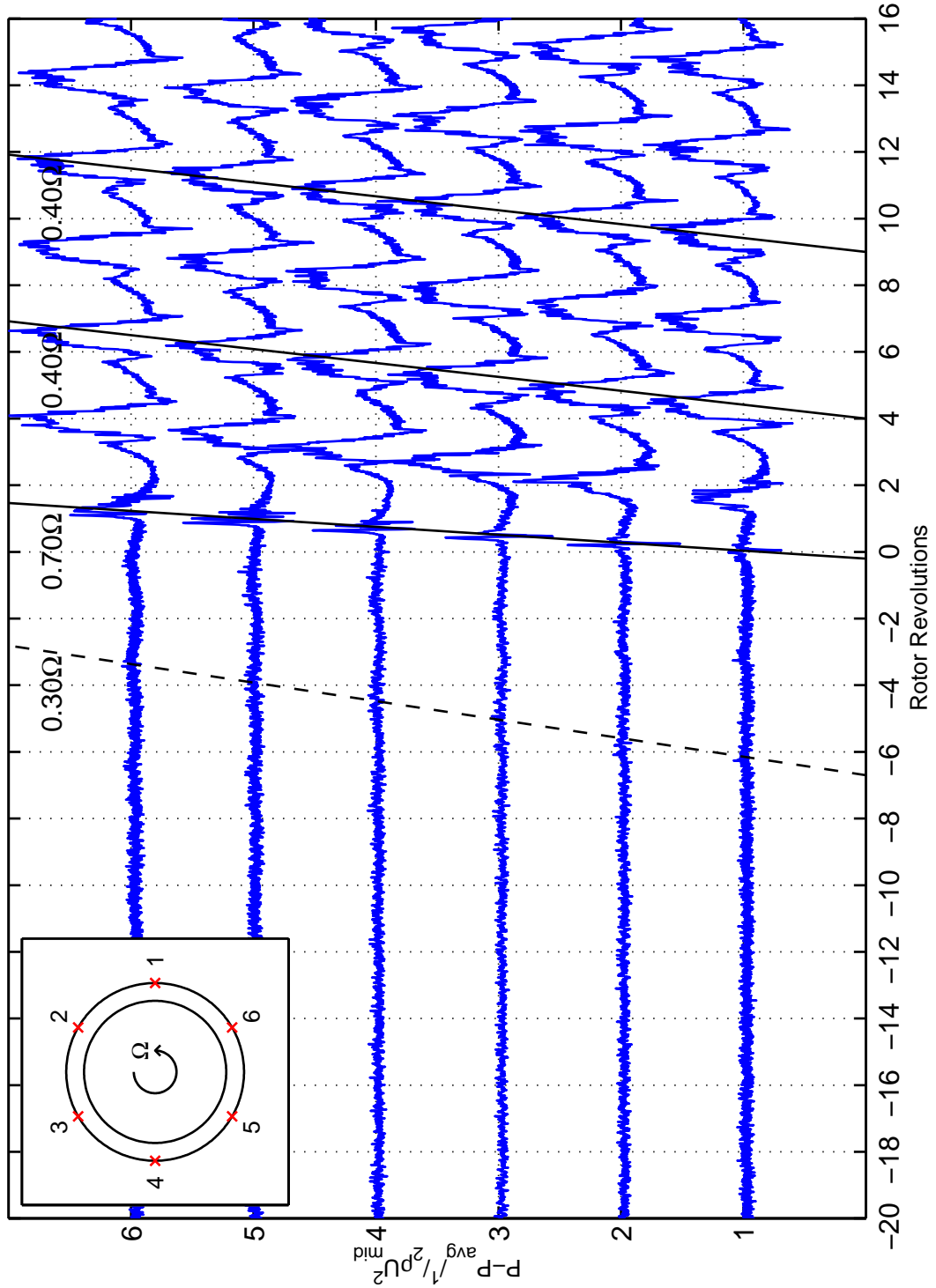


Figure 5.34: Stall inception event in the **Gallimore** stage. Unsteady casing static pressures measured 12% of C_x upstream of the rotor shown. Black dashed and solid lines track the propagation of pre-stall disturbances and stall cells respectively.

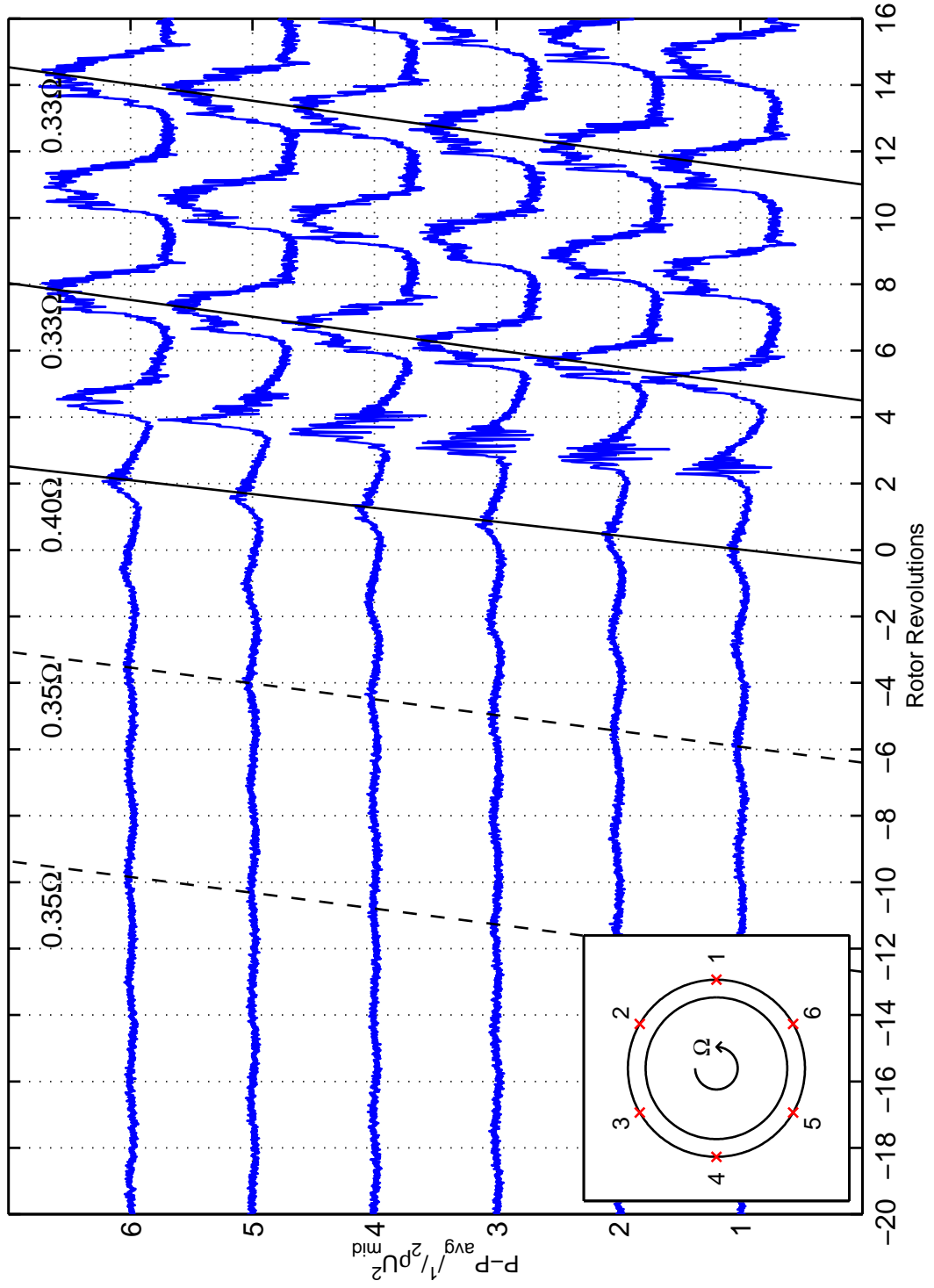


Figure 5.35: Stall inception event in the **Denton** stage. Unsteady casing static pressures measured 10% of C_x upstream of the rotor shown. Black dashed and solid lines track the propagation of pre-stall disturbances and stall cells respectively.

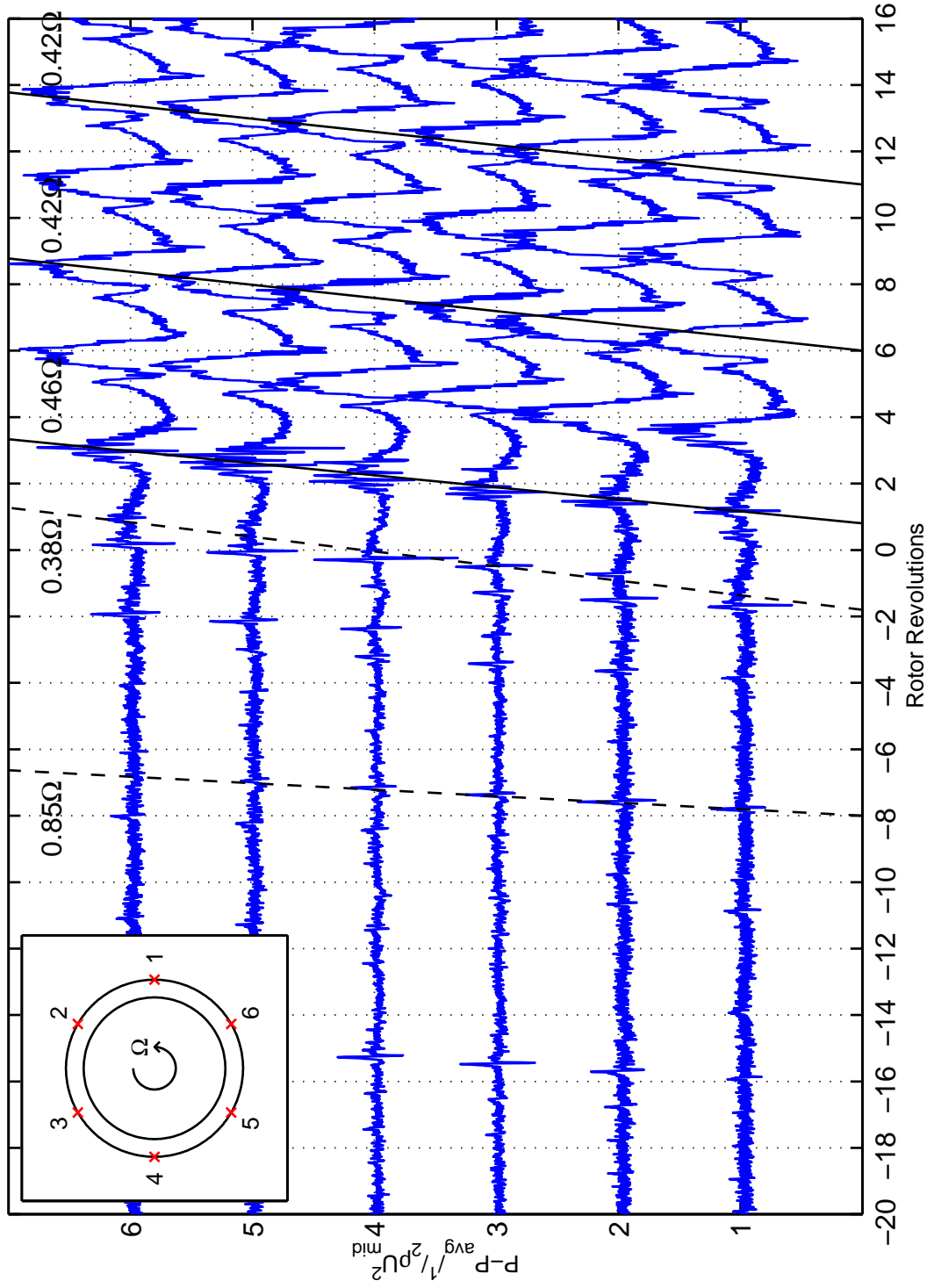


Figure 5.36: Stall inception event in the **Qinetiq** stage. Unsteady casing static pressures measured 20% of C_x upstream of the rotor shown. Black dashed and solid lines track the propagation of pre-stall disturbances and stall cells respectively.

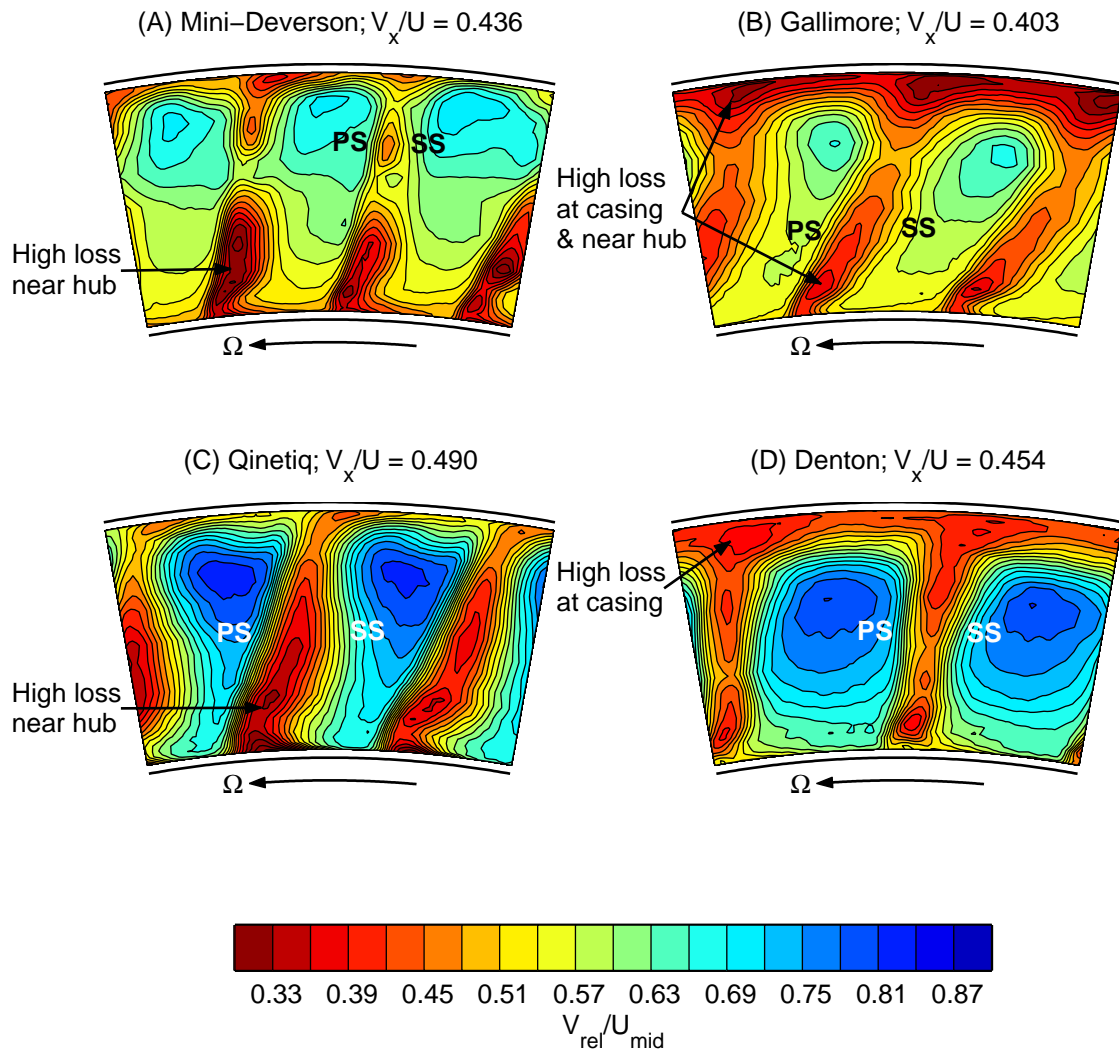


Figure 5.37: Sources of high loss near stall. Rotor exit relative velocity shown.

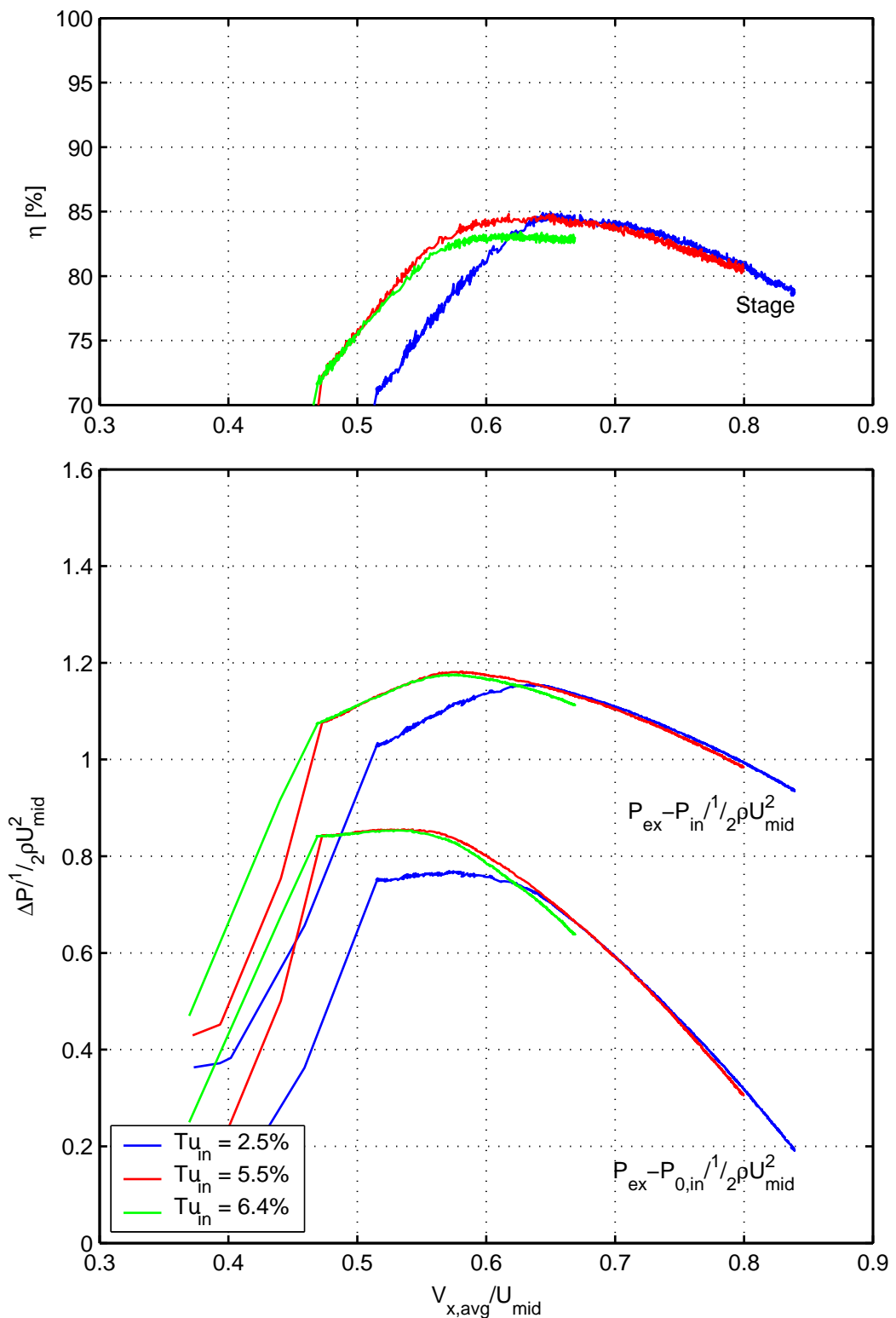


Figure 6.1: The effect of inlet turbulence on the pressure rise and efficiency characteristics of the **Qinetiq** stage.

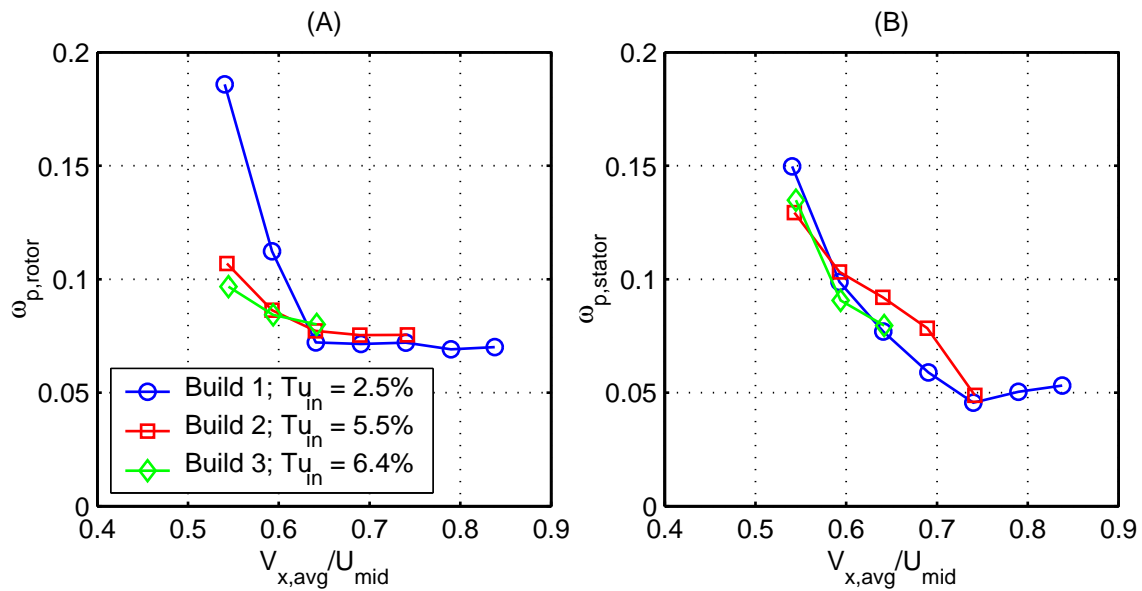


Figure 6.2: The effect of inlet turbulence on (A) the rotor and (B) stator loss coefficients of the **Qinetiq** stage.

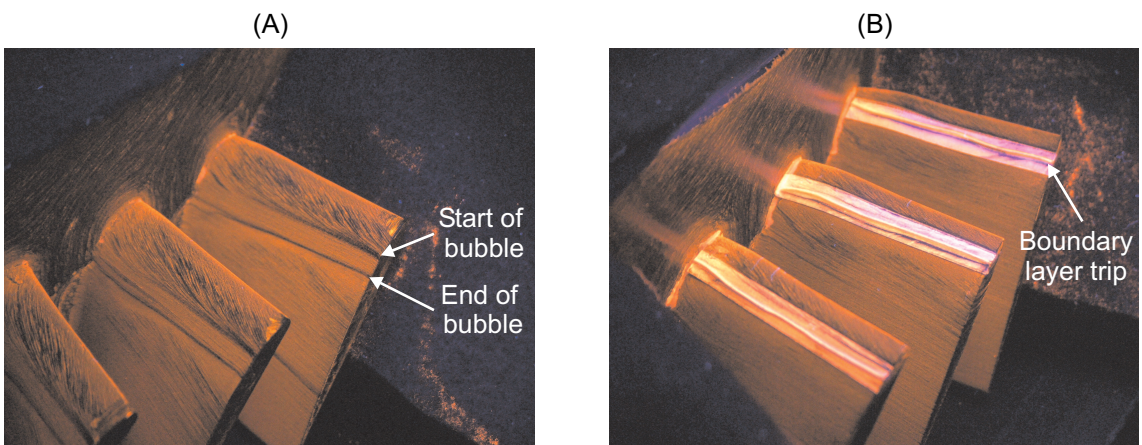


Figure 6.3: Rotor suction surface oil-dye flow visualisation at $\bar{\phi} = 0.638$. (A) Low inlet turbulence. (B) Suction surface boundary layer trip at 11% chord.

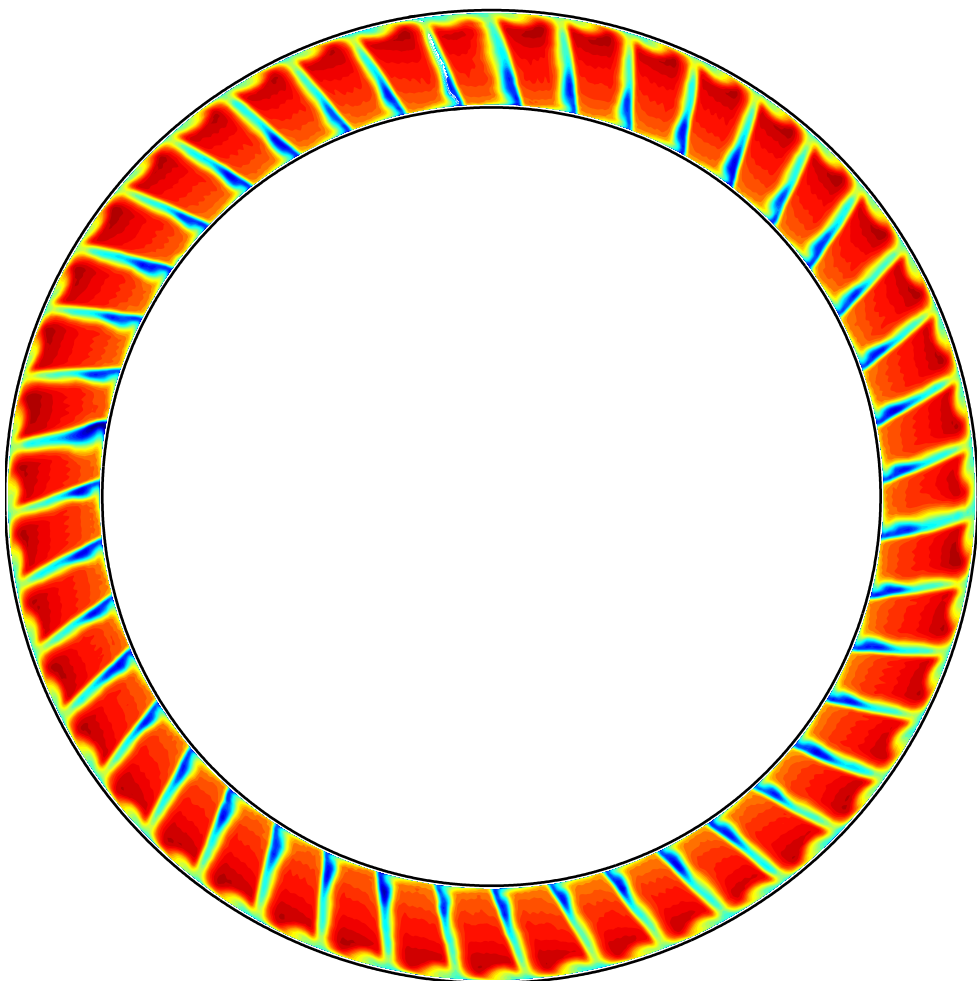
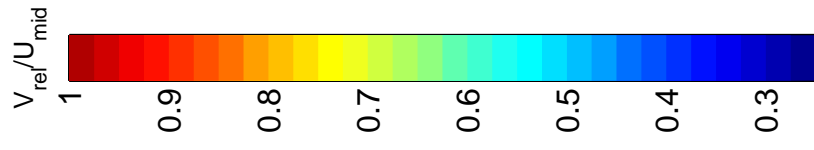


Figure 6.4A: Ensemble averaged rotor exit relative velocity. $\bar{\phi} = 0.638$.

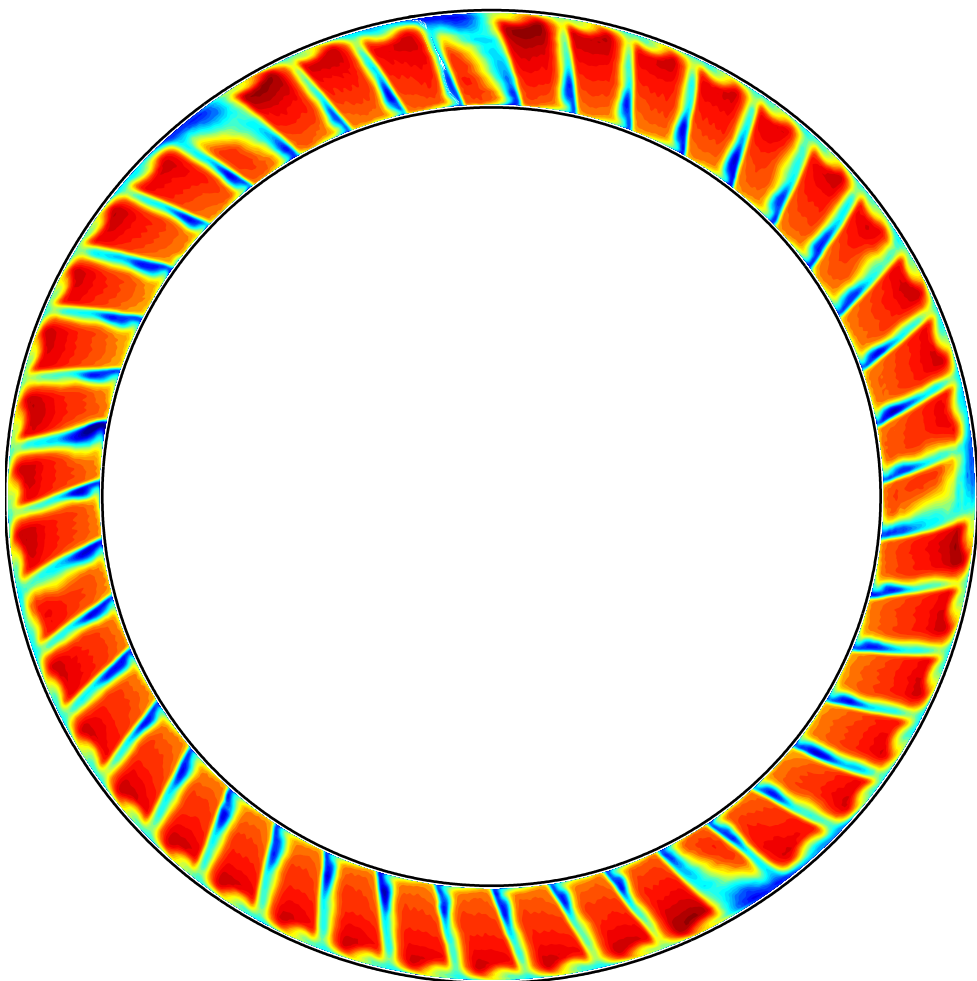
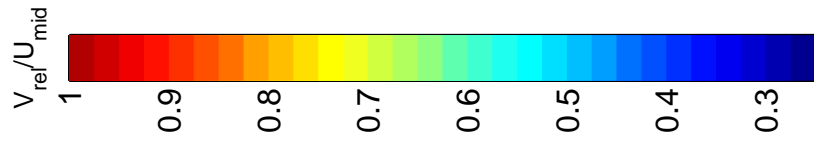


Figure 6.4B: Ensemble averaged rotor exit relative velocity. $\bar{\phi} = 0.613$.

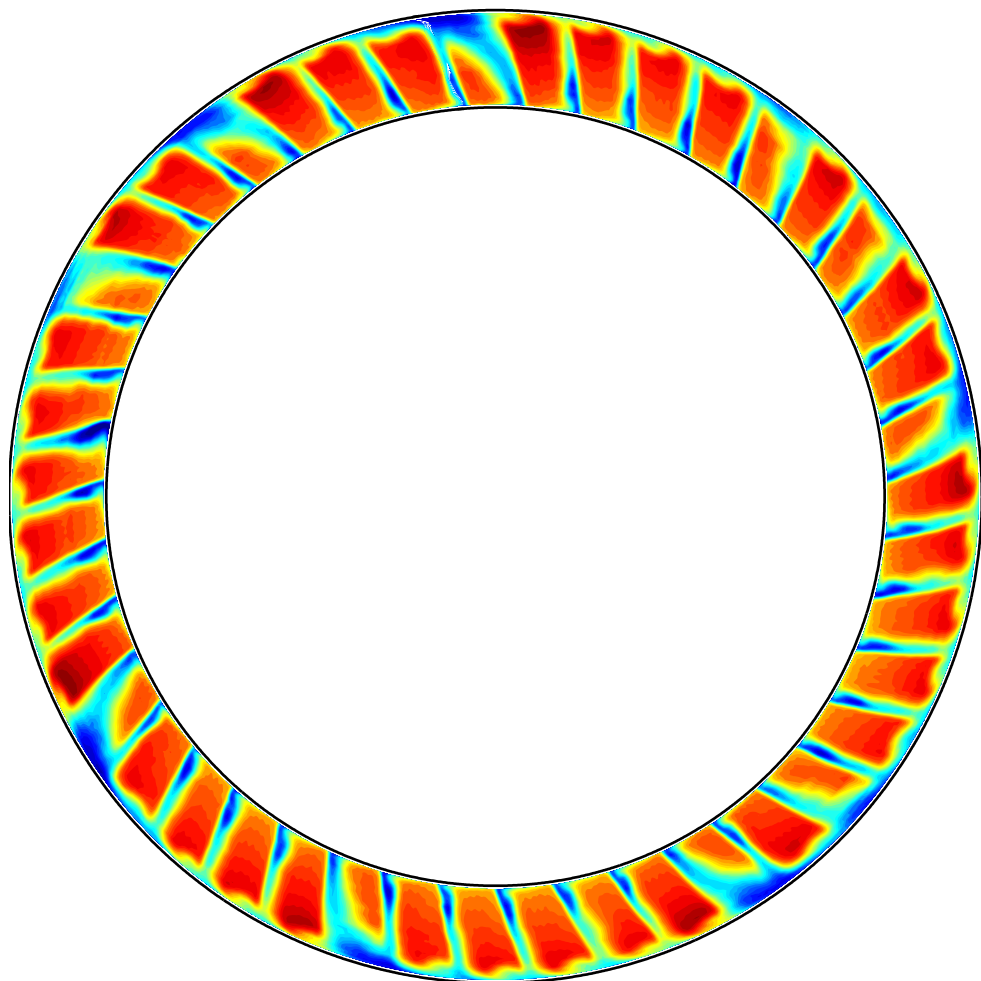
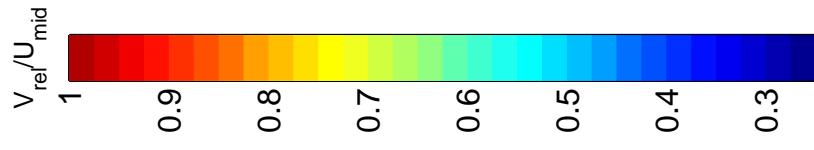


Figure 6.4C: Ensemble averaged rotor exit relative velocity. $\bar{\phi} = 0.589$.

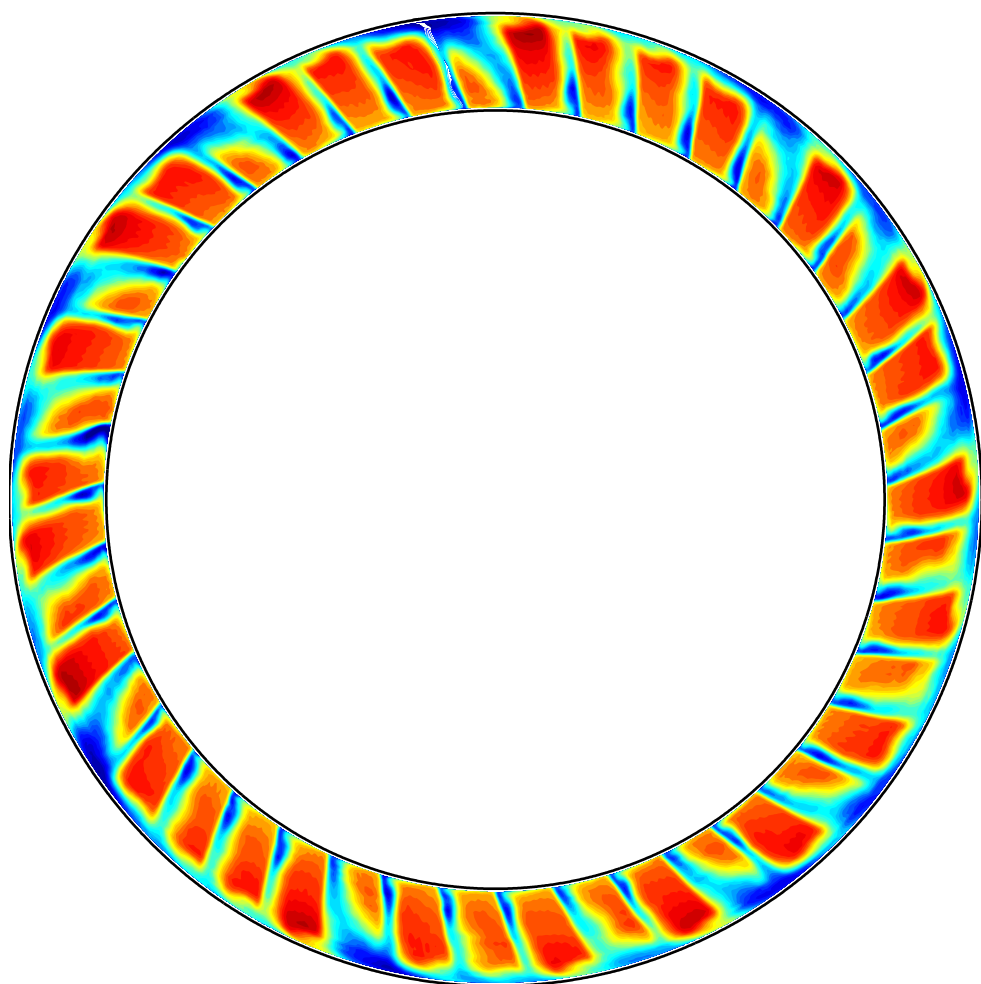
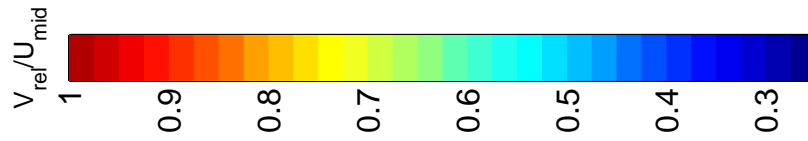


Figure 6.4D: Ensemble averaged rotor exit relative velocity. $\bar{\phi} = 0.564$.

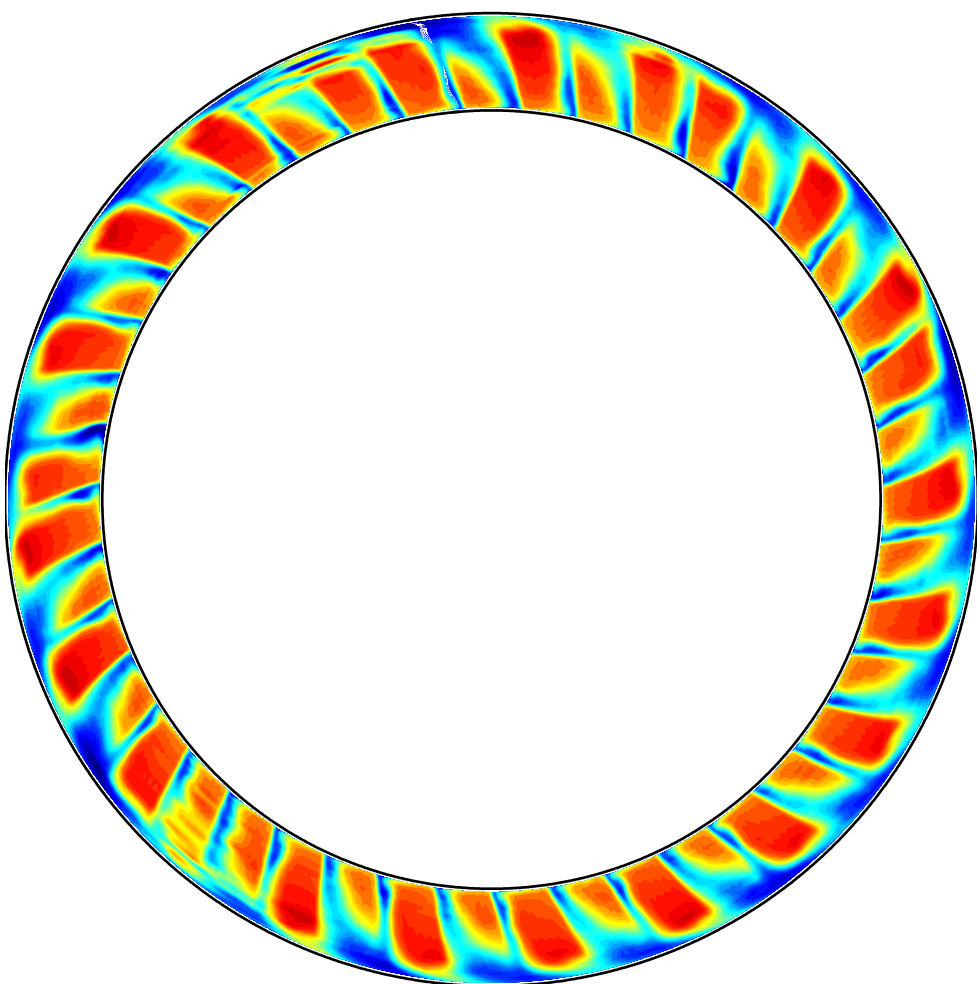
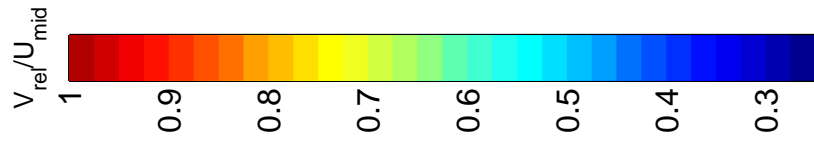


Figure 6.4E: Ensemble averaged rotor exit relative velocity. $\bar{\phi} = 0.540$.

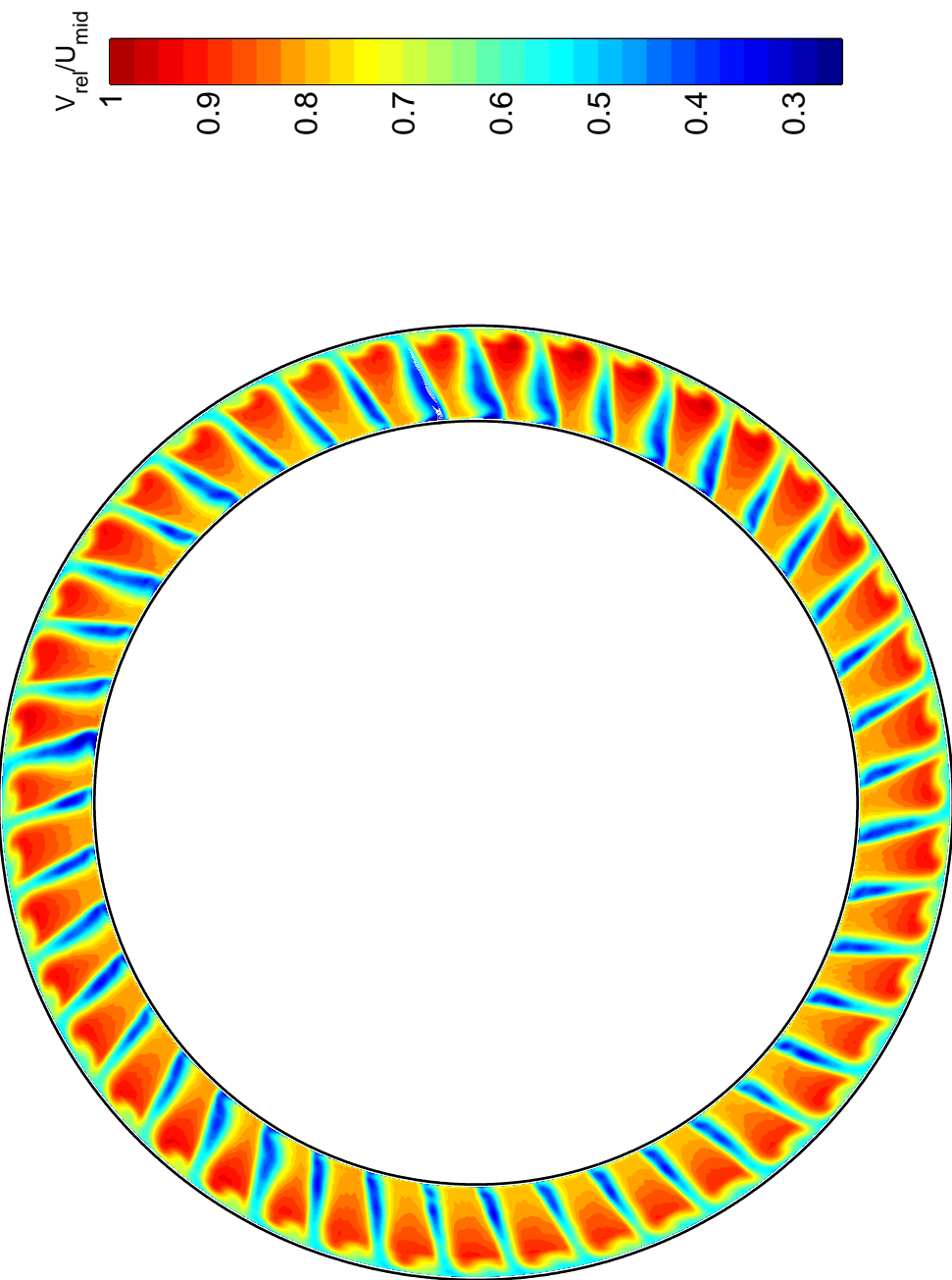


Figure 6.5: Ensemble averaged rotor exit relative velocity with increased inlet turbulence ($Tu_{in} = 6.5\%$). $\bar{\phi} = 0.540$.

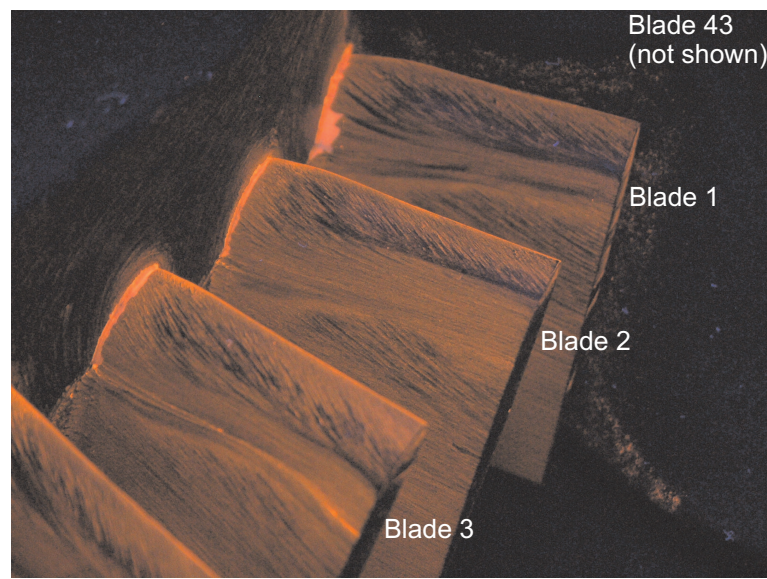


Figure 6.6: Rotor suction surface oil-dye flow visualisation at $\bar{\phi} = 0.540$. Separations present on Blades 2, 4 and 43 (immediately ahead of visible sector).

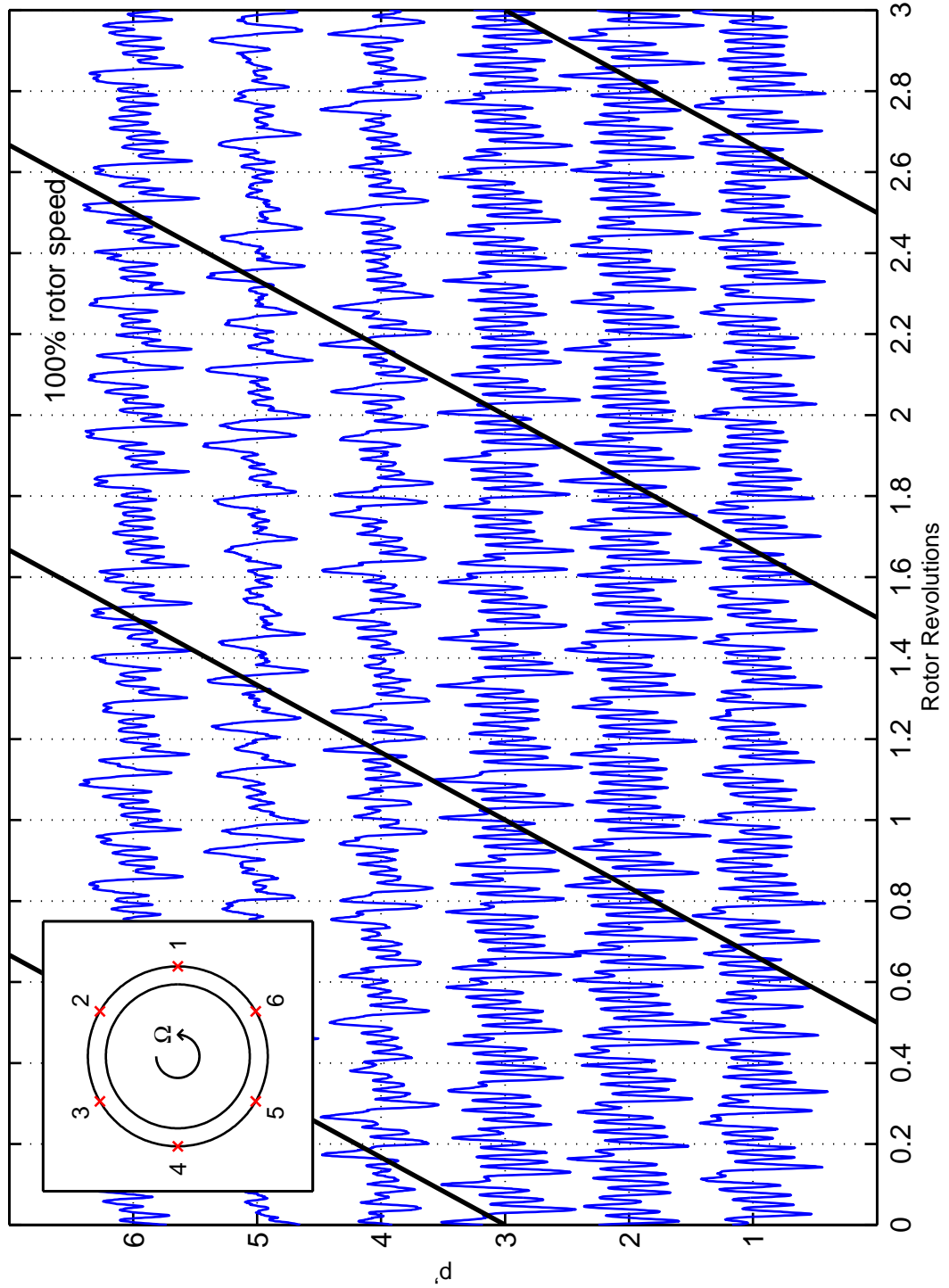


Figure 6.7: Unsteady leading edge casing static pressures. $\bar{\phi} = 0.589$. Bold lines highlight the same disturbance through three revolutions.

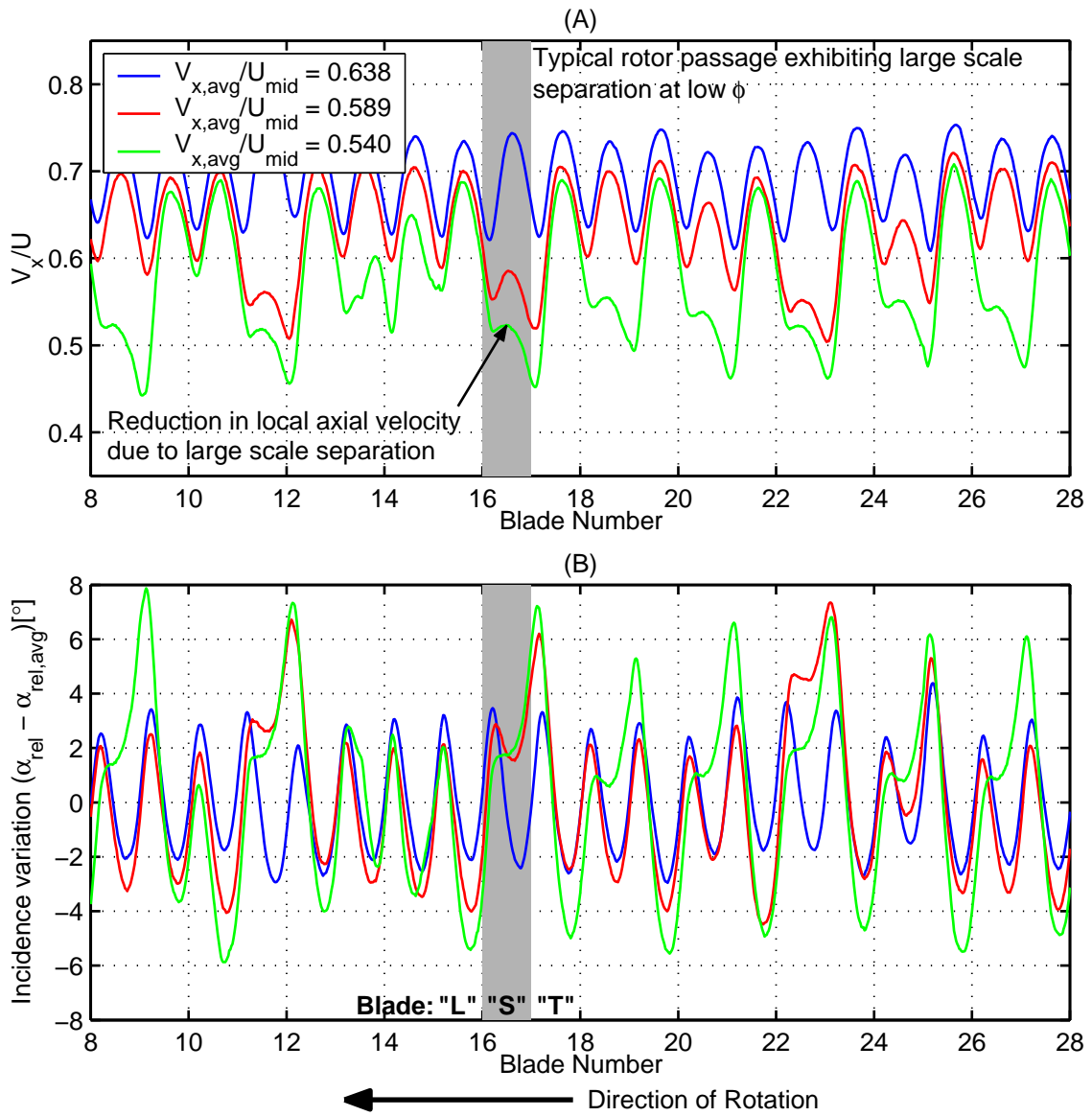


Figure 6.8: Variation in (A) axial velocity and (B) inlet relative flow angle (i.e. incidence) at 75% span (measured 20% of C_x upstream of the rotor leading edge).

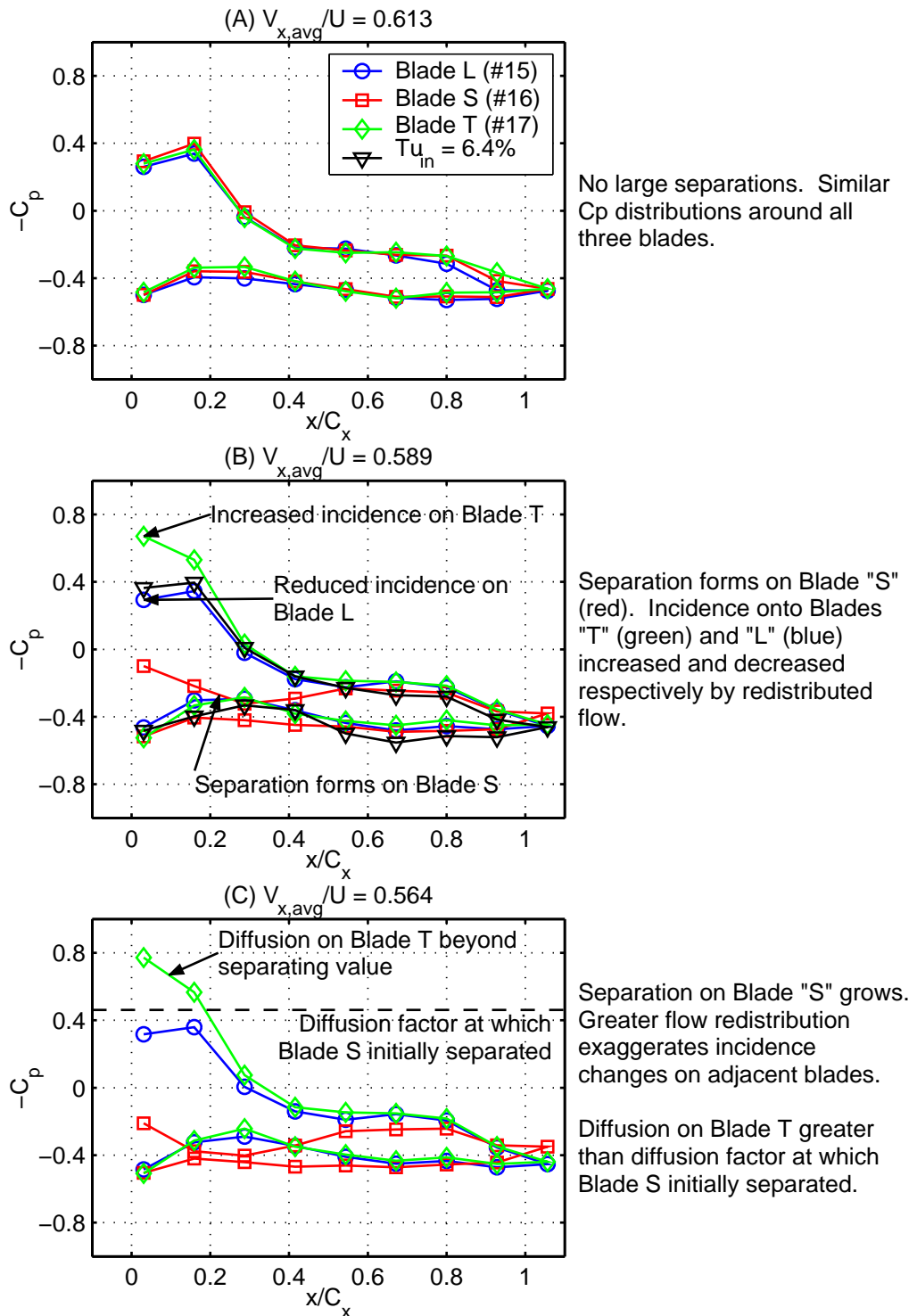


Figure 6.9: Casing static pressure distributions around three blades; (A) before and (B) & (C) after the formation of a large non-periodic separation on Blade "S".

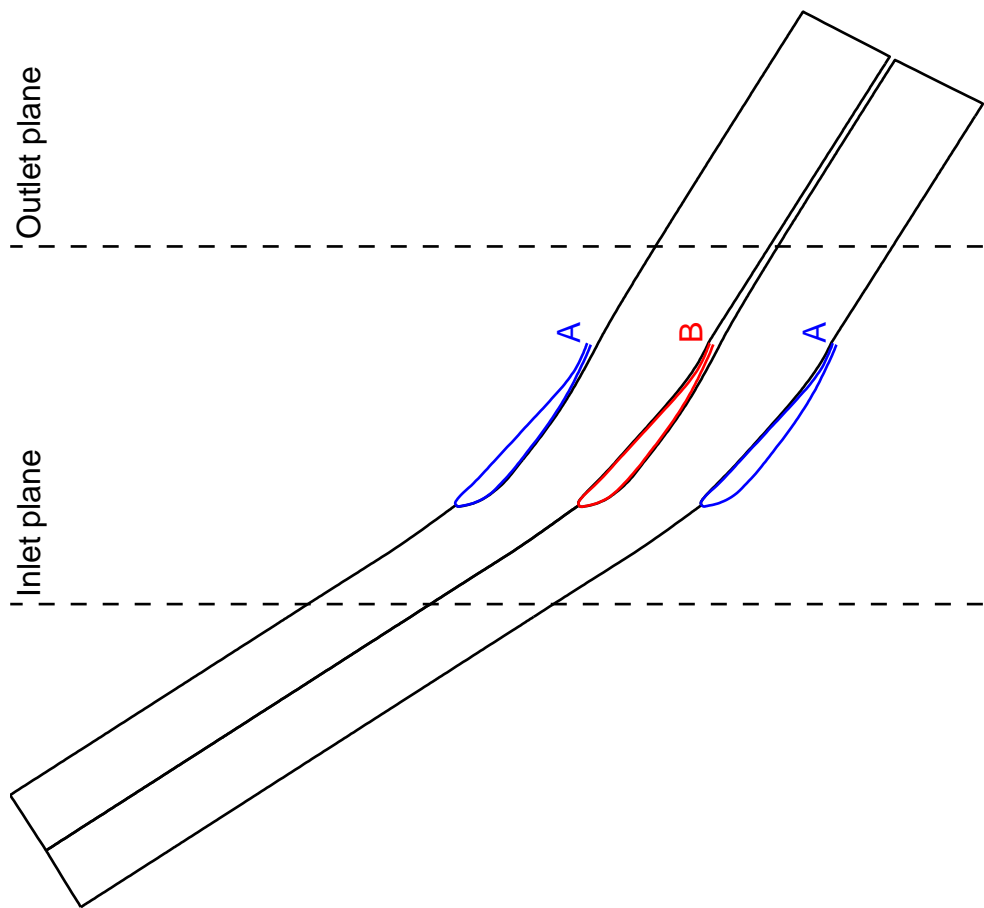


Figure 6.10: Outline of the *MISES* mesh used to simulate two adjacent blades. N.B. Blade B has been re-staggered “open” by 0.2° .

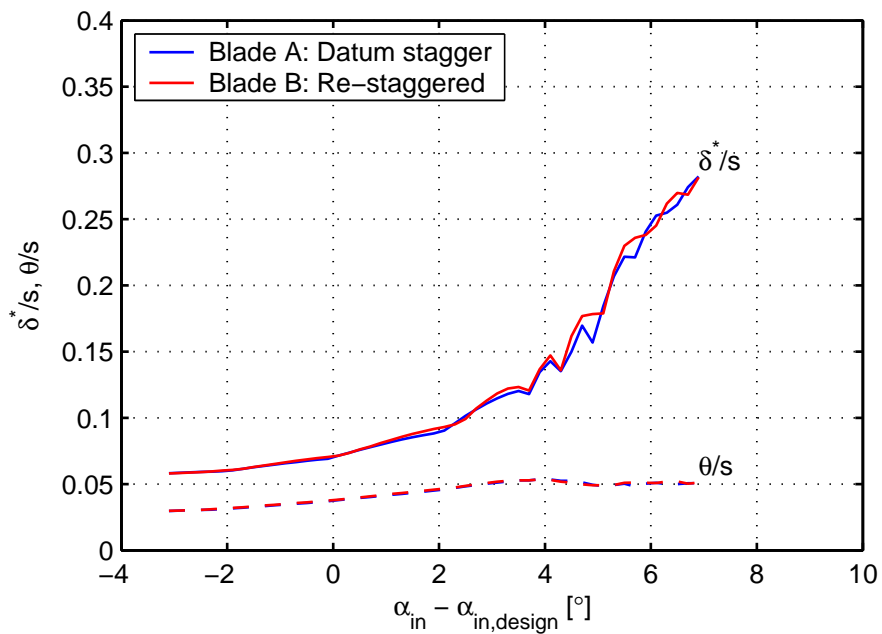


Figure 6.11: Predicted variation in trailing edge displacement and momentum thicknesses with inlet flow angle. Results from “single” blade calculations.

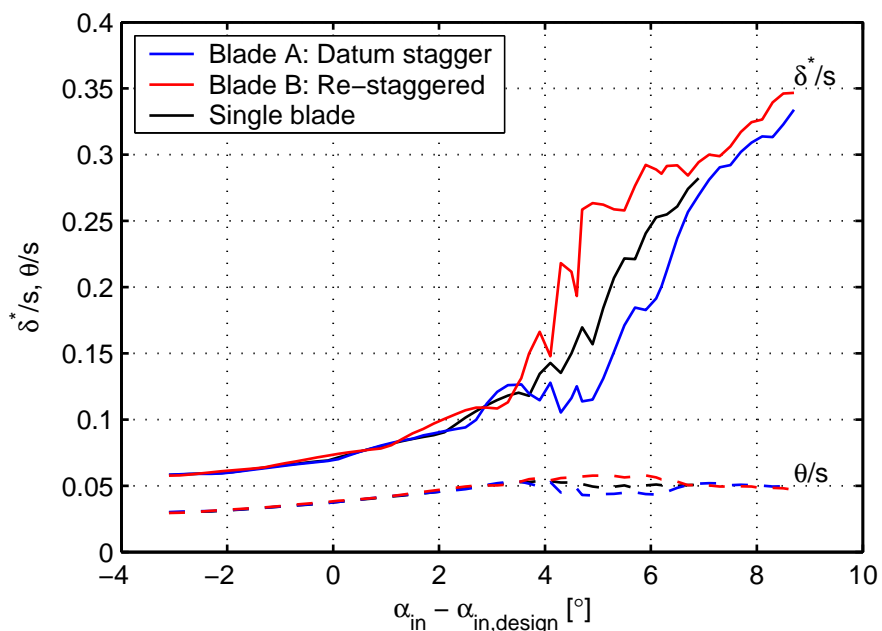


Figure 6.12: Predicted variation in trailing edge displacement and momentum thicknesses with inlet flow angle.

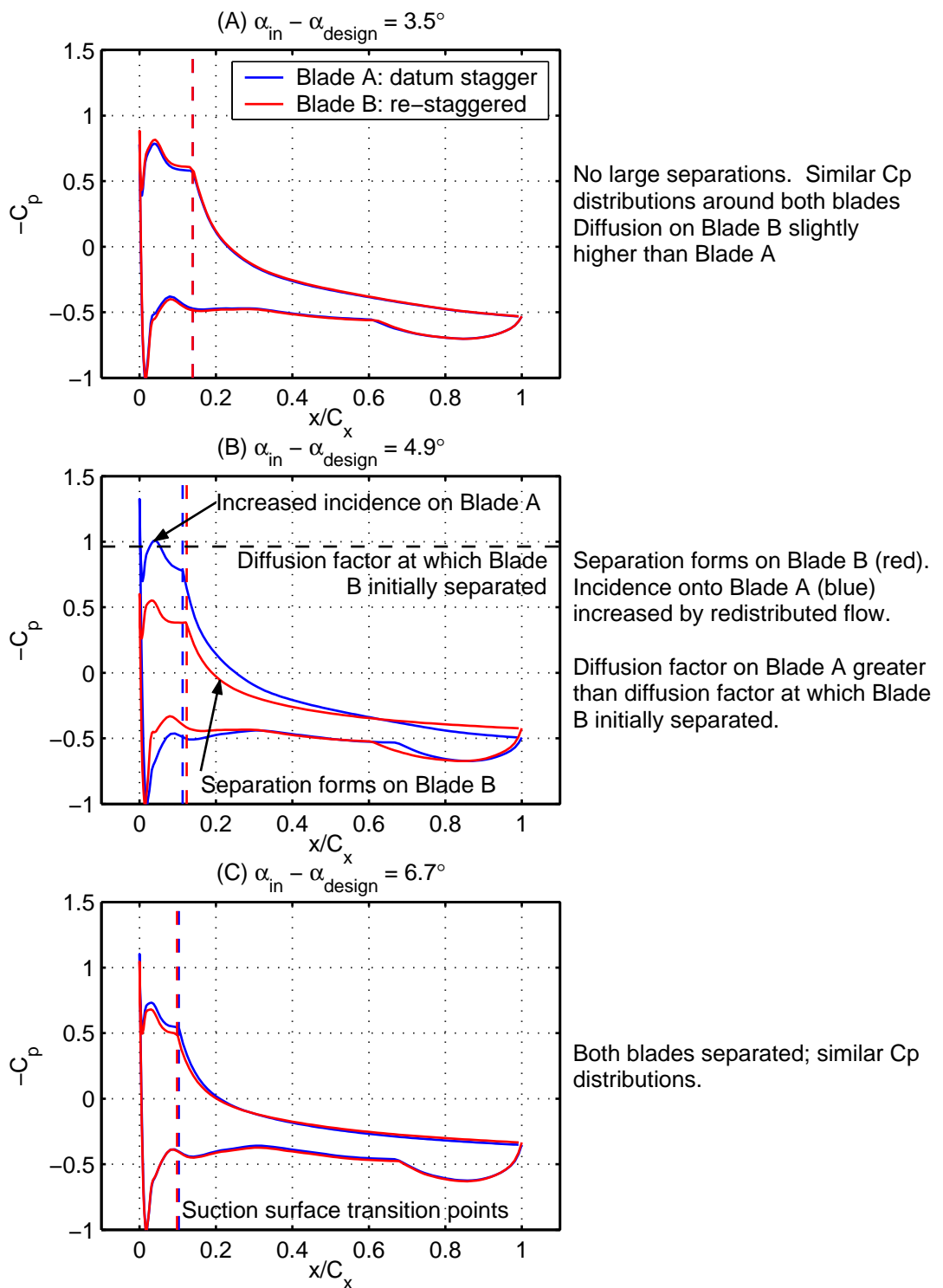


Figure 6.13: Calculated pressure distributions at three inlet flow angles; corresponding to (A) before, (B) during and (C) after the formation of a large non-periodic separation from the suction surface of the re-staggered blade.

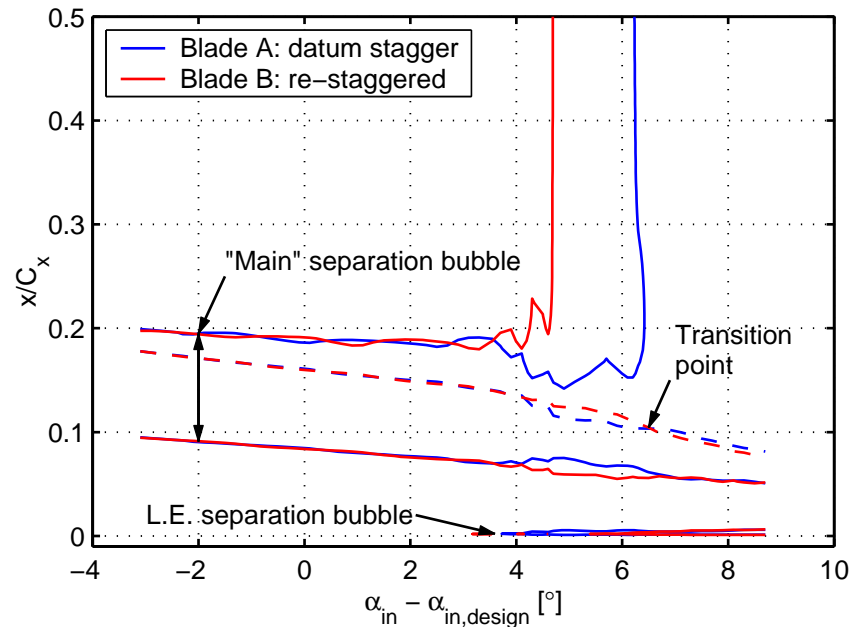


Figure 6.14: Variation in suction surface lines of zero skin friction with inlet flow angle.

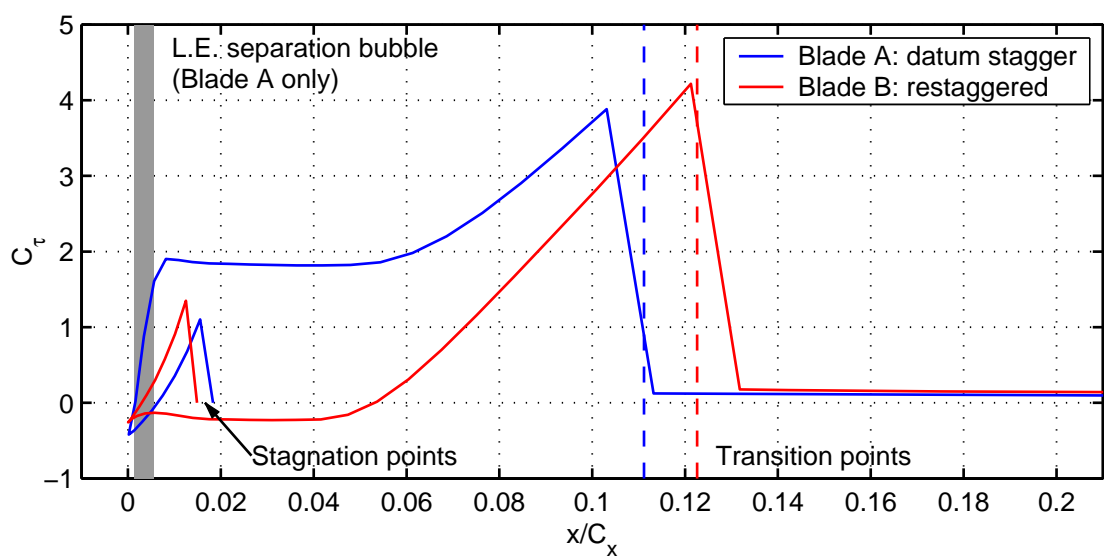


Figure 6.15: MISES Reynolds stress coefficient, C_τ . Shaded area indicates the extent of the leading edge separation bubble on Blade A (datum stagger).

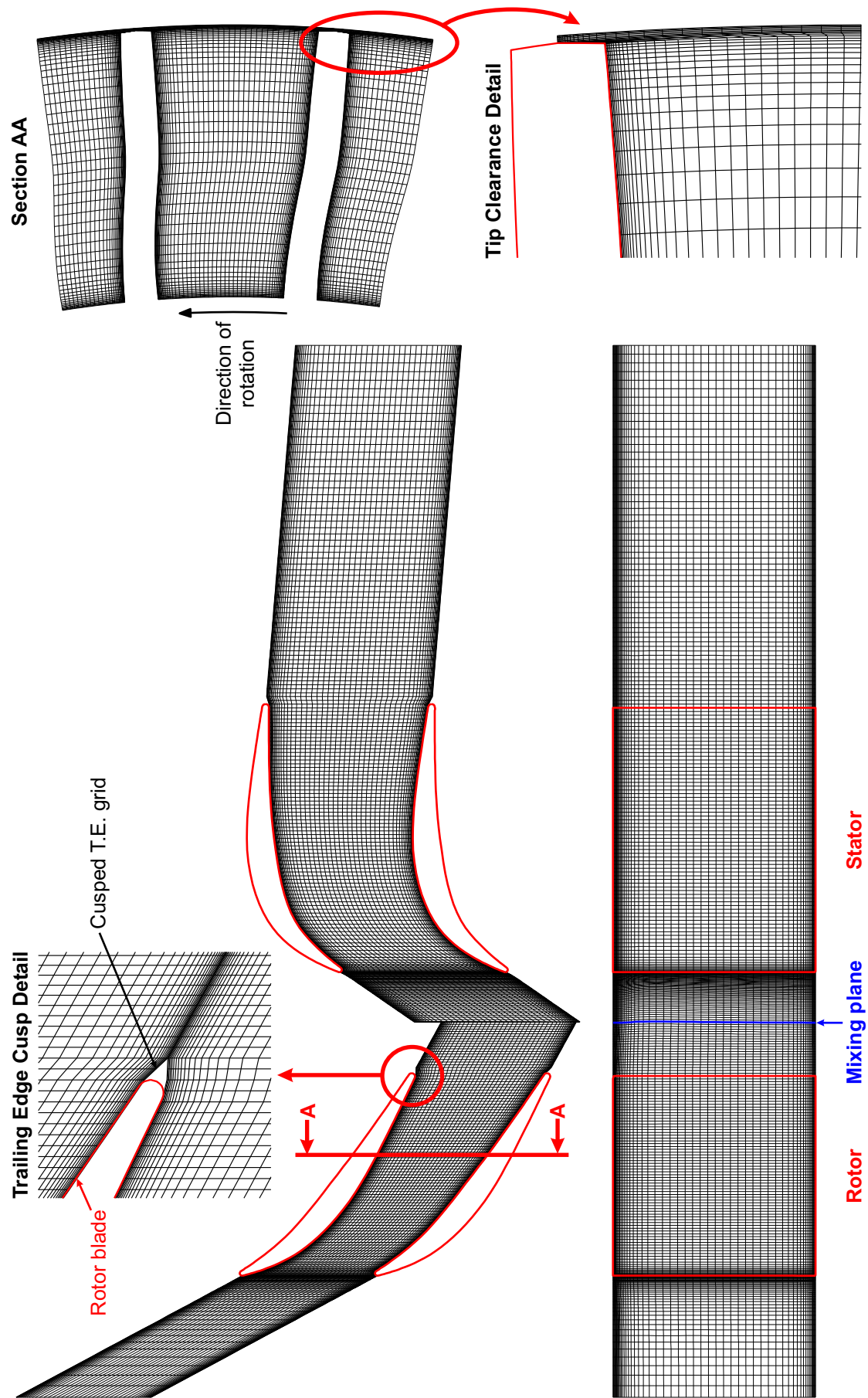


Figure 7.1: A typical *MULTIP* grid

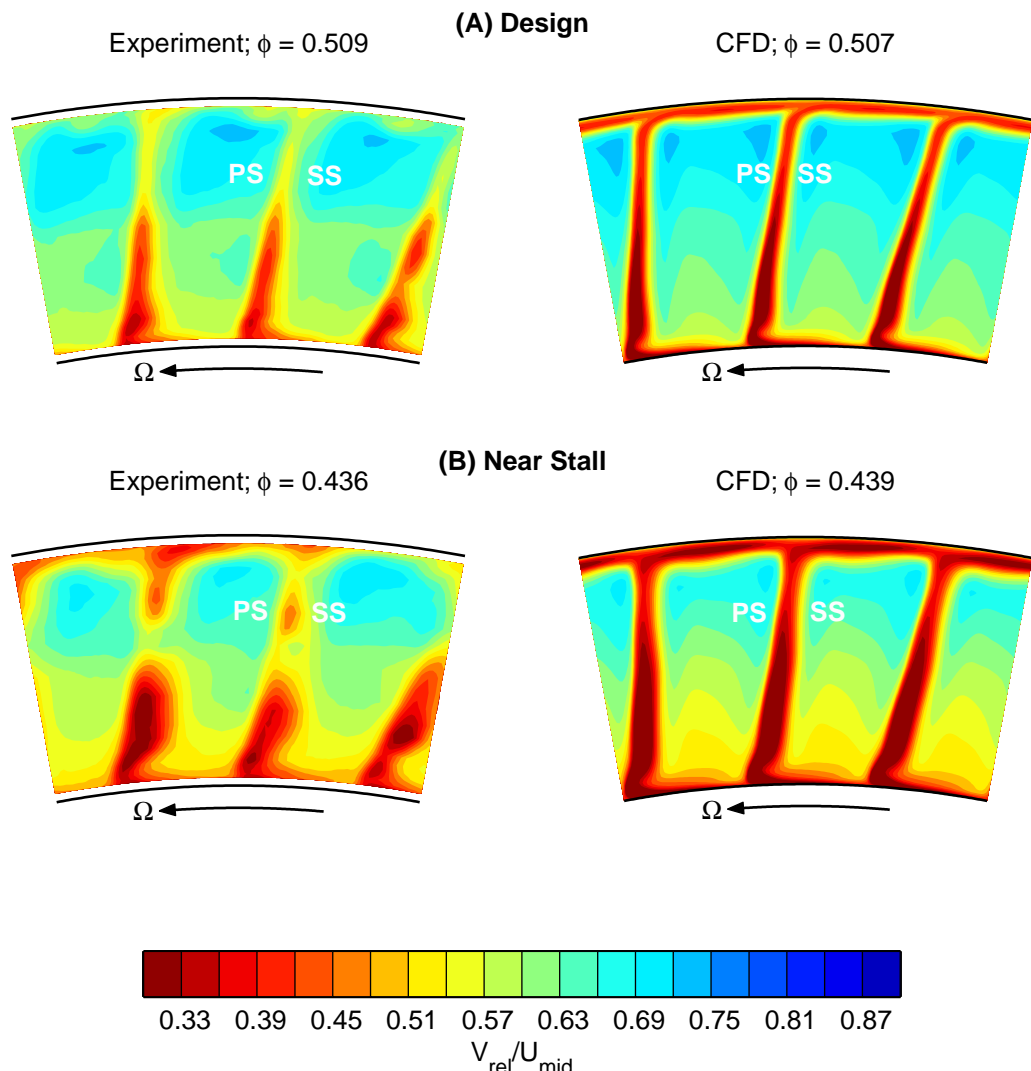


Figure 7.2: Comparison between CFD prediction and experiment downstream of the **Mini-Deverson** rotor at (A) design and (B) near stall operating points.

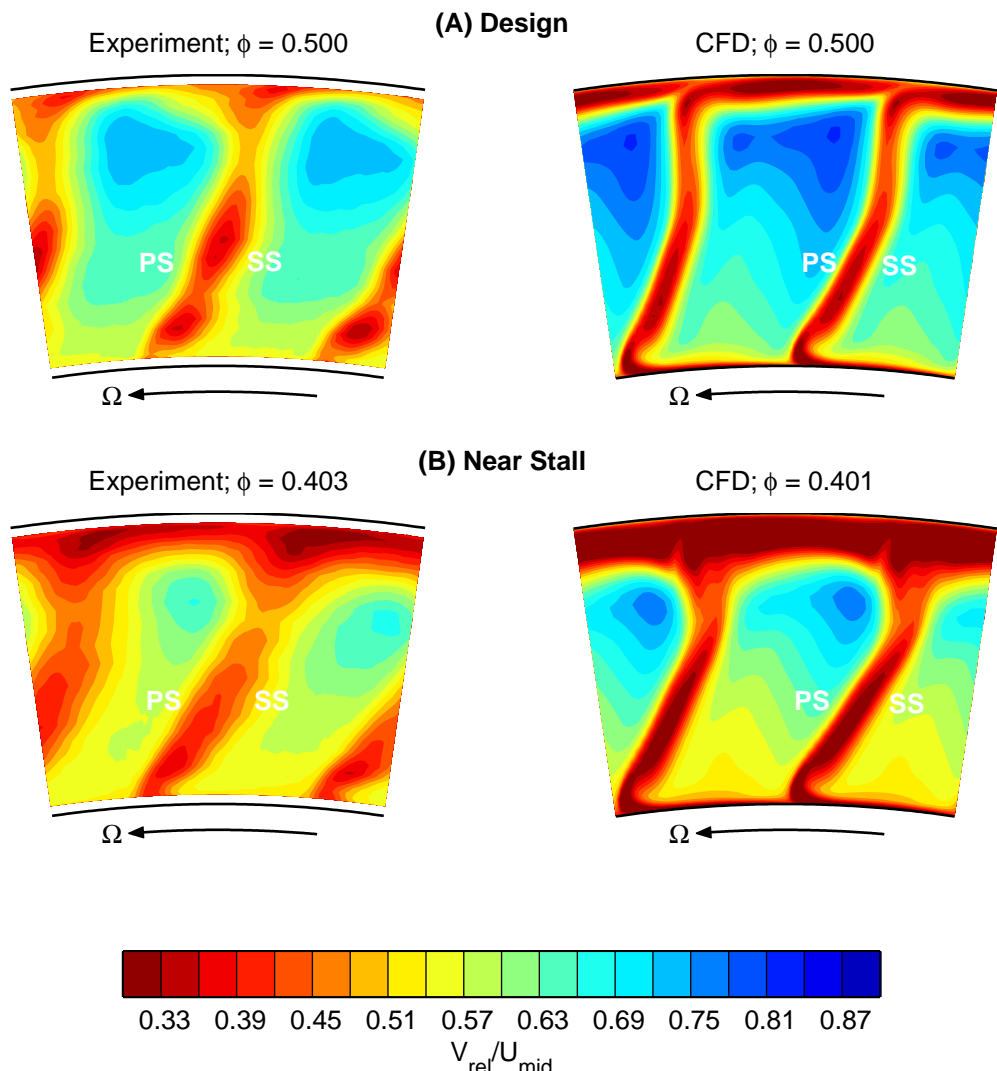


Figure 7.3: Comparison between CFD prediction and experiment downstream of the **Gallimore** rotor at (A) design and (B) near stall operating points.

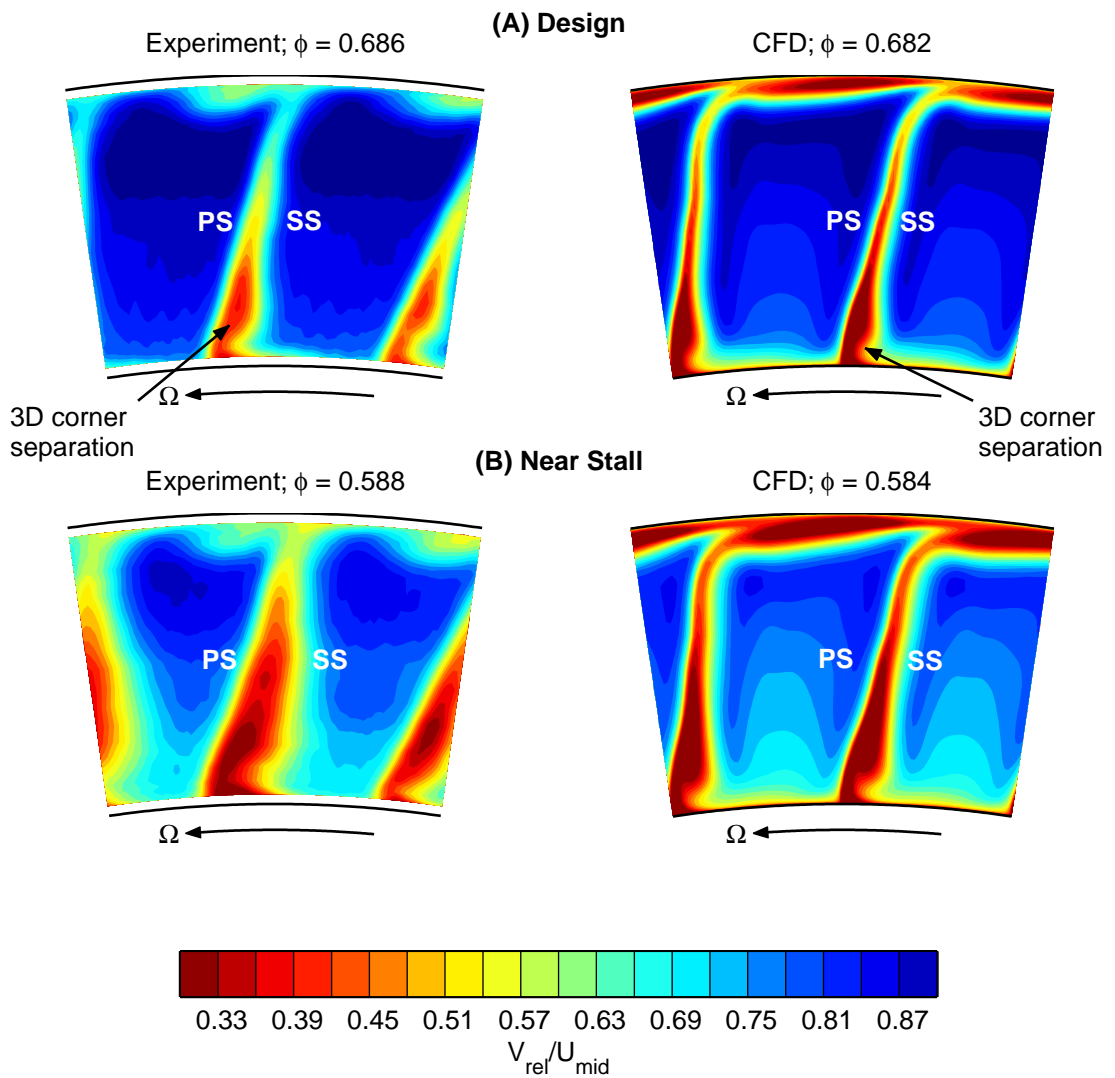


Figure 7.4: Comparison between CFD prediction and experiment downstream of the Qinetiq rotor at (A) design and (B) near stall operating points.

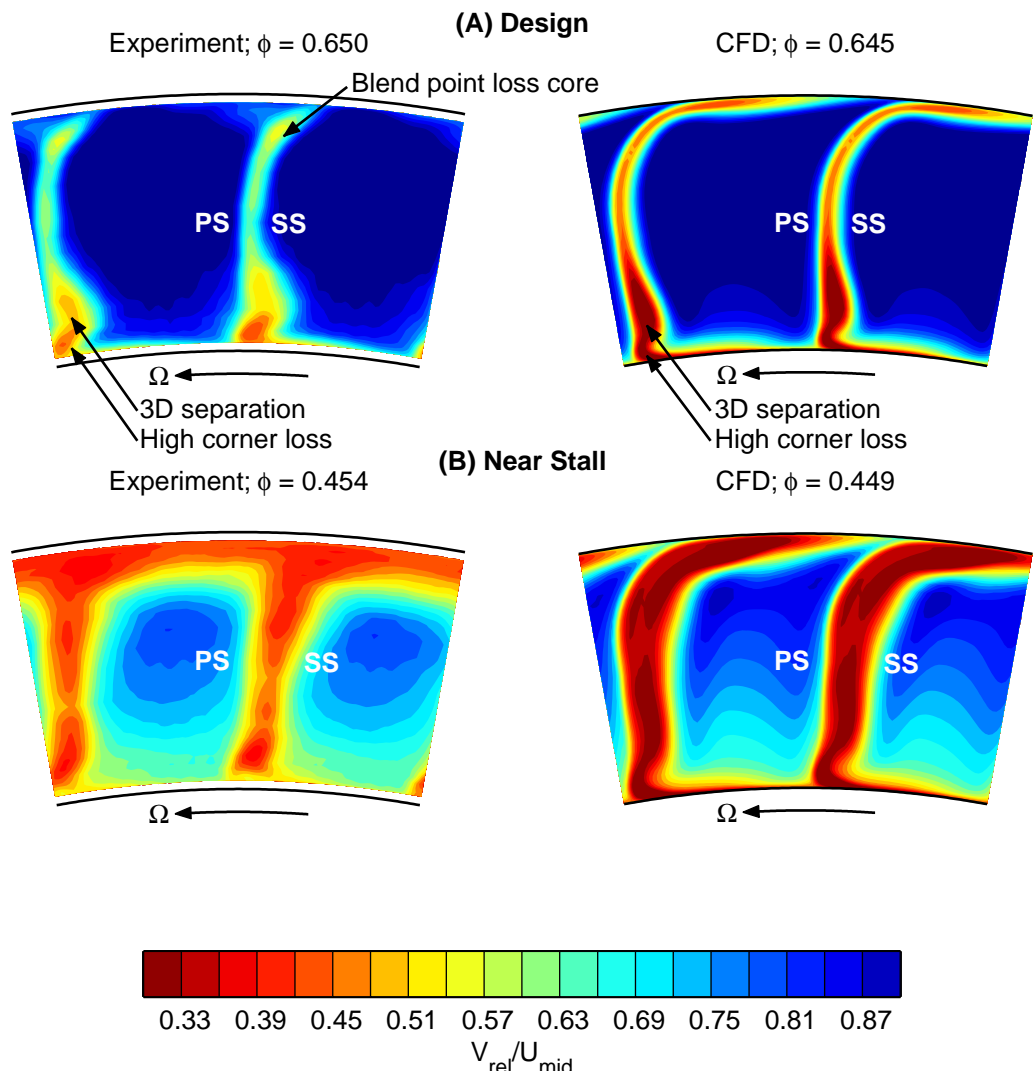


Figure 7.5: Comparison between CFD prediction and experiment downstream of the **Denton** rotor at (A) design and (B) near stall operating points.

Figure 7.6: Comparison between measured and CFD predictions of radial profiles of (A) axial velocity, (B) stagnation pressure rise and (C) relative flow angle downstream of the Mini-Deverson rotor. Dashed line shows metal angle at rotor trailing edge.

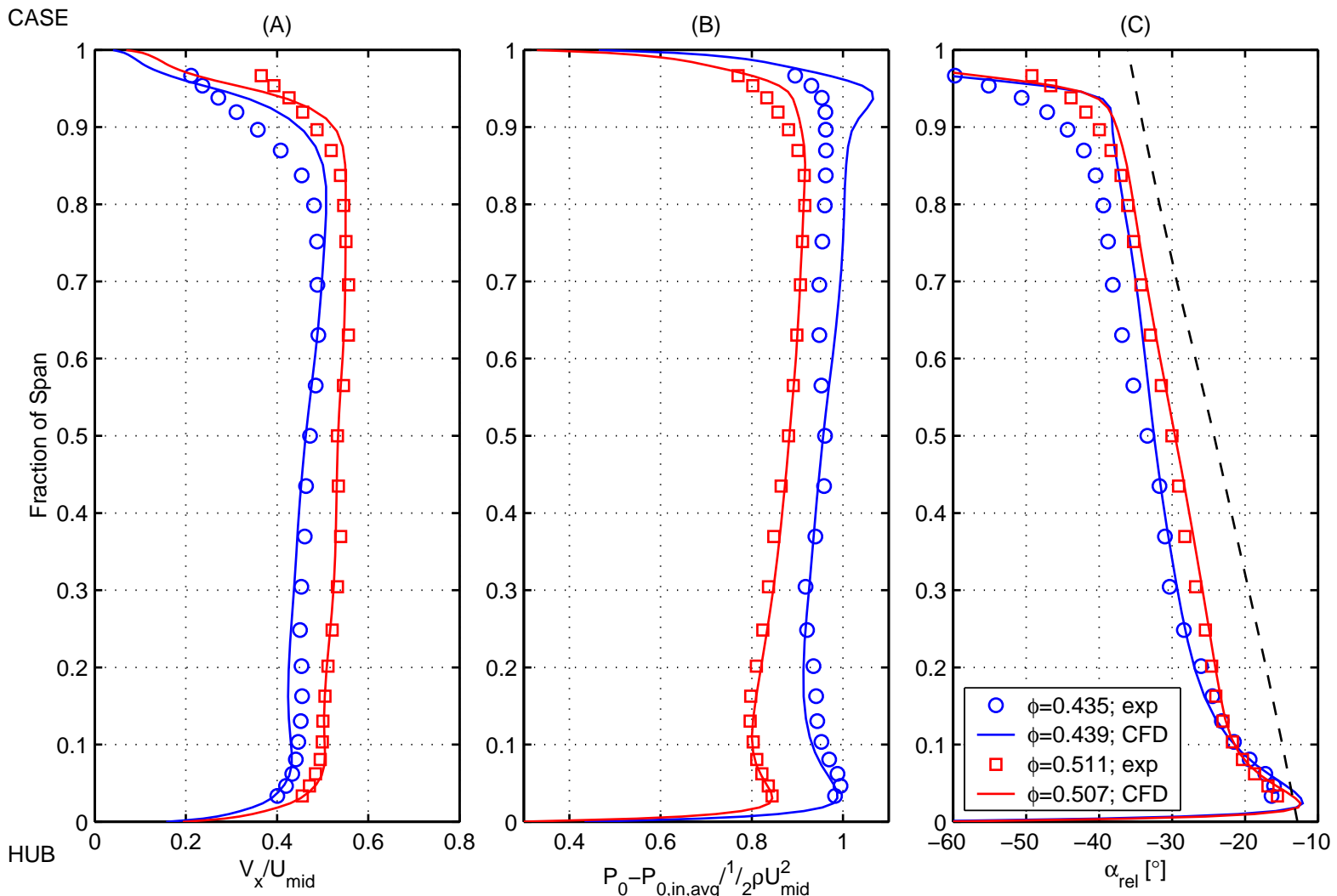


Figure 7.7: Comparison between measured and CFD predictions of radial profiles of (A) axial velocity, (B) stagnation pressure rise and (C) relative flow angle downstream of the **Gallimore** rotor. Dashed line shows metal angle at rotor trailing edge.

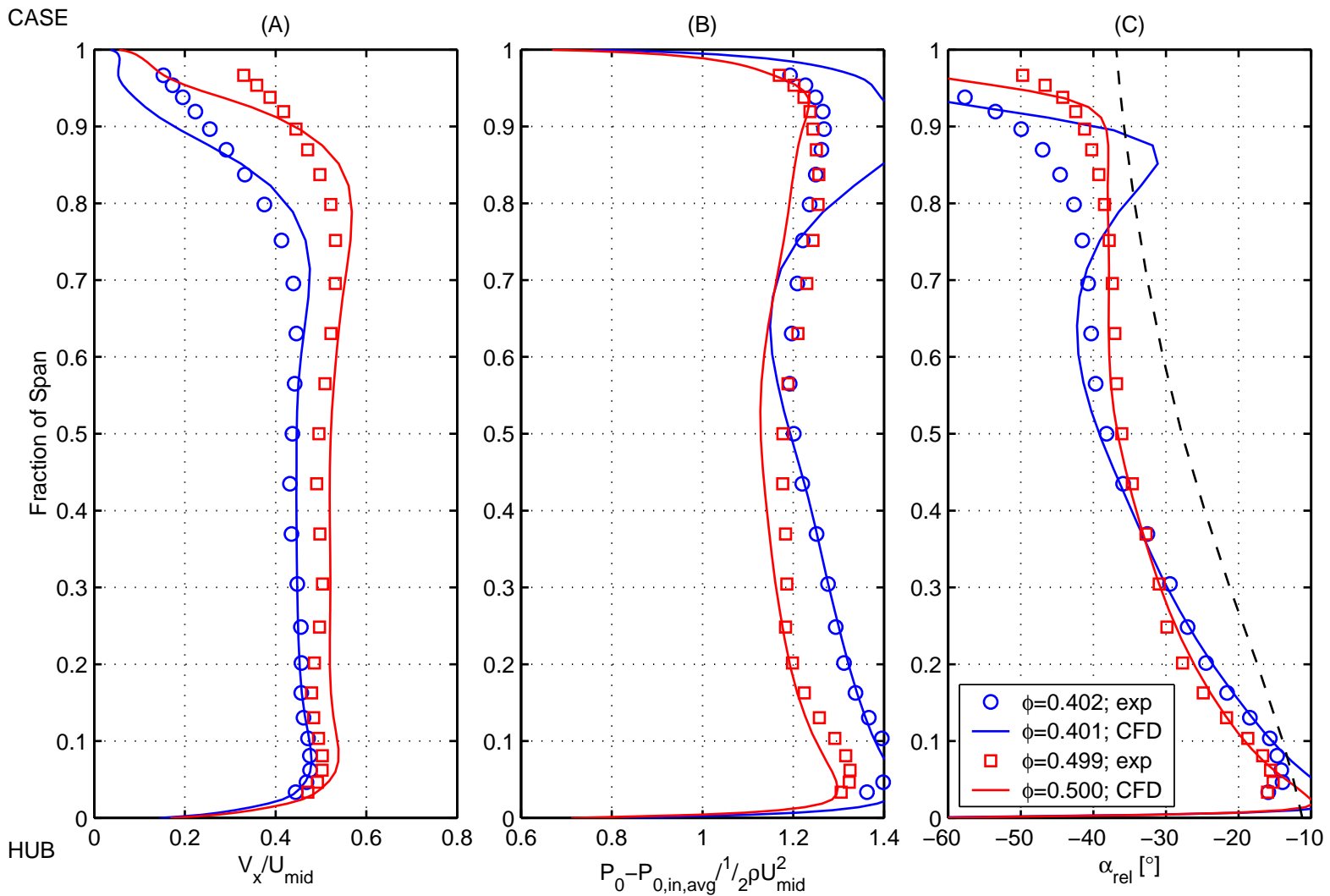


Figure 7.8: Comparison between measured and CFD predictions of radial profiles of (A) axial velocity, (B) stagnation pressure rise and (C) relative flow angle downstream of the **Qinetiq** rotor.

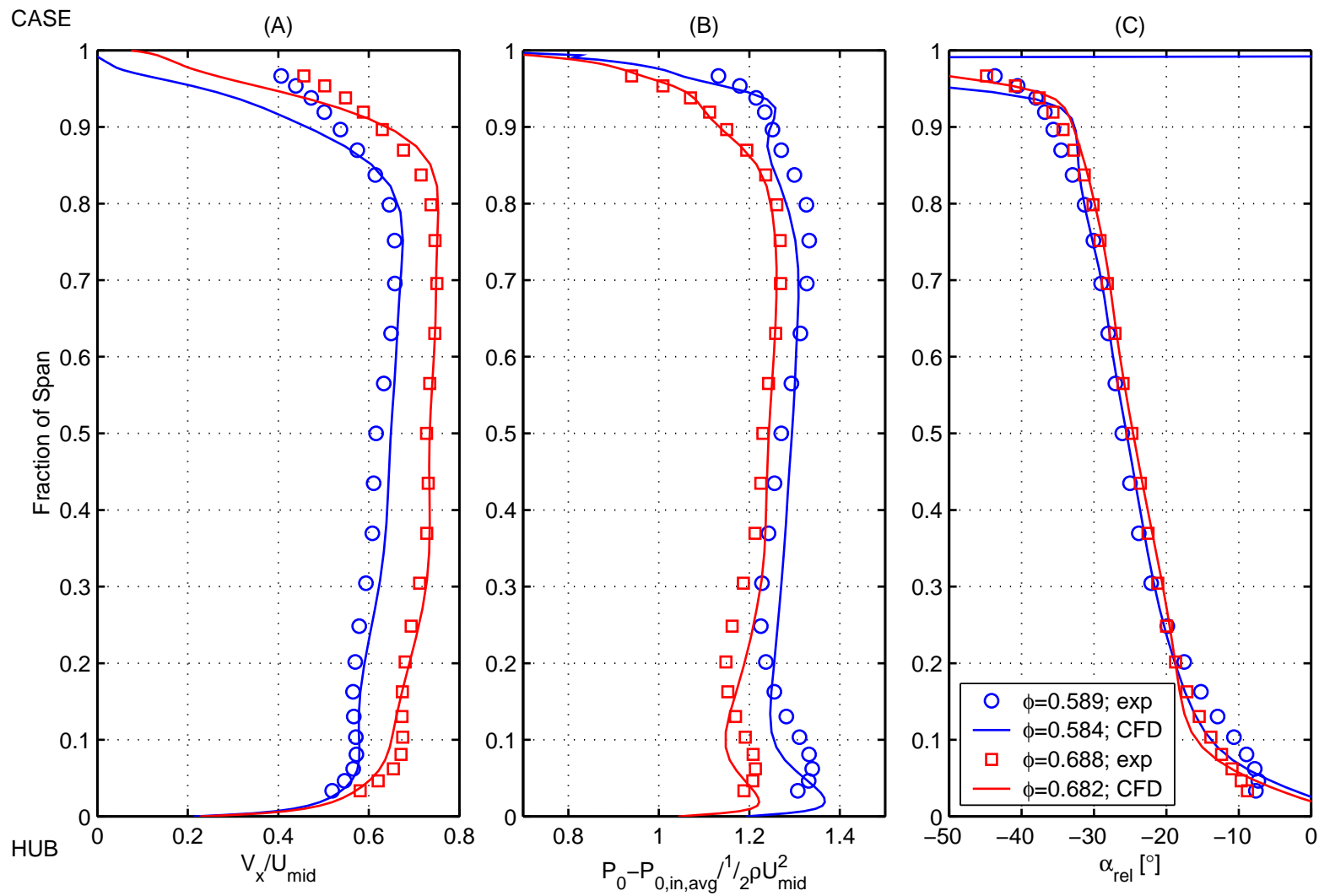
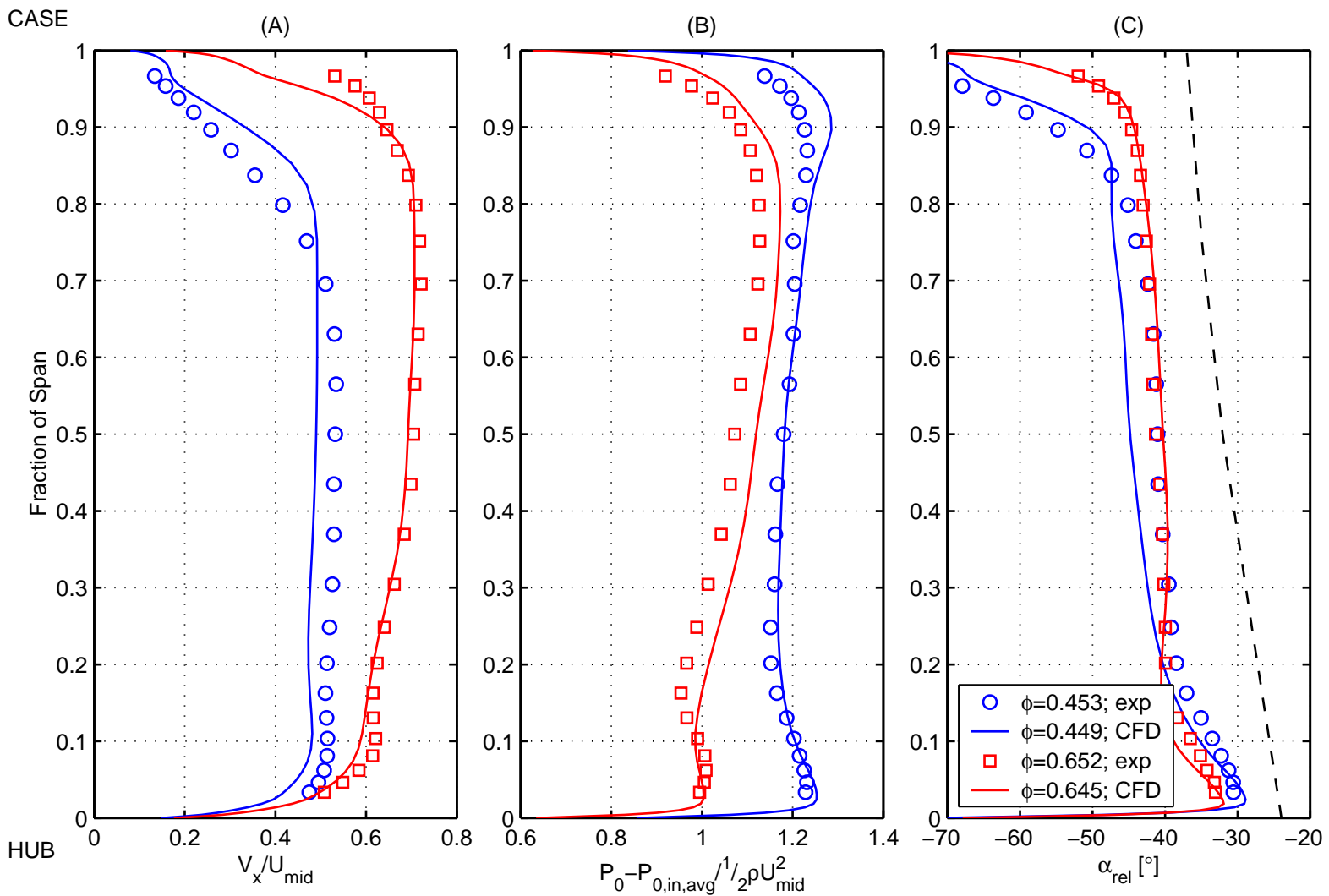


Figure 7.9: Comparison between measured and CFD predictions of radial profiles of (A) axial velocity, (B) stagnation pressure rise and (C) relative flow angle downstream of the Denton rotor. Dashed line shows metal angle at rotor trailing edge.



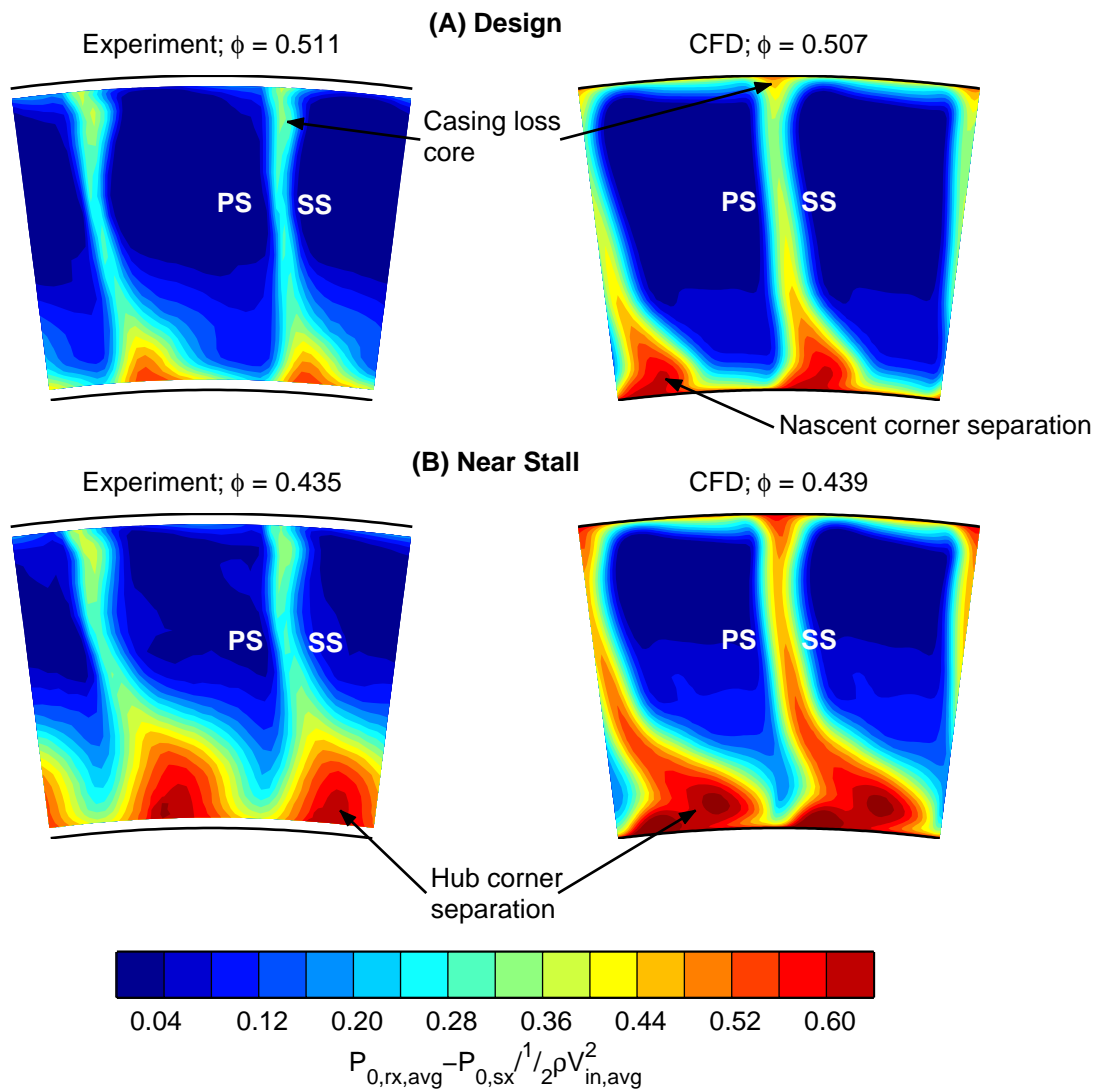


Figure 7.10: Comparison between measured and calculated stagnation pressure loss downstream of the **Mini-Deverson** stator at (A) design and (B) near stall operating points.

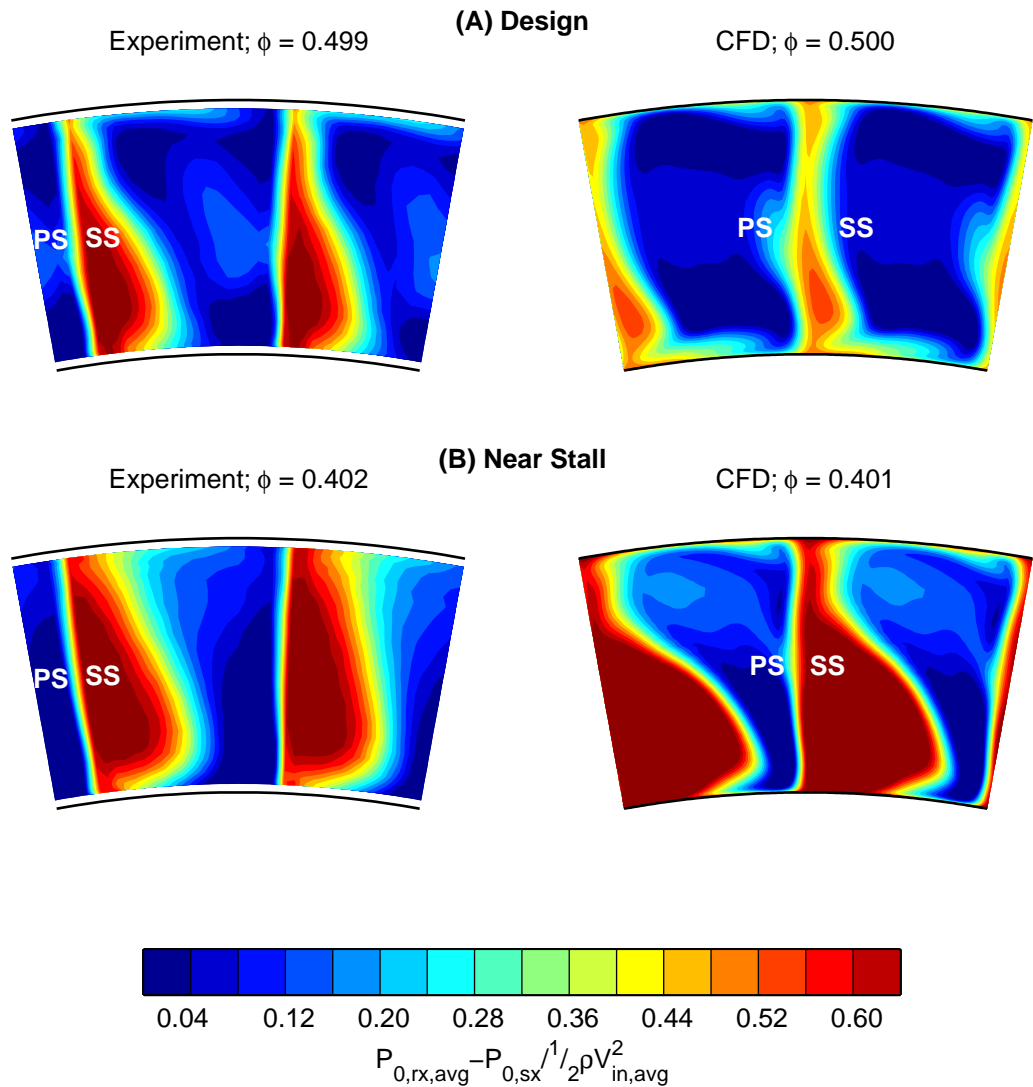


Figure 7.11: Comparison between measured and calculated stagnation pressure loss downstream of the **Gallimore** stator at (A) design and (B) near stall operating points.

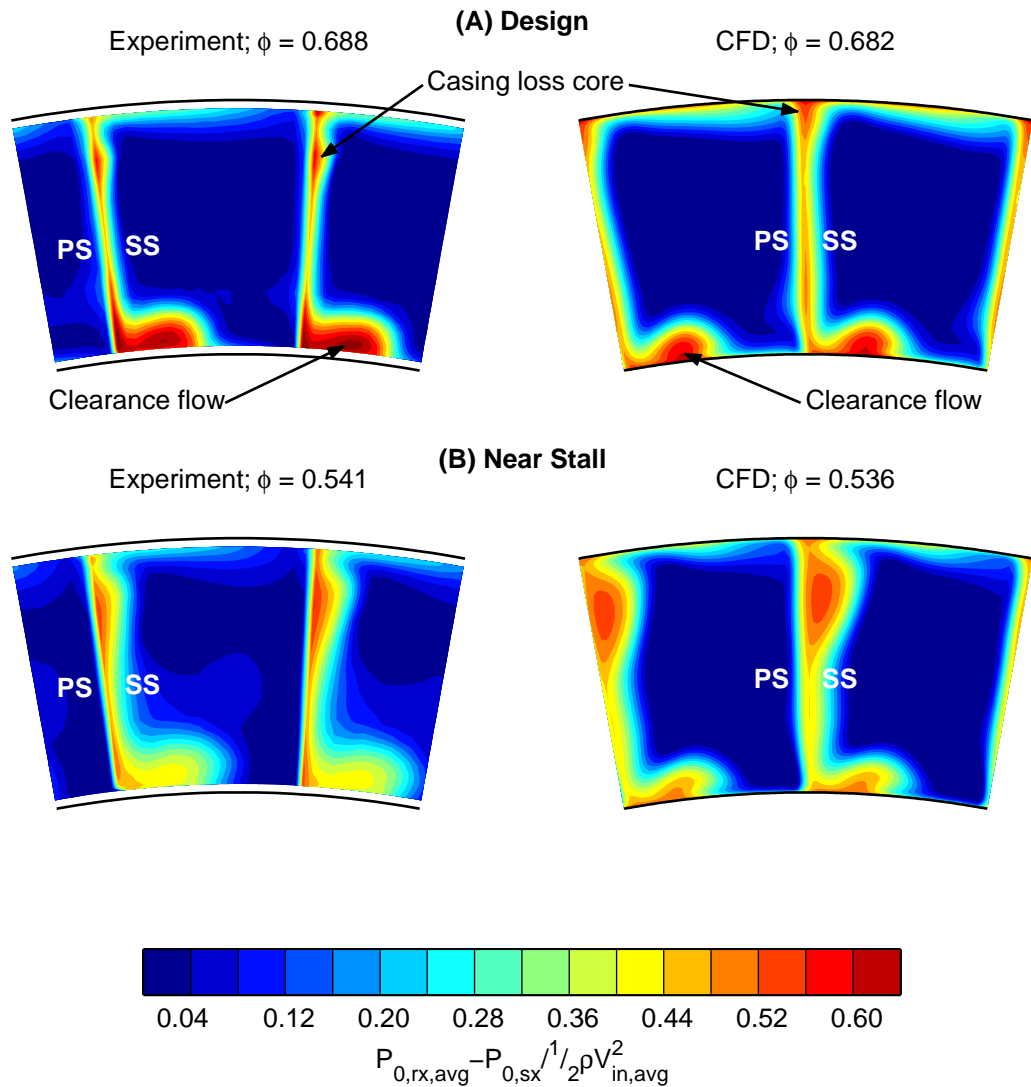


Figure 7.12: Comparison between measured and calculated stagnation pressure loss downstream of the **Qinetiq** stator at (A) design and (B) near stall operating points.

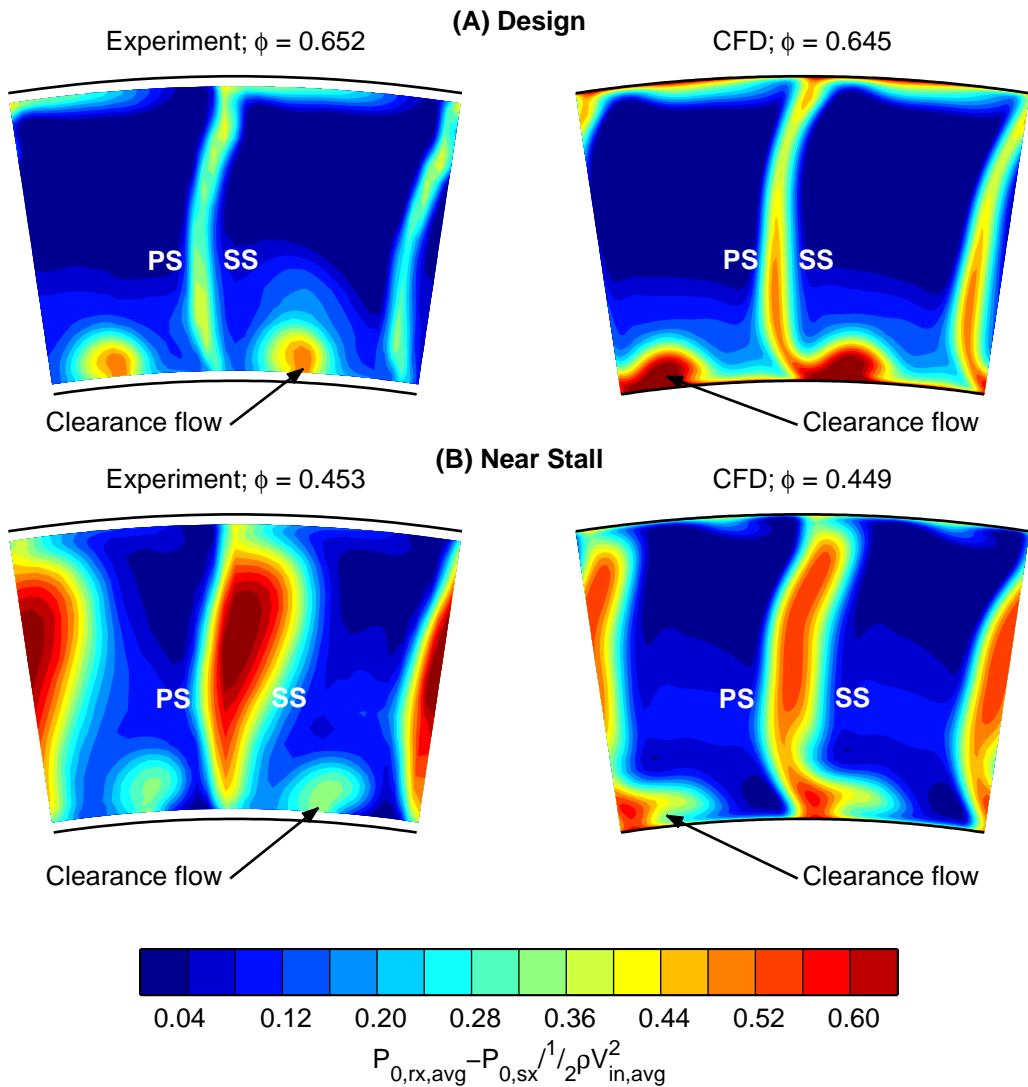


Figure 7.13: Comparison between measured and calculated stagnation pressure loss downstream of the **Denton** stator at (A) design and (B) near stall operating points.

Figure 7.14: Comparison between measured and CFD predictions of radial profiles of (A) axial velocity, (B) stagnation pressure rise and (C) relative flow angle downstream of the Mini-Deverson stator. Dashed line shows metal angle at rotor trailing edge.

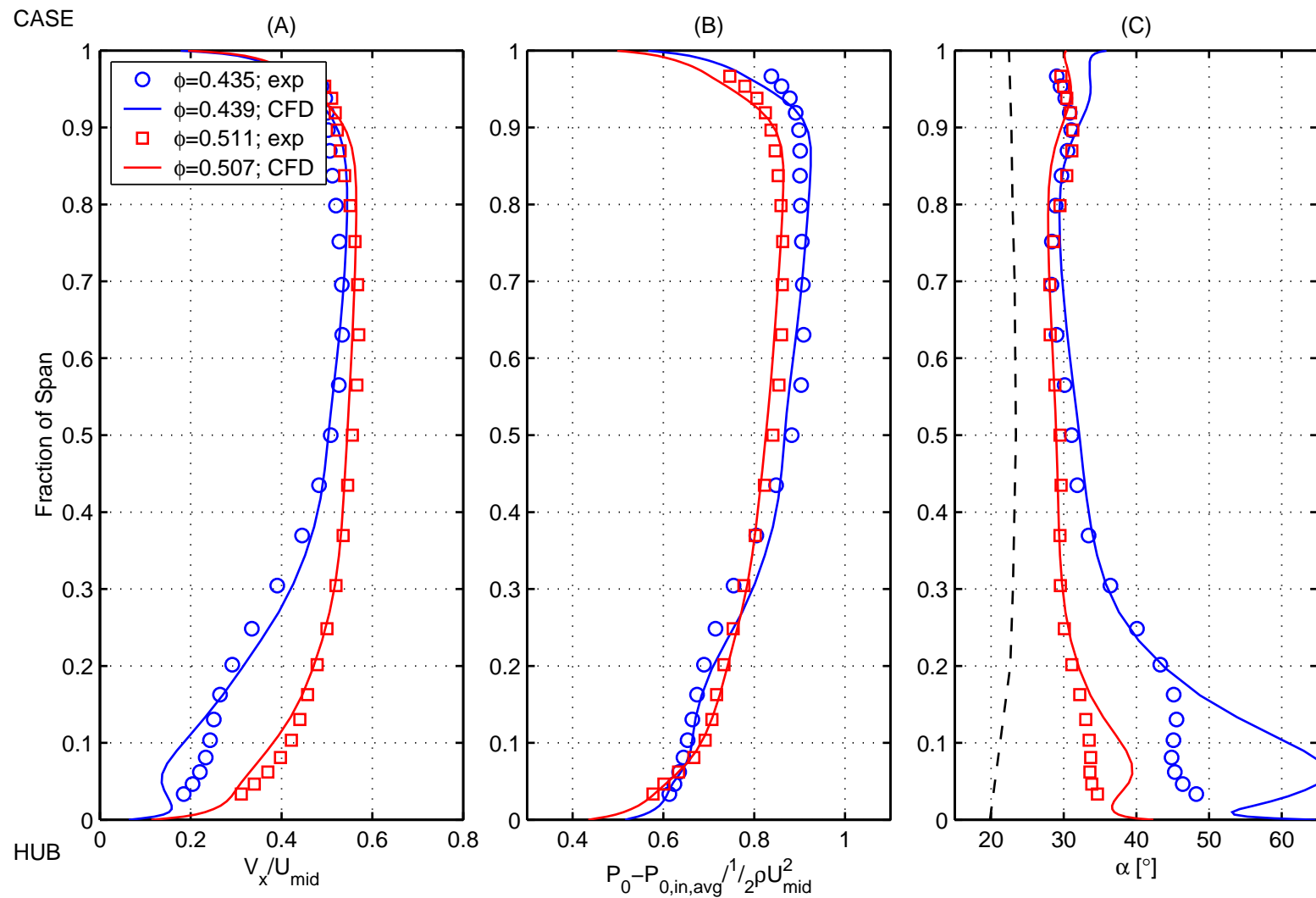


Figure 7.15: Comparison between measured and CFD predictions of radial profiles of (A) axial velocity, (B) stagnation pressure rise and (C) relative flow angle downstream of the Gallimore stator. Dashed line shows metal angle at rotor trailing edge.

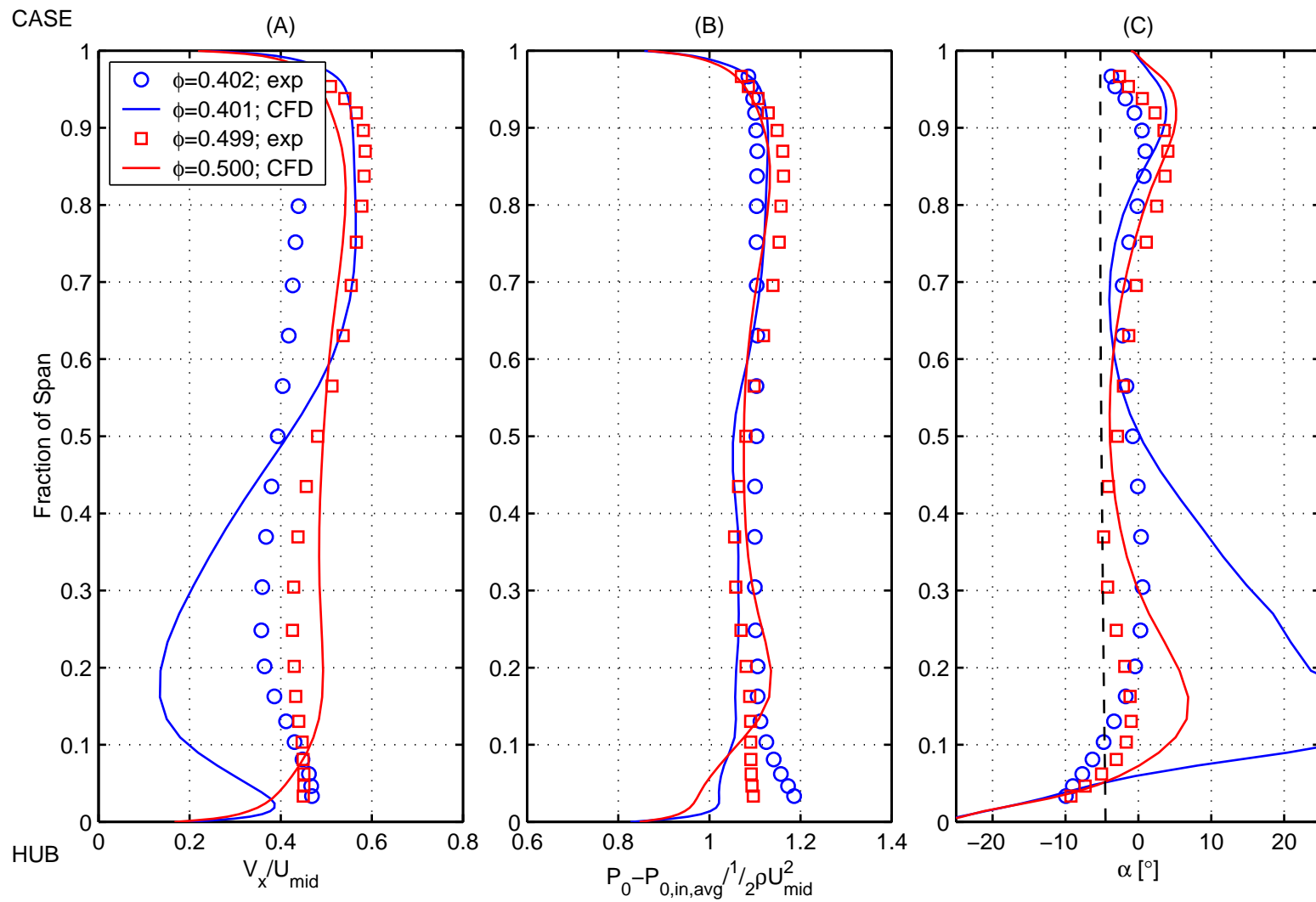


Figure 7.16: Comparison between measured and CFD predictions of radial profiles of (A) axial velocity, (B) stagnation pressure rise and (C) relative flow angle downstream of the **Qinetiq** stator. Dashed line shows metal angle at rotor trailing edge.

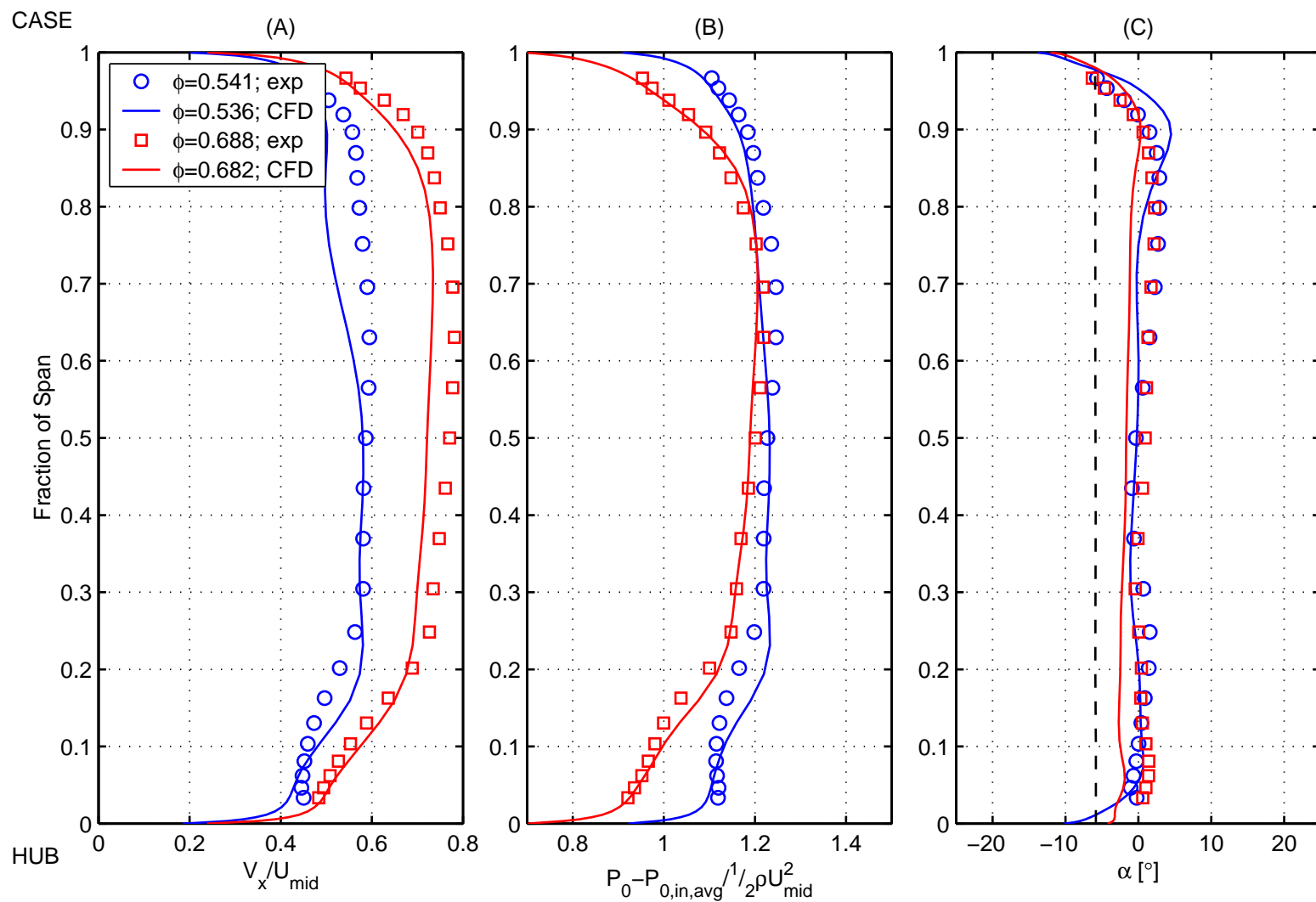
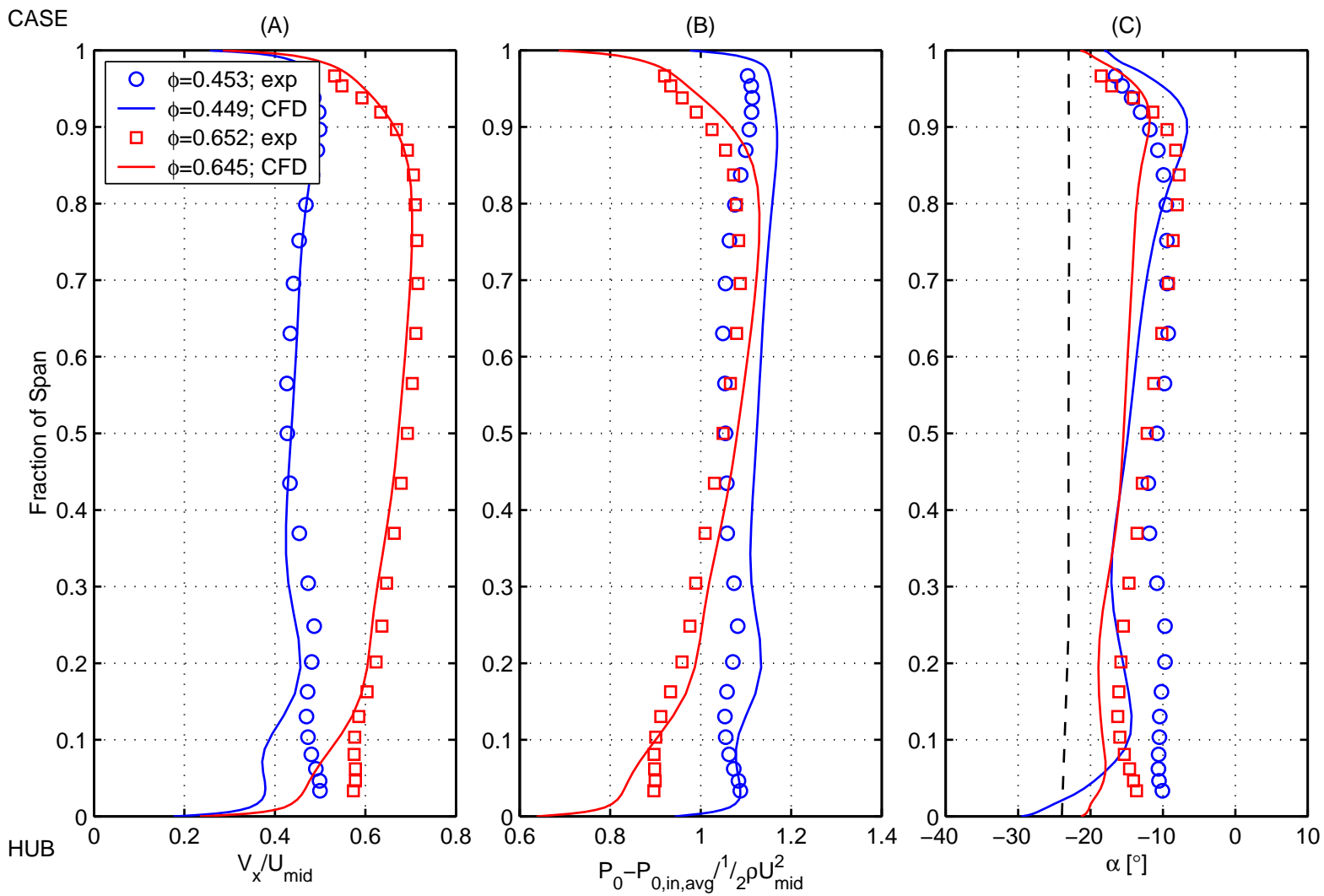


Figure 7.17: Comparison between measured and CFD predictions of radial profiles of (A) axial velocity, (B) stagnation pressure rise and (C) relative flow angle downstream of the Denton stator. Dashed line shows metal angle at rotor trailing edge.



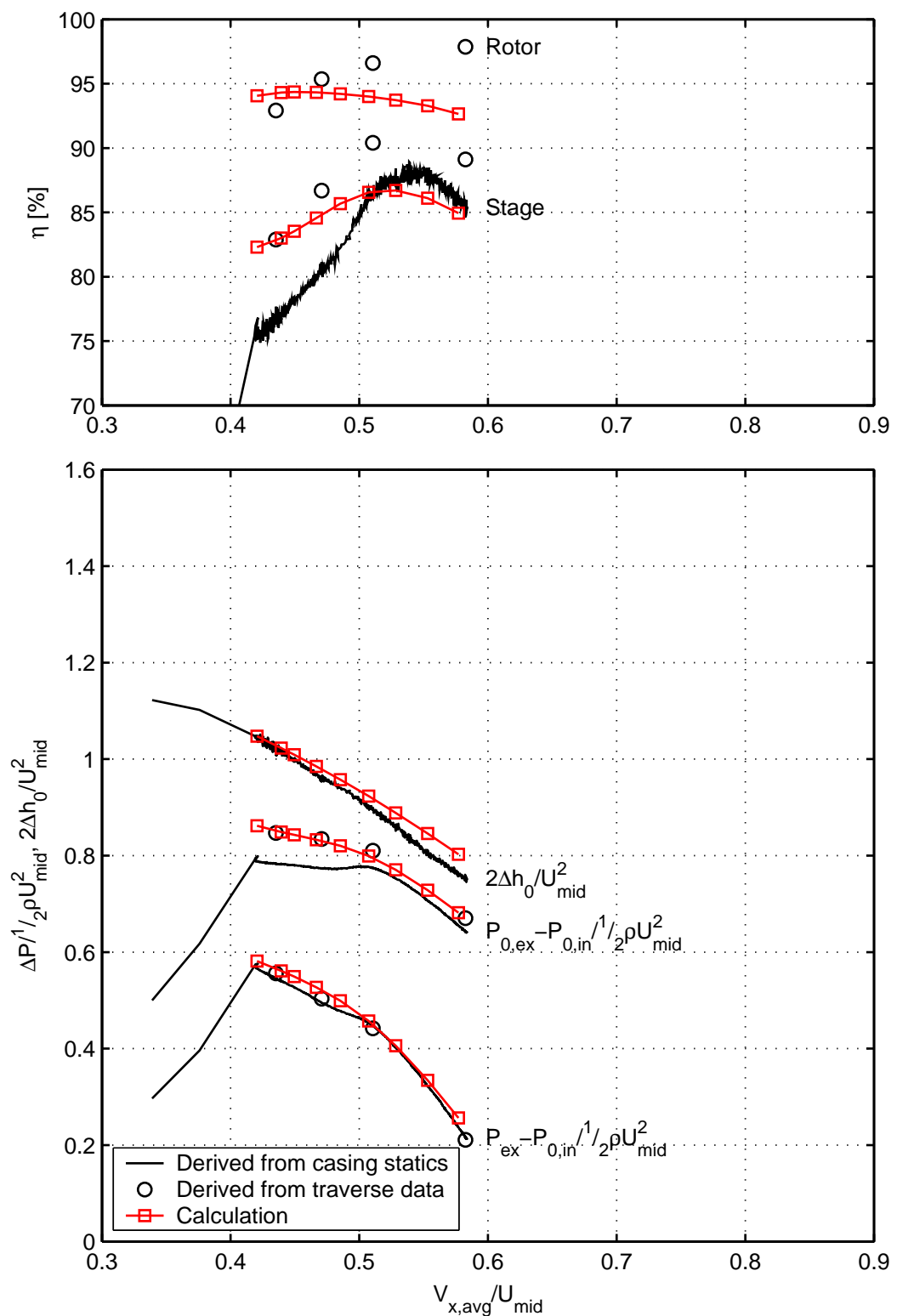


Figure 7.18: Comparison between measured and *MULTIP* predictions of pressure rise, torque and efficiency characteristics for the **Mini-Deverson** stage.

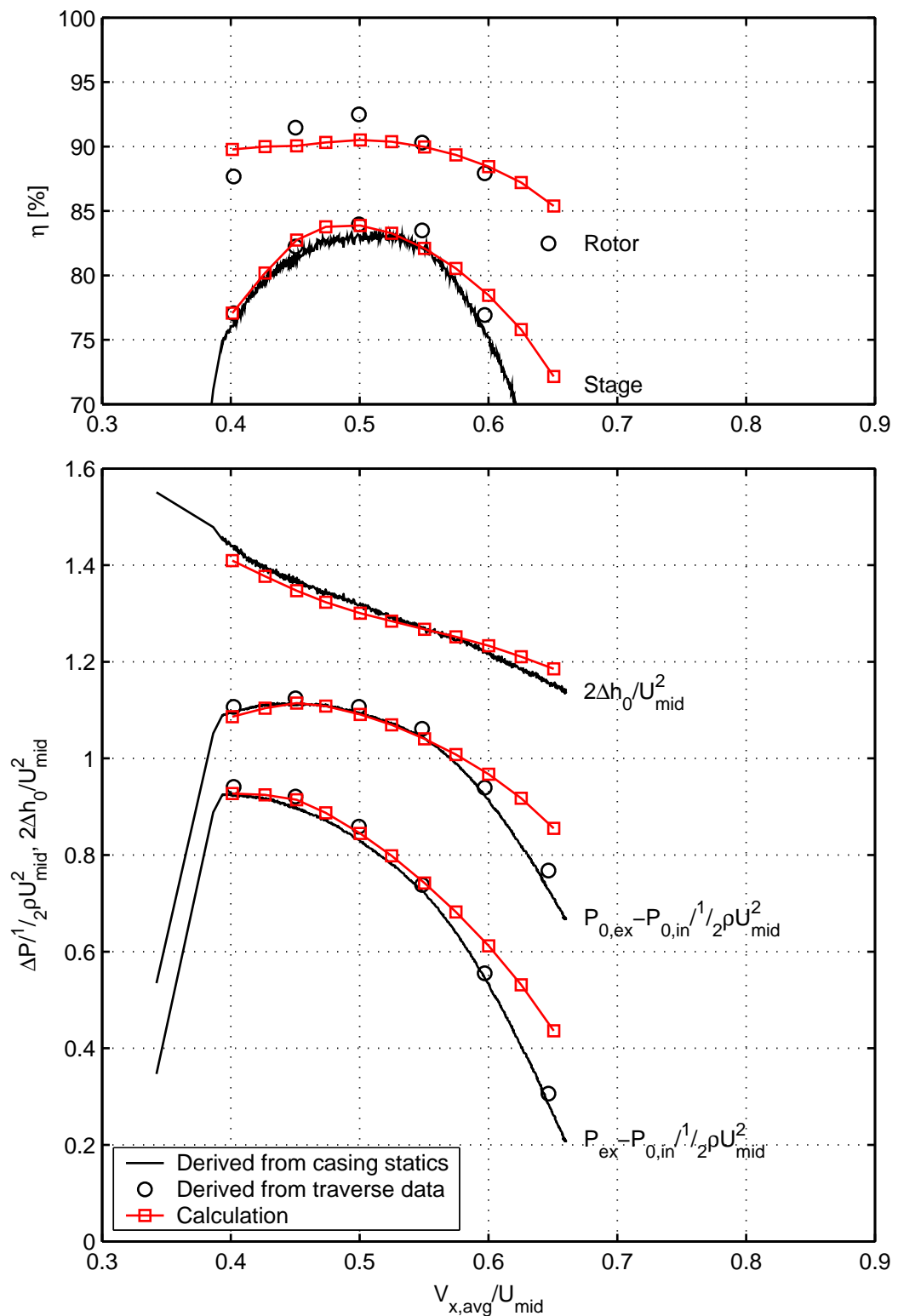


Figure 7.19: Comparison between measured and *MULTIP* predictions of pressure rise, torque and efficiency characteristics for the **Gallimore** stage.

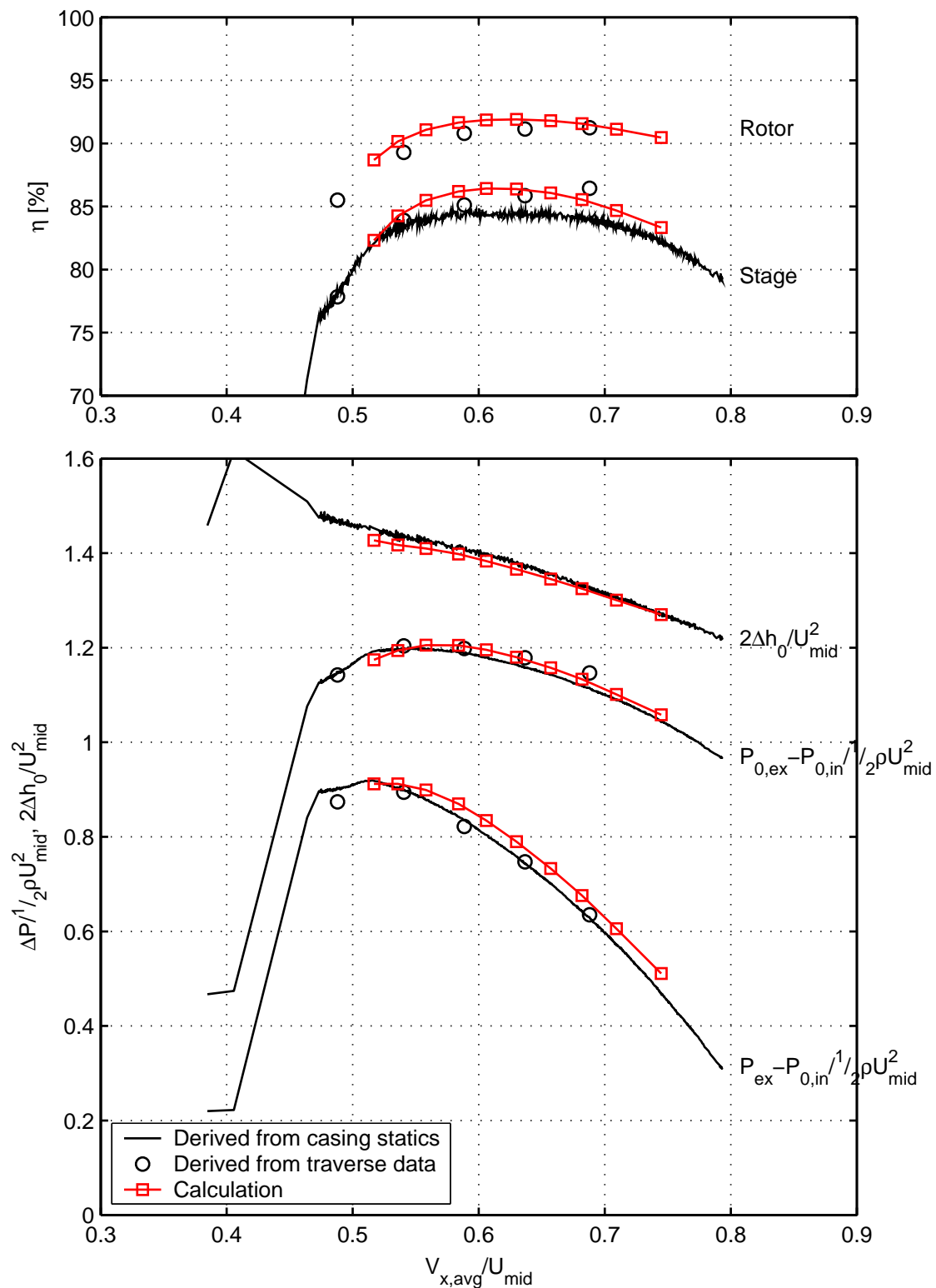


Figure 7.20: Comparison between measured and *MULTIP* predictions of pressure rise, torque and efficiency characteristics for the **Qinetiq** stage.

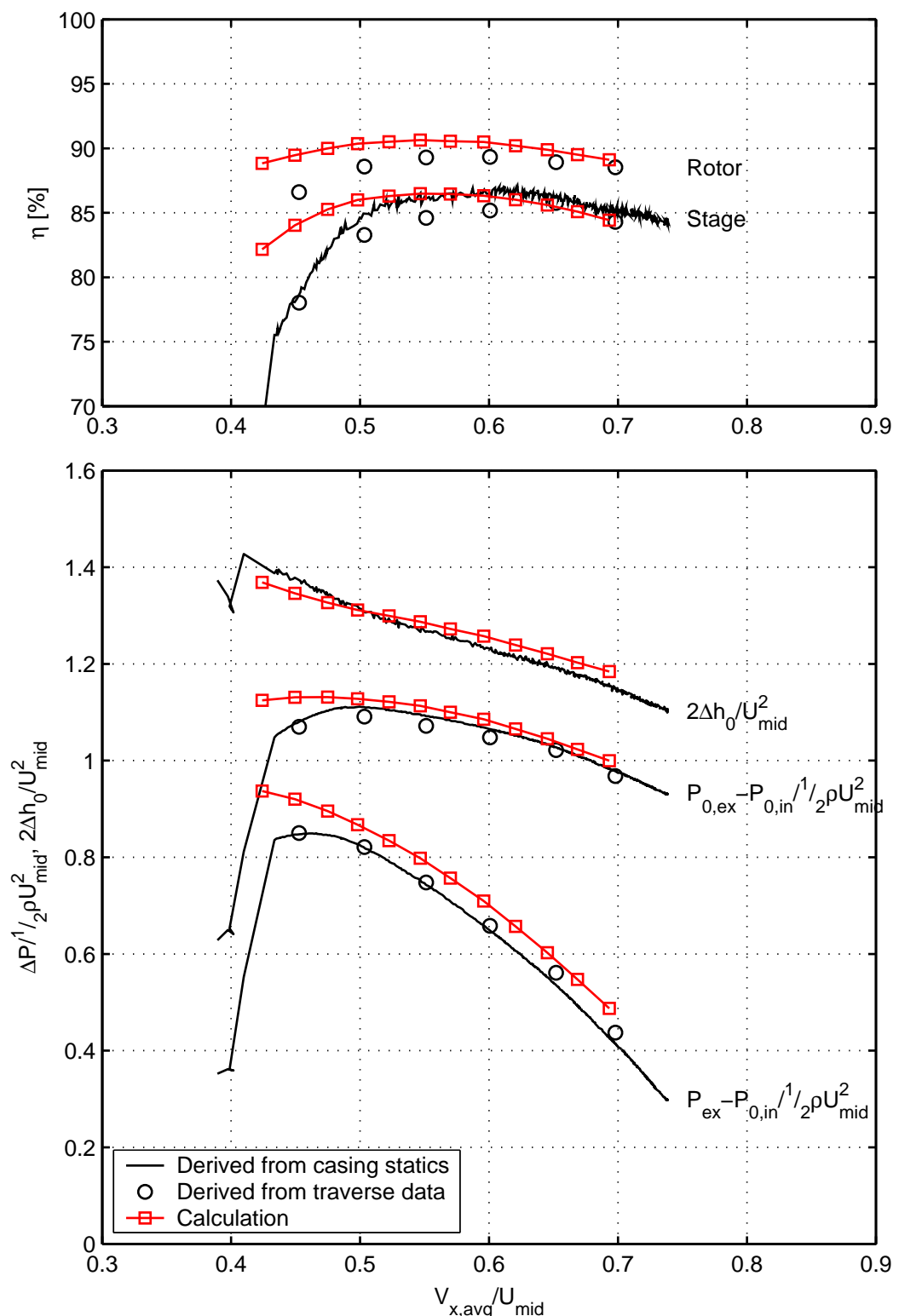


Figure 7.21: Comparison between measured and *MULTIP* predictions of pressure rise, torque and efficiency characteristics for the **Denton** stage.

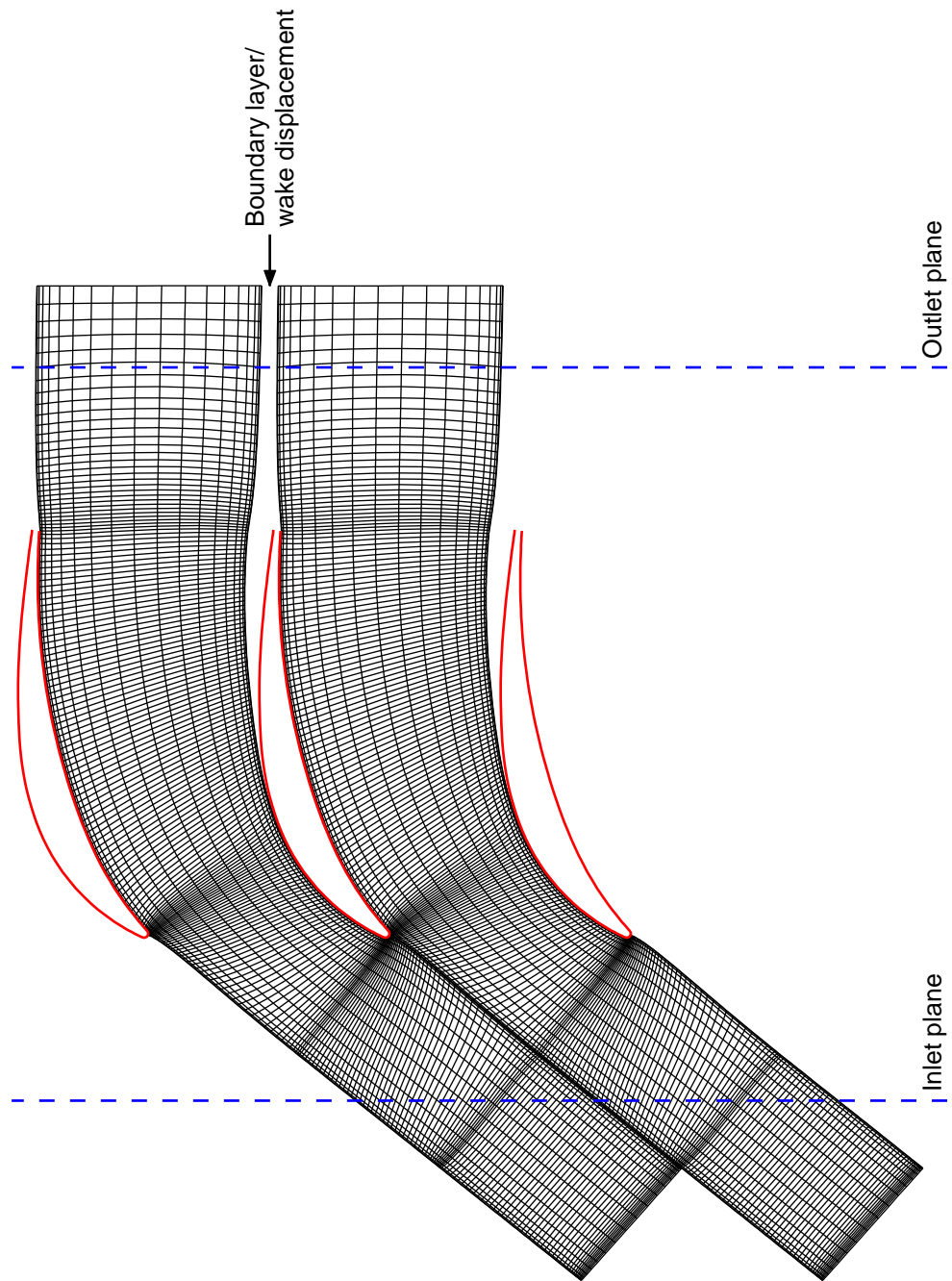


Figure 7.22: A typical *MISES* grid. Qinetiq stator mid-section shown at $\bar{\phi} = 0.535$.

Figure 7.23: Comparison between measured deviation against *MISES* predictions for the stator mid-span section. N.B. Solid symbols denote design point.

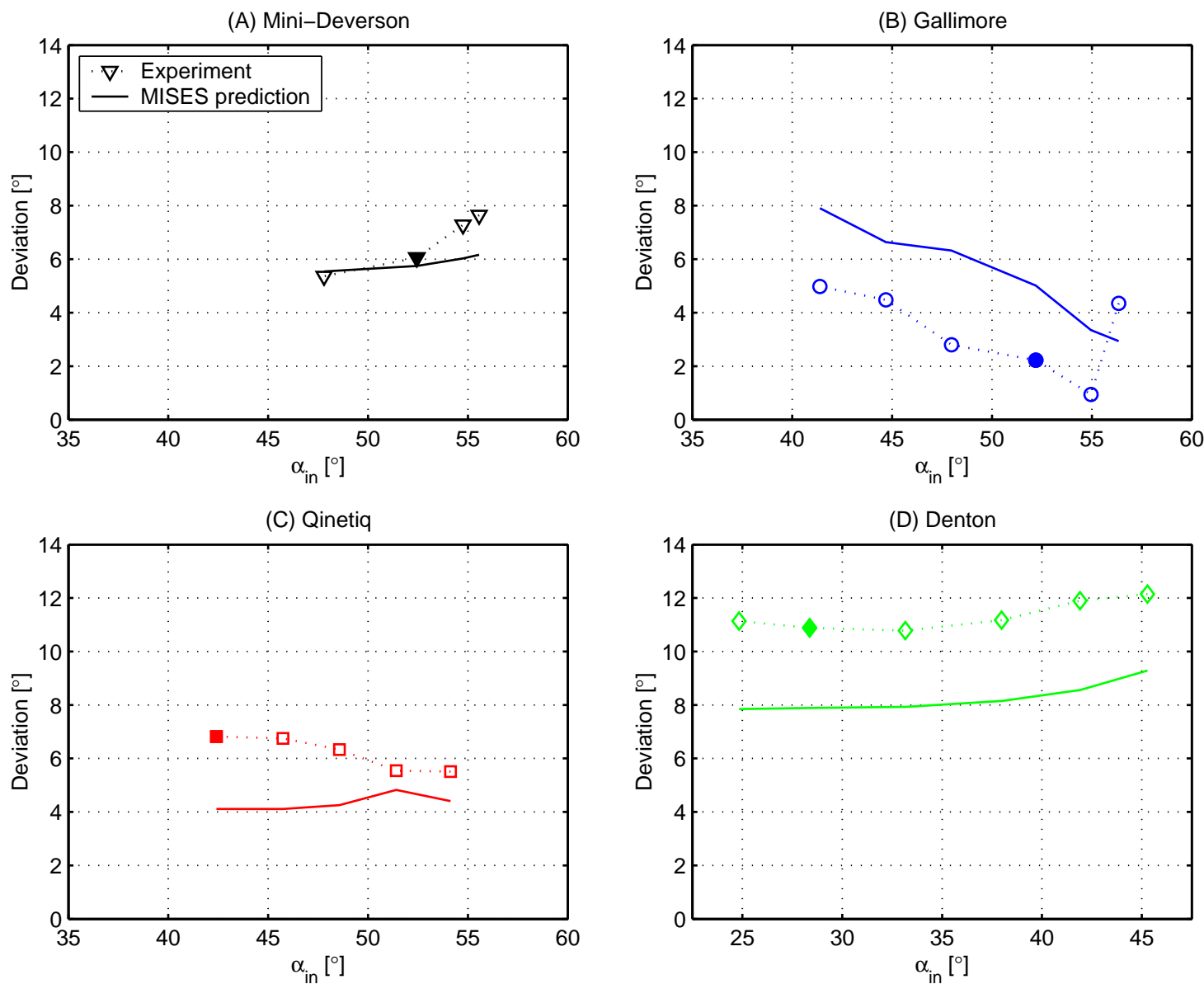
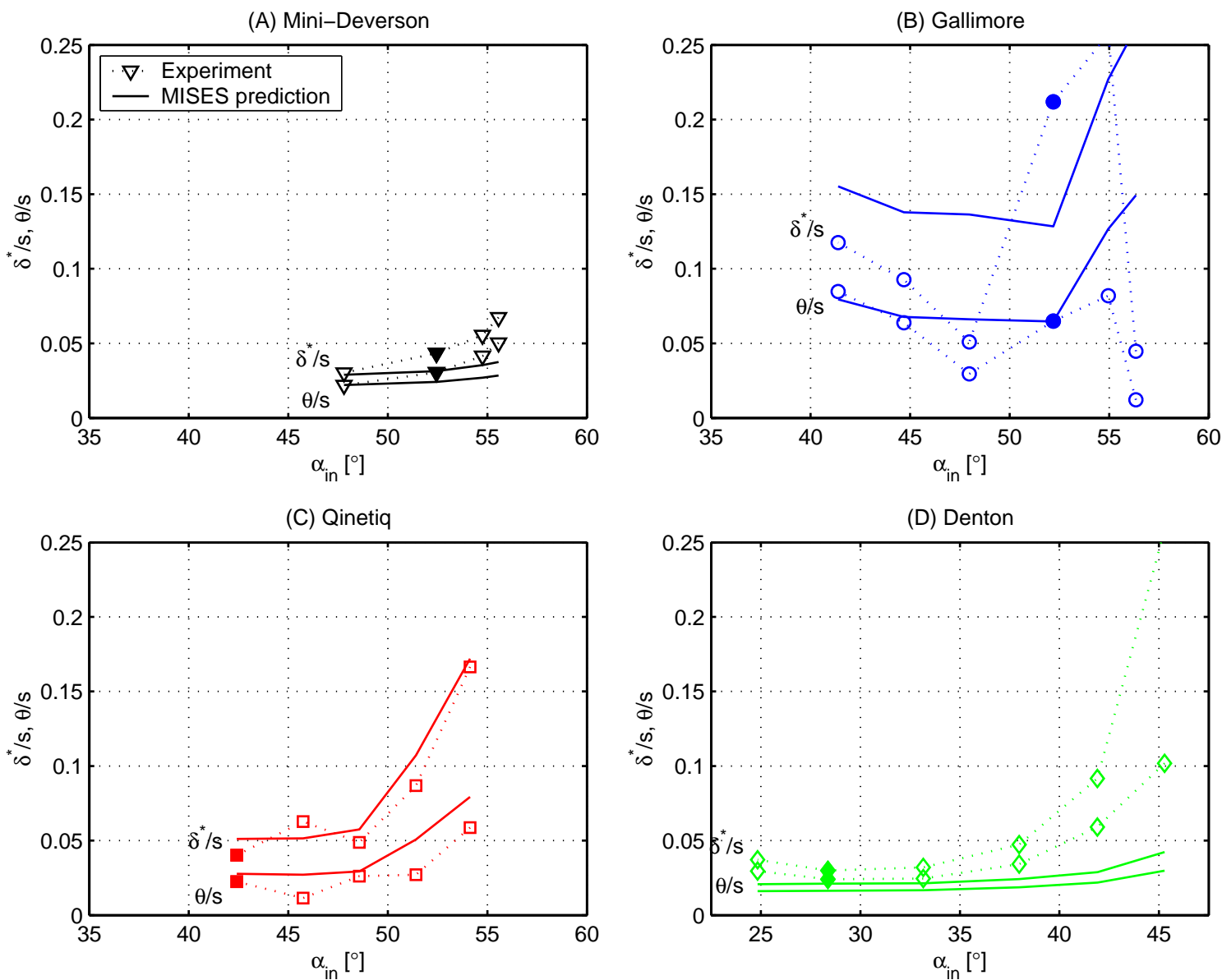


Figure 7.24: Comparison between measured integral wake parameters against *MISES* predictions for the stator mid-span section. N.B. Solid symbols denote design point.



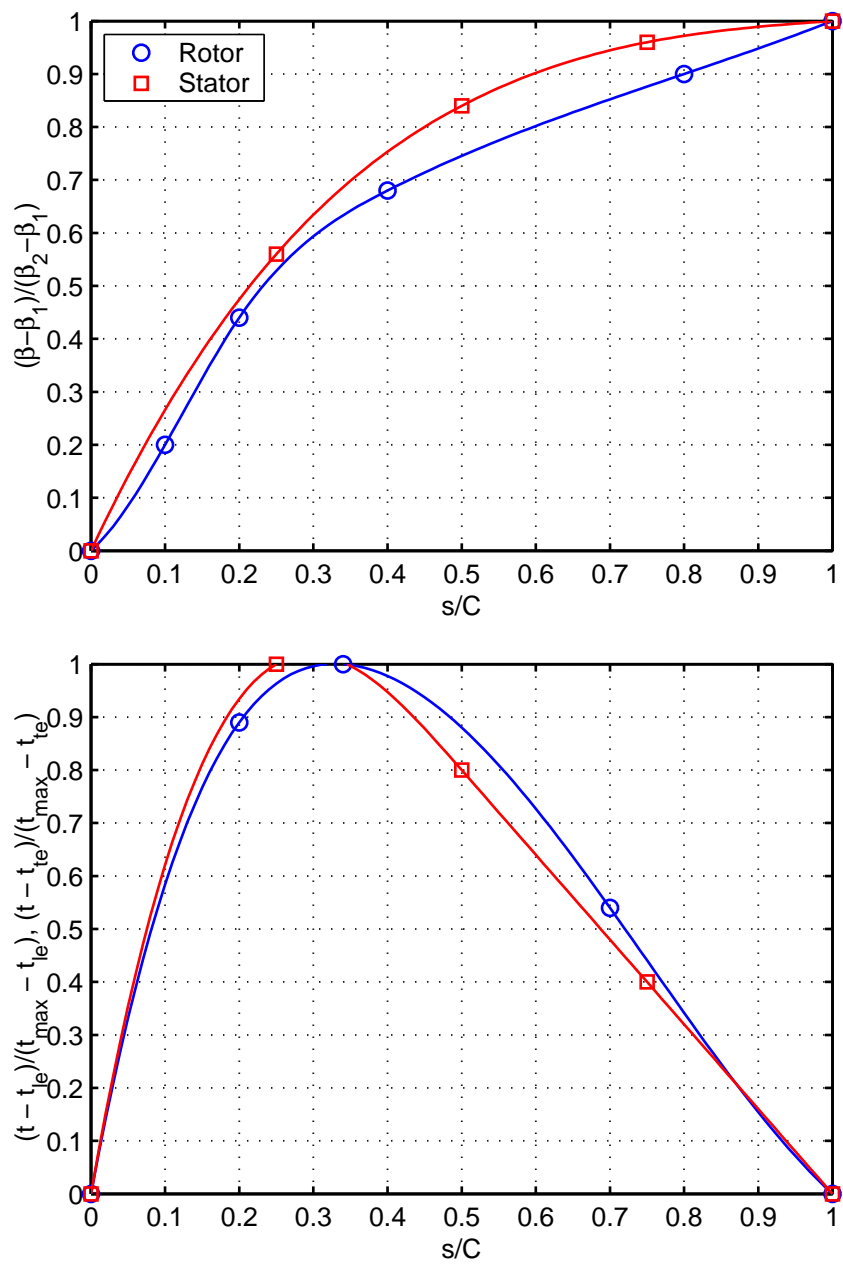


Figure 8.1: Non-dimensional (A) camber and (B) thickness distributions used in the rotor and stator design exercise. Symbols denote spline control points.

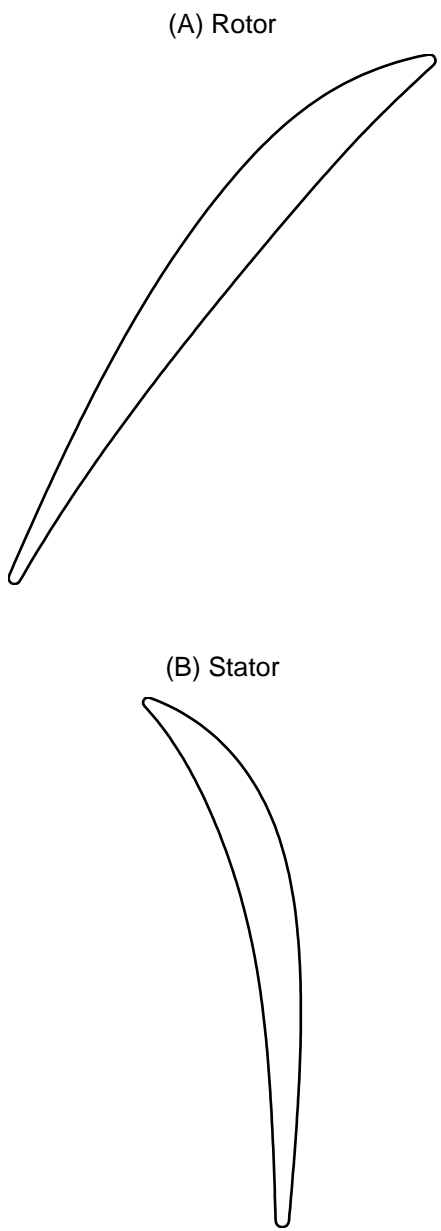


Figure 8.2: (A) Rotor and (B) stator mid-span sections ($\frac{\Delta h_0}{U_{mid}^2} = 0.65$ & $\alpha_{in} = 0^\circ$).

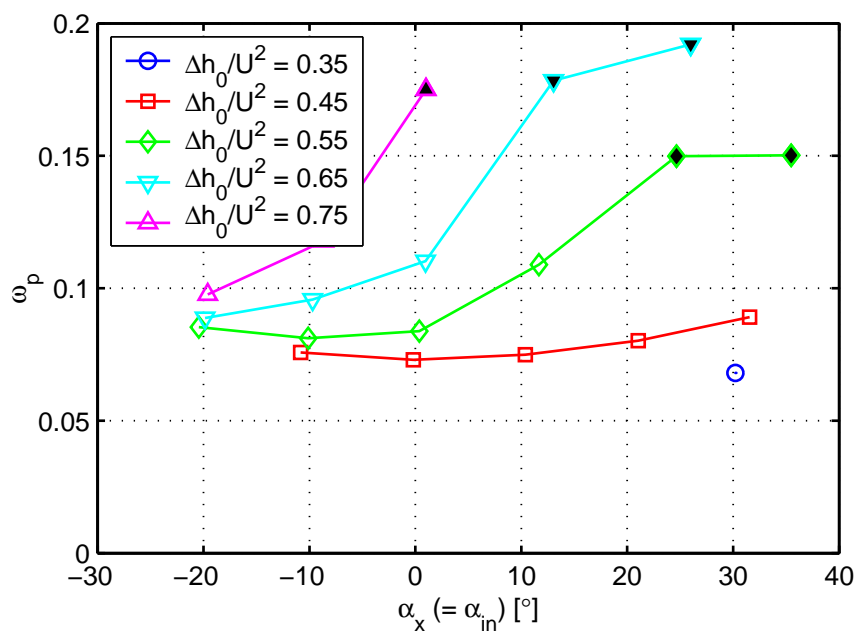


Figure 8.3: Effect of stage loading and stage inlet flow angle (recall in a repeating stage $\alpha_{in} = \alpha_x$) on stator stagnation pressure loss coefficient. Shaded symbols denote the presence of large three-dimensional separations.

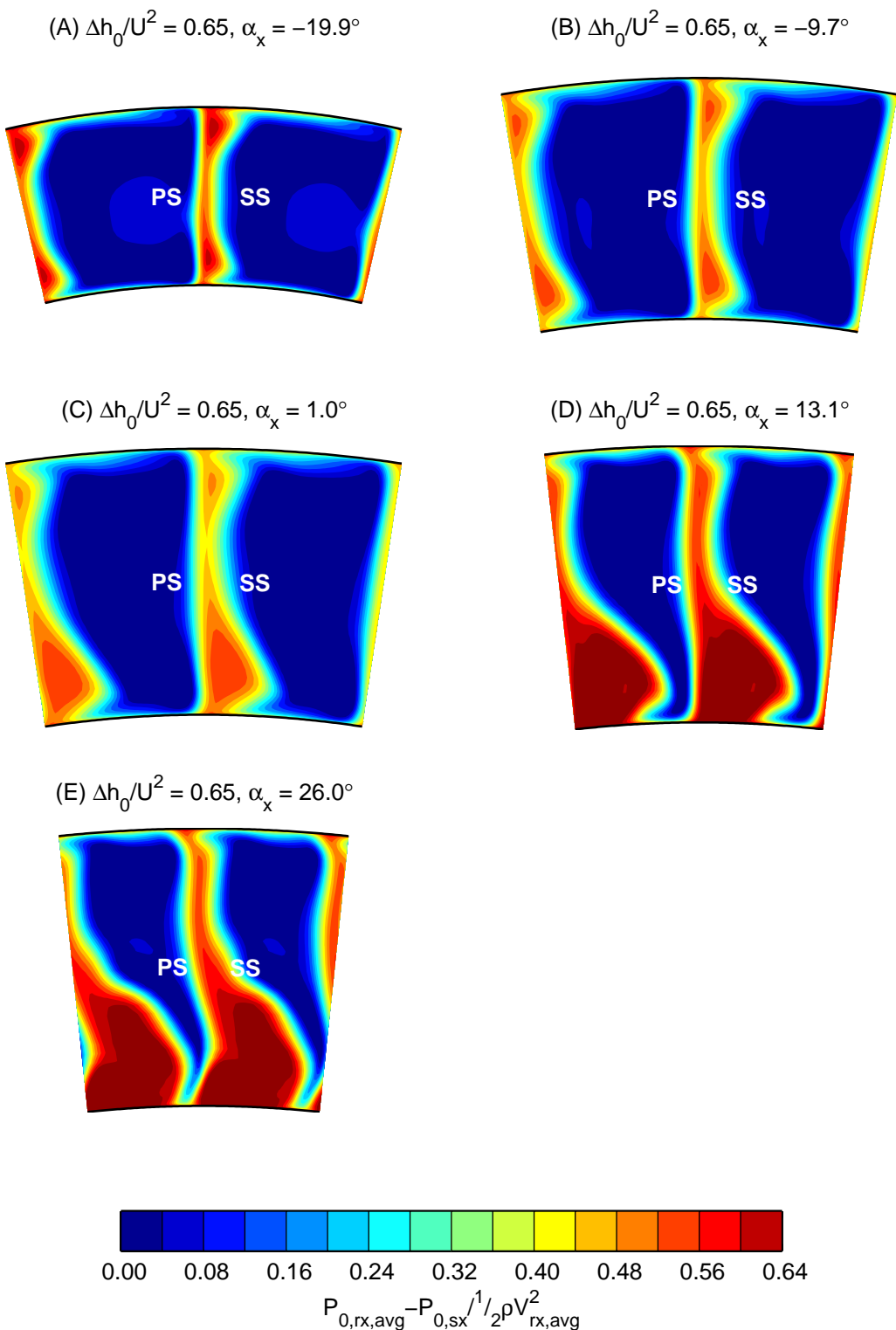


Figure 8.4: Effect of inlet angle on stator exit stagnation pressure for a stator of stage loading equal to 0.65.

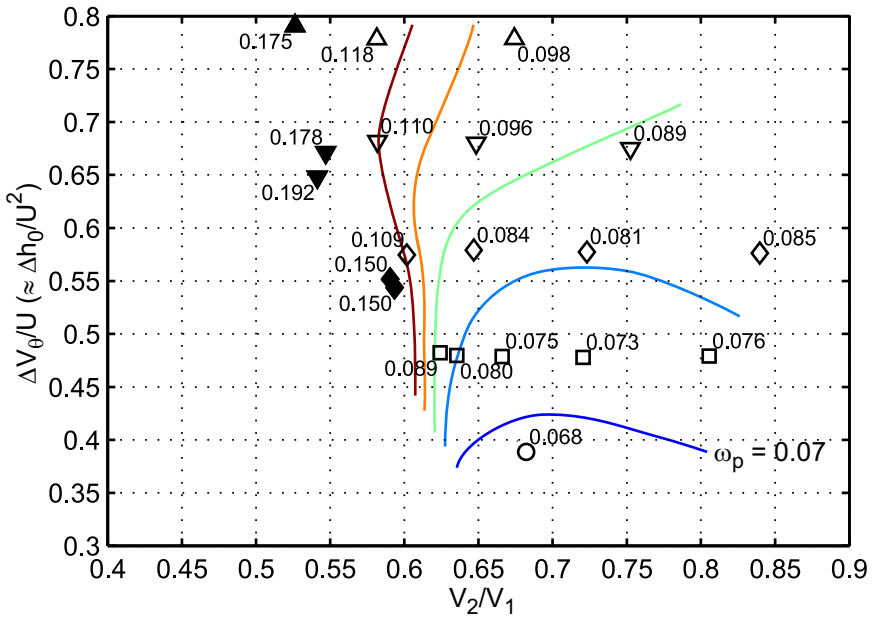


Figure 8.5: The effect of stator loading ($\frac{\Delta V_\theta}{U} \approx \frac{\Delta h_0}{U^2}$) and de Haller number ($\frac{V_2}{V_1}$) on stator loss coefficient (ω_p). Solid lines denote approximate contours of stator loss coefficient (interval = 0.01). Shaded symbols denote the presence of large three-dimensional separations.

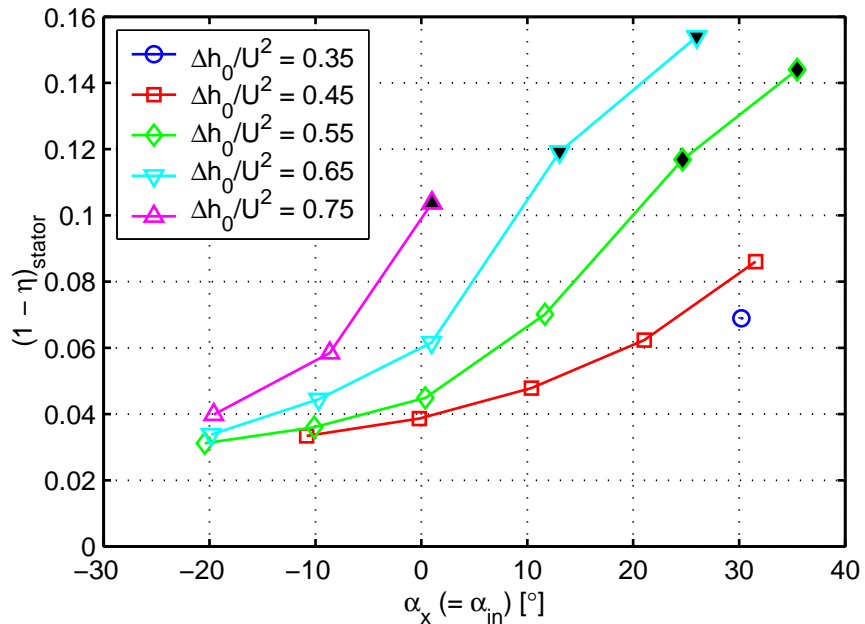


Figure 8.6: Effect of stator loading and stage inlet flow angle (recall in a repeating stage $\alpha_{in} = \alpha_x$) on stator lost efficiency. Shaded symbols denote the presence of large three-dimensional separations.

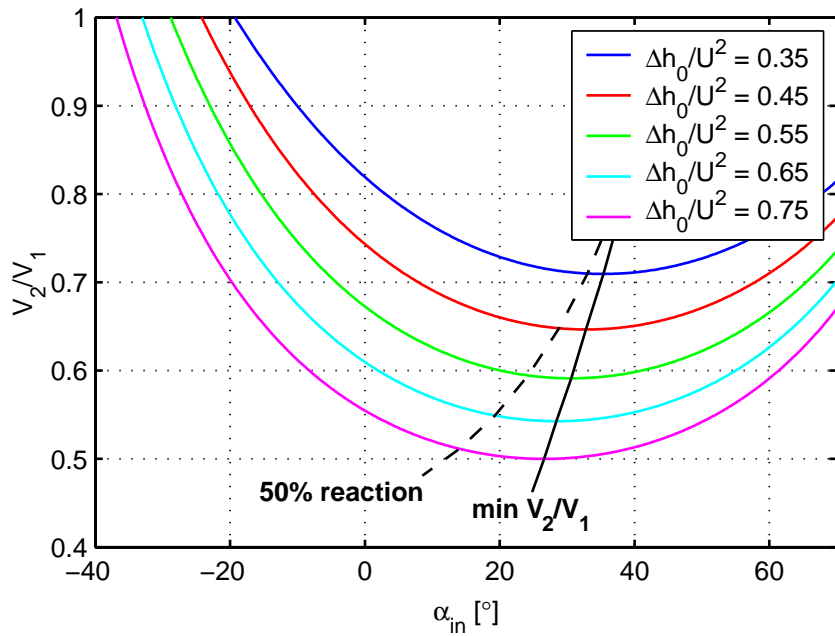


Figure 8.7: Velocity triangle calculations showing the effect of loading ($\frac{\Delta h_0}{U^2}$) and inlet flow angle ($\alpha_{in} = \alpha_x$) on stator de Haller number. Locus of minimum de Haller number and 50% reaction marked with solid and dashed black lines respectively.

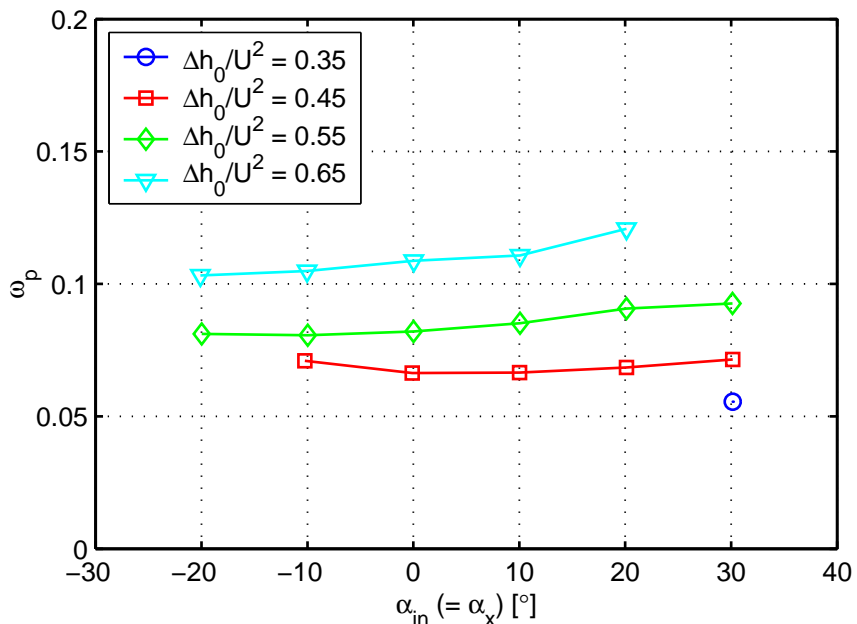


Figure 8.8: Effect of stage loading and inlet flow angle (recall in a repeating stage $\alpha_{in} = \alpha_x$) on predicted rotor stagnation pressure loss coefficient.

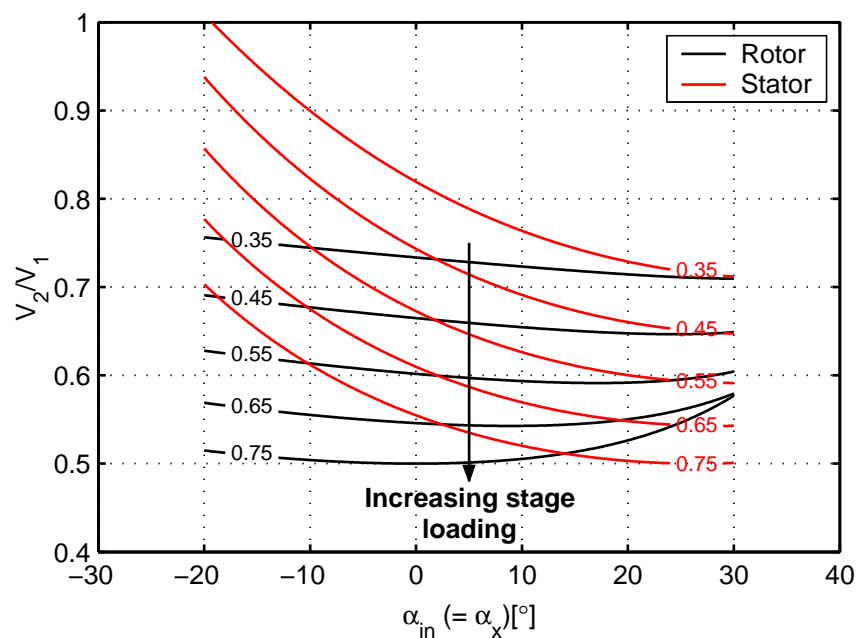


Figure 8.9: Velocity triangle calculations showing the effect of inlet flow angle on rotor and stator de Haller numbers along lines of constant stage loading coefficient.

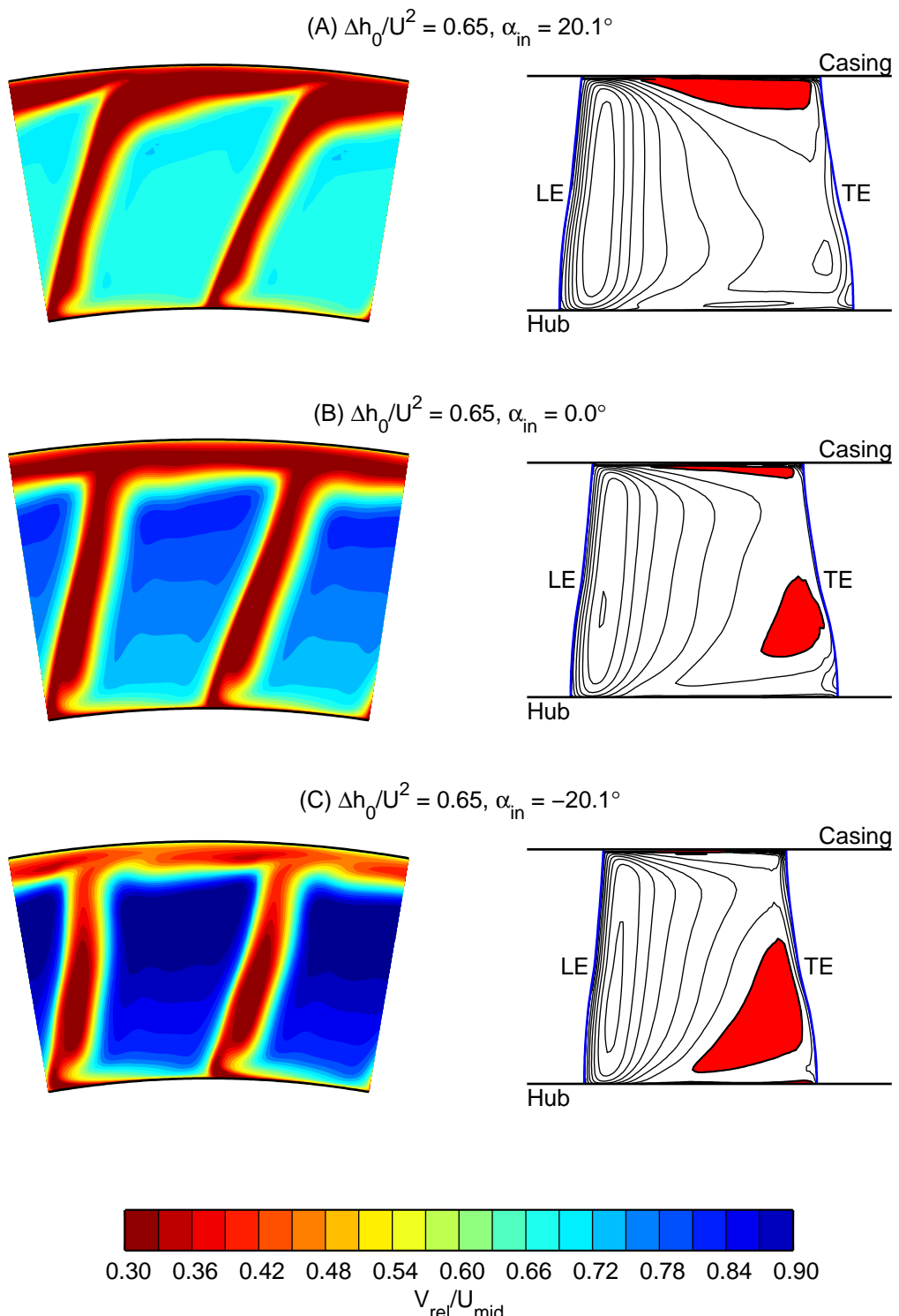


Figure 8.10: Effect of inlet flow angle on contours of relative velocity (left) and suction surface axial velocity (right). Separated regions highlighted in red.

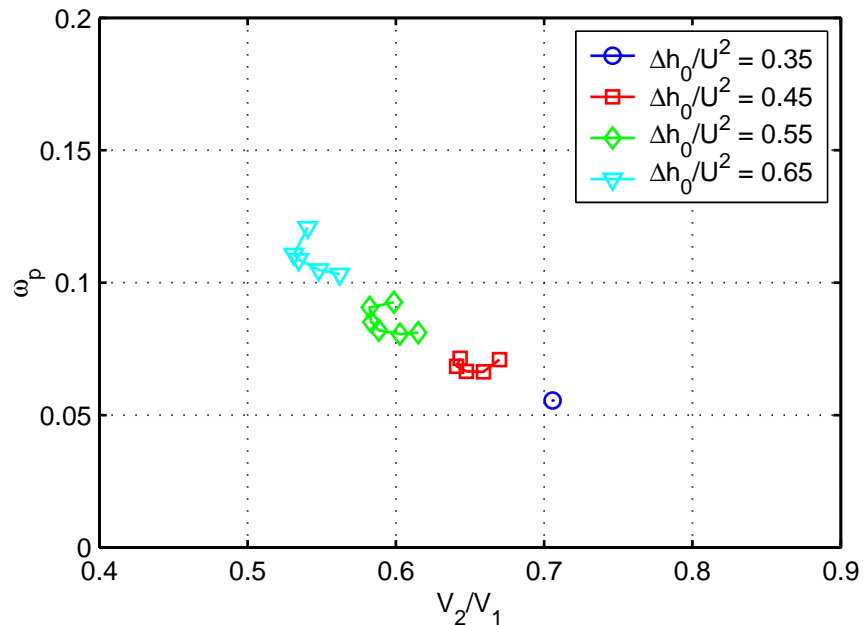


Figure 8.11: The effect of de Haller number ($\frac{V_{2,rel}}{V_{1,rel}}$) on rotor loss coefficient (ω_p).

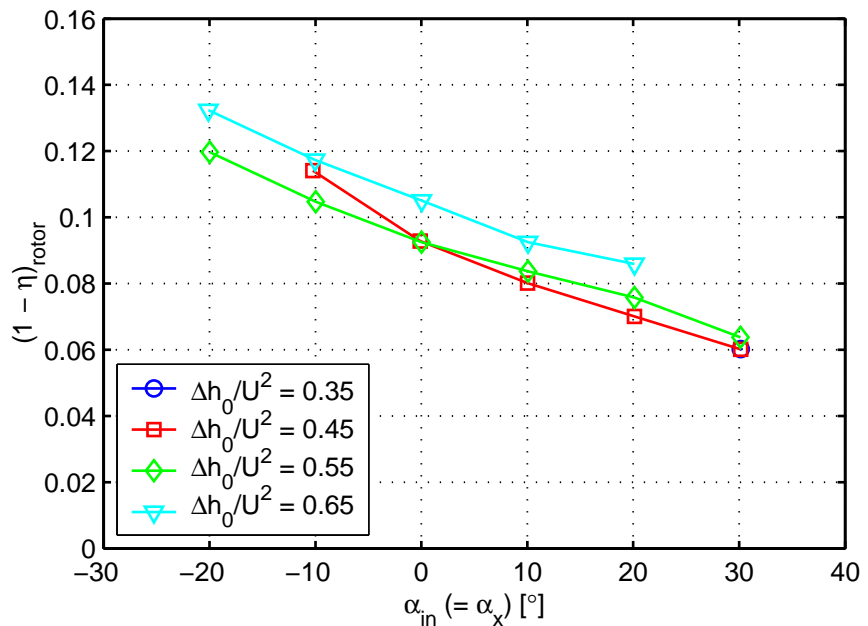


Figure 8.12: Effect of stage loading and stage inlet flow angle (recall in a repeating stage $\alpha_{in} = \alpha_x$) on rotor lost efficiency.

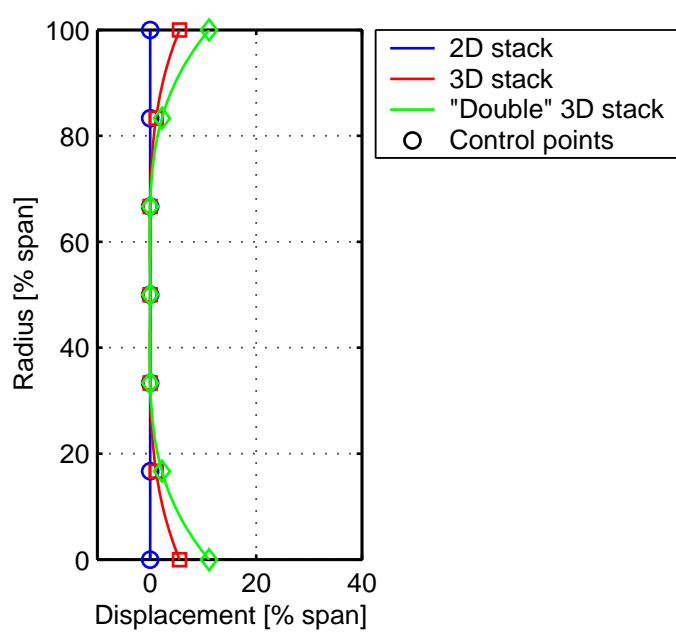


Figure 8.13: Stacking lines used in three-dimensional design study.

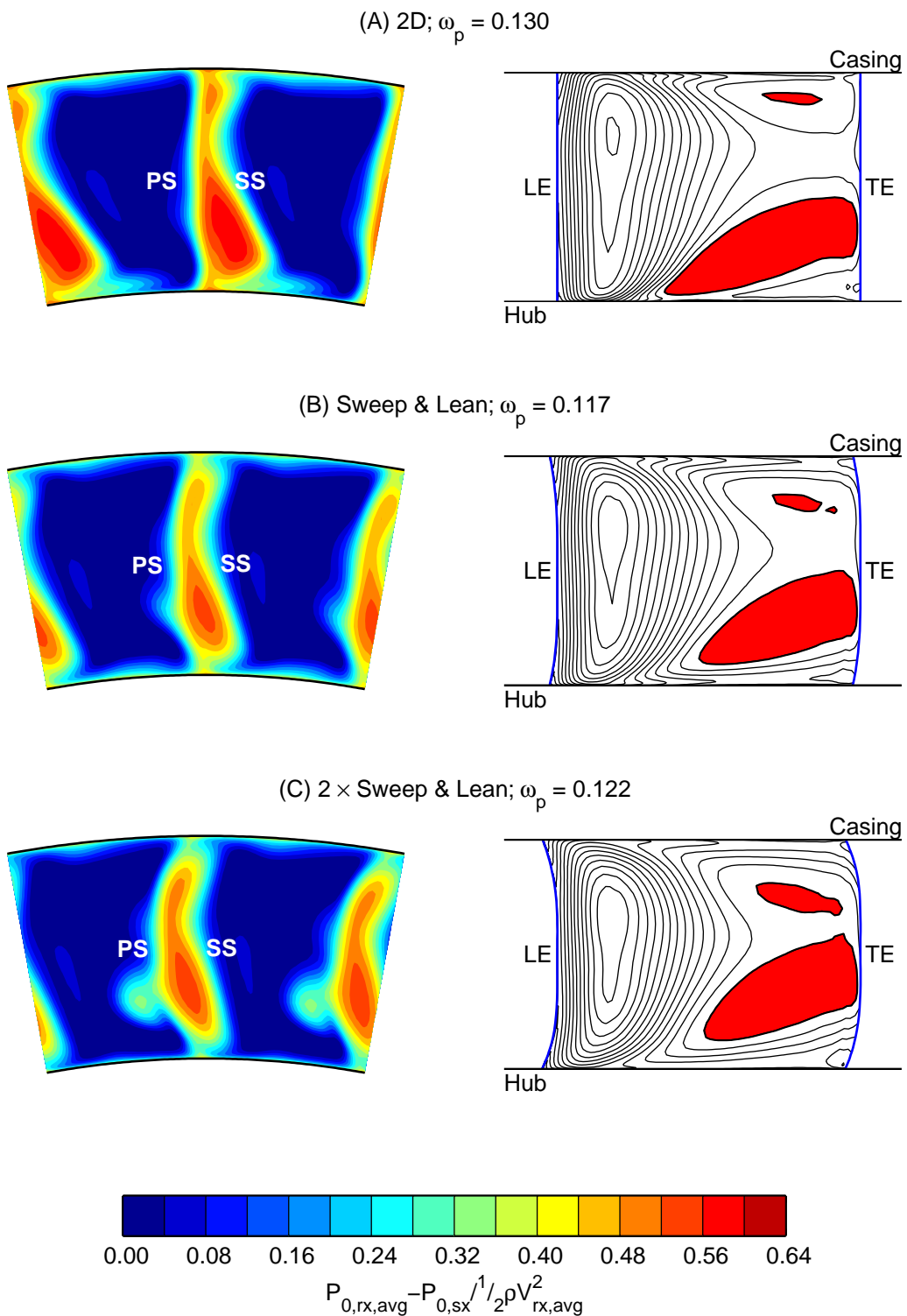


Figure 8.14: Effect of combined sweep and lean on the contours of stator exit stagnation pressure loss (left) and suction surface axial velocity (right) for the Gallimore stator ($\frac{\Delta h_0}{U^2} = 0.65$ & $\alpha_{in} = 0.0^\circ$). Regions of negative axial velocity (i.e. separations) shaded red.

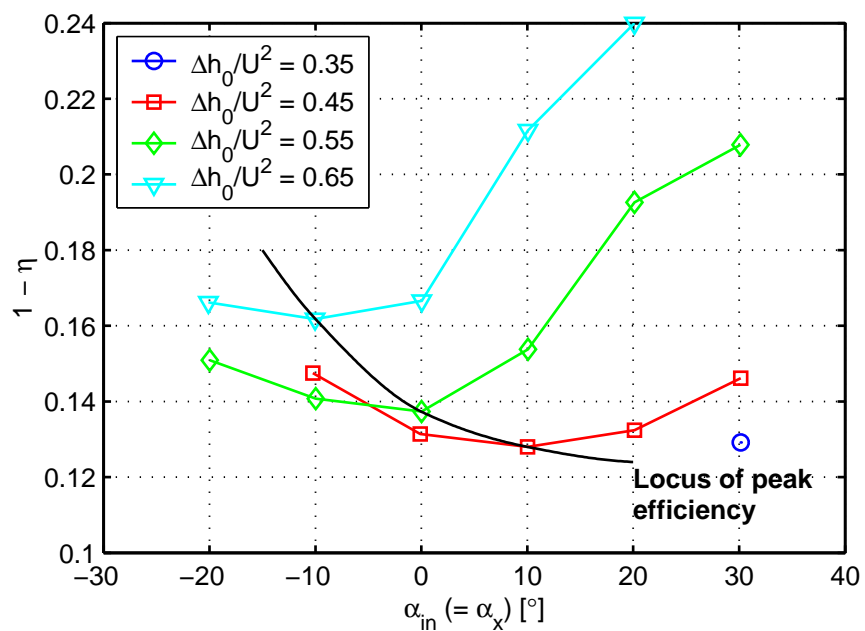


Figure 8.15: Effect of stage loading and inlet flow angle (recall in a repeating stage $\alpha_{in} = \alpha_x$) on predicted stage lost efficiency.

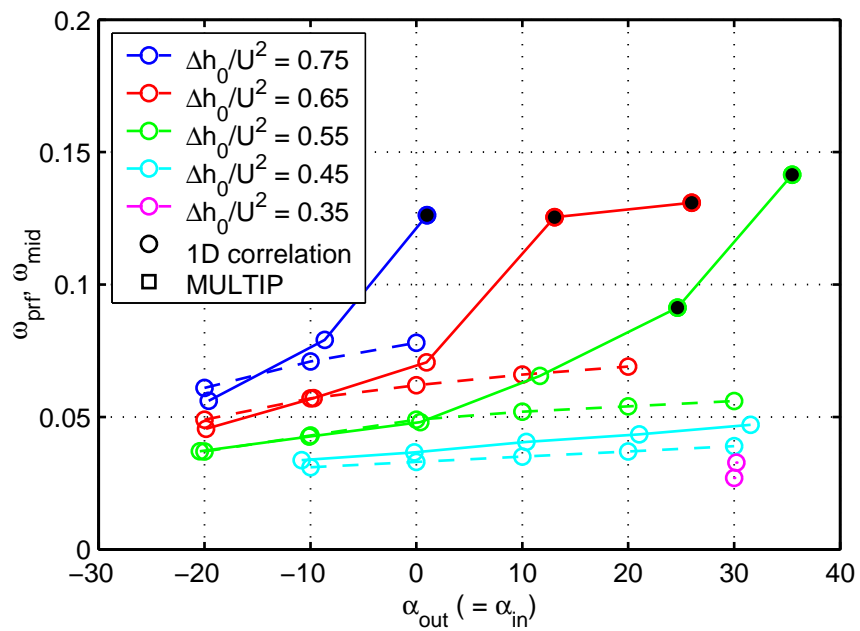


Figure 9.1: Comparison between *MULTIP* (squares) and a one-dimensional (circles) predictions of stator mid-span/ profile loss (assuming repeating stage conditions). Shaded symbols denote the presence of large three-dimensional separations.

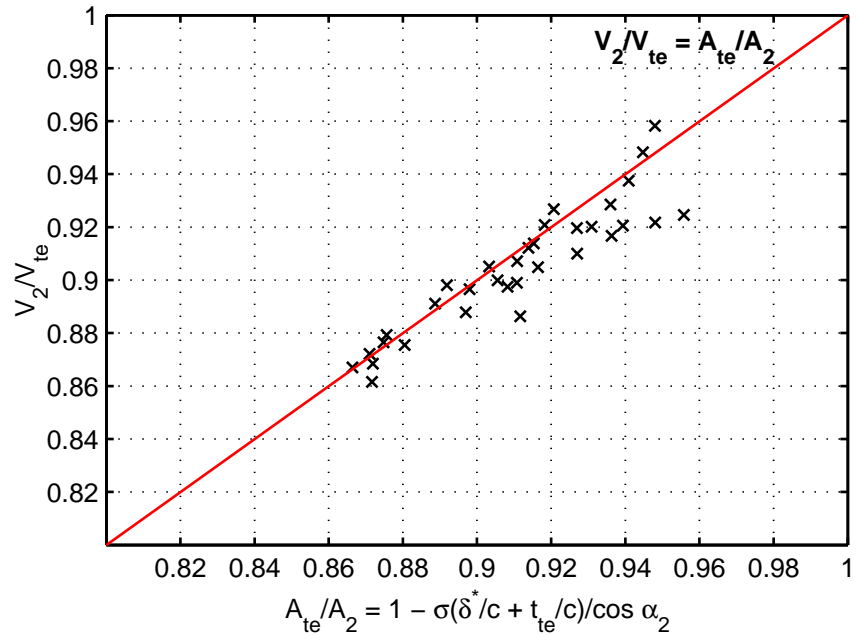


Figure 9.2: Trailing edge velocity against trailing edge blockage for a series of low speed aerofoils.

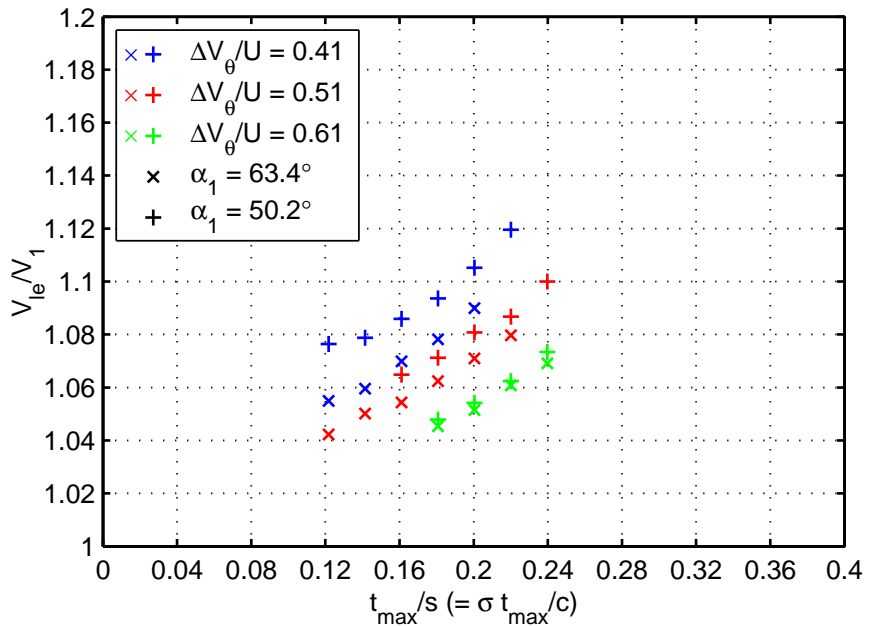


Figure 9.3: Leading edge velocity against blockage (i.e. maximum thickness normalised on pitch) for a series of low speed aerofoils.

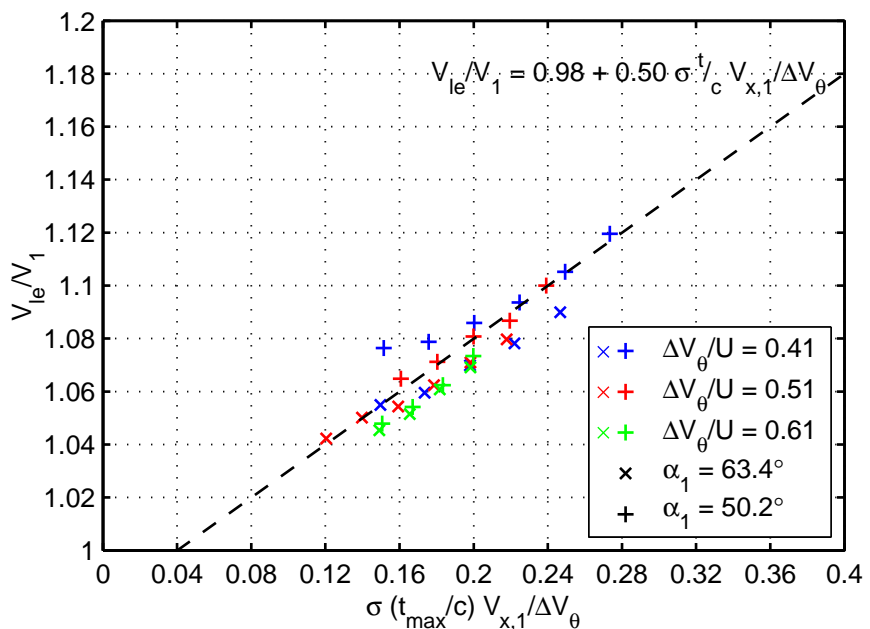


Figure 9.4: Leading edge velocity against correlation parameter, $\frac{\sigma^{t_{max}} V_{x,1}}{\Delta V_\theta}$, for a series of low speed aerofoils.

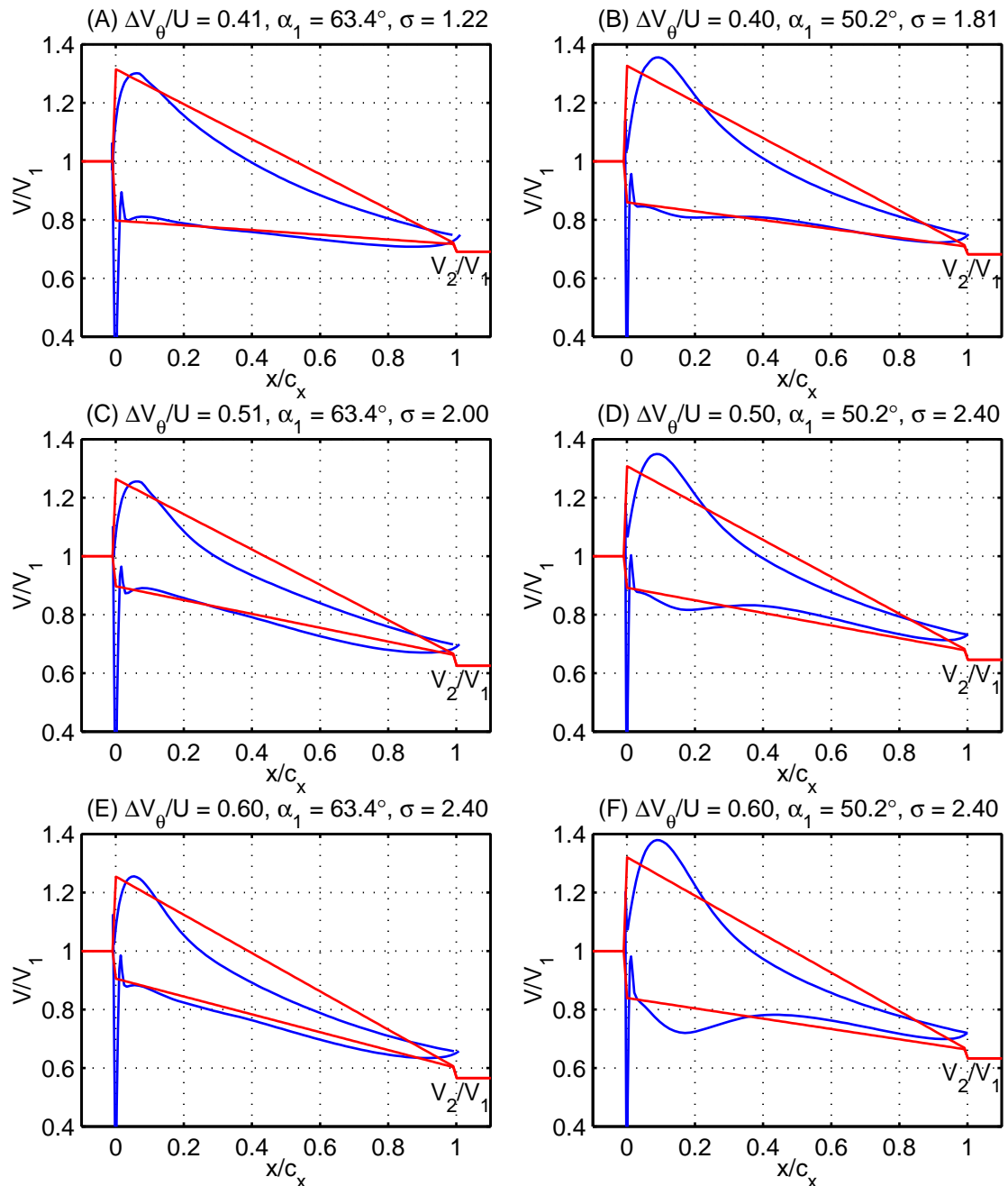


Figure 9.5: Comparison between velocity distributions predicted by *MISES* (blue) and a generic “straight-line” velocity distribution (red).

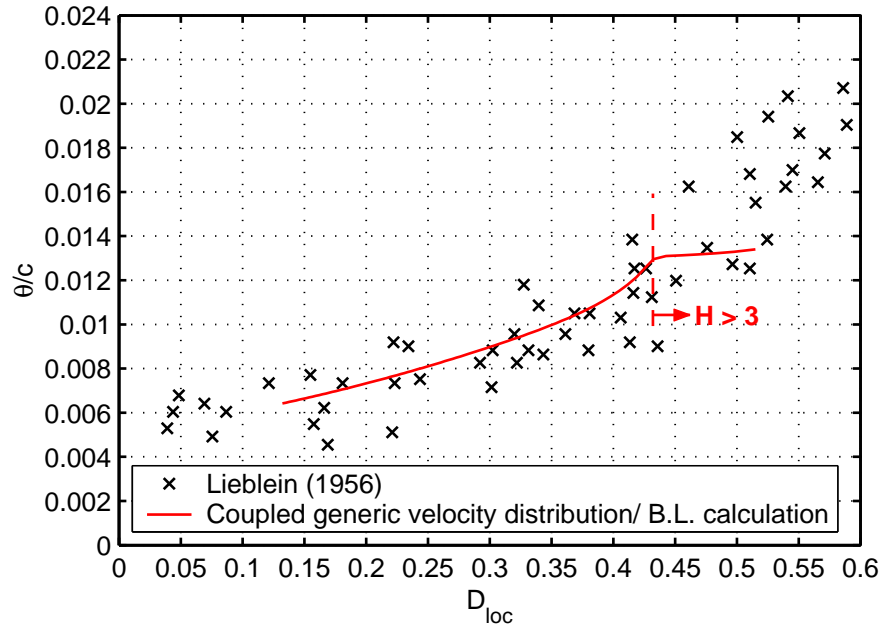


Figure 9.6: Comparison between momentum thickness predicted by a coupled generic velocity distribution/ boundary layer calculation (red) and those measured by Lieblein [63] (black). ($Re = 2.5 \times 10^5$.)

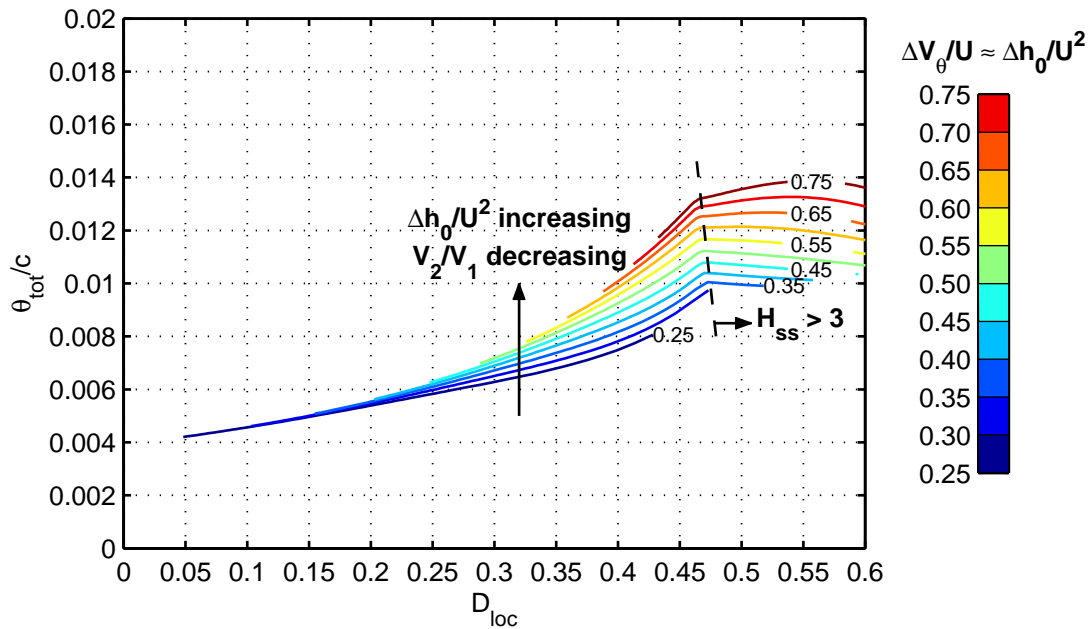


Figure 9.7: Total predicted momentum thickness at the trailing edge against local diffusion factor. Lines of constant $\frac{\Delta V_\theta}{U}$ shown for a blade row with $\alpha_1 = 63.4^\circ$. ($Re = 1.0 \times 10^6$.)

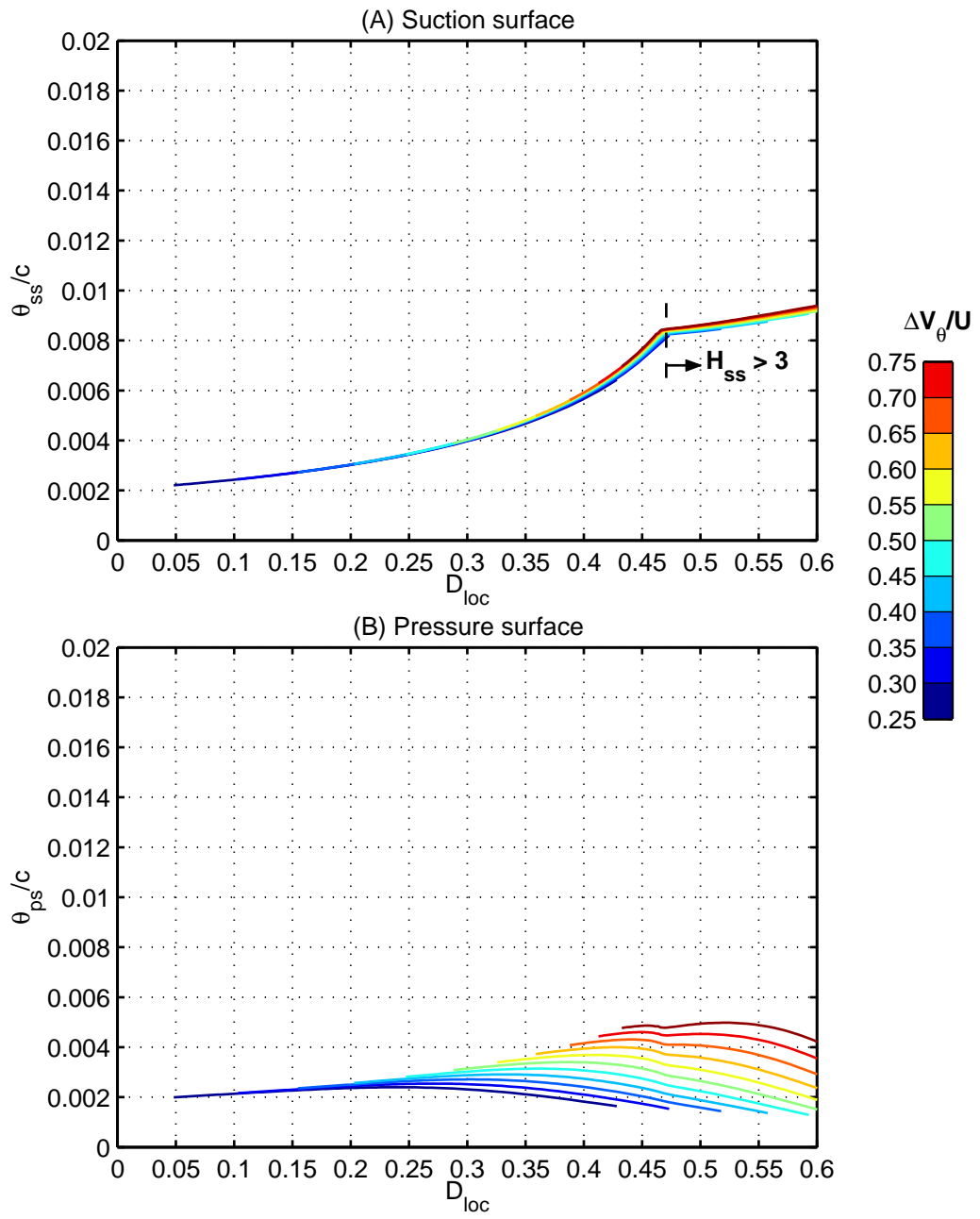


Figure 9.8: (A) Suction surface and (B) pressure surface trailing edge momentum thickness against local diffusion factor. Lines of constant $\frac{\Delta V_\theta}{U}$ shown for a blade row with $\alpha_1 = 63.4^\circ$. ($Re = 1.0 \times 10^6$.)

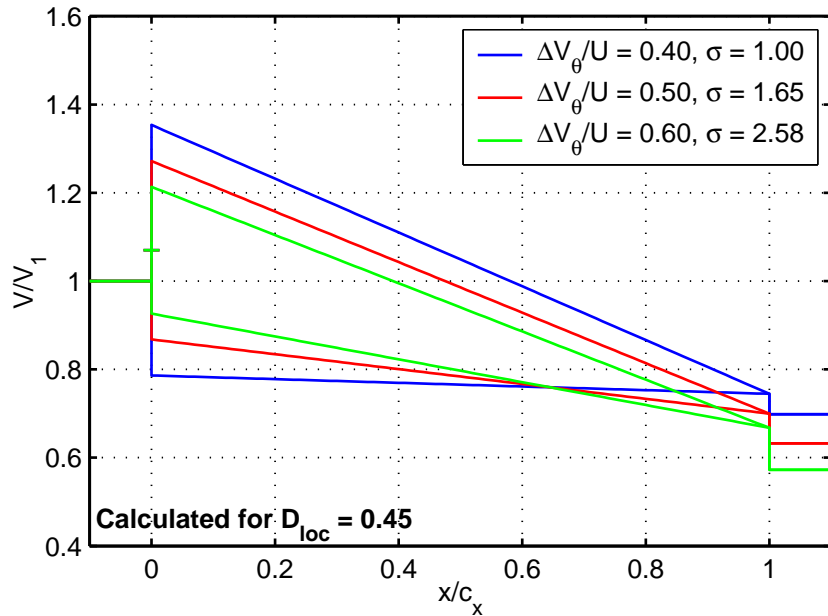


Figure 9.9: Effect of turning ($\frac{\Delta V_\theta}{U}$) on the assumed generic velocity distributions for a series of blades with a constant local diffusion factor of 0.45.

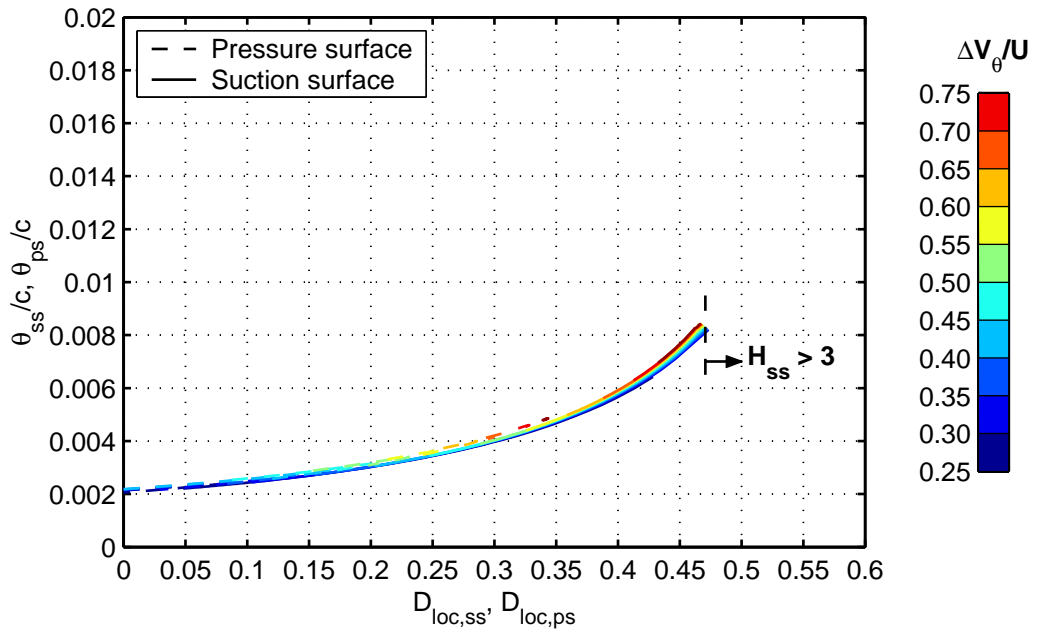


Figure 9.10: Trailing edge suction and pressure surface momentum thickness against suction and pressure surface local diffusion factors respectively. Lines of constant $\frac{\Delta V_\theta}{U}$ shown for a blade row with $\alpha_1 = 63.4^\circ$. ($Re = 1.0 \times 10^6$.)

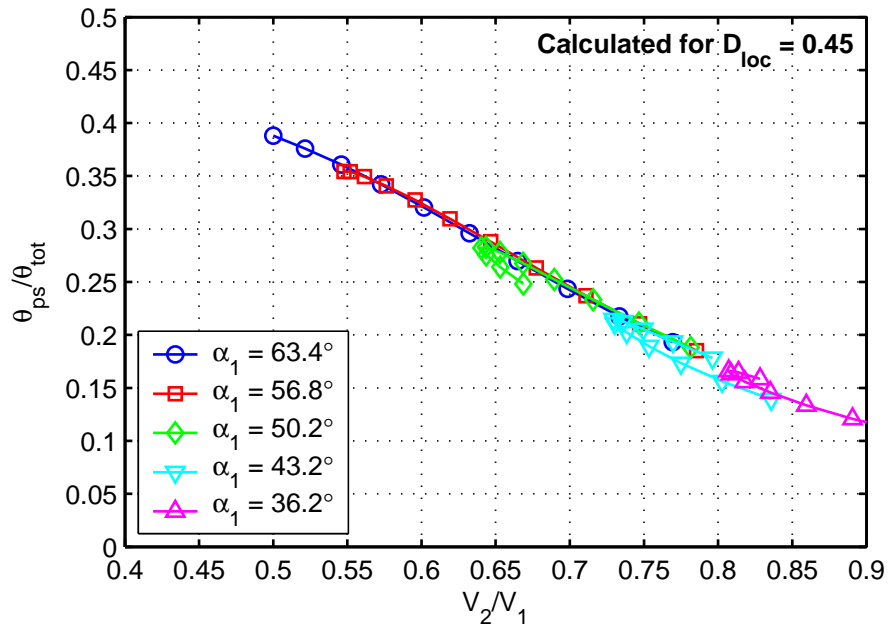


Figure 9.11: Ratio of (predicted) pressure surface to total momentum thickness at the trailing edge (i.e. approximately the fraction of loss attributable to the pressure surface boundary layer) against de Haller number ($\frac{V_2}{V_1}$) for a generic velocity distribution.

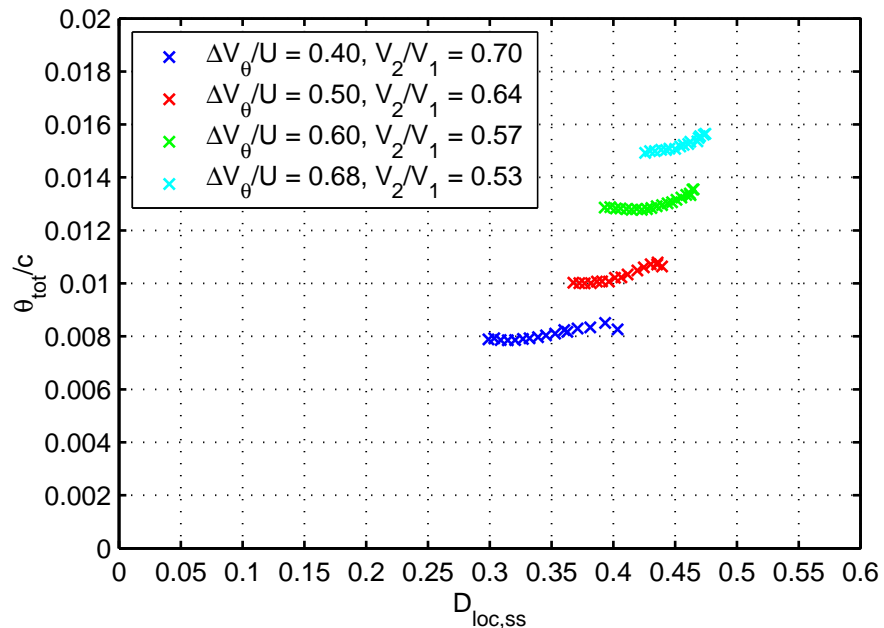


Figure 9.12: Total trailing edge momentum thickness against suction surface local diffusion factor for a series of high-speed blades ($M_{in} = 0.74$).

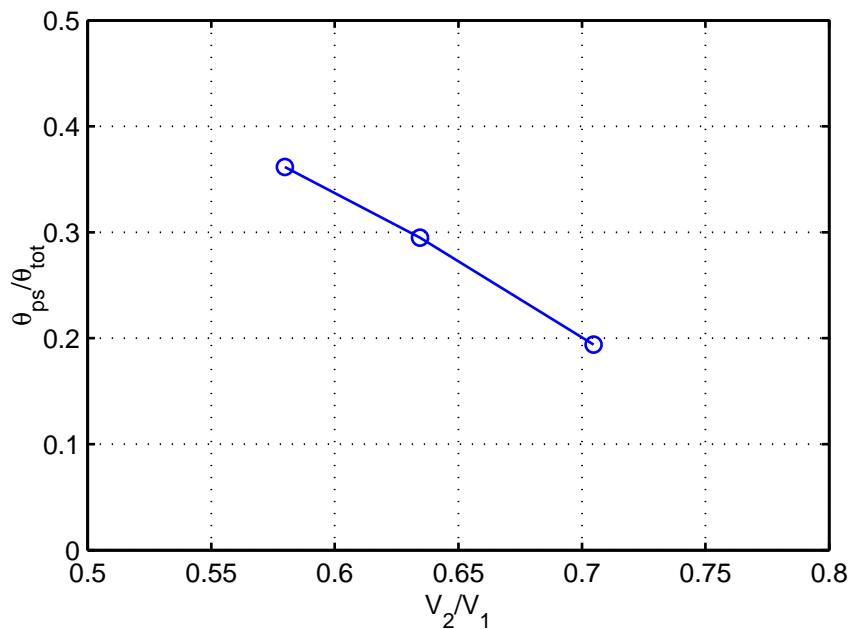


Figure 9.13: Variation in pressure surface momentum thickness as a fraction of the total with de Haller number (i.e. increased loading). Calculated for high-speed blade sections at constant local diffusion factor ($D_{loc} \approx 0.40$).

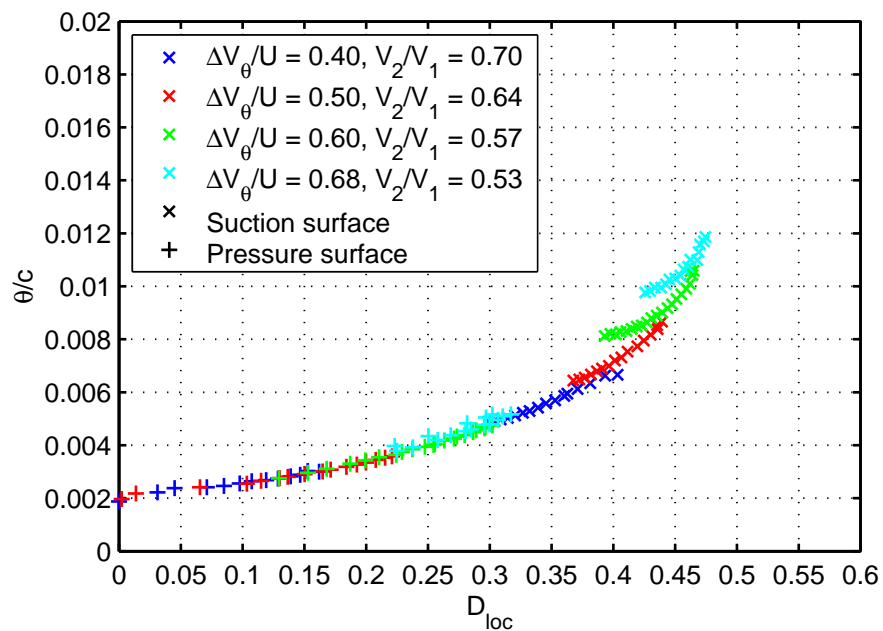


Figure 9.14: Trailing edge suction and pressure surface momentum thickness versus respective local diffusion factors for a series of high-speed blades ($M_{in} = 0.74$). “ \times ” and “+” denote suction and pressure surfaces respectively.

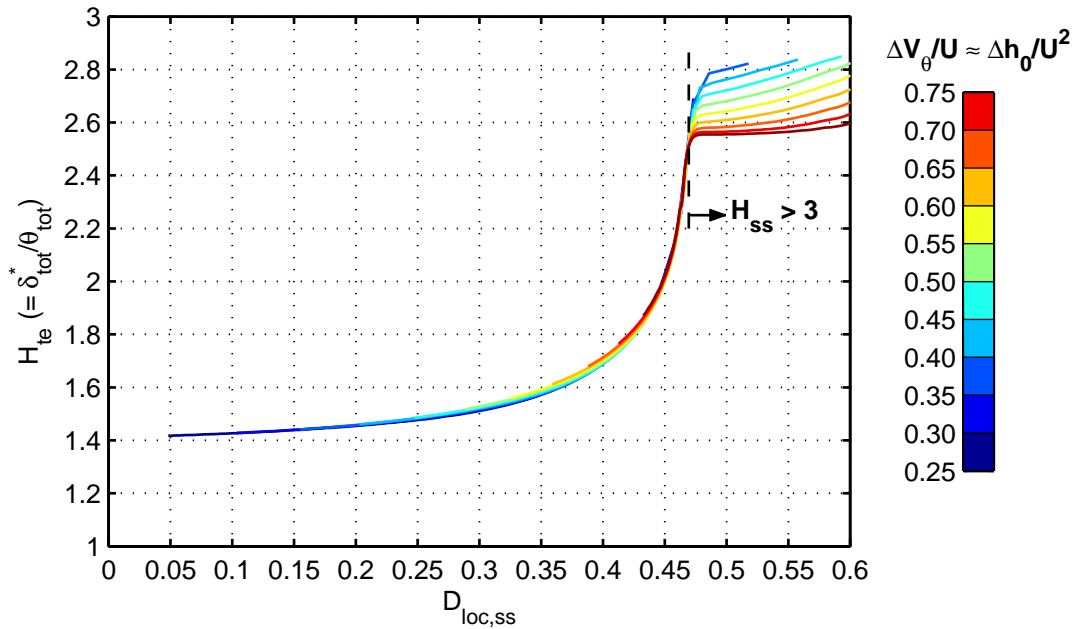


Figure 9.15: Total trailing edge shape factor (H_{te}) plotted against local (suction surface) diffusion factor. Contours of loading, $\frac{\Delta V_\theta}{U}$ shown for a generic velocity distribution model of a blade row with $\alpha_1 = 63.4^\circ$. ($Re = 1.0 \times 10^6$.)

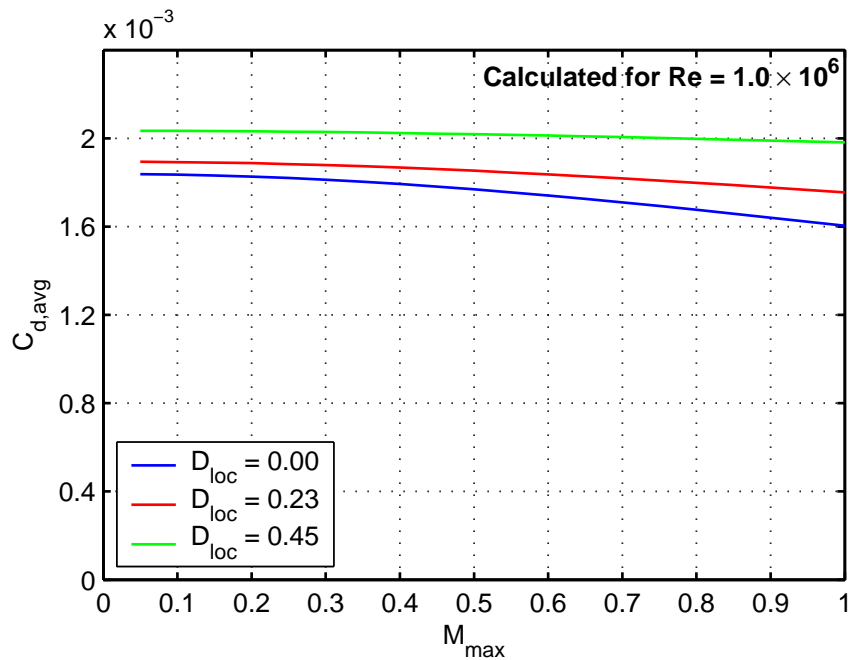


Figure 9.16: Variation in chord-wise averaged dissipation coefficient, $C_{d,avg}$, with Mach number. ($Re = 1.0 \times 10^6$.)

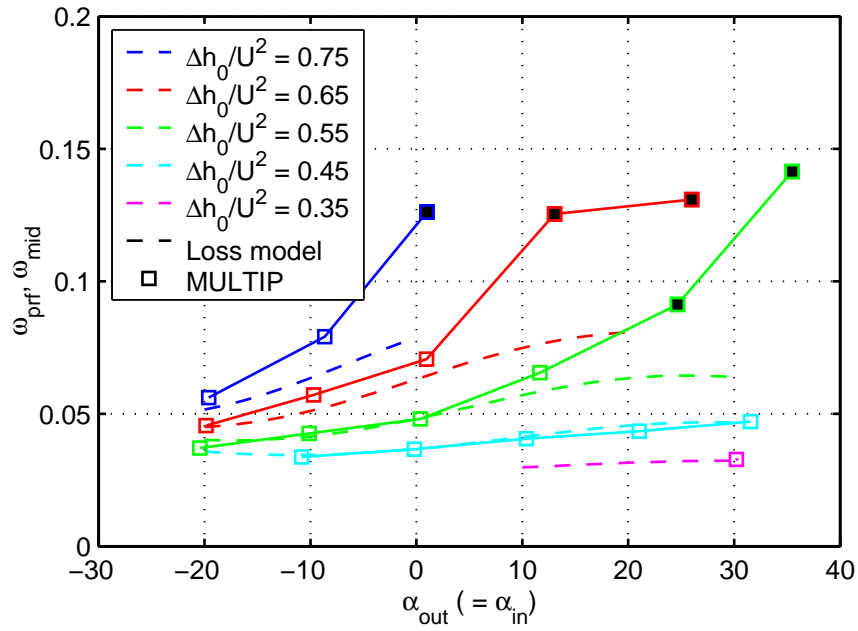


Figure 9.17: Comparison between *MULTIP* predictions of mid-span loss and the coupled generic velocity distribution/ profile loss model of Section 9.4 for a series of stator blades. Shaded symbols denote the presence of large three-dimensional separations.

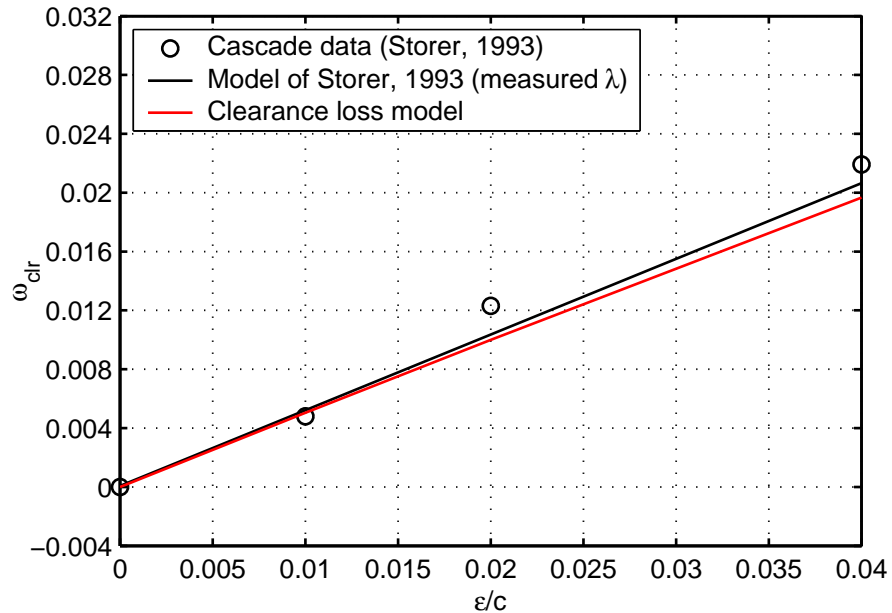


Figure 9.18: Comparison between clearance loss measured by Storer & Cumpsty [87] and that predicted by a simple mixing model for the corresponding generic velocity distribution.

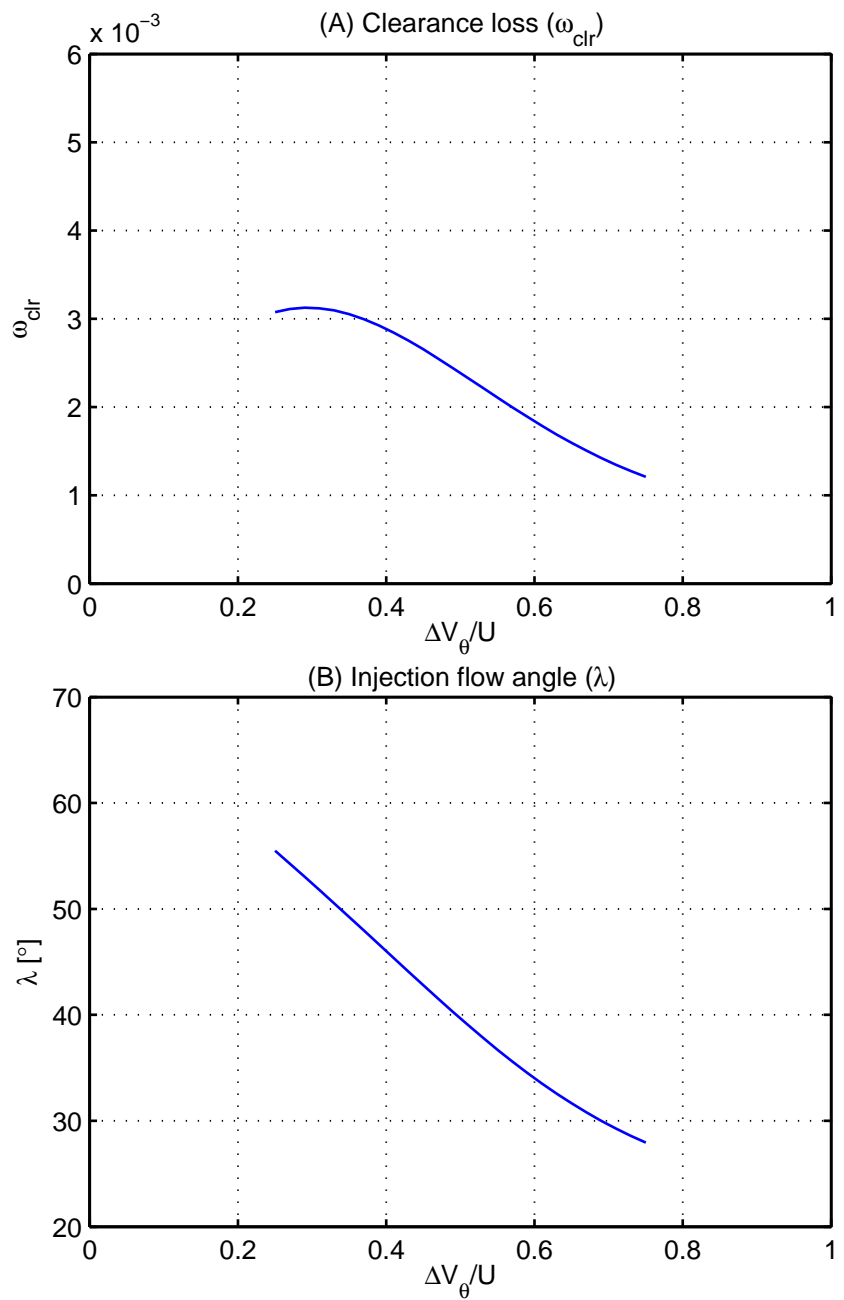


Figure 9.19: Effect of loading ($\frac{\Delta V_\theta}{U} \approx \frac{\Delta h_0}{U^2}$) on estimated clearance flow. Calculated for a blade row with inlet flow angle and local diffusion factor equal to 63.4° and 0.45 respectively.

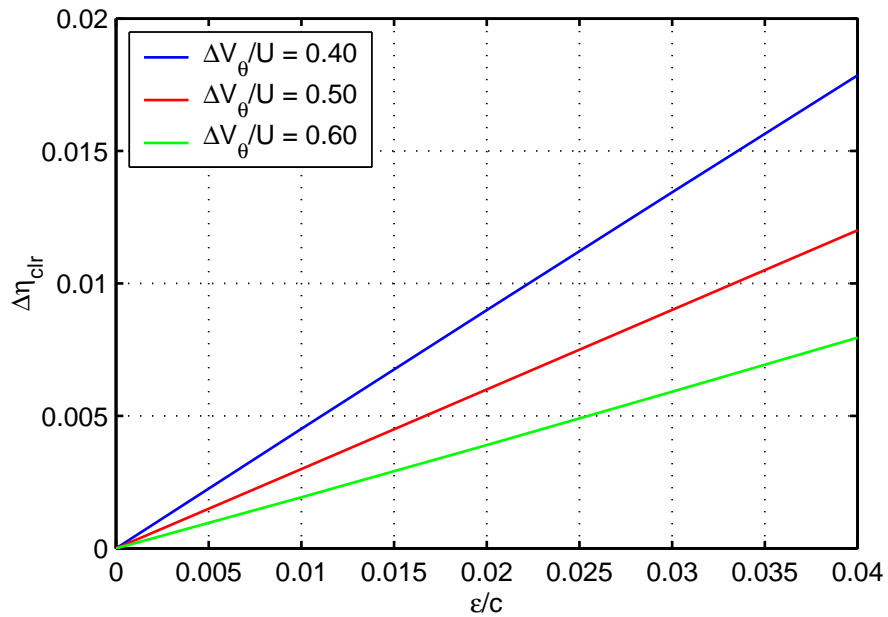


Figure 9.20: Predicted variation in lost efficiency due to clearance losses ($\Delta\eta_{clr}$) with increasing clearance gap ($\frac{\epsilon}{c}$).

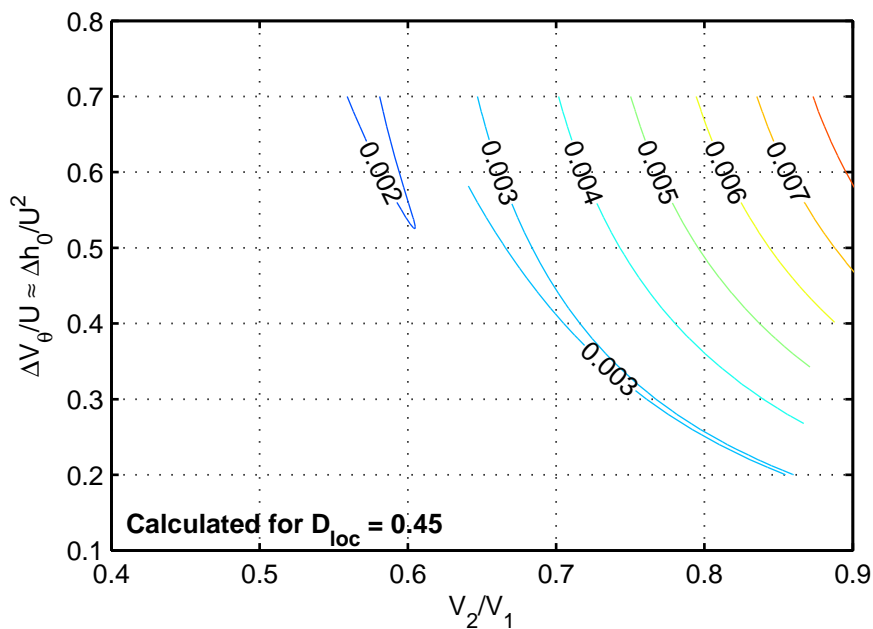


Figure 9.21: Effect of de Haller number ($\frac{V_2}{V_1}$) and loading ($\frac{\Delta V_\theta}{U} \approx \frac{\Delta h_0}{U^2}$) on contours of tip clearance loss coefficient.

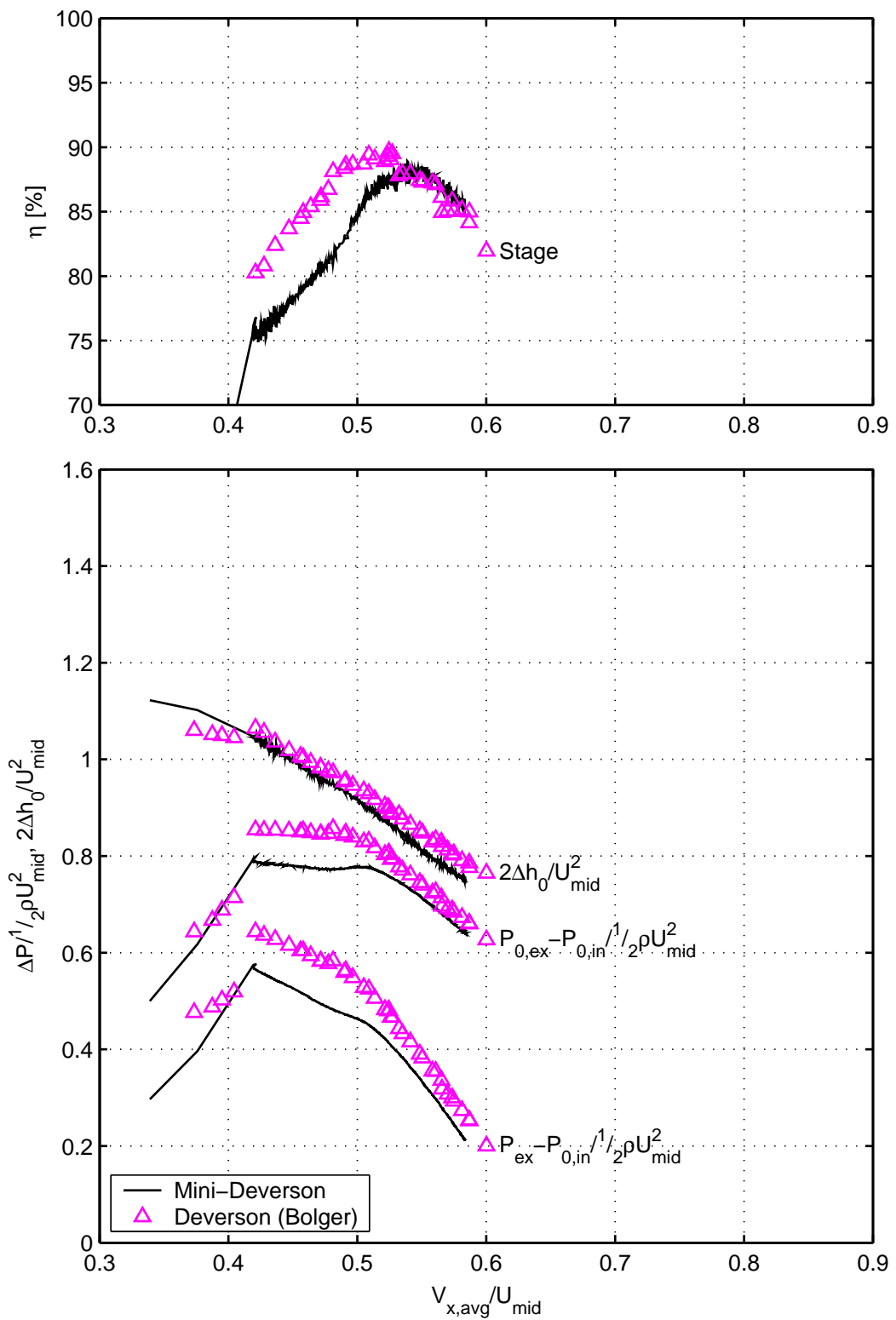
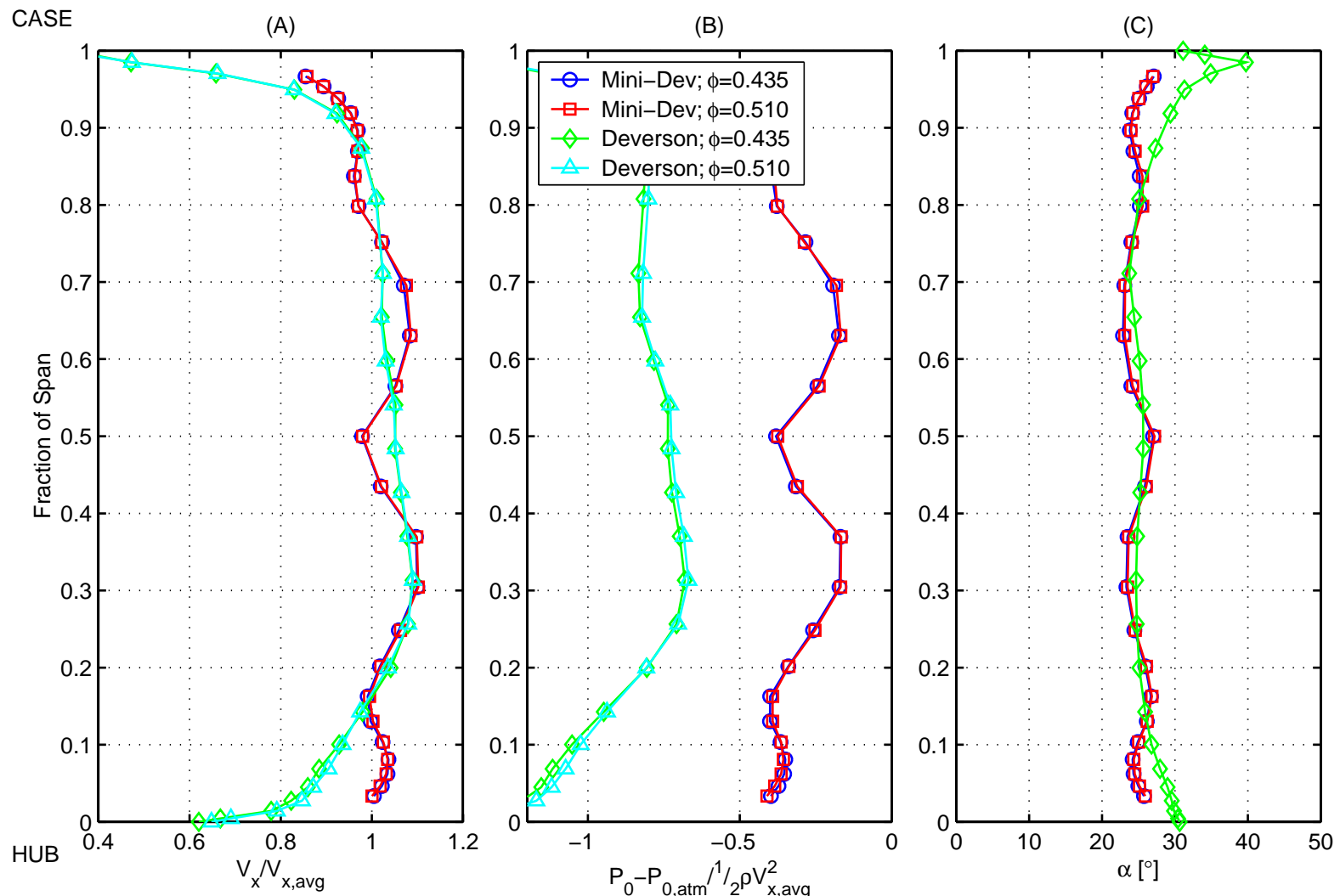


Figure A.1: Comparison between pressure rise, torque and efficiency characteristics of the **Mini-Deverson** and original **Deverson Build II** stage (measured by Bolger [4]). N.B. pressure rise and efficiency values are those derived from the casing static pressure.

Figure A 2: Comparison between the conditions at inlet to the Mini-Deverson and Deverson Build II stage (measured by Bolger [4]).



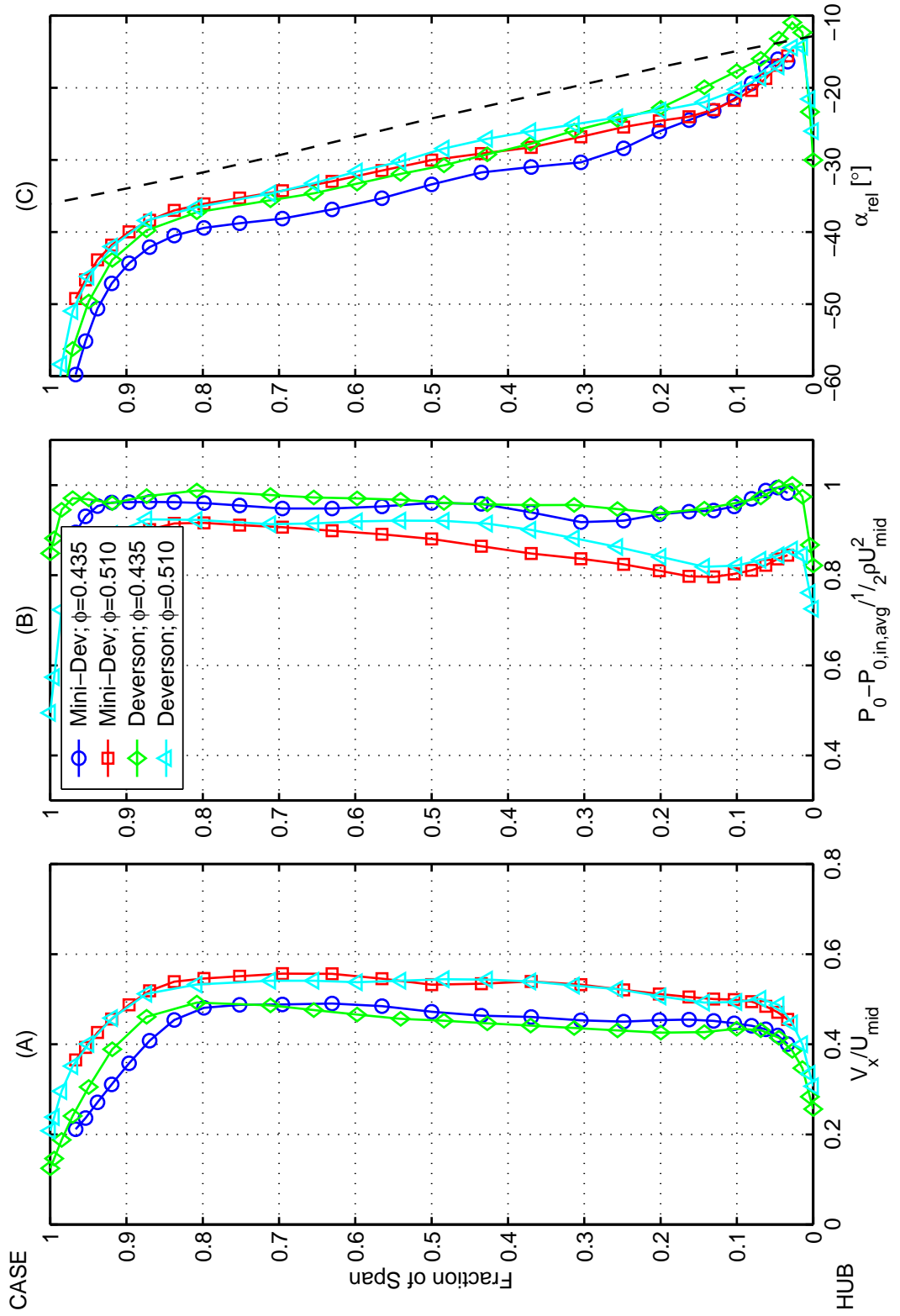


Figure A.3: Comparison between radial profiles of (A) axial velocity, (B) stagnation pressure rise and (C) relative flow angle downstream of the **Mini-Deverson** and **Deverson Build II** rotors. Deverson Build II data taken from Bolger [4]. The dashed line shows metal angle at rotor trailing edge.

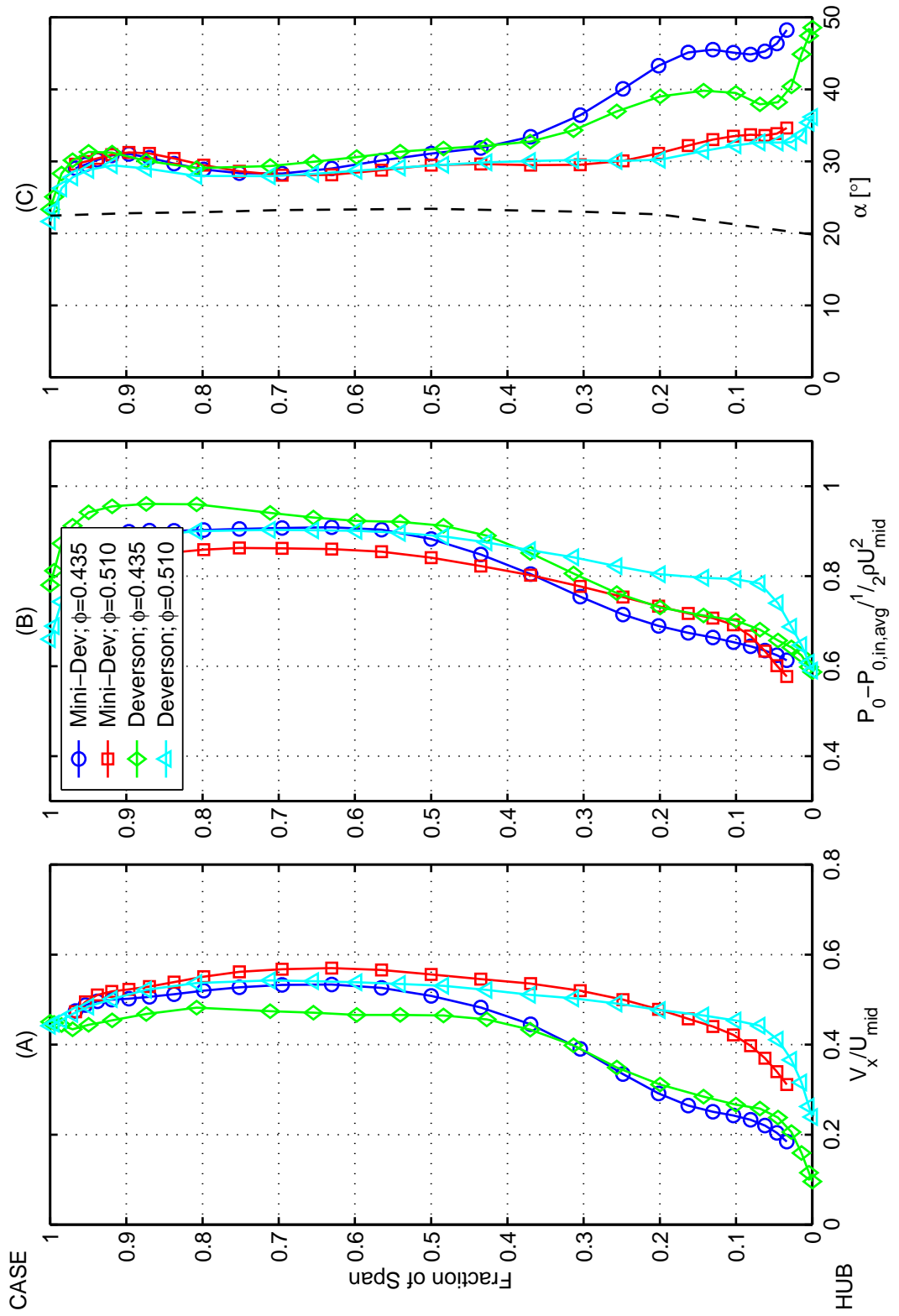


Figure A.4: Comparison between radial profiles of (A) axial velocity, (B) stagnation pressure rise and (C) absolute flow angle downstream of the **Mini-Deverson** and **Deverson Build II** stators. Deverson Build II data taken from Bolger [4]. The dashed line shows metal angle at stator trailing edge.

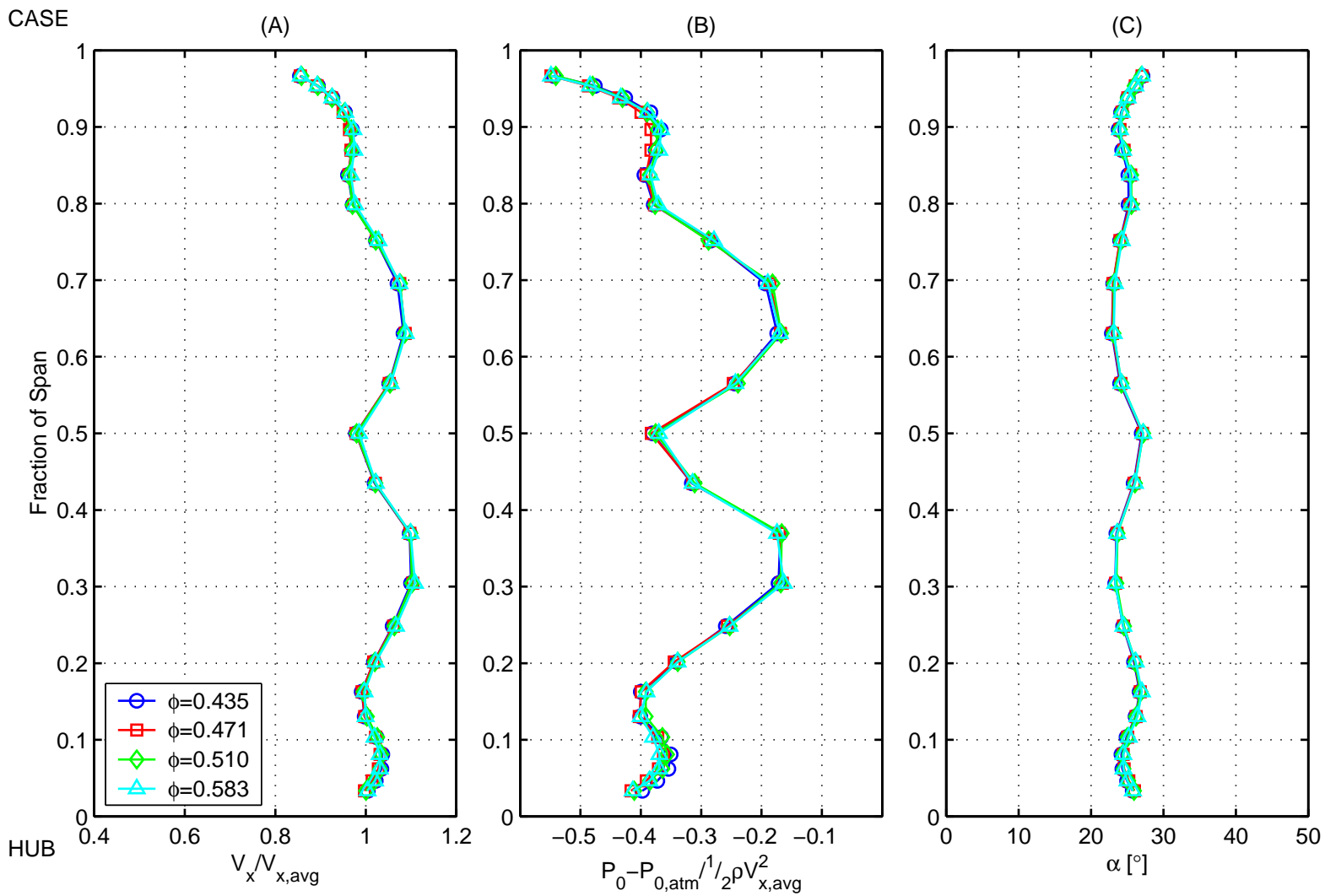


Figure B.1: Inlet conditions to the Mini-Deverson stage.

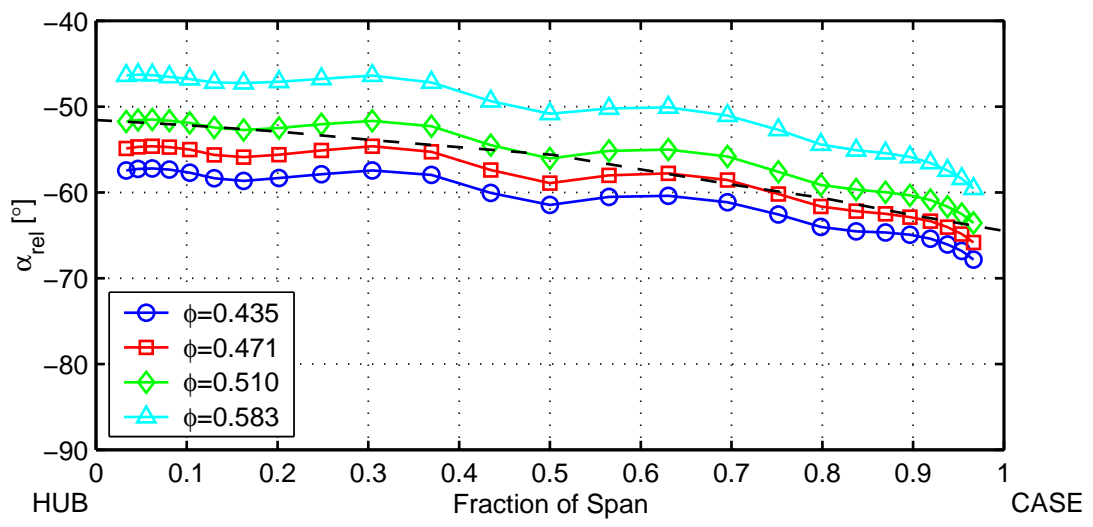


Figure B.2: Radial profiles of flow angle at inlet to the **Mini-Deverson** rotor. Dashed line shows metal angle at rotor leading edge.

Figure B.3: Radial profiles of (A) axial velocity, (B) stagnation pressure rise and (C) relative flow angle downstream of the Mini-Deverson rotor. Dashed line shows metal angle at rotor trailing edge.

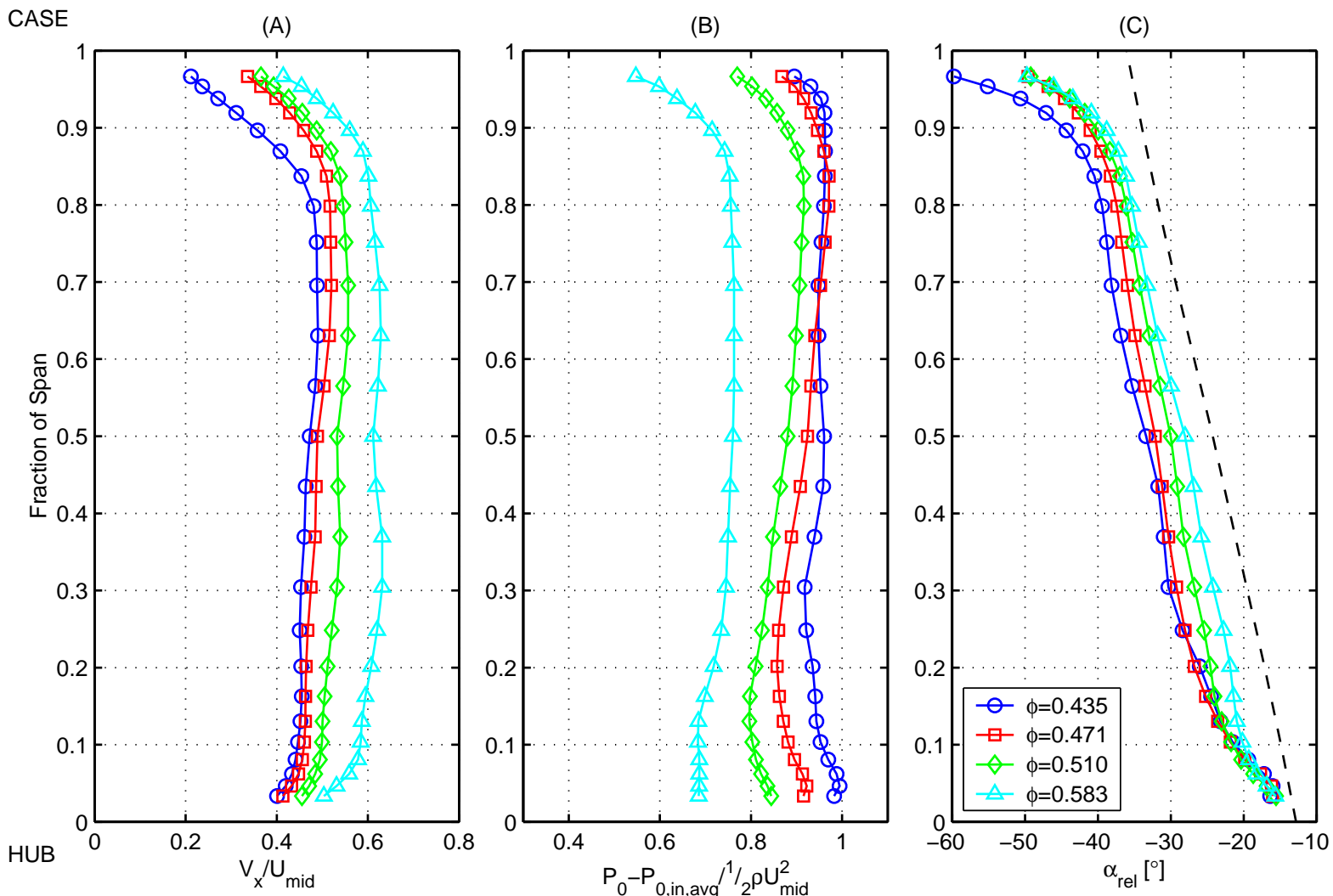
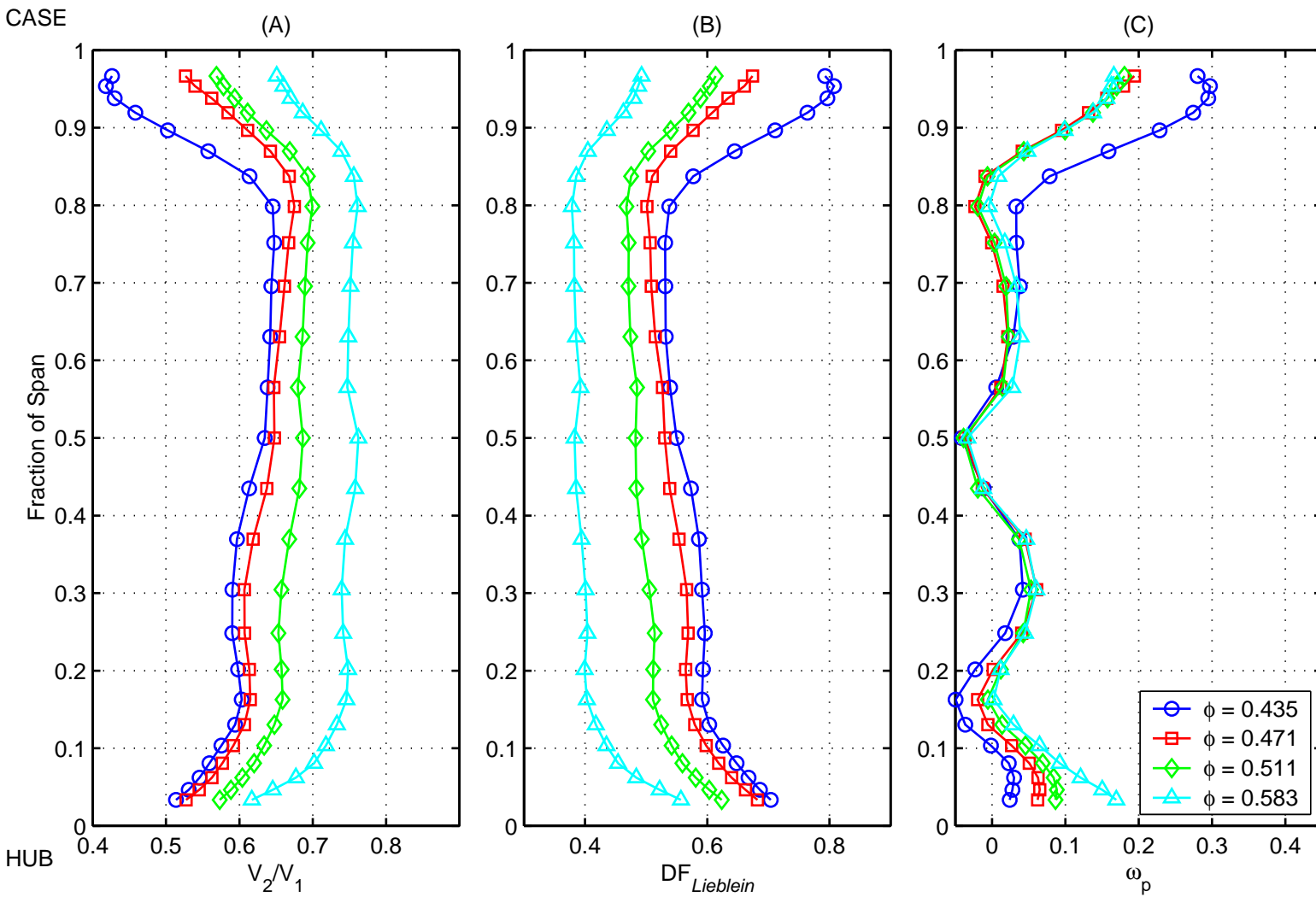


Figure B.4: Mini-Deverson rotor performance; Radial profiles of (A) de Haller number, (B) Lieblein diffusion factor and (C) stagnation pressure loss coefficient.



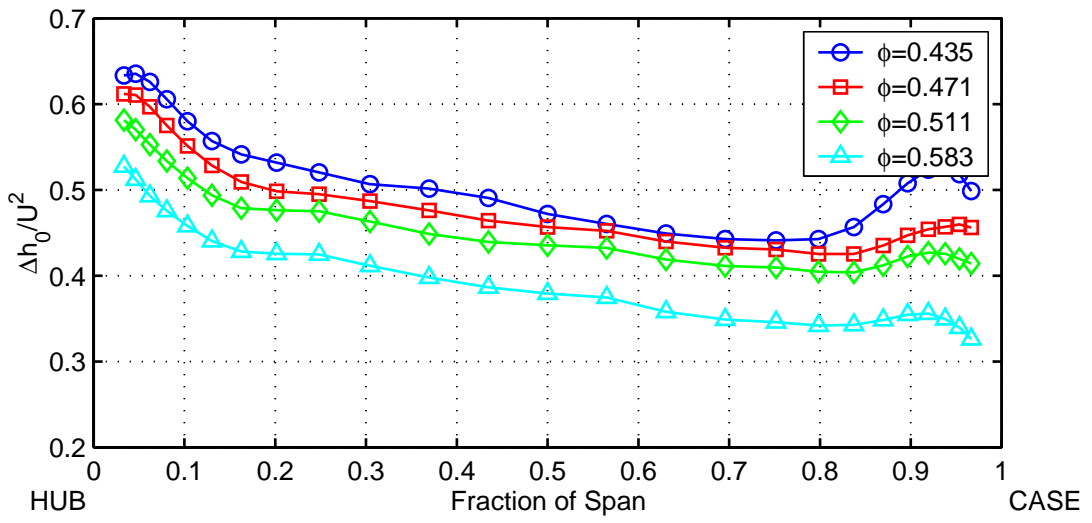


Figure B.5: Span-wise variation in stage loading coefficient ($\frac{\Delta h_0}{U_2^2}$) measured across the **Mini-Deverson** rotor.

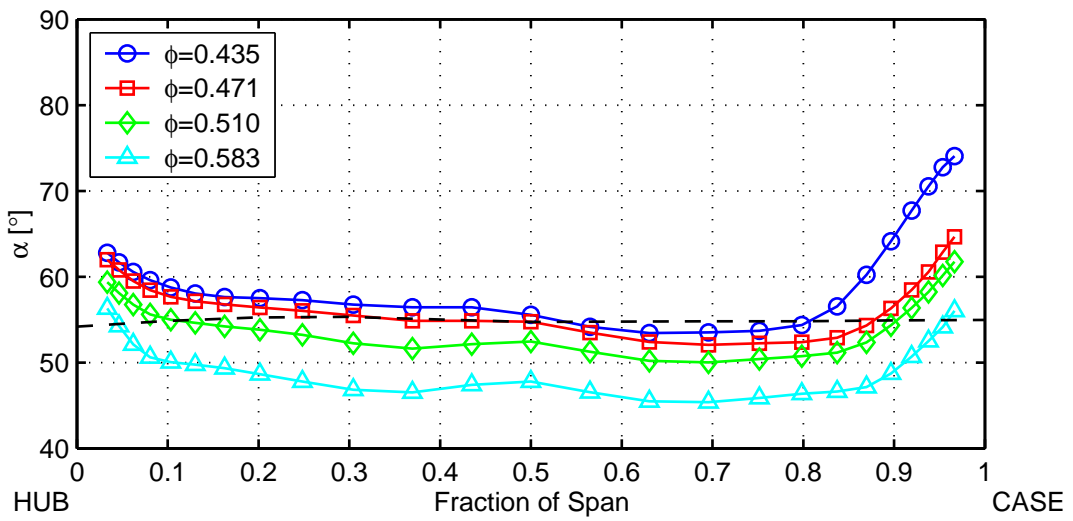


Figure B.6: Radial profiles of flow angle at inlet to the **Mini-Deverson** stator. Dashed line shows metal angle at stator leading edge.

Figure B.7: Radial profiles of (A) axial velocity, (B) stagnation pressure rise and (C) relative flow angle downstream of the Mini-Deverson stator. Dashed line shows the metal angle at stator trailing edge.

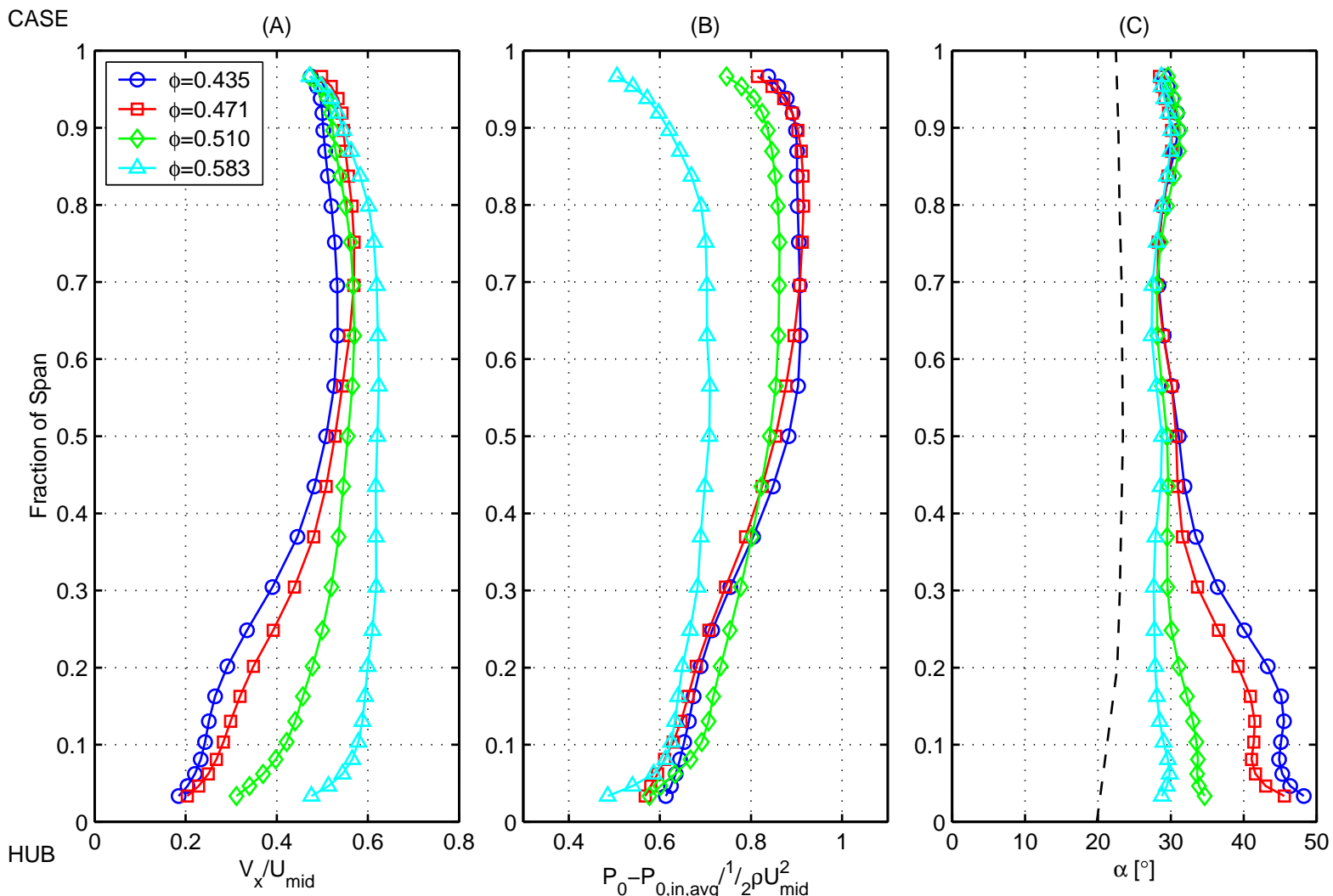


Figure B.8: Mini-Deverson stator performance; Radial profiles of (A) de Haller number, (B) Lieblein diffusion factor and (C) stagnation pressure loss coefficient.

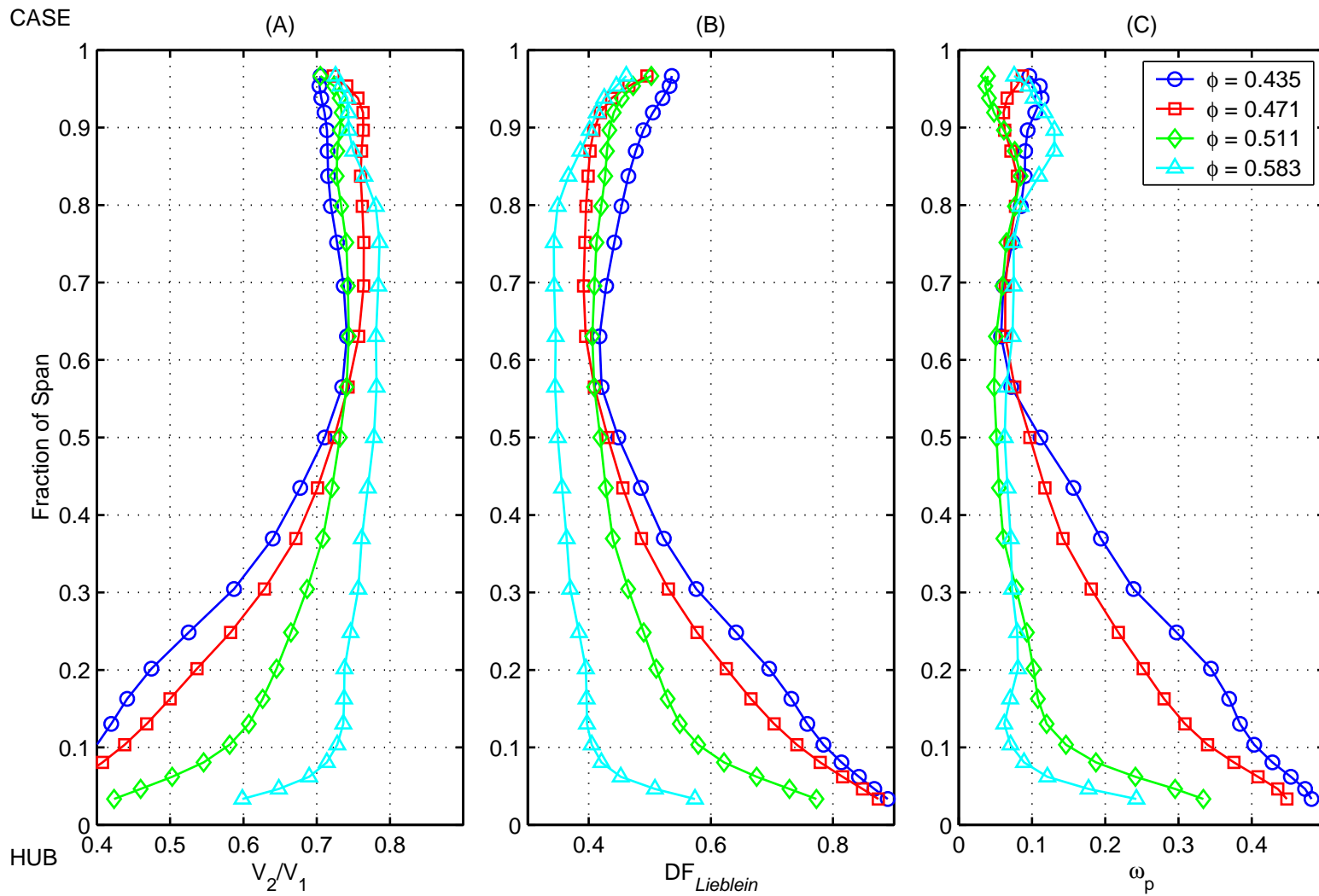
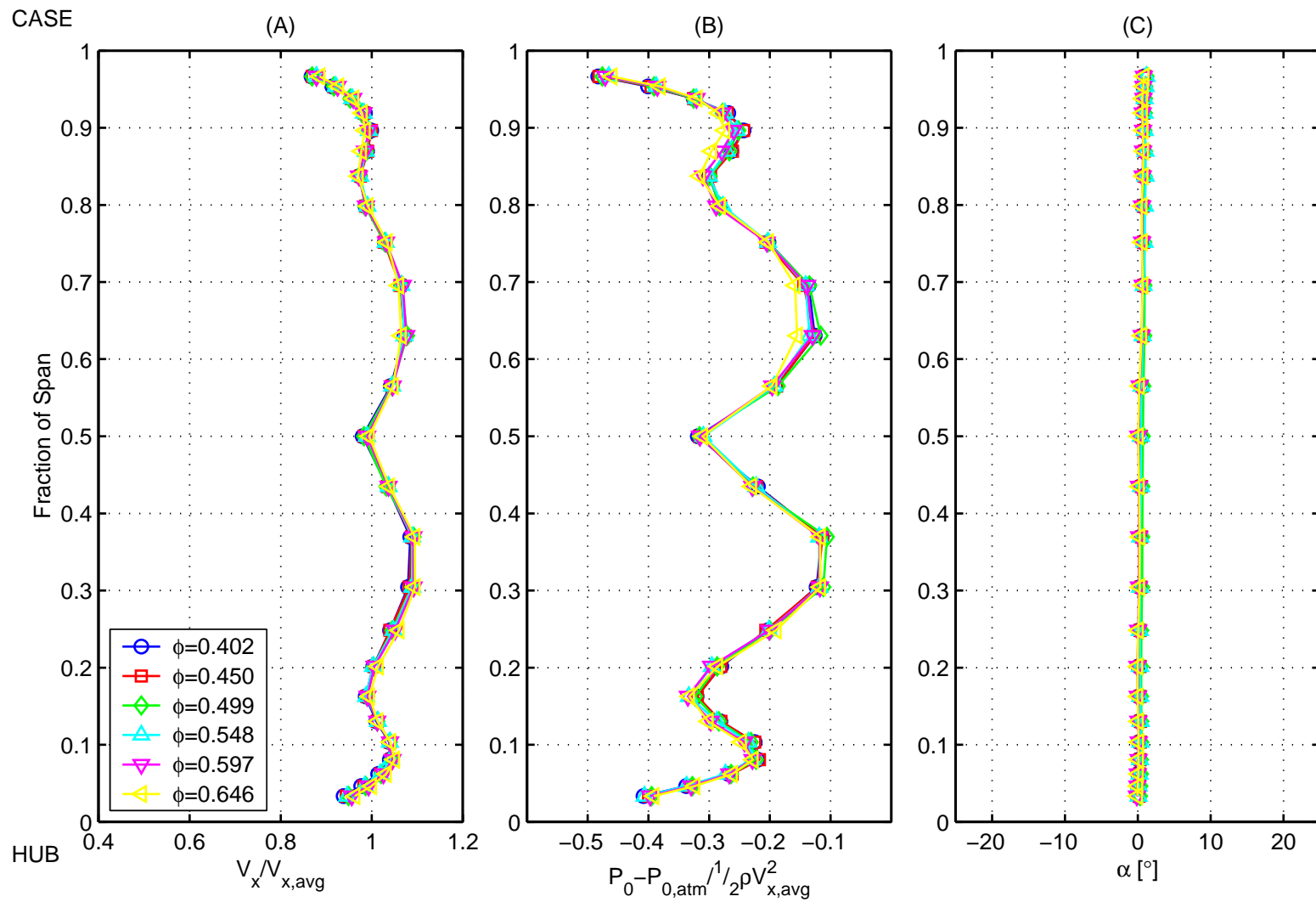


Figure B.9: Inlet conditions to the Gallimore stage.



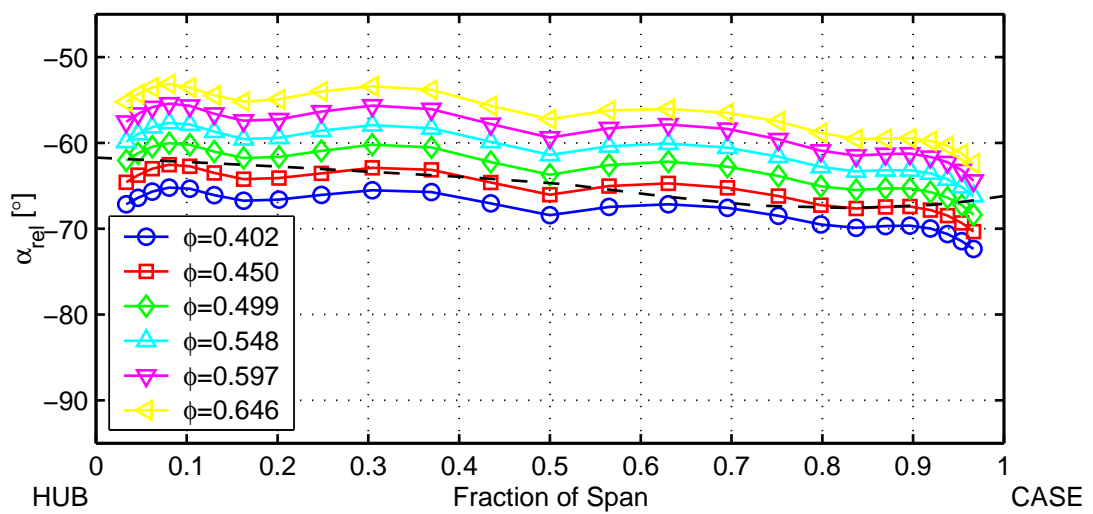


Figure B.10: Radial profiles of flow angle at inlet to the **Gallimore** rotor. Dashed line shows metal angle at rotor leading edge.

Figure B.11: Radial profiles of (A) axial velocity, (B) stagnation pressure rise and (C) relative flow angle downstream of the Gallimore rotor. Dashed line shows metal angle at rotor trailing edge.

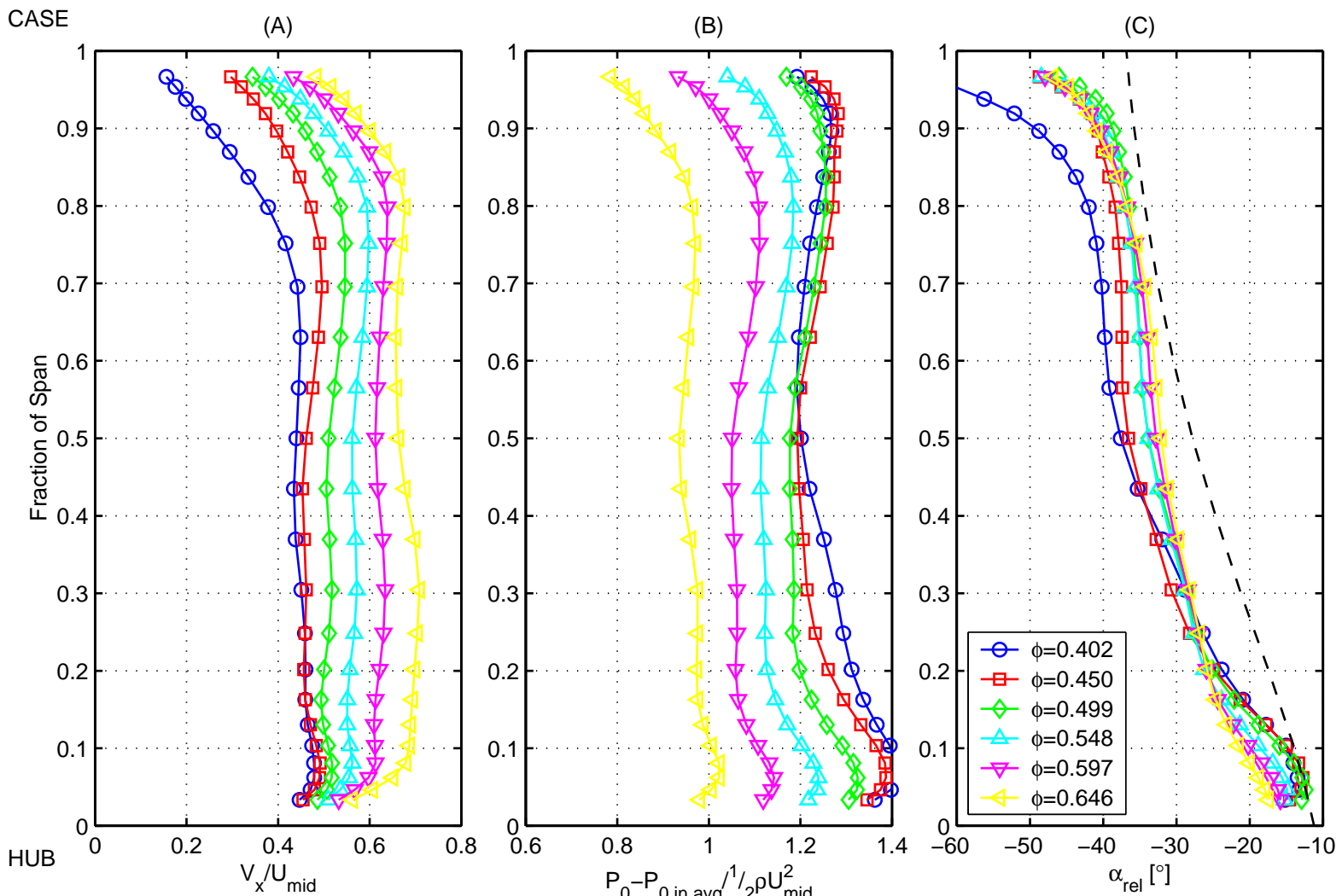
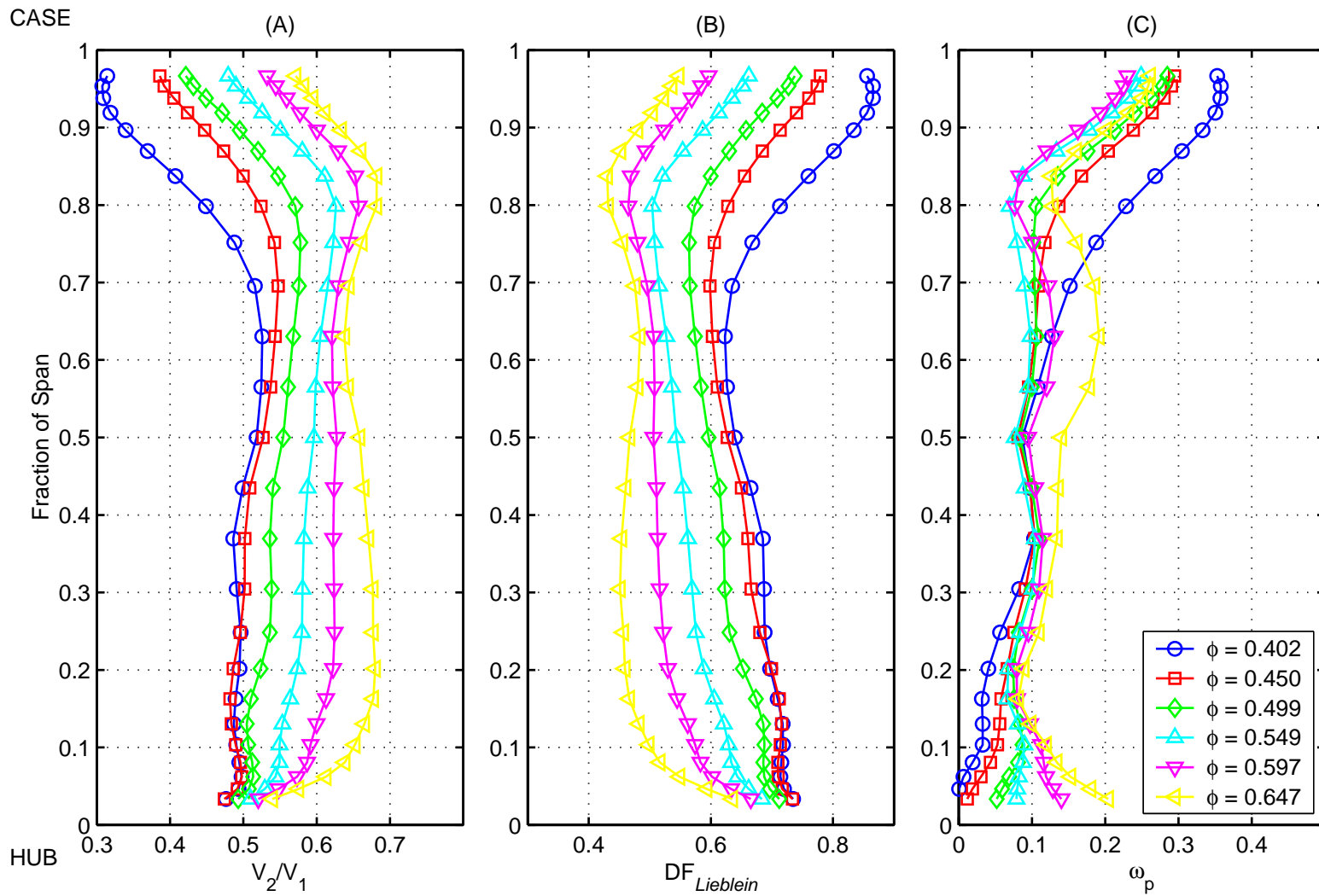


Figure B.12: Gallimore rotor performance; Radial profiles of (A) de Haller number, (B) Lieblein diffusion factor and (C) stagnation pressure loss coefficient.



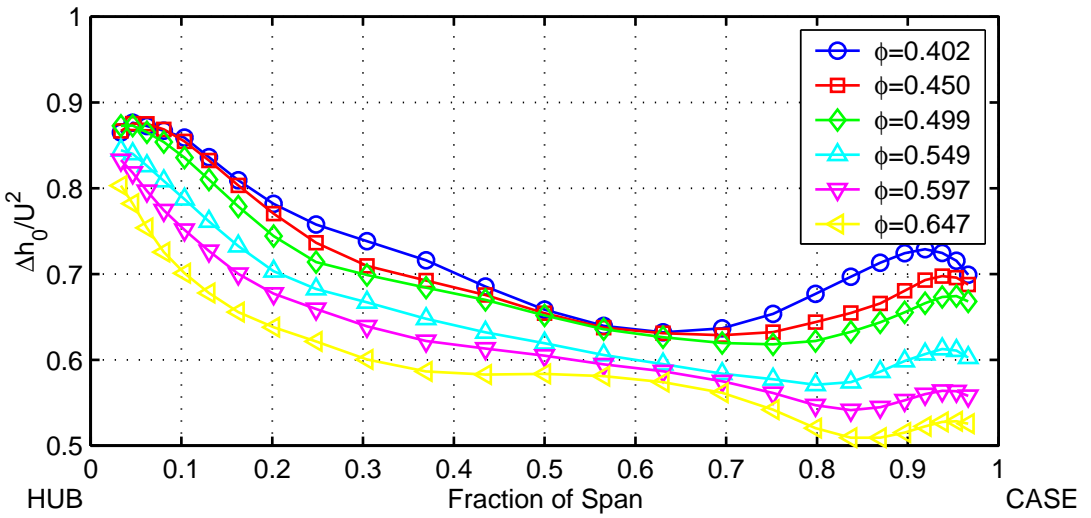


Figure B.13: Span-wise variation in stage loading coefficient ($\frac{\Delta h_0}{U_2^2}$) measured across the **Gallimore** rotor.

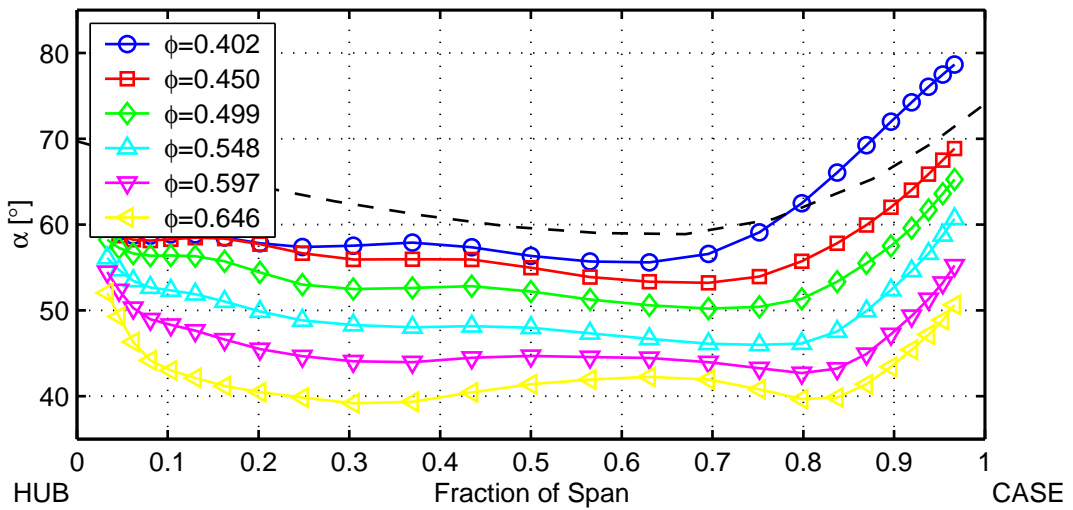


Figure B.14: Radial profiles of flow angle at inlet to the **Gallimore** stator. Dashed line shows metal angle at stator leading edge.

Figure B.15: Radial profiles of (A) axial velocity, (B) stagnation pressure rise and (C) relative flow angle downstream of the **Gallimore** stator. Dashed line shows the metal angle at stator trailing edge.

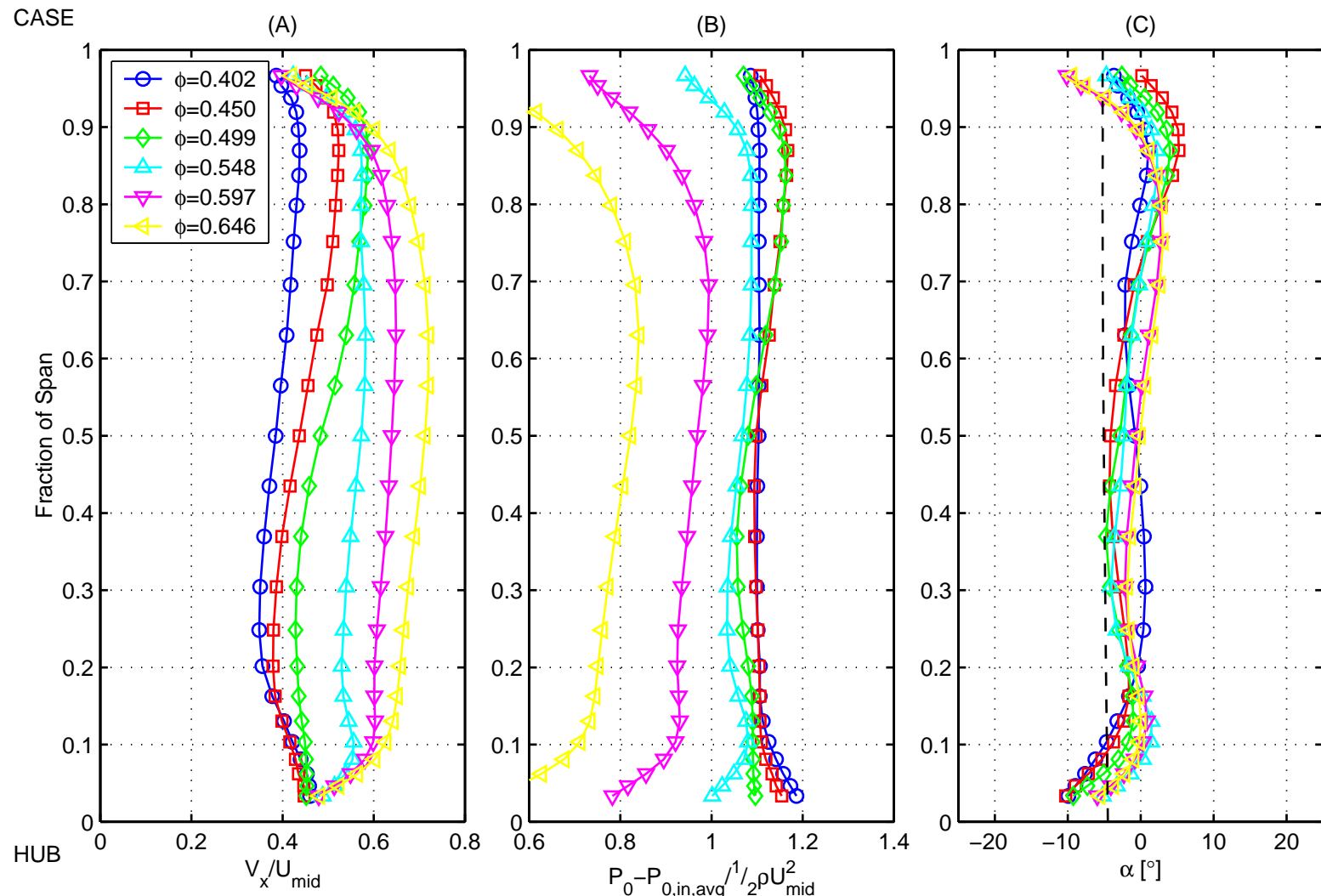


Figure B.16: Gallimore stator performance; Radial profiles of (A) de Haller number, (B) Lieblein diffusion factor and (C) stagnation pressure loss coefficient.

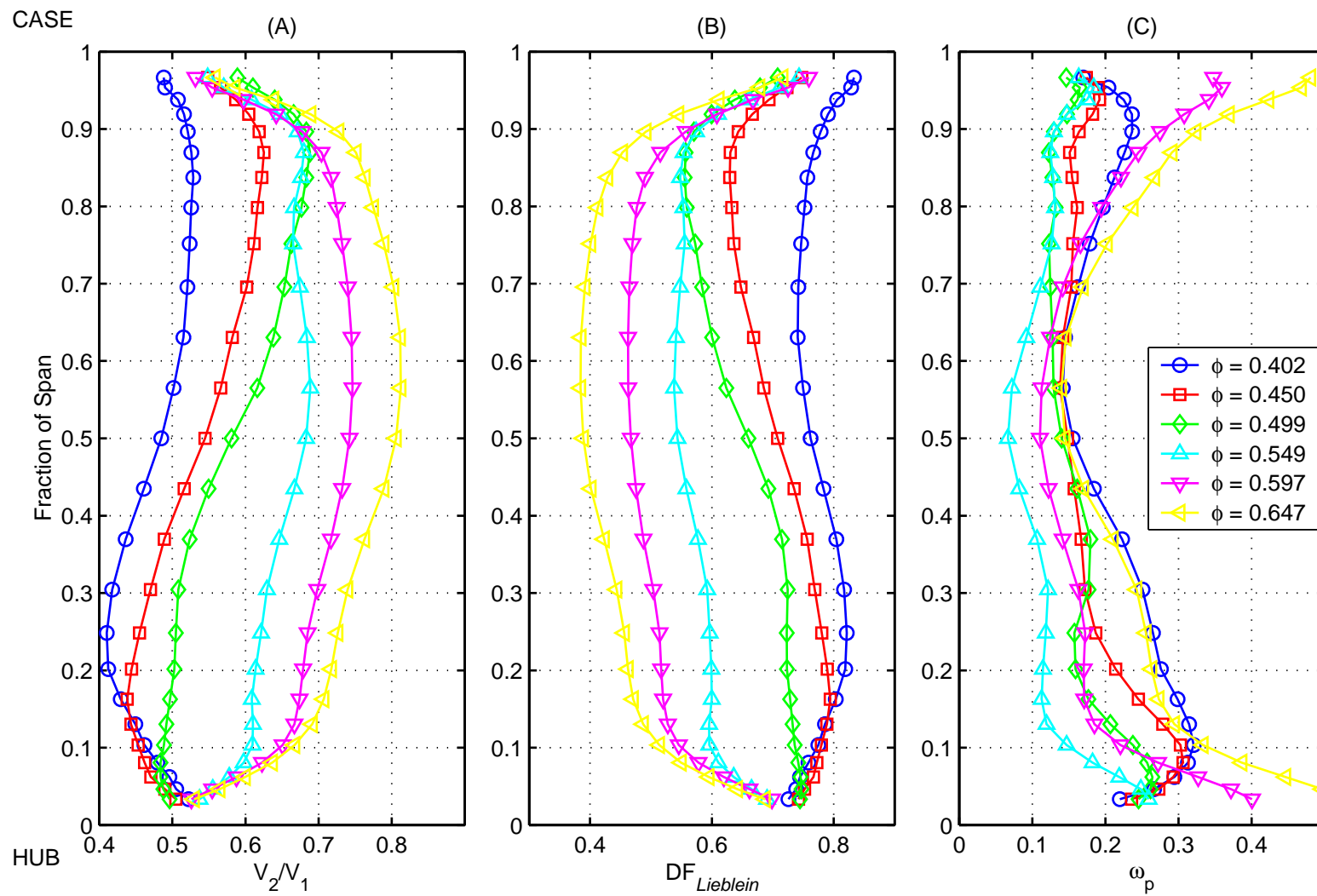
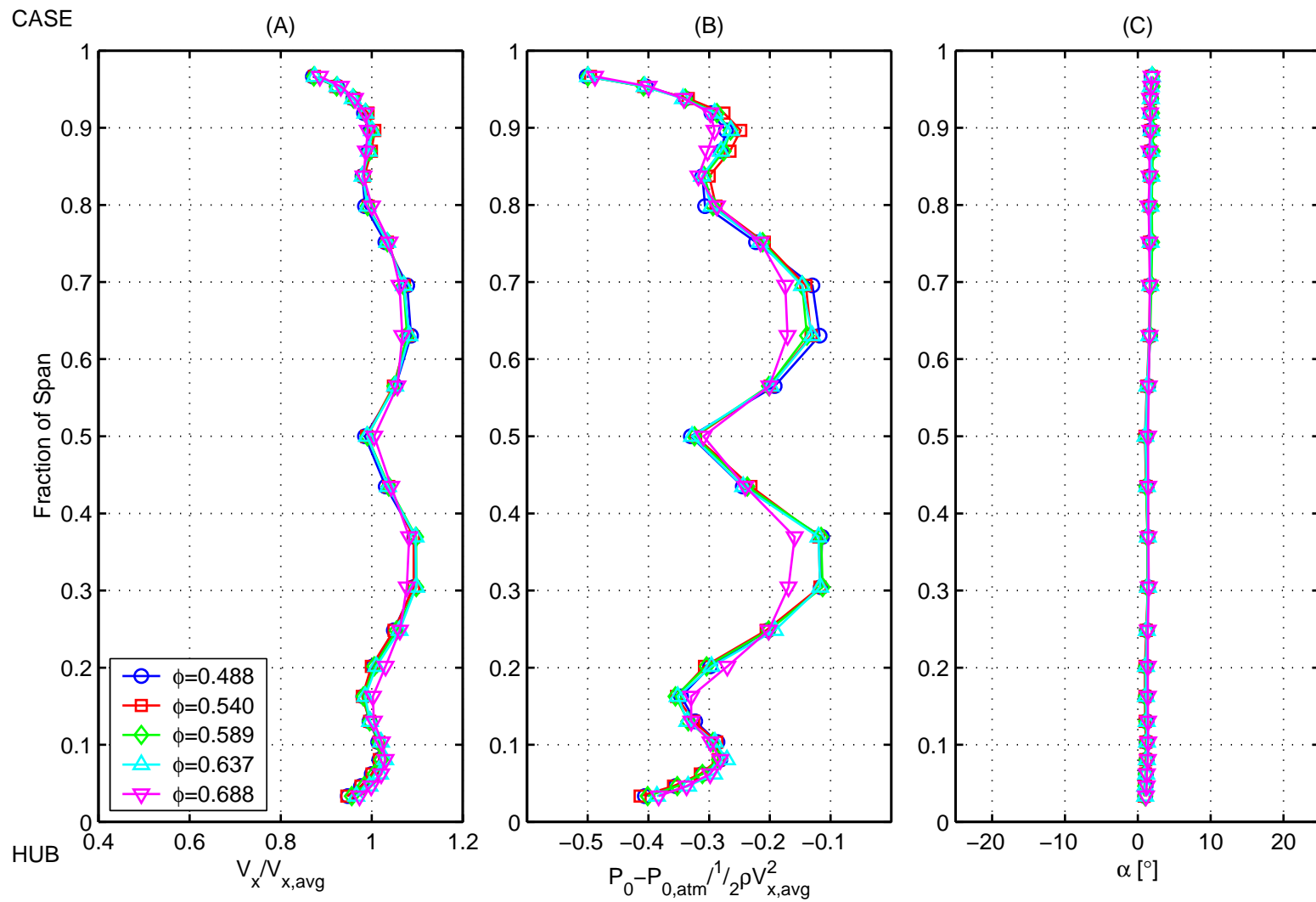


Figure B.17: Inlet conditions to the Qinetiq stage.



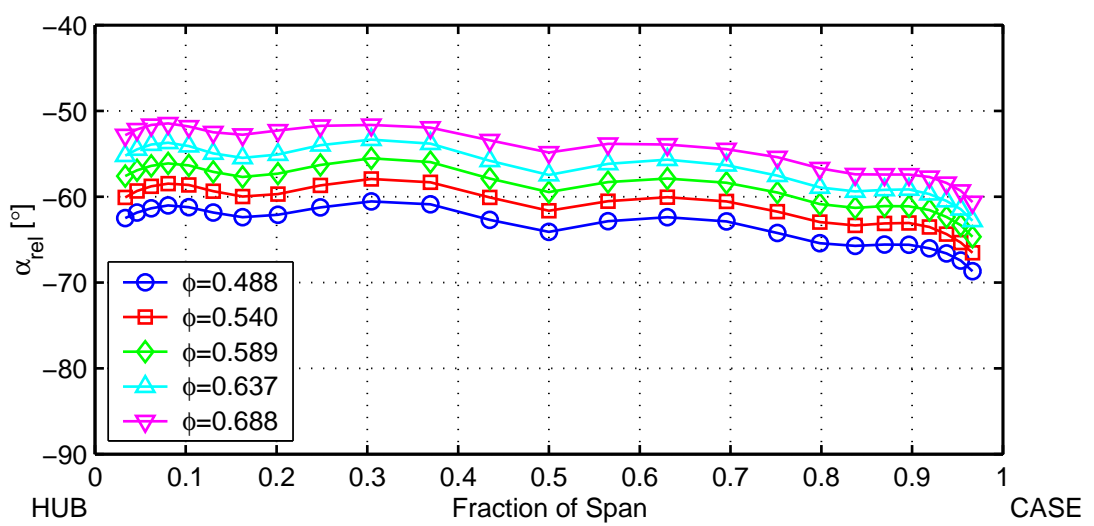


Figure B.18: Radial profiles of flow angle at inlet to the **Qinetiq** rotor.

Figure B.19: Radial profiles of (A) axial velocity, (B) stagnation pressure rise and (C) relative flow angle downstream of the **Qinetiq** rotor.

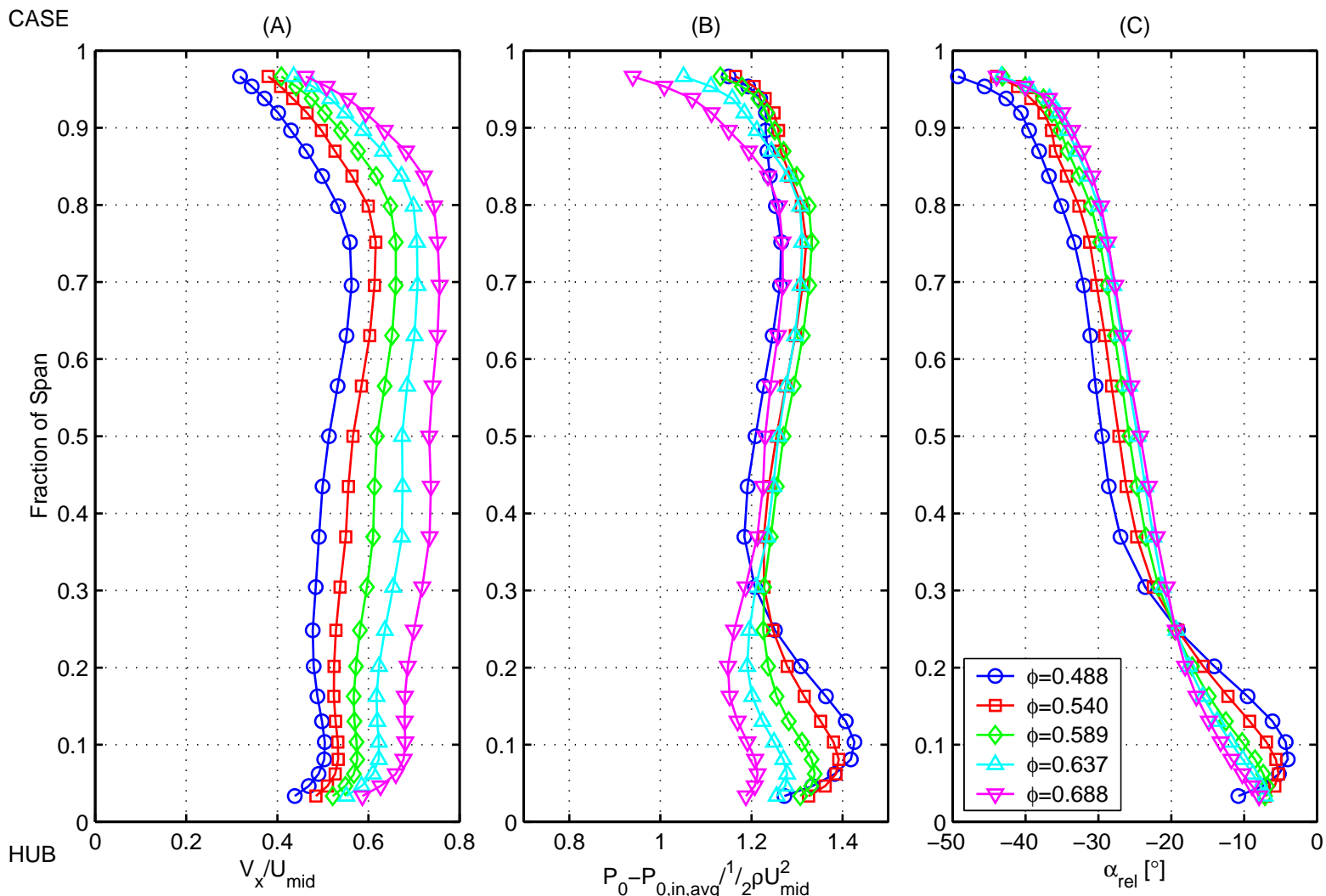
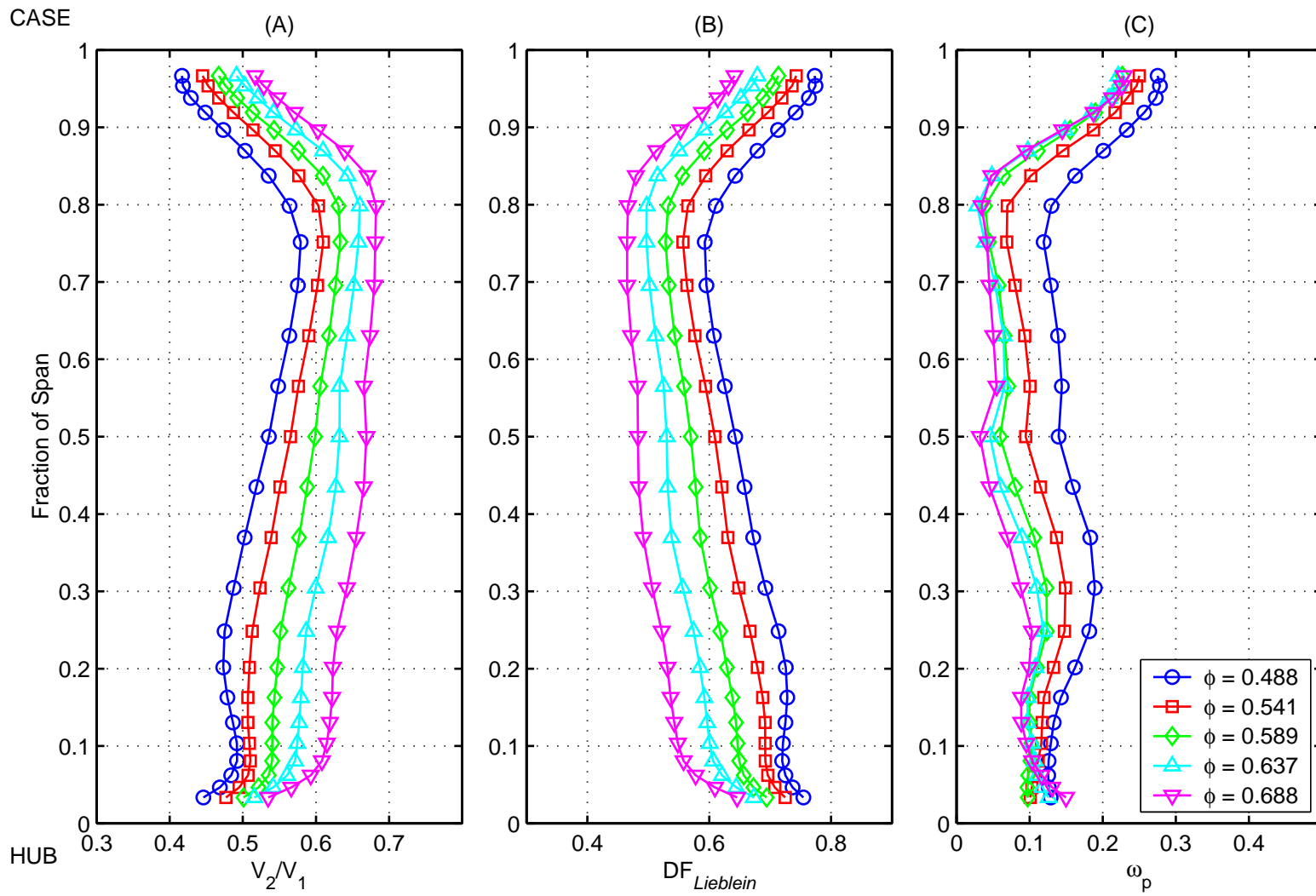


Figure B.20: **Qinetiq** rotor performance; Radial profiles of (A) de Haller number, (B) Lieblein diffusion factor and (C) stagnation pressure loss coefficient.



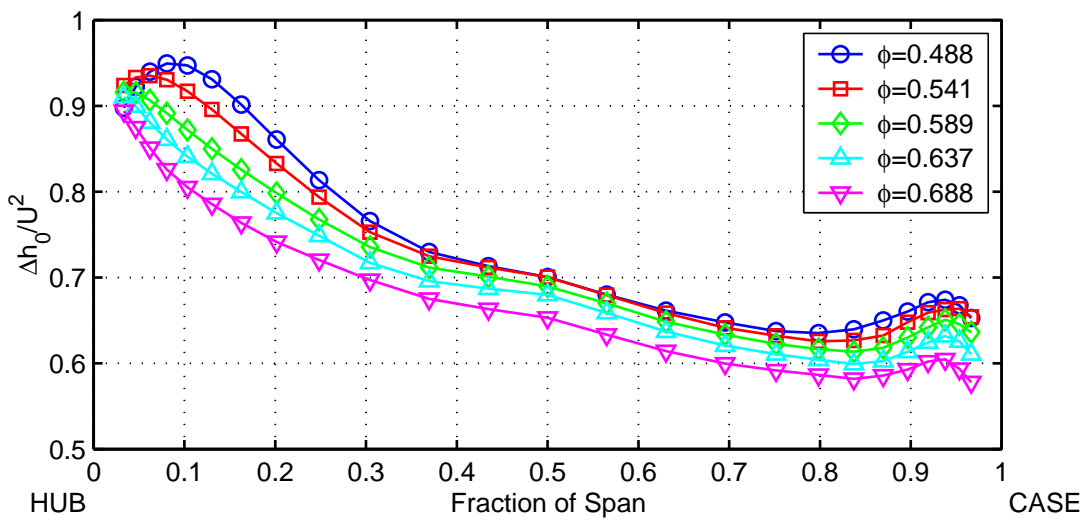


Figure B.21: Span-wise variation in stage loading coefficient ($\frac{\Delta h_0}{U_2^2}$) measured across the **Qinetiq** rotor.

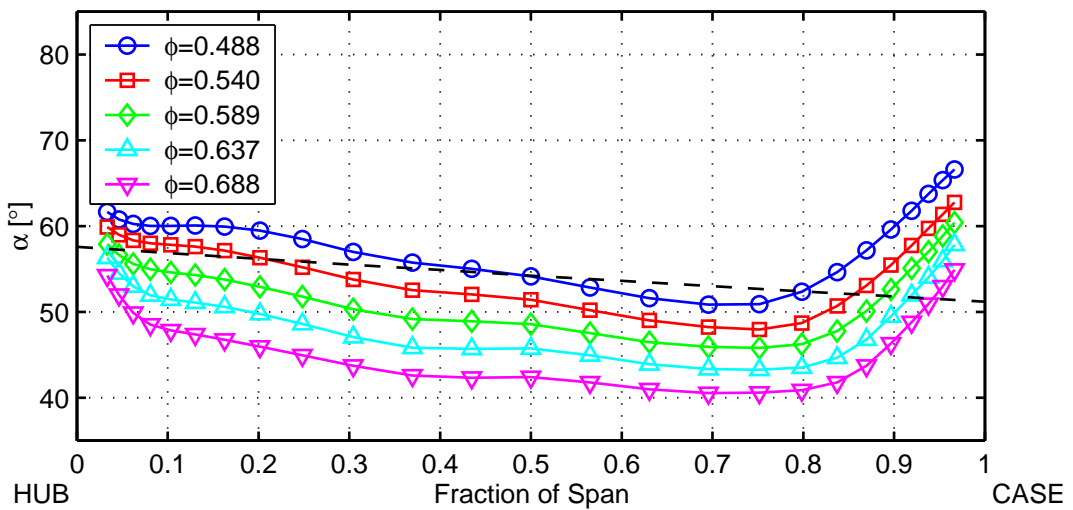


Figure B.22: Radial profiles of flow angle at inlet to the **Qinetiq** stator. Dashed line shows metal angle at stator leading edge.

Figure B.23: Radial profiles of (A) axial velocity, (B) stagnation pressure rise and (C) relative flow angle downstream of the **Qinetiq** stator. Dashed line shows the metal angle at stator trailing edge.

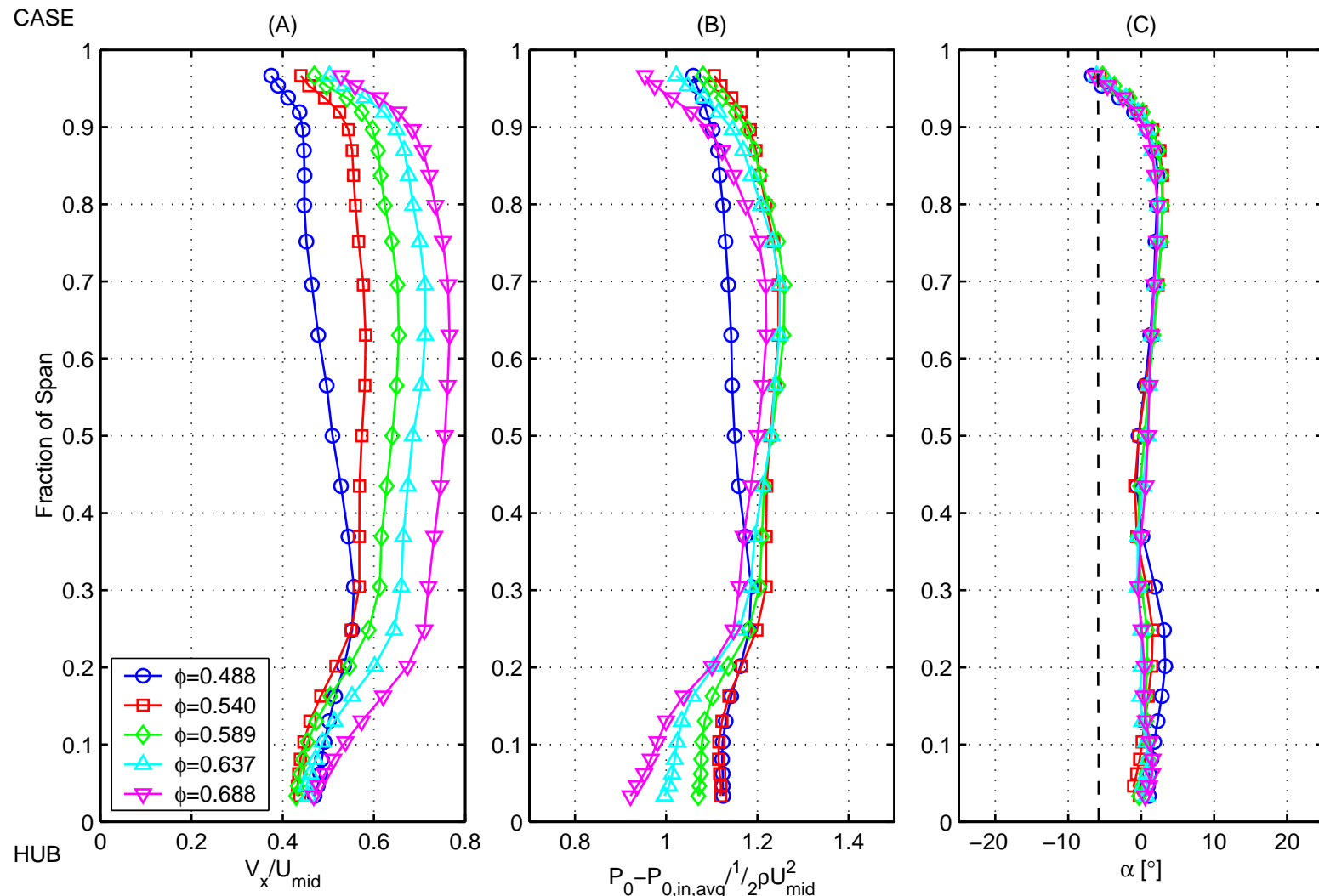


Figure B.24: **Qinetiq** stator performance; Radial profiles of (A) de Haller number, (B) Lieblein diffusion factor and (C) stagnation pressure loss coefficient.

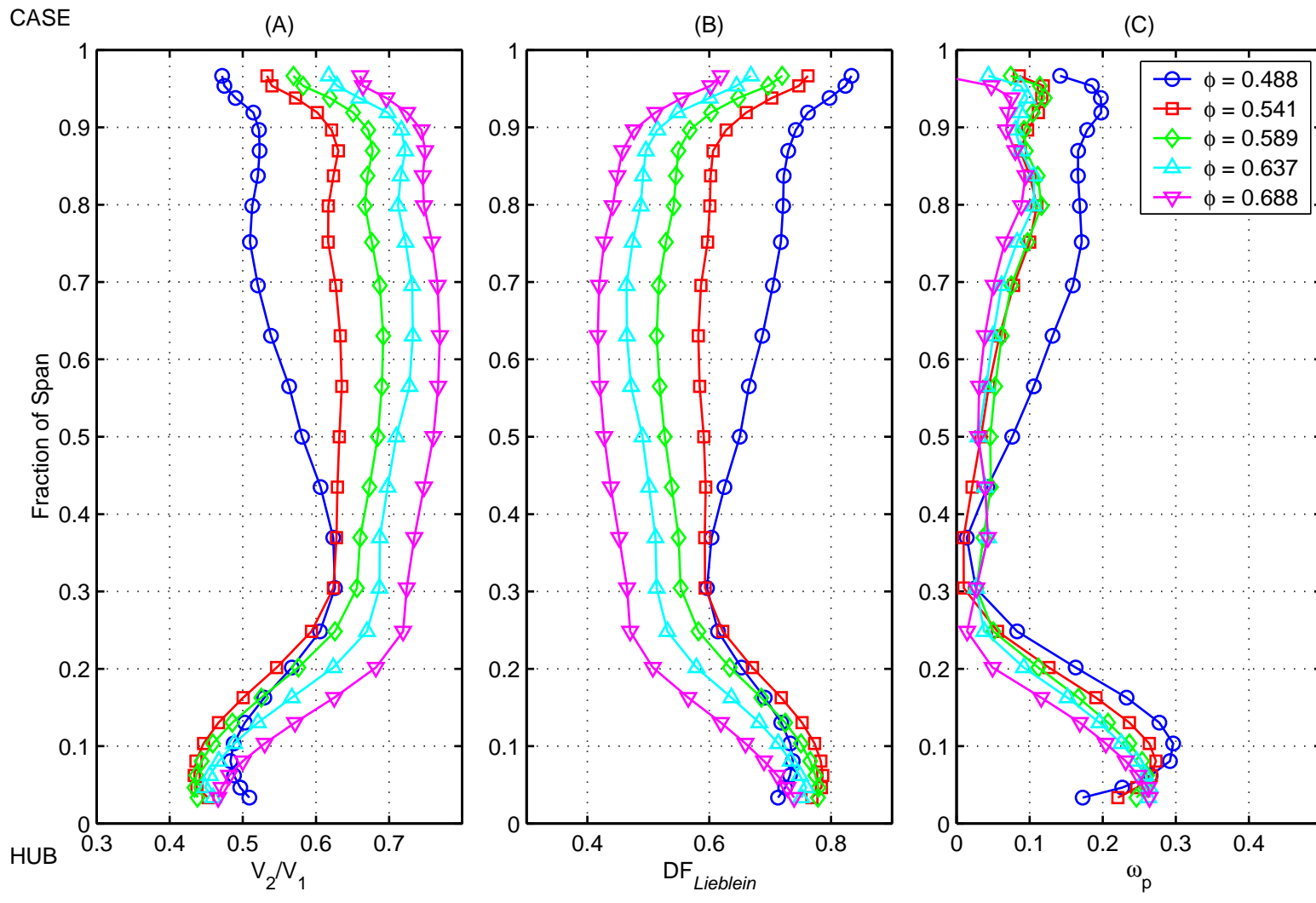
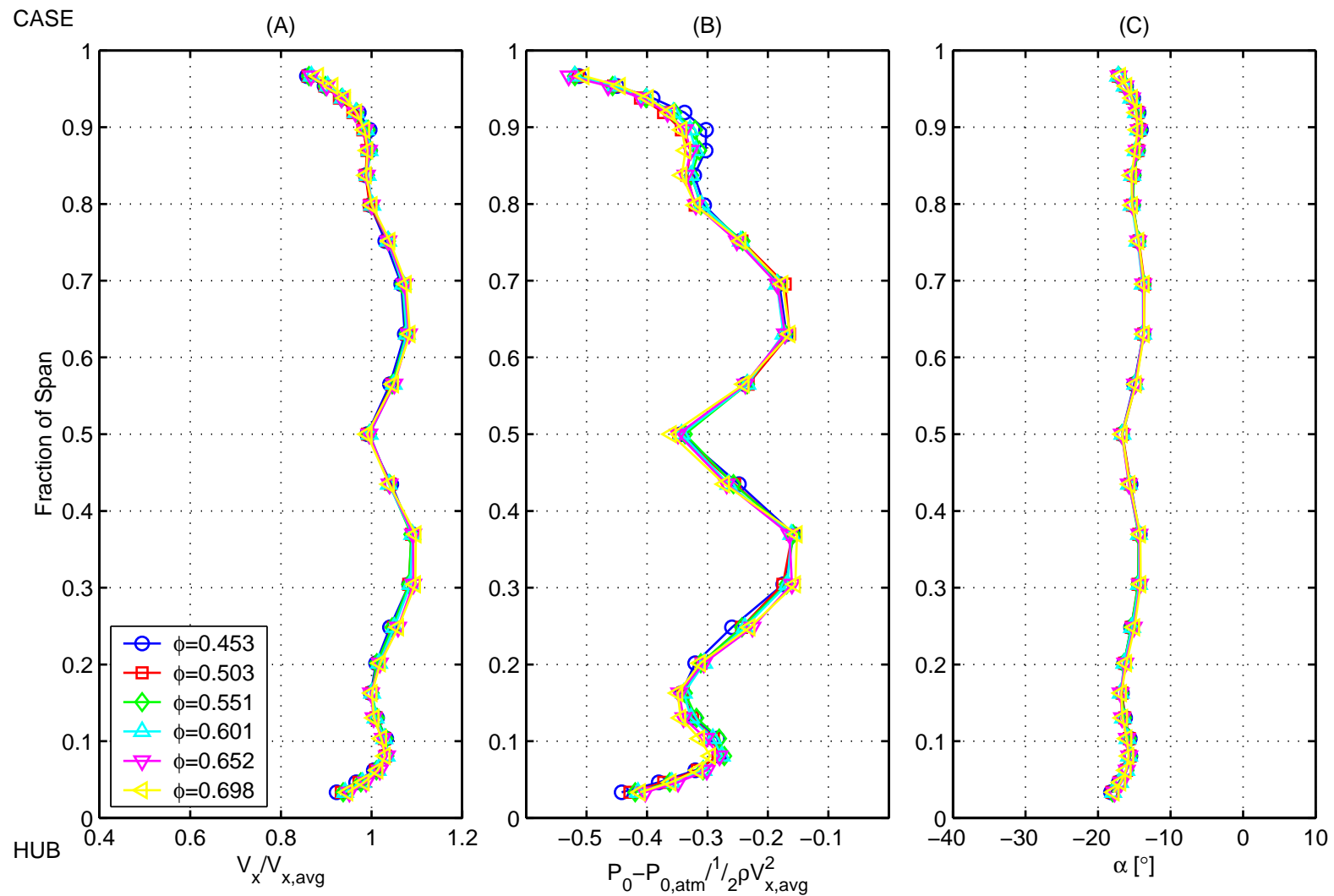


Figure B.25: Inlet conditions to the Denton stage.



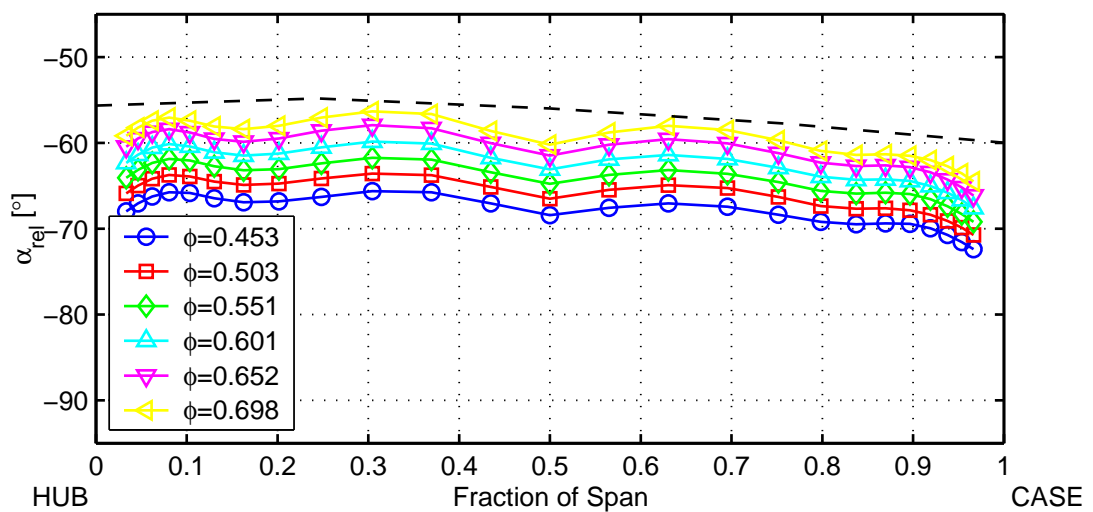


Figure B.26: Radial profiles of flow angle at inlet to the **Denton** rotor. Dashed line shows metal angle at rotor leading edge.

Figure B.27: Radial profiles of (A) axial velocity, (B) stagnation pressure rise and (C) relative flow angle downstream of the **Denton** rotor. Dashed line shows metal angle at rotor trailing edge.

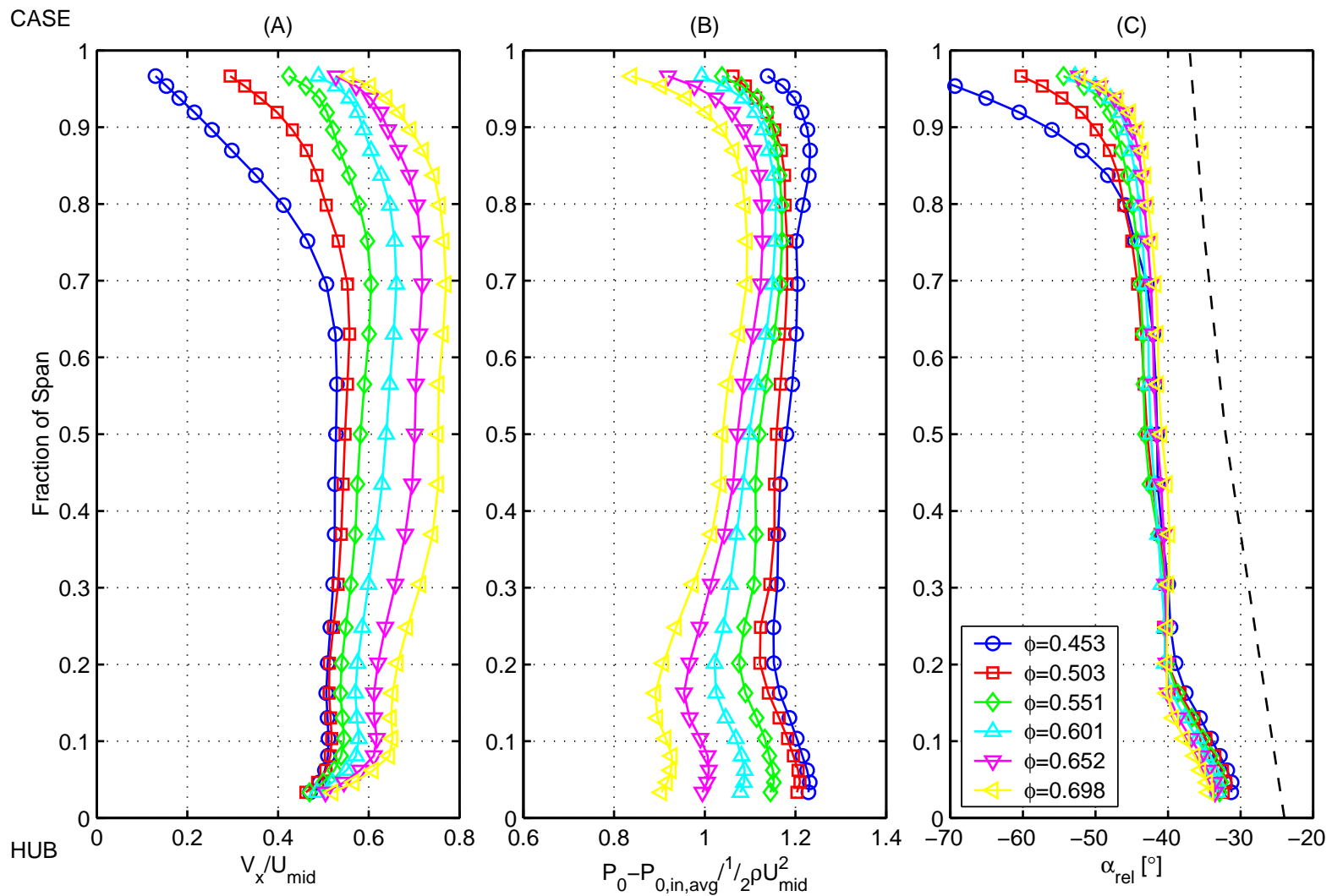
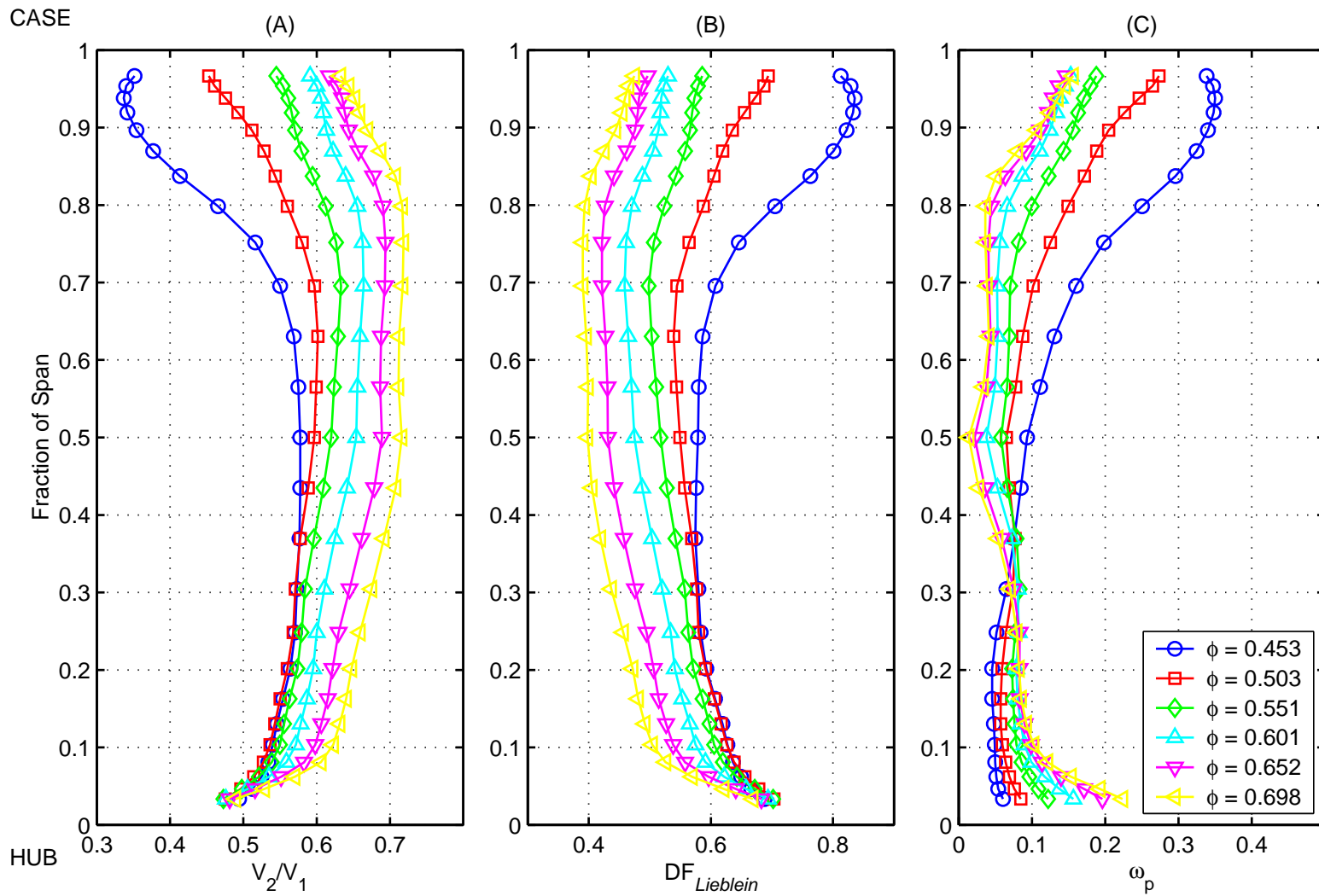


Figure B.28: Denton rotor performance; Radial profiles of (A) de Haller number, (B) Lieblein diffusion factor and (C) stagnation pressure loss coefficient.



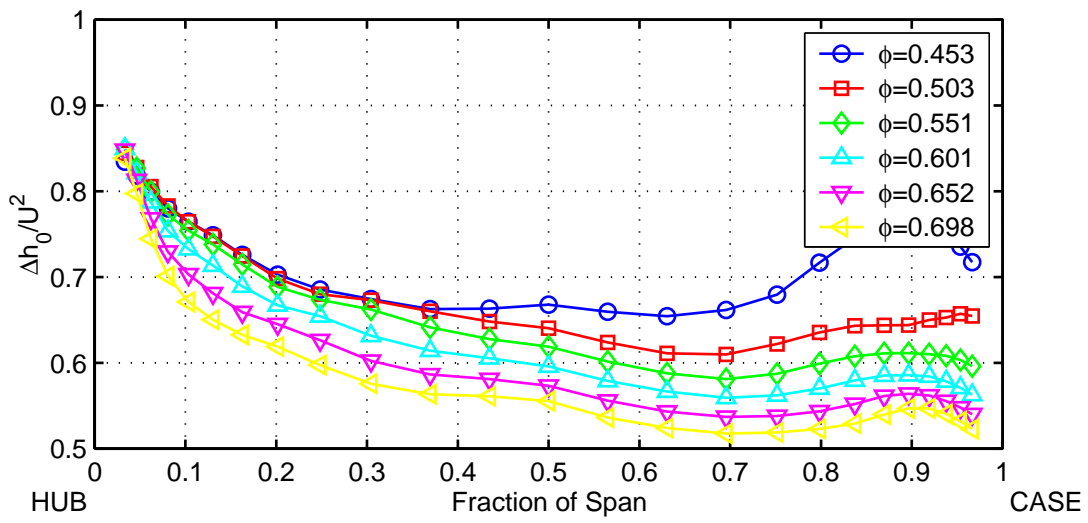


Figure B.29: Span-wise variation in stage loading coefficient ($\frac{\Delta h_0}{U_2^2}$) measured across the **Denton** rotor.

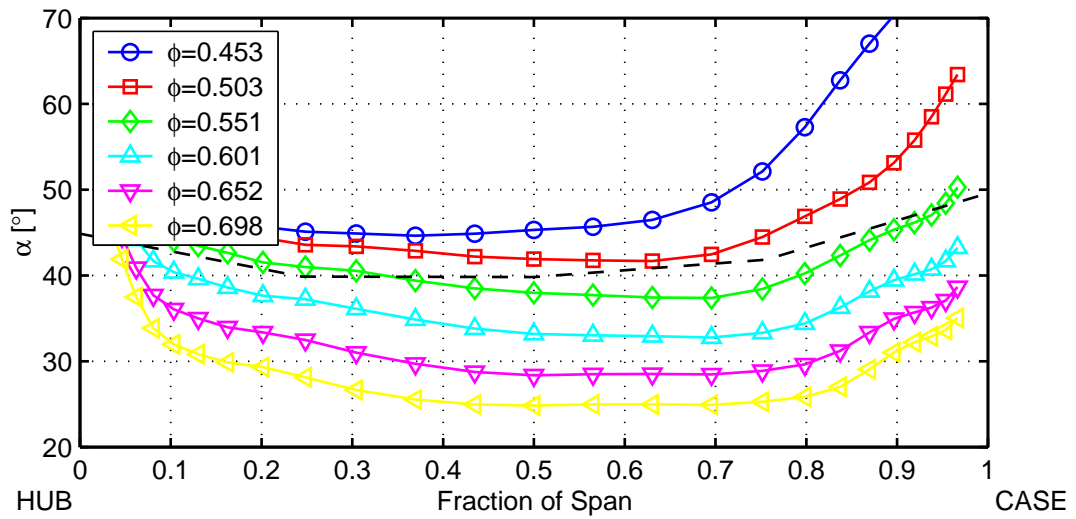


Figure B.30: Radial profiles of flow angle at inlet to the **Denton** stator. Dashed line shows metal angle at stator leading edge.

Figure B.31: Radial profiles of (A) axial velocity, (B) stagnation pressure rise and (C) relative flow angle downstream of the Denton stator. Dashed line shows the metal angle at stator trailing edge.

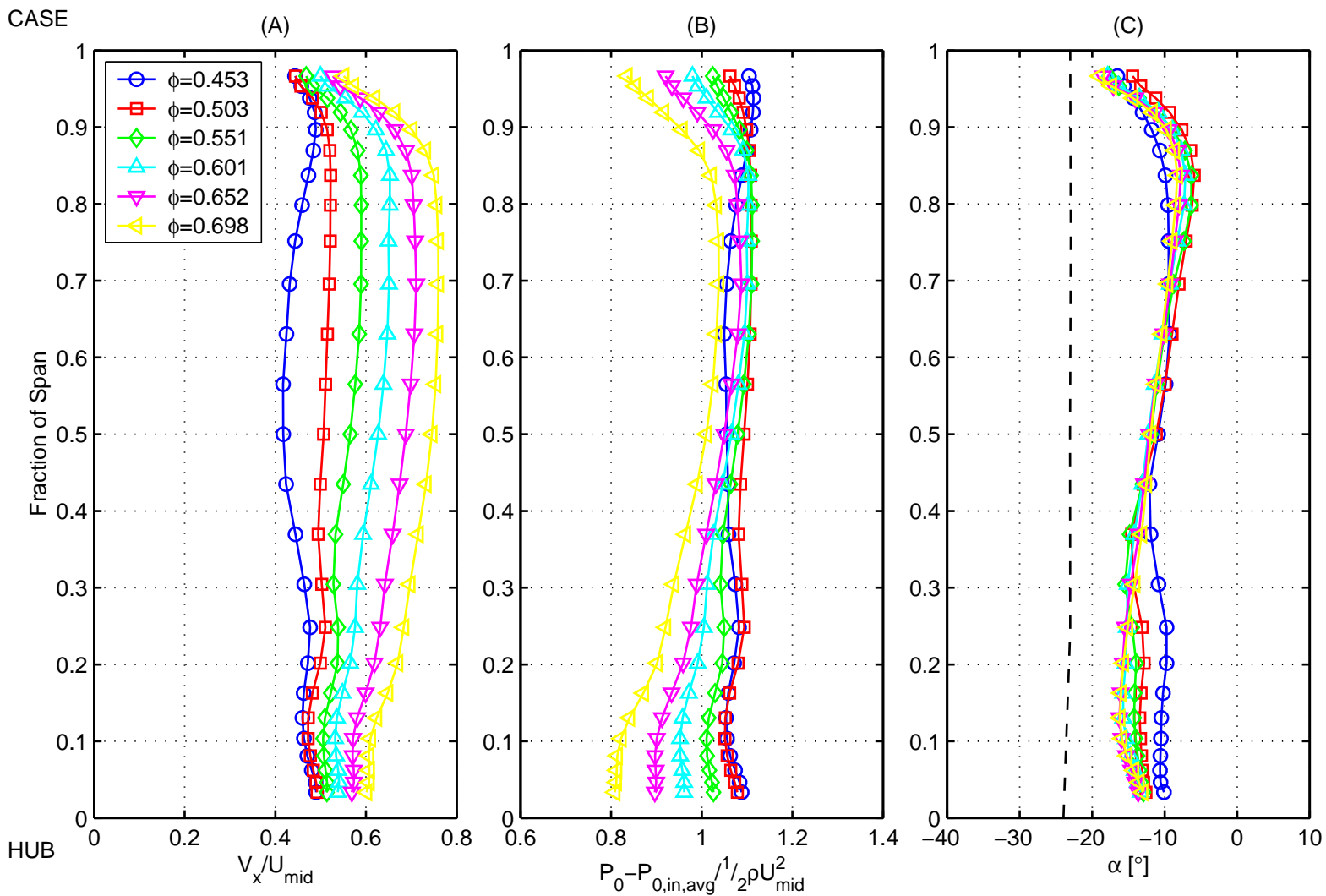


Figure B.32: Denton stator performance; Radial profiles of (A) de Haller number, (B) Lieblein diffusion factor and (C) stagnation pressure loss coefficient.

